VOL.
3
1957

THE PHYSICS AND CHEMISTRY OF SOLIDS

AN INTERNATIONAL JOURNAL

VOLUME 3 1957

Editor-in-Chief HARVEY BROOKS *Cambridge, Mass.*

Associate Editors
H. B. G. CASIMIR, *Eindhoven* · G. J. DIENES, *Brookhaven* · JACQUES FRIEDEL, *Paris*
L. D. LANDAU, *Moscow* · E. M. LIFSHITZ, *Moscow*

Editorial Advisory Board

U.S.A.: L. Apker, Schenectady · J. Bardeen, Illinois · D. S. Billington, Oak Ridge · Leo Brewer, Berkeley, Calif. · N. Cabrera, Virginia · I. Estermann, Washington, D.C. · J. C. Fisher, Schenectady · Conyers Herring, New Jersey · A. R. von Hippel, Cambridge, Mass. · J. H. Hollomon, Schenectady · W. V. Houston, Houston · H. B. Huntington, Troy · John G. Kirkwood, Yale · K. Lark-Horowitz, Purdue · A. W. Lawson, Chicago · B. T. Matthias, New Jersey · Joseph E. Mayer, Chicago · David Pines, Princeton R. Smoluchowski, Pittsburgh · D. Turnbull, Schenectady · J. H. Van Vleck, Harvard · B. E. Warren, Cambridge, Mass. · Eugene P. Wigner, Princeton · B. H. Zimm, Schenectady.

United Kingdom: M. Born, Edinburgh · A. Charlesby, Shrivenham, Berks · W. J. Dunning and F. C. Frank, Bristol · H. K. Henisch, Reading · H. Jones, London · J. W. Mitchell, Bristol · A. B. Pippard, Cambridge M. H. L. Pryce, Bristol · F. C. Tompkins, London.

France: E. F. Bertaut, Grenoble · A. Guinier, Paris · Louis Néel and Louis Weil, Grenoble.

Germany: Ulrich Dehlinger, Stuttgart · R. Hilsch and G. Leibfried, Göttingen · E. Mollwo, Erlangen H. Pick, Stuttgart · M. von Laue, Berlin · H. Welker, Erlangen.

Italy: F. G. Fumi, Palermo.

Japan: Toshinosuke Muto, Tokyo.

The Netherlands: A. Michels and G. W. Rathenau, Amsterdam. *Sweden:* J. O. Linde, Stockholm · Per-Olov Löwdin, Uppsala.

Switzerland: G. Busch and P. Scherrer, Zürich. *U.S.S.R.:* G. S. Zhdanov, Moscow.

PERGAMON PRESS NEW YORK · LONDON · PARIS · LOS ANGELES

NOTES FOR CONTRIBUTORS

I. GENERAL

1. Submission of a paper to the *Journal of the Physics and Chemistry of Solids* will be taken to imply that it represents original research not previously published (except in the form of an abstract or preliminary report), that it is not being considered for publication elsewhere, and that if accepted, it will not be published elsewhere in the same form, in any language, without the consent of the editor-in-chief. It should deal with original research work in the field of the physics and chemistry of solids.

2. Papers should be submitted to the appropriate regional editor (all English-language papers to be sent to the U.S. editor).

3. Papers will be published as quickly as possible after acceptance, and, subject to space being available, should appear in the following issue, if this is due for publication not earlier than three months after the acceptance date. Short communications under the heading of "Letters to the Editors" will receive priority for publication, and will be published in the issue following receipt, if accepted not later than the beginning of the month preceding publication.

4. Fifty free reprints of each paper are supplied. Additional copies can be obtained at a reasonable cost if ordered when proofs are returned. A reprint order form will accompany first proofs.

II. SCRIPT REQUIREMENTS

1. Papers submitted should be concise and written in a readily understandable style. Scripts should be typed and double spaced and submitted in duplicate to facilitate refereeing.

It will be appreciated if authors clearly indicate any special characters used. An abstract, not exceeding 200 words, should be provided in the language of the paper. French and German papers should be submitted with English abstract and titles, but if this is not possible the abstract will be translated by the publishers. To conserve space, authors are requested to mark less important parts of the paper, such as details of experimental technique, methods, mathematical derivations, etc. for printing in small type. The technical description of methods should be given in detail only when such methods are new. Authors will receive proofs for correction when their papers are first set; page proofs will be sent only when the amount of alteration makes it advisable.

2. Illustrations should not be included in the typescript of the paper, and legends should be typed on a separate sheet. Line drawings which require redrawing should include all relevant details and clear instructions for the draughtsman. If figures are already well drawn it may be possible to reproduce them direct from the originals, or from good photo-prints if these can be provided. It is not possible to reproduce from prints with weak lines. Illustrations for reproduction should normally be about twice the final size required. Photographs should only be included where they are essential.

Tables and figures should be so constructed as to be intelligible without reference to the text. Every table and column should be provided with an explanatory heading. Units of measure must always be clearly indicated. The same data should not be published in both tables and figures. The following standard symbols should be used on line drawings since they are easily available to the printers: ○, ●, +, ×, □, ■, △, ▲, ◇, ◆, ▽, ▼.

4. References are indicated in the text by superior numbers in parentheses, and the full reference should be given in a list at the end of the paper in the following form:

1. HILL R. *J. Iron St. Inst.* **158,** 177 (1948).
2. PEARSON C. *The Extrusion of Metals.* Chapman and Hall, London (1944).

Abbreviations of journal titles should follow those given for *Physics Abstracts.* It is particularly requested that authors' initials, and appropriate volume and page numbers, should be given in every case.

Footnotes, as distinct from literature references should be indicated by the following symbols—*, †, ‡, ‡‡, commencing anew on each page; they should *not* be included in the numbered reference system.

5. Due to the international character of the journal no rigid rules concerning notation and spelling will be observed, but each paper should be consistent within itself as to symbols and units.

VOL
3
195

VOL.
3
1957

VOL
3
195

CONTENTS

NUMBERS 1/2

E. A. TAFT and H. R. PHILIPP: Photoelectric emission from the valence band of some alkali halides 1

JEAN-FRANÇOIS LAURENT ET JACQUES BÉNARD: Autodiffusion des ions dans les cristaux uniques des halogénures de potassium et des chlorures alcalins 7

J. D. DUNITZ and L. E. ORGEL: Electronic properties of transition-metal oxides—I. Distortions from cubic symmetry 20

S. GELLER and M. A. GILLEO: The crystal structure and ferrimagnetism of yttrium-iron garnet, $Y_3Fe_2(FeO_4)_3$ 30

M. H. FRANCOMBE: Lattice changes in spinel-type iron chromites 37

EDGAR F. WESTRUM, JR. and D. M. GRIMES: Low temperature heat capacity and thermodynamic properties of zinc ferrite 44

L. E. ORGEL: The crystal structures of manganese and the actinide elements 50

S. TRIEBWASSER: Free energy, internal fields and ionic polarizabilities in $BaTiO_3$ . . . 53

R. N. HALL: Variation of the distribution coefficient and solid solubility with temperature . . 63

E. M. PELL: Solubility of lithium in germanium 74

E. M. PELL: Solubility of lithium in silicon 77

C. J. GALLAGHER: Electrolysis of copper in solid silicon 82

J. J. LANDER: Concentration of hydrogen and semi-conductivity in ZnO under hydrogen-ion bombardment 87

P. KISLIUK: The sticking probabilities of gases chemisorbed on the surfaces of solids . . . 95

ROBERT W. KEYES: Elastoresistance effects in a germanium–silicon alloy 102

F. G. ALLEN and A. B. FOWLER: Variation of contact potential with crystal face for germanium . 107

HENRY J. BOWLDEN: Detailed balance in non-vertical transitions 115

WALTER BALTENSPERGER: Correlations between thermal voltage fluctuations in a circuit . . 118

GEORGE H. VINEYARD: Frequency factors and isotope effects in solid state rate processes . . 121

J. E. AUBREY and R. G. CHAMBERS: Cyclotron resonance in bismuth 128

I. T. STEINBERGER, E. A. BRAUN and E. ALEXANDER: Gudden-Pohl and memory effects in an infra-red stimulated phosphor 133

D. M. GRIMES: Reversible properties of polycrystalline ferromagnets—I. Theory of the expected variation of the reversible properties with magnetization 141

Letters to the Editors:

F. MOSER, N. R. NAIL and F. URBACH: Note on the darkening of silver chloride . . . 153

A. W. LAWSON: On the high temperature heat conductivity of insulators 155

W. P. DOYLE: The absorption spectrum of solid antimony trisulphide 156

J. H. WERNICK and K. E. BENSON: New semiconducting ternary compounds . . . 157

SIMON LARACH and ROSS E. SHRADER: Chemical evidence for a barrier in electro-luminescent zinc sulfide phosphors 159

Book Review:

"Small-Angle Scattering of X-rays", by A. GUINIER and G. FOURNET (reviewed by A. R. LANG) . 161

Contents Lists of Volume 2, Nos. 1 and 2 162

VOL. 3 1957

NUMBERS 3/4

E. A. LYNTON, B. SERIN and M. ZUCKER: The superconductive critical temperature and the electronic specific heat of impure tin 165

A. B. PIPPARD: The effect of alloying on the superconducting transition temperature of tin . . 175

THEODORE G. CASTNER and WERNER KÄNZIG: The electronic structure of V-centers 178

F. J. MORIN and HOWARD REISS: Precipitation of lithium in germanium 196

GEORGE L. HALL: Distortion around point imperfections in simple crystals 210

ROY F. POTTER: The ionic character and elastic moduli of zinc blende lattices 223

D. G. THOMAS: Interstitial zinc in zinc oxide 229

F. K. LOTGERING and E. W. GORTER: Solid solutions between ferromagnetic and antiferromagnetic compounds with NiAs structure 238

A. W. LAWSON: Correlation of ΔS and ΔV in simple activated processes in solids 250

R. R. HAERING and P. R. WALLACE: The electric and magnetic properties of graphite . . . 253

A. M. GAROFALO and J. S. PLASKETT: Interaction energy of point imperfections in metals due to the free electrons 275

D. H. TOMBOULIAN, D. E. BEDO and W. M. NEUPERT: $M_{2,3}$ absorption spectra of the elemental solids Cr through Ge 282

J. E. WORSHAM, JR., M. K. WILKINSON and C. G. SHULL: Neutron-diffraction observations on the palladium hydrogen and palladium deuterium systems 303

DONALD S. MCCLURE: The distribution of transition metal cations in spinels 311

J. D. DUNITZ and L. E. ORGEL: Electronic properties of transition-metal oxides—II. Cation distribution amongst octahedral and tetrahedral sites 318

R. W. SCHMITT and I. S. JACOBS: Low temperature, electrical and magnetic behavior of dilute alloys of Mn in Cu 324

Book Review:

"Physical Properties of Crystals: Their Representation by Tensors and Matrices" by J. F. NYE (reviewed by W. L. BOND) 338

Papers to be published in future issues 339

AUTHOR INDEX TO VOLUME 3

(B) denotes a book review

ALEXANDER, E. 133
ALLEN, F. G. 107
AUBREY, J. E. 128
BALTENSPERGER, WALTER 118
BEDO, D. E. 282
BÉNARD, JACQUES 7
BENSON, K. E. 157
BOND, W. L. 338 (B)
BOWLDEN, HENRY J. 115
BRAUN, E. A. 133
CASTNER, THEODORE G. 178
CHAMBERS, R. G. 128
DOYLE, W. P. 156
DUNITZ, J. D. 20, 318
FOWLER, A. B. 107
FRANCOMBE, M. H. 37
GALLAGHER, C. J. 82
GAROFALO, A. M. 275
GELLER, S. 30
GILLEO, M. A. 30
GORTER, E. W. 238
GRIMES, D. M. 44, 141
HAERING, R. R. 253
HALL, GEORGE L. 210
HALL, R. N. 63
JACOBS, I. S. 324
KÄNZIG, WERNER 178
KEYES, R. W. 102
KISLIUK, P. 95
LANDER, J. J. 87
LANG, A. R. 161 (B)
LARACH, SIMON 159
LAURENT JEAN-FRANÇOIS 7
LAWSON, A. W. 155, 250
LOTGERING, F. K. 238
LYNTON, E. A. 165
MCCLURE, DONALD S. 311
MORIN, F. J. 196
MOSER, F. 153
NAIL, N. R. 153
NEUPERT, W. M. 282
ORGEL, L. E. 20, 50, 318
PELL, E. M. 74, 77
PHILIPP, H. R. 1
PIPPARD, A. B. 175
PLASKETT, J. S. 275
POTTER, ROY F. 223
REISS, HOWARD 196
SCHMITT, R. W. 324
SERIN, B. 165
SHRADER, ROSS E. 159
SHULL, C. G. 303
STEINBERGER, I. T. 133
TAFT, E. A. 1
THOMAS, D. G. 229
TOMBOULIAN, D. H. 282
TRIEBWASSER, S. 53
URBACH, F. 153
VINEYARD, GEORGE H. 121
WALLACE, P. R. 253
WERNICK, J. H. 157
WESTRUM, EDGAR F. 44
WILKINSON, M. K. 303
WORSHAM, J. E., JR. 303
ZUCKER, M. 165

VOL.
3
1957

VOL
3
195

J. Phys. Chem. Solids Pergamon Press 1957. Vol. 3. pp. 1–6.

PHOTOELECTRIC EMISSION FROM THE VALENCE BAND OF SOME ALKALI HALIDES

E. A. TAFT and H. R. PHILIPP

General Electric Research Laboratory, Schenectady, New York

(*Received* 26 *April* 1957)

VOL. 3 1957

Abstract—Photoelectric emission from the valence band, previously measured for CsI, has been investigated in the other alkali iodides and several other halides. As in CsI, the yields rise rapidly from the threshold to values of order 0·1 electron/incident photon. For the iodides, concurrent measurements of reflectivity and optical absorption agree with MARTIENSSEN's recent results and show detail consistent with interband transitions. Approximate values for the energy difference between the bottom of the conduction band and the vacuum level are deduced.

INTRODUCTION

IN AN earlier paper,[1] we described the photoemission from CsI. Large yields, observed for $h\nu > 6$ eV, were independent of defects in the samples and were attributed to emission from the va ence band. Concurrent optical absorption data showed a comparatively small edge consistent with band-to-band transitions if the electron affinity of CsI was estimated to be small (i.e., if the bottom of the conduction band lay only slightly below the vacuum level). This paper reports similar data on the other alkali iodides in which the electron affinity is larger, of order 1 eV.

MARTIENSSEN[2] has recently made an elegant and extensive investigation of the optical absorption of the alkali iodides. At 20°K, the absorption edge for CsI shows up more clearly than in reference 1. Furthermore, it appears to be double in structure with components at $h\nu = 6{\cdot}24$ and 6·31 eV. (In addition, the second absorption peak near 6 eV is also doubled.) In this paper, we continue to relate this double edge in CsI to band-to-band transitions and treat it as analogous to the very clear single edges found by MARTIENSSEN[2] at roughly the same photon energy for iodides of Rb, K, and Na.[3]

Along with our photoelectric data on the iodides we present optical absorption and reflectance data taken at 300°K and at 80°K. They are point-by-point measurements and are not as detailed as MARTIENSSEN's recording-spectrophotometer results on absorption at 20°K. Within this limitation, however, they corroborate his findings. The reflectance results are useful for comparing evaporated films with single crystals. Except for interference effects in the films (see Fig. 4), results for the two kinds of surfaces were identical. To facilitate discussion of trends in the electronic energy structures, tentative new data for LiI are included.[4] For purposes of comparison, intrinsic photoemission data are also presented for all the potassium halides and for those cesium salts having the CsCl structure.

EXPERIMENTAL

Vacuum tubes of three different designs were employed. (1) Cylindrical diodes, fitted with cleaved LiF windows,* were used to determine the spectral distribution of photoelectric yield at 300°K. Emission measurements were made on evaporated films with the spectral range extended to greater than 11 eV with the aid of a vacuum monochromator[5] kindly placed at our disposal by P. D.

* Windows, cleaved from single crystals obtained from the Harshaw Chemical Company, were sealed to a $\frac{5}{8}$ in. diameter extension from the tube envelope with Dennison's red sealing wax. Bake temperatures were limited but system pressures of 10^{-7} mm Hg were readily obtainable. Tubes with quartz bubble windows showed the same behavior to 8 eV. The alkali halides do not seem to be very sensitive to vacuum conditions, but we must avoid any claim that these surfaces, although reproducible, were atomically clean.

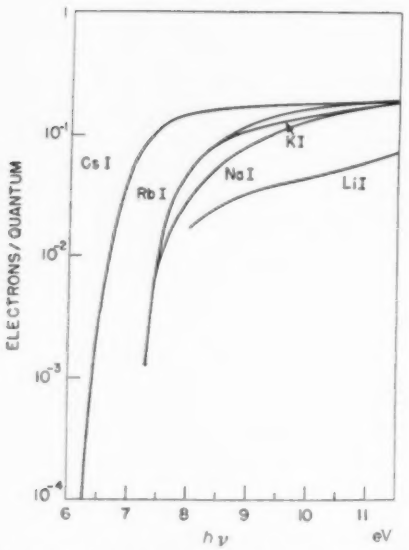

FIG. 1. Spectral distribution of the photoelectric yield for the alkali iodides.

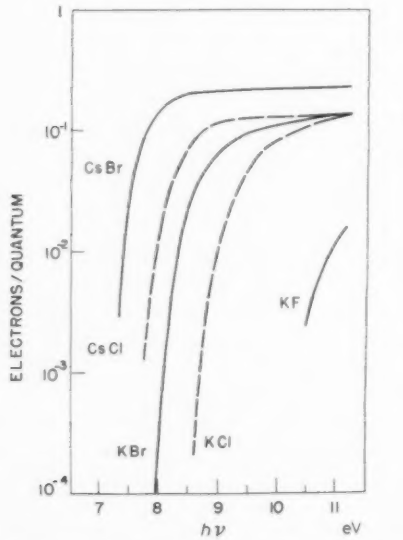

FIG. 2. Spectral distribution of the photoelectric yield for the potassium halides and for several cesium salts.

JOHNSON. (2) A double window tube, described in a previous paper,[1] provided data on the optical absorption of thin films in the temperature range 80 to 500°K. (3) Tubes used to measure reflectance over the temperature range 80 to 500°K held single crystals or evaporated films (on Al_2O_3 crystals) in vacuum behind fused-quartz windows, through which measurements were made.

RESULTS

Spectral distribution of the photoelectric yield

The spectral distribution of the photoelectric yield for the alkali iodides is shown in Fig. 1. For comparison purposes, data on other halide samples are shown in Fig. 2. The curves are all similar in shape. There is an initial rapid increase in yield which levels off at values near 0·1.*† This emission is an intrinsic property of the emitter, independent of crystal impurities and imperfections, and is attributed here to electrons ejected from the valence band. The threshold for this high-yield process is a measure of the energy difference between the top of the valence band and the vacuum level. The shift in the threshold for corresponding potassium and cesium halides is slightly less than 1 eV and will be referred to in a later discussion of the electron affinity.

When *F*-centers are deliberately added to these salts by irradiation in the first fundamental absorption band, a measurable yield appears at lower quantum energy.[6] For completeness, the yield for a KI sample containing about 10^{19} *F*-centers cm^{-3} is shown in Fig. 3. Assuming that each incident photon produces one excited electron, the plateau value for the valence band yield indicates that the excited electrons have roughly a 10 per cent chance of appearing outside the surface. If one assumes the same escape probability for the exciton-induced yield, 2×10^{-3} at the first absorption peak, one concludes that the efficiency of energy transfer to *F*-centers is low in these KI samples, of order 0·02. The energy distribution of the exciton-induced

* Emission from the valence band of LiI appears to be roughly coincident with that from the iodides of Rb, K and Na at yields below 10^{-2}; the threshold may be slightly lower. Processes involving *F*-centers or other defects sometimes complicate the measurements below $h\nu = 7{\cdot}5$ eV. For KF the currents are small and the results of Fig. 2 are only qualitative.

† Spectral distribution data on single crystals of both NaCl and KCl have been obtained at Cornell University by J. W. TAYLOR and P. L. HARTMAN to whom we are indebted for discussion of their work. Our KCl results are in good agreement with theirs.

VOL.
3
1957

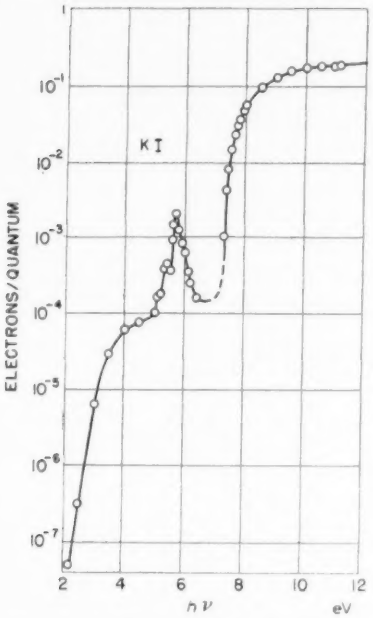

FIG. 3. Spectral distribution of the photoelectric yield for a KI sample containing $\sim 10^{19}$ F-centers cm^{-3}.

yield is considerably different from the valence band yield, however, and the actual value may be somewhat higher.[7]

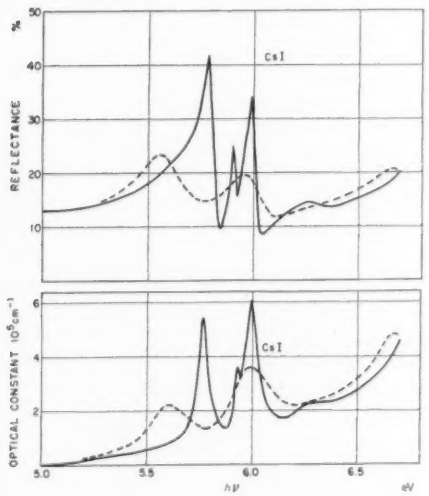

FIG. 4a

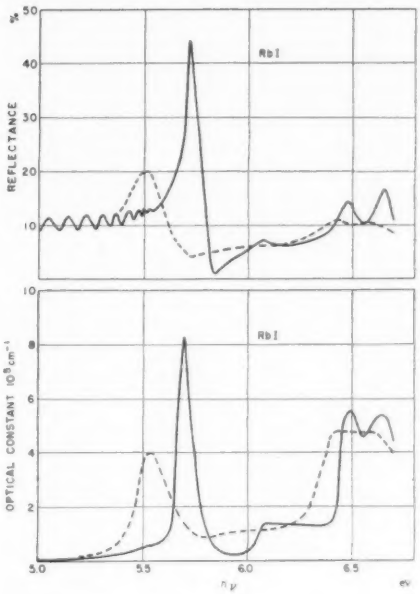

FIG. 4b

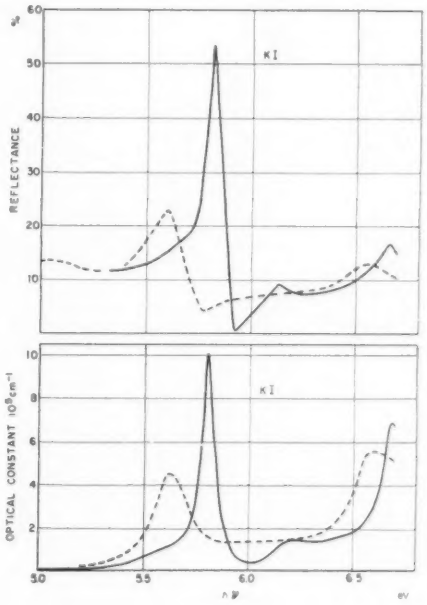

FIG. 4c

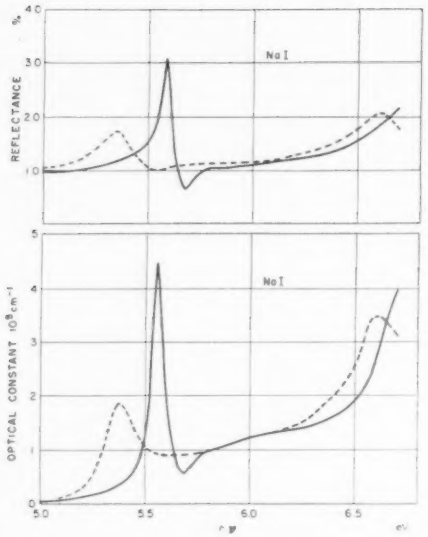

FIG. 4d

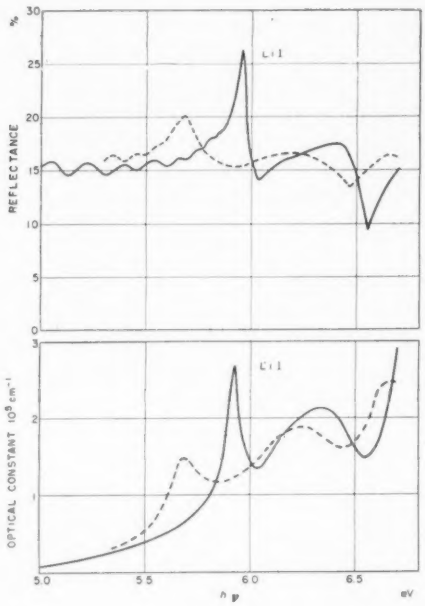

FIG. 4e

FIG. 4. Reflectance and optical absorption of the alkali iodides at 300°K (dotted curves) and 80°K (solid curves). Reflectance data are presented for single crystals, except for RbI and LiI, where measurements were made only on annealed evaporated films. Interference effects appears in these films in the region of optical transparency. Optical transmission data for annealed evaporated films are plotted as estimated absorption constant; no correction has been made for surface effects such as reflectance. The values were roughly calculated from interference colors and tube geometry.[1]

Optical properties

Absorption constants for evaporated, annealed alkali-iodide films are shown in Fig. 4. (No corrections have been made for reflection loss; the absolute values are rough estimates.) The results agree with MARTIENSSEN's. The doubling of the second absorption peak of CsI (which we previously overlooked[1]) barely shows up at 80°K, as MARTIENSSEN has pointed out. The weaker double structure of the absorption edge we were not able to resolve with our techniques, but the edge itself is clear. For RbI and KI, the double peak is missing, and the absorption edge (MARTIENSSEN lists these as "stufe") is very pronounced. It moves closer to the first peak in NaI and becomes less distinct. For LiI it appears to have moved under the first peak, which is weaker. The reflectance data are consistent with these results, showing better resolution of the doublet for CsI.[8]*

DISCUSSION

We obviously cannot assign unique threshold photon energies to the valence band photoemission or to the optical absorption edge in the absence of a more quantitative treatment of these effects. Useful comparisons may be made, nevertheless, by arbitrarily noting the values of $h\nu$ at which the photoemission is 10^{-3} electron/photon and at which the optical absorption constant rises more or less step-wise near a value of 10^5 cm^{-1}. Table 1 shows such values, the photoelectric thresholds (column 1) being given for 300°K and

* The room temperature results for KI are in agreement with early reflectance measurements of HILSCH and POHL.

Table 1

Crystal	1	2	3	4	5
CsI	6·4 eV	6·3*	0·1	5.76	0·5
RbI	7·3	6·1	1·2	5·69	0·4
KI	7·3	6·2	1·1	5·80	0·4
NaI	7·3	5·8	1·5	5·55	0·2
LiI	7·3	5·9†	1·4	5·92	0·0

1. Photoelectric threshold for valence band emission at 300°K.
2. Optical absorption edge at 80°K.
3. Electron affinity.
4. First fundamental absorption peak at 80°K.
5. Exciton ionization energy.

* At 20° MARTIENSSEN shows two edges at 6·24 and 6·31, respectively.

† Taken as coincident with the exciton peak.

the absorption edges (column 2) for 80°K. (Photoelectric thresholds at 80°K would be roughly 0·2 eV higher,[1] a correction which we neglect in view of the coarseness of this procedure). The photoelectric threshold fixes the valence band relative to the vacuum level, and the optical absorption edge corresponds to the valence-conduction band gap. The difference is the electron affinity (column 3) of the crystal, which has a very small value for CsI but a larger one for the other salts. The estimates tend to be too small rather than too large.

In Fig. 4 of the paper by HARTMAN, NELSON and SIEGFRIED[8] there appears an interesting feature in the optical absorption of KCl which looks somewhat like the absorption edge in KI. Assuming for the moment that the two cases are comparable, we arrive at an electron affinity of 0·2 eV for KCl using the photoelectric threshold 8·7 eV from Fig. 2 above.

For LiI, the optical absorption edge is ill-defined and has been taken in Table 1 as coincident with the first absorption peak. The absorption spectrum bears some resemblance to those of the silver salts, for which the discrete first exciton peak is not clearly separated from the continuum as it is in RbI for example.[9]‡ The valence band is the 5*p* band of the iodine ions, which is broadened as these ions are packed more closely in LiI.[10] Thus, one expects the absorption edge to be less sharp than for the heavier iodides. (We notice incidentally that the high-frequency dielectric constant of LiI is higher than for any other alkali halide; it approaches that of the silver halides.) To display the pertinent trends more clearly in Table 1, we plot the difference in energy (column 5) between the first absorption peak (column 4) and the absorption edge (column 2). Keeping in mind the unsophisticated definitions adopted here, we call this the "exciton ionization energy".

We have not discussed in any precise way the character of the band-to-band optical transitions that we associate with the optical absorption edge and the succeeding continuum. We should remark, however, that a recent calculation of the electronic energy structure of KCl by HOWLAND[11] shows that both direct and indirect optical transitions could originate near the top of the valence band without differing greatly in energy.

Another subject which is worth further scrutiny is the behavior of the photoemission in the vicinity of the absorption edge and at the position of the absorption peaks lying beyond the edge. At 80°K the iodides show a slight rise (of order 30 per cent) in the photoelectric yield at the absorption edge when *F*-centers are present in the sample. (This effect is not clear in Fig. 3 for KI since this curve is for 300°K. It appears weakly in Fig. 1 of the last paper of reference 6).

At the present time this small rise looks like a peak in the yield near 6 eV rather than like a plateau that follows the optical absorption beyond the edge. There may conceivably be an unresolved optical peak at this point, though we are reluctant to believe this in view of MARTIENSSEN's detailed work at 20°K. In any case, we summarize by saying that optical absorption in the immediate vicinity of the edge stimulates photoemission from *F*-centers for reasons not yet understood.

For KI, irradiation in the second optical absorption peak at 6·7 eV, which lies beyond the edge, does not appear to stimulate photoemission from *F*-centers, at least with efficiency comparable to that found in the first peak. Experiments in the vicinity of the valence band emission threshold are difficult, however, and we have therefore shown this region in Fig. 3 as a dashed line to indicate it as tentative.

‡ Dr. W. MARTIENSSEN also has kindly sent us absorption data taken by Y. OKAMOTO at Göttingen on these salts.

Acknowledgements—We are grateful to Dr. W. MARTIENSSEN for an advance copy of his paper and for comments on his work. We are indebted to P. HARTMAN and J. TAYLOR for interesting discussions of their work. We particularly thank L. APKER for many helpful discussions throughout the course of this work.

REFERENCES

1. PHILIPP H. R. and TAFT E. *J. Phys. Chem. Solids* **1,** 159 (1956).
2. MARTIENSSEN W. *J. Phys. Chem. Solids* **2,** 257 (1957).
3. HILSCH R. and POHL R. *Z. Phys.* **59,** 812 (1930); SCHNEIDER E. and O'BRYAN H. *Phys. Rev.* **51,** 293 (1937); MARTIENSSEN W. *Nachr. Akad. Wiss. Göttingen. Math. Physik* **11,** 257 (1955); FESEFELDT H. *Z. Phys.* **64,** 626 (1930); FISCHER F. *Z. Phys.* **139,** 328 (1954).
4. HILSCH R. and POHL R. W. *Z. Phys.* **59,** 812 (1930); SCHNEIDER E. and O'BRYAN H. *Phys. Rev.* **51,** 293 (1937).
5. JOHNSON P. D. *J. Opt. Soc. Amer.* **42,** 278 (1952).
6. APKER L. and TAFT E. *Phys. Rev.* **79,** 964 (1950); **81,** 698 (1951); **82,** 814 (1951); PHILIPP H. R. and TAFT E. *Phys. Rev.* **106,** 671 (1957).
7. In this connection see INCHAUSPE N. and MAURER R. J. *Air Force Technical Note* OSR-TN-55-281; TEEGARDEN K. J. *Phys. Rev.* **105,** 1222 (1957).
8. HILSCH R. and POHL R. W. *Z. Phys.* **57,** 145 (1929); HARTMAN, NELSEN, and SIEGFRIED *Phys. Rev.* **105,** 123 (1957).
9. TUTIHASI S. *Phys. Rev.* **105,** 882 (1957).
10. O'BRYAN H. and SKINNER H. *Proc. Roy. Soc.* **A176,** 229 (1940); MOTT N. F. and GURNEY R. W. *Electronic Processes in Ionic Crystals* p. 79. Oxford University Press, London (1940).
11. HOWLAND L. P. *Quarterly Progress Report, Solid State and Molecular Theory Group* p. 23. M.I.T., Cambridge, Mass. (1957). We are indebted to Dr. HOWLAND for stimulating conversations.

VOL
3
195

J. Phys. Chem. Solids Pergamon Press 1957. Vol. 3. pp. 7–19.

AUTODIFFUSION DES IONS DANS LES CRISTAUX UNIQUES DES HALOGÉNURES DE POTASSIUM ET DES CHLORURES ALCALINS

JEAN-FRANÇOIS LAURENT et JACQUES BÉNARD

Laboratoire de Chimie Minérale B, 11, rue Pierre Curie, Paris

(*Received* 11 *February* 1957)

VOL. 3 1957

Abstract—The self-diffusion of both ions in potassium halides and alkali chlorides has been measured as a function of temperature. Radioactive tracers were used, samples being obtained by slicing the specimen with a microtome. For all temperatures and for all compounds except caesium chloride the diffusion constant for the cation exceeds that for the anion. In all cases the activation energy for cation self-diffusion is smaller than for the anion. In each series of compounds increasing the ionic radius of one constituent produces a decrease in activation energy for both ions.

In the series of potassium halides a linear relationship is found between the sum of the activation energies of both ions and the plastic yield strength as measured by the minimum pressure needed to attain compaction of the powder. In each series of compounds the sum of the activation energies is also a linear function of the fusion temperature of the compound.

Résumé—L'étude de l'autodiffusion des deux ions dans les halogénures de potassium et les chlorures de métaux alcalins, en fonction de la température, a été réalisée, grâce à l'emploi des isotopes radioactifs, par la méthode de découpage des échantillons au microtome. Pour chaque composé, à l'exclusion du chlorure de césium, et quelle que soit la température, la vitesse de diffusion des cations est toujours supérieure à celle des anions; de même l'énergie d'activation du processus d'autodiffusion des cations est dans tous les cas inférieure à celle des anions. Dans chaque série—halogénures de potassium et chlorures alcalins—l'accroissement du rayon ionique de l'ion variable produit une diminution de l'énergie d'activation de diffusion des deux ions lorsque l'on passe d'un sel à l'autre.

D'autre part, une relation simple a été établie dans la série des halogénures de potassium entre la pression minimum qu'il faut appliquer à des poudres des différents composés pour obtenir des pastilles de densité maximum, et la somme des énergies d'activation des deux ions composants. Cette somme qui correspond à l'énergie nécessaire pour qu'un couple d'ions diffuse au même instant est aussi dans chaque série une fonction linéaire de la température de fusion des différents halogénures.

Depuis quelques années, les expériences sur les phénomènes de diffusion dans l'état solide se sont multipliées, grâce à l'emploi des radioéléments artificiels. Si l'on veut mieux comprendre le mécanisme du déplacement des atomes dans les réseaux cristallins, il est nécessaire en effet d'effectuer des expériences de plus en plus précises et sur des séries de composés homologues, de façon à obtenir des résultats susceptibles d'être comparés entre eux. C'est dans ce but que nous avons mesuré les variations de l'autodiffusion des ions en fonction de la température, dans un certain nombre d'halogénures alcalins monocristallins. Jusqu'à ce jour, aucune étude systématique ne semblait avoir été effectuée sur l'ensemble des halogénures alcalins; seules existaient des études indépendantes sur le chlorure de sodium,[1,2,3,4] le chlorure de potassium,[5,6,7] le bromure de sodium[2,8] et l'iodure de potassium.[9]

Nous nous sommes proposés, pour notre part, de soumettre à une étude systématique deux séries de composés possédant chacune un ion commun. Dans l'une le cation, en l'espèce le potassium, reste le même; elle comporte le fluorure le chlorure, le bromure et l'iodure de potassium. Dans l'autre l'anion, en l'espèce le chlore, reste

le même; elle comporte le chlorure de sodium, le chlorure de potassium et le chlorure de césium. Dans chaque cas, notre étude a porté à la fois sur l'autodiffusion de l'anion et sur celle du cation. Les expériences, à l'exclusion de celles concernant le fluorure de potassium et le chlorure de césium, ont été effectuées sur des cristaux uniques.

PARTIE 1

1. RAPPEL DE NOTIONS FONDAMENTALES

La deuxième relation de Fick est facilement applicable à l'étude de l'autodiffusion, le coefficient de diffusion étant en effet dans ce cas indépendant de la concentration. On peut donc écrire :

$$\frac{\partial C}{\partial t} = D\frac{\partial^2 C}{\partial x^2}. \qquad (1)$$

L'intégration de l'équation (1) est possible sous réserve que la quantité Q de matière diffusante déposée à la surface du solide constitue une couche très mince, et que l'étendue du milieu diffusant puisse être considérée comme infinie vis à vis de la profondeur de pénétration des ions. Dans ces conditions, l'équation (1) peut s'écrire

$$C = \frac{Q}{\sqrt{\pi Dt}} \exp\left(-\frac{x^2}{4Dt}\right) \qquad (2)$$

dans laquelle C est la concentration de l'élément diffusant à la distance x de l'interface, t le temps en secondes pendant lequel s'est effectuée la diffusion et D le coefficient de diffusion en $cm^2\ sec^{-1}$ à la température $T°K$ de l'expérience. Or la concentration de l'élément radioactif en un point donné du solide est proportionnelle à la radioactivité de cet élément en ce point. Si cette dernière est exprimée par le nombre A d'impulsions par minute, dans un système de mesure déterminé, l'équation (2) devient:

$$\text{Log } A = K - \frac{x_2}{4Dt}.$$

La courbe $\log A = f(x^2)$ permet de déterminer D, d'après l'expression:

$$D = \frac{x_2^2 - x_1^2}{\log_{10} A_1 - \log_{10} A_2}\left[\frac{10^{-10}}{3{,}31 \cdot t}\right]. \qquad (3)$$

Dans cette expression x_1 et x_2 représentent les distances séparant l'interface des points du solide où la radioactivité de l'élément diffusant est respectivement A_1 et A_2, et t représente la durée de diffusion. Si x est mesuré en 1/100 de mm et t en heures, D se trouve exprimé en $cm^2\ sec^{-1}$. Les coefficients de diffusion obéissent d'autre part à la loi générale d'Arrhénius et l'on a :

$$D = D_0 \exp\left(-\frac{Q}{RT}\right).$$

Dans cette expression D_0 est un terme indépendant de la température, généralement appelé terme de fréquence et Q l'énergie d'activation du processus élémentaire de transfert d'une particule d'une position d'équilibre à la position d'équilibre la plus proche.

2. MÉTHODES EXPÉRIMENTALES

D'après la formule (3), il suffit pour déterminer D de connaitre l'activité A de l'isotope ayant diffusé à la distance x de l'interface. La détermination du coefficient de diffusion à une température donnée $T_K°$ comporte cinq opérations successives que nous allons décrire:

(a) *Préparation du milieu de diffusion*

Pour le chlorure, le bromure et l'iodure de potassium, ainsi que pour le chlorure de sodium, les mesures ont été effectuées sur des cristaux uniques de grandes dimensions préparés au Laboratoire d'Essais du Conservatoire National des Arts et Métiers (Paris) par fusion de sels de haute pureté; on doit noter que la solidification lente entraine par rapport à la composition initiale du sel une purification supplémentaire. Les cristaux ainsi obtenus se clivent aisément suivant une face (100); on utilise des prismes de $13 \times 13 \times 5$ mm. Les faces clivées sont aplanies au préalable par une abrasion sur du papier émeri très fin et usé; le polissage final est effectué sur une peau de chamois humectée d'alcool dilué, puis d'alcool absolu. Les échantillons sont ensuite chauffés pendant une cinquantaine d'heures de 10 à 20° au dessous du point de fusion du sel étudié, avec montée et baisse de température très lentes (24 heures). Les échantillons de chlorure de césium et de fluorure de potassium sont préparés en comprimant dans des moules en acier spécial des poudres de ces substances sous des pressions de 15000 kg/cm^2 de façon à obtenir la densité maximum. Les pastilles obtenues, qui ont un diamètre de 13 mm et une hauteur d'environ 5 mm, sont ensuite traitées comme des cristaux uniques.*

(b) *Dépôt de l'isotope radioactif*

Le Commissariat à l'Energie Atomique (France), nous

* Le chlorure de césium de haute pureté nous a été fourni par Monsieur HACKSPILL, Professeur honoraire à la Sorbonne, à qui nous adressons nos vifs remerciements.

a fourni les divers radioéléments utilisés dans cette étude sous les formes suivantes : ^{36}Cl : HCl*; ^{82}Br : NH_4Br*; ^{131}I; NaI* (sans entraineur); ^{22}Na est préparé par irradiation du magnésium par les deutons; ^{42}K : $K_2{}^*Co_3$; ^{137}Cs : Cs*Cl (sans entraineur). Ces produits sont amenés sous la forme du sel à étudier, lequel est ainsi rendu radioactif soit par l'anion, soit par le cation. La mesure de la diffusion de l'ion fluorure dans le fluorure de potassium n'a pu être réalisée par suite de l'inexistance d'un isotope de période suffisamment longue. Les sels radioactifs sont mis en suspension dans l'alcool. Le dépôt s'effectue par évaporation rapide d'une goutte de cette suspension chaude sur une face de clivage de l'échantillon à étudier, porté lui-même vers 80°C. Il se forme ainsi une mince dépôt dont l'épaisseur très régulière est d'une dizaine de microns. La formation de ce film est presque instantanée et il a été vérifié que l'isotope radioactif ne pénétrait pas dans le solide par échange isotopique avant le traitement de diffusion.

VOL. 3 1957

(c) *Chauffage de l'échantillon*

L'échantillon ainsi préparé est placé dans une capsule de platine et la face sur laquelle a été fait le dépôt est recouverte par une plaquette de platine. Le résultat obtenu est exactement le même, que la contreface soit une face de clivage du sel ou une plaquette de platine. L'ensemble capsule-échantillon est introduit dans un bloc métallique en nickel ou en acier inoxydable puis le tout est placé dans un four maintenu à la température désirée. La régulation du four est assurée par un système à tige dilatable assurant une stabilité de la température à ± 1°C. La mesure de la température est effectuée à l'aide d'un couple thermoélectrique étalonné dont la soudure chaude est placée au voisinage immédiat de l'échantillon; la mesure de la température est faite à $\pm 0{,}2$°C avec un système potentiométrique d'opposition. Cette précision est indispensable pour évaluer correctement les énergies d'activation. Il est nécessaire de réduire de 1 heure 30 le temps de chauffe total pour tenir compte de la période de mise en température du système.

Le traitement thermique de diffusion étant achevé, l'échantillon est sorti du four et *les effets de bord sont éliminés* par clivage ou grattage d'une couche de 1 mm sur le pourtour.

(d) *Découpage de l'échantillon: mesure de x*

Le découpage des échantillons est effectué à l'aide d'un microtome, le rasoir d'acier étant remplacé par l'arête coupante d'une lame de verre. Cette méthode qui permet d'obtenir des tranches de 1/300 de mm a été décrite en particulier par CHEMLA.[1] En général, plusieurs coupes sont accumulées, et chaque mesure d'activité s'opère sur des épaisseurs découpées de 1 à 4/100ème de mm. Le réglage de l'échantillon parallèlement au plan de coupe se fait à l'aide d'une lunette autocollimatrice. La poudre radioactive est recueillie dans des coupelles en aluminium et pesée sur une balance au 1/10 mg de manière à rapporter l'activité à un poids connu de substance.

(e) *Mesure de l'activité*

L'activité des prélèvements successifs est mesurée à l'aide d'un compteur cloche à fenêtre mince. Avant la mesure, la poudre est étalée soigneusement dans le fond de la coupelle à l'aide de deux gouttes d'alcool. Les valeurs de A sont obtenues en rapportant chaque mesure à un même poids de substance, en général 10 mg; connaissant ainsi les activités A correspondant aux distances qui séparent chaque plan de coupe de l'interface, on calcule le coefficient de diffusion D à la température de l'expérience, à l'aide de la formule (3).

3. CALCUL DU COEFFICIENT DE DIFFUSION

Les courbes $\log A = f(x^2)$ permettent de calculer le coefficient de diffusion. La figure 1 donne quelques exemples de ces courbes ainsi que des conditions expérimentales dans lesquelles elles ont été obtenues. Les deux courbes supérieures représentent l'une (à droite) l'autodiffusion de l'ion bromure, l'autre (à gauche) celle de l'ion potassium dans le bromure de potassium. Dans les deux cas, les expériences ont eu lieu à des températures voisines de celle du point de fusion de KBr (1021°K). Pour la diffusion de K^+, l'échantillon a été chauffé pendant 10,8 heures (soit 9,3 heures de chauffe effective) à 993°K; une radioactivité appréciable est encore décelable à une distance de 50/100 mm de l'interface; le coefficient de diffusion est $3 \cdot 10^{-9}$ cm^2 sec^{-1}. Pour la diffusion de Br^-, le cristal a été chauffé pendant 15,5 heures (soit 14 heures de chauffe effective) à 1005°K; bien que la température ait été plus élevée dans ce cas, le coefficient de diffusion qui est $2 \cdot 10^{-9}$ cm^2 sec^{-1} est bien inférieur au précédent. Les deux courbes inférieures représentent, l'une (à droite) l'autodiffusion de l'ion chlorure, l'autre (à gauche) celle de l'ion potassium, dans le chlorure de potassium. Les expériences ont eu lieu à une température relativement éloignée du point de fusion de KCl (1041°K). Pour la diffusion de K^+ l'échantillon est chauffé pendant 57,5 heures (soit 56 heures de chauffage effectif) à 783°K; le coefficient de diffusion est $1 \cdot 10^{-11}$ cm^2 sec^{-1}; il n'est plus possible de déceler de radioactivité à une profondeur supérieure à 6/100 mm. Pour la diffusion de Cl^-, l'échantillon a été chauffé pendant 64 heures (soit 62,5 heures de chauffage effectif) à 790°K; le coefficient de diffusion est $3{,}5 \cdot 10^{-12}$ cm^2 sec^{-1}; la radioactivité du chlore n'est plus décelable au delà de 5/100 mm.

Dans toutes les mesures, la détermination du

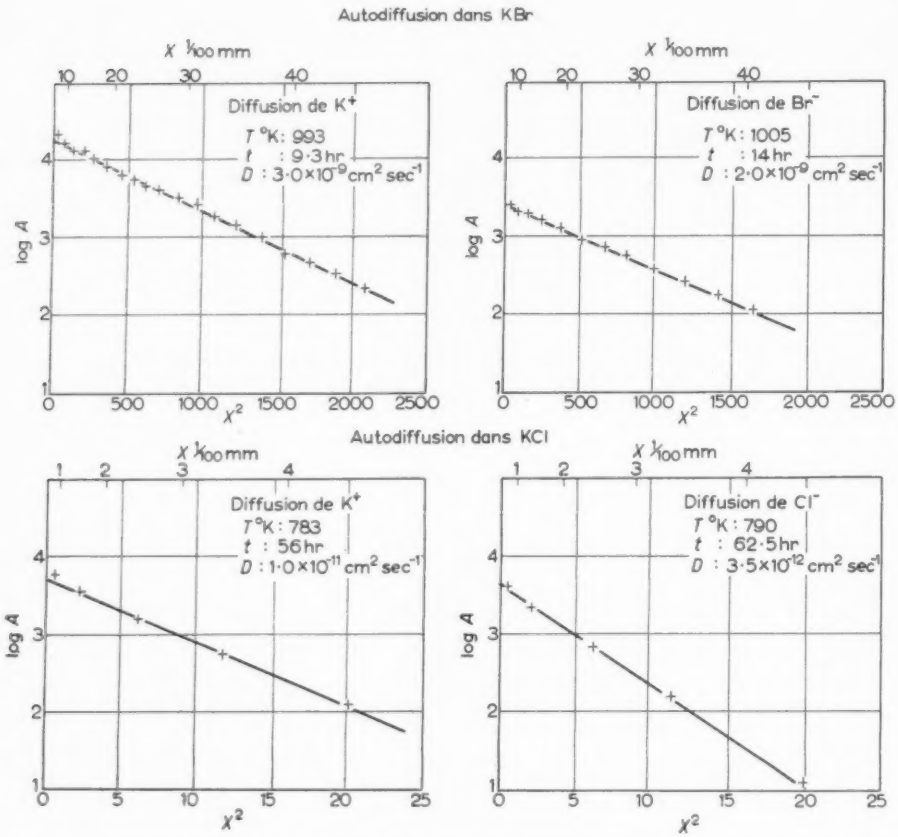

FIG. 1. Exemples de courbes de pénétration des ions par autodiffusion dans le bromure et le chlorure de potassium.

coefficient de diffusion était faite, comme il a été dit plus haut, perpendiculairement à la face (100) qui est la face de clivage des cristaux employés. Nous avions vérifié, dans un travail antérieur,[4] que dans le chlorure de sodium, la valeur du coefficient de diffusion est indépendante de l'orientation suivant laquelle a lieu la migration des ions.

4. CALCUL DE L'ÉNERGIE D'ACTIVATION

Connaissant les coefficients d'autodiffusion des différents ions en fonction de la température, il est facile de déterminer l'énergie d'activation du processus d'autodiffusion pour chaque type d'ion dans chaque composé. Dans la figure 2 se trouvent rassemblées les courbes Log $D = f(1/T_K{}^0)$ dont la pente permet le calcul de cette énergie.

Autodiffusion des ions dans KI

$$D_{KI}^{K^+} = 10^{-5} \exp(-14800/RT);$$

$$D_{KI}^{I^-} = 1{,}2 \,.\, 10^{-3} \exp(-25700/RT).$$

Autodiffusion des ions dans KBr

$$D_{KBr}^{K^+} = 10^{-2} \exp(-29000/RT);$$

$$D_{KBr}^{Br^-} = 2 \,.\, 10^{-2} \exp(-33000/RT).$$

Autodiffusion des ions dans KCl

$$D_{KCl}^{K^+} = 4 \,.\, 10^{-2} \exp(-34000/RT);$$

$$D_{KCl}^{Cl^-} = 10 \exp(-46000/RT).$$

Autodiffusion de K^+ *dans* KF

$$D_{KF}^{K^+} = 2 \exp(-41000/RT).$$

VOL. 3 1957

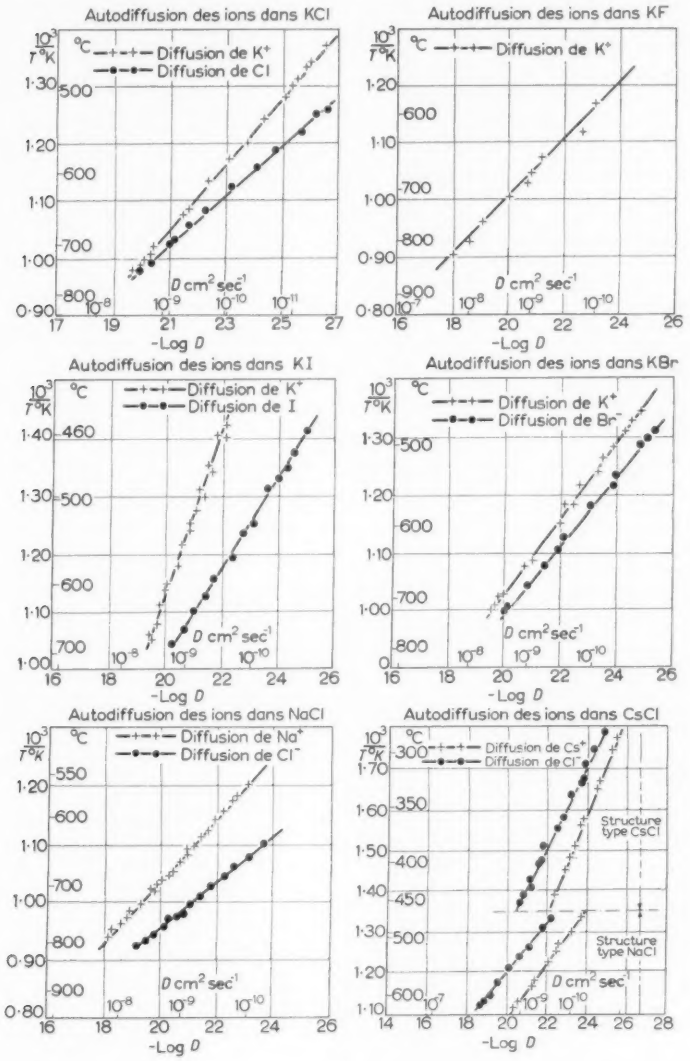

FIG. 2.

Autodiffusion des ions dans NaCl

$$D^{Na^+}_{NaCl} = 0{,}5 \exp(-37000/RT);$$

$$D^{Cl^-}_{NaCl} = 110 \exp(-51400/RT).$$

Autodiffusion des ions dans CsCl *cubique centré* ($t < 465°C$)

$$D^{Cs^+}_{CsCl} = 10^{-5} \exp(-16000/RT);$$

$$D^{Cl^-}_{CsCl} = 1{,}3 \cdot 10^{-3} \exp(-20000/RT).$$

Autodiffusion dés ions dans CsCl *cubique à faces centrées* ($t > 465°C$)

$$D^{Cs^+}_{CsCl} = 10^{-1} \exp(-32000/RT);$$

$$D^{Cl^-}_{CsCl} = 0{,}7 \exp(-36000/RT).$$

En ce qui concerne le fluorure de potassium et le chlorure de césium, il n'a pas été possible d'opérer sur des échantillons monocristallins. Toutefois,

compte tenu de résultats rapportés dans nos publications antérieures[4,9] et de recherches en cours, il est très probable que la valeur du coefficient de diffusion de l'ion K^+ ainsi déterminée dans le fluorure de potassium polycristallin est la même que celle que l'on observerait dans un cristal unique. Le cas du chlorure de césium est plus complexe. En effet, si les valeurs des énergies d'activation mesurées sur les échantillons polycristallins sont vraisemblablement identiques à celles que l'on devrait observer dans un cristal unique, il n'en est plus de même pour les termes de fréquence D_0, qui doivent être très légèrement supérieurs à ceux que l'on devrait observer dans un cristal unique.

APPROXIMATION DES VALEURS DES ÉNERGIES D'ACTIVATION

La dispersion des valeurs du coefficient de diffusion autour de la courbe $\text{Log}\, D = f(1/T_K{}^0)$ permet de se rendre compte de la précision des résultats. Dans les cas les plus défavorables, notamment pour le fluorure de potassium dont la manipulation est rendue difficile du fait de son caractère hygroscopique, les valeurs de D s'écartent au maximum de 20 pour cent des valeurs données par la courbe; pour le chlorure de sodium au contraire l'écart n'est que de 10 pour cent pour les points les plus défavorisés.

Compte tenu de la dispersion des points expérimentaux sur les diagrammes $\text{Log}\, D = f(1/T)$, on peut envisager pour les différentes valeurs des énergies d'activation, les incertitudes suivantes :

$Q^{K^+}_{KI} = (14800 \pm 700)$ cal/ion;
$Q^{I^-}_{KI} = (25700 \pm 700)$ cal/ion.
$Q^{K^+}_{KBr} = (29000 \pm 1000)$ cal/ion;
$Q^{Br^-}_{KBr} = (33000 \pm 500)$ cal/ion.
$Q^{K^+}_{KCl} = (34000 \pm 1000)$ cal/ion;
$Q^{Cl^-}_{KCl} = (46000 \pm 700)$ cal/ion.
$Q^{K^+}_{KF} = (41000 \pm 2000)$ cal/ion.
$Q^{Na^+}_{NaCl} = (37000 \pm 1000)$ cal/ion;
$Q^{Cl^-}_{NaCl} = (51400 \pm 600)$ cal/ion.
$Q^{Cs^+}_{CsCl} = (16000 \pm 1000)$ cal/ion; type c.c.
$Q^{Cl^-}_{CsCl} = (20000 \pm 700)$ cal/ion. type c.c.
$Q^{Cs^+}_{CsCl} = (32000 \pm 2000)$ cal/ion; type c.f.c.
$Q^{Cl^-}_{CsCl} = (36000 \pm 2000)$ cal/ion. type c.f.c.

PARTIE II

L'examen de la figure 2 dans laquelle sont rassemblés tous les résultats expérimentaux suggère à première vue deux observations fondamentales.

(a) *Dans les composés étudiés, à l'exception du chlorure de césium, les cations diffusent plus vite que les anions à une température donnée*; le rapport de leurs vitesses de diffusion $D^{\text{cations}}/D^{\text{anions}}$ augmente d'autre part très vite lorsque la température diminue. Ce phénomène confirme le fait bien connu que la conductibilité électrique à basse température correspond presque exclusivement à la migration des cations.

(b) *Dans tous les composés étudiés et dans le domaine de température exploré, l'énergie d'activation du processus d'autodiffusion des anions est toujours supérieure à celle des cations.* De plus en extrapolant les courbes $\text{Log}\, D = f(1/T)$ au point de fusion, $T_{(F)}$, de chaque sel on trouve des coefficients de diffusion très semblables pour tous les ions. Par exemple pour les trois sels de potassium, on obtient les coefficients suivants :

Sel	$D^{T_{(F)}}_{X^-}$	$D^{T_{(F)}}_{Y^+}$
KCl	$3 \cdot 10^{-9}$	$3 \cdot 10^{-9}$
KBr	$2{,}5 \cdot 10^{-9}$	$4 \cdot 10^{-9}$
KI	$2 \cdot 10^{-9}$	$5 \cdot 10^{-9}$

La discussion des résultats se fera en considérant d'une part la série des halogénures de potassium et d'autre part celle des chlorures alcalins.

1. SÉRIE DES HALOGÉNURES DE POTASSIUM

Cette étude a porté, comme il a été dit plus haut, sur le fluorure, le chlorure, le bromure et l'iodure de potassium. Nous nous sommes proposés en premier lieu de comparer dans cette série les

énergies d'activation d'autodiffusion Q d'une part du cation commun K^+ et d'autre part des différents anions.

Lorsqu'un ion se déplace dans le réseau, d'une position normale à la position lacunaire la plus voisine, il doit franchir une barrière de potentiel; ce franchissement suppose la rupture au moins partielle des liaisons qu'il échangeait avec ses voisins dans sa position initiale. Si l'on admet que ces liaisons sont purement électrostatiques, leur énergie doit être en première approximation proportionnelle à l'inverse de la distance d qui sépare les centres de gravité de deux ions antagonistes contigus. Il semblait donc *a priori* intéressant d'étudier dans la série des sels de potassium la variation de Q en fonction de $1/d$, pour les différents ions (diagramme supérieur de la figure 3). La courbe 1 dans le diagramme de la figure 3(a) se rapporte à la variation de l'énergie d'activation Q^+ du cation K^+ commun, la courbe 2 à celles Q^- des différents anions. On notera que la valeur $Q_{KF}^{F^-}$: 90000 ± 10000 cal/ion, figurant sur cette courbe, a été obtenue par extrapolation, la mesure directe de la diffusion de l'ion fluorure n'étant pas réalisable par la méthode des traceurs radioactifs. Bien que cette extrapolation entraine une incertitude appréciable pour la valeur annoncée, nous verrons par la suite que cette dernière s'intègre bien dans l'ensemble de nos résultats.

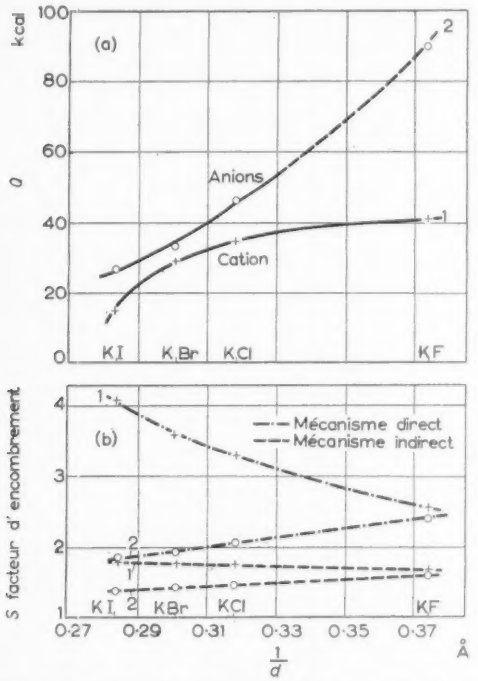

FIG. 3. *Diagramme* (a) : Variation de l'énergie d'activation d'autodiffusion des ions en fonction des énergies de Coulomb relatives à chaque couple d'ions des différents composés.

Courbe 1 : Énergie d'activation Q^+ de l'ion positif commun K^+.

Courbe 2 : Énergie d'activation Q^- des différents ions négatifs.

Diagramme (b) : Variations du facteur d'encombrement des ions pour les mécanismes de diffusion direct et indirect en fonction de l'inverse de la distance interionique des différents composés.

Courbes 1 : Facteur d'encombrement de l'ion positif commun K^+.

Courbes 2 : Facteur d'encombrement des différents ions négatifs.

Les courbes ainsi obtenues indiquent que les énergies d'activation du processus de diffusion du cation et des anions diminuent dans cette série lorsque le rayon de l'anion s'accroit. Cette variation correspond donc bien à un relâchement des forces de liaison à mesure que le volume de l'ion négatif augmente. De plus elle est en bon accord avec le sens de la variation des termes de fréquence D_0 qui diminuent très rapidement lorsque le rayon de l'anion s'accroit (paragraphe 4).

Les courbes 1 et 2 de la figure 3a ne sont pas des droites et présentent des courbures opposées. Il est possible d'expliquer l'allure de ces courbes en considérant l'encombrement de l'espace réticulaire qui se conjugue à l'action des forces de liaison pour entraver le déplacement des ions. Pour passer d'une position d'équilibre à la position d'équilibre contiguë, l'ion diffusant doit s'élever transitoirement à un état d'énergie qui correspond au maximum de la barrière de potentiel qu'il doit franchir. En simplifiant à l'extrême, on peut admettre que cet accroissement d'énergie résulte du développement des forces de répulsion lors du passage de cet ion au travers de son entourage d'ions antagonistes. Ces forces dépendent à la fois de la dimension de l'ion migrateur et de l'espace dont celui-ci dispose pour effectuer son déplacement élémentaire en l'absence de toute déformation. Elles peuvent être représentées par une expression de la forme $S = r_1/\Sigma$ dans laquelle r_1 est le rayon ionique de l'ion diffusant et Σ une fonction simple de la

géométrie du réseau. S sera appelé *facteur d'encombrement*. Dans les systèmes étudiés un ion occupant initialement une position A (figure 4) peut aller occuper une position vacante et équivalente H du réseau par deux voies principales; il peut d'une part se rendre directement de A en H,

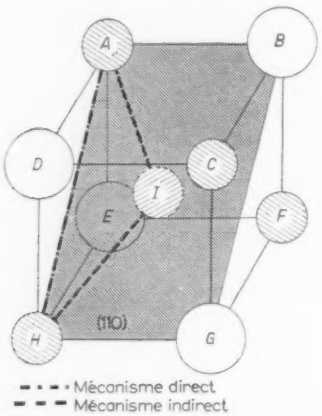

FIG. 4. Représentation simplifiée du réseau cristallin montrant les deux mécanismes principaux de diffusion des ions.

ce qui l'oblige à passer entre les deux ions antagonistes D et E (mécanisme direct); il peut d'autre part emprunter un chemin détourné, en occupant intermédiairement la position interstitielle I, ce qui l'oblige cette fois à passer successivement entre les ions antagonistes D, B, E et D, G, E (mécanisme indirect). Dans chaque cas le facteur d'encombrement S a été calculé : pour le mécanisme direct on a $\Sigma = (d\sqrt{2}/2) - r_2$ pour le mécanisme indirect $\Sigma = (d\sqrt{6}/3) - r_2$, r_2 étant le rayon ionique de l'ion antagoniste de l'ion diffusant Dans tous les cas le processus direct est caractérisé par un facteur d'encombrement supérieur à celui du processus indirect. Ce dernier semble donc le plus probable. On a indiqué dans le tableau ci-joint les valeurs de S calculées pour chacun des deux mécanismes.

Dans le diagramme b de la figure 3, on a porté les différentes valeurs de S ainsi calculées pour les deux mécanismes de diffusion en fonction de $1/d$ Les courbes 1 correspondent à la diffusion du cation et les courbes 2 à celle des anions. Ces courbes montrent que lorsqu'on passe de l'iodure au fluorure, le facteur d'encombrement diminue pour

Sel	S anion diffusant		S cation diffusant	
	Processus direct	Processus indirect	Processus direct	Processus indirect
KF	2,43	1,60	2,51	1,62
KCl	2,04	1,46	3,25	1,75
KBr	1,95	1,43	3,50	1,80
KI	1,86	1,39	4,05	1,85

la diffusion du cation et augmente pour celle de l'anion et ceci quelque soit le mécanisme envisagé.

Les remarques précédentes permettent d'expliquer l'allure des courbes de la figure 3a. En effet on peut penser que si le facteur d'encombrement était le même, soit S_i, pour les ions de même polarité dans tous les sels de la série, les courbes $Q = f(1/d)$ seraient des droites en première approximation, car seules interviendraient les énergies de liaison. Un facteur d'encombrement S plus grand que S_i conduit à mettre en jeu une énergie supérieure à celle qui correspondrait à $S = S_i$; par contre, un facteur d'encombrement S inférieur à S_i conduit à mettre en jeu une énergie inférieure. Donc, même si les énergies de liaison étaient identiques dans le fluorure et dans l'iodure de potassium, l'ion potassium devrait se déplacer plus facilement dans le fluorure, puisque d'après les courbes 1 de la figure 3(b) $S_{KF}^{K+} < S_{KI}^{K+}$, ce qui entraine une diminution de l'énergie d'activation. La courbe $Q^+ = f(1/d)$ doit donc s'aplatir pour les valeurs de $1/d$ élevées, ce que justifient nos expériences (courbe 1 figure 3a).

On peut de même appliquer ce raisonnement à la diffusion des anions. L'intervention du facteur d'encombrement a ici pour effet d'apporter une entrave supplémentaire à la diffusion de l'ion fluorure dans le fluorure de potassium par rapport à celle de l'ion iodure dans l'iodure de potassium; ceci entraine donc une augmentation relative de l'énergie d'activation et justifie du même coup l'allure de la courbe 2 de la figure 3(a). La notion d'encombrement permet donc d'expliquer d'une manière très satisfaisante l'allure des courbes $Q^+ = f(1/d)$ et $Q^- = f(1/d)$. Cependant il faut remarquer que cette notion ne peut s'appliquer qu'à la comparaison du déplacement d'ions de même polarité. La seule considération des rayons

ioniques ne permet pas en effet expliquer la grande différence de mobilité des ions négatifs et des ions positifs, ce qui conduit à penser que le mécanisme de leur diffusion est essentiellement différent.

Relations entre l'autodiffusion et la déformation plastique

Dans des expériences ultérieures, il a été possible de relier les énergies d'activation des processus d'autodiffusion des ions aux énergies à mettre en jeu pour provoquer la déformation plastique de ces réseaux. A la suite de recherches effectuées à la même époque au laboratoire[2,9] sur des échantillons d'halogénures alcalins polycristallins, nous nous sommes trouvés dans l'obligation de tracer les courbes de variation des densités apparentes des poudres comprimées en fonction des pressions de compression (figure 5). La pression minimum qu'il

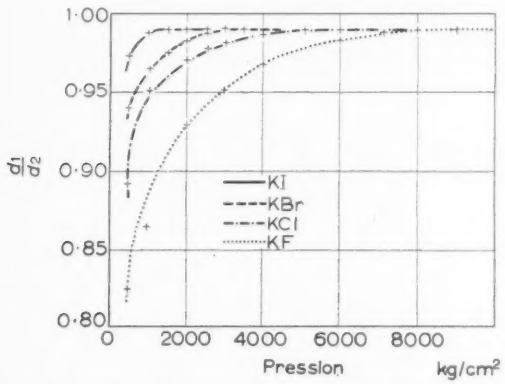

FIG. 5. Variation du rapport d_1/d_2 en fonction de la pression de compression des poudres des différents halogénures (d_1 : densité apparente de la pastille comprimée d_2 : densité du monocristal).

faut exercer sur un agrégat polycristallin pour atteindre le rapport le plus élevé de la densité mesurée à la densité du monocristal représente l'effort fourni pour que les espaces vides existant entre les grains puissent être totalement comblés à la faveur du glissement plastique des plans réticulaires. La pression P atteint les valeurs suivantes pour chaque sel :

Sel	KI	KBr	KCl	KF
P kg/cm²	1300	2700	4300	8000

Il semble que ces valeurs très différentes les unes des autres puissent être reliées aux caractéristiques des processus d'autodiffusion. Le glissement d'une rangée d'ions, de polarité alternée, le long d'une rangée contiguë met en effet en jeu, à l'origine, une énergie d'activation globale qui peut être considérée en première approximation comme la somme des énergies d'activation relatives au déplacement individuel des cations et des anions. Si le terme $\exp(-W/RT)$ représente la probabilité pour qu'un ion migre d'une position à la position voisine, le terme $\exp(-W^+/RT) \cdot \exp(-W^-/RT)$, soit $\exp -(W^+ + W^-)/RT$, représente la probabilité pour qu'un couple d'ions se déplace simultanément. Si l'on tente d'assimiler ces énergies W^+ et W^- aux énergies d'activation d'autodiffusion des deux ions Q^+ et Q^-, une relation simple doit apparaitre entre la somme $Q^+ + Q^-$ et la pression P. Si l'on représente sur un diagramme (figure 6) les variations de P en fonction de la

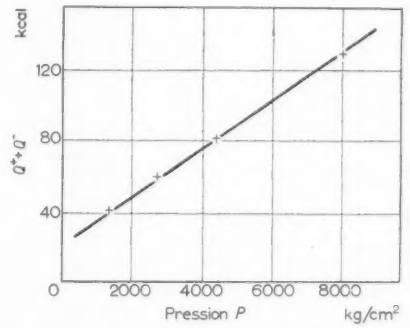

FIG. 6. Variation de la somme des énergies d'activation d'autodiffusion des deux ions de chaque sel en fonction de la pression de compression minimum permettant d'obtenir la densité la plus élevée possible pour une pastille comprimée des différents halogénures.

somme $Q^+ + Q^-$, on constate effectivement que cette variation est linéaire.

Il est d'autre part intéressant de relier la pression P aux énergies de liaison exprimées en fonction de $1/d$ (figure 7(a)) L'examen de la courbe montre que P est proportionnelle à $1/d$. Ceci se justifie bien si l'on admet que P représente l'effort minimum nécessaire pour rompre les liaisons qui s'opposent au glissement des plans réticulaires.

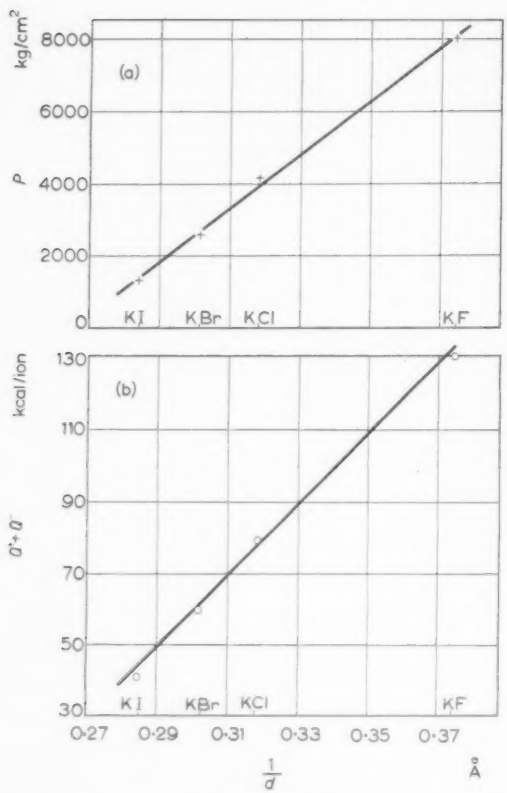

FIG. 7. *Diagramme* (a) : Variation de la pression de compression P en fonction des énergies de Coulomb relatives à chaque couple d'ions des différents composés.

Diagramme (b) : Variation de la somme des énergies d'activation d'autodiffusion des deux ions de chaque halogénure en fonction des énergies de Coulomb relatives à chaque couple d'ions des différents composés.

Relation entre la somme $Q^+ + Q^-$, les énergies de liaison et le point de fusion

L'étude précédente nous a montré que P est une fonction linéaire de $1/d$ et de $Q^+ + Q^-$ il en résulte que la somme $Q^+ + Q^-$ est aussi une fonction linéaire de $1/d$, d'ailleurs l'examen de la figure 7(b) confirme bien ce raisonnement. On peut se demander pourquoi la somme $Q^+ + Q^-$ est sensiblement linéaire en fonction de $1/d$; alors que Q^+ et Q^- ne sont pas proportionnelles à $1/d$ (figure 3a). Cette linéarité n'est cependant pas surprenante si l'on tient compte du fait que les écarts à la linéarité des courbes de la figure 3(a) proviennent comme nous l'avons dit, de l'intervention d'un factuer d'encombrement S qui entraine des corrections de sens opposé pour les anions et pour les cations. Un phénomène mettant en jeu un transport simultané de l'anion et du cation doit par conséquent être dans une certaine mesure indépendant de ce facteur; les valeurs de la somme $S^+ + S^-$ figurant dans le tableau ci-joint confirment d'ailleurs cette interprétation.

Sels	KF	KCl	KBr	KI
Mécanisme direct	4,94	5,29	5,45	5,91
Mécanisme indirect	3,22	3,21	3,23	3,24

Le fait que les valeurs de la somme $S^+ + S^-$ dans l'hypothèse du mécanisme indirect sont constantes quel que soit le sel envisagé, confirme la vraisemblance de ce mécanisme de diffusion.

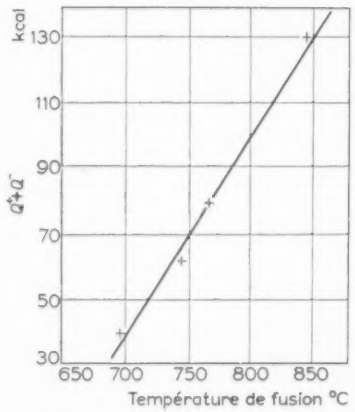

FIG. 8. Variation de la somme des énergies d'activation d'autodiffusion des deux ions des différents halogénures en fonction de leur température de fusion.

Nous avons également représenté sur une courbe (figure 8) la variation de la température de fusion de chaque sel en fonction de la somme $Q^+ + Q^-$; l'examen de la figure montre que cette variation est linéaire. Ce résultat n'est pas essentiellement différent du précédent si l'on songe que la fusion d'un sel comporte elle aussi à l'origine la rupture simultanée d'une partie des liaisons existant entre les différents ions dans l'édifice cristallin.

2. SÉRIE DES CHLORURES ALCALINS

L'étude a porté sur le chlorure de sodium, le chlorure de potassium et le chlorure de césium. Par suite de l'existence du point de transformation du chlorure de césium vers 465°C deux séries de valeurs ont été obtenues pour ce sel, l'une se rapportant à la variété cubique centrée de basse température et l'autre à la variété cubique à faces centrées de haute température. Seules les valeurs relatives à cette dernière variété dont la structure est identique à celle des autres chlorures étudiés ici, seront prises en considération pour l'étude de cette série. Les valeurs relatives à la variété de basse température et l'étude au voisinage du point de transformation seront examinées brièvement à la fin de ce chapitre.

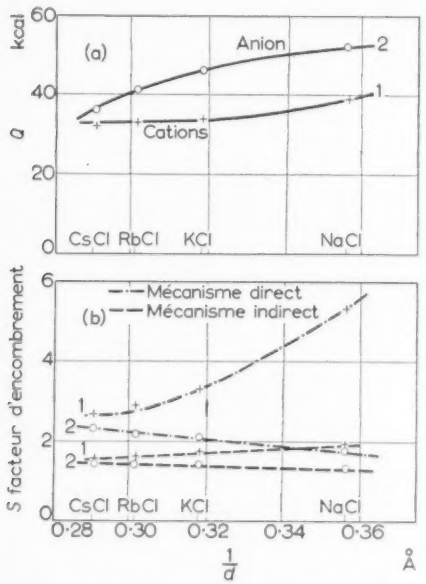

FIG. 9. *Diagramme* (a) : Variation de l'énergie d'activation d'autodiffusion des ions en fonction des énergies de Coulomb relatives à chaque couple d'ions des différents composés.

Courbe 1 : Énergie d'activation Q^+ des différents ions positifs.

Courbe 2 : Énergie d'activation Q^- de l'ion négatif commun Cl^-.

Diagramme (b) : Variation du facteur d'encombrement des différents ions pour les mécanismes de diffusion direct et indirect en fonction de l'inverse de la distance interionique des différents composés.

Courbes 1 : Facteur d'encombrement des différents ions positifs.

Courbes 2 : Facteur d'encombrement de l'ion négatif commun Cl^-.

L'exposé sera identique à celui envisagé au paragraphe précédent. Nous comparerons en premier lieu les énergies d'activation d'autodiffusion Q d'une part pour l'anion commun Cl^- et d'autre part pour les différents cations, en étudiant les variations de Q^+ et de Q^- en fonction de $1/d$ (figure 9(a)). La courbe 1 de la figure 9(a) se rapporte à la variation de l'énergie d'activation Q^+ des différents cations, la courbe 2 à celle Q^- de l'anion Cl^-. On remarquera que les valeurs relatives au chlorure de rubidium, $Q^{Cl^-}_{RbCl} = 42000 \pm 1000$ cal/ion et $Q^{Rb^+}_{RbCl} = 33000 \pm 1000$ cal/ion figurant sur ces courbes ont été obtenues par interpolation ce qui explique leur précision relativement élevée. Ces courbes montrent que les énergies d'activation d'autodiffusion des ions diminuent lorsque le rayon ionique du cation s'accroit, le rayon ionique de l'anion Cl^- restant le même. Cet effet est identique à celui que nous avons signalé au paragraphe précédent, et peut se justifier par un raisonnement analogue.

Les facteurs d'encombrement correspondant au mécanisme de migration directe et indirecte ont été calculés suivant les indications données plus haut et sont rassemblés dans le tableau ci-joint.

Sel	S anion diffusant		S cation diffusant	
	Processus direct	Processus indirect	Processus direct	Processus indirect
NaCl	1,74	1,34	5,27	1,94
KCl	2,03	1,46	3,24	1,75
RbCl	2,13	1,50	2,85	1,68
CsCl	2,42	1,54	2,68	1,62

Les différentes valeurs de S, pour les deux mécanismes de diffusion envisagés, sont portées dans le diagramme 9(b) en fonction de $1/d$. Les courbes 1 correspondent à la diffusion des cations et les courbes 2 à celle de l'anion. Ces courbes montrent que, quel que soit le mécanisme envisagé, le facteur d'encombrement diminue pour la diffusion de l'anion et augmente pour celle des cations lorsque l'on passe du chlorure de césium au

chlorure de sodium. A partir de ces résultats l'allure des courbes 1 et 2 de la figure 9(a) est facile à expliquer. Si les énergies de liaison étaient les mêmes dans le chlorure de sodium et dans le chlorure de césium, l'ion chlorure devrait se déplacer plus facilement dans l'halogénure de sodium que dans celui de césium puisque, d'après les courbes de la figure 9(b), $S^{Cl^-}_{CsCl} > S^{Cl^-}_{NaCl}$, ce qui entraine une diminution de l'énergie d'activation. La courbe $Q^- = f(1/d)$ doit donc s'aplatir pour les valeurs élevées de $1/d$, ce qui est effectivement observé (courbe 2, figure 9a). De même l'intervention du facteur d'encombrement a pour effet d'apporter une entrave supplémentaire à la diffusion de l'ion sodium dans le chlorure de sodium par rapport à celle de l'ion césium dans le chlorure de césium, puisque $S^{Na^+}_{NaCl} > S^{Cs^+}_{CsCl}$; ceci entraine donc une augmentation relative de l'énergie d'activation et justifie l'allure légèrement relevée de la courbe 1 de la figure 9(a). La notion d'encombrement permet donc, ici encore, d'expliquer d'une façon satisfaisante l'allure des courbes $Q^+ = f(1/d)$ et $Q^- = f(1/d)$.

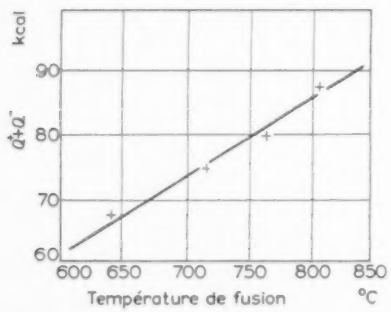

FIG. 10. Variation de la somme des énergies d'activation d'autodiffusion des deux ions des différents halogénures en fonction de leur température de fusion.

Ces résultats nous apportent en outre une confirmation du mécanisme de diffusion par la voie indirecte. En effet, l'examen des courbes 1 et 2 de la figure 9(a) montre que celles-ci s'écartent en fait assez peu de la linéarité, ce qui doit correspondre, comme nous l'avons déjà dit, à des facteurs d'encombrement relativement voisins pour les différents sels de la série; le mécanisme indirect répond parfaitement à cette conclusion.

Dans cette série de composés il n'a pas été possible d'étudier la plasticité par compression, le chlorure de rubidium changeant de structure sous forte pression et le chlorure de césium existant sous une forme cristalline différente à basse température. Mais on peut constater que la température de fusion des sels varie ici encore linéairement en fonction de la somme $Q^+ + Q^-$ (figure 10).

Transformation allotropique du chlorure de césium

La transformation allotropique du chlorure de césium qui passe de la structure cubique centrée (type CsCl) stable à basse température, à la structure cubique à faces centrées (type NaCl) de haute température a été étudiée par de nombreux auteurs[10,11,12,13] par diverses méthodes: mais il ne semble pas qu'une étude comparée des coefficients d'autodiffusion dans les deux phases ait été faite. Nous avons mesuré l'autodiffusion des deux ions en fonction de la température dans les domaines de stabilité des deux structures. D'après les courbes obtenues (figure 2) le point de transformation se situe à 466 ± 3°C ce qui s'accorde bien avec les résultats des autres auteurs. Lorsqu'on passe de la structure cubique centrée de basse température, à la structure cubique à faces centrées de haute température, la vitesse de diffusion des deux ions diminue. Si l'on se place près de la température de transformation, et de part et d'autre de celle-ci, le rapport des coefficients de diffusion est voisin de 10 aussi bien pour l'ion chlorure que pour l'ion césium. D'après les valeurs données au paragraphe 4 de la première partie, l'énergie d'activation du processus d'autodiffusion de chacun des deux ions est plus grande pour la structure de haute température que pour la structure de basse température. On peut également remarquer que dans les deux phases et dans le domaine de température étudié, l'ion chlorure diffuse plus vite que l'ion césium bien que son énergie d'activation soit plus élevée.

RÉFÉRENCES

1. CHEMLA M. Thèse, Paris (1954).
2. MAPOTHER D., CROOKS N., et MAURER R. *J. Chem. Phys.* **18,** 1231 (1950).
3. MURIN A. et LUR'E B. *Dokl. Akad. Nauk. S.S.S.R.* **73,** 933 (1950).
4. LAURENT J. F. et BÉNARD J. *C.R. Acad. Sci., Paris* **241,** 1204 (1955).
5. ASCHNER J. F. Thèse, University of Illinois, Urbana (1954).
6. ARNIKAR H. J. et CHEMLA M. *C.R. Acad. Sci., Pari* **242,** 2132 (1956).

7. WITT H. *Z. Phys.* **134,** 117 (1953).
8. SCHAMP H. W. et KATZ E. *Phys. Rev.* **94,** 828 (1954).
9. NOYER F. et LAURENT J. F. *C.R. Acad. Sci., Paris* **242,** 3068 (1956).
10. WEST C. D. *Z. Krist.* **88,** 94 (1934).
11. MENARY J. W., UBBELOHDE A. R., et WOODWARD J. *Proc. Roy. Soc.* **A208,** 158 (1951).
12. JOHNSON J. W., AGRON P. A., et BREDIG M. A. *J. Amer. Chem. Soc.* **77,** 2734 (1955).
13. HARPUR W. W. et UBBELOHDE A. R. *Proc. Roy. Soc.* **232,** 310 (1955).

VOL.
3
1957

J. Phys. Chem. Solids Pergamon Press 1957. Vol. 3. pp. 20–29.

ELECTRONIC PROPERTIES OF TRANSITION-METAL OXIDES—I

Distortions from cubic symmetry

J. D. DUNITZ* and L. E. ORGEL†

(*Received* 29 *March* 1957)

Abstract—The distortions from cubic symmetry which occur in certain transition-metal oxides, particularly those with the spinel structure, are discussed in terms of crystal (ligand) field theory. It is shown that many such distortions, including all the large ones, are related in a simple fashion to the electronic configuration of the metal ion and may be considered to arise as a consequence of a Jahn-Teller type of distortion.

INTRODUCTION

MUCH of the crystal chemistry of ionic compounds can be rationalized by the simple electrostatic theory in which the ions are regarded as charged, polarizable, almost rigid spheres to which a definite ionic radius can be assigned. In this theory the lattice energy is represented as the sum of the electrostatic (Madelung) potential, the polarization energy, and the Born repulsion energy arising from the incompressibility of the ions. In the case of transition-metal oxides, the simple electrostatic theory is incapable of accounting for much of the evidence. The spinels, for example, present a number of puzzling features which can in no way be interpreted by it. Thus, the chromites appear to be all normal spinels while the ferrites are inverted (see p. 25 for a description of the spinel structure); aluminates are normal except for $NiAl_2O_4$ which is inverted; Mn_3O_4 is a tetragonally distorted spinel elongated in the [001] direction in contrast to Fe_3O_4 which is cubic; $ZnMn_2O_4$, $CuFe_2O_4$, and $NiCr_2O_4$ are distorted in a similar fashion but $CuCr_2O_4$ distorts in just the reverse manner. (The crystal chemistry of spinels has recently been reviewed by GORTER.[1]) In these examples the charge of the transition-metal ion remains constant and the ionic radius changes only slightly so that it seems reasonable to examine the detailed electronic structure of the metal ion and to enquire whether a theory of its interaction with the crystal environment can account for the otherwise puzzling experimental evidence. In this series of papers we shall show that much of the physical and crystal chemistry of transition-metal oxides can, in fact, be rationalized by the application of crystal field theory along the general lines which have already proved successful in discussing co-ordination compounds. As far as we are aware, the only other approach of this type is that of ROMEIJN[2] who discussed the distribution of ions between the tetrahedral and octahedral sites in spinels in terms of a somewhat simplified version of the theory suggested by VAN SANTEN and VAN WIERINGEN.[3] He did not discuss distortions from cubic symmetry. GOODENOUGH and LOEB[4] have accounted for some of these, but on the basis of a rather special theory of chemical bonding which does not seem to be applicable generally. We shall show in this paper that their results and a number of others follow without the need for any special assumptions, by a generalization of a theory which we have already used to account for the stereochemistry of cupric and manganic co-ordination compounds.[5,6,7]

* Davy Faraday Research Laboratory, The Royal Institution, 21 Albemarle Street, London, W.1, England.

† University Chemical Laboratory, Pembroke Street, Cambridge, England.

VOL. 3 1957

CRYSTAL (LIGAND) FIELD THEORY

The electrostatic or crystal field theory was originally developed to account for the magnetic properties of the compounds of rare-earth and transition-metal ions.[8, 9, 10] During the past five years it has been applied with considerable success to the interpretation of spectroscopic, thermodynamic, and stereochemical data on discrete transition-metal complexes. In the course of this development, the fundamental basis of the theory has been extended to take into account the effect of covalent bonding in addition to the purely electrostatic effects of the environment. The name "ligand field theory" has been suggested[6] to distinguish the more complete from the purely electrostatic theory. Recent reviews[6, 11, 12, 13, 14] cover a wide range of applications to discrete co-ordination compounds.

The theory is also applicable to such solids as transition-metal oxides, fluorides, etc., in so far as these may be regarded as nearly ionic crystals. Before considering the problem in greater detail, we emphasize that the crystal-field stabilizations which we shall discuss constitute only a small fraction of the total lattice energy. We therefore make no attempt to predict the basic structural types of the various oxides since they are determined by the Madelung energy, etc., but limit ourselves to comparing different members of a series of compounds which have the same basic crystal structure, particularly the spinel structure. We shall show that certain characteristic differences between apparently analogous compounds are predicted by the theory.

We begin with an elementary account of crystal field theory, stressing those aspects which are specially relevant to the problems of crystal chemistry.

OCTAHEDRAL FIELDS

When a transition-metal ion is surrounded by six negative ions (e.g. oxide ions) in a regular octahedral arrangement, the five d orbitals no longer have the same energy but are split into two groups, a lower triplet, t_{2g}, and an upper doublet, e_g. The physical basis for this splitting is simply the electrostatic repulsion between the d electrons and the surrounding negative ions. The e_g orbitals ($d_{x^2-y^2}$, d_{z^2}) point directly at these ions and are thus destabilized. The t_{2g} orbitals (d_{xy}, d_{xz} and d_{yz}) point in directions where the field is least, i.e. between the ions, and are therefore stabilized (Fig. 1).

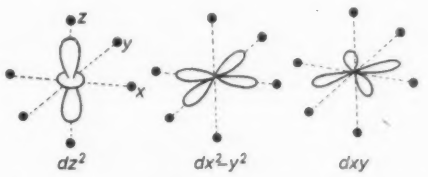

FIG. 1. Approximate charge densities of d orbitals in an octahedral complex: from left to right, d_{z^2}, $d_{x^2-y^2}$ and d_{xy} (d_{xz} and d_{yz} are exactly equivalent to d_{xy} but lying in the xz and yz planes respectively). The first pair, which point directly at the surrounding ions, form the doubly degenerate e_g orbital which is energetically less stable than the triply degenerate t_{2g} orbital formed by d_{xy}, d_{xz} and d_{yz}.

Although this simple picture does not take covalent bonding into account, its inclusion does not affect the fundamental result.[14] It can be shown from molecular-orbital theory that covalent bonding leads to exactly the same kind of splitting, into a lower, nonbonding, t_{2g} orbital and an upper, antibonding, e_g orbital. Only the magnitude of the energy separation between the two is affected. This quantity is actually determined experimentally, by analysis of spectroscopic data. For hydrated divalent ions it is about 10,000 cm^{-1} and for hydrated trivalent ions about 20,000 cm^{-1} with a rather wide range of variation, e.g. 7,800 cm^{-1} for Mn^{+2}, 11,500 cm^{-1} for V^{+2}.[14] Spectroscopic studies to be discussed in Part II show that the splitting is roughly the same in corresponding oxides and hydrates.

As successive electrons are introduced into the d shell they occupy the lowest available orbitals compatible with the total spin associated with the metal ion. In the "ionic" complexes with which we deal here, this is the same as the spin of the isolated metal ion. The configurations $(t_{2g})^m(e_g)^n$ where m and n are integers (Table 1) are exact for electron configurations other than d^2 and d^7, where nonintegral values apply in weak crystal fields.[3] The fields actually realized in oxides are sufficiently large to make the integral representation a good approximation even in these cases. We shall be particularly concerned with the configurations produced by d^4 and d^9, $(t_{2g})^3(e_g)^1$ and

$(t_{2g})^6(e_g)^3$ respectively, which are orbitally degenerate due to the partial occupation of the antibonding pair of e_g orbitals.

TETRAHEDRAL FIELDS*

The set of d orbitals is split into a doublet e orbital (d_{z^2}, $d_{x^2-y^2}$) and a triplet t_2 orbital (d_{xy}, d_{xz}, d_{yz}) by the electrostatic repulsion between the d electrons and the four negative ions placed at the vertices of a regular tetrahedron. In Fig. 2 the symmetrical relationship of d_{xy}, d_{xz} and d_{yz} is shown. The order of the levels is just the reverse of that in the octahedral case but the separation is smaller. BALLHAUSEN[15] has shown that the purely electrostatic theory leads to the value 4/9 for the ratio between the $e-t_2$ separation in a tetrahedral complex and the $t_{2g}-e_g$ separation in the corresponding octahedral complex, if the internuclear distance is supposed to be unchanged. This ratio would be somewhat different if covalent bonding were taken into account but there is evidence that the value 4/9 is quite close to that which really occurs.[16] The configurations for tetrahedral complexes, $(e)^m(t_2)^n$ listed in Table 1 are exact except for d^3 and d^8 and perhaps approximately correct even in these cases. We shall be particularly concerned with configurations which are degenerate with respect to the antibonding t_2 orbitals, i.e. $(e)^2(t_2)^1$, $(e)^2(t_2)^2$, $(e)^4(t_2)^4$ and $(e)^4(t_2)^5$.

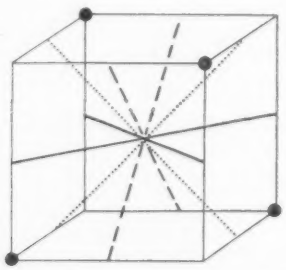

FIG. 2. Showing the symmetrical relationship of the d_{xy}, d_{xz} and d_{yz} orbitals which form the triply degenerate t_2 orbital in a tetrahedral complex.

* The assignment of the labels t_1 and t_2 to the two threefold degenerate representations in the group T_d is arbitrary and no convention seems to have been universally adopted. Here we use t_2 for the representation corresponding to the d_{xy}, d_{xz}, and d_{yz} orbitals. This is contrary to the convention adopted earlier by one of us (ORGEL L. E. *J. Chem. Phys.* **23**, 1004 (1955)) but seems to be employed somewhat more generally than the other.

THE JAHN-TELLER EFFECT

JAHN and TELLER[17] have shown that if the electronic state of a non-linear molecule is orbitally degenerate then there is always at least one vibrational co-ordinate along which the molecule may distort so as to lower its energy. In other words, the ground state of a non-linear molecule cannot be orbitally degenerate in its static equilibrium position. They have also shown that the degree of distortion increases with the bonding or antibonding power of the degenerate electrons.

The physical basis of the Jahn-Teller theorem is best illustrated by considering a definite example. The electronic ground state of the cupric ion (d^9) surrounded by a regular octahedron of negatively charged ligands is $(t_{2g})^6(e_g)^3$, degenerate with respect to the antibonding e_g orbitals. If the four ligands in the xy plane move towards the metal ion and the two along the z axis simultaneously move away, then by the electrostatic arguments employed before, the e_g doublet splits into two levels, d_{z^2} being somewhat stabilized and $d_{x^2-y^2}$ destabilized. A corresponding splitting of the lower triplet also occurs, leading to the situation shown in Fig. 3. By distorting from regular

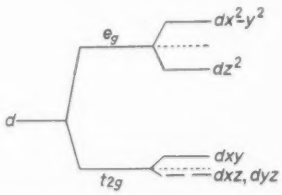

FIG. 3. Splitting of d orbital energy levels in a regular octahedral field and in tetragonal field with $c/a > 1$.

octahedral symmetry so as to leave the uppermost $d_{x^2-y^2}$ orbital only singly occupied, the complex is stabilized and the distortion proceeds until the extra stability gained in this way is just balanced by the energy required to stretch and compress the bonds. The opposite distortion producing four long bonds and two short ones would also seem to be quite compatible with the theory. In fact, however, it does not seem to occur, in cupric complexes at any rate.[7] ÖPIK and PRICE,[18] in a much more detailed study of the Jahn-Teller effect, have shown that the greater stability of the elongated tetragonal distortion may be ascribed to the effect of the non-harmonic nature of the

electrostatic potential between the central atom and the ligands.

Since the magnitude of the Jahn-Teller distortion depends on the bonding or antibonding power of the degenerate electrons, it will vary from one transition-metal ion to another, according to the electronic configurations. In octahedral co-ordination the t_{2g} orbitals are relatively non-bonding and consequently only small distortions are to be expected from the orbitally degenerate configurations $(t_{2g})^1$, $(t_{2g})^2$, $(t_{2g})^4(e_g)^2$, and $(t_{2g})^5(e_g)^2$ produced by 1, 2, 6 and 7 d electrons respectively. VAN VLECK has studied the first two cases in considerable detail and our qualitative conclusions are confirmed by his results.[19] The configurations $(t_{2g})^3(e_g)^1$ and $(t_{2g})^6(e_g)^3$, produced by 4 and 9 d electrons respectively, are degenerate with respect to the e_g orbitals which are strongly antibonding and should produce larger distortions. Even in the purely electrostatic theory it is clear that the Jahn-Teller distortion must be much larger for e_g than for t_{2g} electrons. (Compare the orientation of the $d_{x^2-y^2}$ orbital with that of the d_{xy} orbital in Fig. 1. The former is directed towards the negatively charged ions in the xy plane and so is much more effective in shielding them from the central cation.) This difference seems to be confirmed by VAN VLECK's calculations on the excited states $(t_{2g})^2(e_g)^1$ of the chromic ion.

In tetrahedral co-ordination it is the e orbitals which are non-bonding and the t_2 orbitals which are antibonding. Large distortions from regular tetrahedral symmetry are therefore expected to occur only for configurations which are degenerate with respect to the latter, i.e. for $(e_2)^2(t_2)^1(T_2)$, $(e)^2(t_2)^2(T_1)$, $(e)^4(t_2)^4(T_2)$ and $(e)^4(t_2)^5(T_1)$ produced by 3, 4, 8 and 9 d electrons respectively. The type of distortion required to remove the degeneracy here depends on whether the state is T_1 or T_2.

To destroy the threefold degeneracy it is sufficient to introduce any distortion which destroys the cubic symmetry of the complex. For the present, however, we shall consider only tetragonal distortions since rhombohedral distortions do not appear to be of importance in spinels. A tetragonal distortion preserves one of the fourfold alternating S_4 axes of the tetrahedron but destroys the threefold rotation axes, and the degenerate triplet orbital t_2 splits into a doublet and a singlet. Whether the doublet or the singlet lies lower depends on the ratio c/a. If $c/a < 1$ the tetrahedron is flattened. In the limit, as $c/a \to 0$, it becomes a square lying in the (001) plane. The d_{xy} orbital, concentrated in this plane is therefore destabilized; the d_{xz} and d_{yz} orbitals form a degenerate doublet which is stabilized. This type of splitting is shown in Fig. 4 whence it is evident

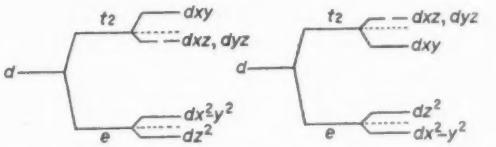

FIG. 4. Splitting of d orbital energy levels in a regular tetrahedral field and in tetragonally distorted fields with $c/a < 1$ (left) and $c/a > 1$ (right). These distortions may be described as flattening or elongation respectively of the tetrahedron along an S_4 axis.

that the orbital degeneracy is removed for T_1 states but not for T_2 states which still retain twofold degeneracy. The opposite distortion, tetragonal with $c/a > 1$, elongates the tetrahedron along an S_4 axis and produces just the reverse splitting, i.e. the singlet d_{xy} orbital is stabilized and the d_{xz}, d_{yz} doublet is destabilized. This leaves a double degeneracy for T_1 states but completely removes the degeneracy for T_2 states. The types of distortion caused by a single electron or hole in the t_2 orbitals (T_2 or T_1 states respectively) are shown diagrammatically in Fig. 5.

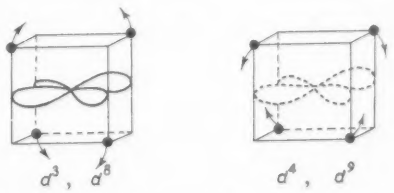

FIG. 5. Effect of (a) a single electron in the t_2 orbital (T_2 state), (b) a single hole in the t_2 orbital (T_1 state) on the stereochemistry of a tetrahedral complex. Only tetragonal distortions are considered.

The results of this discussion are summarized in Table 1.

THE JAHN-TELLER EFFECT IN CRYSTALS

In an isolated complex, of octahedral or tetrahedral symmetry, the Jahn-Teller effect may lead to the existence of a set of equivalent,

Table 1

No. of d electrons	Octahedral Configuration	Octahedral State	Distortion	Tetrahedral Configuration	Tetrahedral State	Distortion
1	(t_{2g})	T_{2g}	a	(e)	E	a
2	$(t_{2g})^2$	T_{1g}	a	$(e)^2$	A_2	0
3	$(t_{2g})^3$	A_{2g}	0	$(e)^2(t_2)$	T_2	b
4	$(t_{2g})^3(e_g)$	E_g	b	$(e)^2(t_2)^2$	T_1	c
5	$(t_{2g})^3(e_g)^2$	A_{1g}	0	$(e)^2(t_2)^3$	A_1	0
6	$(t_{2g})^4(e_g)^2$	T_{2g}	a	$(e)^3(t_2)^3$	E	a
7	$(t_{2g})^5(e_g)^2$	T_{1g}	a	$(e)^4(t_2)^3$	A_2	0
8	$(t_{2g})^6(e_g)^2$	A_{2g}	0	$(e)^4(t_2)^4$	T_2	b
9	$(t_{2g})^6(e_g)^3$	E_g	b	$(e)^4(t_2)^5$	T_1	c

Configurations, states, and type of Jahn-Teller distortion expected for n d electrons in octahedral and tetrahedral co-ordination. Explanation of letters describing distortion:

0, distortion zero except through higher-order mechanisms
a, distortion small
b, distortion large, tetragonal $c/a > 1$
c, distortion large, tetragonal $c/a < 1$

degenerate, distorted configurations which minimize the electrostatic energy. For the tetragonal distortions which we have considered, there are three such equivalent distortions, one along each of the cubic axes. The internal motion of a molecule in such a case would lead to each configuration occurring with equal probability.

Suppose now a Jahn-Teller distortion to be associated with each of a collection of ions arranged in a cubic lattice. Each ion undergoes a set of equivalent distortions and, provided that these are not too large, distortions of individual ions will not interact appreciably. In this situation, at a given instant, each ion will be in one of three equivalent configurations independent of the state of its neighbours, and the cubic symmetry of the lattice is retained in the statistical sense. To X-rays, the lattice would appear to be cubic, although with an abnormally high "temperature factor". If the distortions are sufficiently large, however, interactions between neighbouring ions become more important and we have the possibility of a co-operative phenomenon with consequent decrease in entropy on ordering. Below some transition temperature the lattice may then adjust itself so as to trap each ion in one definite configuration. We believe that this is the cause of the distortions from cubic symmetry which we discuss later in detail.

OXIDES WITH THE SPINEL STRUCTURE

The spinels afford a clear-cut test of our theory since the transition-metal ions in them can be varied widely without any concomitant change in the basic crystal structure. For this reason, we shall discuss them first, rather than the simpler perovskite and rocksalt structures.

The basic crystal structure is that of the mineral spinel, $MgAl_2O_4$. It is cubic, space group O_h^7 ($F3dm$) with the atoms distributed as follows:[20, 21]

8 metal ions in (a), 000: $\frac{1}{4}\frac{1}{4}\frac{1}{4}$: f.c.c.

16 metal ions in (d), $\frac{5}{8}\frac{5}{8}\frac{5}{8}$: $\frac{5}{8}\frac{7}{8}\frac{7}{8}$: $\frac{7}{8}\frac{5}{8}\frac{7}{8}$: $\frac{7}{8}\frac{7}{8}\frac{5}{8}$: f.c.c.

32 oxygen ions in (e), uuu: $u\bar{u}\bar{u}$: $\bar{u}u\bar{u}$: $\bar{u}\bar{u}u$
$\frac{1}{4}-u, \frac{1}{4}-u, \frac{1}{4}-u$: $\frac{1}{4}-u, \frac{1}{4}+u, \frac{1}{4}+u$
$\frac{1}{4}+u, \frac{1}{4}-u, \frac{1}{4}+u$: $\frac{1}{4}+u, \frac{1}{4}+u, \frac{1}{4}-u$: f.c.c.

The structure can be described as an approximately close-packed arrangement of oxygen ions with metal ions distributed amongst two kinds of interstices A and B, with tetrahedral and octahedral co-ordination respectively. The eightfold positions (a) are the tetrahedral sites, and the sixteenfold positions (d) octahedral. With $u = 0{\cdot}375$, the oxygens are in perfect cubic closest packing but usually u is slightly greater than this ideal value,

the oxygen ions moving in a [111] direction away from the nearest A site.

The unit cell contains 8 formula units XY_2O_4. If the 8 X ions occupy the A sites and the 16 Y ions the B sites, the structure is described as a "normal" spinel, $X(Y_2)O_4$. If, on the other hand, the tetrahedral A sites are occupied by 8 of the 16 Y ions, with the remaining 8 Y ions and the 8 X ions distributed amongst the octahedral B sites, the structure is described as an "inverted" spinel, $Y(XY)O_4$. A theory of the distribution of ions between tetrahedral and octahedral sites may be based on crystal field theory and will be described in Part II of this series.

Oxidic spinels have been prepared containing the following transition-metal ions:[1, 22] Mn^{+2}, Fe^{+2}, Co^{+2}, Ni^{+2}, Cu^{+2}, Zn^{+2}, V^{+3}, Cr^{+3}, Mn^{+3}, Fe^{+3}, Co^{+3}, Ti^{+4}, V^{+4}. From the previous discussion, we may expect large deviations from cubic symmetry to occur for the configurations d^4 and d^9 for ions in octahedral sites, and for d^3, d^4, d^8 and d^9 for ions in tetrahedral sites. The experimental evidence is that of the many compounds studied, the following spinels containing transition-metal ions deviate from cubic symmetry at room temperature or above, $CuFe_2O_4$, $CuCr_2O_4$, $NiCr_2O_4$, Mn_3O_4, $ZnMn_2O_4$. We shall now consider these individually.

Copper ferrite

Although copper ferrite, $CuFe_2O_4$, has the cubic spinel structure above 760°C, it becomes tetragonally distorted below this point. The c/a ratio increases with decrease in temperature and attains the value 1·06 (referred to the face-centred cell) at room temperature[23] when the structure is virtually completely inverted[24, 25] i.e. the Cu^{+2} ions occur almost entirely in the octahedra B sites while the Fe^{+3} ions occupy both octahedral and tetrahedral sites. PRINCE and TREUTING,[21] by a careful analysis of the neutron diffraction data, have shown that the oxygen octahedra are elongated parallel to the c axis but that the FeO_4 tetrahedra are undistorted, with the same dimensions as are found in the cubic inverse ferrites.

GOODENOUGH and LOEB[4] have suggested that the tetragonal distortion of copper ferrite is due to the tendency of the copper ion to form square covalent bonds. Our own theory predicts that a large tetragonal distortion with $c/a > 1$ should always be associated with octahedrally co-ordinated Cu^{+2} ions. The two theories thus lead in this case to the same result and the experimental evidence does not distinguish between them.

It should be mentioned, however, that, contrary to GOODENOUGH and LOEB's assertion, the occurrence of square coplanar cupric compounds is quite rare. We have shown in an earlier paper[7] that the distorted octahedral arrangement, with four nearer and two more distant ligands, is much more common and suggested that the square coplanar compounds might well be considered merely as a limiting case, with two ligands removed completely, rather than as a special class.

Since the considerations of this paper apply to fluorides in as much as they too can be regarded as essentially ionic complexes, it is of great interest that the cubic fluorite-like structure proposed by EBERT and WOITINEK[26] for copper fluoride, CuF_2, in which each Cu^{+2} ion is surrounded by 8 fluorines arranged at the corners of a cube, has recently been shown to be incorrect. The Cu^{+2} ion in such an environment would possess an orbitally degenerate ground state and would be expected to distort in such a way as to remove the degeneracy. A very recent re-investigation of the CuF_2 structure by BILLY and HAENDLER,[27] shows that it is actually a distorted version of the rutile structure in which each Cu^{+2} ion is surrounded by 4 fluorine neighbours at 1·93Å and 2 at 2·27Å in a distorted octahedral arrangement. The analogous difluorides of Mn^{+2}, Fe^{+2}, Co^{+2}, Ni^{+2} and Zn^{+2}, for which the Jahn-Teller effect is expected to be either absent or very small, possess the undistorted rutile structure in which the co-ordination of the fluorine ions about the metal ions is almost regular.[28]

Copper chromite

A tetragonal distortion of the spinel structure of copper chromite, $CuCr_2O_4$, was found by GREENWALD (see MCGUIRE, HOWARD and SMART[29]) who reported an axial ratio c/a of about 1·1. GOODENOUGH and LOEB[4] assumed copper chromite to be inverse and again attributed the tetragonal distortion to the tendency of the Cu^{+2} ion to form four square coplanar bonds by virtue of partial covalent bonding. Their interpretation cannot, however, be reconciled with more recent experimental evidence. In the first place, since Cr^{+3}

has perhaps a greater tendency than any other transition-metal ion to occupy octahedral sites,[2, 30] there seems to be no *a priori* reason to assume that copper chromite is inverted. MIYAHARA and OHNISHI[25] have recently established that, contrary to GOODENOUGH and LOEB's assumption, 90 per cent of the Cu^{+2} ions in copper chromite occur in tetrahedral sites and that, moreover, the tetragonal distortion is associated with an axial ratio of 0·91 i.e. the distortion is in the opposite sense to that in copper ferrite.

Our theory predicts that the T_1 degeneracy of tetrahedral Cu^{+2} is removed by a flattening of the tetrahedron to make $c/a < 1$ (Table 1). No distortion of the oxygen octahedra around the Cr^{+3} ion is expected from the Jahn-Teller effect. The tetragonal distortion of copper chromite is therefore attributed to the tendency of the CuO_4 tetrahedra to distort in such a way as to flatten them towards a square planar arrangement. If the space group of $CuCr_2O_4$ is the same as that of $CuFe_2O_4$, D_{4h}^{19}—$I4_1/amd$,[24] this can be done while leaving the CrO_6 octahedra more or less regular by suitable choice of the oxygen parameters.

As far as we are aware, the only other example of tetrahedrally co-ordinated Cu^{+2} ion which has been established occurs in crystals of Cs_2CuCl_4.[31] Here the $CuCl_4^{-2}$ ion consists of a tetrahedron distorted by flattening which removes the threefold axes but preserves an S_4 axis, just as in the above case. The crystal structure is closely related to that of Cs_2CoCl_4 except that the $CoCl_4^{-2}$ tetrahedra are much more nearly regular.[32] Thus the distortion which we propose may be quite general for tetrahedral Cu^{+2} compounds. We should expect similar distortions to occur in tetrahedral Cr^{+2} compounds if they exist.

The behaviour of spinels with the composition $CuFe_{2-x}Cr_xO_4$ has been studied by MIYAHARA and OHNISHI[25] and is particularly interesting. We have seen that for $x = 0$ we have a tetragonal distortion with $c/a = 1{\cdot}06$. The distortion decreases on addition of chromium and disappears at $x = 0{\cdot}4$. For values of x between 0·4 and 1·4 the structure appears to be cubic and the tetragonal distortion again sets in for $x > 1{\cdot}4$ but with c/a less than unity until at $x = 2$ it attains the terminal value of 0·91. Since, for $x = 0$ the spinel is almost completely inverted and for $x = 2$ it is almost normal this process must be accompanied by a continuous displacement of copper by chromium in the octahedral sites, the displaced copper ions being transferred to tetrahedral sites. The two extreme cases have already been discussed. In the intermediate range the theoretical description of the observed behaviour is more complicated. As x decreases from 2 to 1·4 the number of tetrahedral Cu^{+2} ions decreases and so the mean distortion decreases although the tetragonal structure remains stable. At $x = 1{\cdot}4$, the number of tetrahedral Cu^{+2} ions becomes too small to maintain a noncubic structure. The Jahn-Teller mechanism is still operative for both tetrahedral and octahedral Cu^{+2} ions, but their now random distribution in the structure means that, for any ion, each of the three tetragonal distortions occurs with equal probability, so that the structure is statistically cubic. At $x = 0{\cdot}4$, the distortions of the octahedrally co-ordinated Cu^{+2} ions are again able to stabilize a noncubic structure, but now with a quite different c/a ratio.

Tetragonal spinels containing manganic ions

Both Mn_3O_4 and $ZnMn_2O_4$ are tetragonally deformed spinels with c/a ratios of 1·16 and 1·14 respectively and unusually high transition temperatures of more than 1000°C.[33] The X-ray results for the latter compound indicate that the zinc ions occupy the tetrahedral sites, and since the two compounds form complete solid solutions it may be inferred that in Mn_3O_4 the tetrahedral sites are also occupied by divalent ions. Of the two structures $X[Mn^{+2}Mn^{+4}]O_4$ and $X[Mn_2^{+3}]O_4$ the former is regarded as more likely by VERVEY *et al.* who attributed the tetragonal distortions to an ordering of Mn^{+2} and Mn^{+4} ions among the octahedral sites.[34] GOODENOUGH and LOEB, however, have shown that this structure is incompatible with the physical properties and attribute the tetragonal distortion to the tendency of Mn^{+3} ions to form square covalent bonds.[4]

Our theory predicts a large tetragonal distortion with $c/a > 1$ for Mn^{+3} ions in octahedral co-ordination and thus supports the second formula $X[Mn_2^{+3}]O_4$. The same axial ratio occurs in Mn_2O_3 which is a tetragonally deformed spinel with 1/9 of the sites unoccupied,[33] i.e. $Mn_{\frac{8}{3}}^{+3}O_4$. We believe, with GOODENOUGH and LOEB, that the vacancies occur mainly in tetrahedral sites and that the octahedral sites are thus occupied by Mn^{+3}

ions to produce the distortion from cubic symmetry.

As far as we are aware, all the octahedral complexes containing Mn^{+3} ions which have been examined exhibit a similar distortion. BUERGER has shown that in crystals of manganite, MnO(OH) the metal ions are surrounded by four oxygen atoms at distances of 1·85 to 1·92Å and two more distant oxygens at 2·30Å in a distorted octahedral arrangement.[35] For another modification of MnO(OH), groutite, the X-ray analysis is not sufficiently accurate to determine the co-ordination with certainty but COLLIN and LIPSCOMB[36] admit the possibility that the oxygen octahedra may be distorted. A marked distortion occurs in manganic fluoride, MnF_3, where the Mn—F distances are reported[37] as two at 1·79, two at 1·91 and two at 2·09Å. We believe that the elongated tetragonal distortion will prove to be quite general for manganic compounds with octahedral co-ordination.

Nickel chromite

LOTGERING[22] has reported that nickel chromite, $NiCr_2O_4$ becomes tetragonal below 310°C. The axial ratio c/a is 1·025 at room temperature, 15° below the transition point, and presumably increases on further lowering of the temperature. According to ROMEIJN,[2] this compound is a normal spinel so that the Ni^{+2} ions occur almost exclusively in tetrahedral sites. The distortion is in the opposite sense to that in copper chromite, in agreement with our prediction (p. 23) that if the distortions from cubic symmetry are tetragonal then opposite distortions should occur for tetrahedrally co-ordinated ions in T_1 and T_2 states. For Ni^{+2} with the configuration $(e)^4(t_2)^4$ a tetragonal distortion with $c/a > 1$ is predicted, in agreement with the experimental result. This would be difficult to rationalize on the basis of GOODENOUGH and LOEB's theory[4] since any tendency of the Ni^{+2} ions in tetrahedral sites to form four coplanar bonds would presumably lead to flattening of the tetrahedra and hence an axial ratio of less than unity, as in the case of the copper compound.

No other example of tetrahedrally co-ordinated Ni^{+2} has so far been established with certainty by diffraction methods, so that it is not yet possible to say whether this type of distortion is of general occurrence.

OXIDES WITH THE PEROVSKITE STRUCTURE AMO_3

The ideal perovskite structural unit consists of a primitive cube with A, a large alkali, alkaline earth, or rare earth cation, at 000, M, generally a transition-metal ion, at $\frac{1}{2}\frac{1}{2}\frac{1}{2}$, and oxide ions at $\frac{1}{2}\frac{1}{2}0$, $\frac{1}{2}0\frac{1}{2}$ and $0\frac{1}{2}\frac{1}{2}$. Many compounds, titanates and niobates ($BaTiO_3$, $CaTiO_3$, $SrTiO_3$, $PbTiO_3$, $KNbO_3$, $NaNbO_3$) deviate from ideal cubic symmetry[38] but these deviations, which are invariably associated with ferroelectric effects, cannot be interpreted as Jahn-Teller distortions.

A distorted perovskite structure has also been found for samples of $LaMnO_3$ and (La, Ca)MnO_3 which contain a high proportion of Mn^{+3} ion.[39] The actual distortion is quite complicated but is approximately described as tetragonal, with $c/a<1$, and with a doubling of all three axes. A distortion of the MnO_6 octahedra to give two short bonds along the [001] direction and four longer ones in the *ab* plane would account for the observed axial ratio but not for the unit cell dimensions. GOODENOUGH[40] has provided a most convincing analysis of the neutron diffraction results[41] in terms of a model in which the Mn^{+3} ions form four short bonds, of which two are parallel to the *c* axis and the other two alternately along *a* and *b*, and two longer ones alternately along *b* and *a*. The individual octahedra are thus distorted in the usual manner but are coupled together to account for the doubling of the cell edges. Although GOODENOUGH's argument is based on his theory of partial covalent bonding, it could follow equally well from our own theory since Mn^{+3} with configuration $(t_{2g})^3(e_g)^1$ in octahedral co-ordination would be predicted to distort in just the same sense as that assumed by GOODENOUGH. We shall not discuss the other structures which occur in the $(Ca_xLa_{1-x})MnO_3$ system since GOODENOUGH has given a brilliant analysis of the situation. It is perhaps worth noting that similar distortions are to be anticipated for perovskite structures containing the Fe^{+4} ion.

TRANSITION-METAL MONOXIDES

At high temperatures all the transition-metal monoxides have the rocksalt structure with the exception of CuO, tenorite, in which each Cu^{+2} ion is surrounded by four oxygens lying in a plane.[42] This may be regarded as an extreme

example of the tetragonal distortion predicted for Cu^{+2}. Copper oxide is the only transition-metal monoxide for which large deviations from cubic symmetry are predicted, apart from CrO whose structure is still unknown. We expect CrO to depart from cubic symmetry at sufficiently low temperatures, and just possibly to crystallize with the tenorite structure. At high temperatures, cupric oxide forms a range of solid solutions in other transition-metal monoxides. These solutions, unlike those which do not contain cupric copper, show marked deviations from cubic symmetry.[43] We do not understand them in detail since the X-ray results are both complicated and incomplete, but we do believe that they are to be attributed to the Jahn-Teller distortions.

Several oxides show *very small* deviations from the rocksalt structure at low temperatures. Rhombohedral distortions occur in MnO (below 80°K), FeO (below 200°K) and NiO (below 500°K) while CoO becomes tetragonal, $c/a < 1$, below 290°K.[44] These distortions are much smaller than those which occur, for example, in the spinels, and are associated with a complex magnetic ordering process, the nature of which is still not quite clear.[45] In any case, they cannot arise solely as a consequence of the Jahn-Teller effect which would provide virtually no distortion in MnO and NiO and just the opposite distortion, with $c/a > 1$, in CoO to that which is observed, assuming that there is no doubling of the unit cell edges. Clearly a full discussion of these small distortions must take into account the effect of spin-orbit coupling and the interactions between metal ions.

CONCLUDING REMARKS

We have shown that all the available information on the distortions from cubic symmetry of transition-metal oxides, with the exception of that referring to certain small distortions which occur at low temperatures and which are often associated with magnetic ordering and ferroelectric effects, can be understood in terms of crystal (ligand) field theory. Our treatment is a very simplified one which takes into account only the *d* orbital directional properties and energies in fields of octahedral and tetrahedral symmetry. Spin-orbit coupling has been neglected although in certain cases, particularly for tetrahedral complexes, it may lead to splittings which are quite comparable with, although smaller than, the crystal field splittings. The distortions from cubic symmetry depend on the effect of the anisotropic electron density distributions of incompletely filled subshells on the surrounding ligands. We believe, however, that the principles which emerge from our treatment are quite general and will apply equally well to many other ionic solids. They form, in a sense, a second-order correction to the now well-recognized rules concerning octahedral, tetrahedral and square co-ordination. GOODENOUGH and LOEB's treatment of distortions in octahedral environments[4] has much in common with our own theory. The postulation of new types of chemical bonding, however, seems too special and does not permit applications to be made to tetrahedral complexes.

REFERENCES

1. GORTER E. W. *Philips Res. Rep.* **9,** 295 (1954).
2. ROMEIJN F. C. *Philips Res. Rep.* **8,** 304 (1953).
3. VAN SANTEN J. H. and VAN WIERINGEN J. S. *Rec. Trav. Chim. Pays-Bas* **71,** 420 (1952).
4. GOODENOUGH J. B. and LOEB A. L. *Phys. Rev.* **98,** 391 (1955).
5. ORGEL L. E. *J. Chem. Soc.* 4756 (1952).
6. ORGEL L. E. *Proc. Tenth Solvay Conference in Chemistry, Brussels* p. 289. (1956).
7. ORGEL L. E. and DUNITZ J. D. *Nature, Lond.* **179,** 462 (1957).
8. BETHE H. A. *Ann. Phys. Lpz.* **3,** 133 (1929).
9. VAN VLECK J. H. *Phys. Rev.* **41,** 208 (1932).
10. PENNEY W. G. and SCHLAPP R. *Phys. Rev.* **41,** 194 (1932).
11. MOFFITT W. and BALLHAUSEN C. J. *Ann. Rev. Phys. Chem.* **7,** 107 (1956).
12. NYHOLM R. S. *Proc. Tenth Solvay Conference in Chemistry, Brussels* (1956).
13. BJERRUM J. and JORGENSEN C. K. *Rec. Trav. Chim. Pays-Bas* **75,** 658 (1956).
14. GRIFFITH J. S. and ORGEL L. E. *Quart. Rev. Chem. Soc.* In press.
15. BALLHAUSEN C. J. *Dan. Mat. Fys. Medd.* **29,** No. 4 (1954).
16. JORGENSEN C. K. Private communication.
17. JAHN H. A. and TELLER E. *Proc. Roy. Soc.* **A161,** 220 (1937).
18. ÖPIK U. and PRYCE M. H. L. *Proc. Roy. Soc.* **A238,** 425 (1957).
19. VAN VLECK J. H. *J. Chem. Phys.* **7,** 472 (1939).
20. BRAGG W. H. *Phil. Mag.* **30,** 305 (1915).
21. *International Tables for X-ray Crystallography* Kynoch Press, Birmingham (1952).
22. LOTGERING F. K. *Philips Res. Rep.* **11,** 190 (1956).

23. Weil L., Bertaut E. F., and Bochirol L. *J. Phys. Radium* **11,** 208 (1950).
24. Prince E. and Treuting R. G. *Acta Cryst.* **9,** 1025 (1956).
25. Miyahara S. and Ohnishi H. *J. Phys. Soc. Japan* **12,** 1296 (1956).
26. Ebert F. and Woitinek H. *Z. Anorg. Chem.* **210,** 269 (1933).
27. Billy C. and Haendler H. M. *J. Amer. Chem. Soc.* **79,** 1049 (1957).
28. Stout J. W. and Reed A. S. *J. Amer. Chem. Soc.* **76,** 5279 (1954).
29. McGuire T. R., Howard L. N., and Smart J. S. *Ceramic Age* **60,** 22 (1952).
30. Dunitz J. D. and Orgel L. E. *J. Phys. Chem. Solids* To be published.
31. Helmholz L. and Kruh R. F. *J. Amer. Chem. Soc.* **74,** 1176 (1952).
32. Porai-Koshits M. A. *Trud. Inst. Krist. Akad. Nauk S.S.S.R.* **10,** 117 (1954).
33. Mason B. *Amer. Min.* **32,** 426 (1947).
34. Vervey E. J. W., Braun P. B., Gorter E. W., Romeijn F. C., and van Santen J. H. *Z. Phys. Chem.* **198,** 6 (1951).
35. Buerger M. J. *Z. Krist.* A **95,** 163 (1936).
36. Collin R. L. and Lipscomb W. N. *Acta Cryst.* **2,** 104 (1949).
37. Hepworth M. A., Jack K. H., and Nyholm R. S. *Nature, Lond.* **179,** 211 (1957).
38. Megaw H. *Acta Cryst.* **5,** 739 (1952); **7** 187 (1954).
39. Yakel H. L. *Acta Cryst.* **8,** 394 (1955).
40. Goodenough J. B. *Phys. Rev.* **100,** 564 (1955).
41. Wollan E. O. and Koehler W. C. *Phys. Rev.* **100,** 545 (1955).
42. Tunell G., Posnjak E., and Ksanda C. J. *Z. Krist.* **90,** 120 (1935).
43. Bertaut F. and Delorme C. *C.R. Acad. Sci., Paris* **233,** 356 (1951); **238,** 1829 (1954).
44. Greenwald S. *Acta Cryst.* **6,** 396 (1953).
45. Li Y. Y. *Phys. Rev.* **100,** 627 (1955).

VOL. 3 1957

J. Phys. Chem. Solids Pergamon Press 1957. Vol. 3. pp. 30–36.

THE CRYSTAL STRUCTURE AND FERRIMAGNETISM OF YTTRIUM-IRON GARNET, $Y_3Fe_2(FeO_4)_3$

S. GELLER and M. A. GILLEO

Bell Telephone Laboratories, Incorporated, Murray Hill, New Jersey

(*Received* 3 *April* 1957)

Abstract—A refinement of the crystal structure of yttrium-iron garnet (cubic space group—*Ia3d*) has been carried out by application of the least-squares method of calculation to single-crystal X-ray data. The oxygen parameters are $x = -0{\cdot}027_4$, $y = 0{\cdot}057_2$, $z = 0{\cdot}149_2$; the tetrahedral iron-oxygen distance is 1·88 Å, the octahedral iron-oxygen distance is 2·00 Å and the yttrium-oxygen distances are 2·37 and 2·43 Å. None of the oxygen polyhedra is regular even though the space group would allow the tetrahedra and octahedra to be regular simultaneously.

Interionic distances and angles which are important to the interaction between magnetic ions have been calculated. The strongest interactions probably occur between Fe^{3+} in 16(*a*) and 24(*d*) positions and between Fe^{3+}, 24(*d*), and M^{3+}, a magnetic rare-earth ion substituted for yttrium, in the 24(*c*) positions. Interactions between crystallographically equivalent ions are all small. The number of interactions per Fe^{3+} ion per formula unit is 3/5 that in a spinel "ferrite" and, correspondingly, the Curie temperature observed is 0·64 that of magnetite.

No change of symmetry is observed up to 900°C, and the behavior of the lattice constant, a_0 vs. T is consistent with the presence of a Curie transition.

INTRODUCTION

CONSIDERABLE interest in the rare earth-iron garnets has existed since their discovery[1,2] particularly because they constitute a new family of cubic ferrimagnetic compounds which belong to space group $O_h(10)$–*Ia3d* which was not previously encountered in studies of magnetic oxides. There are now the possibilities of testing previously established ideas of magnetic interactions on these new compounds and of expanding some of these ideas because these compounds represent the first case in which rare-earth ions are known to contribute to the spontaneous magnetization.[1,3,4,5]

A quantitative understanding of the interaction between magnetic ions requires an accurate determination of the positions of all ions. For yttrium-iron garnet this has been made possible by the availability of single crystals produced by NIELSEN.[6]

The excellent and extensive work of MENZER[7] on the natural garnets established the structure, although, because X-ray diffraction intensities from powders were used, great accuracy could not be attributed to the O^{2-} ion parameters.

The first extensive and definitive investigation of the role of yttrium and aluminum in the garnet structure was made by YODER and KEITH[8] who studied the system

$$(Mn_{3-x}Y_x)\,Al_2\,(Si_{3-x}Al_x)O_{12}.$$

They succeeded in synthesizing the compound $Y_3Al_2(AlO_4)_3$, an yttrium-aluminum garnet. Later, KEITH and ROY,[9] in an investigation of reaction products of rare-earth and transition-metal oxides, produced garnets: $Y_3Ga_2(GaO_4)_3$, $Sm_3Al_2(AlO_4)_3$, $Sm_3Ga_2(GaO_4)_3$. Attempts by the latter authors to produce the garnet $Sm_3Fe_2(FeO_4)_3$ were unsuccessful.

Recently BERTAUT and FORRAT[1] discovered that spontaneous magnetization, originally attributed by others to a perovskite-like phase, actually originated in a garnet phase which was present. This phase had probably resulted from incomplete reaction of the mixed oxides. In these Laboratories the ferrimagnetism in rare earth-iron garnets was discovered independently and in a different way which has been described in a previous communication.[2] Our magnetic data on $Y_3Fe_2(FeO_4)_3$ are

in agreement with those of ALÉONARD, BARBIER and PAUTHENET.[5] The work of PAUTHENET on gadolinium-iron garnet[3] has clarified the interpretation of data previously in disagreement with that of GILLEO on $GdFeO_3$.[10] Recent work by BERTAUT and PAUTHENET[11] establishes the magnetic properties and cell sizes of a large number of rare earth-iron garnets.

A neutron diffraction study of yttrium-iron garnet has been carried out by BERTAUT *et al.*[12] and by PRINCE[13] of these Laboratories. A neutron diffraction study must establish the oxygen parameters and the magnetic structure.* The results of the two investigations are essentially in agreement with regard to the magnetic nature of the $Y_3Fe_2(FeO_4)_3$, but there are differences in the oxygen parameters. The single crystal analysis, which should give more accurate results, leads to a set of oxygen-ion parameters which, except for the x-co-ordinate, lie between the two sets obtained by the different authors.

EXPERIMENTAL

The crystal used to obtain the data for this analysis is a sphere of 0·23 mm diameter made from a single crystal produced by NIELSEN. To obtain adequate intensity of the most important reflections in reasonable exposure time, CoK_α radiation was used. The crystal was aligned along a [110] direction and all odd-numbered layer-line† photographs were taken about this direction. The intensities were estimated visually by comparison with an intensity scale. The following factors were applied to the layer-line data to convert intensities to $|F|^2$ values: LORENTZ-polarization, TUNELL rotation,[14] absorption, and spot extension corrections.[15] Tables prepared by BOND[16] were used for the absorption correction. Because several reflections were common to two or more photographs, it was a simple matter to put all reflections on the same scale. Further data for determination of the space group were obtained from Buerger precession photographs taken with a [100] direction as the precession axis.

High temperature experiments

Samples used in these experiments were prepared by coprecipitation of the hydroxides from nitric acid solution. The washed mixture of hydroxides was dried at 200°C, ground in an agate mortar, heated gradually to 600°C over a period of 4 hr, kept at 600°C for two hours and then reground. Samples were prepared in pellet form and fired at 1450°C for 16 hr in oxygen. Powder taken from one of the pellets was put into a thin-walled glass capillary‡ which was mounted in a high temperature camera designed and built by BOND of these Laboratories. Lattice constants were determined from photographs taken at various temperatures (Fig. 4) with CoK radiation.

REFINEMENT OF THE STRUCTURE

The symmetry of the single crystal photographs is O_h–$m3m$ and only the following types of reflections are present: (hkl), $h+k+l = 2n$; ($hk0$), $h = 2n$, $k = 2n$; (hhl), $l = 2n$, $2h+l = 4n$. Thus $O_h(10)$–$Ia3d$§ is uniquely established as the most probable space group for $Y_3Fe_2(FeO_4)_3$. The room temperature lattice constant, which was determined from a powder photograph, is 12·376 Å (probably $\pm$0·004 Å). There are eight formula units in the cubic unit cell; the corresponding X-ray density is 5·17 g/cm^3.

The results of this analysis and that of PRINCE[13] indicate that $Y_3Fe_2(FeO_4)_3$ is isostructural with the natural garnets. In the garnet type structure the Y^{3+} ions occupy positions 24(c), Fe^{3+} ions occupy positions 24(d) and 16(a), and oxygen ions occupy positions 96(h). Of these positions only the 96(h) involve parameters (x, y, z) which must be refined.

It is fortunate that in this structure there is a substantial number of reflections which have contributions from the oxygen ions only. These have two indices odd and the third divisible by 4. Furthermore there is an even larger number of reflections to which there is no contribution from the 16(a) Fe^{3+} ions. The contribution from the remaining ions is eight times the difference between the scattering of yttrium and iron. These were, therefore, the only reflections used in the refinement. Those to which the metal atoms contribute very heavily have been given zero weight.

The contributions of the oxygen ions to the structure amplitudes were calculated on the IBM 650 computer using PRINCE's parameters (Table 1). The programming and calculation were carried out by BOOTH.[17] The

* The previously unknown yttrium neutron scattering cross section must also be determined. For this reason a neutron diffraction study of $Y_3Al_2(AlO_4)_3$ has also been carried out by PRINCE.

† WEISSENBERG.

‡ A fused silica capillary was used for the photograph taken at 600 and 900°C (Fig. 4).

§ Below the Curie temperature, the crystal possesses spontaneous magnetization in one direction in each magnetic domain so that the symmetry cannot be truly cubic even though deviations from cubic symmetry are not detected by X-ray diffraction.

scattering factors for the yttrium and iron ions were obtained from the International Tables[18] and for oxygen ions from the paper by BERGHUIS *et al.*[19] Corrections were made for ionicity; these were, of necessity, somewhat arbitrary. Because several of the reflections resulted exclusively from oxygen ion contributions, it was not too difficult to estimate a temperature factor for the oxygens and a scale factor by which the observed structure amplitudes were placed on an absolute basis. The temperature factor so deduced for the oxygen ions was 2·0 Å². In the initial calculations zero temperature factors were assumed for the Y^{3+} and Fe^{3+} ions, although it was recognized that this was physically impossible.

Table 1. Oxygen parameters obtained by neutron diffraction

	x	y	z
PRINCE[12]	—·028	0·060	0·151
BERTAUT *et al.*[12]	—·029	0·054	0·148

Some time after PRINCE had obtained the oxygen parameters from neutron diffraction data, the results of BERTAUT *et al.*[12] appeared (Table 1). The differences between the y and z parameters of these two sets are rather substantial and amount to 0·07 and 0·04 Å respectively. Calculations of structure amplitudes were carried out with the parameters of BERTAUT *et al.* It appeared that neither set was entirely satisfactory as far as the X-ray data were concerned. Examination of the results indicated that the set of parameters which would best satisfy the X-ray data probably would be somewhere between the two sets.

The oxygen parameters obtained by PRINCE were used as a starting point for the least-squares refinement of the structure. These calculations were carried out on the IBM 704 computer. The main program used was that devised by Dr. D. SAYRE of IBM*; the auxiliary program for space group $O_h(10)$–*Ia3d* was worked out by Miss D. C. LEAGUS of these Laboratories and the calculation carried out by Mr. A. H. HATCH of IBM. The reflection amplitudes involved had two indices odd and the third divisible by 2. Thus only (*hhl*) reflections were weighted one-half. All other (*hkl*) reflections were weighted one except those which were not observed. These were given very low weights, and were included in the calculation because only then would the program give the calculated structure amplitude for these reflections. After the first iteration, changes in co-ordinates were very small, so that we had confidence in the final parameters. The results of the last three iterations are given in Table 2. The values given in the last row of this table are considered to be the final ones.

A comparison of calculated with observed structure amplitudes is given in Table 3. If the (*hhl*) structure factors are weighted one-half and the unobserved reflections counted as one-half the minimum observable reflections, the discrepancy factor, $(\Sigma \| |F_0| - |F_c| \| / \Sigma |F_0|)$, is 9·2 per cent. If the unobserved reflections are excluded, 8.5 per cent is the result. The discrepancy factor for the sixteen observed reflections resulting from oxygen-ion contributions only is 9·2 per cent. As calculated from the least-squares data, the errors in co-ordinates are

$$\sigma(x) = \sigma(y) = \sigma(z) = 0{\cdot}0009.$$

Apparently the evidence speaks for high accuracy of the oxygen parameters, even though it is possible, and even probable, that the accuracy is not quite as high as indicated by the numbers.

It is worth noting that the agreement for the reflections from oxygen-ions only is as good as it is for the other reflections. Also the interaction of the positional and temperature parameters appears to be negligible. Intensities for neutron diffraction

* Only diagonal terms in the least-squares matrix are computed.

Table 2. Results of last three least-squares iterations

Oxygen co-ordinates			Temperature factors Å²			Scale factor, K	Discrepancy factor R (per cent)*
x	y	z	O^{2-}	Y^{3+}	Fe^{3+}		
—0·0272	0·0571	0·1490	2·11	0·179	0·598	0·993	10·8
—0·0276	0·0572	0·1494	2·03	0·148	0·655	0·983	9·7
—0·0274	0·0572	0·1492	2·05	0·161	0·631	0·988	9·6

* These values are actually high. They do not consider the half-weighting of the (*hhl*) amplitudes and do include the unobserved reflections counted as half the minimum observable F.

Table 3. Comparison of calculated with observed structure amplitudes

(*hkl*)	Amplitude Obs.	Amplitude Calc.	(*hkl*)	Amplitude Obs.	Amplitude Calc.	(*hkl*)	Amplitude Obs.	Amplitude Calc.
121	84·1	−100·5	671	< 31·5	20·4	581	46·3	−49·1
123	57·9	−68·3	673	60·2	−71·1	583	60·5	−71·0
125	169·9	−160·7	677	26·1	−34·8			
127	83·8	−89·6	679	95·8	85·4	691	86·1	80·1
129	55·3	−58·7						
1,2,11	95·0	−95·8	781	25·3	−25·5	7,10,1	90·3	84·7
1,2,13	24·8	−38·5	783	< 25·6	−4·6	7,10,3	71·1	68·7
			785	< 21·6	6·2	7,10,5	50·0	56·1
233	59·0	−71·5						
235	145·6	−141·7	891	39·7	−42·7	8,11,1	< 8·7	−6·6
237	30·0	24·5	893	< 18·7	−4·0			
239	73·3	−76·8	895	14·4	19·9	161	182·5	207·3
2,3,11	68·0	66·6				1,6,11	68·4	67·3
2,3,13	68·5	−76·9	9,10,1	61·9	−71·2			
						277	90·5	92·5
341	86·1	95·4	147	38·0	42·3	279	40·0	−46·9
345	< 33·4	−15·4	149	51·3	−56·5	2,7,11	81·4	82·2
347	41·5	43·8	1,4,11	26·5	−21·4			
349	38·5	−38·7	1,4,13	< 8·7	6·0	381	< 34·9	−17·8
3,4,11	23·8	20·3						
			255	125·4	−141·9	5,10,1	128·0	−106·6
451	26·0	−25·1	257	48·7	41·0	5,10,3	79·9	−71·9
457	59·1	59·7	259	61·4	−69·9	5,10,5	59·5	−59·1
459	< 25·6	−11·0	2,5,11	76·2	74·3			
4,5,11	< 16·3	−8·1				299	91·6	−93·8
			361	46·4	−44·1			
561	78·5	86·8	363	56·2	−59·5	3,10,1	62·4	61·6
563	39·4	41·5	369	77·0	−70·0	3,10,3	74·3	89·4
565	120·4	117·4	3,6,11	116·8	−109·6			
567	115·6	112·9				5,12,1	< 16·2	−7·4
569	75·3	75·6	479	< 20·1	−4·6	5,12,3	27·5	29·8
5,6,11	62·4	69·5	4,7,11	31·3	35·3			

which were calculated with the oxygen parameters obtained by the analysis described herein are still in good agreement with the intensities observed by PRINCE.[13]

DISCUSSION

In the garnet structure each of three positive-ion positions is associated with a different co-ordination polyhedron of oxygen ions: for Y^{3+}[24(*c*)] an eight-cornered twelve-sided figure (Fig. 1); for Fe^{3+} [16(*a*)] an octahedron (Fig. 2); for Fe^{3+} [24(*d*)] a tetrahedron (Fig. 3). None of these polyhedra is regular with respect to edge length even though the oxygen parameters would permit the octahedra and tetrahedra to be regular

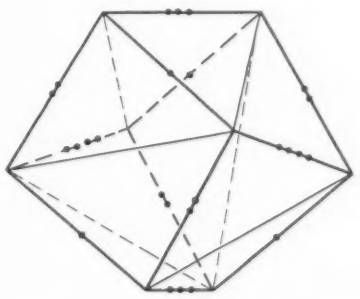

FIG. 1. Co-ordination polyhedron of oxygen ions about the yttrium ion

(· 2·68, · · 2·81, · · · 2·87, · · · · 2·96 Å).

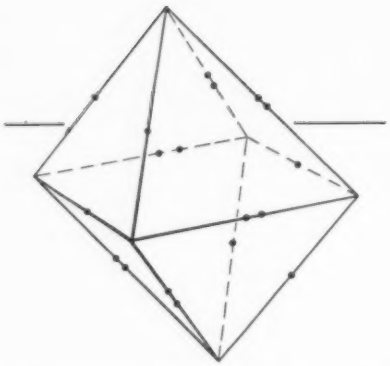

FIG. 2. Co-ordination octahedron of oxygen ions about an $Fe^{3+}(a)$ ion (· 2·68, ·· 2·99 Å).

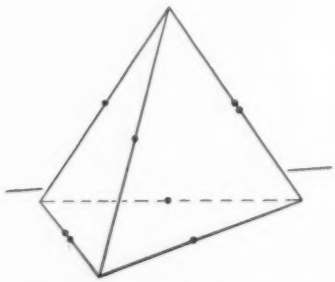

FIG. 3. Co-ordination tetrahedron of oxygen ions about an $Fe^{3+}(d)$ ion (· 3·16 Å, ·· 2·87 Å).

simultaneously.[7] However in the latter two polyhedra all center-to-corner (Fe^{3+}–O^{2-}) distances are equal (Table 4): for the octahedra 2·00 Å; for the tetrahedra 1·88 Å. There are two different O^{2-} Fe^{3+}–O^{2-} angles in each case: for octahedra 87·2° and 96·6°; for tetrahedra 99·9° and 114·3°. Each oxygen ion is common to two eight-cornered polyhedra, one octahedron and one tetrahedron. Thus each oxygen ion has as nearest positive-ion neighbors two Y^{3+}, one $Fe^{3+}(a)$ and one $Fe^{3+}(d)$ ions (Tables 4 and 5). This feature of the structure is most important to the magnetic properties.

The "exchange" interaction of two magnetic ions, Me, through an oxygen ion between them was first conceived by KRAMERS[20] and has since been more extensively studied by ANDERSON[21] and VAN VLECK.[22] In this interaction the overlap of the $2p$ electrons (with dumbbell-shaped distribution) of the oxygen ion with the electronic distribution of the magnetic ions is an important feature.

Table 4. Nearest-neighbor interionic distances in yttrium-iron garnet

Ion	Interionic distances (Å)
Y^{3+}	$4Fe^{3+}(a)$ at 3·46 $6Fe^{3+}(d)$ at 3·09(2), 3·79(4) $8O^{2-}$ at 2·37(4), 2·43(4)
$Fe^{3+}(a)$	$2Y^{3+}$ at 3·46 $6Fe^{3+}(d)$ at 3·46 $6O^{2-}$ at 2·00
$Fe^{3+}(d)$	$6Y^{3+}$ at 3·09(2), 3·79(4) $4Fe^{3+}(a)$ at 3·46 $4Fe^{3+}(d)$ at 3·79 $4O^{2-}$ at 1·88
O^{2-}	$2Y^{3+}$ at 2·37, 2·43 $1Fe^{3+}(a)$ at 2·00 $1Fe^{3+}(d)$ at 1·88 $9O^{2-}$ at 2·68(2), 2·81, 2·87, 2·96, 2·99(2), 3·16(2)

Table 5. Interionic angles in yttrium-iron garnet

Ions	Angles (°)
$Fe^{3+}(a)$–O^{2-}–$Fe^{3+}(d)$	126·6
$Fe^{3+}(a)$–O^{2-}–Y^{3+}*	102·8
$Fe^{3+}(a)$–O^{2-}–Y^{3+}†	104·7
$Fe^{3+}(d)$–O^{2-}–Y^{3+}*	122·2
$Fe^{3+}(d)$–O^{2-}–Y^{3+}†	92·2
Y^{3+} –O^{2-}–Y^{3+}	104·7
$Fe^{3+}(a)$–O^{2-}–$Fe^{3+}(a)$ (4·41)‡	147·2
$Fe^{3+}(d)$–O^{2-}–$Fe^{3+}(d)$ (3·41)	86·6
$Fe^{3+}(d)$–O^{2-}–$Fe^{3+}(d)$ (3·68)	78·8
$Fe^{3+}(d)$–O^{2-}–$Fe^{3+}(d)$ (3·83)	74·7
$Fe^{3+}(d)$–O^{2-}–$Fe^{3+}(d)$ (3·83)	74·6

* Y^{3+}–O^{2-} distance = 2·43 Å.

† Y^{3+}–O^{2-} distance = 2·37 Å.

‡ Numbers in parentheses are the longer $Fe^{3+}(a$ or $d)$–O^{2-} distances. The shorter distances (Table 4) are $Fe^{3+}(a)$–O^{2-} = 2·00, $Fe^{3+}(d)$–O^{2-} = 1·88 Å.

The interaction increases with the overlap and, accordingly, will be greatest for short Me–O distances and for Me_1–O–Me_2 angles near 180°. Therefore in yttrium-iron garnet the strongest interaction (Table 5) will probably occur between $Fe^{3+}(a)$ and $Fe^{3+}(d)$ for which the $Fe^{3+}(a)$–O^{2-}–$Fe^{3+}(d)$ angle is 126·6°. Because interaction of this type is

known to be negative in ferrites, as was first recognized by NÉEL,[23] and because there are $3Fe^{3+}(d)$ and $2Fe^{3+}(a)$ ions per formula unit, there should be a net magnetic moment corresponding to that of one Fe^{3+}, i.e. $5\mu_B$. Verification of this expectation is found in measurements of the saturation magnetization, $\sigma_{\infty,0}$, reported by ALÉONARD *et al.*[5] and by us.[2] The neutron diffraction studies of BERTAUT *et al.*[12] and PRINCE[13] of these Laboratories establish that the alignment of the ionic moments is as assumed.

If yttrium is replaced by a rare-earth ion, M^{3+}, we might expect a strong interaction only with $Fe^{3+}(d)$ ions for which the M^{3+}–O^{2-}–$Fe^{3+}(d)$ angle is 122·2° (Table 5). In this case $\sigma_{\infty,0}$ would correspond to $3n_B(M^{3+})$–5 per formula unit as has been observed by PAUTHENET[4] for all rare-earth ions from Gd to Lu and verified by us for Gd.

In a comparison of the garnets with the ferrites, several important differences in magnetic interaction are noticed. There is probably no appreciable interaction between magnetic ions in equivalent sites in a garnet structure since either oxygen-magnetic ion distances are too large or the Me_1–O–Me_2 angle is nearly 90° (Table 5). In the spinel structure, each octahedral iron ion can interact appreciably with twelve other octahedral iron ions. YAFET and KITTEL[24] first suggested that simple parallel and anti-parallel alignment of magnetic ion moments may not occur in this case. Non-parallel moments of Cr^{3+} in octahedral sites were first observed in $CuCr_2O_4$ by PRINCE.[25]

Another difference in these two structures is found in the number of other magnetic ions with which a given ion simultaneously interacts most strongly. In a formula unit of garnet each of two octahedral ions, 16(*a*), interacts with six tetrahedral ions, 24(*d*), and each of three tetrahedral ions interacts with four octahedral ions, corresponding to a total of twenty-four interactions. In a formula unit of spinel each of two octahedral ions, 16(*d*), interacts with six tetrahedral ions, 8(*a*), and each tetrahedral ion interacts with twelve octahedral ions, also corresponding to a total of twenty-four interactions. However, there are five magnetic ions per formula unit of yttrium-iron garnet, but only three in a spinel. Therefore the number of interactions per ion and, consequently, the strength of interaction per magnetic ion in garnet is 3/5 that in spinel. Because the strength of interaction $J \simeq kT_c$, a lower Curie temperature, T_c, would therefore be expected for yttrium-iron garnet ($T_c = 545°K$)* for which it is 0·64 that of magnetite (848°K).†

The comparison of the interaction distances and angles in the yttrium-iron garnet with those in a spinel may be made by referring to the case of manganese ferrite ($MnFe_2O_4$) for which HASTINGS and CORLISS[26] have accurately determined the oxygen parameter. In this material the Me(*a*)–O–Me(*d*) angle is 123·0° compared with Me(*a*)–O–Me(*d*) angle of 126·6° for yttrium-iron garnet (Table 5). The distance of an oxygen ion from positive ions in the tetrahedral sites in manganese ferrite is 1·95 Å compared with 1·88 Å for yttrium-iron garnet. The larger value would be expected in manganese ferrite because about 80 per cent of the tetrahedral sites are occupied by Mn^{2+},[26] an ion of larger radius than Fe^{3+}. The octahedral ion-oxygen ion distance is 2·01 Å in the ferrite and 2·00 Å in the garnet.

The ferrimagnetism of yttrium-iron garnet is distinguished from that of ferrites in another important way. In the garnet each $Fe^{3+}(a)$ ion interacts only with $Fe^{3+}(d)$ ions, i.e. all 16(*a*) or 24(*d*) ions are not only crystallographically but also magnetically equivalent. This is never the case for the 16(*d*) ions in magnetic ferrites because these ferrites are never entirely normal, i.e. the divalent ions are never solely in the tetrahedral, 8(*a*), positions but a fraction of these ions is distributed at random on the octahedral, 16(*d*), sites.

The yttrium-iron garnet structure is a rather loose one: The X-ray density of $Y_3Fe_2(FeO_4)_3$ is 5·17 g/cm³ with a volume of 236·9 Å³ per formula unit. If one Fe per formula unit could be replaced by a heavier Y with no structure change the density of the resulting $4YFeO_3$ would be 5·40 g/cm³. Actually the density of the perovskite-like compound, $YFeO_3$, is 5·67 g/cm³ and the volume 225·9 Å³.[27] Because no metal ion to oxygen ion distances appear to be unduly long (Table 4) the arrangement of oxygen ions in the garnet appears to be inefficient.

The variation of the lattice constant, a_0, with

* From measurements on a single crystal furnished by Nielsen of these Laboratories.

† The structure dependence of the Curie temperature and the strength of the Fe–O–Fe interaction will be discussed in more detail elsewhere (M. A. GILLEO, to be published).

temperature for yttrium-iron garnet differs from that of a typical natural garnet, grossularite[28] (Fig. 4). The variation of slope of the a_0 vs. T

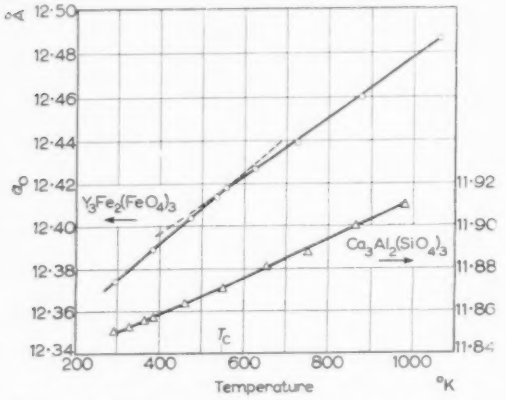

FIG. 4. Lattice constant vs. temperature for yttrium-iron garnet and grossularite.[28]

curve in the neighbourhood of 272°C is consistent with the presence of a Curie transition at this temperature. The precision of the data (±0·004 Å) does not permit us to establish the shape of the curve in more detail than that of the two straight-line approximations employed.

Acknowledgements—The authors wish to thank Dr. J. W. NIELSEN for making available the crystals used in this study, Dr. E. PRINCE for his interest and for supplying us with the results of his neutron diffraction analyses, Messrs. V. B. BALA and D. W. MITCHELL for technical assistance, and Mr. H. M. YATES for the drawings in this paper.

We wish also to thank Dr. CAROLINE H. MACGILLAVRY for her kindness in sending us the mass absorption coefficients of the elements for CoK_α radiation.

REFERENCES

1. BERTAUT F. and FORRAT F. *C.R. Acad. Sci., Paris* **242,** 382 (1956).
2. GELLER S. and GILLEO M. A. *Acta Cryst.* **10,** 239 (1957).
3. PAUTHENET R. *C.R. Acad. Sci., Paris* **242,** 1859 (1956).
4. PAUTHENET R. *C.R. Acad. Sci., Paris* **243,** 1499 (1956); **243,** 1737 (1956).
5. ALÉONARD R., BARBIER J.-C., and PAUTHENET R. *C.R. Acad. Sci., Paris* **242,** 2531 (1956).
6. NIELSEN J. W. In preparation.
7. MENZER G. *Z. Krist.* **69,** 300 (1929).
8. YODER H. S. and KEITH M. L. *Amer. Mineral.* **36,** 519 (1951).
9. KEITH M. L. and ROY R. *Amer. Mineral.* **39,** 1 (1954).
10. GILLEO M. A. *J. Chem. Phys.* **24,** 1239 (1956).
11. BERTAUT F. and PAUTHENET R. IEE Convention on Ferrites, London, England (29 Oct.–2 Nov. 1956); see also BERTAUT F. and FORRAT F., *C.R. Acad. Sci., Paris* **224,** 96 (1957).
12. BERTAUT F., FORRAT F., HERPIN A., and MÉRIEL P. *C.R. Acad. Sci., Paris* **243,** 898 (1956).
13. PRINCE E. To be published.
14. TUNELL G. *Amer. Mineral.* **24,** 448 (1939).
15. PHILLIPS D. C. *Acta Cryst.* **9,** 819 (1956).
16. BOND W. L. *International Tables for X-ray Crystallography* Vol. II. To be published.
17. BOOTH D. P. Conf. on Use of IBM 650 for Crystal Structure Analysis Computations, Univ. of Pittsburgh, 6 Feb., 1957.
18. *Internationale Tabellen zur Bestimmung von Kristallstrukturen* Gebrüder Borntraeger, Berlin (1935).
19. BERGHUIS J., HAANAPPEL I. M., POTTERS M., LOEPSTRA B. O., MACGILLAVRY C. H., and VEENENDAAL A. L. *Acta Cryst.* **8,** 478 (1955).
20. KRAMERS H. A. *Physica* **1,** 182 (1934).
21. ANDERSON P. W. *Phys. Rev.* **79,** 350 (1950).
22. VAN VLECK J. H. *J. Phys. Radium* **12,** 262 (1951).
23. NÉEL L. *Ann. Phys., Paris* **3,** 137 (1948).
24. YAFET Y. and KITTEL C. *Phys. Rev.* **87,** 290 (1952).
25. PRINCE E. To be published.
26. HASTINGS H. M. and CORLISS L. M. *Phys. Rev.* **104,** 328 (1956).
27. GELLER S. and WOOD E. A. *Acta Cryst.* **9,** 563 (1956).
28. SKINNER B. J. *Amer. Mineral.* **41,** 428 (1956).

J. Phys. Chem. Solids Pergamon Press 1957. Vol. 3. pp. 37–43.

LATTICE CHANGES IN SPINEL-TYPE IRON CHROMITES

M. H. FRANCOMBE

Communication from the Staff of the Research Laboratories of The General Electric Company Limited, Wembley, England

(*Received* 25 *February* 1957)

Abstract—X-ray powder studies have been made of structure deformations arising on cooling spinel-type iron chromite compounds with compositions of the form $FeFe_{2-x}Cr_xO_4$ below room temperature. Approximate measurements of Curie temperatures have also been carried out over the entire composition range $x = 0$ to $x = 2$.

A tetragonal distortion with c/a greater than one is first detected at $x = 1{\cdot}0$ and increases in magnitude up to $x \geqslant 1{\cdot}3$. With higher values of x the deformation is orthorhombic and results from a separate [001] expansion and [100] contraction, giving the sequence cubic → tetragonal → orthorhombic on cooling. As x is increased to 2 the second of these deformations predominates and in $FeCr_2O_4$ the lattice distortion is tetragonal with c/a less than one.

The nature and magnitude of the distortions are considered in relation to the probable cation distribution in tetrahedral and octahedral sites. The observed structure changes in these compounds are difficult to explain on the theory of covalent bonding of either octahedral or tetrahedral cations. It is suggested that the deformations may arise from strong negative *B–B* type interactions of the form Fe^{3+}–Fe^{3+}, Fe^{3+}–Cr^{3+} or Cr^{3+}–Cr^{3+} operating through super-exchange or semicovalent-exchange mechanisms.

1. INTRODUCTION

LATTICE distortions have been shown to occur in a number of spinel-type magnetic oxides on cooling through some critical temperature, and are usually associated with magnetic, electrical conductivity or thermal anomalies. Thus in magnetite (Fe_3O_4) the crystal structure has been shown by TOMBS and ROOKSBY[1] to distort from cubic to approximately rhombohedral symmetry on cooling below −160°C. Most of the other examples of such structure changes reported in the literature appear to involve distortions to tetragonal symmetry. In this class may be listed $CoFe_2O_4$,[2] which is slightly distorted at −183°C, and $CuFe_2O_4$,[3] $ZnMn_2O_4$[4] and $NiCr_2O_4$[5] which undergo similar transitions at appreciably higher temperatures, i.e. 760°C, 1025°C and 35°C respectively.

Recently some preliminary X-ray observations on tetragonal distortions, produced on cooling to −183°C, in spinel-type iron chromites possessing the general formula $FeFe_{2-x}Cr_xO_4$, have been reported.[6] The effects are seen in such iron chromites when the value of x lies within the range $1 \leqslant x \leqslant 2$. With the composition $x = 1{\cdot}2$ the structure deformation is accompanied by a relative expansion in the [001] crystallographic direction but for pure ferrous chromite ($x = 2$) a marked relative contraction in the [001] direction (making $c/a < 1$) is observed.

In the present paper the results are given of a more detailed X-ray study of the low-temperature structure changes in these iron chromites, and possible explanations of the phenomena are discussed.

2. PREPARATION OF SAMPLES

Powder specimens of good homogeneity and purity were prepared both by thermal decomposition of solid solutions of Fe_2O_3 and Cr_2O_3 in nitrogen and by reducing such sesquioxide solid solutions with iron powder using a method similar to that reported by RIGBY, LOVELL and GREEN[7] in their preparation of ferrous chromite.

The first method consisted in carefully mixing ferric oxide and chromic oxide by milling in a steel ball-mill for 50 hr, or grinding by hand under acetone, and firing the mixture for 4 hr at about 1000–1100°C in air. X-ray powder photographs of the products showed only a single homogeneous haematite-type phase to be present. The spinel-type iron chromite was then obtained by decomposing the sesquioxide solid solution for 18

hr at 1250°C in dry, oxygen-free nitrogen. The molar proportions of original oxide used were calculated from the appropriate equation, as in the following example for which $x = 1{\cdot}2$.

$$2{\cdot}2Fe_2O_3 + 0{\cdot}8Cr_2O_3 = \underbrace{1{\cdot}2Fe_3O_4 + 0{\cdot}8FeCr_2O_4 + \tfrac{1}{2}O_2}_{2Fe^{2+}Fe^{3+}_{1\cdot2}Cr_{0\cdot8}O_4}.$$

As values of x were increased beyond 1·2 the thermal decomposition did not proceed to completion and appreciable quantities of the haematite-type phase remained.

For compositions containing more chromium i.e. with $x > 1{\cdot}2$, the solid solutions were reduced by carefully mixing them with the appropriate amounts of iron micropowder (particle size $< 1\mu$) under acetone and firing the mixtures for 2–4 hr in open silica boats in dry nitrogen at 1250°C. The reaction may be represented by the equation,

$$Fe + (4-3/2x)Fe_2O_3,\ 3/2xCr_2O_3 = 3Fe_{3-x}Cr_xO_4.$$

Small quantities of boric oxide were used as a flux to promote sintering and to encourage crystal growth. In each case good homogeneous products were obtained which were free from the sesquioxide. Compositions stated in the following sections are in each case nominal and are based on the above reaction equation.

3. EXPERIMENTAL

X-ray studies both at room temperature and low temperatures were carried out with 19 cm powder cameras, using either cobalt or chromium radiations. For exposures at low temperatures the techniques employed were, (a) that described by TOMBS[8] in which the powder specimen is bathed in liquid oxygen or nitrogen fed from a nickel capillary tube, and (b) the gas-cooling method described recently by the author.[9]

Approximate measurements of Curie temperatures were made (to an accuracy of ± 5°C) by a method similar to that used by HARWOOD[10] in his study of lanthanum manganites. For Curie points above room temperature the powders, contained in small aluminium foil tubes, were heated in a furnace and then allowed to cool slowly. The temperature at which they were attracted by a magnet pole-piece placed close to the mouth of the furnace was recorded by using a copper-constantan thermocouple embedded in the powder. For Curie points below room temperature the furnace was replaced by a Dewar flask containing liquid oxygen or nitrogen.

4. THE SYSTEM $Fe_3O_4/FeCr_2O_4$

The chemistry and variation of unit-cell parameters with composition in the system $Fe_3O_4/FeCr_2O_4$ have been studied in some detail by YEARIAN, KORTRIGHT, and LANGENHEIM,[11] who prepared their samples by reducing Fe_2O_3/Cr_2O_3 solid solutions in mixed CO/CO_2 atmospheres. Fig. 1 shows graphically how the a_0 unit-cell parameter for the spinel structure varies with x in the formula $FeFe_{2-x}Cr_xO_4$. The values obtained for preparations described here differ somewhat from those of YEARIAN *et al.* in regions 1 and 2 of the

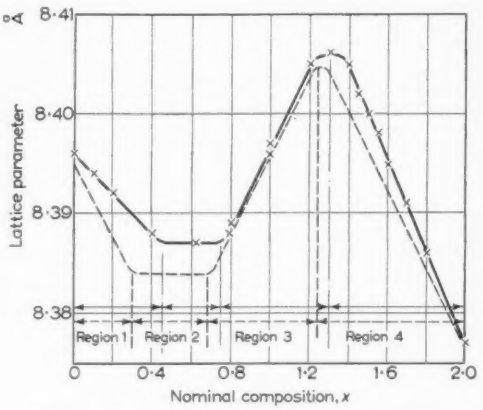

FIG. 1. Lattice parameters of compositions $FeFe_{2-x}Cr_xO_4$.
× × × Present values.
– – – YEARIAN *et al.*[11]

curve, but for compositions with values of x lying between 0·8 and 2·0 the agreement is fairly close. In any case the general trend of the lattice parameter variation appears to be well substantiated.

The curve may be divided into four well-defined linear portions and YEARIAN *et al.* have explained this in terms of the change, in four distinct stages, from the "inverse" ferrite composition of magnetite ($Fe^{3+}[Fe^{2+}Fe^{3+}]O_4$) to the completely "normal" cation arrangement in ferrous chromite ($Fe^{2+}[Cr^{3+}_2]O_4$). Thus over region 1 of the curve as x increases the ferric ions on the B sites are probably being replaced by chromic ions. The resulting solid solutions retain a completely inversed structure of the form $Fe^{3+}[Fe^{3+}_{(1-x)}Cr^{3+}_xFe^{2+}]O_4$. Regions 2 and 3 are two stages over which the cation distribution gradually changes to the normal type, this process being completed at the end of region 3($x \sim 1{\cdot}3$). All compositions over the last linear region of the curve are assumed to have the normal type of structure represented by the formula $Fe^{2+}[Fe^{3+}_{(2-x)}Cr^{3+}_x]O_4$.

Using these assumptions the approximate cation distributions were calculated along the lines suggested by YEARIAN *et al.* for compositions $x =$ 1·0–2·0 and are shown in Table 1.

Table 1

Composition x	a_0 at 20°C $\pm$0·001(Å)	Approximate cation distribution	Structure at −183°C
0	8·396	$Fe^{3+}[Fe^{2+}Fe^{3+}]O_4$	Approx. Rhombohedral
0·1–0·8	See Fig. 1.	~	Cubic
1·0	8·397	$Fe^{2+}_{0·6}Fe^{3+}_{0·4}[Fe^{2+}_{0·4}Fe^{3+}_{0·6}Cr^{3+}_{1·0}]O_4$	↑
1·2	8·405		
1·3	8·406	$Fe^{2+}[Fe^{3+}_{0·7}Cr^{3+}_{1·3}]O_4$	Tetragonal ($c/a > 1$)
1·4	8·405		↓
1·45	8·402		↑
1·50	8·400	$Fe^{2+}[Fe^{3+}_{0·5}Cr^{3+}_{1·5}]O_4$	
1·55	8·398		Orthorhombic
1·60	8·395		
1·70	8·391		↓
1·80	8·385		
2·0	8·377	$Fe^{2+}[Cr^{3+}_2]O_4$	Tetragonal ($c/a < 1$)

5. LOW TEMPERATURE X-RAY RESULTS

5.1. *Structure of solid solutions at* −183°C

X-ray powder photographs were taken of several different solid solutions in the composition range $0 < x \leqslant 2·0$ with the powder specimen held at −183°C, throughout the exposure. For $x = 0·1$ high-angle X-ray diffraction lines remain sharp and unsplit at −183°C, so that the rhombohedral-type distortion found in magnetite at this temperature has become vanishingly small or does not occur. This is also true of other compositions in the range $0·1 < x \leqslant 0·8$. At $x = 1·0$, however, slight splitting of the X-ray diffraction lines again becomes detectable, this time indicating a new tetragonal-type distortion.

With further increase in the chromium content up to $x = 1·3$ the magnitude of the tetragonal-type distortion is appreciably increased. At $x = 1·4$ there are feeble indications of line-splitting effects rather more complex than those due to a tetragonal structure. At this stage the symmetry is probably more accurately described as pseudo-tetragonal (truly orthorhombic). It now becomes apparent that the observed orthorhombic deformation arises from the combined operation of two dilatation effects, differing in magnitude and directed along different ⟨100⟩ cubic axes. The tetragonal and orthorhombic unit-cell dimensions for this series of compositions were calculated from the splitting of diffraction lines with Σh^2 of 27 and 32. In general, determinations from the two line groups agreed to within $\pm$0·002Å, but the limits of accuracy of the absolute values of the lattice parameters are probably a little greater than this.

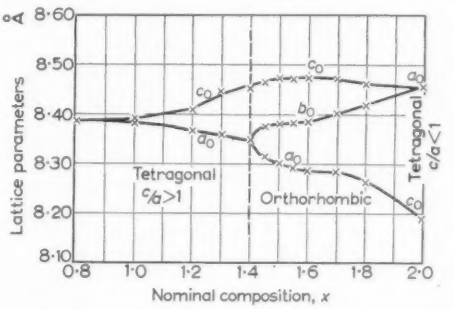

FIG. 2. Lattice parameters at −183°C for compositions $FeFe_{2-x}Cr_xO_4$.

The graph, Fig. 2, illustrates the manner in which the tetragonal and orthorhombic structure-cell dimensions determined at −183°C vary with composition over the range $x = 0·8$ to 2·0. In this graph it can be seen how the tetragonal structure assumed by compositions with $x \leqslant 1·4$ changes progressively as x increases, towards the different tetragonal structure of $FeCr_2O_4$, with an axial ratio well below one, which was reported on an earlier occasion.[6]

5.2. *X-ray studies between* 20°C *and* −183°C

The variation of lattice parameters with change of temperature has been studied on three of the solid solutions, viz. $x = 1{\cdot}2$, $1{\cdot}6$ and $2{\cdot}0$. The results are presented graphically in Figs. 3, 4 and 5.

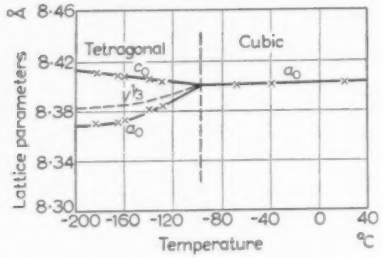

FIG. 3. Lattice parameters of $Fe_{1{\cdot}8}Cr_{1{\cdot}2}O_4$.

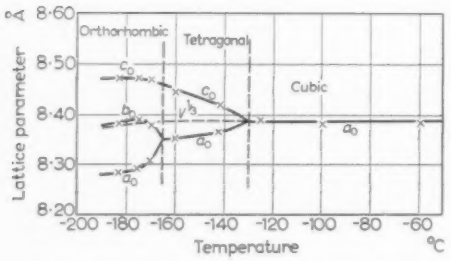

FIG. 4. Lattice parameters of $Fe_{1{\cdot}4}Cr_{1{\cdot}6}O_4$.

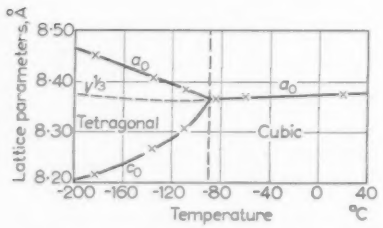

FIG. 5. Lattice parameters of $FeCr_2O_4$.

For the $x = 1{\cdot}2$ composition the transition in structure from cubic to tetragonal on cooling takes place at about −95°C. The change is continuous and line-splitting effects in the X-ray powder photographs increase gradually as the temperature is decreased down to −183°C. The c/a axial ratio attains a value of 1·005 at −183°C.

Pure ferrous chromite, $FeCr_2O_4$ also undergoes a tetragonal deformation on cooling, but here the change is accompanied by a relative contraction instead of expansion in the [001] crystallographic direction of the cubic unit cell, the axial ratio becoming less than unity. As can be seen from Fig. 5, the transition is again a fairly gradual one first appearing at about −90°C, and c/a decreases smoothly with fall in temperature, reaching a value of 0·968 at −183°C.

In order to investigate the mechanism by which the orthorhombic deformation is produced on cooling, the composition $x = 1{\cdot}6$ was chosen for study at temperatures between 20°C and −183°C. This choice was made chiefly on the grounds that the orthorhombic a_0, b_0 and c_0 parameters at −183°C differed from each other to a greater extent than for the other solutions in the series. The graph, Fig. 4, shows that the change to orthorhombic symmetry occurs in two steps. Thus on cooling to about −130°C the structure changes from cubic to tetragonal with an axial ratio greater than one. As the temperature is further lowered the axial ratio increases until at about −165°C a fairly abrupt transition to the orthorhombic structure takes place. The maximum tetragonal axial ratio reached, just above the lower transition temperature, is $c/a = 1{\cdot}013$.

The lattice distortion effects involved in these two structure transitions seem to be such that a marked relative expansion in the [001] crystallographic direction at −130°C is followed, at −165°C by a simultaneous relative expansion and contraction in the [010] and [100] directions respectively.

6. MAGNETIC MEASUREMENTS

Approximate values of Curie temperatures were determined for the entire range of compositions from pure $Fe_3O_4 (x = 0)$ to $FeCr_2O_4 (x = 2)$. These are presented graphically in Fig. 6 together with available data on structure transition temperatures. The Curie points for Fe_3O_4 and $FeCr_2O_4$ agree closely with those given by BOZORTH[12] and LOTGERING[13] respectively.

Although it is not possible to reach any conclusions regarding the nature of the structure deformations from Curie temperatures alone, the graph shows whether the structure transitions occur in the paramagnetic or ferromagnetic region. Also it can be inferred, from the fall in Curie temperature with increase in the value of x, that as the $FeCr_2O_4$ composition is approached the principal

ferrimagnetic interaction occurring between tetrahedral and octahedral cations of the spinel lattice becomes weaker.

7. INFLUENCE OF CATION DISTRIBUTION ON DISTORTIONS

Consideration of the lattice parameter/composition relationship shown in Fig. 2, in association with the cation distributions listed in Table 1, indicates that the type of distortion of the structure cell produced on cooling is closely dependent upon the distribution of atoms amongst the *A* and *B* sites of the structure.

As the value of x increases from 1·0 to 1·3 the value of the tetragonal axial ratio increases considerably. This corresponds, as shown in Table 1 to the gradual removal of Fe^{3+} ions from the *A* sites and Fe^{2+} ions from the *B* sites. At the same time the number of Cr^{3+} and Fe^{3+} ions in the *B* sites increases, the latter reaching a maximum at $Fe^{3+}_{0\cdot7}$($x = 1\cdot3$).

As the chromium content increases further from $x \leqslant 1\cdot4$ to $x = 2\cdot0$ the tetragonal distortion involved changes from a type with c/a greater than unity to one with c/a less than unity. At the same time the overall distortion of the lattice observed at −183°C becomes progressively greater in magnitude.

From these observations, even without knowing the origin of the forces causing these deformations, we may conclude that, at least in the composition range $x = 1\cdot3$ to 2·0, the cation distribution on the *B* sites of the spinel lattice probably governs the type and magnitude of the lattice distortions produced.

8. DISCUSSION

Various explanations have been advanced to account theoretically for the distortions produced in spinel-type structures on cooling. Thus in Fe_3O_4 VERWEY and HAAYMAN[14] concluded, on the basis of electrical conductivity measurements, that ordering of the Fe^{2+} and Fe^{3+} ions occurs in octahedral sites of the spinel lattice on cooling below −160°C. VERWEY[15] predicted that such ordering should produce a tetragonal distortion, while BICKFORD[16] suggested that the distortion might be orthorhombic. GOODENOUGH and LOEB[17] have used VERWEY's model together with the conception of covalent bond formation for the Fe^{3+} ions in tetrahedral sites to explain the orthorhombic distortion reported by ABRAHAMS and CALHOUN.[18] Unfortunately any such ideas involving ordering of 3*d* electrons are difficult to extend to structures with mixed *B*-site cation distributions, such as $Fe[CoFe]O_4$ and $FeFe_{2-x}Cr_xO_4$.

GOODENOUGH and LOEB have also proposed an explanation of the tetragonal distortions observed in Mn_3O_4, $CuFe_2O_4$, $CuCr_2O_4$ and $ZnMn_2O_4$ in terms of covalent bonding effects in the octahedral sites. The tetragonal deformation is assumed to arise from the tendency on cooling for the octahedral cation to form square covalent bonds with four of its nearest neighbour anions and ionic bonds with the other two anions. At the structure transition temperature the ionic bonds become "frozen" into a definite direction in the lattice, which then becomes identified with the c axis of the new tetragonal unit cell. The deformation is positive in the direction of the ionic bonds and thus c/a is greater than one.

Chromium ions, however, do not show this tendency and the hypothesis breaks down when applied to $NiCr_2O_4$[13] and $FeCr_2O_4$, both of which probably possess normal structures. Moreover X-ray studies by BERTAUT and DELORME[19] have shown that $CuCr_2O_4$ not only possesses a normal cation distribution but also a structure cell with an axial ratio below one. Even if, as has been suggested,[20] the tetragonal deformation of this structure were due to strong covalent bonding of the divalent Cu ions in the tetrahedral sites, such bonding is not likely to occur for divalent Fe or Ni ions.

An alternative interpretation of the effects may possibly be found in antiferromagnetic ordering of spin moments in the spinel lattice. Thus ROOKSBY and WILLIS[2] have drawn attention to the similarity of the low temperature deformations in Fe_3O_4 (a principal [111] expansion) and $CoFe_2O_4$ (a [001] contraction) to those in the corresponding antiferromagnetic monoxides FeO and CoO. Antiferromagnetic interaction between spin moments in spinels has been considered by YAFET and KITTEL[21] who suggested a model in which the *A* and *B* lattices of the spinel structure could be regarded as composed of sublattices. Negative-type interactions between the sublattices, either for *A* or *B* type ions, can be shown to account for apparent anomalies in magnetic behaviour in several of the spinel-type ferrites and chromites.[22,13]

HASTINGS and CORLISS,[23] using neutron diffraction techniques, have in fact detected an antiferromagnetic ordering of spin moments on the *B* sites in normal-type $ZnFe_2O_4$ at low temperature. Also from specific heat and magnetic data obtained by MCGUIRE, HOWARD, and SMART[24] there seems good reason to suppose that similar ordering effects are responsible for the tetragonal distortion produced on cooling $NiCr_2O_4$.[13] In this substance the structure changes very sharply to tetragonal ($c/a > 1$) just below 35°C. LOTGERING has made magnetic measurements on $FeCr_2O_4$ but reports no anomaly similar to that found for $NiCr_2O_4$. The structure deformation in $FeCr_2O_4$, however, is smaller in magnitude and occurs more smoothly than that in $NiCr_2O_4$, so that the magnetic anomaly, if originating from similar causes, might be expected to be somewhat smaller and therefore have been missed.

We can interpret the data shown graphically in Figs. 2–5 in terms of deformations comprising anisotropic expansions or contractions directed along cubic ⟨100⟩ axes in the spinel-type unit cell. For compositions in the range $x = 0{\cdot}8$ to $1{\cdot}3$ the tetragonal distortion results from a relative expansion along the [001] direction of the unit cell, this then becoming the *c* axis. The magnitude of this effect increases up to $x \geqslant 1{\cdot}4$, at which composition a second [100]-type deformation becomes involved, producing the orthorhombic structure observed at −183°C. The low-temperature X-ray study of the composition $x = 1{\cdot}6$ (Fig. 4) reveals that the second distortion probably occurs as a relative contraction along one of the *a* axes of the tetragonal unit cell, and at a lower temperature than the first structure change.

Further data on the transition temperatures for compositions intermediate between $x = 1{\cdot}6$ and $2{\cdot}0$ are not yet available, but the present results indicate that, with increasing chromium content the second distortion effect becomes predominant, the first [001]-type expansion gradually disappearing. Also the temperature at which the [100] contraction occurs rises as the composition $FeCr_2O_4$ is approached. With pure $FeCr_2O_4$ the low-temperature structure change arises entirely from this relative contraction, in a direction identified with the orthorhombic *a* axis. As shown in Fig. 3 the orthorhombic b_0 dimension now becomes equal to the c_0 dimension and the symmetry may now be referred to a tetragonal structure cell having its *c* axis as the deformation direction.

It may be possible to explain these structure changes on arguments similar to those used by YAFFET and KITTEL,[21] by picturing strong negative *B*–*B* type interactions to occur between spin moments on interpenetrating sublattices. Over the solid solution series examined such interactions could be of the form Fe^{3+}–Fe^{3+}, Fe^{3+}–Cr^{3+} or Cr^{3+}–Cr^{3+} and would presumably operate by means either of a superexchange[25] or semicovalent exchange[17] magnetic coupling, involving oxygen ions situated between the cations on the sublattices.

It is not clear how such antiferromagnetic ordering on the *B* sites may be affected by changes in the strength of the *A*–*B* type interactions or by replacement of Fe^{3+} by Cr^{3+} ions on the *B* sites as *x* increases in value from 0·8 to 2·0. From the fact that the ferrimagnetic Curie temperature falls throughout the series with increasing chromium content (Fig. 6) it appears that the *A*–*B* type interactions become progressively weakened. The maximum tetragonal distortion (at −183°C) with an axial ratio greater than one appears to be reached with a composition of $x \sim 1{\cdot}3$. This probably corresponds to a maximum number of Fe^{3+} ions in the *B* sites (Table 1) and thus to a maximum Fe^{3+}–Fe^{3+} or Fe^{3+}–Cr^{3+} interaction in these sites. As *x* is further increased the Cr^{3+}–Cr^{3+} type interaction increases, coinciding with the strengthening of the [100] contraction and with the removal of the relative [001] expansion.

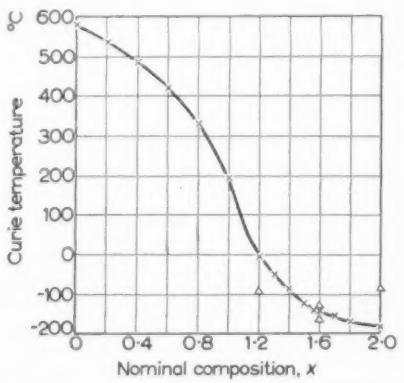

FIG. 6. Curie temperatures for compositions $FeFe_{2-x}Cr_xO_4$.
× × × Curie temperatures.
△ Structure transition temperatures.

Reference to the graph, Fig. 6, shows that for compositions with $x < 1{\cdot}4$ the structure changes in the ferromagnetic region, i.e. below the temperature at which the principal ferrimagnetic ordering effect between spin moments on the spinel *A* and *B* sites is assumed to occur. If, as has been suggested above, the deformation originates from strong negative *B*–*B* interactions, it must be concluded that below the Curie temperature, in these solid solutions, states of ferrimagnetism and antiferromagnetism coexist. A similar condition might arise in Fe_3O_4 and $CoFe_2O_4$ where the structure deformations also occur in the ferromagnetic region.

It is obviously desirable to supplement these studies with careful thermal and magnetic measurements, particularly of susceptibility and magnetic moments. Further work along the lines described above could be attempted on $NiCr_2O_4$ and $CuCr_2O_4$ compositions in which the *B*-site Cr^{3+} ions are replaced by small amounts of Fe^{3+} ions. It would also be interesting to study the effect produced on the tetragonal structure deformation of $NiCr_2O_4$ by replacing Ni^{2+} ions both by Fe^{2+} ions and also by a non-magnetic ion such as Zn^{2+} or Mg^{2+}. Observations on the resulting changes in the deformations should enable firmer conclusions to be reached concerning their origin.

VOL. 3 1957

REFERENCES

1. Tombs N. C. and Rooksby H. P. *Acta Cryst.* **4**, 474 (1951).
2. Rooksby H. P. and Willis B. J. M. *Nature, Lond.* **172,** 1054 (1953).
3. Bertaut E. F. *J. Phys. Radium* **12,** 252 (1951).
4. Mason B. *Amer. Min.* **32,** 426 (1947).
5. Delorme C. R. *C.R. Acad. Sci., Paris* **241,** 1588 (1955).
6. Francombe M. H. and Rooksby H. P. *Nature, Lond.* **178,** 586–587 (1956).
7. Rigby G. R., Lovell G. H. B., and Green A. T. *Iron and Steel Inst. Spec. Rep. No.* 32. p. 93 (1946).
8. Tombs N. C. *J. Sci. Instrum.* **29,** 364 (1952).
9. Francombe M. H. *J. Sci. Instrum.* **34,** 35 (1957).
10. Harwood M. G. *Proc. Phys. Soc.* **B68,** 586–592 (1955).
11. Yearian H. J., Kortright J. M., and Langenheim R. H. *J. Chem. Phys.* **22,** 1196–1198 (1954).
12. Bozorth R. M. *Ferromagnetism* p.246. Nostrand, New York (1951).
13. Lotgering F. K. *Philips Res. Rep.* **11,** 190–249 (1956).
14. Verwey E. J. W. and Haayman P. W. *Physica* **8,** 979 (1941).
15. Verwey E. J. W. *Nature, Lond.* **144,** 327 (1939).
16. Bickford L. R. *Phys. Rev.* **78,** 449 (1950).
17. Goodenough J. B. and Loeb A. L. *Phys. Rev.* **98,** 391–408 (1955).
18. Abrahams S. C. and Calhoun B. A. *Acta Cryst.* **6,** 105 (1953).
19. Bertaut E. F. and Delorme C. *C.R. Acad. Sci., Paris* **239,** 504–505 (1954).
20. Goodenough J. B. Private communication (1956).
21. Yafet Y. and Kittel C. *Phys. Rev.* **87,** 290 (1952).
22. Gorter E. W. *Philips Res. Rep.* **9,** 295, 321, 403 (1954).
23. Hastings J. M. and Corliss L. M. *Phys. Rev.* **102,** 1460 (1956).
24. McGuire T. R., Howard L. N., and Smart J. S. *Ceramic Age* **60,** 22 (1952).
25. Kramers H. A. *Physica* **1,** 182 (1934).

J. Phys. Chem. Solids Pergamon Press 1957. Vol. 3. pp. 44–49.

LOW TEMPERATURE HEAT CAPACITY AND THERMODYNAMIC PROPERTIES OF ZINC FERRITE*

EDGAR F. WESTRUM, JR. and D. M. GRIMES

University of Michigan, Ann Arbor, Michigan, U.S.A.

(*Received* 4 *February* 1957)

Abstract—The heat capacity of zinc ferrite ($ZnFe_2O_4$) has been determined over the range 5 to 350°K. Molal values of C_p,S^0, and $H^0-H_0^0$ computed from the thermal data are $32{\cdot}99\pm0{\cdot}03$ cal/deg., $36{\cdot}01\pm0{\cdot}03$ cal/deg., and $18{\cdot}00\pm0{\cdot}02$ cal, respectively, at 298·15°K. A co-operative thermal anomaly associated with antiferromagnetic ordering occurs at 9·5° and extends toward higher temperatures probably as a consequence of persisting short range order.

INTRODUCTION

ZINC ferrite, $ZnFe_2O_4$, crystallizes in the normal spinel structure. A well-tempered zinc ferrite is, therefore, characterized by having the iron atoms located at the centers of octahedra of oxygen atoms and the zinc atoms centered in tetrahedra of oxygen atoms. Conversely, an inverted spinel contains the divalent cation on octahedral sites; since there are twice as many octrahedral sites as tetrahedral sites in the spinel structure, half of the trivalent iron atoms also occupy octrahedral sites. Typically, the inverted spinels are ferrimagnetic and the normal spinels are paramagnetic at room temperature. Since the exchange interactions between cations on octahedral sites are antiferromagnetic in nature, some type of antiferromagnetic ordering may take place in zinc ferrite at low temperatures.

Although the fairly complex magnetic properties of ferrospinels have been extensively investigated by various techniques, few of these measurements have extended below 10°K. Utilization of low temperature adiabatic calorimetry permits both the detection of magnetic transformations and the evaluation of the thermodynamic parameters associated with these phenomena. This calorimetric technique is relatively sensitive, precise and, compared to more direct magnetic measurements (e.g., susceptibility), less subject to being masked by traces of ferromagnetic impurities.

The study of the low temperature thermal properties of a series of nickel-zinc ferrites[1] of empirical formula $Ni_{1-x}Zn_xFe_2O_4$ over the range $x = 0{\cdot}6$ to $x = 0{\cdot}9$ revealed an anomalously high heat capacity in the vicinity of 9°K, the magnitude of which increases rapidly as x approaches unity. Recent measurements by FRIEDBERG *et al.*[2] on a sample approximating zinc ferrite in composition confirmed the obvious extrapolation to $x = 1$ in revealing the existence of an anomalous peak in the heat capacity of zinc ferrite ($ZnFe_2O_4$) with a maximum near 9°K and a prominent "tail" on the high temperature side. Low temperature neutron diffraction studies by HASTINGS and CORLISS[3] have demonstrated the existence of this transition and strongly suggest that it results from an antiferromagnetic ordering.

However, the thermal anomaly reported by FRIEDBERG[4] in zinc ferrite is considerably rounded and broadened compared to other co-operative transformations and reveals no evidence of a discontinuity in the derivative of the heat capacity with respect to temperature. Such deviation from the usual behavior of co-operative transitions might be expected as a consequence of partial inversion of the "normal" spinel structure, of inhomogeneity on an atomic scale, or of deviation from exact

* This work was done with the support of the U.S. Army Signal Corps through the Engineering Research Institute of the University of Michigan. A preliminary report of these studies appears in *Conference on Magnetism and Magnetic Materials* p. 64. American Institute of Electrical Engineers, New York (1955).

stoichiometry in the sample utilized in these measurements. Further investigation of the thermal properties of this substance was, therefore, considered relevant to the understanding of the ordering phenomenon.

EXPERIMENTAL

Preparation of the zinc ferrite

Preliminary investigation revealed the strong dependence on composition of the heat capacity of nickel-zinc ferrites in the vicinity of 10°K. For reasons already indicated,[1] great care was exercised in the preparative technique to obtain, as nearly as possible, a stoichiometric, homogeneous, non-inverted sample of zinc ferrite.

Equimolal quantities of weighed, anhydrous, chemically pure ZnO and Fe_2O_3 were milled in a hardened-steel ball mill using a thin acetone slurry. After passing the slurry through a magnetic separator, the bulk of the acetone was decanted and the remainder evaporated. Cylindrical slugs of about 50 g mass were pressed; the surface layer was removed, and the slugs were fired in air at 1100°C for 14 hr. After furnace cooling, the slugs were sufficiently fragmented in a hardened-steel "diamond mortar" to pass a 30 mesh screen. These granules were reformed into slugs, fired at 1100°C for 12 hr, and gradually allowed to cool in the furnace to 30°C over a period of 16 hr. The resulting ferrite granules were of a uniform reddish-brown color throughout.

Gravimetric chemical determinations showed 46·24 ± 0·1 per cent iron (theoretical: 46·33) and 27·2 ± 0·1 per cent zinc (theoretical: 27·12). Spectro-chemical analyses revealed 0·01 to 0·1 per cent of Al and Mn and 0·001 to 0·01 per cent of Ca, Cu, Mg, Ni, and Si. Stannous chloride redox titration indicates less than 0·1 per cent ferrous iron in the samples.

Cryogenic technique

The Mark I adiabatic cryostat used for these measurements has been described.[5] Measurements were made in a calorimeter (Laboratory Designation W-9) which is similar in design and dimensions to W-6[6] except for the following modifications: only four conduction vanes were used, protection against possible corrosion was achieved by a 0·02 mm gold plate on the interior surfaces, and a weighed quantity of Apiezon T vacuum grease was used to provide thermal conduction in the thermocouple sleeve and in the thermometer-heater well. The calorimeter contained 2·0 cm helium pressure to improve thermal conduction in the sample space. Temperatures were measured with a capsule-type platinum resistance thermometer (Laboratory Designation A-3) inserted within the heater sleeve in the wall. A 150 Ω glass-fibre-insulated, constantan wire was bifilarly wound in a double-thread groove in the heater sleeve. The thermometer was calibrated by the National Bureau of Standards against the International Temperature Scale above 90°K and by comparison at 19 temperatures with the Bureau's platinum thermometers[7] over the range 10–90°K.

Below 10°K we established a provisional temperature scale by fitting the constants in the equation[8] $R = A+BT^2+CT^5$ to the observed resistance of the thermometer at 10°K, the resistance at the boiling point of helium, and dR/dT at 10°K. The temperature scale thus defined probably agrees with the thermodynamic scale to 0·1° below 10°K, 0·03° from 10 to 90°K, and 0·05° from 90 to 400°K.

Measurements of temperature and of electrical energy

Table 1. *Molal heat capacity of zinc ferrite*
(in cal/deg^{-1} g/mole^{-1})

T(°K)	C_p	T(°K)	C_p
Series I		Series III (cont.)	
184·44	24·00	11·82	3·034
193·52	25·00	12·95	2·787
203·27	25·99	13·66	2·635
212·90	26·93	14·70	2·457
222·68	27·80	15·85	2·271
232·53	28·65	16·97	2·127
242·39	29·43	18·31	1·989
252·28	30·16	20·14	1·848
262·21	30·85	22·28	1·755
272·28	31·44	24·45	1·723
282·53	32·10	26·74	1·749
292·86	32·71	29·39	1·848
303·14	33·25	32·55	2·045
313·31	33·77	36·01	2·341
323·41	34·23	39·61	2·716
333·65	34·66	43·47	3·176
343·93	35·11	47·72	3·740
		52·45	4·413
Series II		Series IV	
7·81	2·6		
8·47	3·9	17·04	2·123
8·87	5·9	18·69	1·957
9·18	7·9	52·37	4·298
9·41	9·2	58·05	5·246
9·76	6·5	64·00	6·173
10·18	4·17	69·98	7·115
10·91	3·37	76·16	8·097
		82·61	9·183
Series III		89·79	10·335
		97·61	11·608
5·50	0·58	105·53	12·900
6·24	1·11	111·99	13·917
6·82	1·50	120·25	15·232
7·48	2·08	128·58	16·526
8·46	3·28	137·08	17·81
8·89	5·3	146·07	19·11
9·39	(8·7)	155·56	20·42
9·75	(8·3)	165·25	21·70
10·38	3·86	175·00	22·90
11·10	3·272	184·94	24·06

were made with an autocalibrated White double potentiometer. A timer operated by an electrically driven 240-cycle tuning fork and amplifier automatically indicated the duration of the energy input. Three independent determinations of the heat capacity of the empty calorimeter have been made over the entire temperature range.

RESULTS

The experimental values of the observed molal heat capacity of zinc ferrite are presented in Table 1. These data include small corrections for the slight differences in the amounts of helium and solder between the full and the empty calorimeter and for the finite temperature increments used in the measurements. Since the data are listed in chronological sequence, the temperature increments of the individual determinations can be estimated from the adjacent mean temperatures.

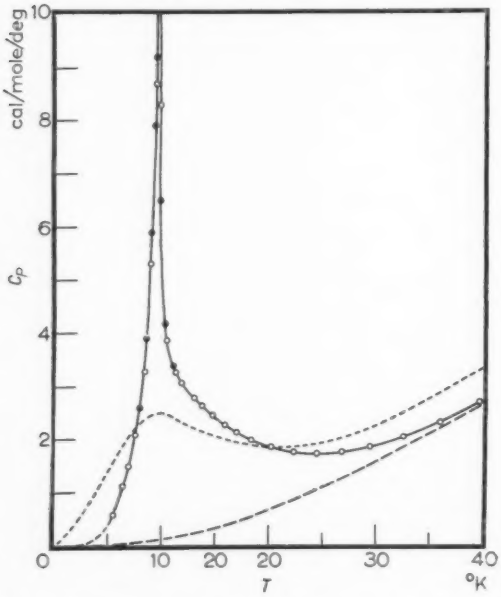

FIG. 1. The molal heat capacity of zinc ferrite from 5 to 40°K. The dotted curve represents the measurements of FRIEDBERG *et al.*[2] and the dashed curve approximates the lattice (vibrational) heat capacity.

The data are expressed in terms of the defined thermochemical calorie equal to 4·1840 absolute joules. The ice point is taken as 273·15°K, and the gram formula weight of $ZnFe_2O_4$ as 241·08. A sample of 163·397 g was employed. Fig. 1 depicts the heat capacity in the vicinity of the observed thermal anomaly.

The molal heat capacity and thermodynamic functions derived by numerical integrations of the heat capacity are listed at rounded temperatures in Table 2. The heat capacity values were read from a smooth curve through the experimental points and are estimated to have a probable error of 0·1 per cent down to 25°K increasing to 1 per cent at 10°K. The probable error may be 10 per cent below 10°K as a consequence of the sharp dependence of heat capacity on temperature over the region of thermal anomaly and the relatively slow establishment of thermal equilibrium in this region. The deviation of the individual experimental determinations from

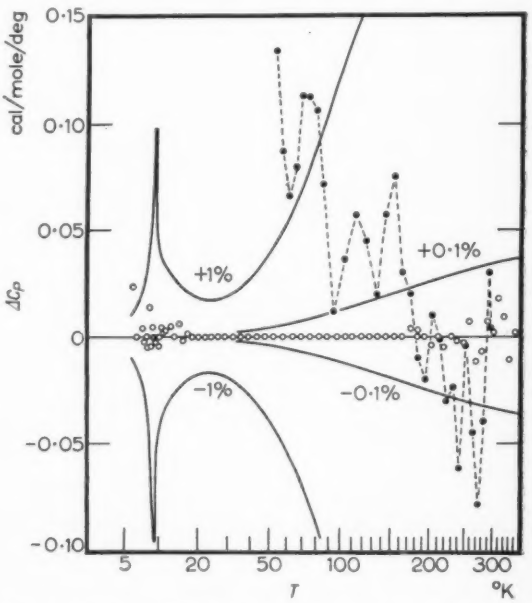

FIG. 2. The deviation of the measured heat capacities of zinc ferrite from smooth curve, i.e.,

$$\Delta C_p = C_{p(\text{experimental determination})} - C_{p(\text{curve})}$$

The open circles represent the individual experimental determinations of this work. The solid circles are those reported by KING.[9]

our smoothed curve are presented in Fig. 2. Solid lines represent deviations of $\pm 0{\cdot}1$ per cent and $\pm 1{\cdot}0$ per cent, respectively. Below 5°K, a Debye third power extrapolation was used to obtain values of the thermodynamic functions. The probable

Table 2. Molal thermodynamic functions of zinc ferrite

T(°K)	C_p (cal/deg.)	S^0 (cal/deg.)	$(H^0-H_0{}^0)$ (cal)	$-\frac{(F^0-H_0{}^0)}{T}$ (cal/deg.)
10	4·68	2·2126	17·69	0·4431
15	2·400	3·4473	32·65	1·2705
20	1·857	4·0520	43·11	1·8966
25	1·724	4·4459	51·92	2·3692
30	1·878	4·7701	60·82	2·7427
35	2·248	5·0852	71·07	3·0548
40	2·758	5·4173	83·53	3·3291
45	3·376	5·7766	98·82	3·5807
50	4·059	6·1673	117·38	3·8197
60	5·552	7·0370	165·29	4·2821
70	7·117	8·0095	228·58	4·7441
80	8·721	9·0639	307·7	5·2173
90	10·368	10·1863	403·2	5·7067
100	12·004	11·363	515·0	6·213
110	13·598	12·583	643·1	6·737
120	15·196	13·835	787·1	7·276
130	16·738	15·112	946·8	7·829
140	18·236	16·408	1121·7	8·396
150	19·658	17·715	1311·2	8·973
160	21·01	19·027	1514·5	9·561
170	22·29	20·339	1731·1	10·156
180	23·48	21·648	1960·0	10·759
190	24·62	22·949	2200·6	11·367
200	25·67	24·239	2452·1	11·979
210	26·65	25·515	2713·7	12·592
220	27·56	26·776	2984·8	13·208
230	28·43	28·020	3264·8	13·825
240	29·25	29·247	3553·3	14·442
250	30·00	30·458	3849·6	15·059
260	30·70	31·647	4153·1	15·673
270	31·34	32·818	4463·4	16·287
280	31·96	33·970	4779·9	16·899
290	32·54	35·102	5102·4	17·507
300	33·08	36·214	5430·5	18·112
350	35·35	41·493	7143·8	21·082
273·15	31·54	33·184	4562·7	16·481
298·15	32·99	36·010	5369·8	18·000

errors in the entropy, enthalpy, and free energy function are estimated to be 0·1 per cent above 100°K, but for internal consistency one more digit has been retained than is justified by the estimated probable error. The effect of nuclear spin and isotope mixing is not included in the entropy and the free energy function.

DISCUSSION

After the completion of these measurements, heat capacity data on zinc ferrite from 51 to 298°K were reported by KING.[9] The deviations of KING's data from our smoothed curve are shown in Fig. 2. The data of KING trend gradually to higher values toward lower temperatures than do the results of the present research; however, the agreement is good at room temperature. By virtue of compensation of these deviations of opposite sign, the entropy increments ($S_{298\cdot16°K}-S_{51°K}$) are in close agreement. Below 51°K, the extrapolated portion of KING's entropy is in error by nearly four units. This emphasizes the desirability of extending heat capacity measurements to the lowest practicable temperatures when such data are intended for evaluation of chemical thermodynamic functions. Isolated experimental points obtained by FRIEDBERG *et al.*[2] over the range 80 to 200°K appear to be at least 5 per cent higher than those reported either in the present work or by KING.

The existence of a typical co-operative type heat capacity anomaly rising to a sharp maximum greater than 9 cal/mole/deg. at 9·5±0·2°K accompanied by a prominent "tail" possibly extending beyond 25°K is characteristic of pure zinc ferrite. However, because thermal equilibrium was so slowly achieved below 10°K, it was desirable to traverse this entire anomaly with a single energy input and then to compare the directly measured enthalpy with that obtained by the integration of the C_p curve (Fig. 1) over the corresponding range. The results of three such tests are summarized in Table 3 and indicate good accord with the heat capacity measured with small temperature increments.

The anomaly as reported by FRIEDBERG *et al.*,[2] is indicated by the dotted line in Fig. 1. The observed difference is probably due to deviations from exact stoichiometry, from inhomogeneity, and/or from partial inversion suggested by the mode of preparation and the reported properties of their sample.[2,4] That the thermal history of the ferrite specimen may have a marked effect on heat capacity over a wide temperature range has recently been demonstrated for lithium-zinc ferrite.[10]

Table 3. Comparison of measured and integrated enthalpy increments

$T_{initial}$(°K)	T_{final}(°K)	$\Delta H_{measured}$	$\Delta H_{integrated}$
5·16	25·23	52·7	51·7
5·03	14·12	31·6	30·0
5·03	16·07	36·7	36·1

Although it is not yet possible satisfactorily to resolve the magnetic and lattice contributions to the specific heat, a rough approximation may be obtained by fitting the higher temperature data with an empirical equation of the type recommended by KELLEY.[11]

The Debye and Einstein function sum proposed by KING[9] was modified to better fit our data. The equation

$$C_p = D(178/T)+3E(390/T)+3E(710/T)$$

fits our data to within 0·5 per cent over the range 130 to 300°K. This approximate lattice heat capacity is presented as a dashed curve in Fig. 1. Attempts to make a similar extrapolation from temperatures substantially lower than 130°K resulted in a calculated lattice heat capacity contribution in excess of the measured total value near 40°K. Hence the estimated value of the lattice contribution is almost certainly high over the entire range.

If the magnetic contribution is estimated as the difference of this and the experimental curve, the magnetic entropy is 2·2 cal/mole/deg. at 10°K, 4·0 at 25°K, and 4·5 at 150°K. The molal entropy increment between the completely disordered paramagnetic states and the ordered antiferromagnetic state is $2R\ln(2S+1) = 7\cdot12$ (cal/mole/deg). The discrepancy between the theoretical value and our rough estimate of the magnetic contribution can readily be explained if we assume the persistence of short range ordering contributions to the thermal properties above 130°K.

These data are thus seen to be in accord with the interpretation of HASTINGS and CORLISS[3] of

the transition from paramagnetic zinc ferrite to an antiferromagnetic state at 9·5°K as a result of the spin interaction of the iron atoms. The anomalously high heat capacity above 9·5°K is consistent with the persistence of short range ordering above the Néel temperature and the interpretation of the diffuse scattering of neutrons observed at liquid nitrogen temperatures as arising from a short-range ferromagnetic interaction.

Note added in proof: The heat capacity here reported is consistent with the results calculated by TACHIKI and YOSIDA, *Progr. Theor. Phys., Osaka* **17,** 223 (1957).

Acknowledgements—The authors appreciate the generous co-operation of Prof. H. W. WELCH, JR. of the Electrical Engineering Department, the assistance of JAMES KUIPER in the preparation of the sample, of Dr. CHIEN CHOU and SEISHO TOMEODA in the cryogenic measurements and of TE FU CHANG in the calculations.

REFERENCES

1. GRIMES D. M. and WESTRUM E. F., JR. Submitted to *J. Phys. Chem.*
2. FRIEDBERG S. A. *et al. Investigations of Thermal and Electrical Properties of Solids at Very Low Temperature* Carnegie Institute of Technology Report (1955).
3. CORLISS L. M. and HASTINGS J. M. *Acta Cryst.* **7,** 674 (1954); *Phys. Rev.* **102,** 1460 (1956).
4. FRIEDBERG S. A. and BURK D. L. *Low Temperature Heat Capacity of Some Normal Spinels* Conference on Magnetism and Magnetic Materials American Institute of Electrical Engineers, New York (1955).
5. WESTRUM E. F., JR. and BEALE A. F., JR. *J. Amer. Chem. Soc.* Submitted.
6. BENJAMINS E. and WESTRUM E. F., JR. *J. Amer. Chem. Soc.* **79,** 287–290 (1957).
7. HOGE H. H. and BRICKWEDDE F. G. *J. Res. Nat. Bur. Stand.* **22,** 351 (1939).
8. OSBORNE N. S., STIMSON H. F., SLIGH T. S., JR., and CRAGOE C. S. *Bur. Stand. Sci. Papers* **20,** 65 (1925).
9. KING E. G. *J. Phys. Chem.* **60,** 410 (1956).
10. WESTRUM E. F. and GRIMES D. M. To be published.
11. KELLEY K. K. *Contributions to the Data on Theoretical Metallurgy XI* U.S. Bureau of Mines Bulletin 477. Washington D.C. (1950).

VOL. 3 1957

J. Phys. Chem. Solids Pergamon Press 1957. Vol. 3. pp. 50–52.

THE CRYSTAL STRUCTURES OF MANGANESE AND THE ACTINIDE ELEMENTS

L. E. ORGEL

The Department of Theoretical Chemistry, University of Cambridge

(*Received* 7 *March* 1957)

Abstract—The crystal structures of manganese and the actinide elements are discussed from the point of view of a recent theory of the electronic structure of body-centred cubic metals. It is shown that the existence of complex structures may be related to the possibility of Jahn-Teller distortions occurring in the body-centred cubic lattice.

VOL
3
195

THE elements of the first transition series other than manganese crystallize in one or more of the face-centred cubic, body-centred cubic or hexagonal close-packed structures.[1] Manganese is body-centred cubic at high temperatures, but as the temperature is lowered becomes stable successively in a face-centred cubic structure which distorts slightly to face-centred tetragonal at low temperatures and then in two complicated structures, the β- and α-phases.[2] This is particularly surprising since chromium with one less electron and iron with one more electron crystallize with the body-centred cubic structure at low temperatures. Iron, in addition, has a face-centred cubic structure at intermediate temperatures but returns to the body-centred cubic structure at high temperatures. Argument by analogy would suggest that manganese should be body-centred cubic at sufficiently low temperatures.

The actinide elements crystallize in a variety of unusual structures. Thorium is body-centred cubic at high temperatures and face-centred cubic at low temperatures,[1] but protoactinium has a unique structure which is derived from body-centred cubic by compression along a fourfold axis.[3] Each atom has ten nearest neighbours, eight corresponding to the nearest neighbours of the body-centred cubic structure and two corresponding to the next nearest neighbours along the z direction. Uranium is body-centred cubic at high temperatures and crystallizes in two complicated structures at lower temperatures.[3,4] The high temperature form of neptunium is probably body-centred cubic.[3] At 550°C a distorted body-centred structure of tetragonal symmetry becomes stable. A further slight change in structure occurs at 278°C, the low temperature form being orthorhombic. Finally, plutonium is body centred at high temperatures. becomes tetragonally distorted with twelve nearest neighbours at 490°C and face-centred cubic at 465°C.[4] At lower temperatures a number of more complicated structures become stable.[4]

In this paper we shall suggest a qualitative explanation of some of these facts which is based on a theory of the structure of body-centred transition metals suggested by GRIFFITH.[5] In the group O_h corresponding to the site symmetry of a body-centred cubic structure the d orbitals on a metal atom form two groups. One comprises the d_{xy}, d_{xz}, and d_{yz} orbitals which transform as t_{2g} while the other consists of the $d_{x^2-y^2}$ and d_{z^2} orbitals which transform as e_g. The t_{2g} orbitals point in the direction of the nearest neighbours and can form σ-bonds with them, while the e_g orbitals point towards the centres of the cube faces and, are unable to form σ-bonds except to the next nearest neighbours. In an infinite lattice the molecular orbitals derived from the e_g and t_{2g} orbitals cannot be separated rigorously, but nonetheless GRIFFITH assumes that the e_g orbitals can be treated as if they interacted only weakly with their environment. He supposes that in chromium the conduction band, made up from the $3d(t_{2g})$, $4s$ and $4p$ orbitals, concontains six electrons per atom. In iron the con-

duction band again contains six electrons per atom but in addition there are two atomic electrons with parallel spin in the e_g orbital. If this is correct one might expect a stable body-centred structure with one e_g electron per atom for manganese at low temperatures. That this is not the case is due, we believe, to the operation of the Jahn-Teller effect.[6] A similar explanation of the complexity of the structures of the actinide elements (and perhaps of tungsten) is also possible if the elements after thorium are assumed to contain e_g d-electrons in their body-centred cubic modifications.

According to the Jahn-Teller theorem if a non-linear molecule is in a geometrical configuration such that its ground state is orbitally degenerate then there exists a distortion of the nuclear framework which removes the electronic degeneracy and in so doing lowers the energy of the molecule. We have previously discussed empirical evidence[7] which shows that in a crystalline ionic solid the Jahn-Teller distortions can become "trapped" as the temperature is lowered in such a way as to cause a second order phase transition. A body-centred cubic metal in which the e_g orbital contains one or three electrons per atom presents a situation exactly analogous to that in an ionic solid in which the metal ion has a degenerate ground state, provided that the e_g orbitals can be treated as atomic orbitals. (The strict conditions for the Jahn-Teller theorem to be applicable are not satisfied, but providing the interaction between e_g orbitals on neighbouring atoms in the undistorted structure is not too large distortions will nevertheless occur.)

Unfortunately it is very difficult to determine the most stable distortion of even a simple molecule produced by the Jahn-Teller mechanism,[8] for this depends on high order terms in both the vibrational potential and the Jahn-Teller stabilization energy. In a crystalline solid the situation is even more difficult, for all atoms are not required to be equivalent in the distorted structure. Nevertheless it is interesting to examine situations in which all atoms do distort in an equivalent way. Suppose first that each atom carries one e_g electron in the d_{z^2} or $d_{x^2-y^2}$ orbital. The crystal will then contract or expand along the z axis to give a tetragonal structure. If the electron is in the d_{z^2} orbital it is fairly clear physically that the lattice must contract in such a way as to establish directed bonds, using the d_{z^2} orbital, to the next nearest neighbours along the z axis. This leads to exactly the structure observed in protoactinium. We therefore believe that in this metal each atom carries one d_{z^2} electron which gives rise to bonds in the direction of the fourfold axis.

Suppose alternatively that each atom carries a $d_{x^2-y^2}$ electron. Then a distortion complementary to that discussed above must occur in which the unit cell contracts in the xy plane. The co-ordination around each atom would then involve twelve other atoms just as is in fact observed in plutonium. This distortion allows the structure to go over continuously into face-centred cubic. We must not, however, conclude that this is the situation in these elements without first discussing the case of metals with three e_g electrons per atom. If two go into the d_{z^2} orbital and only one into the $d_{x^2-y^2}$ orbital then we expect bonding in the xy plane, while if two go into the $d_{x^2-y^2}$ orbital and one into the d_{z^2} orbital we would expect bonding along the z axis. We think that the available evidence is slightly in favour of the configuration $(e_g)^3$ for the body-centred cubic phase of plutonium, but not very strongly so.

The complex structures observed in manganese, tungsten, uranium, neptunium and plutonium are consistent with our explanation but certainly could not have been predicted by it. It is perhaps significant that WYCKOFF has described the α-phase of manganese as distorted body-centred cubic,[1] and that the α and β neptunium structures are closely related to body-centred cubic.[9] In any case, the fact that complex structures occur at those points in the periodic table where partial occupation of the e_g orbitals in body-centred structures might be anticipated makes it seem likely that the effect we have discussed is responsible, at least in part, for their appearance.

In Table 1 we summarize what we believe to be the most probable electron assignments for chromium, manganese, iron, and the actinide elements. For the latter, these assignments are only tentative since the number of electrons in the $5f$ orbital is uncertain. Large distortions from cubic symmetry are not likely to result from the Jahn-Teller effect if only f electron degeneracy is involved.

Our hypothesis could be tested in a number of ways. Thus the electronic degeneracy postulated for manganese and certain other body-centred cubic metals should lead to an extra contribution

Table 1. Possible electron assignments for body-centred cubic forms of transition-metals and actinide elements

Metal	Number of electrons in d^3sp^3 bond	Arrangement in e_g	No. of f electrons
Cr	6	—	0
Mn	6	$(d_{z^2})^1$ or $(d_{x^2-y^2})^1$	0
Fe	6	$(d_{z^2})^1$ $(d_{x^2-y^2})^1$	0
Th	4	—	0
Pa	4	$(d_{z^2})^1$	0
U	?	?	?
Np	4	$(d_{z^2})^2(d_{x^2-y^2})^1$	0
	or 6	$(d_{x^2-y^2})^1$	or 2
Pu	4	$(d_{z^2})^2(d_{x^2-y^2})^1$	0
	or 6	$(d_{x^2-y^2})^1$	or 2

to the entropy of R ln 2. A detailed analysis of thermal measurements on body-centred cubic manganese should show whether or not such a contribution exists, although the conventional separation of the entropy into vibrational and electronic terms may not be convenient when the Jahn-Teller effect is operative. Another experimental test of the theory would be provided by the determination of absolute X-ray intensities for body-centred chromium, manganese, and iron. The Jahn-Teller distortions should simulate an abnormally large temperature factor and so lead to unusually low intensities. Finally, X-ray absorption from the L_{II} and L_{III} or M_{II} and M_{III} levels should reveal very narrow d electron bands in the body-centred metals in addition to the broader conduction bands. This seems to be true for iron,[10] but comparable data on other metals are not available.

In the absence of definite confirmation of the theory it does not seem profitable to develop it in greater detail here. If it is confirmed subsequently it should have a wider application to the theory of transition-metal alloys, for example to the σ-phases.

Note added in proof: We must emphasize that we do not suggest that complex structures such as those of α- and β-manganese are determined in detail by the Jahn-Teller effect, but rather that the instability of the simple cubic structure forces the metal to adopt some other more complicated structure. The particular structure which actually occurs will be determined by many factors, of which the Jahn-Teller effect is only one. The occurrence of alloys isostructural with α-Mn but which do not contain transition metals shows clearly that some factor other than the Jahn-Teller effect must be important in stabilizing the α-Mn structure.

Acknowledgements—I am indebted to Mr. J. S. GRIFFITH, Professor H. C. LONGUET-HIGGINS, and Dr. R. WEISS for many valuable discussions and to Professor HARVEY BROOKS for bringing much of the experimental evidence to my notice.

REFERENCES

1. WYCKOFF R. W. G. *Crystal Structures* Interscience, New York (1948).
2. SULLY A. H. *Manganese* Butterworths, London (1955).
3. SEABORG G. T. and KATZ J. J. *The Actinide Elements* McGraw Hill, New York (1954).
4. *Progress in Nuclear Energy—Metallurgy and Fuels* (Ed. H. M. FINNISTON and J. P. HOWE) Pergamon Press, London (1956).
5. GRIFFITH J. S. *J. Inorg. Nucl. Chem.* **3,** 15 (1956).
6. JAHN H. A. and TELLER E. *Proc. Roy. Soc.* A**161,** 220 (1937).
7. DUNITZ J. D. and ORGEL L. E. *Nature, Lond.* **179,** 462 (1957).
8. ÖPIK U. and PRYCE M. H. L. *Proc. Roy. Soc.* A**238,** 425 (1957).
9. ZACHARIASEN W. H. *Acta Cryst.* **5,** 660 (1952).
10. CARTER D. E. and GIVENS M. P. *Phys. Rev.* **101,** 1469 (1956).

J. Phys. Chem. Solids Pergamon Press 1957. Vol. 3. pp. 53–62.

FREE ENERGY, INTERNAL FIELDS AND IONIC POLARIZIBILITIES IN $BaTiO_3$

S. TRIEBWASSER

I.B.M. Watson Laboratory at Columbia University, N.Y. 25, N.Y.

(*Received* 16 *January* 1957)

Abstract—The electronic and ionic polarizations and the ionic polarizibilities of $BaTiO_3$ are calculated allowing for the atomic displacements found from neutron diffraction data. The internal Lorentz fields are found at the displaced atomic sites. In addition SLATER's method for deriving the free energy from an ionic potential function is extended to include terms of the sixth power in the displacement of the ions. The resulting free energy function for a clamped crystal is compared with the experimentally derived function for the free crystal by reducing the latter to the former by means of relations between the clamped and free coefficients. From this comparison the coefficients a, b_1 and b_2 in SLATER's notation and the additional coefficients of the sixth power terms of the ionic potential have been calculated for several cases. It is concluded that the model considered gives qualitative agreement with experiment, and quantitative agreement to the order of accuracy of the approximation.

VOL. 3 1957

1. INTRODUCTION

SLATER[1] and DEVONSHIRE[2, 3] published similar statistical theories of ferroelectricity in $BaTiO_3$. Since the time of their work, much additional data have become available on the mechanical and electrical behavior of excellent single domain crystals. It is now possible to test further whether their treatments yield the principal ingredients of the new experimental results.

We will follow the Slater method primarily because in it the so-called Lorentz corrections to the internal fields are applied taking into account the actual geometry of the lattice. This treatment is modified and extended here as follows:

(1) The Lorentz corrections are calculated for the displaced positions of the various ions.

(2) The potential function describing the energy of a displaced ion is expressed to one further term in the power series expansion.

(3) Provision is made for all ions to undergo displacement rather than restricting ourselves to the case of the Ti ion alone.

2. ASSUMPTIONS

The following assumptions are made in arriving at the results given here:

(1) The crystal can be most closely described as partially ionic.

(2) Each atom carries a point charge which is some fraction, f, of the full ionic charge (Ba^{2+}, Ti^{4+}, O^{2-}) and f is the same for all ions in the lattice.

(3) The electronic polarizibilities are those assumed by SLATER.[1]

(4) In any polarization of the crystal, spontaneous or induced, the atomic displacements are proportional to those found by FRAZER, DANNER, and PEPINSKY[4] in their neutron diffraction studies.

(5) All polarizibilities (ionic as well as electronic) are linear except for one of the four* ionic polarizibilities which shall instead be given by a power series relationship between P and E for that ion.

It is further understood that in all calculations the state of the polarized crystal is regarded as a small deformation of the cubic phase. The simplification of the calculations which results is the

* In this work we shall be concerned only with the cubic and tetragonal phases. Under these circumstances the four atoms are Ba, Ti and two species of O's.[1]

reason for choosing this phase as the reference state. The information derived from these calculations is meaningful in discussing the behavior of the solid in all its phases. It has been well established by MERZ[5] from measurements in the vicinity of the cubic to tetragonal transition temperature that a single continuous free energy function is sufficient to explain the observed phenomena (double hysteresis loops) in each phase separately and in the transitions between them. Even stronger verification of the sufficiency of a single function is contained in the work of HUIBREGTSE and YOUNG.[6] They observed P–E hysteresis curves and the dielectric constant in the region of the orthorhombic to tetragonal transition temperature and found that with a free energy function of the form

$$F(P,T) = F_0(T)+A(P_x^2+P_y^2+P_z^2)+ B(P_x^4+P_y^4+P_z^4)+ D(P_y^2P_z^2+P_z^2P_x^2+P_x^2P_y^2)+ C(P_x^6+P_y^6+P_z^6)+G[P_x^2(P_y^4+P_z^4)+ P_y^2(P_z^4+P_x^4)+P_z^2(P_x^4+P_y^4)] \quad (1)$$

one could explain their excellent experimental data in detail. Furthermore, the coefficients A, B and C found in their work agree quite well with those found earlier[7] from measurements in the cubic phase just above the tetragonal-cubic transition temperature. These latter measurements did not involve D and G since only one component of P is non-zero. It has been found that a similar situation exists in $KNbO_3$,[8] a ferroelectric of the perovskite structure which is apparently isomorphic with $BaTiO_3$ in its dielectric behavior.

The underlying philosophy of this work is that we are seeking a starting point in the description of the behavior of $BaTiO_3$ which is expressible in terms of present knowledge of interactions in solids, and at the same time is a reasonable approximation to the real substance. The first two assumptions describe the approximation selected, while the remaining three are required for details in the calculations. Other models have been examined by various authors, but we will reserve discussion of these until our results have been presented.

The third assumption is the one most consistent with the point of view taken here. ROBERTS[9] has given a set of polarizibilities somewhat different from those used here, but it is felt that the method used to arrive at his values is not valid where the internal field differs by so much from that given by the ordinary Lorentz relation ($P/3\epsilon_0$) that the latter are not reasonable approximations to the former.

The fourth and fifth assumptions are related to each other. The implication here is that for the range of polarizations being considered the contribution of each atom is directly proportional to the local electric field at that atom. The slight non-linearity of one of the P–E relationships is considered as a small perturbation on the basic behavior, which is linear. Slater has shown that very small changes in the ionic polarizibility of the titanium atom produced large effects on the dielectric constant. It is just such a slight change with polarization or local field that causes the spontaneous polarization to be confined to some finite value. The part of the total contributed by each atom is, to first order, the same regardless of whether we are talking of the small field-induced polarization in the cubic phase, or the self-induced or spontaneous polarization, since the ratios of the internal fields are virtually independent of the applied field.

3. METHOD

The calculations are divided into three parts. First, the values of the ionic polarizibilities and all the relative polarizations (ionic and electronic) when the crystal has a non-zero polarization in the absence of an externally applied field are found. This yields the linear approximation and gives the free energy to the P^2 term only. The fraction of the total polarization contributed by each atom and the charge carried by each is also found from this calculation.

In the second part a relation between the local field at an atomic site and the ionic polarization of the atom at that site is found. This result is inserted into the equations of the first part to derive the relation between the macroscopically measurable external field and the total polarization. This relation is then integrated to give the free energy in terms of the polarization and the temperature as a power series in P.

Finally we wish to compare this calculated free energy function with the experimentally

derived function as given in equation 1. Since the latter is a result of measurements on the free crystal whereas the former is calculated for a crystal which is clamped (so that the strains are zero) and for which the thermal expansion coefficient is zero, relations must be calculated in order to reduce the experimental results to the case treated theoretically.

4. IONIC POLARIZIBILITIES AND POLARIZATIONS

As has been pointed out by many authors, for a crystal in which polarization is along one of the cubic axes, there are relations between the local fields, the externally applied field and the polarizations in this direction of the following form:

$$\epsilon_0 E_i = \epsilon_0 E + \sum_{k=1}^{4} (a_{ik} P_k + a'_{ik} P_k'). \qquad (2)$$

The subscripts i, k (= 1, 2, 3, 4) refer to the four atoms Ti, Ba, O_a and O_b* respectively. E_i designates the field at the site of the ith atom, P_k the electronic polarization per unit volume due to atom k, and P_k' is the ionic (displacement) polarization per unit volume due to the atom k. The a_{ik} and a'_{ik} are dimensionless numbers which depend on the relative positions in the lattice of the various atoms. Equation (2) is derivable from SLATER,[1] eqs. (16), (17), and (18), except that we do not require $P'_2 = P'_3 = P'_4 = 0$.

If one takes into account the fact that the local fields must be evaluated at the displaced positions of the ions[10] then it can be shown that $a_{11} = a'_{11}$, $a_{22} = a'_{22}$, while $a'_{33} \neq a_{33}$ and $a_{44} \neq a'_{44}$. In all cases, for $i \neq k$, $a'_{ik} = a_{ik}$. KINASE [11] has shown this. His arguments can be completed by observing that for the magnitudes of atomic displacements encountered in $BaTiO_3$ the field at a site is represented with adequate accuracy if one does indeed stop at considering only the dipole term in the multipole expansions of the fields due to ionic displacements. The results for a_{ik} and a'_{ik} can be found in KINASE's paper, equation (9), where the q and p are identical with SLATER's q and p and the u, v, w, and x are the same as P_1, P_2, P_3 and P_4 respectively, while u_0, v_0, w_0 and x_0 are P'_1, P'_2, P'_3 and P'_4 respectively.

Equation (2) can be solved for the P_i in terms of P'_i for the case $E = 0$, since the $\epsilon_0 E_i$ can be written

$$\epsilon_0 E_i = P_i/(\alpha_i/\epsilon_0 V) \qquad (3)$$

where α_i is the electronic polarizibility of the ith atom and V is the volume per unit cell. KINASE[11] has done this and gives the results in matrix form in his eqs. (14) and (15). In view of the fact that these relations between the ionic and electronic polarizations are calculated for the case of a spontaneous polarization while we are treating the region where the spontaneous polarization is zero the question must be raised as to whether the results are applicable. The arguments given by SLATER showing that this is the case apply here equally well.

Now as a consequence of assumptions (2) and (4) we can express all the P'_i in terms of one of them. FRAZER *et al.*[4] found in their neutron diffraction studies of $BaTiO_3$ that the Ti atom is displaced 0·06 Å and the O_a and O_b atoms 0·09 Å and 0·06 Å respectively in the opposite direction, while the Ba atom is undisplaced. This is, of course, not unique since only relative atomic displacements are determined; hence we can anchor some other point in the cell and arrive at different results. However, KAENZIG's[12] X-ray observations on the displacements and temperature factors of the various atoms in the structure indicate that one can really say physically that the Ba atoms are not strongly affected by the ferroelectric transition. Since the ratio of the charges on the Ti, O_a and O_b atoms is 4 : 2 : 2, we can write:

$$P'_2 = 0;\ P'_3 = (3/4)P'_1;\ P'_4 = (1/2)P'_1. \qquad (4)$$

KINASE's equations (14) and (15) can now be written

$$\begin{bmatrix} P_1 \\ P_2 \\ P_3 \\ P_4 \end{bmatrix} = [\gamma] \begin{bmatrix} 1 \\ 0 \\ 3/4 \\ 1/2 \end{bmatrix} \times P'_1 \qquad (5)$$

where $[\gamma]$ is the matrix given numerically by Kinase. From equations (4) and (5) all P's can be expressed in terms of P'_1. The fractional contributions to the total polarization may be calculated from

$$\frac{P_i}{P} = \frac{(P_i/P_1')}{[\sum_1^4 (P_i + P_i')/P_1']}. \qquad (6)$$

A similar relation can be written for any P'_i. The α_i', which we define as the ionic polarizibilities, can be found from the relation

$$E_i = P_i/(\alpha_i/V) = P_i'/(\alpha_i'/V) \qquad (7)$$

where V is as defined in equation (3).

In Table 1 we have tabulated the fraction of the total polarization contributed by each atom, and the polarizibilities per unit volume divided by ϵ_0 (SLATER's X). It is to be noted that the values in Table 1 are actually those required for the tetragonal phase. However, the variation in an appropriate X'_i required to explain the observed

* The O_a are along the Ti–O line parallel to the polarization. There are two O_b atoms per cell in the plane perpendicular to the polar axis (when it exists) which have identical behavior by the symmetry of the tetragonal phase. (See footnote p. 53).

behavior of $BaTiO_3$ is ~ 1 part in 10^5 per degree centigrade so that the X's found here are essentially constant over the region considered.

Table 1. *Polarizibilities, polarizations and field enhancement factor at each atomic site*

		$X = (\alpha/\epsilon_0 V)$	P_i/P	Field enhancement factor
Ti	electronic	0·0365	0·0505	1·38(K − 1)
	ionic	0·0747	0·1034	
Ba	electronic	0·382	0·0118	0·031(K − 1)
	ionic	0	0	
O_a	electronic	0·470	0·4928	1·05(K − 1)
	ionic	0·0739	0·0775	
O_b	electronic	0·470	0·0803	0·165(K − 1)
	ionic	0·303	0·0517	

Also tabulated in Table 1 is a so-called "field enhancement factor". This is a number by which the field applied externally must be multiplied to find the internal field at a given atomic site. It is arrived at as follows: for small fields in the cubic phase we write

$$P = (K-1)\epsilon_0 E \tag{8A}$$

and

$$E_i = (P_i/P) \cdot P(\alpha_i/V)^{-1} \tag{8B}$$

from the definition of α_i. Hence for the paraelectric (cubic) phase:

$$E_i = (P_i/P)(\alpha_i/V)^{-1}(K-1)\epsilon_0 E \tag{8C}$$

or

$$E_i = [(P_i/P)(\alpha_i/\epsilon_0 V)^{-1}(K-1)]E \tag{8D}$$

where K is the dielectric constant and all other quantities are as previously defined. The quantity in equation (8D) in square brackets is the "field enhancement factor". In the case that the polarization is spontaneous the internal local field can be found from equation (8B). As an example at room temperature, where $P = 26\mu C/cm^2$,

$$E_3 = 1{\cdot}0\times 10^6 \text{ stat volt/cm} = 3\times 10^8 \text{ volt/cm} \tag{9}$$

This leads to a polarization energy for the O_a atom of $-1/2(\alpha_0 E_3^2)$ or $1{\cdot}2\times 10^{-12}$ erg/atom. This may be compared with the magnitude of the total coulomb energy per cell in the unpolarized crystal given in DEVONSHIRE[2] (equation 10.1) as $-49{\cdot}1\ (e^2/R)$ where e is the charge of the electron and R the cell constant. This latter formula yields $2{\cdot}8\times 10^{-10}$ erg/cell. Hence we see that the additional electrostatic energy (or rather decrease in electrostatic energy) in the polar state is a small, but not negligible, part of the total.

At this point the fractional ionic character, f. may also be calculated. The contribution of ionic polarization of the ith atom to the total polarization can be written

$$P_i' = (n_i e f \delta_i)/V \tag{10}$$

where n_i is the number of electronic charges carried by atom i if it were completely ionic, e is the electron's charge and δ_i is the displacement of the ith atom from it's unpolarized position. Then from the results of FRAZER *et al.*[4] at room temperature

$$\Sigma P_i' = [(0{\cdot}06\times 4)+(0{\cdot}09\times 2)+2(0{\cdot}06\times 2)]\times \times 10^{-8}\, e.f.V^{-1} \tag{11}$$

From Table 1 ($\Sigma P'_i$) accounts for 28·4% of the total polarization which at room temperature is $26\mu C/cm^2$.[5] Inserting this result into equation (11) we find that f is 0·45.

5. THE FREE ENERGY FUNCTION

The method by which the free energy function for the crystal is found is in essential details identical with that used by SLATER.[1] Briefly, one finds the relation between a local electric field and the polarization of an array of displaceable ions (for example, the Ti lattice) coupled only by having a common temperature. The remainder of the lattice is represented by a steady potential in which each of the ions under consideration moves. The partition sum for this array is written in terms of this potential function. From the partition function the free energy for this array can be found as a function of its polarization and the temperature. The derivative of the free energy with respect to the polarization is the local field. This relates E_c to P'_c where the cth ion is the one with the non-linear P–E relationship.

Assuming that we have found

$$E_c = E_c(P_c', T) \tag{12}$$

where T is the absolute temperature, we substitute equations (7) and (3) into (2) writing the result:

$$P/X = \epsilon_0 E + \sum_{\substack{k=1 \\ k \neq C}}^{4} [a_{ik} + a_{ik}'(X_k'/X_k)]P_k + a_{ic}P_c + a_{ic}'P_c' \qquad (13)$$

where

$$X_i = \alpha_i/(\epsilon_0 V) \text{ and } X_i' = \alpha_i'/(\epsilon_0 V).$$

The four equations (13) are solved for E and P_i in terms of P'_c and the results substituted into

$$\epsilon_0 E + \sum_{\substack{k=1 \\ k \neq C}}^{4} [a_{ck} + a_{ck}'(X_k'/X_k)]P_k + a_{cc}P_c + a_{cc}'P_c' = \epsilon_0 E_c(P_c', T). \qquad (14)$$

It is to be remembered in all this that we are considering only one direction of polarization, namely, along one of the cube axes; hence the scalar equation, The result, in SLATER's notation, is:

$$\epsilon_0(C_5/C_3)E - (C_4/C_3)P_c' = \epsilon_0 E_c(P_c', T). \qquad (15)$$

The ratios (C_5/C_3) and (C_4/C_3) are related to the quantities a_{ik}, a'_{ik}, X_i and X'_i of equations (13). These ratios have been evaluated for the three cases $c = 1$, 3, and 4 corresponding to the nonlinear ionic polarizibility residing with Ti, O_a or O_b respectively. (C_4/C_3) most closely approximates an aggregate Lorentz factor for the crystal, while (C_5/C_3) would be (P/P'_c) where it not for the corrections to a'_{33} and a'_{44} discussed earlier. The results of these calculations are tabulated in Table 2.

To find E_c (P'_c, T) to a number of terms sufficient in view of the present status of experimental results we write for the potential energy of the ion "C":

$$\phi = a(x^2+y^2+z^2) + b_1(x^4+y^4+z^4) + 2b_2(y^2z^2+z^2x^2+x^2y^2) + c(x^6+y^6+z^6) + d_1[x^2(y^4+z^4)+y^2(z^4+x^4)+z^2(x^4+y^4)] + d_2x^2y^2z^2 \qquad (16)$$

where x, y, z are the components of the displacement of the atom from its equilibrium position. The partition sum is found from ϕ, and the local electric field from this result (See SLATER Sec. 2). We finally arrive at:

$$E_c(P_c', T) = 2(a/Nq^2)[1 + kT(3b_1+2b_2)/a^2](Pc') + 4(1/N^3q^4)[b_1 + (15/2)(kT/a)c](P_c')^3 + 6(1/N^5q^6)[c](P_c')^5 \qquad (17)$$

where N is the number of atoms per unit volume and q the charge per atom. This result may be compared with SLATER's equation (11). Terms of the order T^2 have been omitted since their contribution is negligible. In addition, the terms in d_1 and d_2 have been estimated under the assumption that d_1 and d_2 are of the same order of magnitude as c. These terms also turn out to give a negligible contribution to the final results. The term in T in the coefficient of $(P'_c)^3$ eventually leads to a term in the free energy which is of the correct sign and order of magnitude to explain the temperature dependence of the coefficient of P^4 in the observed free energy.[7]

Substituting equation (17) into equation (15) yields a relation between E and P'_c. If we write P'_c as $(P'_c/P)\cdot P$ taking (P'_c/P) from Table 1, the result is a relation between the applied external field E and the total polarization P. The desired result is derived by integrating the thermodynamic relation

$$\partial F(P, T)/\partial P = E(P, T)$$

This yields:

$$F(P, T)_{\text{Strain}=0} = F_0(T) + (c_3|c_5)(P_c'/P)(a/Nq^2) \times [1 + (kT/a^2)(3b_1+2b_2)]P^2 + (c_3/c_5)(P_c'/P)^3(N^3q^4)^{-1}[b_1 + (15/2)(kT/a)c]P^4 + (c_3/c_5)(P_c'/P)^5(N^5q^6)^{-1}[c]P^6 + (c_4/c_5)(P_c'/P)(2\pi)P^2 \qquad (18)$$

where we have substituted $(1/4\pi)$ for ϵ_0. This is equivalent to SLATER's equation (36).

6. COMPARISON WITH EXPERIMENTAL FUNCTION

We wish to compare the relation in equation (18) with the experimentally derived function:

$$F(P, T)_{\text{Stress}=0} = A(T - T_0)P^2 + BP^4 + CP^6 \qquad (19)$$

where

$$A = 3{\cdot}7 \times 10^{-5}(^\circ\text{C})^{-1}$$
$$T_0 = 378^\circ\text{K}$$
$$B = -1{\cdot}89 \times 10^{-12} + 4{\cdot}17 \times 10^{-15}T$$
$$C = 3{\cdot}8 \times 10^{-23} \qquad (19A)$$

all expressed in c.g.s-e.s.u. However, we cannot compare equations (18) and (19) directly since, as discussed above, the latter is measured for a free crystal, while the former is calculated for a crystal with zero strain and zero temperature expansion coefficient. We shall calculate corrections to the A, B, and C coefficients to compare the two expressions (18) and (19).

In order to relate the "free" constants to the "clamped" values a more general free energy function is written in place of equation 18. If we retain only those terms pertinent to our problem this takes the form:

$$F(P,T,x) = A_c P^2 + B_c P^4 + C_c P^6 + (1/2)c_{11}{}^P(x_x{}^2+y_y{}^2+z_z{}^2) + c_{12}{}^P(y_y z_z + z_z x_x + x_x y_y) + g_{11}x_x P^2 + g_{12}(z_z+y_y)P^2 \quad (20)$$

where x_x, y_y, and z_z are longitudinal strains, $c_{11}{}^P$ and $c_{12}{}^P$ are elements of the elastic constant tensor and g_{11} and g_{12} are defined by their occurrence in equation (20). The expression is written for the case of polarization along the x direction, which is in turn one of the cubic axes. The first three terms of equation (20) contain all of equation (18) except for the term $F_0(T)$. Equation (19) would be completed by the addition of terms involving stresses. For the free crystal all stresses are assumed to be zero.

There are two sets of corrections derivable directly from equation (20). These are firstly, the relations between A_c and B_c and the coefficients $A(A_f)$ and $B(B_f)$ of equation (19) and secondly the effect of ordinary temperature expansion on A_c. Since the crystal is not piezoelectric in the reference (cubic) phase, $A_c = A_f$.

The terms of the form $x_x P^2$ lead to a calculable relation between B_c and B_f. DEVONSHIRE[3] equation (2.4) gives relations from which the desired corrections may be calculated. These are as follows:

$$B_f = B_c + (1/2)g_{11}Q_{11} + g_{12}Q_{12} \quad (21)$$

$$g_{11}+2g_{12} = -(Q_{11}+2Q_{12})(c_{11}{}^P+2c_{12}{}^P) \quad (22A)$$

$$g_{11}-g_{12} = -(Q_{11}-Q_{12})(c_{11}{}^P-c_{12}{}^P) \quad (22B)$$

where Q_{11} and Q_{12} are elements of the electrostrictive tensor. The values of $c_{11}{}^P$ and $c_{12}{}^P$ have been given by BOND, MASON, and MCSKIMIN[13] Q_{11} and Q_{12} are calculated from the X-ray data of KAY and VOUSDEN[14] on the c/a ratio of $BaTiO_3$ at room temperature combined with the dilatometric data on the change in volume of the crystal as it goes through the cubic to tetragonal transition as given by SHIRANE and TAKEDA,[15] and the spontaneous polarization results of MERZ.[5] The X-ray and dilatometric data together permit a calculation of the strains associated with the change from the unpolarized to the polarized state.

From the Q's and cP's and equation (22) the g's may be found. The values finally inserted into equation (21) are

$$c_{11}{}^P = 2{\cdot}07 \times 10^{12}$$
$$c_{12}{}^P = 1{\cdot}40 \times 10^{12}$$
$$Q_{11} = 1{\cdot}23 \times 10^{-12}$$
$$Q_{12} = -0{\cdot}45 \times 10^{-12}$$
$$g_{11} = -1{\cdot}26$$
$$g_{12} = -0{\cdot}15$$

all in c.g.s.-e.s.u. The difference between the Q values given here and those in DEVONSHIRE[3] equation (3.1) arises principally from the fact that Devonshire used older spontaneous polarization data.

The resulting relation between B_c and B_f is

$$B_c = B_f + 7{\cdot}1 \times 10^{-13}. \quad (23)$$

Since B_f is negative and about $2{\cdot}5+10^{-13}$ c.g.s. near 120°C it is seen that B_c is positive. It can be shown, as a consequence of this, that the clamped crystal would undergo a second-order transition rather than the first-order one observed for free $BaTiO_3$.

The other major difference between the experimental and theoretical free energy is related to the ordinary temperature expansion and the associated change in the force constants between the ions and a change in the density of atoms. These two effects usually cannot be separated in the macroscopic experimental data being considered here. The effect on "A" is discussed by DEVONSHIRE (See DEVONSHIRE,[2] p. 1062) and can be expressed as

$$A_{\text{theory}} = A_{\text{exp.}} - (g_{11}+2g_{12})\frac{dx_x}{dT}. \quad (24)$$

From KAY's X-ray data[16]

$$\frac{dx_x}{dT} = 1{\cdot}24 \times 10^{-5}(°\text{C})^{-1} \text{ or}$$

or

$$A_{\text{theory}} = A_{\text{exp.}} - (-1{\cdot}9 \times 10^{-5})\,(°\text{C})^{-1}. \quad (25)$$

It is interesting to note that the sign of the correction is such as to decrease the observed "A". In other words, the effect of the temperature expansion is opposite to that required for the observed Curie-Weiss behavior of the crystals. The effect of the increase in ionic polarizibility as the lattice expands more than overcomes the effect of the decrease in the density of atoms.

We can make a rough estimate of the effect of the lattice expansion on b_1—and, as a matter of

fact, estimate g_{11}. Looking at equation (20) we see that

$$\frac{\partial}{\partial x_x}\left(\frac{\partial E}{\partial P}\right) = 2g_{11} \tag{26}$$

for the clamped case. From equation (18)

$$\frac{\partial}{dx_x}\left(\frac{\partial E}{\partial P}\right) \cong (2/Nq^2)(c_3/c_5)(P_c'/P)\frac{da}{dx_x} \tag{27}$$

to first order. If the coefficient "a" is derived from a potential energy of interaction of the form λR^{-s} where R is the distance between atoms, then

$$\frac{da}{dx_x} = \frac{da}{dR}\cdot R. \tag{28}$$

For a simple geometrical arrangement such as the Ti atom between two O_a atoms it can be shown quite simply that $(da/dR)\cdot R = -(s+2)a$. Furthermore, from equation (18) near the ferroelectric transition

$$\begin{aligned}&(C_3/C_5)(P'_c/P)(a/Nq^2)\\ &= -(C_3/C_5)(C_4/C_3)(P'_c/P)2\pi\end{aligned} \tag{29}$$

and hence

$$g_{11} = -(C_3/C_5)(C_4/C_3)(P_c'/P)2\pi[-(s+2)]. \tag{30}$$

Table 2. C_4/C_3 and C_5/C_3 for $c = 1, 3, 4$ and from Slater

	Ti		O_a	O_b	Slater
c_4/c_3	−13·36		−13·52	− 3·09	− 5·47
c_5/c_3	9·67	4·96		46·5	3·24

From Tables 1 and 2 the factor in front of $-(s+2)$ is 0·65, 1·3, and 0·13 for the Ti, O_a and O_b ions respectively. The agreement is best for O_b if s is taken from the short range repulsive force to be 9.

In a similar manner it can be shown that

$$\begin{aligned}\left(\frac{1}{b_1}\right)\frac{db_1}{dT} &= \frac{1}{b_1}\frac{db_1}{dx_x}\frac{dx_x}{dT}\\ &= -(t+4)\cdot(1{\cdot}24\times10^{-5})(°C)^{-1}\end{aligned} \tag{31}$$

where t is the exponent that plays the role s plays in the calculation of "a" above. The situation is not as clearcut here since we require a negative b_1. If we assume the important interaction term is due to the ion-dipole energy then t will be 4. This would lead to a fractional change of B in equation (19) (See equation 18) $\sim 10^{-4}$ per degree Kelvin. The experimental result for $(dB/dT)B^{-1}$ is seen from equation (19A) to be more than 10^{-3} per degree Kelvin so that lattice expansion alone does not account for the observed temperature variation of B.

Data from which the relation between C_e and C_f may be calculated are not available. It is assumed that these corrections would not alter the results significantly.

Now comparing equations (18) and (19)

$$\begin{aligned}A_{\text{theory}}(T-T_0) &= (A_{\text{exp}}+1{\cdot}94\times10^{-5})(T-T_0)\\ &= (a/Nq^2)(c_3/c_5)(P_c'/P)[1+(kT/a^2)(3b_1+2b_2)]+\\ &\quad+(c_3/c_5)(c_4/c_3)2\pi(P_c'/P).\end{aligned} \tag{32A}$$

$$\begin{aligned}B_{\text{theory}} &= B_{\text{exp}}+(B_c-B_f)\\ &= -1{\cdot}89\times10^{-12}+(4{\cdot}17\times10^{-15})T+7{\cdot}1\times10^{-13}\\ &= (c_3/c_5)(P_c'/P)(N^3q^4)^{-1}[b_1+(15/2)(kT/a)c].\end{aligned} \tag{32B}$$

$$C_{\text{theory}} = 3{\cdot}8\times10^{-23} = (c_3/c_5)(P_c'/P)^5(N^5q^6)^{-1}c. \tag{32C}$$

These actually constitute 5 equations in the four parameters a, b_1, b_2 and c since equation (32A) and (32B) each lead to two relations. The temperature dependent part of (32B) was used as a consistency check; that is the four remaining relations were used to find a and c and these values to calculate (dB/dT).

Table 3 shows the result for a, b_1, b_2 and c and the resulting (dB/dT) for the three possibilities considered here (Ti, O_a or O_b having the nonlinear ionic polarizibility) and the equivalent result using SLATER's results directly but including the cx^6 term in the potential.

The a's given in Table 3 are calculable from

$$X_i' = (4\pi/V)(n_i^2e^2/2a_i) \tag{33}$$

where n_i is the number of electronic charges carried on atom "i". Equation (33) was used as an overall

Table 3. Coefficients of the potential function, ϕ, and dB/dT. Experimental $dB/dT = 4{\cdot}2\times10^{-15}$

	Ti	O_a	O_b	Slater
a/n^2	$3{\cdot}0\times10^{5}$	$3{\cdot}1\times10^{5}$	$0{\cdot}70\times10^{5}$	$1{\cdot}2\times10^{5}$
b_1/n^4	$-2{\cdot}1\times10^{21}$	$-2{\cdot}6\times10^{21}$	$-7{\cdot}3\times10^{22}$	$-2{\cdot}6\times10^{19}$
b_2/n^4	$2{\cdot}4\times10^{22}$	$1{\cdot}8\times10^{22}$	$1{\cdot}6\times10^{23}$	$9{\cdot}8\times10^{20}$
c/n^6	$3{\cdot}5\times10^{38}$	$7{\cdot}7\times10^{38}$	$4{\cdot}6\times10^{40}$	$5{\cdot}0\times10^{35}$
dB/dT	$0{\cdot}68\times10^{-15}$	$1{\cdot}2\times10^{-15}$	$11{\cdot}1\times10^{-15}$	$0{\cdot}19\times10^{-15}$

arithmetic check, which tests both the accuracy of KINASE's matrix as well as the calculations performed for this work. The results are $X = 0{\cdot}0748$, $0{\cdot}0739$, and $0{\cdot}323$ for Ti, O_a and O_b respectively. The most serious discrepancy is in O_b. The source of error seems to have been in rounding several of the α's and p and q before the machine calculations performed for this work.

It is seen that the coefficient b_1 must be negative regardless of which ion is considered the source of the non-linearity. In no case is the value of b_1 required large enough in magnitude to result in a potential minimum away from the symmetrical position in the lattice.

The (dB/dT) values tabulated are to be compared with the obersved value $(4{\cdot}2\pm10^{-15})$. It is seen that all the results found here are of the same order of magnitude as this value.

The next step in the treatment would be the calculation from our model and the short-range forces in the crystal of the coefficients a, b_1, b_2 and c of equation (16) for the various atoms and a comparison of these results with those of Table 3. Unfortunately exact knowledge of these short-range forces is lacking. DEVONSHIRE[2] discusses the quantity "a" derived from a model of a completely ionic crystal in which short-range repulsive interactions of the form λr^{-9} and van der Waals interactions of the form μr^{-6} in addition to coulomb and ion-dipole forces are taken into account. He comes to the conclusion that O_a is the most loosely bound to its site because the ion-dipole interaction associated with the highly polarizible O ion overcomes the "hard" binding associated with the short-range repulsive force.

KINASE and TAKAHASHI,[17] in a similar treatment assuming a displaceable Ti ion and taking into account only the λr^{-9} and μr^{-6} terms, find a and b_1 to be $5{\cdot}1\times10^{5}$ and $1{\cdot}9\times10^{22}$ c.g.s. respectively. Their results on the tetragonality associated with the onset of spontaneous polarization also indicate that the crystal is about 50 per cent ionic. It is worth noting that on the basis of a model similar to that on which the calculations reported here depend they find reasonable agreement with the atomic displacements and the c/a ratio in the tetragonal phase of $BaTiO_3$.

If only short-range repulsive forces, van der Waals forces and coulomb forces are included, the calculations of b_1 for Ti, O_a and O_b yield a positive value for all cases. If, however, the ion-polarizible sphere interaction is included for the case of the sphere large,[18] then it appears that b_1 is negative for the O_b atom and almost negative for the O_a atom. Reliable quantitative results await the acquisition of a better knowledge of the short-range interactions of atoms in a solid.

7. DISCUSSION

The first question to consider is: How good is the model? It succeeds here in explaining at least qualitatively and, to a fair approximation, quantitatively, most of the experimental observations related to the free energy. There have appeared in the literature several other calculations based on essentially this model which have again at least qualitatively explained the behavior of this and other perovskites. Specifically the spontaneous strain[17] and the relation between ferroelectric and antiferroelectric arrays[11, 19] have been treated.

VOL. 3 1957

Similar earlier treatments are found in the works of KAENZIG[12] and KAY and VOUSDEN.[14] These latter two papers, in addition, concern themselves with what is actually the principal shortcoming of the model, namely, the treatment of short-range interactions.

Also to be considered is whether other models, of which several have been proposed, will do as well or better. JAYNES,[20] in addition to the type of treatment given here, considers the MASON-MATTHIAS[21] model of the "many valleyed" potential of the Ti atom and a model due to Jaynes which considers the TiO_6 octahedra of the structure as a unit. The former model (MASON-MATTHIAS) is analysed at some length by JAYNES. He concludes on the basis of reasonable arguments that neither is the model self-consistent, nor does it agree with the experimental data.

The electronic theory of JAYNES which considers the electronic states of the TiO_6 octahedra, certainly will have to be considered when the short-range forces are treated more accurately. But this treatment cannot by itself tell the entire story since the relative atomic displacements on polarization are not considered. There is no way of associating these displacements with the distortion of electron clouds since the neutron diffraction data sees the nuclei themselves.

There are two other models which should be considered: a treatment due to HAGEDORN[22] and a more qualitative approach due to MEGAW.[23] HAGEDORN considered that the charge on each atom was the important parameter and derived an empirical relation between the charge and the polarizibility. By an iteration procedure in which the dielectric constant and spontaneous polarization data are matched, he arrives at values for the charges, polarizibility and polarization of each ion. The charges found are 0·55, 0·300, —0·365 and —0·125 electronic charges for the B_a, Ti, O_b and O_a ions respectively. This would mean that the structure is hardly ionic at all. It would also mean that a considerable charge rearrangement occurs at the Curie point since in the cubic phase the charges on O_a and O_b must obviously be equal. Furthermore, associated with the large relative charge on Ba is a large polarizibility so that this ion contributes 70% of the total polarization. One would conclude from this that the dielectric behavior of $BaTiO_3$ would be very sensitive to the atom in the Ba site. This is contrary to the conclusions drawn by TAKAGI[19] on calculating the interactions which can be said to "cause" ferroelectricity in the perovskites. He finds that the behavior is quite insensitive to the polarizibility of the atom at this site. In fact WO_3, which is almost a ferroelectric,* has this site vacant.

MEGAW suggests that the onset of the polar state is associated with a change of the character of the bond between the Ti and the surrounding Oxygens. This would mean that the transition from the cubic to tetragonal phase comes about at the crossing of two free energy curves rather than at a point at which one of two minima on a single curve drops below the other. Arguments given in section 2 indicate that the latter is actually the case.

It is concluded that the model used here represents a reasonable approximation to the problem and that ferroelectricity as a phenomenon is explained in a straightforward way in terms of internal fields and reasonable forces between atoms. What is lacking is a more accurate knowledge of these microscopic forces. Ferroelectricity can then be another tool by which these microscopic interactions in solids may be studied.

REFERENCES

1. SLATER J. C. *Phys. Rev.* **78,** 748 (1950).
2. DEVONSHIRE A. F. *Phil. Mag.* **40,** 1040 (1949).
3. DEVONSHIRE A. F. *Phil. Mag.* **42,** 1065 (1951).
4. FRAZER B. C., DANNER, H. R., and PEPINSKY R. *Phys. Rev.* **100,** 745 (1955).
5. MERZ W. J. *Phys. Rev.* **91,** 513 (1954).
6. HUIBREGTSE E. J. and YOUNG D. R. *Phys. Rev.* **103,** 1705 (1956).
7. DROUGARD M. E., LANDAUER R. W., and YOUNG D. R. *Phys. Rev.* **98,** 1010 (1955).
8. TRIEBWASSER S. *Phys. Rev.* **101,** 993 (1956).
9. ROBERTS S. *Phys. Rev.* **81,** 865 (1951).
10. COHEN M. H. *Phys. Rev.* **84,** 368 (1951).
11. KINASE W. *Progr. Theor. Phys., Osaka* **13,** 529 (1955).
12. KAENZIG W. *Helv. Phys. Acta* **24,** 175 (1951).
13. BOND W. L., MASON W. P., and MCSKIMIN H. J. *Phys. Rev.* **82,** 442 (1951).
14. KAY H. E. and VOUSDEN P. *Phil. Mag.* **40,** 1019 (1949).
15. SHIRANE G. and TAKEDA A. *J. Phys. Soc. Japan* **7,** 1 (1952).

* TAKAGI[20] and COHEN[11] discuss the relation between the ferroelectric and antiferroelectric states and point out that it is difficult to choose between them in selecting the lower energy configuration in $BaTiO_3$.

16. KAY H. F. *Acta Cryst.* **1,** 229 (1948).
17. KINASE W. and TAKAHASHI H. *J. Phys. Soc. Japan* **10,** 942 (1955).
18. BOTTCHER C. F. *Theory of Electric Polarization* Elsevier Publishing (1952).
19. TAKAGI Y. *Proc. Int. Conf. on Theoretical Physics* p. 824. Kyoto and Tokyo (1953).
20. JAYNES E. T. *Ferroelectricity* Princeton University Press (1953).
21. MASON W. P. and MATTHIAS B. T. *Phys. Rev.* **74,** 1622 (1948).
22. HAGEDORN R. *Z. Phys.* **133,** 394 (1952).
23. MEGAW H. D. *Acta Cryst.* **5,** 739 (1952); *ibid.* **7,** 187 (1954).

VOL
3
195

J. Phys. Chem. Solids Pergamon Press 1957. Vol. 3. pp. 63–73.

VARIATION OF THE DISTRIBUTION COEFFICIENT AND SOLID SOLUBILITY WITH TEMPERATURE

R. N. HALL

General Electric Research Laboratory, Schenectady, New York, U.S.A.

(*Received* 11 *March* 1957)

Abstract—The distribution coefficient of a solute having a low solid solubility should vary with temperature according to the equation, $\log k = B - A/T$. Analysis of the published solubility data involving germanium and silicon show that this form for the temperature variation of the distribution coefficient is obeyed within the accuracy of the experimental measurements, except, perhaps, in the case of lithium in silicon. The valves which are observed for the constant B can be explained by assuming that the heat of solution in the solid phase has a negative temperature coefficient.

A systematic trend is noted in the behavior of solutes having different distribution coefficients. Families of solubility curves are calculated for germanium and silicon on the assumption that this behavior holds for all slightly soluble impurities in these two crystals.

VOL. 3 1957

INTRODUCTION

IT HAS been recognized for some time that the solidus curve of a binary phase diagram generally exhibits the phenomenon of retrograde solubility when the solid solubility is small.[1] A solubility maximum is observed at a temperature somewhat below the melting point of the pure solvent as the result of the temperature dependence of the distribution coefficient. When small amounts of solute are present in the melt, the freezing temperature is nearly that of the pure solvent, and the amount of solute incorporated in the solid phase is approximately proportional to that in the liquid. With relatively large concentrations of solute, however, the freezing point depression becomes quite large, and the distribution coefficient may decrease to such small values that the concentration appearing in the crystal actually decreases with further solute additions. Such behavior is the rule rather than the exception among strongly segregated solutes.

The need for semiconductor crystals containing accurately controlled amounts of impurities has stimulated interest in the variation with temperature of solid solubilities in these binary systems, and a considerable amount of data on the subject has appeared recently.[2–20] In most cases, the temperature variation of the distribution coefficients calculated from these measurements can be fitted to the equations which have been deduced from thermodynamic arguments.[2–4] However, little has been said regarding the significance of the values which must be assigned to the solubility parameters in order to obtain such a fit.

This paper presents a statistical treatment of solid solubility which may add to the physical understanding of the problem. In addition, a comparison of the measured distribution coefficients in germanium and in silicon reveals a systematic behavior which should be useful in predicting solubilities in systems which have not yet been measured extensively.

In a few cases, the reported solubilities conflict with theoretical expectations. This difficulty prompted a re-examination of the two most serious examples, indium in germanium[9] and lithium in silicon.[18] The new data[12,19] are consistent with the expected behavior, suggesting that similar agreement would result from more careful measurement in the other cases where anomalous behavior has been reported.

VARIATION OF THE DISTRIBUTION COEFFICIENT WITH TEMPERATURE

THURMOND and STRUTHERS[2] obtained the following expression for the distribution coefficient,

which is the ratio of the solute concentration in the solid to that in the liquid at equilibrium:

$$\ln k = \frac{T_m}{T} \ln k_m + (T_m/T - 1)\frac{\Delta S^f}{R} \qquad (1)$$

k_m is the distribution coefficient at the melting point, T_m, of the pure solvent. ΔS^f is the entropy of fusion of the solute, a positive quantity which is comparable in magnitude to the gas constant, R. This expression, which has the form $\log_{10} k = B - A/T$, can be fitted to most of the experimental results. To obtain such a fit, however, the constant, B, must be assigned values which correspond to entropies of fusion that are several times larger than normal, and which have the wrong sign. In the derivation of equation (1), it was assumed that the partial molar heat of solution of the solute in the solid phase was independent of temperature. The values which must be assigned to B can be explained by assuming that the heat of solution has a negative temperature coefficient. This assumption gives rise to a term which appears formally as an entropy of solution, but which, from the point of view of statistical mechanics, has a quite different origin.

In order to provide a better understanding of the physical significance of equation (1), we shall present an alternative derivation. We assume that the distribution coefficient is determined by a Boltzmann factor involving the energy, ΔH, required to transfer a mole of solute atoms from the liquid phase to an appropriate position (interstitial or substitutional) in the solid.

$$k = C \exp(-\Delta H/RT). \qquad (2)$$

C is a statistical factor which is equal to the ratio of the densities of states for solute atoms in the two phases. In view of the greater degree of disorder of the liquid, we should expect C to be somewhat smaller than unity. We shall presently identify it with the quantity $\exp(-\Delta S^f/R)$, which varies between 0·1 and 0·4 for most metals.[21]

In view of the correlation between measured values of distribution coefficients and the degree of misfit in the solvent crystal,[22] it is reasonable to suppose that as the temperature is increased and the interatomic distances in the crystal become greater, the energy, ΔH, should decrease. This argument holds for interstitial or large substitutional solute atoms, and thus applies to all of the binary systems involving germanium or silicon for which solid solubility data are available. For simplicity, we shall assume that ΔH decreases linearly with increasing temperature in the range where experimental results are obtained,

$$\Delta H = \Delta H_0 - \alpha T, \qquad (3)$$

where α is an arbitrary constant which will be used to obtain a fit with the experimental results. Substitution of this expression into equation (2) gives,

$$k = C \exp(-\Delta H_0/RT + \alpha/R). \qquad (4)$$

The distribution coefficient measured at the melting point of the pure solvent, k_m, can be used to replace ΔH_0 in equation (4). Using the knowledge that $k = k_m$ at $T = T_m$, we eliminate ΔH_0 and obtain

$$\ln k = \frac{T_m}{T} \ln k_m + \left(\frac{T_m}{T} - 1\right)\left(-\frac{\alpha}{R} + \ln\frac{1}{C}\right). \qquad (5)$$

This equation is identical to equation (1) except that the coefficient of $(T_m/T - 1)$ contains an additional term which resulted from our assumption that the heat of solution of the solute in the solid phase varied with temperature. This term makes it possible to fit the observed form, $\log_{10} k = B - A/T$, without assigning unreasonable values to the entropy of fusion. The identification of C with $\exp(-\Delta S^f/R)$, which was mentioned earlier, can now be made by comparing equations (1) and (5).

Consider, first, the expression for the temperature variation of the distribution coefficient which is obtained by setting $\alpha = 0$ and $C = 1$.

$$k = (k_m)^{T_m/T}. \qquad (6)$$

This equation, involving the single adjustable parameter k_m, can be expected to display the gross features of the temperature variation of the distribution coefficient. It has the property that $\ln k$ vs. $1/T$ plots as a straight line with an intercept of $k = 1$ at $T = \infty$. Real systems will deviate somewhat from this simple form, but large departures are not to be expected. As indicated by equation (1) and equation (5), the corrections which are likely to be most significant will affect the intercept at $T = \infty$, but will preserve the linearity of a plot of $\ln k$ vs. $1/T$.

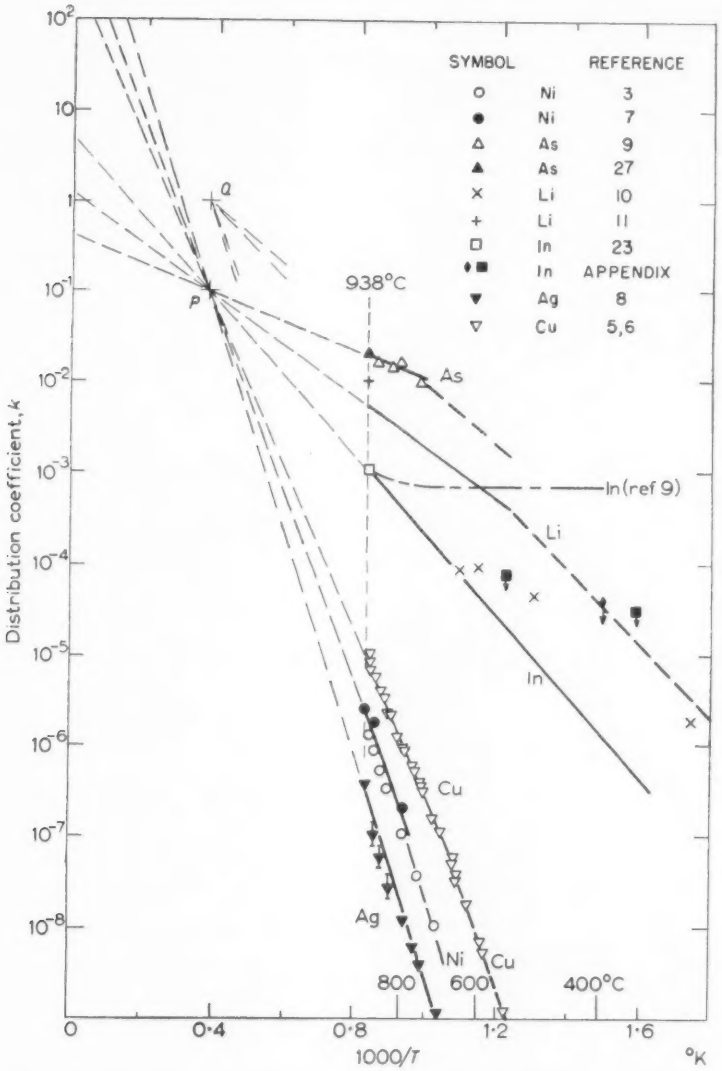

FIG. 1. Temperature variation of the distribution coefficients of several impurities in germanium. The straight lines drawn through the data are solid above the eutectic temperature and dashed below.

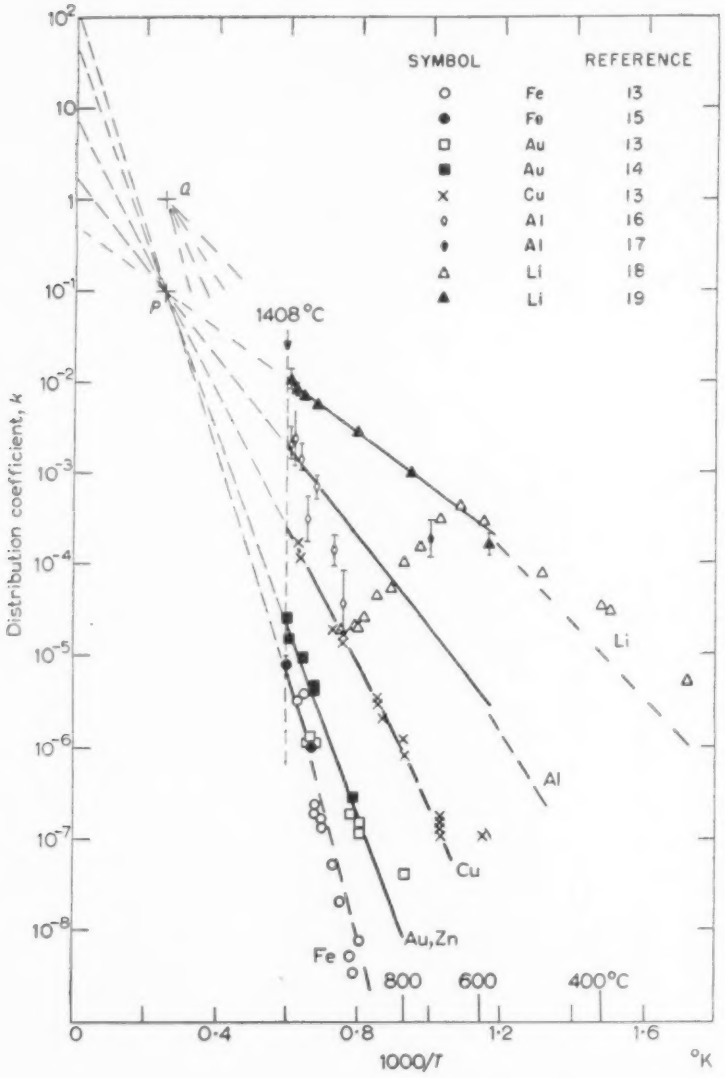

FIG. 2. Temperature variation of the distribution coefficients of several impurities in silicon. The straight lines drawn through the data are solid above the eutectic temperature and dashed below.

Equation (6) is sufficient to give a useful estimate of the temperature variation of the distribution coefficient and the saturation solubility, once any single point has been determined. Thus, a good guess can be made of the solubilities of a large number of impurities on the basis of the melting-point distribution coefficients which have been reported.[23] Furthermore, the nature of the deviations from this formula which may be expected are indicated by equation (5), and estimates can be made of the magnitude of these correction terms.

It will be seen from the discussion of the solubility data that the temperature coefficient of ΔH tends to be larger for the more strongly segregated impurities. The assumption,

$$\alpha = \Delta H_0/T_0, \tag{7}$$

provides a good fit with the experimental results, and leads to a simple construction for plots of $\ln k$ vs. $1/T$. T_0 is a proportionality constant which is independent of ΔH_0, and which, presumably, is related to the coefficient of thermal expansion of the crystal. While equation (7) is purely an empirical relation, it is reasonable to suppose that an impurity which exhibits a large activation energy should be associated with a correspondingly large temperature coefficient. When this equation is combined with (4), we see that all of the curves for different distribution coefficients pass through a single point at $T = T_0$ and $k = C$, as indicated by point P in Figs. 1 and 2. The data which are now available can be fitted by setting $T_0 = 2{\cdot}3\ T_m$ for both germanium and silicon. This fit implies a change of approximately 20 per cent in the heat of solution over a temperature range of 500°C.

TREATMENT OF EXPERIMENTAL RESULTS

Knowledge of the liquidus curve is required in order to calculate the distribution coefficient from solubility data. Rather than referring to individual phase diagrams, which in some cases are not available, it was assumed that the liquidus was that of an ideal solution as given by,

$$\ln(1-x) = \frac{-\Delta H^f}{R}\left(\frac{1}{T}-\frac{1}{T_m}\right), \tag{8}$$

where x is the fraction of solute atoms in the liquid phase, and ΔH^f is the heat of fusion of the pure solvent. For germanium, it was assumed that the melting point was 938°C[24,25] and that the heat of fusion was 7700 cal/mole.[21] For silicon, a melting temperature of 1408°C[19] and a heat of fusion of 11,100 cal/mole[21] were used.

For reasonably dilute solutions ($x < 0{\cdot}1$) involving easily segregated solutes ($k_m < 0{\cdot}1$), departures from ideality are small, and this equation is more reliable than most published phase diagrams. Moderate errors may arise when the concentrations of solvent and solute are comparable ($x \approx \frac{1}{2}$), but in most of the examples which we shall discuss, the experimental liquidus curves give solute concentrations which differ by less than 20 per cent from those calculated from equation (8). In the cases of gold and lithium in silicon, the departures from ideality are somewhat larger, as will be noted in the discussions of these two systems. At still higher solute concentrations, large departures from ideality do not introduce appreciable error because the solute concentration will be close to unity in any event.

At some sufficiently low temperature, the solute phase will change from a liquid to a solid. In all of the systems which we shall examine, this change involves a eutectic transformation in which the solute concentration in the liquid phase is always less than that of the solid phase which replaces it. (The opposite will be true of a peritectic transformation.) Below the eutectic temperature, the distribution coefficient is equal to the solute concentration in the solid solution divided by the concentration in the solid phase which is in equilibrium with it. As the temperature is decreased through the eutectic point, the distribution coefficient must decrease discontinuously, and then continue with a slope which is still largely determined by the energy required to dissolve a solute atom in the host crystal. The distribution coefficient will still be given by an expression like equation (5), with a heat of solution that has essentially the same magnitude and temperature coefficient. However, the constant, C will be approximately unity, since the equilibrium is now between two solid phases. Therefore, it is to be expected that distribution coefficients below the eutectic temperature will tend to converge to a point located near $k = 1$ when extrapolated to high temperatures, as indicated by point Q in Figs. 1 and 2. (Similar behavior has been noted by FINK and FRECHE[26] in the solid solubilities, and hence in the distribution coefficients, of aluminum

alloys measured below the eutectic temperature. In this series of alloys, $T_0 = 3{\cdot}6\ T_m$.)

The discontinuity which occurs in the distribution coefficient at the eutectic temperature is almost imperceptible in each of the systems which we shall examine, because the composition of the solute phase does not change significantly when it solidifies. The change in slope which is to be expected at this temperature can be expressed by the following equation, which is based upon the discussion of the preceding paragraph:

$$\left.\frac{d\ln k}{d(1/T)}\right|_{\text{liq.}} - \left.\frac{d\ln k}{d(1/T)}\right|_{\text{solid}} = T^e\Delta S^e/R \qquad (9)$$

T^e is the temperature of the eutectic transformation, and ΔS^e is an entropy term which must be comparable in magnitude to the entropy of fusion appearing in equation (1).

In presenting the experimental results, straight lines will be drawn through the data points, solid above the eutectic temperature, and dashed below. In general, the change in slope will be barely perceptible with highly segregated impurities, but will be an important effect if k is close to unity. Thus, any system with a solid solubility great enough to be included in a conventional phase diagram can be expected to display a pronounced change of slope at the eutectic temperature.

The binary systems which will be discussed are those for which extensive data are available, or for which the results conflict seriously with the behavior to be expected on the basis of equation (5). The straight lines drawn through the data points are drawn in accord with the empirical relation equation (7), and they therefore all extend through a single point at a temperature well above the melting point. Below the eutectic temperature, the slopes are drawn so as to extend through point Q in accord with equation (9). This construction indicates the manner in which the distribution coefficient should vary if the only temperature dependent quantity is the linear term in the heat of solution, as represented by equations (3) and (7). Moderate departures from this simple behavior can be expected when the solubility is relatively large and where the data cover a considerable range of temperature.

SOLUBILITIES INVOLVING GERMANIUM

Fig. 1 summarizes the data which have been reported for systems involving germanium. Extensive measurements have been made of the solid solubility of copper over a wide temperature range.[4,5,6] Data obtained from radioactive tracer determinations by FULLER *et al.*[5] and from electrical measurements by WOODBURY and TYLER[6] all fall almost exactly along the straight lines which extend through points P and Q.

Nickel is another strongly segregated impurity.[3,7] As in the case of copper, the results are consistent with a straight line having a slight break at the eutectic temperature. Silver behaves similarly, but has an even small distribution coefficient.[8]*

Arsenic is much more soluble in germanium[9,27] and the distribution coefficient shows a correspondingly smaller variation with temperature. Measurements have not been made below the eutectic temperature. The dashed line has been added in order to show the greater apparent effect of a phase change upon the distribution coefficient of a more soluble impurity.

Conflicting evidence has been reported regarding lithium in germanium. REISS, FULLER and MORIN[10] have determined the solubility between room temperature and 650°C. The distribution coefficient calculated from these data has a reasonable slope between 200°C and 300°C, but goes through a maximum near 600°C, which is difficult to understand. Furthermore, these results are not consistent with the reported value at the melting point, $k_m > 0{\cdot}01$.[11] In view of the explanation[19] for a similar anomalous situation regarding lithium in silicon, the data near 600°C will be discounted. A tentative distribution coefficient curve has been drawn which follows the behavior exhibited by Cu, Ag, Ni, and As. It comes close to the values measured at the melting point and at low temperatures.† (Points at 200°C and 250°C fall exactly on this curve, but are beyond the edge of the diagram.)‡

* Five measurements by WOODBURY and TYLER based on analysis of HALL coefficient data are shown. Another point at 648°C falls on the same straight line. The three points with indicated probable errors were determined by CARLSON using radioactive silver.

† The temperature of the eutectic between germanium and a germanium-lithium compound was measured by E. M. PELL as being 525±10°C.

‡ *Note added in proof:* Recent data by PELL fall below this curve by a factor of approximately two. (In press.)

The distribution coefficient of indium in germanium is reported to be almost independent of temperature.[9] However, evidence which will be presented in the Appendix shows that it does decrease rapidly with decreasing temperature. As in the case of lithium, a tentative curve has been drawn through the well-established value at the melting point to indicate the behavior to be expected of indium.

Curves showing the solubilities of zinc, aluminum, gallium, tin and antimony in germanium have been published.[9] These data were obtained by a method similar to that used in determining the indium solubility curve but were omitted from Fig. 1 because they might be subject to similar errors, arising from solute inclusions within the germanium crystals. The arsenic data were used because, from the information available, they appeared to be the most accurate, and because a system having a relatively high solubility was needed in order to establish a reliable intercept for the point, *P*. Actually, the experimental uncertainties are such that the value for the ordinate of this intercept could easily be in error by a factor of two. The value assigned to it is, however, consistent with the thermodynamic arguments which have been presented, and with the position of the similar intercept determined by the more extensive silicon data.

VOL. 3 1957

SOLUBILITIES INVOLVING SILICON

Distribution coefficients calculated from the reported solubilities of several elements in silicon are summarized in Fig. 2. The data representing gold[13,14] would be shifted upward by a factor of approximately 1·4, except very near the melting point, if the measured liquidus were used instead of the values calculated from equation (8). In either case, the results behave as expected within the experimental uncertainties.

The points representing the distribution coefficients of copper[13] and iron[13,15] fall close to straight lines which have a common intersection with the line representing gold. The iron solubility data cover a considerable range of temperature below the eutectic transformation. Here, the equilibrium is between silicon and $FeSi_2$, and the distribution coefficient is equal to three times the solubility, since it is defined as the ratio of the concentration of iron in the silicon phase divided by that in the $FeSi_2$ compound. A much steeper slope would have been obtained if the composition of the iron-rich phase was assumed to be that of an ideal liquid as was done above the eutectic temperature. Within the experimental error, the solubility of iron behaves as expected, both above and below this temperature.

Data on the solubility of aluminum in silicon involve considerable experimental uncertainty but are included because of the importance of this system in connection with the construction of silicon rectifiers and transistors. The line which is drawn to represent the distribution coefficient of aluminum tends to lie above the measurements obtained from diffusion experiments[16] but below a determination based upon a thermal gradient method.[17]*

It has been reported[10,11,18] that the solubility of lithium in solid silicon exhibits a pronounced maximum at 650°C. Distribution coefficients calculated from these data show a corresponding maximum as shown by the open triangles in Fig. 2. At temperatures below the maximum, the distribution coefficient varies in a normal manner. Above this temperature, however, the reported behavior is completely anomalous.† Much greater solubilities at high temperatures have been measured by PELL.[19] His results agree with previous determinations at 600°C, and the temperature variation of the distribution coefficient calculated from his data is similar to those exhibited by other solutes in silicon.‡ In view of the large departures from ideality observed for lithium-silicon solutions,[19]

* *Note added in proof:* Data by D. NAVON and V. CHERNYSHOV fall almost exactly along this line. (In press.)

† The suggestion that the solubility maximum is the result of a phase change[18] is unacceptable. The magnitude of this effect is much too small, as calculated from equation (9). Furthermore, it would only affect the temperature variation *below* the phase change, whereas it is the high temperature behavior which is anomalous.

‡ The absence of the solubility maximum at 650°C invalidates the theory which has been proposed[18] to explain the effect of dissolved boron upon the apparent solubility of lithium at high temperatures. An alternative explanation is that lithium precipitates within the sample as it cools until the concentration still in solution becomes comparable with that of boron. By the time this temperature is reached, the silicon is extrinsic and electron-hole interactions prevent the precipitation of any more lithium by the mechanism discussed by H. REISS *J. Chem. Phys.* **21,** 1209 (1953).

all of the distribution coefficients for this system were calculated on the assumption that it was a regular solution fitted to the known composition of the eutectic.

The slope of the line which represents the distribution coefficient of lithium in silicon below the eutectic temperature is somewhat steeper than is indicated by the data in this temperature range. A reasonable explanation for this discrepancy is that the heat of solution cannot be adequately represented by equation (3) over such a wide temperature range, and that the real distribution coefficient has a small curvature, in addition to the indicated change of slope.

The solubility of zinc in silicon has been measured by FULLER and MORIN.[20] Although these authors felt that the zinc concentration was determined by an equilibrium between zinc vapor and the solid silicon, the observation that a 100-fold change in zinc pressure had no significant effect upon the measured solubility would make it appear probable that a liquid phase was actually present, and that the solubility which was observed was the true solidus curve. On the assumption that this was the case, distribution coefficients were calculated from these solubilities. The results fall along the line which represents the gold distribution coefficient, well within the reported experimental error.*

CONCLUDING REMARKS

Experimental evidence confirms the theoretical expectations that all slightly soluble impurities have distribution coefficients which vary with temperature in accord with the equation, $\log_{10} k = B - A/T$. Only in the case of lithium in silicon, where the data cover a very wide range of temperature, does there appear to be any indication that additional terms involving T are required to fit the results. In an ideal system, B would be zero or slightly negative because of the greater degree of disorder of the liquid phase. In the real systems which have been examined, B is generally positive, and may be as large as two or three, the larger values being associated with solutes having very small distribution coefficients. The magnitude and sign of B can be explained by assuming a reasonable value for the temperature coefficient of the heat of solution of the solute into the solid phase.

In view of the apparent tendency for large values of B to be associated with small distribution coefficients, an attempt was made to fit the solubility data with curves which assume that the temperature dependence of the heat of solution is given explicitly by $\Delta H = \Delta H_0(1 - T/T_0)$, which is the equivalent of equation (7). This assumption causes B to vary with k_m in such a way that all distribution coefficient curves pass through a single point at $T = T_0$. Inspection of Figs. 1 and 2 shows that all of the data involving germanium and silicon can be fitted in this way, within experimental error.

The values for the heat of solution, ΔH_0, its temperature coefficient, $\Delta H_0/T_0$†, and the melting-point distribution coefficient, k_m, which correspond to the solid lines drawn in Figs. 1 and 2 are summarized in Tables 1 and 2.

Table 1. Germanium solid solutions

Solute	ΔH_0 kcal/mole	$\Delta H_0/T_0$ cal/mole-deg.C	k_m
As	7·4	2·6	$2{\cdot}0\times10^{-2}$
Li	13	4·7	5×10^{-3}
In	20	7·3	$1{\cdot}0\times10^{-3}$
Cu	41	15	9×10^{-6}
Ni	47	17	$2{\cdot}4\times10^{-6}$
Ag	56	20	3×10^{-7}

Table 2. Silicon solid solutions

Solute	ΔH_0 kcal/mole	$\Delta H_0/T_0$ cal/mole-deg.C	k_m
Li	13·5	3·5	$1{\cdot}0\times10^{-2}$
Al	23	5·9	$2{\cdot}0\times10^{-3}$
Cu	34	8·9	$2{\cdot}5\times10^{-4}$
Zn	48	12	$2{\cdot}3\times10^{-5}$*
Au	48	12	$2{\cdot}3\times10^{-5}$
Fe	56	14	8×10^{-6}

* This value should be decreased by a factor of two if zinc is a double acceptor.

* Recent experiments by R. O. CARLSON indicate that zinc is a double acceptor in silicon. The solubilities reported by FULLER and MORIN should therefore be decreased by a factor of two.

† This term is represented by the symbol, σ, in equations (14) and (15) of Ref. 2.

Although the linear relation between the heat of solution and its temperature coefficient cannot be expected to be exact, it is nevertheless reasonable to suppose that the distribution coefficients of other solutes will exhibit similar tendencies. Accordingly, sets of solid solubility curves have been calculated for germanium and silicon, assuming a family of distribution coefficients which vary logarithmically with $1/T$ and pass through the point $k = 0{\cdot}1$ at $T = 2{\cdot}3\ T_m$, and making use of the liquidus curve for an ideal solution, equation (8). These solubility curves are shown in Figs. 3 and 4, plotted on a

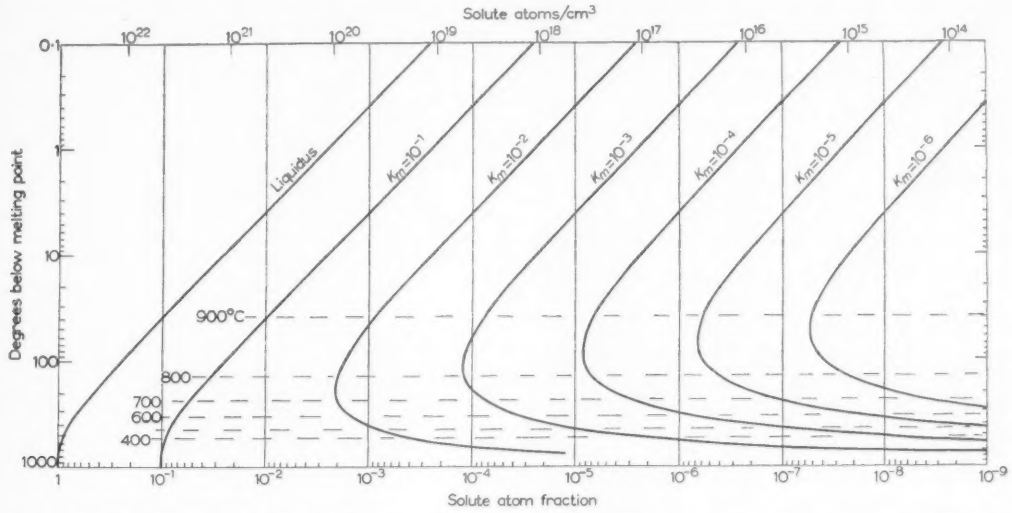

FIG. 3. Calculated solid solubility curves for germanium. The parameter, k_m, is the distribution coefficient at the melting point of pure germanium.

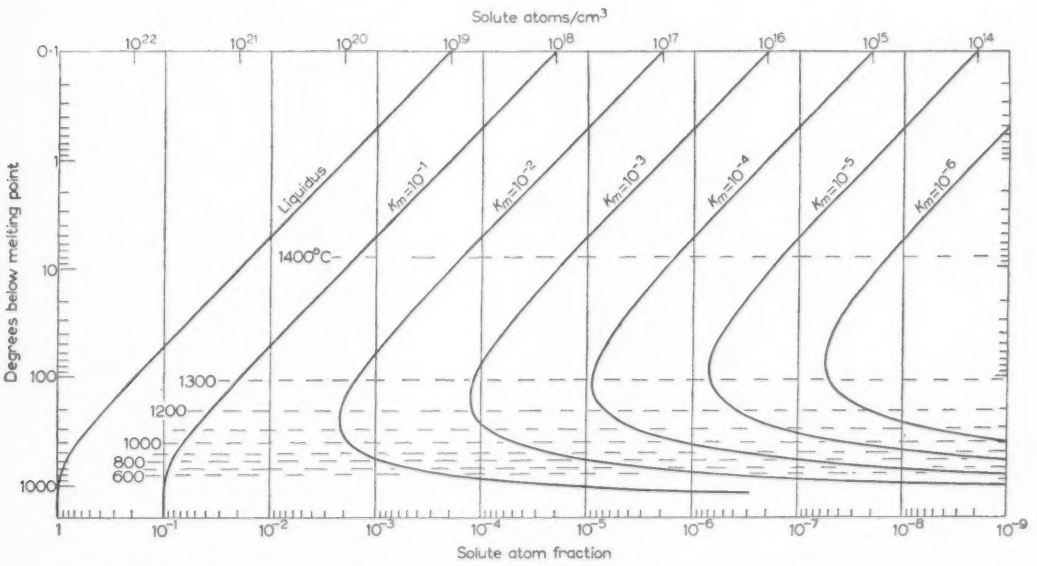

FIG. 4. Calculated solid solubility curves for silicon. The parameter, k_m, is the distribution coefficient at the melting point of pure silicon.

log-log scale so as to emphasize the regions of the phase diagram which are of greatest interest for semiconductor purposes. By construction, all of the lines drawn through the data points in Figs. 1 and 2 above the eutectic temperature correspond exactly to the families of curves which are drawn in Figs. 3 and 4. The liquidus curve is included in order to facilitate a determination of the melting point depression when the solute concentration is so small that this temperature difference cannot be measured directly.

Acknowledgements—The author is indebted to R. O. CARLSON, C. B. COLLINS, E. M. PELL, A. G. TWEET, W. W. TYLER, and H. H. WOODBURY for numerous helpful discussions and for permission to make use of hitherto unpublished data. A large part of the experimental work discussed in the appendix was performed by Miss A. D. WARNER and Miss S. SCHWARZ.

APPENDIX: THE LOW-TEMPERATURE SOLUBILITY OF INDIUM IN GERMANIUM

It is a well-established fact that small additions of aluminum or gallium have a profound effect upon the emitter efficiency of indium junctions alloyed to germanium at temperatures in the neighborhood of 400°C.[28,29] Experiments performed in this laboratory[30] have shown that atomic fractions of gallium as small as 4×10^{-4} have a distinct effect. (More dilute alloys were not investigated.) These experiments indicate that the distribution coefficient of indium is smaller than that of gallium at this temperature by a factor which is no greater than 4×10^{-4}. (This conclusion depends upon the assumptions that the activity of gallium in an indium solution is equal to its mole fraction, and that the effect of the addition of the gallium is to increase the number of acceptors included in the regrowth germanium, without increasing the lifetime in this region.) Since it can be assumed that the distribution coefficient of gallium at 400°C is no greater than $0{\cdot}10$[9,22,23] it follows that indium has a coefficient which is at most 4×10^{-5}, probably it is many times smaller than this. This conclusion is represented by the solid diamond in Fig. 1.

Additional evidence has been obtained by the author from measurements of germanium crystals grown from an indium-rich solution. Twenty-gram melts of indium, contained in quartz test-tubes in a hydrogen atmosphere were saturated with germanium at temperatures between 400°C and 600°C, and then cooled at a rate of 25°C/hr. Germanium crystals which nucleated in the melt and floated to the top were removed after they had grown to a length of two or three millimeters and etched free of the exterior coating of indium, using HCl. Selected crystals were ground to the size of bars approximately 1 mm long and 0·2 mm square and etched to reveal the presence of indium inclusions. Indium contacts were fused to the ends of those bars which appeared to be free of inclusions and resistivity values were determined by measuring the resistance between the indium contacts. Indium concentrations were calculated from these values, using the known relation between resistivity and acceptor concentration.* The results showed considerable scatter, much more than could be accounted for by uncertainties in the electrical measurements or the sample dimensions. Presumably, the scatter was primarily caused by undetected indium inclusions within the samples, and this was proved to be the case in some instances by further chemical etching of several of the bars. Of the 20 determinations which were made, 17 indicated acceptor concentrations between 10^{18} and $5\times10^{18}/cm^3$. The average concentration calculated for crystals grown in a temperature interval close to 550°C was $2{\cdot}6\times10^{18}/cm^3$, whereas samples grown near 360°C contained approximately half this concentration of acceptors. Since the presence of indium inclusions will indicate more acceptors than are really present in solution, these two values represent only upper limits to the indium solubility, as indicated by the two solid squares in Fig. 1. The indium which was used was obtained from the Indium Corporation of America. Crystals grown from "99·97 per cent pure" indium could not be distinguished from those grown from "99·9975 per cent pure" indium.

REFERENCES

1. MEIJERING J. L. *Philips Res. Rep.* **3,** 281 (1948).
2. THURMOND C. D. and STRUTHERS J. D. *J. Phys. Chem.* **57,** 831 (1953).
3. VAN DER MAESEN F. and BRENKMAN J. A. (Ni in Ge) *Philips Res. Rep.* **9,** 225 (1954).
4. HODGKINSON R. J. (Cu in Ge) *Phil. Mag.* **46,** 410 (1955).
5. FULLER C. S., STRUTHERS J. D., DITZENBERGER J. A., and WOLFSTIRN K. B. (Cu in Ge) *Phys. Rev.* **93,** 1182 (1954).
6. WOODBURY H. H. and TYLER W. W. (Cu in Ge) *Phys. Rev.* **105,** 84 (1957).
7. TYLER W. W. and WOODBURY H. H. (Ni in Ge) *Bull. Amer. Phys. Soc.* Series II, **2,** No. 3 (1957); *Phys. Rev.* **98,** 461 (1955).

* Unpublished data by T. J. SOLTYS, H. H. WOODBURY, and W. W. TYLER, General Electric Research Laboratory, give the following relation between free carrier concentration and the room temperature resistivity of germanium doped with donors or acceptors:

Carrier concentration (cm^{-3}) ..	$1{\cdot}0\times10^{17}$	$1{\cdot}0\times10^{18}$	$1{\cdot}0\times10^{19}$
Resistivity, *n*-type (ohm-cm) ..	0·033	0·0064	0·0018
Resistivity, *p*-type (ohm-cm) ..	0·057	0·011	0·0028

8. Woodbury H. H., Tyler W. W., and Carlson R. O. (Ag in Ge). Unpublished data, General Electric Research Laboratory.
9. Thurmond C. D., Trumbore F. A., and Kowalchik M. (Zn, Al, Ga, In, Sn, As, and Sb in Ge) *J. Chem. Phys.* **25,** 799 (1956); Trumbore F. A. *J. Electrochem. Soc.* **103,** 597 (1956).
10. Reiss H., Fuller C. S., and Morin F. J. (Li in Ge and Si) *Bell Syst. Tech. J.* **35,** 535 (1956).
11. Fuller C. S. and Ditzenberger J. A. (Li in Ge and Si) *Phys. Rev.* **91,** 193 (1953).
12. Hall R. N. (In in Ge) Appendix of this paper.
13. Struthers J. D. (Au, Cu, Fe, in Si) *J. Appl. Phys.* **27,** 1560 (1956).
14. Collins C. B., Carlson R. O., and Gallagher C. J. (Au in Si) *Phys. Rev.* **105,** 1168 (1957).
15. Collins C. B. (Fe in Si) General Electric Research Laboratory Memo Report No. P-88, September 6, 1956. Unpublished.
16. Miller R. C. and Savage A. (Al in Si) *J. Appl. Phys.* **27,** 1430 (1956).
17. Trumbore F. A. (Al in Si). Private communication.
18. Reiss H., Fuller C. S., and Pietruskiewicz A. J. (Li in Si) *J. Chem. Phys.* **25,** 650 (1956).
19. Pell E. M. (Li in Si) *Bull. Amer. Phys. Soc.* Series II, **2,** No. 3 (1957); *J. Phys. Chem. Solids* **3,** 77, (1957).
20. Fuller C. S. and Morin F. J. (Zn in Si) *Phys. Rev.* **105,** 379 (1957).
21. Kubaschewski O. and Evans E. *Metallurgical Thermochemistry* (2nd Edition) Wiley, New York (1956).
22. Burton J. A., Kolb E. D., Slichter W. P., and Struthers J. D. *J. Chem. Phys.* **21,** 1991 (1953).
23. Burton J. A. Distribution coefficients in Ge and Si. *Physica* **20,** 845 (1954).
24. Stöhr H. and Klemm W. *Z. Anorg. Chem.* **241,** 305 (1939).
25. Hassion F. X., Thurmond C. D., and Trumbore F. A. *J. Phys. Chem.* **59,** 1076 (1955).
26. Fink W. L. and Freche H. R. *Trans. Amer. Inst. Min. (Metall.) Engrs.* **111,** 304 (1934); Zener C. *Thermodynamics in Physical Metallurgy* Chapter 2. American Society for Metals (1950).
27. Jillson D. C. and Sheckler A. C. *Phys. Rev.* **98,** 229 (1955).
28. Tummers L. J. Nachrichtentechnischen Fachberichten. Beihefte der *F.T.Z.* (Heft *I*) 31–32 (1955).
29. Armstrong L. D., Carlson C. L., and Bentevegna M. *R.C.A. Rev.* **17,** No. 1, 37 (1956).
30. Warner A. D. and Hall R. N. Unpublished data.

VOL. 3 1957

J. Phys. Chem. Solids Pergamon Press 1957. Vol. 3. pp. 74–76.

SOLUBILITY OF LITHIUM IN GERMANIUM

E. M. PELL

General Electric Research Laboratory, Schenectady, New York

(*Received* 30 *April* 1957)

Abstract—The solubility of lithium in germanium has been measured as a function of temperature between 593°C and 899°C. It reaches a maximum impurity atom fraction of $1{\cdot}7\times10^{-4}$ at about 800°C, and the distribution coefficient at the melting point is $(1{\cdot}6$ to $2{\cdot}0)\times10^{-3}$. Lithium content was measured by flame analysis and therefore included Li which precipitated during cooling. Distribution coefficients are in accord with thermodynamic principles when calculated as the ratio of the above solubility data and a liquidus curve calculated from the eutectic point.

Additional information regarding the Li-Ge phase diagram was obtained which indicates the existence of two compounds, $Li_{4n}Ge_n$ (probably Li_4Ge) with a melting point of 750 ± 10°C and $Li_{3n}Ge_n$ (probably Li_6Ge_2) with a melting point of 800 ± 10°C, and a eutectic point at 49 ± 5 atom per cent Li and a temperature of 525 ± 10°C.

INTRODUCTION

THE present report extends the techniques developed for a previous study of lithium solubility in silicon[1] to the study of lithium solubility in germanium. There is some discrepancy between distribution coefficients determined from earlier experiments[2,3] which made it desirable to obtain data in the temperature range between these earlier sets of data. There is also a solubility maximum at about 600°C in one of the earlier observations[3] which we wished to check by chemical means to see if it could have arisen from precipitation of Li during cooling. In addition, the recent work of HALL[4] has indicated the need for better solubility data of low-segregation impurities to confirm our understanding of the solution process.

PROCEDURE

Lithium solubility (solidus)

The experimental techniques were essentially identical to those used in the earlier investigation,[1] differing only in the following respects:

(1) The Ge samples used were much larger than the Si samples of the previous investigation. This was necessary because of the lower solubility of Li in Ge and also because of higher background in the flame analysis of the Ge samples.

(2) The crucible temperature was monitored throughout the diffusion with an attached Pt–Pt 10 per cent Rh thermocouple, in all but the lowest temperature run reported here. This, although not essential, constitutes an improvement over the earlier technique.

(3) In the present series of experiments, no statistical study of reproducibility was made. The error limits indicated in the figures represent limits-of-error for 95 per cent confidence, as estimated by the chemists. (In the previous experiments with Si, statistical analysis indicated that total probable errors, inclusive of all steps in the experiment, were higher than this.)

Lithium-germanium liquidus

For the melting point of Ge we used 937°C.[5,6] The eutectic point was determined by the methods used previously,[1] and was found to lie at 525 ± 10°C, 49 ± 5 atom per cent of Li. The liquidus between these points was calculated by assuming the solution to be "regular", as before; and this liquidus was used in calculating the distribution coefficients.

RESULTS AND DISCUSSIONS

The new solubility data are plotted in Fig. 1, and the log of the distribution coefficient vs. $1/T$ is given in Fig. 2. In Fig. 2, it is seen that a straight line can be drawn which passes through the data and also passes through the point P that has been

discussed by HALL.[4] Such a line gives a distribution coefficient of $2{\cdot}0\times10^{-3}$ at the melting point. If, instead, we draw a line which best fits our data, ignoring point P, the distribution coefficient at the melting point would be $1{\cdot}6\times10^{-3}$. This difference is too small to be significant.

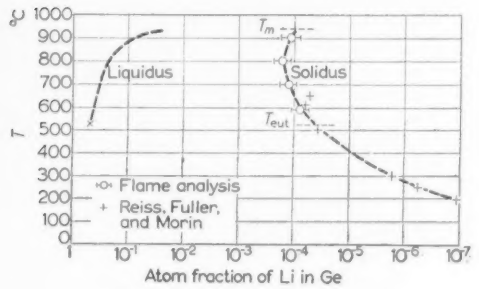

FIG. 1. Solubility of Li in Ge.

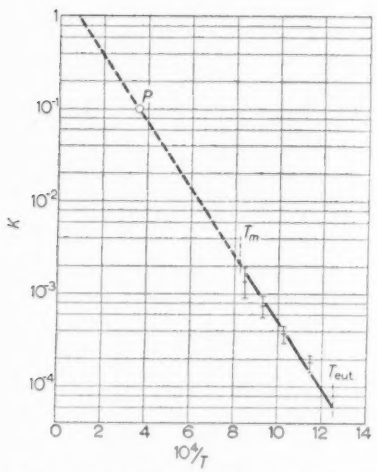

FIG. 2. Distribution coefficient for Li in Ge.

In general, the present data are consistent with the earlier solubility data of REISS, FULLER, and MORIN,[3] but the distribution coefficient at the melting point is appreciably lower than that quoted by FULLER and DITZENBERGER.[2] The slight discrepancy between the present data and the two highest temperature points of reference 3 suggests that Li precipitates during cooling after diffusion at temperatures in excess of 600°C, for the fastest quench cycles used in the earlier experiments.

MISCELLANEOUS NEW INFORMATION ON Li-Ge CHEMISTRY AND PHASE DIAGRAM

This is collected in the Appendix.

CONCLUSIONS

1. The solubility of Li in Ge reaches a maximum atom fraction of $(1{\cdot}7\pm0{\cdot}5)\times10^{-4}$ at about 800°C.

2. The behavior of the distribution coefficient vs. $1/T$ is in accord with thermodynamic principles, and it has a value of $(1{\cdot}6$ to $2{\cdot}0)\times10^{-3}$ at the melting point.

3. There is a Li-Ge eutectic point at 49 ± 5 atom per cent of Li and 525 ± 10°C.

4. Li and Ge form the compounds $Li_{4n}Ge_n$ and $Li_{3n}Ge_n$, the former having a melting point of 750 ± 10°C and the latter a melting point of 800 ± 10°C. Both react with moist room air to form Li_2Co_3.

Acknowledgement—The author wishes to express his appreciation to D. J. LOCKE for performing the measurements.

APPENDIX

(Except where otherwise noted, all experiments were performed using crystalline chips of SiC for "crucibles" in a helium atmosphere.)

1. With clean surfaces, Li reacts with Ge at about 185°C to produce a crystalline powder, with a large increase in total volume and no apparent liquid intermediate phase. This compound has a somewhat gummy consistency, and its melting point is poorly defined but is appreciably lower than that of the compounds prepared as in the paragraphs below; both observations suggest that it contains excess Li. Weight analysis indicates it contains 75 to 85 atom per cent Li, and X-ray powder patterns (which are very poor because the pasty consistency makes it impossible to prepare finely divided powder) indicate it contains $Li_{4n}Ge_n$. It reacts with water but much less violently than $Li_{4n}Si_n$.

2. Li and Ge, when mixed in proportions corresponding to $Li_{4n}Ge_n$, react (when heated) to form a substance with a well-defined melting point of 750 ± 10°C. X-ray powder patterns give strong lines corresponding to d-values of 2·20 and 2·06 Å and medium-strength lines corresponding to 3·98, 3·87, 3·80 and 2·24 Å. (The possibility that some of these lines result from contaminants cannot be excluded.) This material changes to Li_2CO_3 in moist room air (but not in dry), the Ge changing to a form soluble in HCl (probably GeO_2).

3. Li and Ge, when mixed in proportions corresponding to $Li_{3n}Ge_n$, react (when heated) to form a substance with a well-defined melting point of 800 ± 10°C. X-ray powder patterns give a strong line corresponding to a

d-value of 3·80 Å and medium-strength lines corresponding to 3·05, 2·24, and 1·80 Å. This material also changes to Li_2CO_3 in moist room air, but at a slower rate than the $Li_{4n}Ge_n$. Its density is 6 ± 2 g/cm^3.

4. Li and Ge, when mixed in proportions corresponding to $Li_{2n}Ge_n$, react (when heated) to form a substance without a well-defined melting point; in fact, the melting range extends all the way from about 730°C to the eutectic temperature of 525°C, and we conclude that this is not a compound. This constitutes a difference between Li-Ge and Li-Si, the latter forming an $Li_{2n}Si_n$ compound (but not an $Li_{3n}Si_n$ compound.)

REFERENCES

1. PELL E. M. *J. Phys. Chem. Solids* **3,** 77 (1957).
2. FULLER C. S. and DITZENBERGER J. A. *Phys. Rev.* **91,** 193 (1953).
3. REISS H., FULLER C. S., and MORIN F. J. *Bell Syst. Tech. J.* **35,** 535 (1956).
4. HALL R. N. *J. Phys. Chem. Solids* **3,** 63 (1957).
5. GREINER E. S. and BREIDT P. *J. Metals* **7,** 187 (1955).
6. HASSION F. X., THURMOND C. D., and TRUMBORE F. A. *J. Phys. Chem.* **59,** 1076 (1955).

VOL
3
195

J. Phys. Chem. Solids Pergamon Press 1957. Vol. 3. pp. 77–81.

SOLUBILITY OF LITHIUM IN SILICON

E. M. PELL

General Electric Research Laboratory, Schenectady, New York

(*Received* 11 *March* 1957)

Abstract—The solubility of lithium in silicon has been measured as a function of temperature between 592°C and 1382°C. It reaches a maximum impurity atom fraction of $1{\cdot}3\times10^{-3}\pm8$ per cent at about 1200°C, and the distribution coefficient at the melting point is $1{\cdot}0\times10^{-3}$. Li content was measured by flame analysis; comparison of flame analysis results and electrical measurements indicates that serious precipitation occurs during quenching for diffusion temperatures above 650°C. Distribution coefficients are in accord with thermodynamic principles when calculated as the ratio of the above solubility data and a liquidus curve calculated from the eutectic point.

Additional information regarding the Li–Si phase diagram was obtained which indicates a melting point of 720 ± 20°C for $Li_{4n}Si_n$, 750 ± 10°C for $Li_{2n}Si_n$, and a eutectic point at 58 ± 5 atom per cent Li and a temperature of 590 ± 10°C. The melting point of Si is 1408 ± 2°C, based on a literature survey and our own measurements. The melting point of Li_2CO_3, a product of the reaction of $Li_{4n}Si_n$ with room air, was found to be 715 ± 10°C, instead of the 618°C usually quoted.

VOL. 3 1957

INTRODUCTION

THE general shape and behavior of a solid solubility curve is prescribed by thermodynamic principles. In particular, the log of the distribution coefficient vs. $1/T$ should fall along a straight line which, extrapolated to $1/T = 0$, should not be far from unity in value.[1, 2] There may be exceptions to this general principle, but data which appear to violate it must be rigorously checked. We have remeasured the solubility of lithium in silicon[3] to see if it constitutes such an exception, and we have found that previous discrepancies can be explained by precipitation during quenching. We have not been able to prevent such precipitation (in fact, our Hall effect measurements, which are not sensitive to precipitated Li, reproduce the earlier measurements very closely), but by using flame analysis to measure the Li content we have been able to include this precipitated Li in our measurements.

PROCEDURE

1. *Lithium solubility (solidus)*

Li was prealloyed to Si at about 600°C in a hydrogen bottle. This temperature is sufficient to cause the voluminous and powdery $Li_{4n}Si_n$ which forms at about 200°C to remelt and alloy with the Si. The Si used was in the form of roughly a $\frac{1}{8}$ in. cube, and the Li amounted to about 20 atom per cent of this, except at the highest diffusion temperatures, where the prealloyed Li had to be reduced to as little as 5 atom per cent to prevent complete melting of the sample. Lithium hydride formation during prealloying was insignificant; use of helium instead of hydrogen did not affect our results.

The prealloyed sample was placed in a $\frac{1}{2}$ in. diameter $\times 1$ in. molybdenum crucible, spacing the Si from the crucible walls with crystals of silicon carbide. Argon was flowed in to replace the air, and a closely fitting molybdenum cover was added. Crucible and cover were inserted into the cool end of a quartz tube furnace heated by a graphite heater in its own separate concentric quartz compartment. (Fig. 1) After flushing the furnace with argon, the sample was moved into the hot zone for the Li diffusion. In one run, the argon atmosphere was replaced with helium, using an inverted crucible to prevent trapping of air; the results were identical to those with argon.

The closed crucible technique was chosen to prevent Li loss by evaporation. Known data on Li evaporation rates in vacuum suggest that it could easily be troublesome even under an atmosphere and at our lower diffusion temperatures. On the other hand, an experimental check of Li evaporation from a prealloyed sample in our furnace indicates that it is not serious until about 1100°C, and that the evaporation rate is about 10^{-5} of the rate in vacuum; such a low rate is surprising and may be caused

by the inhibiting effect of an oxide layer. In an earlier set of experiments using the sandwich diffusion technique,[3] appreciable erosion of the quartz furnace walls by Li vapor was observed after many runs at 1000°C.

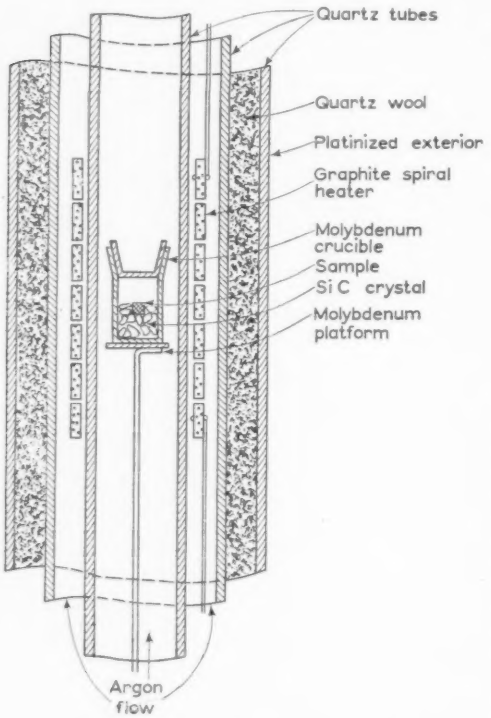

FIG. 1. Schematic cross-section of diffusion furnace with sample.

Since we wished to go up to 1400°C, use of a closed crucible seemed imperative. No attempt was made to seal the crucible; slow leakage was relied upon to reduce Li loss sufficiently. Since quartz erosion was not noticeable, it is felt that Li loss was negligible.

The crucible material, molybdenum, was chosen because of its inertness to Li. There was no macroscopic evidence of Li attack even near 1400°C, though frequent cracking of crucibles at this temperature may have been caused by some more subtle reactions between Li and Mo. Since Mo alloys with Si, it was necessary to prevent the Si from touching the crucible. This was accomplished with silicon carbide crystals, which showed no macroscopic reaction with either Li or Si.

Diffusion times were chosen with the aid of known diffusion data[4] so as to achieve Li concentrations roughly 90 per cent of equilibrium, and the resulting Li analyses were raised 10 per cent in compensation. The possibility of being far short of equilibrium was checked by doubling the diffusion time for one run at 1000°C; there was no change in Li concentration within the probable error of a single determination (±13 per cent).

The oven temperature was monitored before each run with a Pt–Pt 10 per cent Rh thermocouple which was calibrated against the melting points of gold (1063°C) and nickel (1455±1°C on 1927 International Temperature Scale,[5] or 1453±1°C on 1948 International Temperature Scale).* These temperature readings and the power input to the heater were subsequently calibrated against thermocouple measurements of the crucible temperature itself (it was not convenient to measure the crucible temperature directly during the diffusion runs because of the desirability of moving the crucible into and out of the hot zone while the oven remained sealed against the entry of room air). The difference between the thermocouple oven-temperature measurement and the actual crucible temperature was as much as 18°C at 1400°C and is attributable to the temperature gradient in this furnace. It is believed that the calibrated temperatures are accurate to ±4°C, based on experimental attempts to reproduce a desired temperature.

During the diffusion period, Li diffused from a region of molten Li-Si alloy into the solid Si until the solubility limit was reached. The crucible and sample were then removed to the cool part of the furnace and allowed to cool by radiation, conduction, and convection. This cooling period was amply short to prevent Li loss from the sample by diffusion, the excess Li either remaining in solution or forming precipitates. The sample was then differentially etched in $HF–HNO_3$ (1 : 3) etch to remove the previously molten alloy region. (The alloy region etched much more rapidly, and at the sacrifice of but a small fraction of the Si, this proved to be an easy and reliable method for removing the alloy.)

The remaining Si, with its dissolved and precipitated Li, was then analysed by an outside laboratory,† using flame analysis. The quoted limit-of-error for 95 per cent confidence, for our size samples, was ±20 p.p.m. This estimate of error was checked statistically with ten samples diffused at 1000°C. The statistical study indicated a mean probable error in each determination of ±13 per cent, which is about three times the probable error estimated by the analysts for this Li content. The difference is attributable to unknown errors in our diffusion techniques and/or errors in the analysts' estimates of error.

* We used the procedure wherein a small piece of pure nickel is used to bridge the ends of the thermocouples, with the nickel physically isolated from the Pt by short pieces of tungsten to prevent alloying, the melting point being indicated by a sudden open circuit. With nickel, a slightly-reducing atmosphere should be used—even as little as 0·24 per cent oxygen in the nickel will depress the melting point 20°C. On the other hand, if the atmosphere is too reducing, it will embrittle the Pt. We found 1 per cent H_2 in A to be satisfactory.

† Large Steam Turbine Generator Materials and Processes Laboratory, General Electric, Schenectady.

2. *Lithium-silicon liquidus*

To determine the distribution coefficient, one must also know the liquidus. One can obtain good values for the distribution coefficient by using the liquidus for a perfect solution, as long as one remains in the region of dilute solution. An approximate knowledge of the eutectic point (or any other point on the liquidus), plus accurate knowledge of the melting point, permits one to obtain somewhat better values for the distribution coefficient. We therefore desired to know the melting point and the eutectic point.

Melting point of silicon. This was found by raising the temperature in small steps until the Si sample collapsed. The molybdenum crucible used in the previous experiments was replaced with a tantalum crucible to prevent possible contamination of the Si with evaporated molybdenum oxide. This crucible contained a quartz cup for the Si and was supplied with an attached thermocouple calibrated against the melting points of gold and nickel. We found the melting point to be 1409 ± 2°C. This was not a refined technique, but the results compare favorably with more careful determinations which give 1408 ± 2°C,† 1409 ± 2°C,* 1410°C,† and 1408 ± 5°C.‡ We consider 1408 ± 2°C to be the best present value for the melting point.

Eutectic point. This was determined only roughly, by two experiments. In the first, the solidification temperature was measured for a series of alloys varying between 50 and 67 atomic per cent of Li. This was done in a bell jar under He by probing the sample while going both up and down through the melting point. The solidification temperature will lie close to either the solidus or a eutectic temperature. From this experiment we were able to conclude that the eutectic temperature was 590 ± 10°C and that the eutectic mixture was 58 per cent Li or less. The second experiment consisted in alloying a known amount of Li to a known amount of Si at a series of temperatures above 600°C and then differentially etching off the alloy to find how much Si had been alloyed. This method worked best at lower temperatures where the differential etching effect was greatest, and comparison of the results with a theoretical liquidus indicated that the eutectic mixture was 58 atom per cent Li or more. Considering both experiments, we conclude that the eutectic point lies at 590 ± 10°C, 58 ± 5 atom per cent of Li.

RESULTS

The present data are tabulated in Table 1, and in Fig. 2 we have plotted the solubility of Li in Si as determined by the present experiment and also as measured in earlier experiments. Below 650°C, our data and earlier data are in good agreement, but above this temperature the present data indicate smoothly increasing (retrograde) solubility, reaching a maximum of $1{\cdot}3\times10^{-3}$ at about 1200°C. We have also included electrical measurements of Li content, using the Hall effect, in our relatively slowly quenched samples; and it is seen that the results lie parallel to the earlier solubility data based on electrical resistivity measurements of more rapidly quenched samples. One datum point from a special experiment (in which we used a sandwich technique for the diffusion and a special furnace to permit rapid quenching by dropping the sample into ethylene glycol) is also exhibited, and it is seen that this Hall measurement of Li content is in excellent agreement with the earlier data. This dependence of dissolved Li content (using the Hall effect) upon quench rate, in conjunction with the much higher total Li content as measured chemically, is almost incontrovertible evidence of precipitation during quenching. It may be of interest to note that our rapidly quenched samples were extremely brittle, all but the one crumbling during the measurements; slowly quenched samples were mechanically durable, but the high-diffusion-temperature samples with high Li content (mostly precipitated) etched more rapidly than the original

* F. Hoffman and A. Schulze[6] obtained 1411 ± 2°C with a calibrated thermocouple and 1409 ± 2°C with a pyrometer. These values are to be reduced 2°C because of the change in the International Temperature Scale in 1948.

† H. Stöhr and W. Klemm[7] found 1412° for the melting point, which is to be reduced 2°C because of the change in the temperature scale.

‡ M. Hansen, H. D. Kessler, and D. J. McPherson,[8] obtained 1410 ± 5°C by an incipient melting technique, which is to be decreased 2°C because of the change in the temperature scale (private communication from McPherson states that the melting points of nickel and platinum based on the 1927 scale were used in their calibrations).

Table 1. *Tabulation of experimental data*

T(°C)	$10^4/T$(°K)	Calculated liquidus (atom fraction)	Solidus (atom fraction)	Distribution coefficient
1382±4	6·04	0·046±·006	$5{\cdot}6\times10^{-4}\pm8\%$	$1{\cdot}22\times10^{-2}$
1333±4	6·23	0·108±·005	$8{\cdot}6\times10^{-4}\pm13\%$	$8{\cdot}0\times10^{-3}$
1283±4	6·43	0·158±·004	$1{\cdot}05\times10^{-3}\pm8\%$	$6{\cdot}7\times10^{-3}$
1185±4	6·86	0·241±·003	$1{\cdot}3\times10^{-3}\pm8\%$	$5{\cdot}4\times10^{-3}$
987±4	7·94	0·371±·003	$1{\cdot}0\times10^{-3}\pm4\%$	$2{\cdot}7\times10^{-3}$
790±4	9·40	0·478±·002	$4{\cdot}5\times10^{-4}\pm10\%$	$9{\cdot}4\times10^{-4}$
592±4	11·57	0·578±·002	$9{\cdot}0\times10^{-5}\pm30\%$	$1{\cdot}56\times10^{-4}$

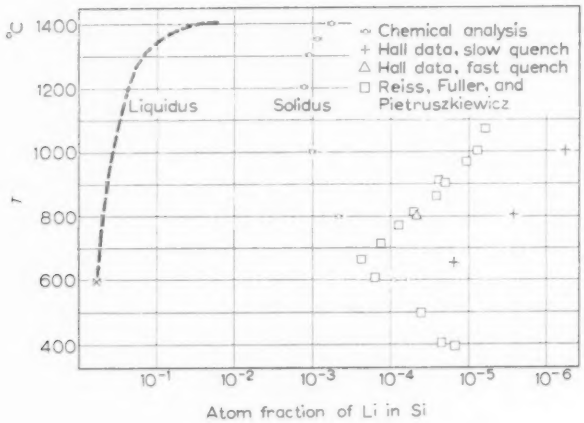

FIG. 2. Solubility of Li in Si.

Si and to a matte surface instead of the usual shiny surface.

Using the values for melting point and eutectic point discussed earlier, the remainder of the liquidus curve was determined by assuming the solution to be "regular",* and this liquidus was used in calculating the distribution coefficient. It is known from thermodynamic principles that the distribution coefficient, k, should follow, approximately, the relation $\ln k = (T_m/T) \ln k_m$, where T_m is the melting point in °K and k_m is the distribution coefficient at the melting point.[2] We have accordingly plotted $\ln k$ vs. $1/T$ (Fig. 3), and the results are seen to be in good agreement with the theory.

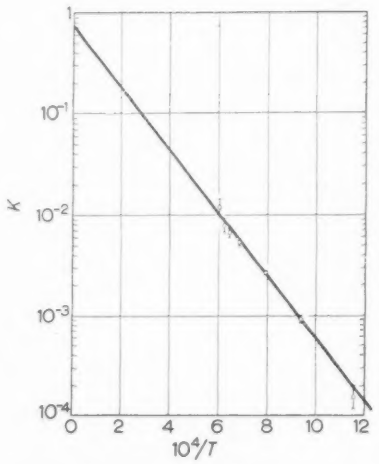

FIG. 3. Distribution coefficient for Li in Si.

* For an example of such a calculation, see C. D. THURMOND *J. Phys. Chem.* **57**, 827 (1953).

Miscellaneous new information on Li–Si chemistry and phase diagram

In performing the above experiment, we obtained some data pertaining to Li–Si chemistry which does not appear to have been published previously. This is collected in the Appendix.

CONCLUSIONS

(1) The solubility of Li in Si is greater than previously realized, reaching a maximum atom fraction of $1{\cdot}3\times10^{-3}\pm8$ per cent at about 1200°C.

(2) The behavior of the distribution coefficient vs. $1/T$ is in accord with thermodynamic principles. At the melting point, it has a value of $1{\cdot}0\times10^{-2}$.

(3) The melting point of Si is 1408 ± 2°C on the 1948 International Temperature Scale.

(4) There is a Li–Si eutectic point at 58 ± 5 atom per cent of Li and 590 ± 10°C.

(5) Using typical fast quench techniques, Li is unavoidably precipitated from solution when the sample is quenched from temperatures above about 650°C.

(6) $Li_{4n}Si_n$ has a melting point of 720 ± 20°C and it reacts with room air to form Li_2CO_3 plus a Si compound; Li_2CO_3 has a melting point of 715 ± 10°C; $Li_{2n}Si_n$ has a melting point of 750 ± 10°C.

Acknowledgements—The author wishes to express his appreciation to D. J. Locke for performing the measurements and to many members of the General Physics Research Department of the General Electric Research Laboratory, particularly to R. N. Hall and to R. O. Carlson for valuable discussions. He is indebted to W. C. Dash for most of the silicon.

APPENDIX

(1) With clean surfaces, Li reacts with Si at 185–200°C (probably near the Li melting point of 186°C) to produce a crystalline powder, with a large increase in total volume and no apparent liquid intermediate phase. Weight analysis indicates that this compound is of the composition $Li_{4n}Si_n$, and X-ray powder patterns identify it with a compound of similar composition found by earlier investigators.[9] This compound reacts slowly with room air to produce Li_2CO_3 (50 per cent conversion in 8 hr in room air at 20 per cent R.H.). The product was identified as predominantly the carbonate by weight analysis, X-ray powder pattern, and melting point. (Using C.P. Li_2CO_3, we have found the melting point to be 715 ± 10°C inctead of the 618°C quoted in many handbooks.) The compound $Li_{4n}Si_n$ has a melting point of 720 ± 20°C, measured in He, on sapphire or SiC. It ignites spontaneously in air at temperatures above roughly 100°C, and it reacts violently with water.

(2) A mixture of composition $Li_{2n}Si_n$ (which has been identified as a compound by earlier workers[9]) has a melting point of 750 ± 10°C, as measured on sapphire in He.

(3) The molten alloy on the Si side of the 58 per cent Li eutectic point appears to dissolve large amounts of H_2. When cooled, the H_2 "boils" out near the eutectic temperature; however, the melting points discussed above, and the general behavior of the Li–Si compounds, are not significantly affected by the presence of H_2. This phenomenon does not occur with He.

(4) For alloys richer in Li than $Li_{2n}Si_n$, the only crucible material which we have found to be satisfactory is SiC. On the Si side of this compound, sapphire seems to be satisfactory. Pure alumina reacts with the Li even with 50 atom per cent mixtures.

(5) Any alloy richer in Li than roughly 50 atom per cent can be etched with water; if not too much richer in Si, dilute $HF–HNO_3$ etches are satisfactory.

REFERENCES

1. Thurmond C. D. and Struthers J. D. *J. Phys. Chem.* **57,** 831 (1953).
2. Hall R. N. *J. Phys. Chem. Solids* **3,** 63 (1957).
3. Reiss H., Fuller C. S., and Pietruszkiewicz A. J. *J. Chem. Phys.* **25,** 650 (1956), and references cited therein.
4. Fuller C. S. and Severiens J. C. *Phys. Rev.* **96,** 21 (1954).
5. Wensel H. T. and Roeser W. F. *J. Res. Nat. Bur. Stand.* **5,** 1309 (1930).
6. Hoffman F. and Schulze A. *Phys. Z.* **38,** 901 (1937); *Metallwirtschaft* **17,** 3 (1938).
7. Stöhr H. and Klemm W. *Z. Anorg. Chem.* **241,** 305 (1939).
8. Hansen M., Kessler H. D., and McPherson D. J. *Trans. Amer. Soc. Metals* **44,** 518 (1952).
9. Klemm W. and Struck M. *Z. Anorg. Chem.* **278,** 117 (1955). See also Osborg H. *Lithium, Electrochem. Soc.* 1935 (*N.Y.*), for general discussion of Li chemistry.

J. Phys. Chem. Solids Pergamon Press 1957. Vol. 3. pp. 82–86.

ELECTROLYSIS OF COPPER IN SOLID SILICON

C. J. GALLAGHER

General Electric Research Laboratory, Schenectady, New York

(*Received* 17 *April* 1957)

Abstract—The diffusion of copper in silicon can be enhanced or retarded by application of an electric field. Transport measurements indicate that the copper diffuses with a single positive charge at temperatures around 1100°C. The amount of transport observed requires that a large fraction, possibly 50 per cent of the copper in solution, be positively charged and rapidly diffusing. On the basis of these results and the known slight electrical activity produced by copper in silicon at room temperature, we conclude that the charged, rapidly diffusing species of copper is interstitial. Similar experiments with Au and Fe in silicon show no field effect at 1100°C. It is found that copper in germanium diffuses rapidly with a positive charge at 700°C, in agreement with the results reported by FULLER for higher temperatures.

INTRODUCTION

THE experiments described here are concerned mainly with the effect of an electric field on the diffusion of copper in silicon and germanium.

It is well known that copper diffuses rapidly in these materials.[1,2] Detailed studies of the diffusion mechanism have been made extensively in germanium. FULLER and SEVERIENS[3] have reported that the diffusion rate in germanium is influenced by the presence of an electric field, with the copper behaving as a positively charged ion. Recent work has shown that copper penetrates more rapidly into crystals of germanium containing high dislocation densities.[4,5] FRANK and TURNBULL[6] have shown that the experimental results are consistent with a diffusion mechanism in which a relatively low concentration of interstitial copper diffuses rapidly and forms substitutional copper by reacting with vacancies diffusing from various sources such as surfaces and climbing dislocations. The electrically active acceptor copper is presumably the substitutional species.

Similar detailed studies have not been made for silicon. THURMOND and STRUTHERS[2,7] have studied the solubility and find it to be 2×10^{-5} at 1200°C. However, the concentration of electrically active centers in crystals saturated at 1200°C and then quenched is of the order of 10^{14}cm^{-3} at room temperature.[8] Thus, there are of the order of 10^{18} atoms per cm^3 electrically inactive copper for saturated samples quenched from high temperature. The copper is either precipitated as a separate phase, or present as neutral single atoms or clusters. DASH has shown that copper precipitates on dislocations even in rapidly quenched samples.[9]

EXPERIMENTAL

There has been no experimental information about the charge state of the copper in silicon at high temperatures. The *p-n* junction method used by FULLER in germanium could not be applied because of the low electrical activity. However, the direct transport of copper through silicon can be measured, and the influence of an electric field observed.

The experiment consisted of diffusing radioactive ^{64}Cu through silicon between a plane source and a plane sink, under steady state conditions. An electric field was maintained in the material by

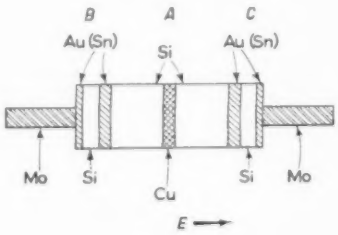

FIG. 1.

d.c. which also served to heat the sample. For this geometry the diffusion equation is readily solved and the measured amount of copper transported can be related to the product of the diffusion constant and the concentration at the source.

The experimental arrangement is shown in Fig. 1. The source is at the center (A), two sinks are provided (B and C). In this way diffusion with the field and against it could be observed under the same temperature and field conditions. The end blocks were provided to ensure uniform temperature and field in the samples.

The source consisted of an excess of ^{64}Cu in $Cu(NO_3)_2$ solution applied to each of the inner blocks. The sink consisted of gold or tin plated on the faces at B and C. THURMOND and LOGAN[10] have shown that gold and tin act as getters for copper in germanium. Experiments described later in this report show that these metals are also effective getters for copper in silicon. The end pieces were also completely plated with tin or gold to ensure good electrical contact and to provide extra solvent. Contact was made by spring loaded molybdenum rods held against the end pieces as shown.

All four pieces of the sample were enclosed by flat quartz plates, 0·040 in. thick. The cross-section dimensions of the silicon were made uniform to within 0·5 ml to get maximum contact with the quartz. It was found in separate experiments with longer diffusion paths that an appreciable fraction of the transport occurred in the gaseous atmosphere around the sample if there was no shielding. The shielding reduced this to a negligible amount.

The shielded sample was mounted on a water cooled block which also held the electrical contact rods. A hydrogen atmosphere was used. Temperatures were read with an optical pyrometer through the quartz, and corrected by comparing with a sample in a furnace of known temperature.

The conductivity data of MORIN and MAITA[11] were used to calculate the electric field at the known current density. Fields of about 1·5 V/cm were obtained at temperatures of 1100 to 1200°C, with current densities of 250 to 350 A/2. The samples were approximately square in cross-section, with an area of about 0·2 cm². The length of the diffusion path varied for different samples, as did the diffusion time.

The effectiveness of gold and tin as getters for copper in silicon was demonstrated by diffusing copper through silicon wafers with regions of tin and gold plated on the other side. Autoradiograms of the plated side showed very little activity outside the plated regions. A typical autoradiogram is shown in Fig. 2.

SOLUTION OF DIFFUSION EQUATION

The one-dimensional diffusion equation can be used for computing the total transport with the effect of the field included.

The appropriate equation for the concentration, c, is

$$\frac{dc}{dt} = D\frac{d^2c}{dx^2} - \mu E\frac{dc}{dx} = -\frac{dJ}{dx} \tag{1}$$

where J is the particle current density and μ the mobility. The field, E, may have either sign. The boundary conditions are

$$\begin{aligned} C(0,t) &= C_0 \\ C(L,t) &= 0 \\ C(x,0) &= 0. \end{aligned} \tag{2}$$

The number of atoms per unit area (m) collected at the sink is given by the time integral of the current at $x = L$, which can be written*

$$m = \int_0^t J(L,t')\,dt = \frac{C_0 L e^{\pm|\beta|/2}}{2\sinh|\beta|/2}\left\{\alpha^2|\beta| - (\coth|\beta|/2 - 2/|\beta|) - \right.$$

$$\left. - \sum_{n-1}^{\infty}(-1)^n 4\sinh(|\beta|/2)\exp[-\alpha^2(n^2\pi^2+\beta^2/4)]\frac{n^2\pi^2}{(n^2\pi^2+\beta^2/4)^2}\right\} \tag{3}$$

* The author is indebted to Dr. F. S. HAM of this Laboratory for helpful discussions of this problem.

$$\beta = \frac{\mu EL}{D},$$

$$x^2 = \frac{Dt}{L^2}.$$

The sign of β in the term outside the brackets is established by the direction of the field. The terms inside are independent of the field direction. This establishes the important point that the ratio of the transport along the field to that against the field is independent of the time, and is the same regardless of whether steady-state conditions have been obtained. The ratio of the numbers of atoms in the negative and positive sinks is thus given simply by

$$\frac{m^-}{m^+} = e^{\beta} = \exp\frac{LE\mu}{D}.$$

Thus, from the ratio m^-/m^+ we obtain μ/D and, assuming the validity of the Einstein relation $\mu/D = q/kT$, we obtain a value of q, where q is the charge carried by the diffusing atom.

RESULTS

The results of seven runs for copper in silicon are shown in Table 1.

The second and third columns give the number of atoms transported per cm² for the negative and positive sinks, respectively. It is clear that the copper prefers the negative sink and thus must carry a positive charge while diffusing. The last column gives the ratio of the charge calculated as described above to the charge on the electron. The average value of this ratio is 1:10, from which we conclude that the fast diffusing copper atom carries a single positive charge.

The experimental determination of this ratio is subject to less error than the evaluation of either amount of transport separately. There are several corrections and sources of error in the individual measurements which need to be considered:

(1) It is difficult to be certain that steady-state conditions have been established. The two correction terms in equation 3 reduce the total transport, but the reduction depends on the diffusion constant. We cannot be sure that the diffusion constant of $3 = 10^{-5}$ cm²/sec reported by FULLER and STRUTHERS is the appropriate one to apply.

(2) We cannot be sure that the concentration given by STRUTHERS' solubility data is the appropriate one to use in equation 3. This would be equivalent to saying that all of the copper is charged.

(3) The effective cross-section area of the sample is less than the geometric area because of the thermal gradient between the surface and the center.

(4) There are losses from the sinks due to evaporation, as shown by the activity of the enclosing quartz. This loss is assumed proportional to the amount in the sink, and hence does not affect the ratio.

(5) The boundary conditions at the source are not necessarily independent of time. In practice, it is difficult to get enough copper on at the source to keep the level up to saturation. Too much copper would lead to melting along the surface, with resultant convection transport.

If we calculate the amount of transport from equation 3, using $D_0 = 3 \times 10^{-5}$ cm²/sec and C_0 as obtained from STRUTHERS' data, the calculated values are greater than the measured values by factors ranging from 2 to 30. Hence, it seems best to rely on separate experiments if we wish to decide what fraction of the copper is charged and what is the appropriate diffusion constant.

Field-free transport

These experiments used 0·030 in. disks of silicon, about 1 cm in diameter, with ^{64}Cu plated on one side and tin or gold plated on the other. They

Table 1

T (°C)	E (V/cm)	$m^- \times 10^{-16}$ (cm^{-2})	$m^+ \times 10^{-14}$ (cm^{-2})	m^-/m^+	$\ln(m^-/m^+)$	q/q_0
1000	1·96	11	15	71	4·3	0·83
1060	1·43	1·8	5·2	36	3·6	1·15
1080	1·49	2·9	2·9	108	4·7	0·94
1090	·89	5·8	7·1	82	4·4	1·30
1125	1·44	3·1	7·6	40	3·7	1·23
1135	0·99	1·5	3·0	48	3·9	1·22
1200	1·46	1·5	7·3	19	2·9	1·03

VOL.
3
1957

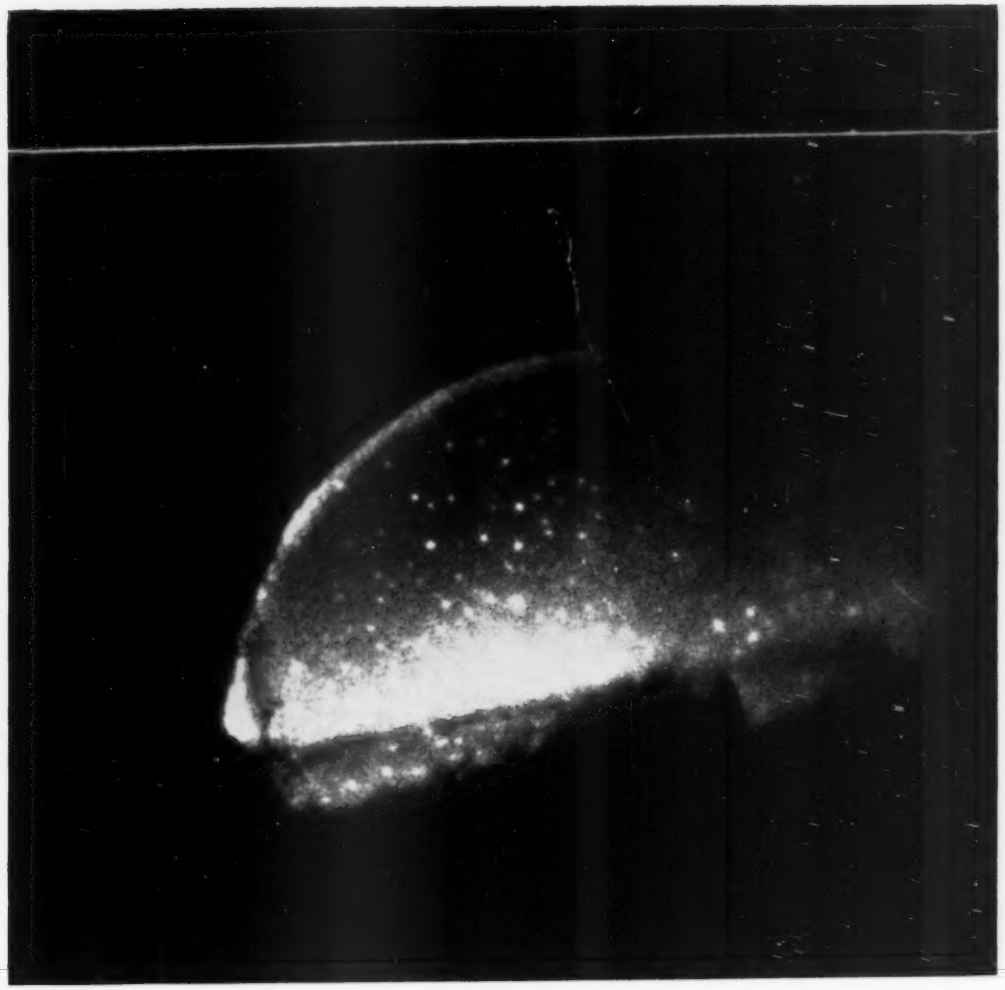

FIG. 2.

[*Facing Page* 84

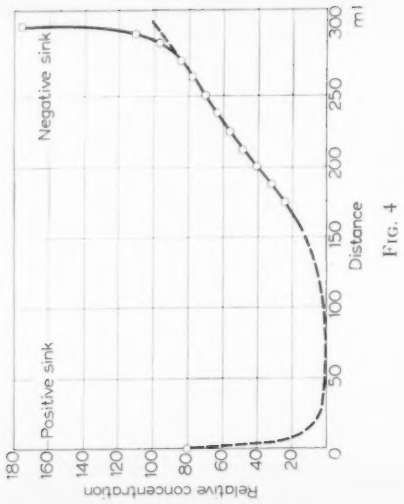

FIG. 4

FIG 3

Facing Page 85]

VOL
3
195

were enclosed in quartz plates and heated for appropriate times at 1100°C in H_2. The value of DC_0 calculated from the relation

$$DC_0 = \frac{ml}{t}$$

averaged for four samples was $1{\cdot}1 \times 10^{13}(\text{cm/sec})^{-1}$. The value of DC_0 from THURMOND and STRUTHERS' data may be as large as $2{\cdot}5 \times 10^{13}(\text{cm/sec})^{-1}$, which implies that at least 35 per cent of the soluble copper moves at the fast diffusion rate. The remaining question to settle concerns the fraction of the copper which is charged.

Drift experiment

A bar of silicon was saturated with ^{64}Cu at 1100°C. The bar was then ground on all faces to remove excess activity and etched, heated to 1120°C with d.c. for 12 min. A lengthwise section was then cut from the bar and a contact autoradiogram made, as shown in Fig. 3. The negative sink shows a heavier accumulation of Cu than the positive. Also, there is a gradient of Cu in the bar, increasing toward the negative end. This we interpret as the trailing edge of the initially square pulse of copper as it drifts in the field.

There is a greater density along one edge of the sample. This we attribute to the greater cooling at this side since the shielding quartz plate was not as thick as those on the other faces. There would thus be some copper precipitated here which would not diffuse readily, as indicated by the uniform distribution of density.

A densitometer trace of the autoradiogram was made along the center line. The measured densities were compared with a series of calibration autoradiograms made by various exposures of samples of the same thickness which were uniformly saturated with Cu at 1120°C. The relative intensities are shown in Fig. 4, plotted against distance from the positive sink.

If we take the distance to the half-way point on the trailing edge as the distance traveled by the pulse, we calculate a mobility of $2{\cdot}7 \times 10^{-4}$ cm²/V sec at 1120°C, with a corresponding diffusion constant of $3{\cdot}2 \times 10^{-5}$ cm²/sec as calculated from the Einstein relation. Since this was measured for the charged species only, we conclude from this experiment that a large fraction of the fast diffusing copper is positively charged. It is unlikely that the effective diffusion constant is greater than about 5×10^{-5} cm²/sec. The fraction is thus greater than 60 per cent so that certainly more than 20 per cent of the total copper is charged. The true fraction is probably in excess of 50 per cent. It would seem logical to identify the charged copper as interstitial, in which case the ratio of substitutional to interstitial copper could well be less than unity.

Copper in germanium

A number of runs were made for copper diffusing in germanium at 700°C in an electric field using plated tin for a sink. We have verified the conclusion of FULLER *et al.* that the copper diffuses with a positive charge, but the data for the ratios of the transport along and against the field are much more scattered than in the silicon case. This may be due in part to the sample-to-sample variations in structure, which would change the effective diffusion constant. We cannot say whether the charge is single or double.

Iron and gold in silicon

We have carried out similar experiments in silicon using ^{59}Fe and ^{198}Au as tracers. These diffuse rapidly but they show no field effect at 1100°C.

SUMMARY

(1) We find that copper diffuses in silicon at 1100°C with a positive charge.

(2) At least 35 per cent of the dissolved copper can diffuse rapidly, and more than 60 per cent of this fraction is positively charged.

(3) The diffusion of iron and gold in silicon is not affected by an electric field at 1100°C.

(4) Copper diffuses in germanium with a positive charge at 700°C.

Acknowledgements—The author wishes to express his appreciation to Mr. JOHN SOBIESKI for his able assistance with the experimental work, and to Dr. A. G. TWEET for many helpful discussions.

REFERENCES

1. FULLER C. S. and STRUTHERS J. D. *Phys. Rev.* **87,** 526 (1952).
2. STRUTHERS J. D. *J. Appl. Phys.* **27,** 1560 (1956).

3. FULLER C. S. and SEVERIENS J. G. *Phys. Rev.* **96, 21** (1954).
4. TWEET A. G. and GALLAGHER C. J. *Phys. Rev.* **103,** 828 (1956).
5. FULLER C. S. and DITZENBERGER J. A. *J. Appl. Phys.* **28,** 40 (1957).
6. FRANK F. C. and TURNBULL D. *Phys. Rev.* **104,** 617 (1956).
7. THURMOND C. D. and STRUTHERS J. D. *J. Phys. Chem.* **57,** 831 (1953).
8. CARLSON R. O. Private communication.
9. DASH W. C. *J. Appl. Phys.* **27,** 1193 (1956).
10. THURMOND C. D. and LOGAN R. A. *J. Phys. Chem.* **60,** 591 (1956).
11. MORIN F. and MAITA J. P. *Phys. Rev.* **96,** 28 (1954).

VOL
3
195

J. Phys. Chem. Solids Pergamon Press 1957. Vol. 3. pp. 87–94.

CONCENTRATION OF HYDROGEN AND SEMICONDUCTIVITY IN ZnO UNDER HYDROGEN-ION BOMBARDMENT

J. J. LANDER

Bell Telephone Laboratories, Inc. Murray Hill, N.J.

(*Received* 24 *April* 1957)

Abstract—Steady-state concentrations of hydrogen produced in ZnO by bombardment with the ions H_1^+, H_2^+, and H_3^+ have been determined as a function of temperature, ion current and ion energy by measurement of conductivity. Relative to the solubility obtained in normal hydrogen, the bombardment-induced concentrations are extremely high at low temperatures, e.g., higher by five orders of magnitude at 200°C.

This behavior of ZnO under hydrogen ion bombardment results from two factors: (a) ions of sufficient velocity penetrate efficiently the surface barrier to normal reaction, and (b) the barrier to escape of hydrogen through the surface is high. The barrier to escape, found to be 0·58 eV, is partly "chemical" and partly electrical in nature, the electrical part resulting from surface charge. In agreement with the latter concept, it was observed that treatments in oxygen altered the results in the expected direction. The technique provides a novel method for measuring surface barriers to chemical reaction.

1. INTRODUCTION

HYDROGEN diffuses into and increases the conductivity of ZnO.[1,2] Diffusion is rapid. The donor center has an ionization energy of about 0·05 eV. The mobility of the electrons under normal conditions is known with fair accuracy. Thus the solubility of hydrogen is easily determined from conductivity measurements. It increases with increasing temperature, reaching a value of 1×10^{17} atoms per cm^3 at 600°C in one atmosphere of hydrogen. The heat of solution is 0·80 eV per atom. The system is an excellent one to use in the study of a variety of problems in solid state solution chemistry.

Effects produced by hydrogen-ion bombardment are reported in this paper. The work is concerned mainly with bulk effects, though surface effects were also encountered. The interest grew out of the following argument. The rate of solution of hydrogen in ZnO is determined in part by reactions occurring at the crystal surface. Hydrogen forms a relatively stable complex believed to be the hydroxyl group.[2] It seems likely that an appreciable surface barrier to reaction exists and that atomic hydrogen, or hydrogen ions, can efficiently bypass such a surface barrier. If so, much higher "solubilities" should be obtained by bombardment and they should increase with decreasing temperature.

These systems are irreversible. Consider what appear to be the important reactions taking place when ZnO is bombarded with H_1^+. The ions react to form the donor centers, but in the reverse reaction hydrogen is not desorbed as hydrogen ions. Hydrogen gas is evolved and at saturation the amount is equal in hydrogen content to the current of hydrgen ions reacting with the crystal. Thus studies of the system yield reaction rates and activation energies for reaction rates, which are determined by heights of energy barriers.

There is a practical interest in the general field of reactions with activated hydrogen (or other elements). The doping of semiconductors by ion bombardment offers sets of very special results. Another example is the gettering of hydrogen in vacuum tubes. Most cool metal parts (nickel, molybdenum) will have an increased capacity for hydrogen arriving as a steady stream of ions, or as atomic

hydrogen, if surface barriers to escape are sufficiently high.

In this work single crystals of ZnO were bombarded with H_1^+, H_2^+, and H_3^+. These ions were obtained separately from a small mass spectrometer. Conductivity was measured and solubilities calculated as before.[2] Positive identification of the donor center was made by measuring its diffusion coefficient. Other effects of some interest are reported; for example, properties of H_1^+, H_2^+, and H_3^+.

2. MATERIALS AND APPARATUS

Crystals of ZnO were taken from the stock used in the earlier work.[2] In diameter, they ranged from 2 to 6 mil, and they were about 1 cm long. Those with initial conductivities of about 0·02 $(\Omega\,\text{cm})^{-1}$ were chosen.

Hydrogen for the mass spectrometer was obtained by diffusion of hydrogen through a hot nickel tube. In all tests the pressure of hydrogen was about 2×10^{-3} mm of Hg.

Conductance measurements were generally made by the two probe method because under hydrogen bombardment contacts were ohmic. However, the more precise diffusion data were obtained in the same apparatus used in the earlier work,[2] and the four probe method was used.

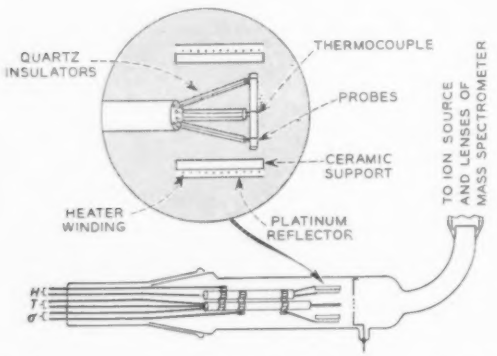

FIG. 1. Apparatus in which the crystal is bombarded.

The mass spectrometer is sketched in Fig. 1. It is a 90° fixed magnetic field instrument with a 3 cm radius of curvature. The field used was about 900 gauss. Thus H_1^+ appeared at about 700 V, H_2^+ at about 350, and H_3^+ at about 230. The beam defining slits (about 40 mil wide) produced a width of peaks at half intensity of about 5 V. Ion current was controlled by adjusting ionizing electron current (up to 5 mA). The crystal was maintained at ground potential. The grid immediately in front of the crystal was normally set at −300 V with respect to the ionization chamber. This helped to maintain a high ion current to the crystal even at low bombarding potentials where space charge effects are more serious. Effects of bombarding energies below about 20 V are not reported because of the wide distribution in energy of the ions. The equipment used was limited in the high range to about 750 V.

The crystal was supported in a small cylindrical furnace by its two leads of 2 mil Pt wire and a Pt–Pt Rh thermocouple made of 2 mil wires. All these wires were normally attached with platinum paste (baked on in air at 600°C). Quartz capillary tubes covered these lead wires from the ceramic support to the crystal. It was estimated that the exposed portions of wires and the paste contacts drew about 30 per cent of the ion current when the smaller crystals were used.

The crystal was surrounded at a distance of one centimeter by metal surfaces which were kept at ion repelling potentials. In Fig. 1 it is to be observed that the needle-like crystal is perpendicular to the axis of the cylindrical heater (and ion repeller). A second apparatus was built with a cylindrical heater (and ion repeller) having a wide slit through which ions entered, and the crystal was placed along the axis of the heater. These two designs gave the same results. It is believed therefore that bombarding currents were approximately uniform in both.

Current to the crystal was measured with a feedback type electrometer-amplifier. The maximum available currents were about 1×10^{-7} A of H_2^+ or H_3^+ and about 1×10^{-8} A of H_1^+.

The largest errors in the work are believed to be due to fluctuations in temperature and bombarding current. Under some conditions surface damage, or an effect which operates in the same sense, was not negligible, but a quantitative study of its results was not made.

3. RESULTS

3.1 *Diffusion and saturation*

In a typical run the crystal was first annealed at about 500°C. This served to remove hydrogen from a previous run and to anneal "surface damage" occurring when a run was made at high current density or bombarding voltage. Without such treatment results could not be reproduced.

Mass spectrometer adjustments were made at the high temperature to produce the desired current of an ion at the desired energy. The crystal was cooled to the test temperature. The electron ionizing current was switched on and conductivity vs. time measurements were made. The results generally fitted simple diffusion theory very well. For a cylinder the predicted time to 50 per cent saturation is obtained from $Dt/r^2 = 0{\cdot}060$ and to 96 per cent saturation from $Dt/r^2 = 0{\cdot}50$. After reaching 96 per cent or more of saturation, measurements were often made of the hydrogen

evolution rate after the beam was switched off. These agreed well with simple diffusion theory.

Typical curves showing the approach to saturation are given in Fig. 2. Diffusion coefficients

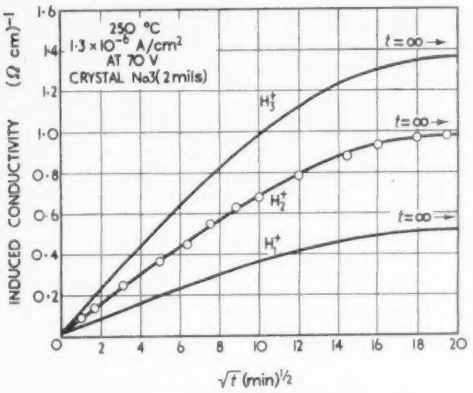

FIG. 2. Increase in conductivity during bombardment with H_1^+, H_2^+, and H_3^+ ions.

calculated from such curves agreed well with those reported in reference 2 and shown in Fig. 3. The equation for the line given is

$$2D = 0{\cdot}063e^{-0{\cdot}91e/kT} \text{ cm}^2/\text{sec}. \qquad (1)$$

The factor $2D$ is used because diffusion of electrons is space charge limited.

To demonstrate further that saturation was a bulk effect a crystal saturated with a high concentration of hydrogen was etched about 10 per cent. The conductance was reduced by about 10 per cent.

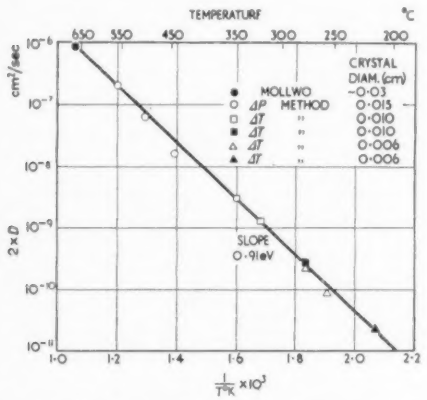

FIG. 3. Diffusion coefficients of hydrogen in ZnO.

It was observed that intense bombardment at lower temperatures turned clear colorless crystals to a beautiful amber color which was a property of an extremely thin surface layer. This color persisted after removal of hydrogen. The color vanished after a few seconds of etching by 0·1 per cent nitric acid. This removes a few thousand angstroms of crystal. A contribution to conductivity by this colored layer was not detected in this one test.

It will be noted from data to be given that many runs could be made with a single crystal with a diameter of 0·005 cm. No gradual deterioration of the crystal was observed and subsequent microscopic examination revealed no changes in the appearance of the crystal.

3.2 *Comparison of* H_1^+, H_2^+ *and* H_3^+

Fig. 2 contains curves of conductivity as a function of time obtained with H_1^+, H_2^+, and H_3^+ at the same ion currents, temperature, and bombarding voltage. The crystal (No. 3) had a diameter of 0·0044 cm. For the temperature of 250°C twice the diffusion coefficient is $1{\cdot}0\times10^{-10}$ cm²/sec. Thus the time to 50 per cent of saturation is about 3000 sec. The total ion current, equal to 1×10^{-8} A, corresponds to a calculated current density of $1{\cdot}3\times10^{-6}$ A per cm². The most interesting feature of these results is their relative simplicity. The ratios of saturation conductivities are 0·52 : 1·00 : 1·41 or nearly 1 : 2 : 3. This was found to hold well at higher temperatures if the bombarding voltage was high enough. At 400°C about 300 V was required.

Thus a range of conditions exists in which the bombardment induced conductivity is, to a good approximation, independent of the ion used if current is expressed as atom current.

Most of the work was done with H_2^+ because the yield of this ion from the spectrometer was ten times that of H_1^+. The purpose was not entirely to use higher current densities but also to keep down the temperature and therefore the evaporation rate of the spectrometer filament (to postpone the time for repairs).

3.3 *Saturation conductivity as a function of bombarding voltage*

Saturation conductivities as a function of bombarding voltage of H_2^+ are given in Fig. 4 for 250°C and 420°C. At both temperatures there is a linear

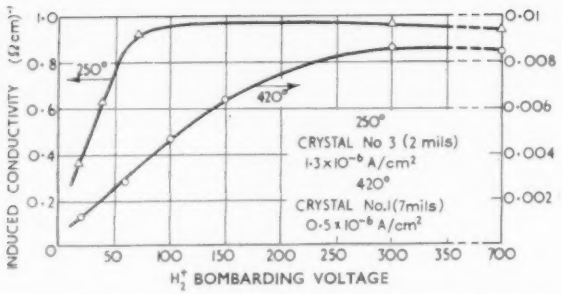

FIG. 4. Conductivity at saturation as a function of bombarding voltage of H_2^+.

range in the low voltage region. In the 250°C curve a relatively sharp break to a constant value occurs at about 70 V. At 420°C a constant value is obtained but the change from a linear dependence is much more gradual and the transition region is near 250 V. Scattered results at intermediate temperatures and with another crystal were in agreement with this trend.

There is some ambiguity in results obtained above the break. Saturation conductivity values tend to decrease with continued bombardment. This effect is discussed further in the next section.

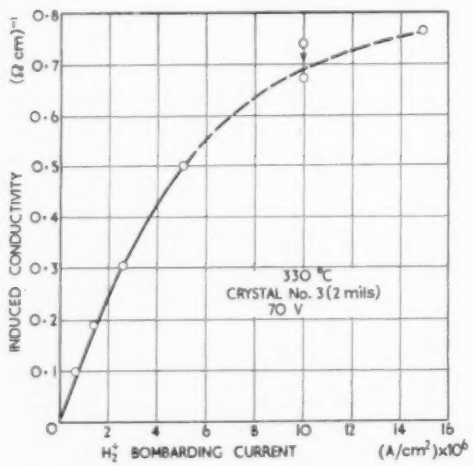

FIG. 5. Conductivity at saturation as a function of bombarding current of H_2^+.

3.4 *Saturation conductivity as a function of bombarding current. Surface damage*

Results from a series of runs at 330°C and 70 V are given in Fig. 5. A range of linear increase is observed up to a current density of about 3×10^{-6} A per cm^2.

The departure at higher currents is believed to be due, at least in part, to "surface damage". Two points are given for 10×10^{-6} A per cm^2. The first is the observed value at the estimated 96 per cent of saturation time. On continued bombardment conductivity did not rise by the expected 4 per cent. It drifted to the lower value which was reached at double the time taken to reach the first point. This is interpreted as a gradually increasing impedance to flow of ions into the crystal, or as a gradually decreasing impedance to the escape of ions which have entered and reacted with the crystal. It may result from a changing electrical barrier (produced by secondary processes) or from a true surface damage (for example flaws which impede inward flow).

This effect was often observed, but only when bombarding voltage or current density were relatively high. It is characterized by a premature slowing up of the diffusion process followed (sometimes) by a drift downwards of conductivity. The dependence on neither temperature nor type of ion was studied. Various observations, such as effectiveness of annealing at 500°C and absence of microscopically observable damage after many hours of bombardment, suggest that not many atom layers were affected.

The curves of Fig. 2 are believed to be relatively free of this effect because they were obtained at low bombarding current and moderate voltage. There was no difficulty in repeating results in this range, even without a preliminary anneal.

One suspects that several damaging effects might

lead to a gradual deterioration of the crystal, for example: surface misalignment, sputtering and chemical reduction. No visual evidence of such effects was found. One crystal (No. 3) was bombarded for about 10^5 sec with an average current of about 2×10^{11} H_2^+ ions/sec in experiments ranging through 250 to 420°C, and with bombarding energies up to 300 V. Microscopic examination showed no evidence of etching. Thus sputtering and chemical reduction were not efficient under these conditions.

3.5 *Efficiency of the bombardment process*

The process is very efficient, as can be shown by comparing ion current with rate of increase of donor concentration near zero time. It is found in Fig. 2 that specific conductivity increased by about 0·030 $(\Omega\,\text{cm})^{-1}$ in the first 5 sec for a current of H_2^+ equal to $1{\cdot}3\times10^{-6}$ A per cm². Taking room temperature mobility as 200 and an inverse three-halves power dependence on temperature (following results obtained by A. R. HUTSON[3]) the relation between number of donors and conductivity is

$$n = 9{\cdot}6\times10^{12}T^{3/2}\sigma. \qquad (2)$$

Thus the increase in number of donors was about $3{\cdot}3\times10^{15}$ per cm³. The actual volume of the sample between probes was about $6{\cdot}0\times10^{-6}$ cm³. Therefore the actual increase was $2{\cdot}0\times10^{10}$ donors. The estimated current to this region is $6{\cdot}0\times10^{-9}$ amperes. Therefore $2{\cdot}0\times10^{10}$ donors were produced by $6{\cdot}0\times10^{-9}\times5/1{\cdot}6\times10^{-19} = 2{\cdot}0\times10^{11}$ ions. Taking a shorter time interval, starting from zero time, yields higher efficiencies. Five seconds was chosen as having experimental significance.

It appears likely that in the higher range of bombarding voltages almost all incoming ions penetrate the crystal surface and react to form the donor complex.

3.6 *Saturation conductivity as a function of temperature*

Values of saturation conductivities at higher bombarding voltages (where they are independent of voltage) and at lower current densities (where they increase linearly with current) seem to be the proper data to plot as a function of temperature. Results are given in Fig. 6 for H_1^+ and H_2^+ and converted to donors per cm³ of ZnO in Fig. 7. Equation (2) has been used to make the conversion. The activation energy is found to be 0·58 eV.

The solubilities under ion bombardment are also compared with values obtained in H_2 gas. The

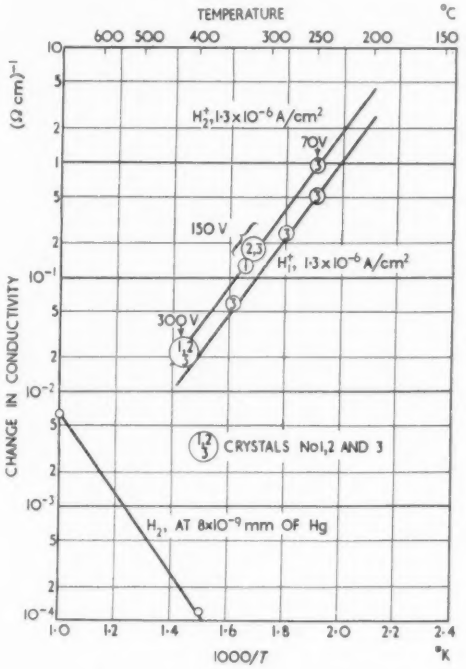

FIG. 6. Change with temperature of conductivity at saturation.

basis chosen for the comparison is numbers of atoms striking the surface. A current of $1{\cdot}3\times10^{-6}$ A/cm² of H_2^+ is equal to 8×10^{12} molecules per cm²/sec, or a hydrogen gas pressure equal to $2\times10^{-7}/\sqrt{T}$ mm of Hg. The lines drawn in Figs. 6 and 7 for this pressure were obtained from reference 2 using the one-quarter power dependence on pressure. For normal crystals, with relatively high initial conductivities, a one-half power dependence is expected because of the "common ion" effect.

Thus the "solubility" of hydrogen in ZnO under hydrogen ion bombardment increases with decreasing temperature and in the low temperature range is enormously greater than that obtained with an equivalent amount of normal hydrogen.

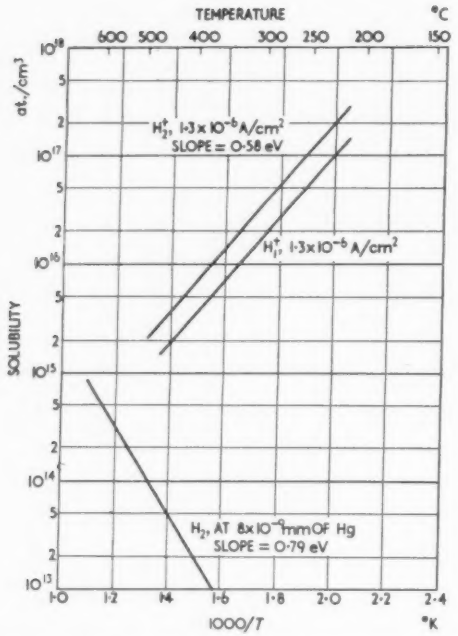

FIG. 7. Change with temperature of concentration of hydrogen in ZnO produced by bombardment compared with solubility of hydrogen at an equivalent atomic current to the surface.

4. INTERPRETATION

4.1 *Kinetics of the bombardment process*

The kinetics of the bombardment process, in the range of the above experiments, can be described by a simple model. It was observed that the conversion of bombarding ions to donors was very efficient (Section 3.5). When the diffusion process is complete (at saturation) the number of bombarding ions is equal to the number of desorbed molecules. Therefore, the boundary condition at the surface is

$$I = -D\frac{dn}{ds} + k_{-1}n, \qquad (3)$$

where I is the ion (H_2^+) current per cm², n is the donor concentration, dn/ds is the concentration gradient normal to the surface and k_{-1} is the evaporation rate constant. The evaporation rate is written as proportional to concentration because solubility was observed to be proportional to the bombarding current, at least through a large part of the experimental range.

It follows that the activation energy (0·58 eV) calculated from the slope of the curve of Fig. 7 is the activation energy for the evaporation process, since dn/ds is negligible at saturation.

4.2 *Diffusion and the surface barrier*

At this point one may well ask whether diffusion coefficients calculated from simple theory (Section 3.1) are valid, since a more complete treatment must take into account the surface barrier in the form of the boundary condition given in equation 2. Solutions of the more general equation are available, but they will not be required here. It is sufficient to note that the simpler treatment is valid if $D\,dn/ds$ is small compared to $k_{-1}n$ during most of the process. If it is, then surface concentration reaches the limiting value rapidly and this value may be used as the surface boundary condition, as is done in the simpler treatment.

Table 1 contains values of $D\,dn/ds$ calculated from the simpler diffusion equation, and the value of $k_{-1}n$ which is reached rapidly if $D\,dn/ds$ is negligible. Data from Fig. 3 and Fig. 7 are used. The crystal is assumed to have a diameter of 0·005

Table I

T (°C)	D (cm²/sec)	S (atoms/cm³)	$D(dn/ds)$ (atoms/cm²)		$k_{-1}n$ (atoms/cm²)	Percent of saturation	
			1 sec	100 sec		1 sec	100 sec
200	$1·0\times10^{-11}$	$4·4\times10^{17}$	$2·2\times10^{12}$	$2·2\times10^{11}$	4×10^{13}	0·13	1·3
300	$7·0\times10^{-10}$	$4·0\times10^{16}$	$1·9\times10^{12}$	$1·9\times10^{11}$	,,	1·2	12
400	$1·5\times10^{-8}$	$7·0\times10^{15}$	$1·5\times10^{12}$	$1·5\times10^{11}$	,,	5·2	45

cm, and data are for the H_2^+ ion with bombarding current equal to $1{\cdot}3\times10^{-6}$ A/cm².

A comparison of values of diffusion rate at the surface with evaporation rate shows that throughout the experimental range the diffusion rate is much smaller than the evaporation rate, therefore the barrier should not distort the simple diffusion process appreciably. Furthermore it seems unlikely that this effect can be measured directly in this type of experiment. The trouble is that the diffusion coefficient and the "solubility", which determine the flow rate, are so balanced that the flow rates are almost independent of temperature at constant time. One must search in an initial time interval much smaller than 1 sec. In very small crystals k can dominate the rate effects.

VOL. 3 1957

4.3 *Comparison of hydrogen ion bombardment and molecular hydrogen reaction kinetics*

The equilibrium equation for the reaction of molecular hydrogen with ZnO may be written

$$H_2(g) \underset{k_{-1}}{\overset{k_1}{\rightleftharpoons}} 2H^+(s)+2e^- \qquad (4)$$

$$K_1 = [H^+]^2[e^-]^2/p_{H_2}.$$

The heat of solution per atom is about 0·8 eV and this is the difference in energy between the barrier to the forward reaction and that to the reverse reaction. Assuming that the ion bombardment result (0·58 eV) is a measure of the barrier to the reverse reaction, the barrier to the forward reaction is about 1·4 eV.

It was concluded from the ion bombardment results that the evaporation rate at the surface is proportional to donor concentration. It has been argued that the ionized donor center is probably an hydroxyl ion. The argument is based on the need for finding the hydrogen atom in a relatively stable complex. This model suggests that the rate determining step in the reverse reaction is the breaking of the hydroxyl bond. If these are independent events then the overall rate is expected to be proportional to donor concentration.

An electrical barrier is also expected in ZnO, since it is known that surface charge can vary widely (THOMAS and LANDER[4]). The expected positive charge must repel ionized hydrogen. This barrier height is at most about 0·2 eV for a ZnO crystal at 250°C having a conductivity of 1 $(\Omega\,\text{cm})^{-1}$, equilibrium conditions being assumed.

Extrapolation of the "solubility" curve for ion bombardment (Fig. 7) toward higher temperature ultimately yields a value less than that expected for the equivalent pressure of molecular hydrogen. But this is impossible if bombardment is one hundred per cent efficient and the two processes have the same evaporation rates, since the reaction with molecular hydrogen must be far less than 100 per cent efficient in this temperature range. It is concluded that the evaporation rate constants for the two processes cannot be identical.

5. EFFECT OF ATOMIC HYDROGEN

A hot tungsten filament operated in hydrogen did, under various conditions, increase the conductivity of crystals by a small amount, even when there was no detectable ion current. This is believed to be due to atomic hydrogen. It was not studied systematically because of the difficulty of measuring concentrations of atomic hydrogen.

6. EFFECTS OF OXYGEN

It was noted in section 4.3 that part of the barrier to hydrogen evaporation should be electrical in nature, due to repulsion between positive surface charge and ionized hydrogen in solution. This charge may be from adsorbed hydrogen ions or zinc ions produced by reduction. In any case it should be more or less neutralized if oxygen is added to the system.

In the experimental arrangement at hand it was not possible to bombard crystals with hydrogen while exposing them to relatively high pressures of oxygen. To obtain high enough bombarding currents hydrogen pressures of the order of 1×10^{-3} mm of Hg were required. The pressure of 1×10^{-4} mm of oxygen had no observable effect on saturation conductivity, when the hydrogen pressure was 1×10^{-3} mm, but an oxygen pressure of 1×10^{-3} mm reduced the saturation conductivity by about 50 per cent and was just as effective at higher bombarding voltages where penetration of the ions beneath the surface is believed to be more efficient.

Large effects were also produced by heating the crystal in low pressures of oxygen at higher temperatures (instead of in vacuum) before bombardment. It was found that heating in the range from 500°C up reduced the saturation conductivity subsequently produced by the normal bombardment

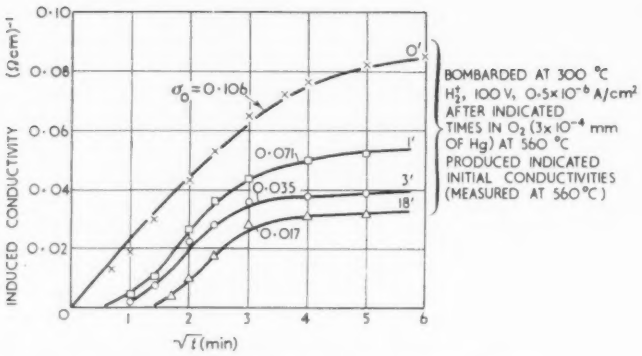

FIG. 8. Effect of treatment in oxygen at 560°C on conductivity produced by bombardment at 300°C.

conditions. Typical results for treatments at 560°C are given in Fig. 8. The results depended on time and temperature in the expected way (for example 18 min at 500°C was equivalent to 1 min at 560°C). Moreover such treatment also produced an induction period, as shown in Fig. 8. This amounts to a displaced zero for the diffusion process. The largest value is about three minutes. Conductivities resulting from the oxygen treatments also correlate with the effects. These values, given in the figure, are largely "surface" conductivities because in the particular crystal studied bulk conductivity was very low. The crystal could be restored to its normal condition by an equivalent heat treatment in vacuum.

Since treatment at 300°C in oxygen had no effect on the subsequent bombardment process it is concluded that the higher temperature treatments either removed donors or introduced acceptors below the surface. The problem of the neutral condition is not solved by these measurements, but it appears as though acceptors (e.g. zinc vacancies) were introduced by the treatment and that the induction period results because the bombarding ions must first neutralize these acceptors before the normal diffusion process can proceed. One is tempted to equate the integrated current flowing during the induction period with the number of acceptors introduced by the oxygen treatment. If this interpretation is essentially correct and the technique has more general application, then it provides a useful way to "titrate" acceptors.

REFERENCES

1. MOLLWO E. *Z. Phys.* **138,** 478 (1954).
2. THOMAS D. G. and LANDER J. J. *J. Chem. Phys.* **25,** 1136 (1956).
3. HUTSON A. R. *Bull. Amer. Phys. Soc.* II **1,** 381 (1956).
4. THOMAS D. G. and LANDER J. J. *J. Phys. Chem. Solids* **2,** 318 (1957).

J. Phys. Chem. Solids Pergamon Press 1957. Vol. 3. pp. 95–101.

THE STICKING PROBABILITIES OF GASES CHEMISORBED ON THE SURFACES OF SOLIDS

P. KISLIUK

Bell Telephone Laboratories Incorporated, Murray Hill, New Jersey

(*Received* 26 *April* 1957)

Abstract—A theory of the sticking probability is presented which differs from those in the literature in that the rates of migration and desorption for physisorbed molecules when they are above sites occupied by chemisorbed molecules are not assumed to be equal to these rates when they are above unoccupied sites for chemisorption. It is shown that this treatment, without invoking surface heterogeneity, has some of the flexibility of that of EHRLICH, which assumes a surface on which there are regions of high sticking probability and regions of negligible sticking probability. The present approach does not have the difficulty inherent in EHRLICH's model in explaining a surface density of adsorbed atoms nearly equal to the surface density of the atoms of the substrate. The expression thus derived for the sticking probability as a function of coverage is compared with data from the literature for nitrogen on tungsten.

INTRODUCTION

IN THE consideration of a complex phenomenon such as chemisorption which involves several kinds of interactions on surfaces of some degree of heterogeneity and which may require several adjacent adsorption sites for molecules which dissociate on adsorption, it is probably not practicable to proceed from first principles to develop a satisfactory theory. To extract from the experimental observations a mechanism which may at least contain the ideas most important to a reasonable understanding it may be worthwhile to develop the consequences of an admittedly oversimplified model but one which, it is hoped, will not sacrifice the essential features obtained experimentally.

To explain the observed sticking probabilities of N_2 on tungsten BECKER[1,2] has proposed a model in which every molecule impinging on the metal surface is captured by the relatively weak attractive forces leading to physisorption. It may then either pass into the chemisorbed state or be desorbed. Using reasonable values from the literature for the energies of physi- and chemi-sorption of nitrogen and oxygen on most metals it can be shown that after a reasonable length of time at room temperature the number of molecules chemisorbed greatly exceeds the number physisorbed. The sticking probability is defined as the ratio of the number per second which are becoming chemisorbed to the number per second which are arriving at the surface at any instant.*

The most striking experimental facts from the study of N_2 on W[1,2,3,4] that one can explain on such a model are:

1. The sticking probability is relatively insensitive to changes in coverage over a considerable range of coverage at room temperature and below.
2. The sticking probability is a monotonically decreasing function of temperature at the lowest measurable coverage.

The second point is significant because from other considerations one might expect a non-negligible activation energy for chemisorption.[2,5]

* The temperature range in which this view of the sticking probability is valid at pressures of 10^{-8} mm Hg and below is between $T_{\text{lower}} \approx \epsilon_{\text{phys}}/30\,k$ where ϵ_{phys} is the binding energy of physisorption and $T_{\text{upper}} \approx \epsilon_{\text{chem}}/30\,k$ where ϵ_{chem} is the binding energy of chemisorption. Below this range physisorbed molecules are present in numbers comparable to those chemisorbed and must be experimentally distinguished if we are to count only those chemisorbed as "stuck". Above this range the rate of desorption of chemisorbed molecules is no longer negligible compared to the rate of chemisorption.

This model has been further developed by EHRLICH[6] who concludes that the most likely explanation of the observed curves of the sticking probability as a function of coverage and of temperature is obtained by assuming a patchy surface with regions of rapid chemisorption, identified tentatively with lattice steps, and regions with a negligible rate of chemisorption. However this author concedes that this model requires further development to explain the observed density of adsorbed molecules in a completed monolayer which is of the order of the number of tungsten atoms on the surface. It will be shown in the present paper that, on somewhat different assumptions, it is possible to get agreement with the experimental facts equivalent to that obtained in reference (6) without resorting to a model with a patchy surface.

2. SIMPLE THEORY

We will consider a molecule which does not dissociate on chemisorption and which, when chemisorbed, occupies one of a finite number of distinct identical sites on the surface. At this stage the sites need not be related to a particular configuration of substrate surface atoms. However, no more than one chemisorbed molecule may occupy a site.

Let the probability that a molecule physisorbed above an empty site be chemisorbed before it is desorbed or passes on to a new site be P_a, and the similar probability of desorption be P_b.* The probability that a molecule will proceed to the next site from an empty site is then:

$$P_c = 1-P_a-P_b. \tag{1}$$

Similarly, let P_a', P_b' and P_c' be the corresponding probabilities for a molecule physisorbed over a filled site. We are assuming $P_a' = 0$, so that:

$$P_c' = 1-P_b'. \tag{2}$$

When a molecule arrives at the surface from the gas phase the probability that the site on which it is first physisorbed be already filled by a chemisorbed molecule is θ, the fractional coverage. Thus we have:

$$\left.\begin{aligned}
&\text{Probability of being chemisorbed on first site,}\\
&\quad P_{a1} = (1-\theta)P_a\\
&\text{Probability of evaporating from the first site,}\\
&\quad P_{b1} = (1-\theta)P_b+\theta P_b'\\
&\text{Probability of moving on to second site,}\\
&\quad P_{c1} = 1-P_{a1}-P_{b1}\\
&\qquad = 1-P_a-P_b+\theta(P_a+P_b-P_b').
\end{aligned}\right\} \tag{3}$$

Now the probability that the second site be filled is not completely independent of whether or not the first was filled. If, for example, $P_b = P_b'$, a site next to a filled site is a bit more likely to be filled by the next molecule than a site next to an empty site because of the additional possibility of being stopped at the original site by chemisorption if it is empty. Thus the probability of the nth event is dependent on the $n-1$ previous events *and the likelihood of any particular route to a given distribution depends not only on the events required, but also on the order in which the events take place.* Such a process is called a "generalized Markoff process"[7] and is beyond the mathematical powers of the present author to handle in this case. We will therefore assume that the probability that the second site be already filled is independent of whether the first was filled or empty, i.e., equal to θ, even though we know this is unlikely to be strictly the case and that this probability is determinable in principle from our basic assumptions. This approximation is most likely to be valid near $\theta = 0$ and $\theta = 1$ when the distribution of the few filled or vacant sites, respectively, must be nearly random, and is weakest near $\theta = 0{\cdot}5$ where there may be some clumping or "anti-clumping", but these effects may be negligible for the cases of physical interest. In principle this assumption could be tested *a posteriori* when the various probabilities are evaluated by comparison with experiment.

With this further assumption, then, the probabilities relevant to the second site visited are:

* These probabilities are not merely proportional to the inverse of the corresponding rates since they also depend on the average time spent at a site, which time is not assumed to be necessarily the same for filled as for empty sites—i.e., the barrier to migration for a physisorbed molecule may be different at the two types of site as well as the rates of desorption and chemisorption.

$$P_{a2} = P_{c1}(1-\theta)P_a$$
$$P_{b2} = P_{c1}\{(1-\theta)P_b+\theta P_b'\}$$
$$P_{c2} = P_{c1}\{1-P_a-P_b+\theta(P_a+P_b-P_b')\} = P_{c1}^2. \quad (4)$$

By iteration of this procedure we arrive at the sticking probability which is the sum of the probability of chemisorption on the first, second, third ... etc. site visited by the physisorbed molecule.

$$S = P_{a1}+P_{a2}+P_{a3}\ldots = P_a(1-\theta)(1+P_{c1}+P_{c1}^2\ldots)$$
$$= \frac{P_a(1-\theta)}{1-P_{c1}} = \frac{(1-\theta)P_a}{P_a+P_b-\theta(P_a+P_b-P_b')} \quad (5)$$

When $\theta = 0$ we have:

$$S_0 = P_a/(P_a+P_b), \quad (5a)$$

defining S_0, so that after a rearrangement of terms we have

$$S/S_0 = \left(1+\frac{\theta}{1-\theta}\,\frac{S_0P_b'}{P_a}\right)^{-1} = \left(1+\frac{\theta}{1-\theta}K\right)^{-1}.* \quad (6)$$

This equation gives a family of curves of S/S_0, vs. θ in terms of a single parameter $K = S_0 P_b'/P_a = P_b'/P_a+P_b$. In principle one can evaluate S at coverage approaching zero and the coverage corresponding to $\theta = 1$ from experiment. The data of S vs. number of molecules per cm² can then be reduced to a plot of S/S_0 vs. θ. If the above theory is applicable, the points will fall on a curve corresponding to a single value of the parameter K. Equation 6 is plotted for various values of this parameter in Fig. 1.

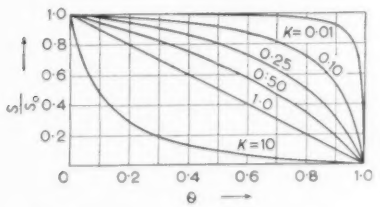

FIG. 1. A plot of

$$S/S_0 = \left(1+\frac{\theta}{1-\theta}K\right)^{-1} \quad \text{(equation 6).}$$

3. CORRESPONDENCE BETWEEN THE DIFFERENT TYPES OF THEORY

In the language of exponential rate theories such as those used by BECKER and EHRLICH, which involve the assumption that the physisorbed molecules are in thermal equilibrium with the surface, let:

Frequency per admol of migration from clean site,

$$F_c = K_c e^{-\epsilon_m/kT}$$

Frequency per admol of chemisorption on a clean site,

$$F_a = K_a e^{-\epsilon_a/kT}$$

Frequency per admol of evaporation from a clean site,

$$F_b = K_b e^{-\epsilon_p/kT} \quad (7)$$

and similarly from a filled site:

$$F_c' = K_c' e^{-\epsilon_m'/kT}$$
$$F_b' = K_b' e^{-\epsilon_p'/kT}$$

where ϵ_m is the energy barrier height to migration from an empty site, etc.

The average time spent above an empty site is then

$$\tau = \frac{1}{F_a+F_b+F_c}, \quad (8)$$

and that over a filled site

$$\tau' = \frac{1}{F_b'+F_c'}.$$

The various probabilities defined earlier are then

$$P_a = F_a\tau,\ P_b = F_b\tau,\ P_c = F_c\tau$$
$$P_b' = F_b'\tau',\ P_c' = F_c'\tau'. \quad (9)$$

* An unpublished manuscript has recently been brought to my attention in which D. G. BILLS and N. P. CARLETON arrive at a formally identical result for a different, but related, problem.

$$\left.\begin{aligned} S_0 &= \frac{P_a}{P_a+P_b} = \frac{K_a e^{-\epsilon_a/kT}}{K_a e^{-\epsilon_a/kT}+K_b e^{-\epsilon_p/kT}} \\ &= \frac{1}{1+K_b/K_a e^{(\epsilon_a-\epsilon_p)/kT}} \\ \frac{S_0}{1-S_0} &= \frac{K_a}{K_b} e^{(\epsilon_p-\epsilon_a)/kT}. \end{aligned}\right\} \quad (10)$$

Equation 10 is equivalent to expressions given by BECKER[1,2] and EHRLICH.[1,6,9] However, the parameter K of equation 6 which is the unique feature of the present treatment is given by:

$$\begin{aligned} K &= \frac{S_0 P_b'}{P_a} = \frac{P_b'}{P_a+P_b} = \frac{F_b'\tau'}{(F_a+F_b)\tau} \\ &= \frac{F_a+F_b+F_c}{F_a+F_b} \times \frac{F_b'}{F_b'+F_c'} \end{aligned} \quad (11)$$

which clearly does not reduce further without additional simplifying assumptions.

If, in particular, we assume the probabilities of migration F_c and F_c' to be negligibly small, we find $K = 1$, corresponding to the simplest possible case (Fig. 1), in which S is proportional to $1-\theta$.

To find the case corresponding to the treatments of BECKER and EHRLICH we assume first that the most likely fate of an admol on any site is that it migrate to a neighboring site, i.e., both F_c and F_c' much greater than F_a, F_b, or F_b'. Now in these theories one does not distinguish between the various probabilities over filled and empty sites; therefore one has implicitly assumed that $F_b = F_b'$, $F_c = F_c'$. Putting both these and the fact that F_c is much greater than F_a into equation 8 we find $\tau \approx \tau'$. Thus $P_b \approx P_b'$ and

$$K \approx \frac{P_b}{P_a+P_b} = 1-S_0. \quad (12)$$

When such a theory is applied to a uniform surface, there is little freedom of choice to fit the curves; out of the manifold of curves of equation 6 (Fig. 1) only one with K nearly equal to $1-S_0$ may be applied.

Both EHRLICH's treatment and ours require that S approach zero linearly as θ approaches unity which will be shown in the next section to offer some difficulty in comparison with experiment. In the present case, from equation 6 we find:

$$(S/S_0)_{\theta\to 1} \to (1-\theta)/K. \quad (13)$$

In summary, earlier treatments implicitly assume by using the thermodynamics of rate processes in a simple manner that the rate of desorption over a filled site is equal to that over an empty site. To allow sufficient freedom to fit the data EHRLICH[6] then assumes a distribution of active and inactive patches, specified by two parameters giving the fraction of the area occupied by active patches and the size of each individual patch. If these sites are identified with lattice steps, one arrives at the aforementioned difficulty in explaining the relatively high observed coverage. In the present theory the freedom necessary to fit the specific data is obtained by assuming the various probabilities to be not necessarily the same over filled and empty sites, arriving at the single adjustable parameter K. In this theory all sites are available so there is no difficulty with the observed coverage.

4. COMPARISON OF THEORY WITH EXPERIMENTS AT ROOM TEMPERATURE

Values of S_0 and the surface density when S is a specified fraction of S_0 found for N_2 on W by various experimenters who may reasonably lay claim to have started with atomically clean surfaces are given in Table 1.

Table 1. *Chemisorption of* N_2 *on tungsten at room temperature*

Reference	S_0	$N_{0.001}$	$N_{1/2}$
		molecules/cm²	molecules/cm²
BECKER and HARTMAN[3]	0·55	$2{\cdot}5\times10^{14}$	$1{\cdot}6\times10^{14}$
EHRLICH[4]	0·11	$2{\cdot}05\times10^{14}$	$0{\cdot}8\times10^{14}$
EISINGER[9]	0·35	$3{\cdot}05\times10^{14}$	$1{\cdot}8\times10^{14}$

$N_{0.001}$ is surface density chemisorbed when $S \approx 10^{-3} S_0$. (Fortunately the α-phase reported by EHRLICH[4] is small enough in population so that it is only a small correction to the total.)

$N_{1/2}$ is the surface density when $S = 1/2\, S_0$.

It is clear that there is no obvious universal value of the coverage corresponding to a completed

layer or of S_0 to be drawn from this data. This may be due to differences in crystal orientation, roughness, etc., especially since EHRLICH used wire while the others used ribbons.* Thus the values of $N_{0\cdot001}$ and $N_{1/2}$ for ribbons are in reasonable agreement.†

If the shapes of the experimental curves of S vs. the surface population corresponded to one of the curves of equation 6 (Fig. 1), one could choose a set of values of the parameters S_0, $N_\theta = 1$, and K to fit each of these sets of data. Typical curves of S vs. coverage from the literature are given in Fig. 2. It is clear that the experimental values of S_0 lead to values of K much too large to fit the shapes of the experimental curves if K is taken equal to $1-S_0$ (equation 12). Thus further freedom is necessary to fit the data even in the region of low θ. Either the patchy surface of EHRLICH, the independent K of the present treatment, or some other additional parameter must be invoked.

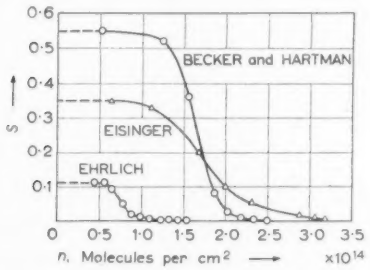

FIG. 2. Experimental data on the sticking probability of N_2 on W as a function of the surface density of N_2 at room temperature.

By fitting three experimental points to equation 6, one at the lowest measured coverage and the other two in the knee of the curve where S has become appreciably less than S_0, "experimental" values of S_0, K, and $N_{\theta=1}$ have been deduced. These are presented in Table 2.

We note, in addition to the discrepancy between K and $1-S_0$, that $N_{\theta=1}$ obtained in this manner is much closer to $N_{1/2}$ than it is to $N_{0\cdot001}$. The tail at large coverage may be due to an effect not contemplated in this theory which nevertheless does not greatly affect the form of the curve at low coverage. It may be appropriate to regard the coverage corresponding to $N_{1/2}$ as the completion of a unit of coverage (i.e. a "monolayer" or "one θ unit") rather than that corresponding to $N_{0\cdot001}$ (see reference 2).

The ratio $K/(1-S_0)$ according to the present theory is equal to P_b'/P_b. This quantity is also listed in Table 2 and is found to be of order 0·1 or less. Thus the physisorbed molecule is apparently more likely to evaporate from a site unoccupied by a chemisorbed molecule than from an occupied one. This seems contrary to intuition in that one might expect the forces leading to physisorption to be somewhat stronger over an empty site than over a filled one. The explanation is that the barrier to migration away from an empty site may be sufficiently greater than the corresponding barrier at a filled site that the greater time spent over an empty

* Unpublished experiments by C. D. HARTMAN and H. D. HAGSTRUM indicate that both the sticking probability at low coverage and the coverage where the sticking probability decreases appreciably are approximately half as great for wires as they are for ribbons. See also reference 9a.

† J. T. EISINGER informs me that for several ribbons contained in different volumes at different pressures the density of molecules in a completed monolayer is much more consistently repeatable than is S_0. Thus in applying EHRLICH's treatment one must conclude that the fraction of the surface upon which adsorption may take place is one of the more repeatable quantities characterizing the adsorptive properties of the surface.

Table 2. Quantities derived from the curves of Fig. 2.

Reference	K	S_0	$1-S_0$	$K/1-S_0$	$N_{\theta=1}$
					molecules/cm²
BECKER and HARTMAN	0·015	0·55	0·45	0·03	$1\cdot65\times10^{14}$
EHRLICH	0·095	0·11	0·89	0·11	0·8
EISINGER	0·04	0·35	0·65	0·06	1·8

site, and consequent greater opportunity to evaporate, more than compensates any greater attractive force. Thus $\tau \gg \tau'$, leading to small values of K (equation 11) and, to the extent that this simplified theory is applicable to N_2 on tungsten, the molecule may be pictured as skittering around over the filled sites rapidly until it arrives at an empty site where it may rest in the physisorbed state for a relatively long time before being desorbed, chemisorbed or resuming its travels on the surface.

Unfortunately this would cause the layer to build up in patches, making questionable the validity of the assumption of a random distribution of filled sites used in Section 2.

In the region of large coverage, as touched upon earlier regarding the discrepancy between $N_{0.001}$ and $N_{\theta=1}$, none of these curves are similar to Fig. 1 in shape. There is a tail which apparently approaches the $S = 0$ axis asymptotically rather than at a finite slope as required by both EHRLICH's treatment and that presented here if the probabilities involved (or equivalently the entropies and energies of activation in EHRLICH's treatment) are not considered to be functions of coverage.

The suggestion that the energies of activation are a function of coverage is by no means new. In fact the terms "activated" and "chemical" adsorption were regarded as synonomous until chemical adsorptions with negligible activation energy were observed by improving the techniques of obtaining clean surfaces, whereupon the earlier observations were attributed to partially covered surfaces.[10,11] The only additional point to be made here is that such an assumption may be useful in fitting the observed curve of sticking probability vs. coverage to theory.

The alternate possibility that the additional adsorption responsible for the tail is of a different sort, e.g., a distinguishable second layer, is made untenable by the flash-off experiments which show no new peak at lower temperatures appearing when this region of adsorption is attained; in fact EHRLICH[4] finds that the relatively weakly adsorbed α-state *decreases* at high coverage.

The interpretation would indeed be further complicated if there were more than one state of adsorption present in appreciable numbers (as, for example, more than one layer), but for N_2 on W at the experimental pressures and times this does not appear to be the case.[2,4,11a,12]

5. EXPERIMENTS AT VARYING TEMPERATURES

The activation energy as a function of coverage may in principle be found approximately from the measured slopes of $\ln S/(1-S)$ vs. $1/kT$ at various fixed values of θ. Returning to the model proposed by BECKER this slope is simply $(\epsilon_p - \epsilon_a)$ (equation 10 extended to coverages greater than zero). If we assume ϵ_p to be independent of coverage, the variation of this slope with θ is due entirely to the variation of ϵ_a with θ.

The published data on S as a function of T are, however, rather scanty,[3,6] and suffer, in so far as our present purpose is concerned, by the uncertainty in θ introduced by the variability of the observed number in a completed "layer". In other words, the data presently available are not sufficiently precise, fine-grained, and reproducible to warrant such a treatment.

6. ATTEMPTS TO FIT EXPERIMENTAL CURVES AT HIGH COVERAGE BY FURTHER SIMPLIFYING ASSUMPTIONS

If, as appears reasonable, we assume F_b, F_c, F_b', F_c' to be weak functions of θ while F_a is a strong monotonically decreasing function of θ, then K is a monotonically increasing function of θ (equation 11), so that we move downward among the curves of Fig. 1 with increasing θ and the behavior of Fig. 2 could conceivably be approximated.

However, to achieve any significant increase in K, for example from about 0·01 to more than unity which would appear from Figs. 1 and 2 to be necessary to fit the curves, we then must have $F_a(\theta = 0) \gg F_b$ (equation 11). This implies that

$$S_0 = \frac{F_a(\theta = 0)}{F_a(\theta = 0) + F_b} \approx 1,$$

contrary to observation (Table 1). This appears to be a blow to our hopes of fitting the curve by a reasonable assumption as to the behavior of the activation energy as a function of coverage.

Several ways out of this dilemma appear reasonable:

(1) The assumption that the physisorbed molecules are in thermal equilibrium with the surface may not be justified.

(2) Effects due to the requirement for two empty

sites when N_2 dissociates on chemisorption may be important in this region.[10]

These two points will be discussed in a future publication.

(3) The tail may be due to crystal faces exposed on a relatively small fraction of the surface which have a low sticking probability, i.e. patchiness invoked to explain this small effect rather than as an essential of the process also important at low coverages.

(4) Perhaps only a fraction of the order of 10 per cent → 50 per cent of the impinging molecules are physisorbed, the rest being reflected on the first bounce. (This is related to point (1).) The sticking probability for those molecules which become physisorbed could then be very nearly unity at $\theta = 0$. Variations in S_0 between different experiments might then be attributed to differences in surface microgeometry, and even a simple theory in which $K = 1 - S_0$ (equation 12) assuming a uniform surface might remain tenable. However, some evidence that nearly all impinging molecules may be physisorbed is reviewed in reference 6, p. 6.

(5) For H_2 on W and certain other systems chemisorption when the coverage is considerable may cause the desorption of a neighboring chemisorbed molecule which would have had a negligible probability of desorption in the absence of the gas.[13–15] In this case the observed sticking probability near $\theta = 1$ is the difference between those chemisorbed and those desorbed, the latter being a considerable contribution. Clearly this would invalidate any of the treatments thus far considered in this region. Experiments with labeled isotopes might clarify this matter.

Other possibilities which may be of importance but are not taken into account are forces between the physisorbed molecules and chemisorbed molecules on nearby sites,[10] a possible tendency for new sites to be created when molecules are chemisorbed,[16] or a tendency for easier formation of surface bonds near chemisorbed atoms,[17,18] all of which have been suggested in the literature. In the opinion of the author these considerations are not likely to be strong enough to greatly alter the situation, but this clearly is a matter for further experiment and calculation to decide.

7. CONCLUSION

An alternative formulation of the theory of sticking probabilities has been presented and applied to the experimental data for nitrogen on tungsten. This treatment achieves some of the flexibility of EHRLICH's assumption of a patchy surface without the concommitant difficulty in explaining the large coverage which approaches that of tungsten atoms in the surface and is one of the more repeatable experimental quantities. It has been shown that both theories are incapable of explaining the form of the sticking probability curve on a nearly complete monolayer without additional considerations.

Acknowledgements—The author would like to thank J. A. BECKER, J. T. EISINGER and H. D. HAGSTRUM for helpful discussions.

REFERENCES

1. BECKER J. A. in *Structure and Properties of Solid Surfaces* p. 459. University of Chicago Press (1952).
2. BECKER J. A. in *Advances in Catalysis* Vol. VII. Academic Press, New York (1955).
3. BECKER J. A. and HARTMAN C. D. *J. Phys. Chem.* **57,** 157 (1953).
4. EHRLICH G. *J. Phys. Chem.* **60,** 1388 (1956).
5. LENNARD-JONES J. E. *Trans. Faraday Soc.* **28,** 333 (1932).
6. EHRLICH G. *J. Phys. Chem. Solids* **1,** 3 (1956).
7. CHANDRASEKHAR S. *Rev. Mod. Phys.* **15,** 1 (1943).
8. EHRLICH G. *J. Phys. Chem.* **59,** 473 (1955).
9. EISINGER J. Unpublished data.
9a. EHRLICH G. and HICKMOTT T. W. *J. Chem. Phys.* **26,** 219 (1957).
10. ROBERTS J. K. *et al.*, reviewed in MILLER A. R. *Adsorption of Gases on Solids* Cambridge University Press (1949).
11. BEECK O. *et al.* reviewed by WHEELER A. in *Structure and Properties of Solid Surfaces* University of Chicago Press (1952).
11a. HICKMOTT T. W. and EHRLICH G. *J. Chem. Phys.* **24,** 1263 (1956).
12. BECKER J. A. Unpublished results.
13. ELEY D. D. and RIDEAL E. *Proc. Roy. Soc.* **A178,** 429 (1941).
14. COUPER A. and ELEY D. D. *Proc. Roy. Soc.* **A211,** 536, 544 (1952).
15. MOLINARI E. *Gazz. Chim. Ital.* **85,** 930 (1955).
16. LANDSBERG P. T. *J. Chem. Phys.* **23,** 1079 (1955).
17. COULSON C. A. and BALDOCK C. R. *Disc. Faraday Soc.* **8,** 27 (1950).
18. POLLARD W. G. *Phys. Rev.* **56,** 324 (1939).

VOL. 3 1957

J. Phys. Chem. Solids Pergamon Press 1957. Vol. 3. pp. 102–106.

ELASTORESISTANCE EFFECTS IN A GERMANIUM-SILICON ALLOY

ROBERT W. KEYES

Westinghouse Research Laboratories, Pittsburgh 35, Pennsylvania

(*Received* 26 *April* 1957)

Abstract—The large piezoresistance effect in a Ge 0-04 Si alloy has been measured and found to be proportional to T^{-1} between 77°K and 300°K and to be 15 per cent greater than in pure Ge. Various origins for this difference are examined, and, using some evidence from the elastogalvanomagnetic effects, it is concluded that at least part of the difference is due to intervalley scattering of the alloy type in the alloy.

VOL
3
195

INTRODUCTION

RECENTLY single crystals of germanium-silicon alloys in a variety of compositions have been prepared.[1,2] These alloys are semiconductors with electrical properties[3,4] similar in many respects to those of silicon or germanium. In alloys with a silicon content of less than 10 per cent the parameters which describe the conduction band minima are essentially the same as the corresponding parameters in pure germanium.[4,5,6] In other words, the addition of small amounts of silicon to germanium does not appear to change the conduction band structure significantly.

The electron mobility, however, is a rapidly varying function of the alloy composition. The addition of a few per cent of silicon to pure germanium decreases the mobility sharply. The mobility at 300°K of a Ge - 9 per cent Si alloy is only half of the lattice scattering mobility of germanium according to GLICKSMAN.[4]

In view of the similarity in the band structures of dilute solutions of silicon in germanium and pure germanium it appears that the decrease in mobility which results from the addition of the silicon must be due to scattering of the electrons by the silicon atoms.[3,4] It has been shown[7,8,9] that various aspects of the elastoresistance effects are sensitive to details of the carrier scattering mechanism. In an effort to obtain a more complete picture of the scattering of electrons by silicon atoms in dilute silicon-germanium alloys we have measured the piezoresistance effect and some other relevant electrical properties in such an alloy.

EXPERIMENTAL

We obtained from Dr. S. M. CHRISTIAN of the RCA Laboratories some samples of a Ge-Si alloy containing 4 per cent silicon. The material was *n*-type, containing about 4×10^{15} donors per cm^3. A resistivity traverse of a specimen showed considerably more inhomogeneity than is found in a high quality specimen of pure germanium. An X-ray powder diffraction pattern showed only a single composition with a lattice parameter 0·0126Å less than the lattice parameter of pure germanium. This value is consistent with a Si content of 4 per cent according to the measurements of JOHNSON and CHRISTIAN.[1]

The Hall mobility of our specimens at 300°K was only 1800 cm^2/Vsec, compared to 2700 cm^2/Vsec found by GLICKSMAN for material of the same composition. The reason for this discrepancy is not clear. A measurement of the temperature dependence of the mobility excludes the possibility that there is a significant amount of ionized impurity scattering at 300°K in our samples. We believe that the decreased mobility is due to additionl scattering by some sort of defects in the lattice. Since these alloy crystals are not grown by the Czochralski method, it is not possible to attain with them crystal perfection comparable to that which is common in pure germanium, and it is not surprising that the crystal perfection varies from sample to sample. However, it is necessary to bear in mind that in the discussion which follows the term "alloy scattering" includes this additional scattering of uncertain origin.

The specimens were rectangular parallelipipeds $0{\cdot}1 \times 0{\cdot}14 \times 1{\cdot}0$ cm^3 with a (110) axis in the long direction. In the measurements of the piezoresistance effects the technique of SMITH[10] was closely copied.

The elastoresistance effects

The measurements of elastoresistance and elastogalvanomagnetic effects were all made with the orientation shown in Fig. 1. When $B = 0$, this arrangement is

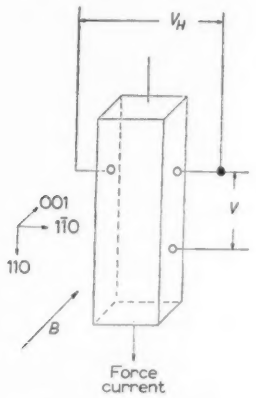

FIG. 1. The sample arrangement used to make the measurements of elastoresistance and elastogalvanomagnetic effects described in the text.

equivalent to SMITH's arrangement C, and we designate the piezoresistance constant which it measures by π_c, i.e., $\pi_c = (1/X)\delta V/V$, where X = longitudinal stress. Two effects of elastic strain on the galvanomagnetic coefficients can also be measured with this arrangement: (1) the piezo-Hall constant with the magnetic field in a (001) direction, $\pi_c^H = (1/X)\delta V_H/V_H$, (2) the elastomagneto-resistance with the magnetic field in a (001) direction, which we characterize by the ratio of the elastomagnetoresistance to the elastoresistance:

$$G = \left(\frac{\delta V(B) - \delta V(0)}{V(B) - V(0)}\right) \Big/ \frac{\delta V(0)}{V(0)}. \qquad (1)$$

The results of the measurement of the piezoresistance constant π_c are shown in Fig. 2. π_c is approximately proportional to T^{-1}. Its value at 300°K is -83×10^{-12} (dyne/cm^2)$^{-1}$, which is to be compared with SMITH's value[10] of -72×10^{-12} (kg/cm^2)$^{-1}$ for pure n-type germanium at 300°K. Since the temperature dependence of π_c is also close to T^{-1} in pure germanium,[11,12] the piezoresistance constant in the alloy is about 15 per cent higher than that in pure germanium throughout the temperature range from 77°K to 300°K.

The measurements of elastogalvanomagnetic effects are more qualitative in nature and the results will be given at the appropriate places in the next section.

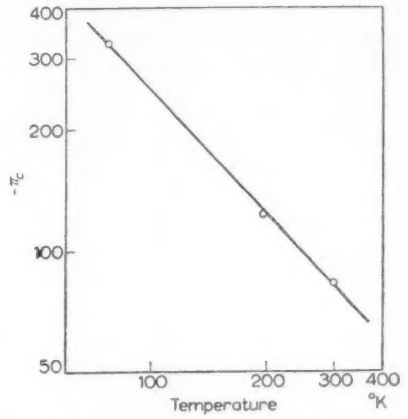

FIG. 2. The piezoresistance coefficient π_c, measured by the arrangement of Fig. 1, at three convenient temperatures. π_c is expressed in units of 10^{-12}(kg/cm^2)$^{-1}$. The slope of the line is $-1{\cdot}02$.

DISCUSSION

We wish now to consider the question of why there is a difference in the piezoresistance constants of pure germanium and the alloy. It appears in the first place that this difference results from a difference in the dimensionless elastoresistance constants, rather than from a difference in elastic constant. A simple interpolation of elastic constants between germanium and silicon gives elastic constants for the alloy within 2 per cent of those for germanium. The elastic constants of silicon differ by less than 30 per cent from those of germanium, and it is difficult to believe that the solution of 5 per cent of silicon in germanium could alter the elastic constants of germanium by more than a few per cent.

We do not believe that the sample inhomogeneity can cause an increase in π_c. In an inhomogeneous sample with the geometry of Fig. 1 the piezoresistance effect might be altered by the existence of inhomogeneity. In some regions of the sample the current would flow, not in the (110) direction, but in some other direction so that the component of the resistivity tensor being measured would not be the (110) (110) component. However a tensile stress in the (110) direction produces its

largest effect on the (110) (110) component of the resistivity tensor, and the mixing of other components into the resistivity measurement could only decrease the effect of the strain. Thus we believe that the inhomogeneity of the sample cannot be the source of the enhanced piezoresistance effect.

Another possibility which must be considered is that the model of the band structure which places all of the conduction electrons in minima on the (111) axes is defective. Although the magnetoresistance measurements of GLICKSMAN[4] are in agreement with this model, we desired a further verification of it. Such a verification could be provided by a determination of the complete elastoresistance tensor; however, the sample of Fig. 1 does not allow such a determination to be made. It has been shown[9] that for conduction by (111) valleys the piezo-Hall constant, π_c^H, defined above vanishes. This result is not true for conduction by electrons in various other multivalley structures, such as (100) or (110) minima. We have therefore measured π_c^H, and found that its value is only $0{\cdot}01\,\pi_c$, in agreement with the model of conduction by electrons in (111) valleys.

The most likely alternative states for the electrons are the minima on the (100) axes, as it is known[13] that these minima are lower in energy with respect to the (111) minima in the alloy than in germanium. The presence of electrons in the (100) valleys would cause a considerable change in the elastoresistance effects. However, if electrons activated into the (100) valleys were contributing to the effects, their number would be a strong function of temperature, and the simple T^{-1} dependence of π_c on temperature would not be expected.

Furthermore, using the energy gap data of JOHNSON and CHRISTIAN[1] we can estimate the number of electrons in the (100) minima. From the data[1] we find that the difference in energy between the (100) and (111) minima in a 4 per cent Si alloy is 0·11 eV. From this energy and the effective masses of germanium and silicon it can be calculated that about 3 per cent of the electrons will be in the (100) minima at 300°K, and that this number will decrease rapidly with decreasing temperature. Thus it is unlikely that the (100) electrons have any important influence on the electrical properties.

Thus we will assume the germanium band structure and examine ways in which the elastoresistance coefficients might be increased by the addition of silicon. The theory of the elastoresistance of germanium has been given by HERRING and HERRING and VOGT.[7] They show that the large elastoresistance coefficient has the value

$$m_{44} = \frac{1}{9}\,\frac{\Xi_u}{kT}\left(\frac{\mu_{\parallel}-\mu_{\perp}}{\mu}\right)\left(1+\frac{\nu}{2}\right), \qquad (2)$$

where Ξ_u is a deformation potential constant, $(\mu_{\parallel}-\mu_{\perp})/\mu$ is the mobility anisotropy of a valley, and ν represents the effect of intervalley scattering. The expression for ν is very complicated and only an approximate evaluation of it for germanium has been made.[7] However, ν has the property that it vanishes if there is no intervalley scattering, and, on the basis of a very simple model which regards the relaxation times as scalars independent of electron energy, ν is the fraction of scatterings which are of the intervalley type.[9] We shall, therefore, regard ν as a rough measure of the fractional amount of intervalley scattering.

We will now proceed to discuss the various terms of equation (2) in order.

The magnitude of the elastoresistance constant is proportional to Ξ_u. If Ξ_u were larger in the alloy than in germanium, the elastoresistance effect would be larger in the alloy. The most direct way to check this possibility would be to look for its other important consequence, namely, a decrease in the lattice mobility. In germanium the lattice mobility is approximately proportional[7] to Ξ_u^{-2}. Thus if the enhancement of the elastoresistance is entirely due to a higher value of Ξ_u in the alloy, the lattice scattering mobility of the alloy should be about 30 per cent less than that of germanium. The lattice mobility of the alloy is not susceptible to direct measurement; it is masked by the scattering due to the silicon atoms.*

It is difficult to evaluate theoretically the possibility of Ξ_u being different in the alloy and in germanium. If the wave functions of the electronic states around the energy minima are changed, Ξ_u

* Since we understand that the problem of the temperature dependence of the electron mobility is under investigation by Dr. GLICKSMAN it will not be pursued any further here.

would also be changed. It might be expected then that, in addition, other parameters which depend on the detailed nature of the wave functions, such as effective mass and energy of the minima, would be altered. The accuracy of the cyclotron resonance[5] and magnetoresistance[4] data is such that a change of the mass parameters by 10 per cent would not be detected. The energy gap of the alloy is 7 per cent greater than the gap of germanium. Thus it is not difficult to believe that a change of Ξ_u by 15 per cent could take place.

In germanium the mobility anisotropy factor is 0·93 of its maximum possible value. Thus, it could account for no more than a 7 per cent increase in the elastoresistance coefficient. Even this amount of increase would require a very extreme anisotropy, which would be difficult to understand.

In germanium ν approaches zero at low temperatures and increases with increasing temperature in the range 150°K–300°K attaining a value between 0·1 and 0·3 at 300°K.[9,12] The non-zero value of ν is a result of phonon-induced intervalley scattering. A higher value of ν in the alloy could account for the enhanced elastoresistance effect.

We can estimate ν by another means. The elastomagnetoresistance parameter G is sensitive to the amount of intervalley scattering.[9] In particular, in the simple energy independent relaxation time model mentioned above[9]

$$G = 1 - 4\frac{\nu}{1+\frac{1}{2}\nu} \qquad (3)$$

for valleys with a large mobility anisotropy. We have measured G and find at 77°K, $G = 0{\cdot}0$ and, at 300°K, $G = -0{\cdot}2$. The corresponding values for pure germanium[9] are at 77°K, $G = 1{\cdot}0$ and, at 300°K, $G = 0{\cdot}5$. These values indicate that ν is indeed larger in the alloy by about 0·2 or 0·3, which is the amount needed to explain the extra elastoresistance. Furthermore, since the energy of the intervalley phonon in Ge is much larger than 77°K, the large value of ν at this temperature excludes the possibility that phonon induced intervalley scattering is involved. We therefore conclude that intervalley scattering of the alloy type accounts for a considerable part of the enhancement of the elastoresistance effect in the alloy.

This conclusion implies that a large fraction of the alloy scattering is of the intervalley type. For, from the mobility data we find that one-third to one-half of the total scattering is of the alloy type. Thus, by attributing 20–30 per cent of the scattering to intervalley scattering we are implying that the probabilities of intervalley and intravalley scattering are comparable for the alloy scattering.

This conclusion is reasonable from a theoretical viewpoint. When a silicon atom is substituted for a germanium atom the difference in potential is large only within one or a few interatomic distances of the silicon atom. Thus the perturbing potential will have large matrix elements between states differing in k by as much as the reciprocal of the lattice parameter. This order of difference in k leads to intervalley scattering.

CONCLUSIONS

Unfortunately, we are unable to draw any accurate quantitative conclusions from our experiments. We have found that in a Ge-Si alloy specimen in which there is appreciable scattering by Si atoms, and perhaps also by other crystal defects, the piezoresistance effect is larger than in pure Ge. There is also a considerable amount of intervalley scattering in the alloy, probably enough to account for the increased piezoresistance effect, although the possibility that a large part of the enhancement of the effect is due to an increased deformation potential constant cannot be excluded.

Acknowledgements—The author is indebted to Dr. S. M. CHRISTIAN of the RCA Laboratories for making available the samples for this experiment, and to E. N. ADAMS and M. GLICKSMAN for helpful discussions.

REFERENCES

1. JOHNSON E. R. and CHRISTIAN S. M. *Phys. Rev.* **95,** 560 (1954).
2. WANG C. C. and ALEXANDER B. H. *Trans. Amer. Inst. Min. (Metall.) Engrs.* Symposium on Semiconductors, New York City, February 15–18 (1954).
3. LEVITAS A. *Phys. Rev.* **99,** 1810 (1955).
4. GLICKSMAN M. *Phys. Rev.* **100,** 1146 (1955); **102,** 1496 (1956); GLICKSMAN M. and CHRISTIAN S. M. *Phys. Rev.* **104,** 1278 (1956).
5. DRESSELHAUS G., KIP A. E., KU H. Y., WAGONER G., and CHRISTIAN S. M. *Phys. Rev.* **100,** 1218 (1955).
6. HERMAN F. *Phys. Rev.* **95,** 847 (1954).

7. HERRING C. *Bell Syst. Tech. J.* **34,** 237 (1955); HERRING C. and VOGT E. *Phys. Rev.* **101,** 944 (1956).
8. DUMKE W. *Phys. Rev.* **101,** 531 (1956).
9. KEYES R. W. *Phys. Rev.* **103,** 1240 (1956).
10. SMITH C. S. *Phys. Rev.* **94,** 42 (1954).
11. KEYES R. W. *Phys. Rev.* **100,** 1104 (1955).
12.* MORIN F. J., GEBALLE T. H., and HERRING C. *Phys. Rev.* **105,** 525 (1957).
13. BROOKS H. and PAUL W. *Bull. Amer. Phys. Soc.* **1,** 48 (1956).

* We are indebted to these authors for the communication of a preprint of their paper.

VOL
3
195

J. Phys. Chem. Solids Pergamon Press 1957. Vol. 3. pp. 107–114.

VARIATION OF CONTACT POTENTIAL WITH CRYSTAL FACE FOR GERMANIUM*

F. G. ALLEN† and A. B. FOWLER

Gordon McKay Laboratory, Harvard University

(*Received* 8 *February* 1957)

Abstract—A method is presented for measuring with high resolution the differences in the areal average work functions of the different crystal faces of any non-insulator available as a fairly large single crystal. The method has been applied to germanium, cleaned by certain techniques in high vacuum, and gives a reproducible pattern of values correlated with crystallographic directions. The results found were $\phi_{(100)} > \phi_{(110)} > \phi_{(111)}$, with $\phi_{(100)} - \phi_{(111)} \cong 0{\cdot}06$ eV, $\phi_{(110)} - \phi_{(111)} \cong 0{\cdot}015$ eV, these values being insensitive to bulk doping. While these differences found for germanium are on the order of one-tenth those known to exist between different faces of tungsten, it must be borne in mind that differences measured on the actual macroscopic faces will in general be less than those between ideal atomic surfaces. Before the face differences in work function for semiconductors can be explained, surface space charge potential and electrostatic dipole barrier at each face must be measured separately.

VOL. 3 1957

INTRODUCTION

MEASUREMENTS of the differences in contact potential or work function between different crystal faces have been reported for the metals copper,[1,2] silver[3] and tungsten,[4,5] all cleaned in high vacuum. These differences have been ascribed[6] to variations with crystal face of the strength of the electric dipole barrier at the surface, formed when the electron cloud spreads out from the positive ion cores of the surface atoms.

It is of interest to study these same differences in the case of typical semiconductors. The situation here might be expected to differ from that for metals in at least two respects: the electrons forming the surface cloud may originate in the valence band of the semiconductor instead of in the conduction band of the metal, so that the arrangement of bonds in the surface may be more important for semiconductors; and the surface potential of the semiconductor may be appreciably affected by a space charge just beneath the surface required to neutralize charge held in surface states.

This paper describes measurements made of the differences in contact potential between macroscopic (100), (110) and (111) faces of germanium single crystals cleaned both by heating and by argon bombardment in high vacuum.

METHOD

The contact potentials of six different faces of a single germanium crystal were measured, one after the other, by the same (vibrating) reference surface using a modification of the Kelvin method,‡[7,8] immediately after cleaning. The experiment was arranged to provide several internal checks on the reliability of its results. First, the six faces were actually three pairs of identical faces. Thus, as long as like faces did not give like values of contact potential, it was known that some of the faces were still contaminated. On the other hand, when a reproducible pattern of values was obtained for the six faces in which like faces were well matched, it could be asserted that

* Work supported jointly by the Navy Department, the Signal Corps of the U.S. Army and the U.S. Air Force under ONR Contract; also, through a fellowship awarded by Union Carbide and Carbon Co.

† Now at Bell Telephone Laboratories, Murray Hill, N.J.

‡ Note that with the null method, contact potentials are measured with zero external field applied.

differences in surface potentials were actually being determined by the crystal properties of the different faces. Second, the effects on contact potential of contamination from gas absorbing on the surface after the initial cleaning could be guarded against by checking the contact potential, after the run was completed, of the first face measured. If this value had not drifted during the run (usually an interval of about twenty minutes), no relative change in contact potential had occurred between the reference surface and germanium and, since the former was a metal (nickel), whose contamination properties are presumably different from those of germanium, one can say that little change had occurred on either surface. Finally, since all faces were on the same crystal, greater precision was possible than in experiments, sometimes reported in the past, in which unlike faces of different crystals are compared, so that small differences in crystal purity or history may introduce large errors in contact potential differences.

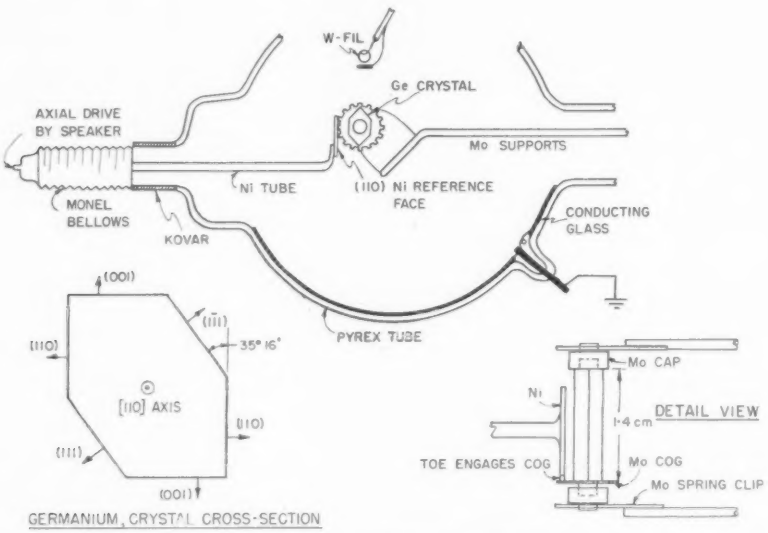

FIG. 1. Apparatus for contact potential experiment.

Tube and apparatus

The arrangement of sample and electrodes in the Pyrex vacuum envelope is shown in Fig. 1. The sample was rotated manually from outside the tube through a flexible bellows to present its different faces for measurement using a tooth and cog arrangement as shown. The reference surface was brought to within a few mils of the germanium face to be measured by a screw-driven adjusting yoke attached to the bellows (not shown). With this close spacing, the capacitance between reference surface and the face being measured was large compared to that between reference surface and all other electrode surfaces in the tube, including the remaining faces of the sample.

Contact potential differences were measured from the d.c. voltage required between germanium and reference surface to produce a null in the a.c. signal generated by the vibrating reference surface through its capacitance to the germanium face. With appropriate circuitry contact potentials were read to 2 or 3 mV.

Preparation of surfaces

The germanium crystals were cut in square bars along the (110) axis with (001) and (1$\bar{1}$0) faces accurate to within a few degrees, on a diamond saw. The (1$\bar{1}$1) faces were cut and all faces brought to within 1 degree of correct orientation by hand-sanding in a small jig on metallographic emery papers, checking orientation as needed with Laue back-scattering X-ray photographs. The sanding was finished with 000 paper (particle size roughly 5μ), and the damaged material removed by etching for two or three minutes in a CP-4* solution. This was followed by a brief etch in pure hydroflouric acid to remove excess germanium oxide left by the action of the nitric acid in CP-4. After a careful rinsing

* CP-4 solution: 25 c.^{3}, HNO_3 conc.; 15 c.^{3}, HAc, glacial; 15 c.^{3} HF conc.; several drops of bromine. A rough check on removal rate of germanium in this etch gave approximately 10μ min.

in distilled water, the sample was mounted, sealed into the tube and the latter evacuated within less than an hour.

The reference surface used with samples *A*, *B* and *C* was a (110) face cut from a large single nickel crystal.* A single crystal face was desirable to minimize variations in work function over its surface. After cutting, sanding and polishing the face mechanically, it was etched in nitric acid long enough to remove the damaged layer, i.e. about twice as long as required to give a sharp Laue X-ray pattern.

Vacuum techniques

After the customary baking of the Pyrex vacuum system at about 400°C several hours and outgassing all metal parts the germanium sample was heated at progressively higher temperatures. Heating was usually carried out by running an a.c. current through the sample (up to 18A) via the molybdenum supports, but occasionally electron bombardment from a tungsten filament (Fig. 1) was also used. It was found that gas was released each time the germanium was heated to a higher temperature, but that this gas evolution always died off in less than about 30 min. A subsequent heating to the same temperature produced no further evolution unless drastic contamination had occurred in the meantime. The nickel reference surface was heated by electron bombardment. Very much larger quantities of gas were evolved from the nickel than from the germanium. After repeated outgassing, pressures as low as $2{\cdot}5\times10^{-10}$ mm Hg were indicated on the Westinghouse Bayard–Alpert gauge, though most of the data reported here were taken at indicated pressures between this figure and 2×10^{-8} mm Hg. Even at the higher pressure, the run could usually be completed before significant drift of the contact potential difference measured on the first face had occurred. This was probably due to the fact that a large surface of freshly evaporated molybdenum was used as a getter during the runs, so that the residual pressure was nearly entirely inert gas.

Positive argon ion bombardments similar to those described by FARNSWORTH *et al.*[9] were used in cleaning the germanium surfaces either to supplement the effects of high temperature heating, or in place of all heating but low temperature baking. An electron ionizing beam of about 6 mA was drawn from the tungsten filament (Fig. 1) to the reference surface at 200V positive, argon gas was admitted to a pressure of about 5×10^{-4} mm Hg and an ion current of 10–100μA was collected on the germanium surface held at −400V. The argon used was "spectroscopically pure" as supplied in sealed flasks, was admitted into a well-evacuated volume through greased glass stopcocks where it was kept in contact with a liquid nitrogen trap for about 20 min† before being admitted through a baked-out all metal valve.[10] Two bombardments of the sample of about three minutes duration each with the sample held in positions differing by 180° were normally employed. The metal valve was then closed and the argon pumped out. Rough calculations assuming a sputtering efficiency of nearly unity[11] predict that this treatment should have removed a few monolayers of germanium or oxide each time it was used. The treatment had to be followed by a brief annealing of the germanium to about 600°C before "good" (see below) contact potential results were obtained. After bombardment the pressure always rose sharply during the first few seconds of heating of the sample, suggesting that a monolayer or more of argon is trapped in or on the surface by the bombardment. The pressure dropped again rapidly, and it was usually possible to start a contact potential run at a pressure of about 2×10^{-8} mm Hg‡ within 5 min after bombardment had ceased.

Table 1. *Data on germanium samples used for contact potential study*

Sample	Resistivity	
	Before study	After study
*A	15–20 ohm-cm type?	1·6 ohm-cm *p*-type
†*B*	0·005 ohm-cm *n*-type (arsenic dope)	0·0065 ohm-cm *n*-type
†*C*	40·0 ohm-cm type?	4·6 ohm-cm *p*-type
†*D*	0·10 ohm-cm *p*-type (indium dope)	sample lost in test

Only the following data were obtained on bulk lifetimes:

Sample *A*: 5μ sec after study.
Sample *C*: 450μ sec before study, 1μ sec after study.

* Purchased from Transistor Products, Inc.
† Supplied by Lincoln Laboratory and M.I.T.

Samples used: effectiveness of heating vs. bombardment

Data on the bulk properties of the four different

* Obtained from Horizons, Inc. While a single crystal face of tungsten or molybdenum, for which the work function has already been established, would have been preferable to nickel, no large single crystals of these metals were then available.

† In some runs, a molybdenum getter film was used in the argon line.

‡ It should be pointed out that this pressure was due to the argon that had been admitted, and that the residual pressure due to active gases was certainly many times less than this.

germanium samples used in this study are given in Table 1. It is seen that the range from extreme *n*-type through intrinsic to extreme *p*-type was covered.

When values of contact potential on the various faces of a germanium sample were first measured after pumping down to a vacuum but before the germanium had been heated above 350°C, they were completely random and differed from one another by as much as 1·4V. After suitable cleaning treatments a "pattern" of face potential values emerged in which like faces matched, unlike faces differed, and the differences were reproducible on many successive cleanings.

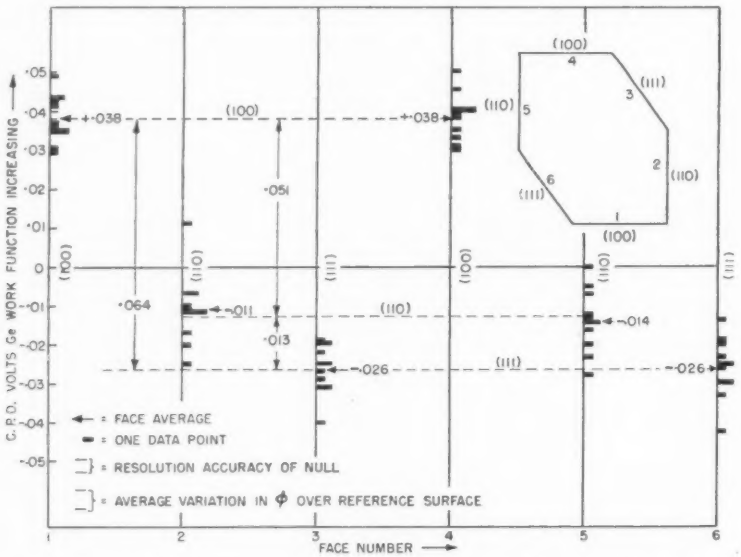

FIG. 2. Relative contact potential of germanium faces; sample *B*.

Calling such a pattern "good", we can summarize the treatments required to produce good patterns on each of the four samples as follows:

Sample A. Heating the germanium resistively 750±50°C for one continuous hour in a vacuum of 10^{-7} to 10^{-8} mm Hg.

Sample B. This sample was heated to 750±50°C for four hours, over many short heatings, and was removed from the tube and re-etched in CP-4 and HF four times, one of these following a repolishing of its faces on 0000 paper before a fairly good face pattern resulted. This pattern was improved but not essentially altered by the argon bombardments and further high temperature heatings that followed the above.

Sample C. A fair pattern was obtained after one argon bombardment and heating to temperatures between 400 and 500°C (following baking the system at 350°C two hr), only about 15 min. The first good pattern resulted after four argon bombardments and heating to temperatures between 500 and 600°C a total time of 40 min. However, subsequent heatings often yielded a poor set of values. This was taken to indicate that gas or impurities in the bulk of the sample had not yet been allowed to diffuse out of the interior.

Sample D. Fair patterns did not result till after two vacuum bakeouts of ~4 hr total at ~400°C and 15 argon bombardments followed by brief anneals to about 500°C. The lack of any high temperature outgassing is believed to explain the fact that the patterns obtained here were not as "good" as those with sample *B*.

From these results it is believed that (a) prolonged heating of germanium in high vacuum at temperatures above 750°C can be expected to produce a reproducible surface, as judged by its contact potential, and (b) that argon bombardment cleans the surface quickly and effectively, but cannot produce a surface that remains clean on subsequent heatings until the bulk material has been thoroughly outgassed. Aside from this disadvantage, it is still very attractive since, with only mild annealing needed, changes in bulk properties and diffusion of impurities into or out of the surface can be minimized.

VOL. 3 1957

PRESENTATION OF RESULTS

The data are presented using the arithmetic mean of the germanium face values for each run as a common zero reference. In this way, the differences in face values are shown directly, and easily compared for all runs. The data taken on sample *B* was the most extensive among the four, and is presented in Fig. 2. Data taken on all runs where cleaning had produced significant matching of values on like faces are plotted, each run yielding six data points, one on each face.* The spread in the data on each face shows that in many runs the faces were not completely clean or regular. However, it was noted on sample *B* that the face values measured after the most carefully conducted argon bombardments of both germanium and nickel surfaces not only showed an excellent matching of faces, but also excellent agreement with the mean values indicated in Fig. 2.† The data on the other samples is not reproduced here because it is in essential agreement with that in Fig. 2. The spread in the data on each face was greater on samples *C* and *D*, where high temperature heating was kept to a minimum, than that shown here for sample *B*.

The data on samples *B*, *C* and *D* can be summarized by giving the differences in the face averaged work functions as follows:‡

	Sample B	*Sample C*	*Sample D*
$\phi_{(100)}-\phi_{(111)}=$	0·064	0·055	0·045
	±·005	±·009	±·009 eV (1)
$\phi_{(110)}-\phi_{(111)}=$	0·013	0·013	0·022
	±·005	±·009	±·009 eV (2)

Sample *A* was an early specimen cut in a square cross-section with two pairs of opposite, parallel faces. One pair was about 7° off the (110), while the other was about 7° off the (111) direction. The fact that "good" patterns were obtained with *A* is considered significant, while the fact that the difference corresponding to (2) above turned out to be 0·040±0·007 eV cannot be directly related to the values found on the other samples without some previous knowledge of the rate of change of work function with angle near a principal direction.

* No attempt has been made to indicate the sequence of runs, since there was no tendency toward change as the runs continued.

† Normally, two or three null measurements, with slightly different spacing and position of the reference surface were made and averaged for each data point.

‡ Samples *A*, *B* and *C* were prepared and measured by the first author; sample *D* was then prepared and measured independently by the second author to rule out personal errors in the method and to extend the study to *p*-type material.

ABSOLUTE WORK FUNCTION FOR GERMANIUM, AND DIFFERENCE BETWEEN SAMPLES

The work function of the cleaned nickel (110) reference surface was always between 0·20 and 0·35 eV higher than the average of the three germanium faces for all samples studied. While the work function of the (110) face of nickel cleaned in high vacuum has not yet been reported, data taken in this study§ indicated that $\phi_{(110)}$ for nickel was higher than the average of several other faces by roughly 0·2 eV. Values reported for the work function of polycrystalline nickel cleaned by heating in vacuum,[12,13] range from 4·6 to 5·2 eV. All this would put our estimate for the work function of germanium between 4·5 and 5·1 eV, a range which brackets the more exact values (4·75±0·1 eV) reported by APKER, TAFT and DICKEY,[14] and DILLON.[15]

An additional check on the germanium work function is available from data taken by the second author on a germanium sample in the form of a *p–n* junction, to be reported later in detail. Here the C.P.D. between the germanium and a graphite reference surface heated to high temperatures in high vacuum gave the results

$$\phi_{\mathrm{Ge}\,(110)}-\phi_{\mathrm{Graphite}}=0{\cdot}04\pm0{\cdot}1\ \mathrm{eV}.$$

In a photo-electric study, TAFT and APKER[16] found the work function of seven samples of graphite outgassed in high vacuum to be

$$\phi_{\mathrm{Graphite}}=4{\cdot}68\pm0{\cdot}2\ \mathrm{eV}.$$

Using this value the present work indicates

$$\phi_{\mathrm{Ge}\,(110)}=4{\cdot}72\pm0{\cdot}3\ \mathrm{eV}.$$

Lastly, it is significant that the average work

§ An attempt was made to apply the technique described in this paper to a single crystal nickel sample to get differences in face work functions.

functions of germanium samples *A*, *B*, *C*, and *D* differed from each other, as measured through the common reference surface, by only about $\pm 0{\cdot}05$ eV, whereas from the position of the Fermi level in the bulk (see Table 1) one might have expected a difference on the order of 0·50 eV, in the absence of surface space charge layers, in going from sample *B* to *D*. Heating the samples in high vacuum undoubtedly reduced the added impurity concentration at the surface by diffusion and evaporation. Rough calculations, however, indicate that even in the worst case—sample *B*—donor (arsenic) concentration at the surface should not have been reduced by more than one or at most two orders of magnitude, which still leaves roughyl 10^{16} donors/c^3, and hence still a strongly *n*-type surface. The treatment of sample *D* should have caused little or no depletion of indium at the surface.*

EFFECT OF GAS CONTAMINATION ON CONTACT POTENTIALS

An interesting and reproducible effect on the contact potentials of sample *B* occurred due to slow contamination by residual gases in the vacuum system (one or two days at 10^{-9} mm Hg), which may be summarized as follows:

(a) $\phi_{Ge(110)}$ *increased* by approximately 0·07 eV.
$\phi_{Ge(100)}$ *decreased* by approximately 0·07 eV.
$\phi_{Ge(111)}$ changed very little.

(b) This contamination was such that a mild heating to between 300 and 400°C drove off gas (as seen by the ion gauge) and restored the pattern of face values to its freshly cleaned condition.

Later, this effect could not be reproduced with sample *C* with any of several known gases introduced as contaminants. Nevertheless, the fact that some gas adsorption processes can change the work function of different crystal faces in opposite directions is significant.

DISCUSSION

(a) *Cleanness of germanium surfaces*

The only direct experimental evidence at hand to suggest that the germanium surfaces as treated in this study were atomically clean is the electron diffraction work on similarly treated germanium surfaces reported by FARNSWORTH *et al.*[9] The reproducibility of the contact potential patterns after each fresh cleaning of a sample and the absence of drift in potential of any face during the run, can be explained either by a truly clean surface, good vacuum and low sticking probability, or by the presence of, say, a stable monatomic oxide film. Such a film may either have remained on the surface throughout all heating and sputtering treatments (which seems doubtful), or it may have formed very rapidly after each sputtering treatment, for example, during the annealing, from impurity gases in the argon.† The fact that the contact potential of particular faces was monitored continually as the germanium cooled from either high (750°C) or medium (500°C) temperature heatings and was never seen to change drastically, throws doubt on the formation of such a film during the cooling. In short, while the authors feel the present evidence is in favor of atomically clean surfaces, further work will probably be needed to settle this question.

As for contamination of the germanium surfaces by either the tungsten or nickel present in the tube, there is internal evidence in the data to show that such effects were not important.

(b) *Actual atomic structure of faces*

The fact that a macroscopic crystal face is cut and lapped parallel to a given plane of the lattice is, of course, no guarantee that the true surface, after cleaning, is ideal on an atomic scale.‡ It is important to note that, since the contact potential measured by the Kelvin method is an areal average of the potential at each point on the surface, the potential differences measured between macroscopic faces in this study will always be *less* than those existing between the corresponding ideal atomic surfaces if the actual surfaces are

* No trends in $\phi_{Ni}-\phi_{Ge}$ were seen to indicate surface impurity content was changing with successive heatings.

† If the adsorption produces surface energy states, as little as one-tenth of one monolayer could "lock" the surface potential and make further adsorption energetically unfavorable.

‡ By an ideal atomic surface is meant one in which all outermost surface atoms lie in a common plane, and in which all lattice sites lying in or beneath the surface plane are filled.

VOL. 3 1957

either rough in a random fashion, or if they are all made up of facets having common preferred faces. Microscopic examination of two samples after the study at a magnification of up to 500 X revealed some waviness and pitting from the etching, but no development of facets. An optical goniometer search also failed to reveal facet structure, but the possibility of facets being present which were small compared to the wavelength of light, and hence unresolvable by optical methods, cannot be ruled out. However, since the surface structure must have changed somewhat during the many heatings and bombardments, and yet the contact potential differences remained nearly constant, it seems unlikely that a facet structure was important in determining contact potential differences between faces.*

(c) *Work function differences*

The difference in contact potential or work function on different faces of the same crystal is due to variation with crystal face of the electron's electrostatic potential energy rise in going from a given point in the interior where no surface effects persist, to a point just outside any face. This potential rise can be broken down into (1) a space charge potential change just inside the surface due to external fields or surface charges, and (2) the dipole potential jump in the electron cloud just outside the positive cores of the surface atoms. In the case of metals, only the latter is important, but for a semiconductor the former may amount to an appreciable fraction of the energy gap, and must be considered in the present case for germanium.

This study gave three types of evidence that space charge layers did exist at the germanium surfaces as treated: (1) the work functions averaged over the faces for samples of widely different dopings differed far less than predicted from the Fermi-level positions in the bulk; (2) the work functions of the faces of the highly-doped *n*-type sample, *B*, did not shift as they should have if no surface space charges existed, on passing from intrinsic to extrinsic temperatures on cooling; (3) the contact potential of at least two samples changed with illumination.[17,18] For sample *B* this change was a decrease in the work function on all three faces on the order of 30 mV at room temperature (100 mV at −40°C), with the (110) face showing a somewhat larger change than the (100) or (111).† From the analysis of this photovoltage[18] one can only conclude that the space charge was of the same sign on the three faces for this sample, and that the bands were probably bent up at the surface by at least 0·10 eV. The relative magnitude of the bending on the different faces cannot be determined from the amplitudes of the photo-voltage without data on the recombination velocity and trap structure on each surface. Such data were not made available by this study. A computation[19] of the electron surface energy state density required to explain the evidence (1) and (2) sets a lower bound of $\sim 5 \times 10^{13}$ states per cm^2 within the forbidden band for a distribution assumed uniform over the band. This could be reduced by an order of magnitude in the extreme case in which all states lie at one level and within kT of the Fermi-level at the surface.

Since we cannot estimate the difference in space charge potential on the different faces, we cannot say how much of our observed differences in work function remains to be attributed to differences in dipole barrier height. The only published work attempting such calculations is that of SMOLUCHOWSKI[20] who was able to show agreement between predictions and results for the sequence of work functions observed on tungsten faces. However, an application of SMOLUCHOWSKI's criterion of the degree of smoothing of the electron cloud for the three germanium faces studied would predict (assuming undistorted, ideal atomic surfaces).

$$\phi_{(111)} > \phi_{(110)} > \phi_{(100)}.$$

This is just the reverse of the results found here. It should be noted that the differences in face work function found for germanium, on the order of 0·06 eV, are an order of magnitude less than

* Electron microscope studies of the surface after bombarding should disclose such submicroscopic facets if they are present, but were unfortunately not made here.

† These changes were rapid with response times on the order of milliseconds. No slow drifts in contact potential with light were seen after the faces had been cleaned, and it is believed that the states involved here are the so-called "Fast Surface States".

those reported for tungsten.[4,5] (Part of this difference may be due to too low a value for the germanium differences due to the averaging effect on non-ideal macroscopic surfaces.)

In view of the pronounced valence bond character of germanium and the fact that the electrons forming the surface cloud are probably in modified valence orbitals, an explanation of surface dipole barrier height differences may well require knowledge of the manner in which severed bonds and even surface atoms[21] rearrange themselves on the various ideal atomic faces.

Acknowledgement—The authors wish to thank H. Brooks, L. Apker, and C. Herring for many helpful discussions, and R. Kingston and D. Stevenson of Lincoln Laboratory and W. F. Leverton and L. Davis of Raytheon Co. for samples and bulk properties measurements.

REFERENCES

1. Rose B. A. *Phys. Rev.* **44,** 585 (1933).
2. Underwood N. *Phys. Rev.* **47,** 502 (1935).
3. Farnsworth H. E. and Winch R. P. *Phys. Rev.* **58,** 812 (1940).
4. Smith G. F. *Phys. Rev.* **94,** 295 (1954).
5. Mueller E. W. *J. Appl. Phys.* **26,** 732 (1955).
6. Herring C. and Nichols M. H. *Rev. Mod. Phys.* **21,** 195 (1949).
7. Zisman W. A. *Rev. Sci. Instrum.* **3,** 367 (1932).
8. Anderson and Alexander *Austral. J. Appl. Sci.* **3,** 201 (1952).
9. Farnsworth H., Schlier R., George T., and Burger R. *J. Appl. Phys.* **26,** 252 (1955).
10. Bills D. G. and Allen F. G. *Rev. Sci. Instrum.* **26–7,** 654 (1955).
11. Wolsky S. P. *Bull. Amer. Phys. Soc.* **1,** 322 (1956).
12. Rentschler H. C. and Henry D. E. *J. Opt. Soc. Amer.* **26,** 30 (1936).
13. Wahlin H. B. *Phys. Rev.* **61,** 509 (1942).
14. Apker L., Taft E., and Dickey J. *Phys. Rev.* **74,** 1462 (1948).
15. Dillon J. A. *Bull. Amer. Phys. Soc.* **1,** 53 (1956).
16. Taft E. and Apker J. *Phys. Rev.* **99,** 1831 (1955).
17. Brattain W. and Bardeen L. *Bell Syst. Tech. J.* **32,** 1 (1953).
18. Garrett C. G. B. and Brattain W. *Phys. Rev.* **99,** 376 (1955).
19. Bardeen J. *Phys. Rev.* **71,** 717 (1947).
20. Smoluchowski R. *Phys. Rev.* **60,** 661 (1941).
21. Schlier R. E. and Farnsworth H. E. *Semiconductor Surface Physics* (Ed. R. H. Kingston) U. of Penna. Press, Philadelphia (1957).

J. Phys. Chem. Solids Pergamon Press 1957. Vol. 3. pp. 115–117.

DETAILED BALANCE IN NONVERTICAL TRANSITIONS

HENRY J. BOWLDEN

Wayne State University, Detroit 2, Mich.; Naval Research Laboratory, Washington 25, D.C.*

(*Received* 4 *February* 1957)

Abstract—After a presentation of the application of detailed balance to direct transitions in solids, the application of the principle to indirect transitions is studied, and it is concluded that the relation between emission and absorption characteristics valid for direct transitions is also valid for indirect transitions. The limitations on the validity of this relation in both cases are set forth.

VOL. 3 1957

1. INTRODUCTION

In recent years, the principle of detailed balance (also known as microscopic reversibility) has gained considerable usage in solid state physics. In most cases[1,2] it is applied as to "direct" (vertical) transitions. In view of the fact that interband transitions in silicon and germanium are most likely of the "indirect" or nonvertical type, involving lattice interactions, a re-evaluation of the theory is in order, to ascertain whether the relations in use for direct transitions are also valid for indirect. The present paper reviews the application of the principle to direct transitions, and then presents a discussion of the problems involved in nonvertical transitions.

2. DIRECT TRANSITIONS

Vertical, or direct, transitions are represented in perturbation theory as first-order effects. We define a transition probability for the process in which a photon q is absorbed and an electron goes from state 1 to state 2 by the relation

$$w_{1\to 2} = n_q C_{12}, \tag{1a}$$

where $w_{1\to 2}$ denotes the transition rate on the assumption that state 1 is occupied and state 2 is unoccupied, n_q is the occupation factor for photons q, and C_{12} contains the absolute square of the matrix element together with the appropriate density-of-states factors.[3] The corresponding quantity for the reverse process is then given by

$$w_{2\to 1} = (n_q+1)C_{12}. \tag{1b}$$

The actual transition rates when the electron occupancies are not as given above are given by

$$\begin{aligned} r_{1\to 2} &= w_{1\to 2} n_1(1-n_2) \\ \text{and} \quad r_{2\to 1} &= w_{2\to 1} n_2(1-n_1), \end{aligned} \tag{2}$$

where n_1 and n_2 are the occupation factors for electrons in the states 1 and 2 respectively. If we denote quantities at thermal equilibrium by primes, we have

$$\begin{aligned} r'_{1\to 2} &= n'_q n'_1(1-n'_2)C_{12} \\ \text{and} \quad r'_{2\to 1} &= (n'_q+1)n'_2(1-n'_1)C_{12}. \end{aligned} \tag{3}$$

For equilibrium, the principle of detailed balance prescribes $r'_{1\to 2} = r'_{2\to 1}$. Cancellation of C_{12} then gives a relation between the photon and electron occupation factors which is easily shown to be satisfied by the Bose-Einstein distribution for photons and the Fermi-Dirac distribution for electrons.

The development of VAN ROOSBROECK and SHOCKLEY[1] sets up two experimental situations, and compares the observed quantities from these two. In the first experiment, the sample is illuminated with radiation q, and the absorption coefficient is measured. In this case, it is assumed that in the steady state the occupation factors of the electrons are not appreciably changed, so that the absorption rate is given by

$$r_{1\to 2} = n_q n'_1(1-n'_2)C_{12} = (n_q/n'_q)r'_{1\to 2}.$$

Strictly speaking, there may be various pairs of

* Present address: National Carbon Research Laboratory, Cleveland, Ohio.

initial and final states such that the indicated transition satisfies the conservation laws for the given incident photon energy. Enumerating these pairs by a symbolic variable k, which may represent several variables, the total absorption rate is given by

$$R_{1\to 2} = \int dk\, r_{1\to 2} = (n_q/n'_q) \int dk\, r'_{1\to 2}$$
$$= (n_q/n'_q)R', \tag{4}$$

where we have written

$$R' = \int dk\, r'_{1\to 2} = \int dk\, r'_{2\to 1}.$$

To obtain the cross-section we must have the incident flux per energy interval, which is equal to the incident density of states of photons multiplied by the occupation factor n_q and by the group velocity.* Dividing the rate (4) by this flux, we obtain for the cross-section

$$\sigma_{1\to 2} = (\pi c/N\epsilon_q)^2(\hbar^3/n'_q)R', \tag{5}$$

where n is the index of refraction and ϵ_q is the photon energy.

The second experiment involves injection of carriers and measurement of the emitted radiation.[4] Assuming that the emitted photons escape without reabsorption, so that n_q may be assumed to retain its equilibrium value, we have for the emission rate, after integrating over k as before.

$$R_{2\to 1} = \int dk \frac{n_2(1-n_1)}{n'_2(1-n'_1)} r'_{2\to 1}.$$

We now assume that the shape of the velocity distribution of carriers is not affected by the conditions of the experiment,† so that the factor $n_2(1-n_1)/n'_2(1-n'_1)$ is a constant.
With this assumption, the emission rate takes the form

$$R_{2\to 1} = \frac{n_2(1-n_1)}{n'_2(1-n'_1)} R',$$

and combining this with equation (5), we have the desired relation

$$R_{2\to 1} = \frac{n_2(1-n_1)}{n'_2(1-n'_1)} \left(\frac{n\epsilon_q}{\pi c}\right)^2 \frac{\sigma_{1\to 2}}{\hbar^3[\exp(\epsilon_q/kT)-1]}. \tag{6}$$

in which we have replaced n'_q by its proper form from the Bose-Einstein statistics. Equation (15) of VAN ROOSBROECK and SHOCKLEY is seen to be a special case of our equation (6).

3. INDIRECT TRANSITIONS

The application of this theory to indirect transitions requires further examination because, for the case of photon absorption, for example, it is possible to have either emission or absorption of a phonon. Since these two transitions involve different initial and final states (differing, at least, in the phonon occupation factors), they cannot be lumped into the sum over intermediate states, but must be treated separately. We require second-order perturbation theory here, but will include such details as the sum over intermediate states, etc., in a symbolic factor. The cases involving phonon emission and absorption, respectively, will be represented by the superscripts (e) and (a). We have, then, for the transition probabilities for the four possible processes:

$$\begin{aligned} w_{1\to 2}^{(e)} &= n_q(n_f+1)\phi_1, \\ w_{1\to 2}^{(a)} &= n_q n_f \phi_2, \\ w_{2\to 1}^{(e)} &= (n_q+1)(n_f+1)\phi_2, \\ w_{2\to 1}^{(a)} &= (n_q+1)n_f\phi_1, \end{aligned} \tag{7}$$

in which n_f denotes the phonon occupation factor, and the equality in pairs of the ϕ-factors, as indicated, is demonstrable with the help of the second-order theory. Here each ϕ-factor includes the complete sum over intermediate states. For the transition rates, we then find

$$\begin{aligned} r_{1\to 2}^{(e)} &= n_q(n_f+1)n_1(1-n_2)\phi_1, \\ r_{1\to 2}^{(a)} &= n_q n_f n_1(1-n_2)\phi_2, \\ r_{2\to 1}^{(e)} &= (n_q+1)(n_f+1)n_2(1-n_1)\phi_2, \\ r_{2\to 1}^{(a)} &= (n_q+1)n_f n_2(1-n_1)\phi_1. \end{aligned} \tag{8}$$

Detailed balance now equates the equilibrium values of the first and fourth of these, and also those of the second and third.

* For details see reference 1.

† This is equivalent to the assumption that the thermalization time for "hot" carriers is small compared to the recombination time, an assumption undoubtedly valid for intrinsic materials, but not so obviously satisfactory for cases involving impurity states.

If we now set up the two experiments previously described, a similar argument will give for the total absorption cross-section

$$\sigma_{1\to 2} = (\pi c/n\epsilon_q)^2(\hbar^3/n'_q)(R'_1+R'_2),$$

where

$$R'_1 = \int dk\, r'_{1\to 2}{}^{(e)} = \int dk\, r'_{2\to 1}{}^{(a)} \qquad (9)$$

and

$$R'_2 = \int dk\, r'_{1\to 2}{}^{(a)} = \int dk\, r'_{2\to 1}{}^{(e)}.$$

The emission rates, assuming again, as before, that the velocity distribution of electrons and phonons is not appreciably altered in the process, is given by

$$R_{2\to 1} = \frac{n_2(1-n_1)}{n'_2(1-n'_1)}(R'_1+R'_2).$$

Thus we are led again to the relation given in equation (6).

4. CONCLUSIONS

We have shown that the emission rate under carrier injection conditions and the absorption cross-section for electromagnetic radiation are related to one another in a definite way, both for direct and indirect transitions, assuming only that the mechanism of carrier injection does not change the shape of the steady-state velocity distribution of carriers appreciably, and that in each experiment only one occupation factor (that of the "incident particles") is altered in steady-state. These assumptions may break down for high impurity concentrations or large deviations from equilibrium. Under such extreme conditions, it would appear that no simple relation exists between the emission rate and absorption cross-section.

Acknowledgements—The author wishes to acknowledge with sincere gratitude the stimulation of frequent discussions with ELIAS BURSTEIN and R. F. WALLIS, and also valuable comments by R. KIKUCHI and J. E. THOMAS, JR.

REFERENCES

1. VAN ROOSBROECK and SHOCKLEY *Phys. Rev.* **94,** 1558 (1954).
2. SHOCKLEY and READ *Phys. Rev.* **87,** 835 (1952).
3. HEITLER W. *Quantum Theory of Radiation* (Third Edition) pp. 136–145. Oxford (1955).
4. HAYNES and WESTPHAL *Phys. Rev.* **101,** 1676 (1956).

J. Phys. Chem. Solids Pergamon Press 1957. Vol. 3. pp. 118–120.

CORRELATIONS BETWEEN THERMAL VOLTAGE FLUCTUATIONS IN A CIRCUIT

WALTER BALTENSPERGER

Instituto Tecnológico de Aeronáutica, São José dos Campos, São Paulo, Brasil

(*Received* 26 *February* 1957)

Abstract—The use of the laws of circuits in the derivation of NYQUIST's formula of thermal noise contains the assumption that the current is the same in all parts of a conductor. This assumption is incompatible with perfect gas models for the conduction electrons in metals, but it can be justified by the collective description of BOHM and PINES for the large distances which correspond to the low frequencies of electronic measurements. Between different fluctuating voltages in a circuit there exist correlations, for which a general method of calculation is given.

1. INTRODUCTION

THE mean square of the fluctuating thermal voltage $V(t)$, which appears between the end-points of an electrical impedance, is given by the formula of NYQUIST[1]

$$\overline{V^2} = \int RG\, dv, \qquad (1)$$

where $G = 4kT$, k being the Boltzmann constant and T the absolute temperature; R signifies the resistive part of the impedance, and the integration extends over the frequency band of the detecting instrument. The original work of NYQUIST, and also a later derivation of CALLEN and WELTON,[2] are not explicit about the theoretical model employed for a conductor. However, their use of the laws of circuits implies the assumption that the current is the same in all points of a conductor. An examination will show, that this is only compatible with models, which have a strong correlation between the positions of the charge carriers.

2. THE FLUCTUATIONS FOR VARIOUS MODELS

What would the fluctuations of the potentials be if the positions of the electrons in a metal were completely uncorrelated, like the particles of a perfect gas? In this case, if N denotes the average number of particles in a certain small volume of a conductor, the root mean square fluctuation of this number is $N^{1/2}$. Thus a part of a conductor with volume 0·1 cm^3, which contains 10^{22} free electrons on the average, would show fluctuations of the order of 10^{11} electrons, representing a charge of 48 e.s.u., and capable of inducing thousands of volts in a nearby voltmeter. This result is not only numerically in error by a factor of order of 10^9, but it is also qualitatively wrong, since the fluctuations here depend on the shape of the conductor instead of its resistence.

For a degenerate Fermi gas the root mean square fluctuation would amount to $(NkT/\zeta)^{1/2}$, where ζ is the Fermi energy. Thus the correlations, which exist between Fermi particles only reduce the above result by a factor, numerically of order of 1/15 for room temperature.

It is important to note that the typical frequencies in the spectrum of these fluctuations are of order of v/l, where v is the mean speed of the electrons and l a typical length of the system. For electrons in a metallic wire $v/l \approx (10^8\text{cm/sec})/(10\text{cm}) = 10^7$ sec^{-1}, which lies in the radio-frequency range, so that a large part of the enormous fluctuations calculated above would really effect electronic detectors.

A completely different result is obtained with the collective description developed by BOHM and PINES.[3] The movement of the electron system is described by the Fourier components $\rho_{\mathbf{k}}$ of the electron density. It is found, that for sufficiently small wave-vectors $\mathbf{k}$, but with the exeption of $\mathbf{k} = 0$, these variables satisfy the equations of independent harmonic oscillations with the plasma frequency

$\omega_P = (4\pi ne^2/m)^{1/2}$, where e, m, and n signify the charge, mass, and the mean density of the electrons, respectively.

Only two types of motion are thus possible: first the movements of an incompressible fluid, and secondly movements which vary the density, but which have a frequency spectrum equal to zero below ω_P. For metals $n \approx 10^{23}\,\mathrm{cm}^{-3}$, so that $\omega_P/2\pi \approx 3 \cdot 10^{15}\,\mathrm{sec}^{-1}$. Such frequencies cannot affect electronic detecting devices, and hence the second type of movement does not contribute to the noise. Incidentally, since $\hbar\omega_P \approx 20$ eV, the plasma oscillations in a metal are not excited at room temperature, but are all in their ground state.

According to the collective description, therefore, only the motions of an incompressible fluid can produce detectable thermal noise. In a wire these motions can be characterized by just one variable, the current, and a circuit with one mesh has only this one relevant degree of freedom. The collective description thus gives the theoretical foundation of the laws of circuits.

3. THE PHYSICAL BASIS OF NYQUIST'S FORMULA

NYQUIST's formula (1) can be derived from thermodynamics and the laws of circuits. These, however, agree only with theoretical models, which do not permit a detectable fluctuation of the charge carriers in the conductors. NYQUIST's formula is incompatible with free electron theories, but in agreement with the collective description of the electron system in metals.

Thermal noise in metals is not due to random motion of the individual electrons. Rather the electron system may be pictured as an incompressible fluid of negligible mass. If the conductor has a resistivity, the fluid interacts with matter. The thermal agitation of matter then furnishes irregular impulses to the fluid. The result is a fluctuating movement of the fluid as a whole in the conductors. The case of an "open circuit" can be included in this picture by considering the voltmeter as an element of high resistence which closes the circuit and in which the current is measured.

These considerations do not invalidate the kinetic derivations of NYQUIST's formula,[4, 5] since these simply use the free electron theory of electrical resistence to establish the interaction between the current and the medium.

NYQUIST's formula can be applied to an arbitrary interval of frequency and to any part of an extended resistence. This shows that there exist generators of voltage in every element of resistence dR and for every interval of frequency $d\nu$. According to equation (1) the total power is the sum of those produced by the elementary generators; thus they are independent. Physically the independence of the generators means, that the thermal motion of matter is uncorrelated for different frequencies as well as in different elements of resistence.

4. CORRELATIONS

As a consequence of the laws of circuits, two fluctuating voltages in a circuit are in general not independent. In the following the correlation between the thermal voltage $U(t)$, measured between A and B, and the voltage $W(t)$ between C and D will be calculated for the circuit shown in Fig. 1.

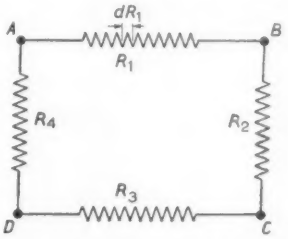

FIG. 1. Circuit with correlated voltage fluctuations.

According to equation (1) the generators of voltage in the element of resistence dR_1 and in the bandwidth $\Delta\nu$ of the detecting instrument produce a voltage dV_1 such that

$$(\overline{dV_1})^2 = G\,\Delta\nu\,dR_1. \tag{2}$$

dV_1 induces a current dI_1 in the circuit

$$dI_1 = dV_1/Y, \tag{3}$$

where

$$Y = R_1+R_2+R_3+R_4, \tag{4}$$

and hence a voltage

$$dU_1 = (1-R_1/Y)\,dV_1 \tag{5}$$

between A and B, and a voltage

$$dW_1 = -(R_3/Y)\,dV_1 \tag{6}$$

between C and D.

Equations (2), (5), and (6) determine the mean value of any expression which is quadratic in the voltages produced by dR_1. In particular the correlation between dU_1 and dW_1 becomes

$$\overline{dU_1 dW_1} = a_1 G\,\Delta\nu\, dR_1 \tag{7}$$

with

$$a_1 = -(R_2/Y)(1-R_1/Y).$$

The coefficients $a_2 = R_1R_3/Y^2$, $a_3 = -(R_1/Y)(1-R_3/Y)$, and $a_4 = a_2$, which relate generators in R_2, R_3, and R_4 to the correlations that these produce, are similarly obtained.

Since different generators are independent, voltages produced by different generators have a vanishing correlation. Hence the correlation between the total voltages is obtained by summing equation (7) over all elements of resistence in the circuit

$$\overline{UW} = \sum_i a_i R_i G\,\Delta\nu \tag{8}$$

which is easily found to be

$$\overline{UW} = -G\,\Delta\nu R_1 R_3/Y. \tag{9}$$

5. CORRELATION BETWEEN TWO THERMAL VOLTAGES AT DIFFERENT TIMES IN A GENERAL CIRCUIT

Given any circuit containing only linear elements with known impedances, the correlation between a voltage $U(t)$ taken between two points A and B and a voltage $W(t+\tau)$ between C and D follows from a generalization of the above method. Any infinitesimal resistence or resistive part of an impedance dR acts in an infinitesimal interval of frequency $d\nu$ as a generator producing a voltage dV with mean square value

$$\overline{(dV)^2} = G\,d\nu dR. \tag{10}$$

Since $dV = dV_0 \cos(2\pi\nu t)$ is of definite frequency, the laws of circuits determine the amplitude and phase of other voltages, which dV induces

$$dU(t) = dV_0\, a \cos 2\pi(\nu t+\alpha) \tag{11}$$

$$dW(t) = dV_0\, b \cos 2\pi(\nu t+\beta). \tag{12}$$

The correlation between these voltages at different times becomes

$$\begin{aligned}\overline{dU(t)dW(t+\tau)} &= (dV_0)^2 ab\,\overline{\cos 2\pi(\nu t+\alpha)\cos 2\pi(\nu t+\nu\tau+\beta)} \\ &= ab\cos 2\pi(\alpha-\beta-\nu\tau)G\,dRd\nu.\end{aligned} \tag{13}$$

The correlation between the total voltages is again obtained by summing equation (13) over all elements of resistence in the circuit and over the frequency band of the detecting instrument

$$\overline{U(t)W(t+\tau)} = \iint ab\cos 2(\alpha-\beta-\nu\tau)G\,dRd\nu. \tag{14}$$

6. LIMITS OF VALIDITY

Measurements of the correlation between two thermal voltages in a circuit provide a direct and obvious test of the theory that the system of charge carriers moves like an incompressible fluid. Its limits of validity are relevant for solid-state physics.

Deviations from the above formulas may be expected for circuits which contain conductors with a low density of charge carriers, such as semiconductors. When the plasma frequency is sufficiently low, the plasma oscillations are thermally excited. For a highly excited plasma, however, the simple results of plasma theory are doubtful, considering that the terms neglected by BOHM and PINES in their "random phase approximation" contain the amplitudes of all oscillations. Certainly, for a sufficiently small density of the charge carriers the independent particle theory becomes acceptable.

At present Prof. JAQUES LIGNON of this Institute is carrying out correlation measurements. His preliminary results with a circuit of metalic wire resistors are encouraging.

Acknowledgements—The author is deeply indebted to Prof. GUIDO BECK for many inspiring discussions. He also profited from comments of Dr. WALTER SCHUTZER and CARL H. WEIS.

REFERENCES

1. NYQUIST H. *Phys. Rev.* **32,** 110 (1928).
2. CALLEN H. B. and WELTON T. A. *Phys. Rev.* **83,** 34 (1951).
3. BOHM D. and PINES D. *Phys. Rev.* **85,** 338 (1952); *Ibid.* **92,** 609 (1953).
4. BERNAMONT J. *Ann. Phys.* **7,** 71 (1937).
5. BAKKER G. J. and HELLER G. *Physica* **6,** 262 (1939).

J. Phys. Chem. Solids Pergamon Press 1957. Vol. 3. pp. 121–127.

FREQUENCY FACTORS AND ISOTOPE EFFECTS IN SOLID STATE RATE PROCESSES*

GEORGE H. VINEYARD

Brookhaven National Laboratory, Upton, New York

(*Received* 8 *February* 1957)

Abstract—The movement of defects in solids on the basis of classical absolute rate theory is re-examined with special attention to many-body aspects. The effective frequency in the Arrhenius expression governing these processes is shown to be, in harmonic approximation, the ratio of the product of the N normal frequencies of the entire crystal at the starting point of a transition to the product of the N-1 normal frequencies of the crystal when it is constrained in a saddle point configuration. The influence of the masses of the various atoms on the effective frequency is investigated. It is shown that an effective mass which depends on the direction of the path through the saddle point in configuration space determines this frequency. In the case of chemical diffusion by the vacancy mechanism the effective mass is approximately the same as the mass of the solute atom, and must always lie between the mass of the solute and the mass of the solvent. It is finally shown that the classical rate theory, even with many-body considerations, is unable to explain the recent observations of LAZARUS and OKKERSE on the isotope effect in the diffusion of iron in silver.

1. INTRODUCTION

THE rate of movement of defects in solids by thermal activation can be calculated on the absolute rate theory.[1–6] In general one finds that individual defect jump rates Γ are given by the equation

$$\Gamma = \tilde{\nu} e^{-\Delta F/kT}. \qquad (1)$$

Here ΔF is the free energy needed to carry the defect from an initial equilibrium position to a saddle point, T is the absolute temperature, k is Boltzmann's constant, and $\tilde{\nu}$ is an effective frequency associated with vibration of the defect in the direction of the saddle point. Even though only one atom jumps in the elementary process, the problem is essentially one of many bodies because the jumping atom is surrounded by other atoms with which it interacts. This fact is readily incorporated in the absolute rate theory in its general form; nevertheless all of the actual discussions of solid state processes with which the writer is acquainted oversimplify the problem by reducing it to a one-body model at some stage in the calculations. After this the frequency either remains loosely defined, which is unnecessary, or is reduced to an Einstein frequency (frequency of the jumping atom when all other atoms are fixed at equilibrium points), which is inaccurate.

The recent discovery of an isotope effect in solid state diffusion,[7] an effect which appears to be anomalously large, focusses attention on the exact meaning of the terms in eq. (1). The purpose of this note is to show that, by a generalization of all the usual arguments $\tilde{\nu}$ and ΔF can be completely defined, within the area of approximation that is appropriate to rate theory, and to derive the more complete expressions for these quantities. The approximations inherent in any rate theory are that well defined states exist for the original system (atom near its starting point) and the transition system (atom near the saddle point). This requires any interactions that are not a part of the phase space under consideration to be sufficiently weak. For usefulness the calculations will be simplified by two further assumptions: (a) At all stages quantum effects will be neglected. (b) At a later stage motions near the saddle point will be treated by the theory of small oscillations—i.e., the vibrations will be assumed to be nearly simple harmonic.

*Work performed under the auspices of the U.S. Atomic Energy Commission.

2. FREQUENCY FACTORS IN SOLID STATE RATE PROCESSES

Various atomic jump processes may be of interest, but the principles are best illustrated by treating a particular case. Consider a crystal containing a vacant lattice site and let Γ be the average rate at which a specific atom adjacent to the vacancy jumps into the vacant site. Let the entire crystal contain $N/3$ atoms, so there are N degrees of freedom, $x_1\ x_2 \ldots x_N$. Let the mass associated with x_j be m_j, and define new coordinates $y_j = \sqrt{m_j}\ x_j$. Let the potential energy of the entire crystal be $\Phi(y_1 \ldots y_N)$. Consider the configuration space of the crystal (N dimensional). Φ possesses a minimum at a point A in this space, corresponding to the atom on its original site, the vacancy on its adjoining site, and every other

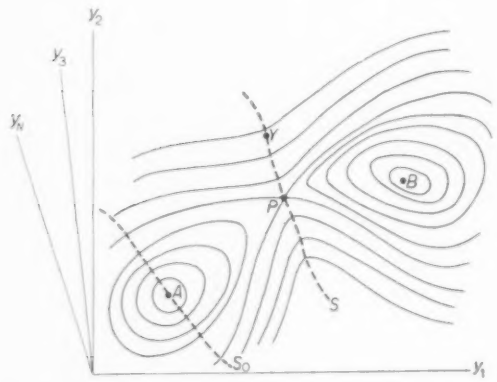

FIG. 1. Configuration space of N dimensions showing, schematically, hyper-surfaces of constant potential energy (solid lines) and imaginary constraining hyper-surfaces (dotted lines).

atom at an equilibrium position (Fig. 1). Φ possesses another minimum at B, which corresponds to the atom and the vacancy interchanged in the crystal and other atoms relaxed again. By topological arguments it is seen that there must be at least one saddle point somewhere between A and B. Also, only one saddle point would be expected for the likely transitions from A to B. Label it P. Two dimensional contours of constant Φ are shown in the figure; it must be remembered that these actually represent $N-1$ dimensional hyper-surfaces.

There now exists a unique hyper-surface S, of dimensionality $N-1$, defined as follows: S passes through P and is perpendicular to the contours of constant Φ everywhere else. S thus separates the region around A from that around B, and any representative point reaching S with finite velocity crosses over into the region around B.

In a system in thermal equilibrium there is a definite number of representative points, Q_A, in the region to the "left" of S, and a definite number, I, crossing S from "left" to "right" per second. The average lifetime, τ, of representative points in region A, and the rate, Γ, of transition from A to B are related as follows:

$$\Gamma = \frac{1}{\tau} = \frac{I}{Q_A}. \tag{2}$$

This Γ, of course, is assumed equal to the desired average jump rate already defined.

In classical systems in equilibrium the position and velocity of a representative point in configuration space are independently distributed, and the density in configuration space, ρ, can be written

$$\rho = \rho_0 e^{-\Phi/kT}, \tag{3}$$

where ρ_0 is a normalizing constant. Then

$$Q_A = \rho_0 \int_A e^{-\Phi/kT}\, dv, \tag{4}$$

where the integration is over the portion of configuration space to the "left" of S.

To calculate I, observe that the number of representative points at any point Y of S, per unit volume, with hyper-velocity $\boldsymbol{V} = \{\dot{y}_1 \ldots \dot{y}_N\}$, within range $d\boldsymbol{V} = d\dot{y}_1 \ldots d\dot{y}_N$ is

$$\rho(Y, \boldsymbol{V})\, d\boldsymbol{V} = \rho_1 e^{-\Phi(Y)/kT} e^{-V^2/2kT}\, d\dot{y}_1 \ldots d\dot{y}_N, \tag{5}$$

where the normalizing constant is

$$\rho_1 = \rho_0 (2\pi kT)^{-N/2}.$$

If an element of S at Y is represented by the vector $d\boldsymbol{S} = \{dS_1 \ldots dS_N\}$ the current of velocity $\boldsymbol{V}$ crossing $d\boldsymbol{S}$ is expression (5) multiplied by $d\boldsymbol{S} \cdot \boldsymbol{V}$, and the total current crossing $d\boldsymbol{S}$ is

$$dI = d\boldsymbol{S} \cdot \int \boldsymbol{V} \rho(Y, \boldsymbol{V})\, d\boldsymbol{V}. \tag{6}$$

Here the integration is over all $\boldsymbol{V}$ such that

$$d\boldsymbol{S} \cdot \boldsymbol{V} > 0. \tag{7}$$

To allow for condition (7) the axes may be rotated so that one, say y_1, is parallel to $d\boldsymbol{S}$ at Y, and then we find

$$dI = \rho_0 (2\pi kT)^{-N/2} e^{-\Phi(Y)/kT}\, dS_1 \times$$

$$\times \int_0^\infty \dot{y}_1 e^{-\dot{y}_1^2/2kT}\, d\dot{y}_1 \prod_{j=2}^{N} \int_{-\infty}^{\infty} e^{-\dot{y}_j^2/2kT}\, d\dot{y}_j \tag{8}$$

$$= \rho_0 \sqrt{kT/2\pi}\; e^{-\Phi(Y)/kT}\, dS_1,$$

where now $dS \equiv |d\boldsymbol{S}| = dS_1$.
Finally,

$$I = \int dI = \rho_0 \sqrt{(kT/2\pi)} \int_S e^{-\Phi(Y)/kT}\, dS, \tag{9}$$

where the integration is over the hyper-surface S. Equations (2), (4), and (9) give

$$\Gamma = \sqrt{\frac{kT}{2\pi}}\, \frac{\int_S e^{-\Phi/kT}\, dS}{\int_A e^{-\Phi/kT}\, dv}. \tag{10}$$

This is in an essentially familiar form—the ratio of two configurational partition functions. The generalization over the usual presentations at this stage is that the configuration space is specifically a many-body space so that the influence of *all* bodies and *all* degrees of freedom is accounted for in principle.

The theory of small vibrations can now be employed to approximate expression (10) in a useful way. Near point A the function Φ may be expanded in Taylor series to second order. By an axis transformation this may be put in the form

$$\Phi \cong \Phi(A) + \sum_{j=1}^{N} \tfrac{1}{2}(2\pi\nu_j)^2 q_j^2, \tag{11}$$

where $q_1 \ldots q_N$ are the normal co-ordinates and $\nu_1 \ldots \nu_N$ are the normal frequencies for vibrations about point A.* Similarly the potential may be expanded about the saddle point P *within the constraining surface* S

$$\Phi \cong \Phi(P) + \sum_{j=1}^{N-1} \tfrac{1}{2}(2\pi\nu_j')^2 q_j'^2, \tag{12}$$

where $q_1' \ldots q_{N-1}'$ and $\nu_1' \ldots \nu_{N-1}'$ are the normal co-ordinates and frequencies for vibrations about P with the constraint S.

With (11) and (12) the partition functions in (10) can be evaluated to give

$$\prod_{j=1}^{N-1} \left(\frac{\sqrt{(2\pi kT)}}{2\pi\nu_j'} \right) e^{-\Phi(P)/kT}, \tag{13}$$

and

$$\prod_{j=1}^{N} \left(\frac{\sqrt{(2\pi kT)}}{2\pi\nu_j} \right) e^{-\Phi(A)/kT}, \tag{14}$$

for the numerator and denominator, respectively. Finally, one finds

$$\Gamma = \left(\frac{\prod_{j=1}^{N} \nu_j}{\prod_{j=1}^{N-1} \nu_j'} \right) e^{-[\Phi(P)-\Phi(A)]/kT}. \tag{15}$$

In this form the transition rate is displayed as a product of an effective frequency,

$$\nu^* = \left(\prod_{j=1}^{N} \nu_j \right) \Big/ \left(\prod_{j=1}^{N-1} \nu_j' \right) \tag{16}$$

and an activation exponential. The activation energy is $\Phi(P) - \Phi(A)$, which is self-explanatory. The effective frequency is very different from a simple Einstein frequency, or any single frequency exhibited in physical space. *It is the ratio of the product of the N normal frequencies of the entire system at the starting point of the transition to the $N-1$ normal frequencies of the system constrained in the saddle point configuration.*

A crude approximation to a normal frequency is found by constraining every x_i but one and allowing this to vibrate. This process provides a set of Einstein frequencies, ν_j^E, and ν_j^E is proportional to $1/\sqrt{m_j}$. If, on this model, the frequencies in the saddle point are the same as those at A, except

* Without loss of generality it may be supposed that the crystal is macroscopically constrained. Consequently there are no free translational or rotational modes and none of the frequencies is zero.

that the mode for motion of the jumping atom in the saddle point direction is missing, ν^* immediately reduces to ν_k^E, the frequency of the moving atom when it was on its original site. This, as noted is proportional to $1/\sqrt{m_k}$ where m_k is the mass of the jumping atom. In this approximation, a simple isotope effect in diffusion would be predicted. On the more complete model, the effect on ν^* of altering the mass of the jumping atom must be estimated in a more sophisticated way. In principle *all* of the normal mode frequencies would be altered and the dependence of each on m_k is complicated. This question is taken up in the next section and a fairly simple answer is shown to exist.

Another dress may be put on the result (10) to make closer contact with the formulation of WERT and ZENER.[3, 4, 6] Let a hyper-surface S_0 be defined passing through A. The choice of S_0 is somewhat arbitrary, but the simplest would appear to be the following: Let S_0 be of the same shape as S with the point corresponding to P located at A, and oriented so that the normal to S_0 at A is along the line of force leading to P. (Fig. 1). Define the constrained configurational partition functions Q_0 and Q_s, as follows:

$$Q_0 = \rho_0 \int_{S_0} e^{-\Phi/kT}\, dS_0, \tag{17}$$

$$Q_s = \rho_0 \int_{S} e^{-\Phi/kT}\, dS. \tag{18}$$

Here $\int_{S_0}$ means integration over the hyper-surface S_0, $\int_S$ means integration over the hyper-surface S. Recognizing that the numerator in (10) is Q_S, and multiplying and dividing the latter by Q_0, one gets

$$\Gamma = \sqrt{\left(\frac{kT}{2\pi}\right)} \frac{Q_0}{Q_A} \frac{Q_S}{Q_0}. \tag{19}$$

Q_S/Q_0 is now precisely the exponential of minus $1/kT$ times the free energy change when the system, constrained to lie on the hyper-surface, is carried from A to P by reversible motion of the constraining hyper-surface. Calling this $\Delta F = \Delta U - T\Delta S$, one has

$$\frac{Q_S}{Q_0} = e^{-\Delta F/kT} = e^{\Delta S/k} e^{-\Delta U/kT}. \tag{20}$$

This displays the activation free energy, entropy, and energy. The effective frequency, $\tilde{\nu}$, comes from the remaining factors in (19),

$$\tilde{\nu} = \sqrt{\left(\frac{kT}{2\pi}\right)} \frac{Q_0}{Q_A}. \tag{21}$$

This again is a ratio of partition functions, the denominator referring to a system of dimensionality one less than the numerator. The previously defined effective frequency, ν^* is related to the present one by

$$\nu^* = \tilde{\nu} e^{\Delta S/k}. \tag{22}$$

For the small vibration approximation

$$\Delta S = k \ln \left(\frac{\prod_{j=1}^{N-1} \nu_j^0}{\prod_{j=1}^{N-1} \nu_j'} \right), \tag{23}$$

where ν_j^0 is the frequency of the jth normal mode for the system constrained to lie on surface S_0. Since, in this approximation,

$$\frac{Q_0}{Q_A} = \sqrt{\frac{2\pi}{kT}} \left(\frac{\prod_{j=1}^{N} \nu_j}{\prod_{j=1}^{N-1} \nu_j^0} \right),$$

this gives

$$\nu^* = \frac{\prod_{j=1}^{N} \nu_j}{\prod_{j=1}^{N-1} \nu_j'},$$

in agreement with the previous result (16).

3. ISOTOPE EFFECT IN ACTIVATED PROCESSES (CLASSICAL TREATMENT)

The preceding analysis has shown that rate processes in a purely classical system undergoing small vibrations depend on products of frequencies of normal modes. We now consider these frequencies in a general way. With the origin taken at an equilibrium point in configuration space, the potential energy of the system can be written, (for small oscillations)

$$\Phi = \Phi_0 + \sum_{i,j=1}^{N} \frac{1}{2} \frac{\beta_{ij}}{\sqrt{m_i}, \sqrt{m_j}} y_i y_j, \tag{24}$$

where β_{ij} is the usual force constant relating the ith cartesian co-ordinate of the system to the jth and has the symmetry $\beta_{ij} = \beta_{ji}$. In the usual way it is shown that the normal frequencies are the roots of the characteristic equation

$$\det[X-(2\pi\nu)^2 I] = 0, \tag{25}$$

where I is the unit matrix and the ij^{th} element of X is $\beta_{ij}/\sqrt{(m_i m_j)}$. By familiar theorems the product of the roots of (25), and hence $\prod_{j=1}^{N} (2\pi\nu_j)^2$ is $\det(X)$. Considering the form of this determinant one sees that $1/\sqrt{m_i}$ factors out of the ith row ($i = 1, 2, \ldots N$) and a similar factor comes out of each column, giving the theorem

$$\prod_{j=1}^{N} \nu_j = \frac{\sqrt{(\det[\beta_{ij}])}}{(2\pi)^N} \prod_{j=1}^{N} \frac{1}{\sqrt{m_j}}, \tag{26}$$

(which is known as the product rule in molecular spectroscopy). The mass dependence of the frequency product is here exhibited explicitly, assuming that the β_{ij} are all independent of mass. From this the numerator in (15) is seen at once to vary as the minus 3/2 power of the mass of the diffusing atom in case of isotopic substitution. The result is general and independent of restrictive assumptions such as an Einstein model.

The denominator in (15) requires more attention. Imposing the stipulated one dimensional constraint at a saddle point reduces the system to a stable one of $N-1$ degrees of freedom, and it is necessary to know which mass has essentially been removed. The constraint is in general not flat, but since P is an equilibrium point, the expansion of Φ to second order about P requires only first order knowledge of the constraining surface. Now consider the saddle point in $x_1 \ldots x_N$ configuration space. S has a normal at P (one dimensional). Let the cosine of the angle between this direction and the axis x_j be c_j. If the representative point moves in this direction a distance $d\xi$ from P, $dx_j = c_j\, d\xi$, and the kinetic energy associated with this direction can be written $\frac{1}{2}m^*\dot{\xi}^2$, where m^* is the effective mass for the direction. Also, the kinetic energy is

$$\sum_{j=1}^{N} \tfrac{1}{2} m_j \dot{x}_j^2 = \sum_{j=1}^{N} \tfrac{1}{2} m_j c_j^2 \dot{\xi}^2,$$

and equating the first and third expressions of kinetic energy one finds

$$m^* = \sum_{j=1}^{N} m_j c_j^2. \tag{27}$$

By the properties of direction cosines $\sum_{j=1}^{N} c_j^2 = 1$, and so m^* is bounded by the smallest and largest masses m_j in the system. Also if the normal to S is parallel to an axis, say x_i, $m^* = m_i$, and if S is nearly parallel to that axis $m^* \cong m_i$, the approximation being generally good because $\sum_j m_j c_j^2$ is an extremum at each axial direction.

Now, without the constraint S, vibration about P has N normal modes (one of imaginary frequency), and the preceding discussion of the product of frequencies applies. Letting β'_{ij} be the force constants in the vicinity of configuration. P, equation (26) gives

$$\prod_{j=1}^{N} \nu_j' = \frac{\sqrt{(\det[\beta'_{ij}])}}{(2\pi)^N} \prod_{j=1}^{N} \frac{1}{\sqrt{m_j}}. \tag{28}$$

Since the normal to S at P is the direction directly across the saddle point, this is also the direction of motion of the normal co-ordinate of the problem that has imaginary frequency. We have labeled this the Nth mode. Introducing the constraint S removes this normal mode without disturbing the others. Thus

$$\prod_{j=1}^{N-1} \nu_j' = \frac{1}{\nu_N'} \frac{\sqrt{(\det[\beta'_{ij}])}}{(2\pi)^N} \prod_{j=1}^{N} \frac{1}{\sqrt{m_j}}. \tag{29}$$

Finally, $\nu_N' = C/\sqrt{m^*}$, where C depends only on the force constants β'_{ij} and m^* is the effective mass for motion in the Nth mode, given by (27). Lumping all the terms that depend on force constants but not on the masses into a new constant C', (29) can be written

$$\prod_{j=1}^{N-1} \nu_j' = \frac{\sqrt{m^*}}{C'} \prod_{j=1}^{N} \frac{1}{\sqrt{m_j}}. \tag{30}$$

If moving through the saddle point along the normal to S means that, at P, only the jumping

atom is in motion in physical space, then the normal to S is along a co-ordinate direction associated with this atom, and m^* equals precisely the mass of the jumping atom. In some crystalline symmetries this might be the true state of affairs, although the displacement of neighbors when an atom is at the saddle point would generally be expected to destroy such symmetry. In any case the jumping atom must have a large share of the motion, hence the approximation $m^* =$ mass of jumping atom should not be bad. If the jumping atom has mass m_1 and all the other atoms have mass $m_2 > m_1$ it is necessary from (27) that $m_1 \leqslant m^* < m_2$. In fact, cartesian axes in physical space can always be chosen such that

$$m^* = c_1^2 m_1 + (1-c_1^2)m_2, \tag{31}$$

where c_1 is the cosine of the angle between the normal of S and axis 1 and is independent of isotopic substitution in m_1.

Combining (30) with (26) in (15) gives

$$\Gamma = \frac{C''}{\sqrt{m^*}} e^{-[\Phi(P)-\Phi(A)]/kT}, \tag{32}$$

where C'' depends on the force constants β_{ij} and β'_{ij}, but does not depend on any of the masses.

To a very good approximation then, it appears that Γ should be inversely proportional to the square root of the isotopic mass of the jumping atom, and to the extent that c_1 is less than 1 the dependence on isotopic mass must be even slower than the square root.

The experiments of LAZARUS and OKKERSE[7] show that the diffusion coefficients of Fe^{55} and Fe^{59} in single crystals of silver at 1156°K are in the ratio of 1·15 to 1. The diffusion coefficients are proportional to the jump frequencies Γ of the impurity atoms, and thus the foregoing analysis leads to the expectation that the ratio of the diffusion coefficients must lie between 1 and the square root of the isotope mass ratio, and would generally be expected to be close to the latter extreme. In the present instance the square root of the mass ratio is 1·035. The experimental results are thus inexplicable by classical rate theory, even when the many body feature of the diffusion process is taken into account. In view of the high temperature and large masses involved the usual quantum corrections to classical rate theory [8–10] would not be expected to make an appreciable difference, although LAZARUS and OKKERSE speculate that an anomalously large tunneling effect might exist in this system. In seeking to explain these results it should be remembered that the diffusion coefficient is also proportional to the concentration of vacancies on sites adjacent to the diffusing atom, and any vibrationally dependent binding between a vacancy and an impurity will increase the concentration around one isotope compared to that around the other. An extra binding of about 0·01 eV around the light isotope as compared with the heavy seems to be required. The work of MONTROLL and POTTS [11] predicts a differential binding at low temperatures of this sign and of roughly this order of magnitude (although their formulas must be pushed beyond their strict domain of validity). At the temperature of this experiment the effect would be very much reduced and no valid calculation of its magnitude exists. The true meaning of the LAZARUS-OKKERSE results thus remains obscure.

One final remark is in order. The preceding discussion of Γ commenced with the assumption that only one atom acquired a new lattice site during the jump, but this restriction is not essential. Two, three, or more atoms might be cooperatively involved in jumping to new sites, and, as long as the topology of the energy contours in configuration space is that of Fig. 1, the discussion through equation (30) remains valid. In a ring mechanism for self diffusion, for example, the effective mass m^* is given by equation (27) and is seen to be identical with the common atomic mass. This has been pointed out before by ZENER.[6] The effect of an isotope in the ring is to alter the jump frequency. If the common mass is m_2 and a single isotope of mass m_1 occurs in a symmetrical ring of n atoms, equations (15), (27), and (30) show that the frequency $\tilde{\nu}$ should be altered, in first approximation, by the factor

$$\frac{\sqrt{m_2}}{\sqrt{[m_1/n + m_2(1-1/n)]}}. \tag{33}$$

Acknowledgement—The writer is indebted to Dr. LAZARUS for stimulating discussions and for communication of results prior to publication.

REFERENCES

1. GLASSTONE S., LAIDLER K. J., and EYRING H. *The Theory of Rate Processes* McGraw-Hill, New York (1941).
2. SEITZ F. *Phase Transformations in Solids* Chap 4. (Edited by R. SMOLUCHOWSKI) John Wiley, New York (1951).
3. WERT C. A., and ZENER C. *Phys. Rev.* **76,** 1169 (1949).
4. WERT C. A. *Phys. Rev.* **79,** 601 (1950).
5. SEEGER A. *Encyclopedia of Physics* Vol. VII, Part 1. Springer-Verlag, Berlin (1955).
6. ZENER C. *Imperfections in Nearly Perfect Crystals* p. 295. (Edited by W. SHOCKLEY, J. H. HOLLOMAN, R. MAURER, and F. SEITZ) John Wiley, New York (1952).
7. LAZARUS D. and OKKERSE B. *Phys. Rev.* **105,** 1677 (1957).
8. BIGELEISEN J. *J. Chem. Phys.* **17,** 675 (1949).
9. BIGELEISEN J. and WOLFSBERG M. *J. Chem. Phys.* **21,** 1972 (1953).
10. BIGELEISEN J. and WOLFSBERG M. *J. Chem. Phys.* **22,** 1264 (1954).
11. MONTROLL E. W. and POTTS R. B. *Phys. Rev.* **102,** 72 (1956).

VOL.
3
1957

J. Phys. Chem. Solids Pergamon Press 1957. Vol. 3. pp. 128–132.

CYCLOTRON RESONANCE IN BISMUTH

J. E. AUBREY and R. G. CHAMBERS

Royal Society Mond Laboratory, Cambridge

(*Received* 29 *March* 1957)

Abstract—AZBEL' and KANER have suggested that the microwave surface impedance of a metal at low temperatures should show periodic variations with magnetic field, if the field is applied parallel to the surface. We report preliminary observations on this effect in bismuth crystals of three different orientations, and show that the results agree reasonably with those expected on the basis of SHOENBERG's measurements of the DE HAAS–VAN ALPHEN effect. A model is proposed for the Fermi surface in bismuth which appears to be consistent with most of the available experimental evidence on this metal.

VOL
3
195

INTRODUCTION

CYCLOTRON resonance experiments in semiconductors have proved very fruitful; in metals, however, they have so far produced relatively little information, because the skin effect considerably modifies and reduces the resonance and complicates its interpretation, particularly under anomalous skin effect conditions. Most experiments have so far been made with the magnetic field H normal to the surface of the metal,[7,11,14] because classical skin-effect theory predicts that the effect should disappear altogether for H parallel to the surface.[2]

Recently, AZBEL' and KANER[3] have suggested that under anomalous skin effect conditions a periodic variation of surface impedance should be observed with H parallel to the surface of the metal, and that the surface impedance $Z = R+iX$ should be given approximately by

$$Z \sim Z(0)[1-\exp(-2\pi i x)\exp(-2\pi x/\omega\tau)]^{1/3} \quad (1)$$

where $x = \omega/\omega_c = m^*c\omega/eH$, and $Z(0)$ is the zero-field impedance. FAWCETT[10] has reported measurements on tin at 24 kMc/s with this geometry which show a single broad maximum in R at a field of about 4 kG; if this is identified with the main peak of (1) it leads to an effective mass m^* of about $0{\cdot}24m_0$. In the present note we report preliminary observations on this type of cyclotron resonance in bismuth at 4°K, and compare the results with those expected theoretically. Bismuth was chosen because its band structure appears to be fairly well established from the work of SHOENBERG,[21] ABELES and MEIBOOM,[1] and HEINE,[12] and because their work indicates that at least some of the energy surfaces are ellipsoidal in form. An ellipsoidal surface has the advantage that for a given field direction m^* is constant over the surface; for more complex surfaces, the variation of m^* over the surface will produce a blurring-out of the resonance,[5] but this complication should be absent in bismuth.

MEASUREMENTS

The frequency used is about 9 kMc/s, and the apparatus and techniques practically identical with those used by PIPPARD[16,17] in studying superconducting tin at this frequency. The specimens are single-crystal rods about 2 mm in diameter and 1·4 cm long, and the r.f. current flow is parallel to the axis of the rod, as is the steady applied field H. From measurements of Q and resonant frequency as a function of H, the variations of $\Delta R/R(0) = [R(H)-R(0)]/R(0)$ and $\Delta X/R(0) = [X(H)-X(0)]/R(0)$ are evaluated. As usual, $X(0)$ itself cannot be evaluated from the measurements, though $R(0)$ can be. Detailed measurements have been made on a specimen with triad axis perpendicular and diad axis parallel to the rod axis ($3_\perp$, $2_\parallel$), and preliminary observations made on specimens of the other two simple orientations ($3_\parallel$, $2_\perp$) and ($3_\perp$, $2_\perp$). Fig. 1 shows

$\Delta R/R(0)$ and $\Delta X/R(0)$ plotted against H up to 10 kG for the $(3_\perp, 2_\parallel)$ orientation. It is clear from the plot of $\Delta R/R(0)$ that at least two separate damped periodic terms are present, one with the main peak at 420 G, the other at about 36 G. The variations in $\Delta X/R(0)$ are less clear-cut, but the same two terms may be distinguished, with the main peaks at somewhat higher fields, about 530 G and 45–65 G. This upward displacement of the reactance peaks is expected from eq. (1): the full lines on Fig. 1 show the theoretical variation of $\Delta R/R(0)$ and $\Delta X/R(0)$ with H for

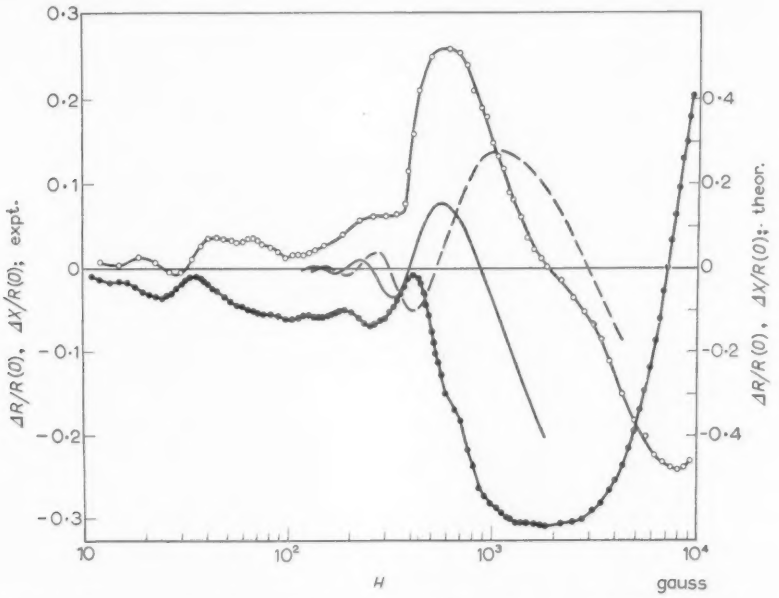

FIG. 1. Variation of surface resistance and surface reactance with field, for $(3_\perp, 2_\parallel)$ orientation. Experimental points (left-hand ordinate scale): ● — $\Delta R/R(0)$; o — $\Delta X/R(0)$. Theoretical curves (right-hand ordinate scale): ———— — $\Delta R/R(0)$; — — — — $\Delta X/R(0)$. Plotted from equation (1), assuming $Z(0) = e^{i\pi/3}$, $\omega\tau = 3$, and $m^*/m_0 = 0{\cdot}11$.

$\omega\tau = 3$, $m^* = 0{\cdot}11m_0$, assuming that $Z(0) \sim e^{i\pi/3}$, i.e. $X(0)/R(0) = \sqrt{3}$, as expected in the extreme anomalous limit where $l \gg \delta_c$ (l: electronic mean free path, δ_c: classical skin depth). This value of m^* has been chosen to give the same period in $1/H$ as that found experimentally for the high-field oscillations of $\Delta R/R(0)$. It will be seen that there is a discrepancy in phase of about $\frac{1}{2}\pi$ between theory and experiment: this is reminiscent of the unexplained phase discrepancy of π in the DE HAAS–VAN ALPHEN (dHvA) effect in Bi[8]; in the present case, however, it may be due partly to the assumption made above that $Z(0) \sim e^{i\pi/3}$. The theoretical ratio $X(0)/R(0) = \sqrt{3}$ is expected only if two conditions are fulfilled: $\alpha = 3l^2/2\delta_c^2 \gg 1$ and $\alpha/\omega^3\tau^3 \gg 1$; otherwise $X(0)/R(0)$ may be either greater or less than $\sqrt{3}$,[9] and the phase of the oscillations of Z will be correspondingly modified. The low-field oscillations in Fig. 1 show a similar phase discrepancy, and correspond to an effective mass $m^* = 0{\cdot}009_7 m_0$.

With the $(3_\parallel, 2_\perp)$ specimen, there is a small peak in $\Delta R/R(0)$ at 92 G, and a broad main peak at about 250 G; above this field the behaviour is qualitatively similar to that shown in Fig. 1, with a minimum in $\Delta R/R(0)$ at about 3·5 kG and thereafter a steady rise up to 10 kG. The $(3_\perp, 2_\perp)$ specimen shows a complex pattern, with peaks in $\Delta R/R(0)$ of irregular height at about 26, 68, 147 and 620 G; $\Delta R/R(0)$ then falls to a minimum at about 5 kG and rises slightly at 10 kG.

These results are summarized in the second

column of Table 1, which also shows, in the third and fourth columns, the results of d.c. resistivity measurements on these specimens. Neither the r.f. nor the d.c. behaviour is greatly affected by tilting the field H by a few degrees relative to the rod axis, or by cooling to 1°K. The last two columns of Table 1 show values of m^*/m_0 and H_p calculated as discussed below.

Table 1. *Summary of experimental results and theoretical predictions*

Orientation	H_p, G	$\rho_{290}(0)/\rho_4(0)$	$\rho_4(10)/\rho_4(0)$†	$100m^*/m_0$	H_p(calc.), G
$(3_\perp, 2_\parallel)$	420, 190, 125; 36, 17	80	2·0	25,0·89 (2)	935, 434, 282; 33·2, 15·4
$(3_\parallel, 2_\perp)$	250, 92	87	5·8	5·46 (3)	199, 92·5
$(3_\perp, 2_\perp)$	620, 147, 68, 26	105	5·2	0·77, 1·54 (2)	54·5, 25·4; 27·2, 12·7

H_p: fields at which peaks occur in surface resistance R (or in $\Delta R/R(0)$). $\rho_T(H)$: d.c. resistivity at T°K in a longitudinal field of H kG. m^*: effective mass expected from DHvA results. 0·89 (2) signifies that two ellipsoids have the same effective mass $m^* = 0{\cdot}0089m_0$. H_p(calc.): values of H_p calculated from m^* as described in the text.

† Specimens $(3_\perp, 2_\parallel)$ and $(3_\parallel, 2_\perp)$ show no appreciable oscillations in $\rho_4(H)$, but specimen $(3_\perp, 2_\perp)$ shows considerable oscillations, with a period in 1/H of $4{\cdot}0\ 10^{-5}$ G^{-1}.

DISCUSSION

The DHvA effect in bismuth[19,21] indicates that the electrons occupy three ellipsoids in k-space. If x and z are chosen along the diad and triad axes, one ellipsoid is given by

$$2m_0E/\hbar^2 = \alpha_1k_x^2+\alpha_2k_y^2+\alpha_3k_z^2+2\alpha_4k_yk_z \quad (2)$$

where according to SHOENBERG the components $\alpha_1 \ldots \alpha_4$ of the reciprocal mass tensor have the values 420, 0·8, 40, −4 respectively, and the Fermi surface at 4°K lies at $E = E_0 = 2{\cdot}83\times10^{-14}$ erg ($\equiv 0{\cdot}017_7$ eV). The other two ellipsoids are obtained by $\pm 120°$ rotations about the z axis. No DHvA effect is observed from the positive holes; according to HEINE[12] this is because the holes have a high effective mass, $\sim 1{\cdot}5$ m_0. For the ellipsoid (2), the value of m^* involved in equation (1) is given by[21]

$$(m_0/m^*)^2 =$$

$$\lambda_1^2(\alpha_2\alpha_3-\alpha_4^2)-2\lambda_2\lambda_3\alpha_1\alpha_4+\lambda_2^2\alpha_1\alpha_3+\lambda_3^2\alpha_1\alpha_2 \quad (3)$$

where $\lambda_{1,2,3}$ are the direction cosines specifying the direction of H relative to the x, y, z axes. The same value of m^* determines the period $\Delta(1/H)$ of the DHvA oscillations; in fact the ratio of periods for the two phenomena should be simply $E_0/\hbar\omega$. Using SHOENBERG's values of α in (3), we obtain the values of m^*/m_0 given in Table 1.† The calculated values of H_p given in the last column of Table 1 are obtained from these values of m^*/m_0 by supposing that the oscillations are given by (1), but displaced by $\frac{1}{2}\pi$ in phase as shown in Fig. 1. There is on the whole reasonable agreement between the calculated and observed values of H_p,‡ except that the peaks at 620 G and 147 G for orientation $(3_\perp, 2_\perp)$ are unaccounted for, and that the high-field peaks for orientation $(3_\perp, 2_\parallel)$ occur at much lower fields than expected, and indicate an effective mass of $0{\cdot}11m_0$ instead of the predicted value of $0{\cdot}25m_0$. This discrepancy may be due to a small misorientation of the specimen, since the predicted value falls rather rapidly from $0{\cdot}25m_0$ if the diad axis is not exactly parallel to the rod; it may, however, indicate an error in SHOENBERG's values of α. The DHvA effect corresponding to this value of m^* (i.e. corresponding

† If the triad axis is not exactly parallel to the rod, the three coincident values of m^* given for $(3_\parallel, 2_\perp)$ rapidly separate: for an error of 2°, there is a spread in m^* of 1·3 : 1, and this probably accounts for the broadness of the observed peak for this orientation.

‡ For orientation $(3_\perp, 2_\perp)$, the DHvA period for $m^* = 0{\cdot}0154m_0$ should be $4{\cdot}25\times10^{-5}$ G^{-1}, in fair agreement with the observed periodicity in $\rho(H)$ of $4{\cdot}0\times10^{-5}$ G^{-1}.

to $\lambda_1 = 1$, $\lambda_2 = \lambda_3 = 0$ in equation (3)) is masked experimentally by the much larger effect from the other ellipsoids with $m^* = 0{\cdot}0089m_0$, and in fact SHOENBERG was never able to observe the effect on m^* of the first term on the right of equation (3), so that the quantities accurately determined in his work (to about ± 4 per cent) were the products $\alpha_1\alpha_i$ ($i = 2, 3, 4$), and E_0. Knowing these, α_1 and thus α_i were found from the absolute amplitude A of the DHvA effect: $\alpha_1 \propto A^2$. This procedure may, however, lead to errors of an order of magnitude or more in α: cf. the results of SHOENBERG[20] on Sn and Ga. If we assume that in fact $\alpha_1 = 168$ instead of 420, and correspondingly $\alpha_{2,3,4} = 2{\cdot}0, 100, -10$, the values of m^* given by (3) are practically unaffected except in the neighbourhood of $\lambda_1 = 1$: for $\lambda_1 = 1$, m^* is reduced from $0{\cdot}25m_0$ to $0{\cdot}1m_0$, in agreement with the observed value of $0{\cdot}11m_0$.

This revision of SHOENBERG's figures also improves considerably the agreement between his model and that found by ABELES and MEIBOOM[1] to fit the galvanomagnetic effects in Bi. They take for the electrons a similar set of ellipsoids to SHOENBERG's, but with $\alpha_4 = 0$ (i.e. the principal axes of the ellipsoids are parallel to the specimen axes, instead of being tilted by 5°45′ about x as in SHOENBERG's model), and $\alpha_1 : \alpha_2 : \alpha_3 = 40 : 1 : 24$, considerably different from SHOENBERG's $420 : 0{\cdot}8 : 40$. The quantities derived by ABELES and MEIBOOM were the mobilities $\mu_i = e\tau\alpha_i/m_0$, and LAX *et al.*[15] have suggested that this discrepancy might be due to anisotropy of τ. But the τ involved in μ_i is itself an appropriate mean of $\tau(k)$; to attain the suggested anisotropy of τ_i would require $\tau(k)$ to be practically zero except for electrons with $k_y \gg k_x, k_z$. Such high anisotropy would lead to a large d.c. magnetoresistance effect for all orientations, and seems incompatible with the very small effect observed e.g. for the $(3_\perp, 2_\parallel)$ specimen; indeed the smallness of this effect is strong evidence that $\tau(k)$ is practically isotropic within each ellipsoid (cf. JUSTI and KOHLER;[13] CHAMBERS[6]). As remarked, the discrepancy is very much reduced if we choose the revised values of α suggested above, which give $\alpha_1 : \alpha_2 : \alpha_3 = 42 : 0{\cdot}5 : 25$.

An attempt to combine the results of SHOENBERG, ABELES and MEIBOOM, and HEINE[12] into a reasonably consistent model leads to the following tentative picture for Bi: for the electrons, the three ellipsoids of eq. (2), with the revised values of α given above and $E_0 = 0{\cdot}017_7$ eV at 4°K; for the holes, one spheroid with the axial ratio suggested by ABELES and MEIBOOM and a density of states of 0·02 per eV per atom,[12] giving

$$2m_0(E_1 - E)/\hbar^2 = \beta_1(k_x^2 + k_y^2) + \beta_3 k_z^2 \qquad (4)$$

with $\beta_1 = 0{\cdot}71$, $\beta_3 = 0{\cdot}19$, and a band overlap $E_1 = 0{\cdot}018_4$ eV. The ratio of densities of states of electrons and holes is then 1 : 27, and if we assume E_1 independent of temperature, we obtain the values for n, the number of electrons or holes per atom, N, the number per cm³, and E_0, the Fermi energy, given in Table 2. The values found for N at 80 and 300°K agree well with the substantially independent values of 4·6 and 22×10^{17} per cm³ found by ABELES and MEIBOOM. If τ is assumed constant within each ellipsoid,

Table 2. Temperature-variation of properties of proposed model

Temperature	No. of electrons or holes per atom	No. of electrons or holes per cm³	Fermi energy
T°K	$n \times 10^5$	$N \times 10^{-17}$, cm^{-3}	E_0, eV
4	0·86	2·46	$0{\cdot}017_7$
80	1·33	3·8	0·028
300	7·7	22	0·068

the observed anisotropy of ρ at room temperature leads to $\tau_e = 1{\cdot}0 \times 10^{-13}$ sec, $\tau_h = 9{\cdot}1 \times 10^{-12}$ sec, and to mean free paths $\bar{l} = \tau\bar{v}$ of the order of $0{\cdot}02 - 0{\cdot}2\ \mu$ for electrons and $0{\cdot}5 - 1\ \mu$ for holes at room temperature, in agreement with the large values found experimentally.[4,18] If τ_e and τ_h increase in the same ratio on cooling to 4°K, we find, e.g. for specimen $(3_\perp, 2_\parallel)$, in which ρ fell by a factor of 80, that at 4°K $\tau_e = 7{\cdot}1 \times 10^{-11}$ sec, $\tau_h = 6{\cdot}45 \times 10^{-9}$ sec (remembering the accompanying change in N). Thus at 9 kMc/s, $\omega\tau_e \sim 4{\cdot}0$, in good agreement with experiment, and $\omega\tau_h \sim 370$. Now equation (4), with the proposed values of β, leads to a value of m^* for the holes of $1{\cdot}4 - 2{\cdot}7m_0$, depending on orientation, corresponding to

a main peak in $\Delta R/R(0)$ at 5·2–10 kG; no peak is observed in this region, but the steep rise in $\Delta R/R(0)$ between 5 and 10 kG suggests a peak not far above 10 kG. With $\omega\tau \sim 370$, we should then expect a long series of "harmonic" peaks at lower fields; the failure to observe these may indicate a non-ellipsoidal Fermi surface for the holes, with a spread of m^* sufficient to blur out all but the main peak. It is clearly desirable to pursue the measurements to higher fields, and we hope to do this shortly.

According to AZBEL' and KANER, the effect should vanish unless the field is parallel to the surface to within an angle $\psi \sim (\delta/r)^{2/3}$, where δ is the skin depth and r the electron orbit radius. For most metals this gives $\psi \sim 1°$ or less, but for Bi, δ is unusually large and r unusually small, giving a much larger value for ψ. For specimen $(3_\perp, 2_\parallel)$, for instance, $R(0) = 0{\cdot}050$ ohm at 4°K, and using PIPPARD's[17] definition of an effective skin depth, $\delta = 10^9\, R/2\pi\omega$, we find $\delta = 1{\cdot}1 \times 10^{-4}$ cm. On the above model, $r = 1{\cdot}4(m_0/m^*)^{\frac{1}{2}} \times 10^{-4}$ cm for the electrons and $0{\cdot}27(m_0/m^*)^{\frac{1}{2}} \times 10^{-4}$ cm for the holes, at the field corresponding to the main peak in $\Delta R/R(0)$. Thus $\delta/r \sim 0{\cdot}1$–$0{\cdot}3$ for the electrons, and ~ 2 for the holes, and we should expect, as found experimentally, that the effect will be relatively insensitive to small errors in field orientation. Finally, we remark that the expression (1) is derived on the assumption that $\delta \ll r$; the phase shift of $\frac{1}{2}\pi$ found in the present work, and the absence of harmonic peaks from the holes, may be due to these large values of δ/r.

It may be noted that the DHVA measurements of SHOENBERG[20] indicate $\tau_e \sim 10^{-12}$ sec at 4°K. If this were the relevant τ for our experiments, we should have $\omega\tau \sim 0{\cdot}06$, and no sign of a resonance would be expected. It has been suggested that SHOENBERG's very small apparent values of τ are due not to collision broadening but to an intrinsic lattice broadening of the quantized energy levels.[5,20] But such an intrinsic broadening would be expected to lead to a very low apparent τ in the present work also, unless very stringent selection rules operate between the broadened levels; our results therefore suggest that lattice broadening may be unimportant and that SHOENBERG's low values of τ have some other explanation.

We should like to thank Dr. D. SHOENBERG for helpful discussion of his DE HAAS–VAN ALPHEN effect measurements. One of us (J.E.A.) is indebted to the D.S.I.R. for a maintenance grant.

REFERENCES

1. ABELES B. and MEIBOOM S. *Phys. Rev.* **101,** 544 (1956).
2. ANDERSON P. W. *Phys. Rev.* **100,** 749 (1955).
3. AZBEL' M. Ya. and KANER E. A. *J. Exp. Theor. Phys.* **30,** 811 (1956).
4. CHAMBERS R. G. *Physica* **19,** 365 (1953).
5. CHAMBERS R. G. *Canad. J. Phys.* **34,** 1395 (1956).
6. CHAMBERS R. G. *Proc. Roy. Soc.* A**238,** 344 (1956).
7. DEXTER R. N. and LAX B. *Phys. Rev.* **100,** 1216 (1955).
8. DHILLON J. S. and SHOENBERG D. *Phil Trans.* A**248,** 1 (1955).
9. DINGLE R. B. *Physica* **19,** 311 (1953).
10. FAWCETT E. *Phys. Rev.* **103,** 1582 (1956).
11. GALT J. K., YAGER W. A., MERRITT F. R., CETLIN, B. B., and DAIL H. W., JR. *Phys. Rev.* **100,** 748 (1955).
12. HEINE V. *Proc. Phys. Soc.* A**69,** 513 (1956).
13. JUSTI E. and KOHLER M. *Ann. Phys.* **36,** 349 (1939).
14. KEYES R. J., ZWERDLING S., FONER S., KOLM H. H., and LAX B. *Phys. Rev.* **104,** 1804 (1956).
15. LAX B., BUTTON K. J., ZEIGER H. J., and ROTH L. M. *Phys. Rev.* **102,** 715 (1956).
16. PIPPARD A. B. *Proc. Roy. Soc.* A**203,** 98 (1950).
17. PIPPARD A. B. *Proc. Roy. Soc.* A**216,** 547 (1953).
18. PIPPARD A. B. and CHAMBERS R. G. *Proc. Phys. Soc.* A**65,** 955 (1952).
19. SHOENBERG D. *Proc. Roy. Soc.* A**170,** 341 (1939).
20. SHOENBERG D. *Phil. Trans.* A**245,** 1 (1952).
21. SHOENBERG D. *Progress in low-temperature physics* Vol. 2, p. 226. Amsterdam.

J. Phys. Chem. Solids Pergamon Press 1957. Vol. 3. pp. 133–140.

GUDDEN-POHL AND MEMORY EFFECTS IN AN INFRA-RED STIMULATED PHOSPHOR

I. T. STEINBERGER, E. A. BRAUN, and E. ALEXANDER

Department of Physics, The Hebrew University, Jerusalem, Israel

(*Received* 29 *March* 1957)

Abstract—Gudden-Pohl effect during stimulation and enhancement of stimulability by the action of an electric field applied during stimulation are observed in Std. VI. Dependence of these effects on voltage and previous history, especially on previous field application is investigated together with the enhancement of stimulability by field application during fluorescence described previously.[17] It is shown that most of the features of electric field action observed may be understood on the basis of the term scheme deduced from thermal and optical evidence.

VOL. 3 1957

1. INTRODUCTION

LIGHT flashes appearing upon application of an electric field on a ZnS type phosphor during phosphorescence have been known since the experiments of GUDDEN and POHL[1] in 1920. The occurrence of this effect seems to be a general property of photoconducting inorganic phosphors.[2] The accepted interpretation of the Gudden-Pohl effect assumes that the field liberates electrons from traps to the conduction band.[3,4,5] The number of electrons in the conduction band is thus momentarily increased. This leads to an increase in the rate of recombination with empty luminescence centres and therefore to enhanced luminescence. A detailed mechanism for the liberation process was proposed by CURIE[4,5] in his theory of electroluminescence. An essentially similar theory of electroluminescence was developed by PIPER and WILLIAMS.[6] In these theories electron avalanche processes are assumed, which should strongly depend on the mean free path of electrons and on the occurrence of strong local fields. As optical and thermal ionization of traps are independent of mean free path, *a priori* no simple correlation would be expected between optical or thermal depths of traps and their effectiveness in the Gudden-Pohl effect. Experiments on ZnS phosphors have led DESTRIAU[3] to the assumption that special traps are active in the Gudden-Pohl effect.

DESTRIAU[7] and VIGEAN and CURIE[8,9] investigated the effect of infra-red and long-wave visible radiation on the Gudden-Pohl effect in ZnS phosphors. They found considerable quenching of the Gudden-Pohl effect both by previous and simultaneous long-wave irradiation.

The use of an infra-red stimulated phosphor for investigating the Gudden-Pohl effect enables one to distinguish between the influence of the density of conduction band electrons and the density of filled traps without change of temperature. The phosphor "Standard VI" (SrS : Eu : Sm)[10] was chosen for this investigation because it represents a relatively well understood system. Chemical and optical evidence has shown that the Eu^{++} ion causes the appearance of the luminescence centres, while the deep traps are associated with the Sm^{+++} ions.[11] Some of these conclusions are supported by Low's experiments on paramagnetic resonance in this phosphor.[12] Standard VI exhibits good stimulability for infra-red radiation of about 1 micron and the quantum efficiency of the stimulation process is about unity. No infra-red quenching of fluorescence is observed.

DROPKIN[13] and BRAUER[14] have deduced a term scheme for Std. VI which shows the following main features: Excitation transfers electrons from the luminescence centres into the conduction band. The electrons will either recombine with the centres or will be trapped. There are two kinds of

traps which play a role in the luminescence process: deep traps associated with samarium ions and shallow traps. At room temperature phonons will gradually transfer electrons from the shallow traps to the conduction band and this will lead to phosphorescence. Electrons from deep traps will be raised to the conduction band by infra-red radiation and this will lead to stimulated emission. This scheme was deduced from optical, thermal and photoconductive evidence and seems well founded. The deep traps provide excellent energy storage. In fact the stimulated light sum does not considerably decrease even if several days elapse between the end of excitation and the beginning of stimulation.[10]

In the present paper experiments are described which show the existence of the Gudden-Pohl effect during stimulated emission in Standard VI. In addition to this new Gudden-Pohl effect a number of effects were recorded in which the phosphor showed a "memory" extending over several hours for the action of an electric field upon it. A systematic investigation of the effects of applying an electric field at different stages of luminescence was undertaken. Most of the observed results may be explained with the help of the term scheme previously deduced. No "special" traps are needed for the explanation and the only additional assumption made is the liberation of electrons by field action from some of the shallow traps into the conduction band.

2. EXPERIMENTAL PROCEDURE

The luminescence brightness was measured by a photomultiplier. The output of the multiplier was fed both into a galvanometer and an oscilloscope and the readings of both these instruments were photographically recorded. Details of the apparatus may be found in a previous paper.[15] The phosphor powder was embedded either in polystyrene or in araldite and pressed between two electrodes, at least one of which was made of conducting glass. The thickness of the cells thus prepared varied between 0·1 and 0·3 mm.

The blue light for excitation was obtained from a 6 volt, 18 watt filament bulb and was filtered by "Wratten 49" and "Chance ON 13" filters and a 2·5 cm thick absorption cell containing a 1/5 N aqueous solution of $CuCl_2$. This combination of filters transmits a spectral band between 3800 and 4900 Å, with maximum transmission at 4600 Å. The excitation was therefore in the absorption band of the europium impurity. The integral intensity at longer wavelengths was under 1 per cent of the total light intensity transmitted. The infra-red light was obtained from a similar bulb and filtered by a "Chance OX 5" filter. Both light sources were equipped with a converging lens system and camera shutters. A combination of "Chance" filters OX 2 and OX 4 and a camera shutter were situated before the photomultiplier IP 21.

Fifty c.p.s. sinusoidal alternating voltages of up to 2000 volts were applied to the phosphor cells. Before each experiment the phosphor had to be stimulated for at least an hour to obtain reproducible results.

3. EXPERIMENTAL RESULTS

The investigated phosphor showed three types of Gudden-Pohl light flashes on application of an alternating electric field. During excitation by blue light (excitation GPE), during phosphorescence (phosphorescence GPE) and finally during stimulation by infra-red radiation (stimulation GPE). These effects will be described in paragraph 3.1. All three types of Gudden-Pohl effect as well as the stimulability were strongly influenced by previously applied electric fields and these "memory" effects will be described in paragraph 3.2.

3.1. *Gudden-Pohl effects*

3.11. Excitation Gudden-Pohl effect. On field application during excitation, the luminescence brightness increases abruptly. This light flash decays within a few tenths of a second to a level below the normal fluorescence brightness and rises within several seconds to a new stationary level which again is lower than the fluorescence brightness without field. We shall call the transient, consisting of the fast rise and decay "excitation GPE", while the stationary lowering of luminescence output will be called "stationary quenching". Oscilloscope records (Fig. 1a) reveal that while the alternating electric field is applied, the light output consists of a slowly varying component and light pulses. There usually are two light pulses during each cycle of the alternating field. The amplitudes of the light pulses decrease continuously with the decrease in light intensity during the GPE and are constant during stationary quenching. In the stationary state the two pulses differ considerably in amplitude, depending on whether the illuminated electrode is positive or negative at the time of the pulse. During the decrease in amplitude the two pulses differ less and the pattern consists essentially of damped sinusoidal waves, while in the

VOL.
3
1957

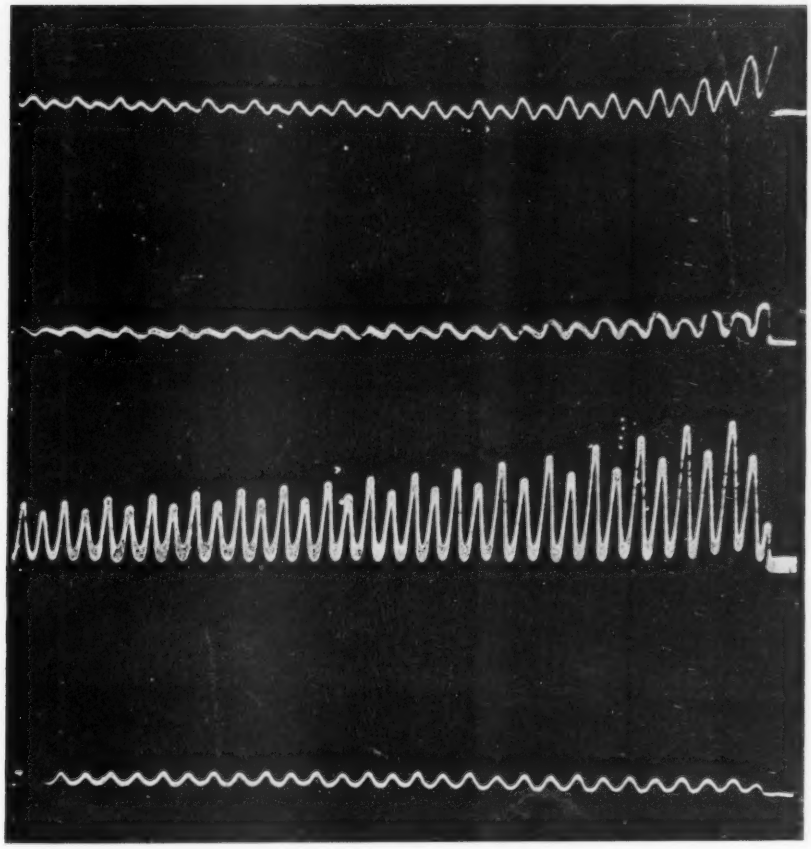

FIG. 1. Brightness waves of Gudden-Pohl effects.

(a) Excitation GPE (field applied during saturated fluorescence).
(b) Phosphorescence GPE (field application began 10 seconds after end of excitation).
(c) Stimulation GPE (field application began 30 seconds after beginning of stimulation).
(d) Stimulation GPE after field had been applied during excitation.

Applied voltage 750 volt RMS on cell of 0·2 mm thickness, 50 c.p.s., two light pulses per cycle. Time scale from right to left.

[*Facing Page* 134

VOL
3
195

stationary state the waves are strongly distorted. This behaviour is rather similar to that of the ZnS phosphors previously investigated.[15,16]

3.12. Phosphorescence Gudden-Pohl effect. When the electric field is applied during phosphorescence, a short light flash consisting of damped waves appears (Fig. 1b). It is very similar to the exitation GPE, i.e. to the fast rise and subsequent decay within a few tenths of a second. Slight quenching of the phosphorescence follows the GPE.

3.13. Stimulation Gudden-Pohl effect. A Gudden-Pohl effect is also observed on field application during stimulated emission. The general features of this new effect resemble those of the other two Gudden-Pohl effects observed in this phosphor. The main difference is in the longer persistence of the stimulation GPE which may last for a few seconds as compared with a few tenths of a second in the case of the excitation and phosphorescence GPE. The stimulation GPE also consists of light pulses and two different pulses are again observed during each cycle of the applied electric field (Fig. 1c). Some weak quenching of the stimulated brightness is observed after the decay of the GPE.

The stimulation GPE does not strongly depend on the time elapsed between the end of excitation and beginning of stimulation, just as the stimulation brightness is not much affected by this time. These facts are shown in Table 1, where the initial

Table 1

Time interval (seconds)	20	80	200	330	2700
Initial stimulated brightness (arbitrary units) . .	25·5	24	26·5	22	21
Maximum amplitude of GPE (same arbitrary units)	12	12	11·5	11	9·5

brightness of stimulated emission and of stimulation GPE are shown in dependence on the time elapsed between end of excitation and beginning of stimulation. The two initial brightnesses remain proportional within the experimental error of 5 per cent.

Fig. 2 shows the dependence of the stimulated brightness and of the stimulation GPE on the duration of excitation. Both reach saturation after 60 sec. This is also the time it takes the fluorescence to reach its equilibrium level under our conditions of excitation.

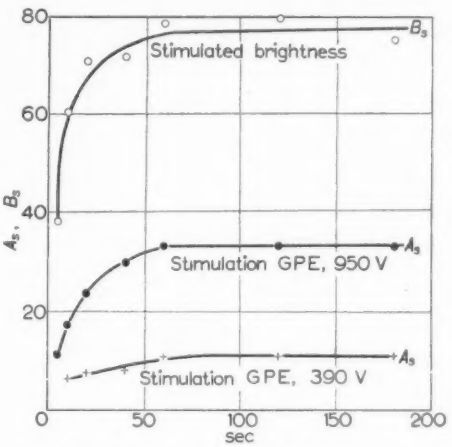

FIG. 2. Dependence of stimulability and stimulation GPE on duration of excitation.
B_s: Initial stimulated brightness, arbitrary units.
A_s: Initial amplitude of stimulation GPE, arbitrary units.
(Field applied after three minutes of stimulation).

It should be emphasized that the occurrence of a strong stimulation GPE in Std. VI is in contrast to

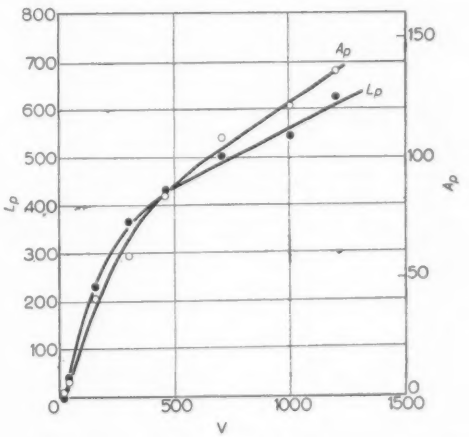

FIG. 3. Voltage dependence of phosphorescence GPE.
L_p: light output integrated over the first twenty cycles.
A_p: maximum amplitude.

the behaviour of ZnS phosphors, where infra-red radiation quenches the GPE.[7]

3.14. *Comparison of some properties of the* GPE *under different conditions.* Fig. 3 shows the dependence of the phosphorescence GPE on the applied voltage, while Fig. 4 shows the voltage dependence

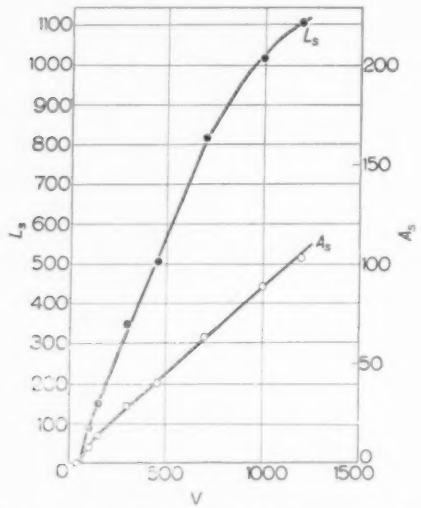

FIG. 4. Voltage dependence of stimulation GPE.

L_s: light output integrated over the first twenty cycles.
A_s: maximum amplitude.

The luminescence brightness at the moment of field application was identical for all experiments represented in Figs. 3 and 4. The same arbitrary units are used in both figures.

of the stimulation GPE. The light output was in both cases integrated over the first 20 cycles only. For the slowly decaying stimulation GPE this is not a true measure of the total light sum. While the phosphorescence GPE as a function of voltage shows a change of slope at about 500 volts, the stimulation GPE increases almost linearly up to higher values of voltage.

The light sum of the phosphorescence GPE decreases with decreasing phosphorescence brightness at the time of field application (Fig. 5). In contrast, the light sum of the stimulation GPE decreases at a much slower rate than the stimulated emission decays (Fig. 6).

3.2 *Memory Effects*

The phosphor investigated shows a memory for

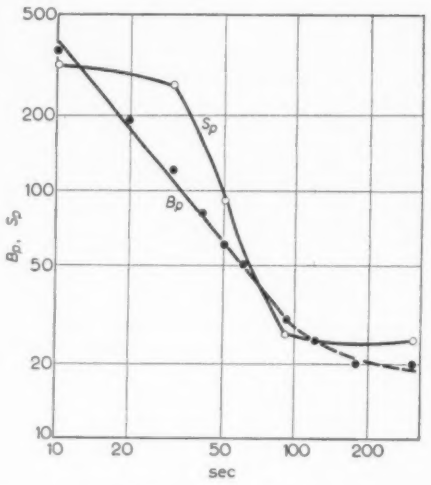

FIG. 5. Time dependence of phosphorescence and phosphorescence GPE.

B_p: phosphorescence brightness, arbitrary units.
S_p: light sum of phosphorescence GPE.

The time is measured from end of excitation.

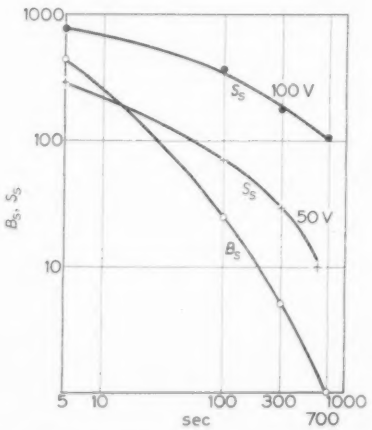

FIG. 6. Time dependence of stimulability and stimulation GPE.

B_s: stimulation brightness, arbitrary units.
S_s: light sum of stimulation GPE, arbitrary units.

The time is measured from beginning of stimulation.

previous field application. This consists of the following facts:

(1) Stimulability is enhanced by an alternating field which had acted during excitation.

(2) The stimulability is enhanced by simultaneous field action. This enhancement also depends on previous field application.

(3) The GPE is quenched by previous field action.

In Fig. 7 experiments are represented which illustrate these effects.

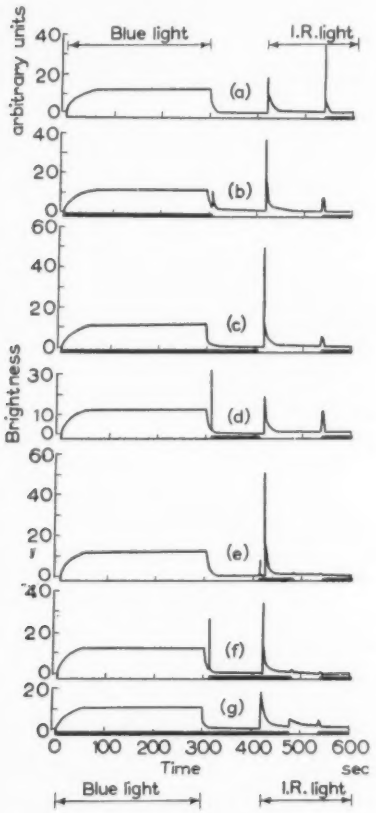

FIG. 7. Luminescence brightness vs. time for field application at different stages of luminescence. Duration of field application marked by thick lines.

In all experiments the phosphor was excited during 300 sec. After 120 sec of phosphorescence infra-red irradiation began, resulting in the stimulation peak ($t = 420$). After another 120 sec ($t = 540$) the field was applied.

We shall separately discuss the influences of previous field application on the stimulability (3.21) and those on the stimulation GPE (3.22).

3.21. Fig. 7(a) shows the luminescence brightness as a function of time when the field is applied at $t = 540$ only.

Fig. 7(b) shows the enhancement of stimulability by the application of an electric field during excitation as previously reported.[17]

Fig. 7(c) shows that the enhancement of stimulability by a previous electric field is more pronounced when the field acts continuously during excitation and phosphorescence.

Fig. 7(d) on the other hand shows that an electric field acting during phosphorescence only has no pronounced influence on subsequent stimulability.

Fig. 7(e) shows the enhancement of stimulability by simultaneous field action, which in this experiment began 5 seconds before stimulation.

In experiment 7(f) this enhancement by simultaneous field is reduced, as the field was switched on 115 seconds before stimulation, i.e. acted during almost the whole duration of phosphorescence.

As Fig. 7(g) shows, no appreciable enhancement was found when the field acted from the beginning of excitation.

A comparison of Figs. 7(g) with 7(c) shows that the enhancement of stimulability by the field action during excitation disappears when the field continues to act during stimulation.

3.22. As comparison of Fig. 7(a) with the remaining figures shows, the stimulation GPE is always quenched by previous field action. Field action during stimulation is the most effective, field action during phosphorescence the least effective in this respect. The light pulses in such a case are shown in Fig. 1(d). It is interesting to note that the decay of the pulse amplitudes is very slow in this instance.

From the above it can be seen that no simple correlation exists between the changes in the stimulation peaks and the following stimulation GPE.

3.23. Various features of the memory effects. The stimulability of Std. VI can be enhanced in two ways: by previous or by simultaneous field action. The characteristics of these two effects are however different. When the stimulability is enhanced by simultaneous field, the light output contains a strong alternating component (not appearing in Fig. 7 because of the time scale used). The appearance of the strong alternating component indicates

that this enhancement effect is correlated with the stimulation GPE. The negative influence of previous fields on this enhancement supports this view.

It seems that in this case the total stimulated light sum is not increased: the initial enhancement is compensated by a faster decay.

The enhancement of stimulability by an electric field acting during excitation was reported previously. This memory-effect persists for many hours. Its voltage dependence shows a threshold and a tendency to saturation (Fig. 2 ref. 17). It can be erased by subsequent blue irradiation (Table 1, ref. 17). We compared light sums with and without previous field and found that previous field action increases not only the initial brightness but also the light sum of stimulation. This increase of the light sum was found to be stronger for short excitation times.

As in several other phosphors,[18] removal of the alternating field sometimes causes a temporary increase of brightness (Fig. 7(b), $t = 305$ sec, 7(g), $t = 480$ sec). This effect is most pronounced during excitation.

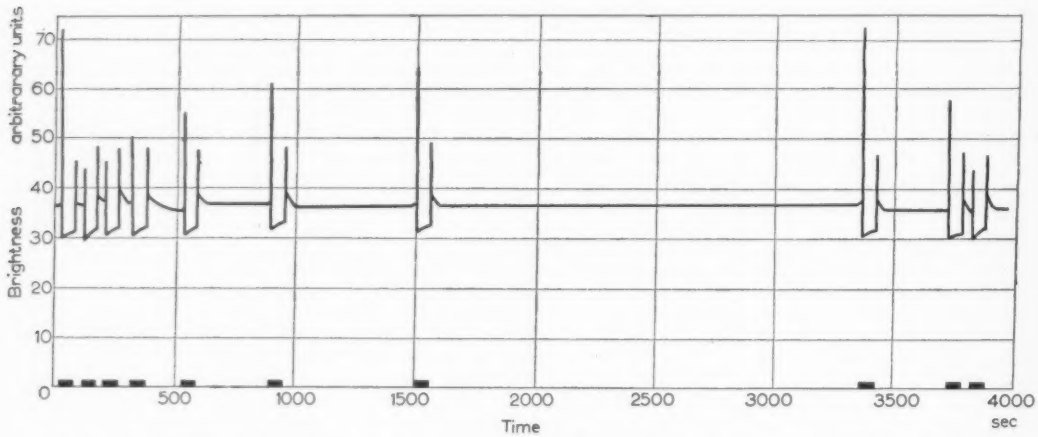

FIG. 8. Influence of field application on fluorescence. Duration of field application marked by thick lines.

Fig. 8 shows a number of experiments on successive field applications during excitation. It can be seen that the excitation GPE is reduced by previous field action. The shorter the interval between successive field applications, the stronger the suppression of the GPE. On the other hand, the stationary quenching of fluorescence and the momentary illumination at field removal are independent of previous field applications.

4. DISCUSSION

The more striking effects of simultaneous or previous field action on Std. VI investigated in this paper are those where the field enhances luminescence, i.e. the three kinds of Gudden-Pohl effect (paragraph 3.1) and enhanced stimulability by simultaneous and by previous field action (paragraph 3.2).

On the other hand quenching effects were observed, e.g. quenching after the GPE, stationary fluorescence quenching and suppressed GPE on field reapplication (Figs. 7, 8).

For the explanation of the Gudden-Pohl effect it has been generally assumed that the field in some way enhances the transfer of electrons from trapping states to the conduction band.

In the following discussion of the various features of the observed effects we shall apply this assumption alone, without making use of a special mechanism for this liberation process.

Experimental evidence of this paper (e.g. Fig. 8) and other work[7,15] indicates that enhancement effects and the stationary quenching of fluorescence by field action are independent phenomena. The brightness increase at field removal seems to be connected with the quenching effect (Fig. 8). MATOSSI[19] has proposed several mechanisms for stationary fluorescence quenching, but no sufficient

experimental evidence has been provided to decide between the different theoretical possibilities. We shall therefore refrain from discussing this matter any further.

We shall now discuss the implications of the previously deduced term scheme for Std. VI (paragraph 1) on the behaviour of this phosphor in an electric field. We shall assume that the field raises electrons from the shallow traps into the conduction band. The depth and number of such traps "reached" by the field will grow with increasing field strength. It seems very probable that only a fraction of the shallow traps ("field sensitive traps") will be located in regions of high local fields and only the electrons in these traps will be acted upon by the electric field.

VOL. 3 1957

4.1. *Gudden-Pohl effects*

The light output at any instant of time is proportional to the product of the number of electrons in the conduction band and the number of empty luminescence centres. During phosphorescence electrons are brought into the conduction band from shallow traps, while during stimulation they are brought to the conduction band from deep traps and a considerable fraction of them is recaptured in shallow traps.[20] If, as assumed, the field enhances the transition from the shallow traps to the conduction band, we should expect an increase in luminescence brightness at the moment of application of the field.

During phosphorescence, the field acts on the electrons in those shallow traps which it can "reach", transfers them to the conduction band and thence they recombine with empty luminescence centres. As there is no mechanism which restores the number of electrons in shallow traps, the increase in light output is short and the subsequent phosphorescence is diminished because of exhaustion of traps. Retrapping decreases the initial amplitude and prolongs the effect.

The stimulation GPE (paragraph 3.13) starts in the same manner, but we would expect it to last far longer, because the shallow traps are continuously refilled from the conduction band.

As may be seen from Fig. 5, the integral light output of the phosphorescence GPE decreases rapidly with decreasing phosphorescence brightness at the moment of field application. This is in contrast to the integral light output of the stimulation GPE (Fig. 6) which decreases much more slowly than the stimulated brightness at the moment of field application. This slow decrease in the light sum of the stimulation GPE with stimulation decay may be understood, considering that the stimulated brightness decreases mainly because of the filling up of luminescence centres and emptying of deep traps, while the number of electrons in shallow traps is a function which varies much more slowly with time. This assumption is justified by calculations carried out by DROPKIN.[13]

A more detailed explanation might be obtained by considering the distribution of electrons in the various shallow traps. From the different voltage dependence of the phosphorescence GPE and the stimulation GPE (Figs. 3 and 4) it may be inferred that the distribution of electrons over various trapping states differ in both cases.

The assumption that the field liberates retrapped electrons from the shallow traps finds further support in the similar dependence of the stimulability and stimulation GPE on excitation time (Fig. 2). The fact that both stimulability and stimulation GPE are nearly independent (for periods of hours) of the time interval between excitation and i.r. irradiation also points to this explanation.

4.2. *Enhancement of stimulability*

The enhancement of stimulability by a field acting simultaneously with stimulation (e.g. Fig. 7(e) $t = 420$) and the subsequent faster decay may also be understood by the enhanced rate of transfer from shallow traps into the conduction band. In this way the "waiting period" of retrapped electrons in shallow traps will be shortened and thereby the rate of filling of centers enhanced.

4.3. *Memory effects*

The enhancement of stimulability by an electric field acting during excitation only can also be explained by our assumption. Enhanced liberation of electrons during excitation from the shallow traps causes a distortion of the dynamical equilibrium in such a way as to decrease the number of electrons in shallow traps and to increase their number in the deep ones. Because of the increased number of filled deep traps remaining after excitation with simultaneous field, the stimulability must increase.

Accordingly, a field which had acted during excitation should weaken the phosphorescence. This was actually observed (Fig. 7b).

The enhancement of infra-red stimulability by an electric field which had acted during excitation is observed even if several hours elapsed between the end of excitation and the beginning of stimulation. This is to be expected according to our explanation, which connects this memory with the normal storage properties of the phosphor. Irradiation by blue light after removal of the field can erase this memory-effect. (ref. 15 Table 1). This process is very slow, as the restoration of the normal equilibrium depends on the slow rate of transfer of electrons from deep traps by blue light.

The stimulation GPE is reduced by previous field action. (Figs. 7 and 8) This effect might be understood on the basis of the given picture by the additional assumption that it is less probable for field liberated electrons to be retrapped in the high field region than in field insensitive traps. This would result in a reduction of the number of electrons in field sensitive traps available for the GPE at field reapplication. The reducing influence of previous field action on the stimulation enhancement by simultaneous field action might be understood on the same lines.

5. CONCLUSION

Our experimental evidence is not sufficient to build up and prove a fully consistent picture which accounts for all details of the observed phenomena.

On the other hand we feel that the above discussion shows that in a well known phosphor the electrophotoluminescence effects may be understood on the basis of a term scheme obtained from optical and thermal evidence alone.

Acknowledgements—In conclusion we would like to thank Professor G. F. J. GARLICK and Dr. W. LOW for extremely helpful discussions, and Dr. L. WEIDENFELD for providing the phosphor samples.

REFERENCES

1. GUDDEN B. and POHL R. *Z. Phys.* **2,** 192 (1920).
2. KRAUTZ E. *Z. Naturforsch* **4,** 284 (1949).
3. DESTRIAU G. *C.R. Acad. Sci., Paris* **211,** 555 (1943).
4. CURIE D. *J. Phys. Radium* **13,** 317 (1952).
5. CURIE D. *J. Phys. Radium* **14,** 672 (1953).
6. PIPER W. W. and WILLIAMS F. E. *Brit. J. Appl. Phys.* Supplement 7, 39 (1955).
7. DESTRIAU G. *Phil. Mag.* **38,** 774 (1947).
8. VIGEAN F. *C.R. Acad. Sci., Paris* **232,** 819 (1951).
9. VIGEAN F. and CURIE D. *C.R. Acad. Sci., Paris* **232,** 955 (1951).
10. URBACH F., PEARLMAN D., and HEMMENDINGER H. *J. Opt. Sci. Amer.* **36,** 372 (1946).
11. STÖCKMANN F. *Naturwissenschaften* **39**, 226 (1952).
12. LOW W. *Phys. Rev.* **98,** 426 (1955).
13. DROPKIN J. J. Final Report on *Photoconduction in Phosphors* Polytechnic Institute of Brooklyn (1954).
14. BRAUER P. *Ann. Phys.* **9,** 227 (1951).
15. STEINBERGER I. T., LOW W., and ALEXANDER E. *Phys. Rev.* **99,** 1217 (1955).
16. DESTRIAU G. *J. Appl. Phys.* **25,** 67 (1954).
17. LOW W., STEINBERGER I. T., and BRAUN E. A. *J. Opt. Soc. Amer.* **44,** 504 (1954).
18. DESTRIAU G. *J. Phys. Radium* **4,** 32 (1943).
19. MATOSSI F. *Phys. Rev.* **94,** 1151 (1954).
20. GARLICK G. F. J. and MASON D. E. *J. Electrochem. Soc.* **96,** 90 (1949).

J. Phys. Chem. Solids Pergamon Press 1957. Vol. 3. pp. 141–152.

REVERSIBLE PROPERTIES OF POLYCRYSTALLINE FERROMAGNETS*†—I

THEORY OF THE EXPECTED VARIATION OF THE REVERSIBLE PROPERTIES WITH MAGNETIZATION

D. M. GRIMES

Department of Electrical Engineering, University of Michigan, Ann Arbor, Michigan

(*Received* 7 *March* 1957)

VOL. 3 1957

Abstract—Using a statistical model, equations are developed for the variation of the reversible susceptibility both parallel with and normal to the biasing magnetization as a function of the magnetization assuming that the susceptibility arises by domain rotation. The results are contrasted with previous results based upon domain-wall motion. It is concluded that the theory points out a new technique for the separation of the origins of the susceptibility. Equations are also given for the expected variation of the differential magnetostriction with magnetization both parallel with and normal to the field and for both domain-wall motion and domain rotation.

Quantitative results depend upon the fraction of the moments oriented in each direction. A function describing this distribution is discussed.

An expression is given for the susceptibility matrix arising from domain rotation as a function of magnetization.

INTRODUCTION

THE reversible properties of polycrystalline ferromagnets result from the ferromagnetic nature of the material when a differential disturbance of some kind is applied. To fit the reversible criterion, internal oscillations to the material must be carried out about fixed equilibrium positions and must be vanishingly small. Thus, reversibility indicates repeatability and, for the special case of a zero-frequency applied disturbance, it implies reversibility in the thermodynamic sense of zero energy dissipation. GANS[1] pointed out that the reversible susceptibility of iron could be closely approximated analytically as a function of the magnetization only, independently of the magnetic history. BROWN[2,3,4] extended GANS' work to include the cases of the derived distribution function $f(\theta)\,d\theta$, the fraction of the presumed equal volume domains oriented between θ and $\theta+d\theta$, and with this knowledge was able to express the reversible susceptibilities and the magnetostriction in terms of the magnetization.

GRIMES and MARTIN[5] extended BROWN's work to include the reversible susceptibility measured both normal and parallel to the magnetization. They compared their results favorably with measurements on several ferrites. In the meantime, TEBBLE and CORNER[6] and STONER[7] pointed out that the reversible susceptibility is not a unique function of the magnetization, but does depend upon the magnetic history. It is the point of view of this paper that although the susceptibilities do indeed depend upon the magnetic history, as a first approximation they can be first considered as functions of the magnetization only. Variations

* Parts of the work described were submitted to the Horace H. Rackham School of Graduate Studies, University of Michigan, in partial fulfillment of the degree of Doctor of Philosophy.

† This work was carried out under the auspices of the Engineering Research Institute. The initial stage of the work was supported by the U.S. Army Signal Corps, the balance by the U.S. Air Force Office of Scientific Research and Development Command under Contract No. AF-18(603)-8. Reproduction in whole or in part is permitted for any purpose of the United States Government.

from this idealized behavior can then be discussed.

It is pointed out that under usual conditions the equations for the parallel reversible susceptibility χ_{rp} and the transverse (normal) reversible susceptibility χ_{rt} as given by BROWN[4] and by GRIMES and MARTIN[5] are applicable when the susceptibility has its origin in domain-wall motion. In this paper the susceptibility matrix is derived as a function of the magnetization when that matrix arises by domain rotation. The diagonal terms give the reversible susceptibilities χ_{rp} and χ_{rt} due to domain rotation.

The expected variation of the parallel differential magnetostriction with magnetization has been computed by BOZORTH and WILLIAMS.[8] They assumed that both the reversible susceptibility and the change in biasing moment had their origin in the rotation of the magnetic moments. In this paper equations are derived for each of the four possibilities when the biasing moment changes by domain-wall motion. The differential magnetostriction of several ferrites has been discussed by VAN DER BURGT.[9]

THE REVERSIBLE QUANTITIES, GENERAL CASE

The susceptibilities

The magnetic properties of a ferromagnet can be described in terms of the function $f(\theta)\,d\theta$, the fraction of the total atomic moments of the material which are oriented between θ and $\theta+d\theta$ with respect to the applied magnetic field. The magnetization is then given by:

$$M = M_s \frac{\int_0^{\pi} f(\theta)\sin\theta\cos\theta\,d\theta}{\int_0^{\pi} f(\theta)\sin\theta\,d\theta} = M_s\langle\cos\theta\rangle \quad (1)$$

where the symbol $\langle\ \rangle$ indicates the weighted average over the polycrystal, M is the gross magnetization, M_s is the spontaneous or saturation moment and θ is the angle between the gross magnetization and the moment vector in question. The validity of equation 1 is limited by the equality of the saturation and spontaneous moments but not by any particular magnetization mechanism. A discussion of $f(\theta)$ will be left until later. The reversible susceptibility measured parallel to the applied magnetic field is:

$$\chi_{rp} = M_s\frac{\partial\langle\cos\theta\rangle}{\partial H} \quad (2)$$

where H is the magnetic field, subject to the condition that the same mechanisms which allow the static value of M to be different from zero also give rise to the reversible susceptibility. The partial derivative indicates that the external stress and the magnetic history of the specimen remain constant. The latter implies that the susceptibility is initially measured opposite in direction to the change in H which brought the material to the position (M, H) at which the measurement was taken. This is assumed to be the susceptibility measured by a vanishingly small alternating field.

The reversible susceptibility for dilute material can also be calculated by applying the usual torque equation to all magnetic dipoles present in the system. This torque equation with the added damping term as given by LANDAU and LIFSHITZ[10] can be written as:

$$\frac{\partial \boldsymbol{M}}{dt} = \gamma(\boldsymbol{M}\times\boldsymbol{H}) - \frac{\gamma\epsilon}{M_s}[\boldsymbol{M}\times(\boldsymbol{M}\times\boldsymbol{H})] \quad (3)$$

where t is the time, γ the magnetomechanical coupling coefficient, and ϵ a dimensionless parameter proportional to the energy loss. It is the usual convention in solving equation 3 to assume that the spontaneous moment is oriented along the z axis and that the effective magnetic field in the z direction is large compared with the applied reversible field. The magnetization from equation 3 can be written as a function of H using matrix notation, as:

$$(M) = (X)(H). \quad (4)$$

Let us now assume that all time varying quantities vary as $e^{i\omega t}$, and, to obtain a diagonalized matrix for (X), we use the co-ordinate system $(x+iy,\ x-iy,\ z)$.[11] Using this notation the operator j represents a time delay of $(\pi/2\omega)$ sec and the operator i represents a $\pi/2$ spatial rotation. The susceptibility matrix then becomes:

$$X_{11} = \frac{M_x+iM_y}{H_x+iH_y} = \frac{M_+}{H_+} = X_+ = \frac{\omega_0}{\omega_1+\dfrac{ij\omega}{1+i\epsilon}}$$

$$X_{22} = \frac{M_x-iM_y}{H_x-iH_y} = \frac{M_-}{H_-} = X_- = \frac{\omega_0}{\omega_1-\dfrac{ij\omega}{1-i\epsilon}} \quad (5)$$

$$X_{33} = X_{12} = X_{13} = X_{23} = X_{21} = X_{31} = X_{32} = 0,$$

where $\omega_0 = \gamma M_s$, $\omega_1 = \gamma H_z$ and ω is the applied radial frequency. The real parts of equation 5 with respect to i represent diagonal terms in the co-ordinate system (x, y, z) and imaginary parts represent off-diagonal terms. Real parts with respect to j represent energy stored and imaginary parts represent energy dissipated.

To extend equation 4 to a polycrystalline medium, let us first average the susceptibility matrix over a polycrystalline sample, and then correct for interdomain effects. The procedure for averaging is to transform the susceptibility matrix from one based upon the z axis to a general matrix in terms of the Euler angles (θ, φ, ψ), then to average the result over a polycrystal. If the subscript d indicates the z axis based system and g the arbitrarily based system, then $M_d = X_d H_d$ and $M_g = aX_d H_d = aX_d a^{-1} H_g = X_g H_g$ where a is the Euler transformation matrix expressed in the system ($x+iy$, $x-iy$, z). Both a and a^{-1} have been computed by PARK.[11] In averaging over a polycrystal, if all angles around the applied field are equally likely (physically this means that if crystalline orientation exists, it has rotational symmetry about the field direction) then all off-diagonal terms of the matrix X_g average to zero and X_g is given by:

$$X_g = \tfrac{1}{4}\begin{bmatrix} \langle(1+\cos\theta)^2\rangle X_+ + \langle(1-\cos\theta)^2\rangle X_-, & 0, & 0 \\ 0, & \langle(1-\cos\theta)^2\rangle X_+ + \langle(1+\cos\theta)^2\rangle X_-, & 0 \\ 0, & 0, & 2(1-\langle\cos^2\theta\rangle)(X_+ + X_-) \end{bmatrix} \tag{6}$$

In an attempt to account for the interactions of neighboring domains whose moments are rotating consider the effective field at a particular domain because of its neighbors. Following PARK[12] let us assume that the neighboring domains have an averaged moment equal to that of the gross material. PARK showed that the interaction could be described as $h = H - \rho M$ where h is the effective magnetic field felt by the domain, H is the applied alternating field, M the macroscopic alternating magnetization and ρ a constant. External demagnetizing factors are describable by a similar equation. Thus it is to be assumed that the term $(-\rho M)$ describes effects due to the external geometry and the internal domain interactions. This can be understood by assuming that the full demagnetizing factor of the domain by itself is only partially cancelled by its contact with neighboring domains. Putting the h's into the susceptibilities:

$$M_g = \frac{X_g}{1+\rho X_g} H_g = \chi_g H_g. \tag{7}$$

The susceptibilities (χ) from equation 7 are formally identical with the susceptibilities (X) of equation 6 when ω_1 is replaced by $(\omega_1 + \rho\omega_0)$. Thus the effect of external demagnetizing factors and nearest-neighbor domain interactions as here considered are describable as an increased effective anisotropy field. This is also true when the effective fields vary throughout the sample.[12]

In terms of the system (x, y, z) and the χ's, the averaged susceptibility matrix is:

$$\chi_g = \tfrac{1}{4}\begin{bmatrix} (1+\langle\cos^2\theta\rangle)(\chi_- + \chi_+), & 2\langle\cos\theta\rangle(\chi_- - \chi_+), & 0 \\ -2\langle\cos\theta\rangle(\chi_- - \chi_+), & (1+\langle\cos^2\theta\rangle)(\chi_- + \chi_+), & 0 \\ 0, & 0, & 2(1-\langle\cos^2\theta\rangle)(\chi_- + \chi_+) \end{bmatrix} \tag{8}$$

For a nonoriented polycrystal in the virgin state it follows that $\langle\cos^2\theta\rangle = 1/3$ and $\langle\cos\theta\rangle = 0$ so equation 8 is proportional to the unit matrix. For saturated material $\langle\cos\theta\rangle = \langle\cos^2\theta\rangle = 1$ and the matrix is the susceptibility matrix of a single crystal.[13] The off-diagonal terms are proportional to the macroscopic magnetization, a fact in agreement with previous calculations of RADO.[14] Since $f(\theta)$ is not known, the diagonal terms cannot be calculated unambiguously from a knowledge of the normalized magnetization only.

Remembering that equation 8 is based upon the biasing magnetization being in the z direction, the transverse and parallel reversible susceptibilities for domain rotation are seen to be

$$\chi_{rt}{}^r = \frac{\chi_- + \chi_+}{4}(1+\langle\cos^2\theta\rangle); \qquad \chi_{rp}{}^r = \frac{\chi_- + \chi_+}{2}(1-\langle\cos^2\theta\rangle) \tag{9}$$

independently of the particular averaging function $f(\theta)$. The susceptibilities are then related by:

$$(\chi_+ + \chi_-) = 2\chi_{rt}{}^r + \chi_{rp}{}^r = 3\chi_0{}^r. \tag{10}$$

where the superscript r's indicate domain rotation, the subscript r's indicate a reversible property and

the subscripts p and t represent parallel and transverse respectively.

The assumptions made in deriving equations 9 and 10 are:

1. that the susceptibility is describable by the small signal solution to the LANDAU-LIFSHITZ equation;

2. that the sum of the biasing field and magnetic anisotropy effects are describable as an effective magnetic field; and

3. that either domain interactions do not exist or that they are describable by the field $(-\rho M)$. Presumably, so long as assumption (2) is valid, assumption (1) will also be.

From equation 10 it is apparent that so long as $(\chi_- + \chi_+)$ remains constant, if $\chi_{rp}{}^r$ is a monotonic decreasing function of M, then $\chi_{rt}{}^r$ will be a monotonic increasing function with ratio of slopes equal (-2).

The magnetostrictions

If a demagnetized sphere of polycrystalline material is magnetized the material ceases to be spherical and becomes elongated or shortened in the field direction. The coefficient λ_s is defined to be:

$$\lambda_s = \frac{\Delta l}{l} = \left(\frac{l_m - l_{sp}}{l}\right)$$

where l_m is the length of the saturated material in the field direction and l_{sp} is the diameter of the sphere. Because parallel-antiparallel orientation changes leave Δl unaltered the angular dependence of the magnetostriction must involve even powers of $\cos\theta$. Under the restricting conditions that the magnetostriction is independent of the crystallographic direction (i.e., $\lambda_s = \lambda_{100} = \lambda_{111}$) then for each crystallite:[15,16,17]

$$\lambda_d = \tfrac{3}{2}\lambda_s(\cos^2\theta - \tfrac{1}{3}). \tag{11}$$

where λ_d is the ratio $\Delta l/l$ for each crystallite as a function of θ. If the effects of microscopic strain interactions are completely described by the determination of $f(\theta)$, then each crystallite separately contributes according to equation 11 and the gross magnetostriction λ_g is given by:

$$\lambda_g = \tfrac{3}{2}\lambda_s(\langle\cos^2\theta\rangle - \tfrac{1}{3}). \tag{12}$$

Subject to the condition that the susceptibility has its origin in the mechanism which produced a gross magnetization other than zero, the parallel differential magnetostriction is given by:

$$d_p = \frac{\partial\lambda_g}{\partial H} = \frac{3\lambda_s}{2}\frac{\partial\langle\cos^2\theta\rangle}{\partial H}, \tag{13}$$

where the partial indicates that the magnetic history and the external stress are constant. Since λ and M are both functions of θ, the differential magnetostriction can also be expressed as:

$$d = \left(\frac{\partial\lambda_g}{\partial H}\right) = \left(\frac{d\lambda_g}{d\theta}\Big/\frac{dM}{d\theta}\right)\frac{dM}{dH}. \tag{14}$$

For alternating differential fields dM/dH is taken to be the reversible susceptibility χ_r. Thus, combining equations 1 and 11 for each crystallite with the bracket in equation 14.

$$d = \frac{3\lambda_s}{M_s}(\chi_r\cos\theta) \tag{15}$$

for each domain. Equation 15 can be combined with the non-averaged values of the susceptibility for each domain corresponding to equation 9, then the product averaged over the polycrystal to obtain:

$$d_p{}^r = \frac{9\lambda_s\chi_0{}^r}{2M_s}[\langle\cos\theta\rangle - \langle\cos^3\theta\rangle] \tag{16a}$$

$$d_t{}^r = \frac{9\lambda_s\chi_0{}^r}{4M_s}[\langle\cos\theta\rangle + \langle\cos^3\theta\rangle]. \tag{16b}*$$

From equation 16 it is apparent that for constant χ_0 the maximum value of d should occur for crossed magnetic fields with $M = M_s$. Since H_{ap} is not negligible for $M = M_s$, this maximum value of $(9\lambda_s\chi_0{}^r/2M_s)$ cannot be attained in nonoriented material.

Results of an effective history field

For many materials, the magnetic moment

* The equation for $d_p{}^r$ is similar in form to the expression for Λ given by BOZORTH and WILLIAMS.[9] Using their approach (a) the biasing moment as well as the differential moment is assumed to vary by rotational processes, (b) it is not clear how the values of 1·37 to 1·60 were obtained for their f, and (c) they put $\langle\cos\theta\rangle^3 = \langle\cos^3\theta\rangle$.

vectors remain oriented very nearly along crystallographically "easy" directions when $M \lesssim M_s/2$. Under these conditions the parallel reversible susceptibility and differential magnetostriction when calculated by equations 2 and 13 must also have magnetic moments in "easy" directions. This criterion is consistent with the movement of domain walls but not with rotation of domains. Thus so long as the static moment is oriented in "easy" directions equations 2 and 13 will be applicable to domain-wall motional effects.

It is convenient to introduce the dimensionless parameter η defined by $\eta = A(H_{ap}+D)$, where H_{ap} is the applied biasing field, A is a constant and D is a history dependent field. It is now necessary to make the restricting assumption that the magnetic history of the sample is completely described by the effective magnetic field D. The physical significance of the parameter η and the field D are discussed in the appendix. This assumption implies that the sum of the component of local moments in the field direction uniquely determines that in all other directions. With this assumption $f(\theta)$ and the resulting $\langle \cos^m \theta \rangle$ will be unique functions of η, and experimental plots of different functions of $\langle \cos^m \theta \rangle$ should eliminate hysteresis effects. Modification of this assumption will be discussed later. Since the $\langle \cos^m \theta \rangle$ are assumed to be unique functions of η, let us define:

$$\begin{aligned} F(\eta) &\equiv \langle \cos \theta \rangle \\ G(\eta) &\equiv \langle \cos^2 \theta \rangle \\ H(\eta) &\equiv \langle \cos^3 \theta \rangle. \end{aligned} \tag{17}$$

The values of M and $\chi_{rp}{}^{w}$ as given in Table 1, row 1, follow from equations 1, 2, and 17. Note that the partial with respect to H is taken at constant D. D is presumed to change with each change in domain configuration. The values for $\chi_{rp}{}^{r}$, $\chi_{rt}{}^{r}$, $d_p{}^{r}$, $d_t{}^{r}$, $d_p{}^{w}$ and the susceptibility matrix in Table 1, row 1, follow from equation 17 and equations 9, 16, 13, and 8 respectively. To compute $\chi_{rt}{}^{w}$ note that when the biasing field is increased by a normal differential field the increasing magnitude is second order in (dH/M) (i.e., $H = \sqrt{[H_{ap}{}^2+(\Delta H)^2]} \cong H_{ap}\sqrt{[1+\frac{1}{2}(\Delta H/H_{ap})^2]}$), but the change normal to H_{ap} is first order in $(\Delta H/H_{ap})$. Thus, for a differential field, the transverse susceptibility can be seen from the similar triangles of Fig. 1, if the field and moment remain parallel:

$$\chi_{rt}{}^{w} \equiv \lim_{\Delta\eta \to 0} A\frac{\Delta M}{\Delta \eta} = \frac{AM}{\eta} = AM_s\frac{F(\eta)}{\eta}. \tag{18}$$

The transverse-field differential magnetostriction due to domain-wall motion follows by a similar argument and is given by:

$$d_t{}^{w} = 3/2\lambda_s \frac{A}{\eta}[G(\eta)-\tfrac{1}{3}]. \tag{19}$$

Upon comparing the parallel and transverse susceptibilities it is apparent that:

$$\chi_{rp}{}^{w} = \chi_{rt}{}^{w}+\eta\frac{d\chi_{rt}{}^{w}}{d\eta}. \tag{20}$$

Thus, if $\chi_{rp}{}^{w}$ is a monotonic decreasing function of M, then $\chi_{rt}{}^{w}$ must also be decreasing in contrast with the expected results from domain rotation.

The differential equation of motion which describes the movement of 180° domain walls is

$$2\mu_0 M_s H = \alpha x+\beta\dot{x}+m\ddot{x} \tag{21}$$

where x represents the spatial co-ordinate of the wall measured from its equilibrium position in the absence of the field, and α, β and m are constants and μ_0 is the permeability of free space. Inherent in equations 18 and 19 is the assumption that $\alpha x \gg (\beta\dot{x}+m\ddot{x})$. The magnetic Q of the material for a sinusoidal applied signal is:

$$Q = \frac{\alpha-\omega^2 m}{\omega\beta}. \tag{22}$$

Thus, so long as the material remains inductive, the Q remains large, and wall-motion processes predominate, equations 18 and 19 will be valid.

FIG. 1. The relationship utilized to determine the transverse properties due to domain-wall motion.

The distribution function $f(\theta)$

The function $f(\theta)\,d\theta$ is, by definition, the fraction of the magnetic moments in the system of interest at an angle between θ and $\theta+d\theta$ with respect to the biasing field. $f(\theta)$ will be constant for nonoriented

Table 1. *The reversible quantities*

	Magnetization	Reversible susceptibility: Wall motion	Reversible susceptibility: Domain rotation	Differential magnetostriction: Wall motion	Differential magnetostriction: Domain rotation
Parallel fields	$M = M_s F(\eta)$	$\chi_{rp}{}^{w} = AM_s \dfrac{dF(\eta)}{d\eta}$	$\chi_{rp}{}^{r} = \dfrac{\chi_- + \chi_+}{2}(1-G(\eta))$	$d_p{}^{w} = \frac{3}{2}\lambda_s A \dfrac{dG(\eta)}{d\eta}$	$d_p{}^{r} = \dfrac{9\lambda_s \chi_0}{2M_s}[F(\eta)-H(\eta)]$
Arbitrary $F(\theta)$ Transverse fields		$\chi_{rt}{}^{w} = AM_s \dfrac{F(\eta)}{\eta}$	$\chi_{rt}{}^{r} = \dfrac{\chi_- + \chi_+}{4}(1-G(\eta))$	$d_t{}^{w} = \frac{3}{2}\lambda_s A \dfrac{1}{\eta}(G(\eta)-\frac{1}{3})$	$d_t{}^{r} = \dfrac{9\lambda_s \chi_0}{4M_s}[F(\eta)+H(\eta)]$
Parallel fields	$M = M_s L(\eta)$	$\chi_{rp}{}^{w} = 3\chi_0 \dfrac{dL(\eta)}{d\eta}$	$\chi_{rp}{}^{r} = 3\chi_0 \dfrac{L(\eta)^*}{\eta}$	$d_p{}^{w} = \dfrac{3d_0}{\eta}\left[\dfrac{L(\eta)}{\eta} - \dfrac{dL(\eta)}{d\eta}\right]$	$d_p{}^{r} = \dfrac{3d_0}{\eta}\left[1 - \dfrac{3L(\eta)}{\eta}\right]$
$f(\theta) = e^{\eta \cos\theta}$ Isotropic material		$\chi_{rt}{}^{w} = 3\chi_0 \dfrac{L(\eta)}{\eta}$	$\chi_{rt}{}^{r} = \frac{3}{2}\chi_0\left(1 - \dfrac{L(\eta)}{\eta}\right)^*$	$d_t{}^{w} = \dfrac{d_0}{\eta}\left[1 - \dfrac{3L(\eta)}{\eta}\right]$	$d_t{}^{r} = \dfrac{3d_0}{2}\left[L(\eta) - \dfrac{1}{\eta}\left(1 - \dfrac{3L(\eta)}{\eta}\right)\right]$
Transverse fields					

Susceptibility matrix

$$\begin{matrix} \dfrac{\chi_- + \chi_+}{4}(1+G(\eta)), & \dfrac{\chi_- - \chi_+}{2}F(\eta), & 0 \\ -\dfrac{\chi_- - \chi_+}{2}F(\eta), & \dfrac{\chi_- + \chi_+}{4}(1+G(\eta)), & 0 \\ 0, & 0, & \dfrac{\chi_- + \chi_+}{2}(1-G(\eta)) \end{matrix}$$

$$\begin{matrix} \dfrac{3\chi_0}{2}\left(1 - \dfrac{L(\eta)}{\eta}\right), & \mathrm{K}L(\eta), & 0 \\ -\mathrm{K}L(\eta), & \dfrac{3\chi_0}{2}\left(1 - \dfrac{L(\eta)}{\eta}\right), & 0 \\ 0, & 0, & 3\chi_0 \dfrac{L(\eta)}{\eta} \end{matrix}$$

* GRIMES D. M. *Bull. Amer. Phys. Soc.* Series II, **1**, 25 (1956).

$^{*}A = \dfrac{3\chi_0}{M_s}$; $d_0 = \dfrac{3\lambda_s \chi_0}{M_s}$; $L(\eta) = \mathrm{ctnh}\,\eta - \dfrac{1}{\eta}$; $(\chi_- + \chi_+) = 3\chi_0$; $(\chi_- - \chi_+) = 2\mathrm{K}$.

material which has been cooled through its Curie temperature in the absence of any magnetic fields. For saturated material $f(\theta)$ will be unity in the field direction and zero in all other directions. If the magnetization is decreased from saturation, the first effect is the rotation of the magnetic moment vectors of the different crystallites towards "easy" crystallographic directions as determined by the anisotropy fields. The exact result as the field is further decreased is open to considerable variation as well as conjecture. However, demagnetizing fields will exist and, if the crystallites are sufficiently large, domain walls will be nucleated. These effects, as well as effective magnetostrictive fields arising from internal strains, will disorder the moments of the system. For single crystals, HEISENBERG[18] has proposed a model based upon the most probable domain behavior, while AKULOV[19] considered a model of either parallel or anti-parallel moments. Since the present system has the additional factor of random crystallite orientation, it is expected that the results will more nearly approximate the model proposed by HEISENBERG.

With the assumption that the domains are all of fixed and equal volume, BROWN[2] has shown that the HEISENBERG model leads to the distribution function

$$f(\theta) = e^{\eta \cos\theta} \tag{23}$$

where η is the same as discussed in the previous section. In the appendix the same distribution function is derived without the restricting equal volume domain assumption, but with other restricting assumptions. For this section equation 23 will be assumed valid; then deviations from this equation are considered to give rise to the remaining hysteresis in plots of the susceptibilities versus the magnetization.

For calculation, we compute the weighted-average values by first averaging over each crystallite, then averaging the crystallite average over the polycrystal. We first assume effectively infinite first order anisotropy fields, then for rotational effects we assume these fields are still small enough to allow a finite moment rotation. The following cases will be considered: Cubic, $K_1 > 0$; cubic, $K_1 < 0$; cubic, an infinite number of possible directions; hexagonal, $K_1 > 0$; hexagonal, $K_1 < 0$; and all moments either parallel or anti-parallel with the field direction. The results are shown in integral form in Table 2 along with the low field expansions and the numerical values for fields effectively infinite but still much less than the anisotropy fields.

The reversible functions

Upon comparing the low field expansion terms for the cubic and isotropic materials, they are identical to the $(7\text{-}m)$ power of η. Further each type assumes infinite anisotropy fields; the [100] oriented material has six possible directions, the [111] oriented material has eight possible directions, and the isotropic material an infinite number of directions. Since for large M the assumption of large anisotropy fields ceases to be valid, the

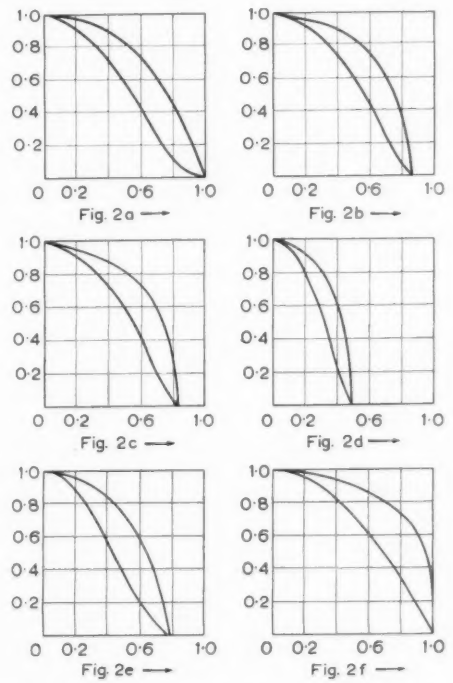

FIG. 2. The variation of the parallel (lower curves) and transverse (upper curves) normalized reversible susceptibilities with normalized magnetization when the susceptibility is due to domain-wall motion. The different figures represent different anisotropy classes. FIG. 2a, isotropic material; FIG. 2b, cubic, $K_1 < 0$; FIG. 2c, cubic $K_1 > 0$; FIG. 2d, hexagonal, $K_1 > 0$; FIG. 2e, hexagonal, $K_1 < 0$, zero basal plane anisotropy; FIG. 2f, all moments parallel or anti-parallel with H.

Table 2. Distribution functions for nonoriented material if $f(\theta) = e^{\eta \cos \theta}$

Anisotropy condition	Isotropic	Cubic $K_1 < 0$	Cubic $K_1 > 0$
$\langle \cos^m \theta \rangle$	$\dfrac{\int d\Omega \cos^\eta \theta \, e^{\eta \cos \theta}}{\int d\Omega e^{\eta \cos \theta}}$	$\displaystyle\int \frac{d\Omega}{4\pi} \frac{\sum_p \left(\sum_i \frac{1}{\sqrt{3}} p_i l_i \right)^m \exp\left(\frac{\eta}{\sqrt{3}} \sum_i p_i l_i \right)}{\sum_p \exp\left(\frac{\eta}{\sqrt{3}} \sum_i p_i l_i \right)}$ $p = \pm 1$ l_i = direction cosine of field to crystalline axis.	$\displaystyle\int \frac{d\Omega}{4\pi} \frac{\sum_i (e^{\eta l_i} + (-1)^m e^{-\eta l_i}) l^m i}{\sum_i (e^{\eta l_i} + e^{-\eta l_i})}$
small η			
$F(\eta) = \langle \cos \theta \rangle$	$\frac{\eta}{3} - \frac{\eta^3}{45} + \frac{2\eta^5}{945} - \frac{\eta^7}{4725} + \cdots$	$\frac{\eta}{3} - \frac{\eta^3}{45} + \frac{2\eta^5}{945} - \frac{17\eta^7}{76{,}545} + \cdots$	$\frac{\eta}{3} - \frac{\eta^3}{45} + \frac{2\eta^5}{945} - \frac{2\eta^7}{8505} + \cdots$
$G(\eta) = \langle \cos^2 \theta \rangle$	$\frac{1}{3} + \frac{2\eta^2}{45} - \frac{4\eta^4}{945} - \frac{2\eta^6}{4725} - \cdots$	$\frac{1}{3} + \frac{2\eta^2}{45} - \frac{4\eta^4}{945} + \frac{2\eta^6}{5103} - \cdots$	$\frac{1}{3} + \frac{2\eta^2}{45} - \frac{4\eta^4}{945} + \frac{2\eta^6}{5670} + \cdots$
$H(\eta) = \langle \cos^3 \theta \rangle$	$\frac{\eta}{5} - \frac{\eta^3}{105} + \frac{4\eta^5}{4725} - \cdots$	$\frac{\eta}{5} - \frac{\eta^3}{105} + \frac{4\eta^5}{5103} + \cdots$	$\frac{\eta}{5} - \frac{\eta^3}{105} + \frac{4\eta^5}{5670} - \cdots$
$\eta \to \infty$			
$F(\infty)$	1·0000	0·8660	0·8312
$G(\infty)$	1·0000	0·7577	0·7009
$H(\infty)$	1·0000	0·6693	0·5991

VOL. 3 195

Table 2. (continued)

Anisotropy condition	Hexagonal $K_1 > 0$	Hexagonal $K_1 < 0$ Zero basal anisotropy	All moments parallel or antiparallel to H_{ap}
$\langle \cos^m \theta \rangle$	$\int \frac{d\Omega}{4\pi} \left(\frac{(e^{\eta l}+(-1)^m e^{-\eta l}) l^m}{e^{\eta l}+e^{-\eta l}} \right)$ l = cosine of angle between C-axis and applied field.	$\int \frac{d\Omega}{4\pi} \frac{\int_0^{2\pi} d\phi (\sin\theta \cos\phi)^m e^{\sin\theta\cos\phi}}{\int_0^{2\pi} d\phi e^{\eta \sin\theta \cos\phi}}$ The integrals over ϕ are expressible in terms of Bessel functions.	$\left(\frac{e^{\eta}+(-1)^m e^{-\eta}}{e^{\eta}+e^{-\eta}} \right)$
small η			
$F(\eta) = \langle \cos\theta \rangle$	$\frac{\eta}{3}-\frac{\eta^3}{15}+\frac{2\eta^5}{105}-\frac{17\eta^7}{2835}+\cdots$	$\frac{\eta}{3}-\frac{\eta^3}{15}+\frac{\eta^5}{84}-\frac{29\eta^7}{15120}+\cdots$	$\eta-\frac{\eta^3}{3}+\frac{2\eta^5}{15}-\frac{17\eta^7}{315}+\cdots$
$G(\eta) = \langle \cos^2\theta \rangle$	0·3333	$\frac{1}{3}+\frac{\eta^2}{30}-\frac{\eta^4}{210}+\frac{\eta^6}{1689}-\cdots$	1·0000
$H(\eta) = \langle \cos^3\theta \rangle$	$\frac{\eta}{5}-\frac{\eta^3}{21}+\frac{2\eta^5}{135}-\cdots$	$\frac{\eta}{5}-\frac{2\eta^3}{105}+\frac{\eta^5}{360}-\cdots$	$\eta-\frac{\eta^3}{3}+\frac{2\eta^5}{15}-\cdots$
$\eta \to \infty$			
$F(\infty)$	0·5000	0·7854	1·0000
$G(\infty)$	0·3333	0·6667	1·0000
$H(\infty)$	0·2500	0·5890	1·0000

assumption of isotropic material should closely approximate the results for cubic material. The reversible functions for isotropic material are listed in Table 1, row 2. The variations of the wall motional and rotational susceptibilities are shown in Figs. 2 and 3, respectively, for each of the six cases. Fig. 4 illustrates the wall motional differential magnetostriction, and Fig. 5 shows the rotational differential magnetostrictions for isotropic material.

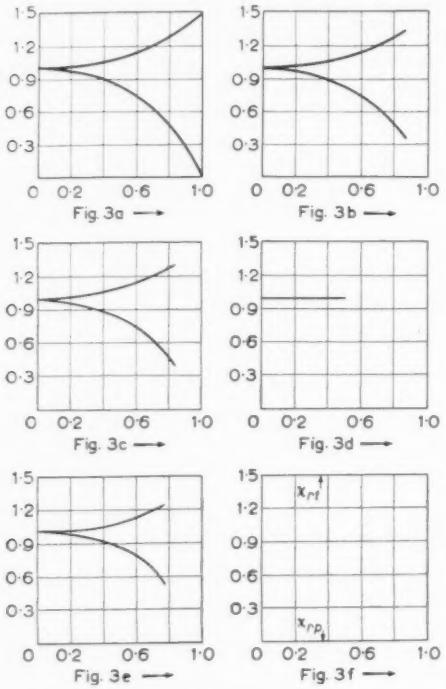

FIG. 3. The variation of the parallel (lower curves) and transverse (upper curves) normalized reversible susceptibility with normalized magnetization when the susceptibility is due to domain rotation. The anisotropy conditions for the figures are the same as in FIG. 2.

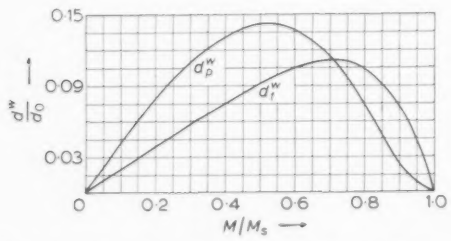

FIG. 4. The variation of the parallel and transverse differential magnetostrictions with magnetization in isotropic material when the susceptibility is due to domain-wall motion.

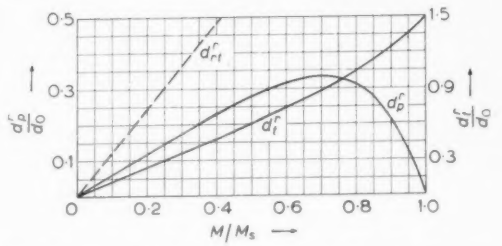

FIG. 5. The variation of the parallel and transverse differential magnetostrictions with magnetization in isotropic material when the susceptibility is due to domain rotation.

The rotational initial susceptibility can be approximated by:

$$\chi_0 = \frac{\mu_0 M_s^2}{3K_1}. \tag{24}$$

Putting equation 24 into the value of d_0 as given in Table 1 yields:

$$d_0 = \frac{\mu_0 \lambda_s M_s}{K_1}. \tag{25}$$

If this form of d_0 is substituted into equation 16a, the coefficient differs from that of the equation given for Λ by BOZORTH and WILLIAMS[8] only by their "small factor" f.

The large values of the rotational reversible properties for crossed fields will not be realized because of the H term in the denominator of the expression for χ_0.

CONCLUSIONS

Theoretical equations are developed for the variation of the reversible susceptibility with magnetization if the susceptibility has its origin in domain rotation or in domain-wall motion. These equations are developed for both parallel and transverse moments. Because of the dependence of transverse field behavior upon susceptibility mechanism, it is concluded that the result provides a new technique for evaluating the relative importance of these two mechanisms (see equations 10 and 20).

Without a detailed knowledge of domain distribution, if the ratios of the slope of transverse and parallel reversible susceptibilities with magnetization is negative, and if only the wall motional and domain rotational mechanisms exist, then the negative ratio can only result from domain rotation. If a more restrictive model is assumed, then correspondingly more detailed results can be calculated. With a detailed model as well as knowledge of the anisotropy constants, the percentage of the susceptibility for each mechanism can be calculated.

Similar results are derived for the differential magnetostrictions under the condition that $\lambda = \frac{3}{2}\lambda_s[\langle\cos^2\theta\rangle - \frac{1}{3}]$. For an ideal moment distribution, the maximum value would arise for transverse fields and domain rotation. In most cases this result would carry over to useable samples. It is expected that a paper will follow comparing experimental susceptibility results on selected ferrite samples with the theory developed here.

An equation is given for the rotational susceptibility matrix applicable to microwave measurements on nonsaturated material on the condition that only nearest-neighbor domain interactions are present and that the total moments of all nearest-neighbor domains to any particular domain be equal to the macroscopic moments.

Acknowledgements—The author wishes to acknowledge PAUL E. NACE for many valuable discussions, Prof. H. W. WELCH, JR. for continued encouragement and Prof. HARVEY BROOKS for his critical reading of the original manuscript.

APPENDIX

Models for considering the normalized volume of material with its magnetic moment between θ and $\theta + d\theta$ have been proposed by HEISENBERG[18] and by AKULOV.[19] BROWN[2,3,4] has attempted to derive, on a model much like that proposed by HEISENBERG, an expression for $f(\theta)$ in a polycrystal. BROWN's model was one of domains with fixed and equal volume. The reasons for using such a model are, primarily, that it can be handled mathematically and that the important features are the energy densities. These energies will vary but little from model to model, so the results derived on the basis of the fictitious model must be expected to carry over to a more realistic one. This appendix uses mathematics similar to BROWN's and obtains the same $f(\theta)$. The model is more realistic but the technique of handling the exchange energy is questionable.

Consider N atomic magnetic moments per unit volume distributed among an unknown but large number of randomly oriented crystallites. If γ represents a particular direction in the macroscopic system and the number of moments oriented in the γ direction is N_γ, then it follows that

$$N = \sum_\gamma N_\gamma. \tag{26}$$

The γ direction denotes different directions in different crystallites.

The effect of the anisotropy energy is to keep the moments of the system aligned along "easy" crystallographic directions. It is to be assumed that all moments remain oriented along these easy directions, and that the effect of the anisotropy energy is entirely described by this assumption.

Another energy is the volume magnetostatic energy, i.e., the energy of a magnetic dipole in a magnetic field. This energy can be written:

$$V_s = \sum_\gamma N_\gamma A H_t \cos\theta \tag{27}$$

where:

A is a constant,
H_t is the total magnetic field,
θ is the angle between the magnetic field and the γ-direction.

The effect of local magnetostatic and magnetostrictive energies throughout the lattice will be to disorder the moments of the system. The number of ways in which the moments of the system can be distributed among N atoms such that N_γ have their moments in the γ-direction is:

$$W = \frac{N!}{\prod_\gamma (N_\gamma!)},$$

which by use of Stirling's approximation becomes

$$\ln W = N \ln N - \sum_\gamma N_\gamma \ln N_\gamma. \tag{28}$$

Equations 26, 27, and 28 are applicable to a paramagnet. For a ferromagnet the exchange energy must also be considered and is given by:

$$V_{ex} = \sum_\gamma \sum_{n.n.} N_\gamma A_{ex}[1-(\Delta\theta)^2]$$

where $\Delta\theta$ represents the angle between nearest-neighbor moments, A_{ex} is the exchange energy and $\sum_{n.n.}$ represents a sum over all nearest-neighbor moments to the moment in question. If at this point domain theory is introduced and intradomain moments are considered to be aligned, then the exchange energy can be written as:

$$V_{ex} = \sum_\gamma s N_\gamma A_{ex} - \frac{\delta}{a}(\Delta\theta)^2 A_{ex} \cdot S\tau \tag{29}$$

where s is the number of nearest neighbors, δ is the wall

thickness, a is the distance between moments, τ is a constant of the order of unity and S is the domain wall area. The sum is exclusive of the walls. Note that the first term of equation 29 is a volume energy term and the second a surface energy term. It is now necessary to make the restricting assumption that the wall area surrounding material oriented in the γ-direction is proportional to N_γ*. With this assumption:

$$V_{ex} = \sum_\gamma N_\gamma(sA_{ex} - D_1) \tag{30}$$

where D_1 is a constant.

Since the magnetoelastic energies and the internal demagnetizing factors act to "randomize" the distribution of the magnetic moments, it is now to be assumed that they act to put the material in a most probable orientation in the sense of an extremum of equation 28. Equations 26, 27, and 30 must also be stable with respect to variations in N_γ. Thus, using the technique of Lagrange multipliers, and putting the sum of all such variations equal zero gives:

$$\delta N_\gamma(B + CAH_t \cos\theta - \ln N_\gamma) = 0$$

where B and C are constants. From this it follows that

$$N_\gamma = \exp(B + CAH_t \cos\theta)$$

and that the fraction of the moments of the system in the γ-direction is:

$$f(\theta) = \frac{\exp(AH_t \cos\theta)}{\sum_\gamma \exp(AH_t \cos\theta)}. \tag{31}$$

In the foregoing discussion, the result of the magnetoelastic energy and the internal demagnetizing fields is not such a "random" orientation as the corresponding thermal problem where the energy of a particular particle is independent of the energy of its momentary nearest neighbor. In a ferromagnet the disorder is a static disorder and the configuration must move through a series of spatially interdependent configurations to arrive at a specified position. Under these circumstances the presence of potential maxima would weight a changing configuration away from an extremum of equation 28 and towards the previous equilibrium position.

If a material is in a most probable configuration in the presence of a magnetic field (H_{ap}), by virtue of being cooled through its Curie temperature in the presence of that field, and the field is changed by ΔH (where ΔH is not small), then the configuration will tend to the limiting value of a most probable configuration for $(H_{ap} + \Delta H)$. However, since potential maxima must first be surpassed (i.e., domain walls must be broken free of localized potential barriers and in some cases nucleated), the configuration will be between that of material in equilibrium in a field H_{ap} and in a field $(H_{ap} + \Delta H)$. If this material represents some most probable configuration for some intermediate field then the effective field can be represented as $(H_{ap} + \alpha\Delta H)$ where $0 \leqslant \alpha \leqslant 1$. The meaning of the "effective history field" D, used to define the parameter η, is $D = (\alpha - 1)\ \Delta H$. The remaining error, after this type of correction, will depend upon the material and upon the magnitude of the ΔH. Discussions are given in references 4 and 5.

* BROWN makes an attempt to make this assumption look reasonable in BROWN W. F., JR. *Phys. Rev.* **55,** 570 (1939).

REFERENCES

1. GANS R. *Phys. Z.* **13,** 1053 (1911).
2. BROWN W. F., JR. *Phys. Rev.* **52,** 325 (1937).
3. BROWN W. F., JR. *Phys. Rev.* **53,** 482 (1938).
4. BROWN W. F., JR. *Phys. Rev.* **54,** 279 (1938).
5. GRIMES D. M. and MARTIN D. W. *Phys. Rev.* **96,** 889 (1954).
6. TEBBLE R. S. and CORNER W. D. *Proc. Phys. Soc.* **63,** 1005 (1950).
7. STONER E. C. *Rev. Mod. Phys.* **25, 2** (1953).
8. BOZORTH R. M. and WILLIAMS H. J. *Rev. Mod. Phys.* **17,** 72 (1945).
9. VAN DER BURGT C. M. *Philips Res. Rep.* **8,** 91 (1953).
10. LANDAU L. and LIFSHITZ E. *Phys. Z. Sowjet.* **8,** 153 (1935).
11. PARK D. *Phys. Rev.* **98,** 438 (1955).
12. PARK D. *Phys. Rev.* **97,** 60 (1955).
13. POLDER D. *Phil. Mag.* **40,** 99 (1949).
14. RADO G. T. *Phys. Rev.* **89,** 529 (1953).
15. KERSTEN M. *Z. Phys.* **76,** 505 (1932).
16. BOZORTH R. M. *Ferromagnetism* p. 634. D. Van Nostrand, New York (1951).
17. BECKER R. and DORING W. *Ferromagnetismus* p. 142. Edward Bros., Ann Arbor (1939).
18. HEISENBERG W. *Z. Phys.* **96,** 287 (1931).
19. AKULOV N. *Z. Phys.* **69,** 78 (1931).

VOL. 3 1957

Note on the darkening of silver chloride*

(*Received* 14 *March* 1957)

In a study of the effect of cationic impurities on the darkening of silver halides,[1]* copper-containing silver chloride[2]† was found to be a particularly interesting system. Very low concentrations of copper can strongly influence the behavior of the crystal, and the effect of the copper depends in a striking and instructive manner on the conditions of preparation.

If silver chloride crystals containing a few parts per million of copper are grown from the melt, or annealed to 400°C, under nitrogen of atmospheric pressure, they show a barely perceptible color; if they are grown or annealed in chlorine under the same conditions, they show a strong yellow-brown coloration. The two states are readily and reversibly converted into each other by annealing under appropriate atmospheres. The spectra of the two states thus obtained are shown in Figs. 1 and 2. It is assumed that they represent the characteristic absorption of cuprous and cupric ions, respectively, dissolved in the silver chloride lattice.‡ This identification is supported by the fact that the crystal in the first state is strongly darkened by exposure to a suitably

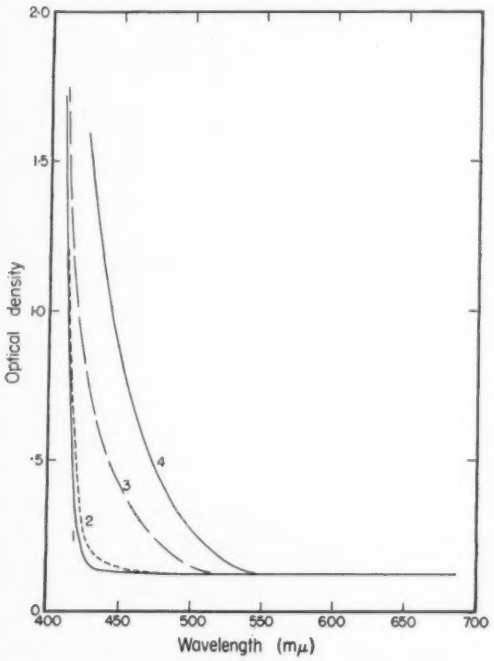

Fig. 1. Absorption spectrum of silver chloride containing cuprous ions. curve 1: pure crystals. curves 2, 3, and 4: Cu^{+} concentrations of 3, 30, and ~ 100 parts per million (in weight). All crystals were annealed in a nitrogen atmosphere. Crystal thickness, 5 mm; measurements at 25°C.

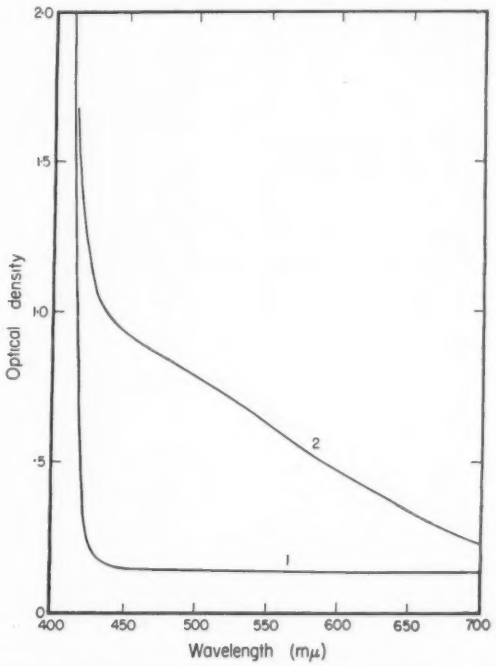

Fig. 2. Absorption spectrum of silver chloride containing cupric ions. curve 1: pure crystal; curve 2: Cu^{++} concentration of 4 p.p.m. Both crystals were annealed in chlorine. Crystal thickness, 8 mm; measurement at 25°C.

* Communication No. 1891 from the Kodak Research Laboratories. This note deals with the darkening in the interior of large crystals and not with the very different behavior of regions close to the surface.

† Reference 2 deals with earlier, incidental observations on copper in silver chloride.

‡ In the melt, too, the two ions are clearly recognizable by their absorption spectra.

absorbed radiation (e.g. 436 mμ), while in the second state no measurable darkening occurs. It is plausible that the Cu^+ ions provide hole traps—or, in chemical parlance, an internal halogen acceptor—which enable stable silver to be formed. The broad absorption band produced by exposure of the copper-sensitized crystal resembles the band first reported by HILSCH and POHL,[3] and attributed to silver. As shown in Fig. 3, the darkening proceeds at first linearly with exposure, then reaches a saturation value. This value is proportional to the Cu^+ concentration, at least from 0·05 to 5 p.p.m.

The purest silver halide crystals which we have prepared[4] show no dependence of the long-wavelength edge of the absorption spectrum[5] upon the atmosphere present in growing or annealing them. Samples grown in chlorine show no photochemical darkening; those grown in nitrogen show an efficient darkening which saturates,

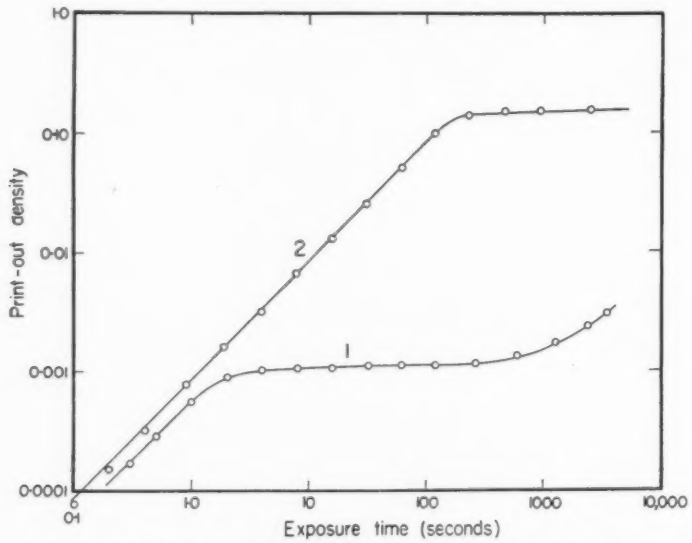

FIG. 3. Darkening of AgCl as a function of exposure. Optical density measured at 600 mμ. Exposure to 3×10^{15} incident photons/cm² sec at 436 mμ; curve 1: pure crystal; curve 2: crystal with 0·2 p.p.m. Cu^+. Crystal thickness, 8 mm; measurement at 25°C. (The second rise in curve 1 represents surface darkening.)

however, at very low, subvisual, levels (see curve 1 of Fig. 3).* It is quite possible that this darkening is caused by residual traces of copper. The same may well be true of some earlier observations of stronger darkening in large silver chloride crystals[6]† and of their yellow coloration upon annealing in chlorine.[7] Some of the most interesting properties of silver chloride crystals are no doubt often controlled by residual impurities and their state of valence.

Few experiments have as yet been made to determine in detail the constitution of the Cu^+ and Cu^{++} centers characterized by the spectra of Figs. 1 and 2. The presence of Cu^+ does not materially change the dark conduction of silver chloride crystals at room temperature, while Cu^{++} enhances it. The conductance of Cu^+ containing crystals is permanently increased by exposure. A corresponding appearance of the Cu^{++} spectrum has not been clearly established. The Cu^+ state is apparently quite stable at room temperature. The Cu^{++} state with the spectrum

* For the measurement of the very low density values recorded in Fig. 3, methods of extreme sensitivity are required which have been described elsewhere, NAIL N. R., MOSER F., URBACH F., *J. Opt. Soc. Amer.* **46**, 218 (1956).

† See also reference 2.

of Fig. 2 is less stable, particularly in strained crystals. There are indications that Cu^{++} ions may occur in two states, differing probably in dispersity and in their association with vacancies or V-centers. These questions and those of interstitial versus substitutional[8] positions of the copper ions require further study which is now under way.

We are much indebted to C. A. DUBOC for helpful discussions, to P. E. GODDARD for pure materials, and to R. L. DEHM for excellent spectrochemical data.

Research Laboratories F. MOSER
Eastman Kodak Company N. R. NAIL
Rochester 4, N.Y. U.S.A. F. URBACH

VOL. 3 1957

REFERENCES

1. NAIL N. R., MOSER F., GODDARD P. E., and URBACH F. *Bull. Amer. Phys. Soc.* **30,** No. 2, 34 (1955).
2. HECHT K. *Z. Physik.* **77,** 235 (1932); STASIW O. and TELTOW J. *Nachr. Akad. Wiss. Göttingen* 93 (1941).
3. HILSCH R. and POHL R. W. *Z. Phys.* **64,** 606 (1930).
4. NAIL N. R., MOSER F., GODDARD P. E., and URBACH F. The Preparation of Silver Halide Crystals of High Purity (to be published in *Rev. Sci. Instrum.* (1957)).
5. MOSER F. and URBACH F. *Phys. Rev.* **102,** 1519 (1956).
6. BROWN F. *Phys. Rev.* **105,** 93 (1957); WAINFAN N. *Phys. Rev.* **105,** 100 (1957).
7. LEHFELDT W. *Nachr. Ges. Wiss. Göttingen* **1,** 171 (1935).
8. TELTOW J. *Z. Phys. Chem.* **195,** 197, No. 3 (1950).

On the high temperature heat conductivity of insulators

(*Received* 24 *April* 1957)

THE kinetic formula for the heat conductivity K of an insulator is given by[1]

$$K = 1/3 c_v l v_s \tag{1}$$

where c_v is the specific heat per unit volume, l the mean free average path of the phonons and v_s is an appropriately averaged velocity of sound.

DUGDALE and MACDONALD[2] have suggested that reasonable values of K are obtained if the mean free path l is more or less empirically taken as

$$l = A_0/\alpha\gamma T \tag{2}$$

where A_0 is the lattice constant, α the thermal expansion coefficient, γ the Gruneisen constant and T is the absolute temperature.

One purpose of this note is to point out that equation (2) may be justified for $T > \theta_D$ by the early work of AKHIESER[3] who showed that in this case [ref. 3, p. 284, equation 29]

$$K = \rho v_s^4/\gamma^2 T\omega_{\max} \tag{3}$$

where ρ is the density and $\omega_{\max}$ is the angular Debye frequency. Replacing $\omega_{\max}$ by $\pi\, v_s/A_0$ and using the Gruneisen relation $\gamma = \alpha/c_v\chi_T$ where the isothermal compressibility χ_T may be roughly related to the velocity of sound by the relation

$$1/\chi_T \cong \rho v_s^2 \tag{4}$$

we see from a comparison of equations (1) and (3) that except for a numerical factor of the order of unity equation (2) must be true for $T > \theta_D$ For $T < \theta_D$, equation (2) is certainly not valid as shown by POMERANCHUK[4] and also by KLEMENS.[5]

Secondly, the author would like to mention that equations (1) and (2) may be combined to yield an alternative form for K, namely

$$K = A_0/3\gamma^2 T\chi_T^{3/2}\rho^{1/2}. \tag{5}$$

This form is more suitable for estimating the pressure dependence of the thermal conductivity $(\partial K/\partial P)_T$ of insulators. The Gruneisen constant may be assumed pressure independent to the extent that the compression of a solid may be adequately described by a quadratic of the form $-\Delta V/V_0 = ap\text{-}bp^2$. Since γ may be computed from a and b, to find K it suffices to know these and A_0.

BRIDGMAN[6] has found a 36 per cent increase of K for NaCl under 10^4 bars pressure at 30°C and 75°C. Using BRIDGMAN's compressibility data on NaCl, we estimate from equation (5) a change of 34 per cent is to be expected. This agreement must be considered as somewhat fortuitous in view of the gross simplifications embodied in the use of equations (2) and (4).

Institute for the Study of Metals A. W. LAWSON
University of Chicago
Chicago 31
Illinois

REFERENCES

1. DEBYE P. *Vortrage über die Kinetische Theorie* B. G. Tuelner, Leipsig (1914).
2. DUGDALE J. S. and MACDONALD D. K. C. *Phys. Rev.* **98**, 1751 (1955).
3. AKHIESER A. *J. Phys., Moscow* **1**, 277 (1939).
4. POMERANCHUK I. *J. Phys., Moscow* **4**, 357 (1941); **6**, 237 (1942).
5. KLEMENS P. G. *Proc. Roy. Soc.* A**208**, 108 (1951).
6. BRIDGMAN P. W. *The Physics of High Pressures* G. Bell, London (1931).

The absorption spectrum of solid antimony trisulphide

(*Received* 10 *April* 1957)

OPTICAL absorption in thin laminae of antimony trisulphide has been measured as part of a study of the properties of some sulphides of arsenic, antimony and bismuth.

Pure antimony trisulphide was prepared by dissolving antimony trichloride in dilute hydrochloric acid, under an argon atmosphere as antimony trichloride solutions are rapidly oxidized by air, and treating the solution with hydrogen sulphide. Antimony trisulphide can be distilled unchanged *in vacuo*(1) and films up to 900 Å thick were prepared by evaporation from a tungsten strip on to fused quartz discs at 10^{-5} mm Hg. The films obtained were perfectly clear, yellow to orange in colour, uniform and free from pin-holes. The absorption of a film was determined in a Beckmann Model DU spectrophotometer by measuring the optical density (the decadic logarithm of the ratio of the intensity of the incident light, I_0, to that of the transmitted light, I_t) of the specimen and quartz disc mount relative to that of a similar quartz disc alone. The spectra are reproducible and Fig. 1 shows the optical density as a function of wavelength from 0·2 to 1μ for three films of different thicknesses. The thickness, t, of the thickest film was determined approximately by weighing and hence absolute values of the absorption coefficient, k, (defined by the equation $I_t = I_0 \cdot e^{-kt}$) were calculated; in Fig. 1 these values of absorption coefficient, which correspond only to the thickest film, are shown alongside those of optical density. The absolute

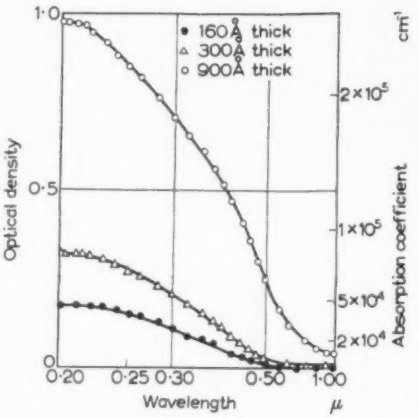

FIG. 1. The absorption spectra of antimony trisulphide films of three different thicknesses. The absorption coefficient scale corresponds to the 900 Å thick film.

● 160 Å thick
△ 300 Å thick
○ 900 Å thick

absorption coefficients so calculated were used to calculate the thicknesses of the other films.

From measurements on films sufficiently thin to permit the determination of the optical spectrum it is not possible to determine accurately the wavelength at which the absorption curve first begins to rise steeply, and thicker films must be used. Fig. 2 gives the absorption from 0·4 to 0·7μ of a film 2500 Å thick and shows that the onset of strong absorption is at 0·525μ.

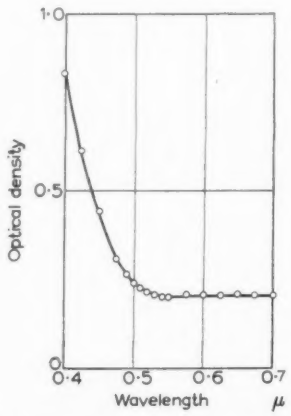

FIG. 2. Absorption of an antimony trisulphide film 2500 Å thick.

Beyond $0{\cdot}525\mu$ there is no significant true absorption. The absorption coefficient of antimony trisulphide at $0{\cdot}7\mu$ is practically zero[2] and antimony trisulphide has excellent transparency for the near infra-red.[3] Thus, in Fig. 1, the apparently large value, about 10^4 cm^{-1}, of the absorption coefficient beyond $0{\cdot}525\mu$ arises from reflection and scattering losses. The smaller absorption of the thinner films in this region shows that reflection losses are negligible and that the apparent absorption in the thicker film is due almost entirely to scattering.

The main features of the spectrum are the sharp rise at $0{\cdot}525\mu$, the continuous increase to $0{\cdot}2\mu$ and the magnitude of the absorption coefficient at this wavelength. The marked flattening of the absorption curve from $0{\cdot}22$ to $0{\cdot}20\mu$ suggests the possibility of a maximum just below $0{\cdot}2\mu$. The absorption coefficient at $0{\cdot}2\mu$ is so large that the absorption must be attributed to the bulk lattice and not to impurities. The threshold of the lattice absorption is $0{\cdot}525\mu$ and the long wavelength photoconductivity threshold is at $0{\cdot}8\mu$.[4] Thus photoconductivity is not associated with lattice absorption and may arise either from lattice imperfections and impurities or from the long wave absorption being due to exciton formation. The absence of any shoulder in the absorption curve suggests that exciton formation is unlikely and it seems more probable that photoconductivity originates from lattice imperfections. In this connection it has been shown that the refractive index is related to the infra-red threshold of sensitivity for a wide range of substances and hence it has been suggested that there are indications that in antimony trisulphide the photoelectrons may arise from lattice imperfections.[5]

The author is indebted to Professor T. S. WHEELER for his continued encouragement.

Department of Chemistry W. P. DOYLE
University College
Dublin

REFERENCES

1. KRAFFT F. and DAMM F. *Ber. Dtsch. Chem. Ges.* **40**, 4775 (1907).
2. FLEISCHMANN R. and SCHOPPER H. *Z. Phys.* **129**, 285 (1951).
3. SCHOPPER H. *Z. Phys.* **131**, 215 (1952).
4. COBLENTZ W. W. *Bur. Stand. Bull.* (*Wash.*) **16**, 595 (1920).
5. Moss T. S. *Proc. Phys. Soc.* B**63**, 167 (1950).

New semiconducting ternary compounds

(*Received* 20 *May* 1957)

WE HAVE synthesized a number of ternary compounds which are found in the natural state. These are enargite, Cu_3AsS_4; famatinite, Cu_3SbS_4; tetrahedrite, Cu_3SbS_3; tennantite, Cu_3AsS_3; wolfsbergite, $CuSbS_2$; and proustite, Ag_3AsS_3. Several new compounds, based on the stoichiometry of these natural compounds, were also synthesized: Cu_3SbSe_4, $CuSbSe_2$, $CuAsS_2$, $CuAsSe_2$, $AgSbSe_2$, $AgSbTe_2$ and Ag_3AsSe_3. All are semiconductors.

The compounds were prepared by melting the stoichiometric amounts of the component elements in sealed quartz tubes containing a nitrogen pressure of approximately 2/3 of an atmosphere. Heating was done slowly so that the major portion of alloying was carried out at temperatures at which the vapor pressures of As, Se, and S were low. The average weight of the ingots made was 50 g. Usually 0·5 g of As, Se, and S were added in excess of the stoichiometric amount to take care of vaporization. However, in nearly all cases, practically no loss was noted after the run.

X-ray powder patterns were taken to establish that the natural-occurring minerals, shown in Table 1, were synthesized. The X-ray data obtained to date for the new compounds are summarized in Table 2. In addition, microscopic examination and thermal analysis data showed that the compounds were single phase. The melting points are shown in Table 3. It was observed during the thermal analyses that all of the compounds, except $CuAsS_2$, exhibited rather low dissociation pressures at as much as 100°C above the melting point; hence, they may be amenable to relatively easy zone refining and single crystal production.

Preliminary resistivity-temperature data on impure polycrystalline specimens indicate that the intrinsic energy gaps lie in the range of 0·2 to 1·0 eV. More accurate data will be obtained with purer single crystal specimens.

Table 1. Natural-occurring minerals synthesized

Name	Formula	Crystal structure	Remarks
Enargite	Cu_3AsS_4	Orthorhombic[1,2]	Structure related to ZnS (Wurtzite) structure.
Famatinite	Cu_3SbS_4	Reported to be cubic[3–6]	Structure information meager.
Tetrahedrite	Cu_3SbS_3	Cubic [1,2]	Structure similar to cubic ZnS, with one-quarter of the sulfur positions unoccupied.
Tennantite	Cu_3AsS_3	Cubic [1,2]	
Wolfsbergite (Chalcostibite)	$CuSbS_2$	Orthorhombic[1,2]	Layer-type structure. Each layer resembling ZnS (Wurtzite) and held together by weak Sb—S bonds.
Proustite	Ag_3AsS_3	Rhombohedral[6,9]	Each As atom forms pyramidal bonds to 3 sulfur atoms. Each sulfur atom is bonded to two Ag atoms.

Table 2. New ternary compounds

Compound	Powder X-ray results
Cu_3SbSe_4	Isostructural with Cu_3SbS_4.
$CuSbSe_2$	Pattern very similar to that of $CuSbS_2$. Some slight differences prevent calling it isostructural with $CuSbS_2$.*
$CuAsS_2$ | $CuAsSe_2$	These two compounds are isostructural. They have a structure related to Zincblende.[11]
$AgSbSe_2$ | $AgSbTe_2$	These two compounds are isostructural and have NaCl structure.[10]
Ag_3AsSe_3	Crystal structure not known.

* $TlSbSe_2$ has been prepared by KOLOMIETS and GORIUNOVA[7] and found to be othorhombic. Tl can have oxidation states of 1 and 3.

Table 3. Melting point data for ternary compounds

Compound	Melting point °C
Cu_3AsS_4	655
Cu_3SbS_4	555
$CuSbS_2$	535
Ag_3AsS_3	480
Cu_3SbS_3	555
Cu_3AsS_3	640
Cu_3SbSe_4	425
$CuSbSe_2$	460
$CuAsS_2$	625
$CuAsSe_2$	415
$AgSbSe_2$	610
$AgSbTe_2$	555
Ag_3AsSe_3	385

It is a pleasure to acknowledge the help of S. GELLER, which included much of the X-ray work and many stimulating discussions. The X-ray work preformed by R. G. TREUTING, Mrs. M. READ, Miss B. PRESCOTT, and V. B. BALA is appreciated. The help derived through discussions with F. J. MORIN, W. G. PFANN, J. H. SCAFF, J. M. WHELAN and the editorial comments of N. B. HANNAY are also appreciated.

J. H. WERNICK and K. E. BENSON

Bell Telephone Laboratories Inc.
Murray Hill, N.J.

REFERENCES

1. WELLS A. F. *Structural Inorganic Chemistry* Oxford (1950).
2. WYCKOFF R. G. *Crystal Structures* Vol. 1 Interscience, New York (1948).
3. DE JONG W. F. *Z. Krist. allogr.* **68,** 522 (1928).
4. WALDO A. W. *Amer. Min.* **20,** 575 (1935).
5. HERMANN C., LOHRMANN O., and PHILLIP H. compilers *Strukturbericht* 2, (1928–1932).
6. *A.S.T.M.* Card for famatinite.
7. KOLOMIETS B. T. and GORIUNOVA N. A. *J. Tech. Phys., Moscow* **25,** No. 6, 984 (1955).
8. HARKER D. *J. Chem. Phys.* **4,** 381 (1936).
9. WERNICK J. H., GELLER S., and BENSON K. E. To be published.
10. GELLER S. and WERNICK J. H. To be published.
11. GELLER S. Private communication.

VOL. 3 1957

Chemical evidence for a barrier in electroluminescent zinc sulfide phosphors

ELECTROLUMINESCENT (EL) zinc sulfide phosphors are usually prepared, prior to crystallization, with relatively large (0·1 per cent) amounts of copper ion, together with a halide coactivator. DESTRIAU[1] has suggested the presence of a surface copper layer, after crystallization, and FROELICH[2] has indicated the incomplete incorporation of copper in the phosphor. The effect of the halide coactivator on the proportion of copper which is incorporated has been reported by LARACH *et al.*[3] Chemical analysis of the surface of EL phosphors was reported by DESTRIAU,[4] who used acid to leach the surface of zinc sulfide powders. Since acid leaching has the inherent possibility of reprecipitation of copper sulfide, the present investigation involved a detailed chemical analysis of the surface of EL–ZnS:Cu:I phosphors, using alkali cyanide as the removal and complexing agent for copper.

Analyses* have shown that the outer layer on the EL phosphor particles consists of copper sulfide, followed by an interdiffused system of copper and zinc sulfides. Thus, the outermost portion is mainly copper sulfide, but as the penetration distance increases, the copper content decreases while the zinc content increases. It is this interdiffused region which can be construed as containing the barrier assumed by many to be essential for EL. The following experiment, outlined schematically in Fig. 1, illustrates the importance of the presence of a large excess of Cu in halide coactivated EL phosphors, not only to promote the formation of the above-mentioned barrier but to shield it from any further destructive action of any excess phase of halide.

* Copper analyses were carried out by Dr. M. C. GARDELS, using a spectrophotometric method, to be published elsewhere. Error of 0·002 per cent was involved.

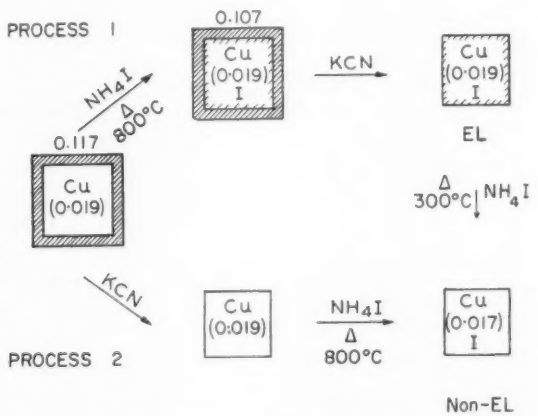

FIG. 1. Barrier effects in ZnS : Cu phosphors. Heavily shaded areas represent excess copper sulfide; lightly shaded areas represent inter-diffused copper-zinc-sulfide.

Non-luminescent ZnS : Cu was prepared by crystallization in H_2S (at 1100°C) in the absence of halide. This material had 0·117 per cent by weight of total copper, and 0·019 per cent incorporated copper. Phosphors were then prepared from this starting material by two different procedures: (1) the first involved the diffusion, at elevated temperatures, of iodide coactivator into the material, followed by digestion with alkali cyanide, while (2) the second process involved digestion with alkali cyanide *before* the iodide diffusion. The resultant phosphors contained, within the limits of the analyses, the same amounts of incorporated copper, and all exhibited comparable photoluminescence and cathodoluminescence, but only the phosphor arrived at in the process (1) was *electroluminescent*.

The EL phosphor arrived at by process (1) was annealed at 300°C, in N_2, with and without halide. The phosphor, annealed without halide, retained its photo- and cathodo-luminescence emission intensity, but showed a decrease in EL emission intensity by a factor of 2.

The phosphor, annealed with halide, while maintaining its photo- and cathodo-luminescence emission intensity, showed a decrease in EL emission intensity by a factor of 30. In both cases, a shift in emission color to longer wavelengths was observed.

Thus, in addition to the effects due to redistribution of copper by thermal diffusion, the phosphor annealed in iodide shows the results of chemical interaction with the surface phase.

Our interpretation of this experiment is that volume iodide was obtained in materials which were prepared by either process, thereby enabling the formation of centers which gave rise to photo- and cathodo-luminescence. During the iodide diffusion, iodide apparently reacts with copper sulfide to give copper iodide, which has an appreciable vapor pressure at the temperature of diffusion. In the case of process (1), sufficient copper, in excess of barrier copper, is available for reaction with any iodide remaining during the period of firing, while in the case of process (2), barrier copper, if existing, is removed, the resulting phosphor being non-electroluminescent.

Thus, for efficient electroluminescence from zinc-sulfide-type phosphors, volume copper activator, volume coactivator, and an interdiffused copper-zinc-sulfide region appears necessary.

SIMON LARACH
ROSS E. SHRADER

RCA Laboratories
Radio Corporation of America
Princeton, N.J.

VOL
3
195

REFERENCES

1. DESTRIAU G. *Phil. Mag.* **38,** 700 (1947).
2. FROELICH H. C. *J. Electrochem. Soc.* **100,** 496 (1953).
3. LARACH S., SHRADER R. E., and HEGYI I. J. *Luminescence Symposium* Paper 40. Electrochemical Society, San Francisco (1956).
4. DESTRIAU G. *Proc. Inst. Radio Engrs.* **43,** 1911 (1955).

Small-Angle Scattering of X-rays. A. GUINIER and G. FOURNET. Translation by C. B. WALKER, with a bibliography by K. L. YUDOWITCH. John Wiley and Sons, New York; Chapman and Hall, London. 1955. xi + 268 pp. with 78 figs.

VOL. 3 1957

THIS book deals principally with the continuous scattering of X-rays at small angles which arises from heterogeneity of electron density in the specimen on a scale of some tens to some hundreds of X-ray wavelengths. As a tool for studying the fine structure of solids, colloids, and even gases, small-angle scattering measurements have found a wide range of applications in the last 20 years, and a quite voluminous literature has grown up. This first comprehensive textbook on the subject, written by two of the leading exponents of the art, makes a timely appearance. It offers a carefully considered and well-balanced review of theory and experiment, and clearly indicates both the potentialities and limitations of small-angle scattering measurements.

A brief introductory chapter followed by a longer one on general theory deal with the underlying X-ray interference theory of small-angle scattering, and occupy the first third of the book. Chapter 3 describes experimental techniques, and the following chapter gives examples of how experimental data have been, or in some cases should have been interpreted. Then comes a brief account of comparisons of small-angle scattering measurements of particle size with those obtained from electron microscope and DEBYE-SCHERRER line-broadening measurements. Applications of small angle scattering measurements in diverse fields are surveyed in the concluding chapter. The extensive bibliography by YUDOWITCH is a revision of that compiled in 1952 for the American Crystallographic Association. It now contains 569 titles.

The treatment of the basic theory is clear and concise and presents a valuable collation and summary of the work of DEBYE, GUINIER, FOURNET, HOSEMANN, KRATKY, and POROD in this field. A central problem in the interpretation of small-angle scattering arises from the presence of both interparticle and intraparticle interference effects. It is emphasized that this situation prohibits a naive interpretation of a maximum on the scattering curve in terms of a characteristic interparticle distance, as has been assumed by some investigators. However, in the favorable case of spherically symmetric identical particles measurements at several particle concentrations can give both the size of the particles and the law governing their spatial separation. Since BABINET's principle applies to an ensemble of particles scattering X-rays at small angles, an ambiguity arises with regard to the particle-pore configuration in dense systems. However, the complementary scatterers have in common the same surface area, and it is shown that this quantity can be derived directly from the intensity of scattering on the tail of the scattering curve. Hence specific surface measurements can be made on catalysts and adsorbents. In common with other methods of measuring particle size, difficulties of interpretation arise from heterogeneity of particle size and shape. On the other hand, this heterogeneity acts advantageously in reducing the effect of interparticle interference. The authors describe promising small-angle scattering studies of macromolecules in solution. Here, the uniformity of particle size and shape, and the possibility of varying concentration, facilitate interpretation of measurements. Other small-angle scattering studies of interest mentioned are those of gases near the critical point, the recent work of TWEET on liquid helium above and below the λ-point, and the measurements on deformed metals which indicate the presence of submicroscopic cavities. It is emphasized, too, that structure models for segregation and precipitation in solid solutions built upon wide-angle X-ray diffraction evidence must be compatible with the small-angle scattering pattern.

With this good basic text available, small-angle scattering studies should now advance in quantity and quality, though to derive real advantage from the theory and interpretative procedures laid out only the very best experimental techniques should be used. The translation from the French has been competently done by C. B. WALKER, and the text is commendably free from typographic errors.

A. R. LANG

CONTENTS LISTS OF VOLUME 2, NOS. 1 AND 2

Volume 2 No. 1

page

N. Sclar et E. Burstein:
Ionisation par choc d'impuretés dans le germanium 1

H. Kanzaki:
Défauts ponctuels dans un réseau cubique à faces centrées—I 24

Gerald W. Sears:
Fusion et solidification de la toluidine *p* 37

Herbert B. Rosenstock:
Points critiques dans un réseau à trois dimensions 44

J. F. Dewald:
Phénomènes transitoires dans la conductibilité ionique de films d'oxyde aux champs élevés 55

L. G. Parratt et E. L. Jossem:
Etats excités par les rayons X ("excitons") et largeur de la bande—de valence dans KC1 . 67

Compte-rendu de réunion
Compte-rendu du Second Congrès sur la Physique des Semi-conducteurs 72

Lettre au Rédacteur 83

Volume 2 No. 2

J. Owen, M. E. Browne, V. Arp et A. F. Kip:
Résonance électronique de spin et mesures de susceptibilité magnétique d'alliages dilues de Mm dans Cu, Ag et Mg 85

W. C. Koehler et E. O. Wollan:
Etude par la diffraction des neutrons des propriétés magnétiques des composes $LaBO_3$, du genre perovskite 100

H. Kanzaki:
Défauts ponctuels dans un réseau cubique à face centrée—II. Diffusion des rayons X . 107

R. G. Shulman:
Calcul des énergies d'un accepteur dans le germanium et le silicium dans l'approximation de liaison forte 115

G. Diemer et W. Hoogenstraten:
Diffusion par excitons et diffusion "ambipolaire" dans les cristaux de CdS 119

H. Ehrenreich:
Diffusion des électrons dans InSb 131

Lettre au Rédacteur
Andreas Kelen: Sur la constante dielectrique des isolants plastiques 150

Volume 2 No. 1

page

И. Скляр и Е. Бурштейн :
Ионизация примесей при столкновениях в германии 1

Х. Канзаки :
Точечные дефекты в кубической гране-центрированной решетке. 1. Искажения в окрестности дефектов 24

Джералд У. Сирс :
Плавление и отвердевание *p*-толуидина 37

Герберт Б. Розеншток :
Критические точки в трех измерениях 44

Дж. Ф. Дьюолд :
Переходные явления в ионной проводимости пленок окислов в сильных полях 55

Л. Дж. Парретт и И. Л. Джоссем :
Состояние, возбуждаемые рентгеновскими лучами („экситоны"), и ширина валентной зоны в KCl 67

Фрэнк Герман :
Отчет о втором симпозиуме по физике полупроводников 72

Письмо в редакцию :
Масаясу Уэта и Масамитсу Хираи: Обесцвечивание центров окраски в кристалле KCl, содержащем U-центры 83

Volume 2 No. 2

Дж. Оуэн, М. Е. Браун, В. Арп, А. Ф. Кипп :
Спин-электронный резонанс и измерение магнитной восприимчивости в твердых слабых растворах Mn в Cu, Ag и Mg 85

В. С. Келер и Е. О. Воллан :
Изучение магнитных свойств перовскито-подобных соединений $LaBO_3$ посредством диффракции нейтронов 100

Х. Канзэйк :
Местные дефекты в гране-центрированной кубической решетке—II. Эффекты в рассеянии γ-лучей 107

Р. Г. Шульман :
Вычисления энергий акцепторов в германии и кремнии в модели плотной упаковки 115

Г. Даймер и В. Хугенстратен :
Амбиполярная и экситонная диффузия в кристаллах CdS 119

Г. Эренрейх :
Рассеяние электронов в InSb 131

Письмо в редакцию :
А. Келен: О диэлектрическом поглощении в пластмассовых изоляторах . 150

VOL. 3 1957

Volume 2 No. 1

page

N. SCLAR UND E. BURSTEIN:
Die Stossionisation von Verunreinigungen in Germanium 1

H. KANZAKI:
Punktförmige Fehlstellen im Flächenzentrierten Gitter—I. Die Verzerrungen in der Umgebung einer Fehlstelle 24

GERALD W. SEARS:
Das Schmelzen und Erstarren bei p-Toluidin 37

HERBERT B. ROSENSTOCK:
Die kritischen Punkte in drei Dimensionen 44

J. F. DEWALD:
Übergangseffekte der Ionenleitfähigkeit von anodischoxydierten Schichten bei hohen Feldstärken 55

L. G. PARRAT UND E. L. JOSSEM:
Durch Röntgenstrahlen angeregte Zustände (exzitonen) und die Breite des Valenzbandes in KCl 67

Briefe an der Herausgeber 83

Volume 2 No. 2

J. OWEN, M. E. BROWNE, V. ARP, UND A. F. KIP:
Messungen der Elektronenspinresonanz und der magnetischen Suszeptibilität von verdünnten Legierungen von Mn in Cu, Ag und Mg 85

W. C. KOEHLER UND E. O. WOLLAN:
Untersuchung der magnetischen Eigenschaften der Perowskit-ähnlichen Verbindungen $LaBO_3$ mit Neutronenbeugung 100

H. KANZAKI:
Punktförmige Fehlstellen im kubisch flächenzentrierten Gitter—II. Ihre Wirkung auf die Streuung von Röntgenstrahlen 107

R. G. SHULMAN:
Berechnung der Akzeptorenenergien in Germanium und Silizium bei starker Bindung . 115

G. DIEMER UND W. HOOGENSTRAATEN:
Ambipolare und Exzitonen-Diffusion in CdS Kristallen 119

H. EHRENREICH:
Die Streuung von Elektronen in InSb 131

Briefe an der Herausgeber 150

VOL
3
195

J. Phys. Chem. Solids Pergamon Press 1957. Vol. 3. pp. 165–174.

THE SUPERCONDUCTIVE CRITICAL TEMPERATURE AND THE ELECTRONIC SPECIFIC HEAT OF IMPURE TIN*†

E. A. LYNTON, B. SERIN, and M. ZUCKER‡

Rutgers University, New Brunswick, New Jersey

(*Received* 16 *April* 1957)

VOL. 3 1957

Abstract—From measurements of the threshold magnetic field as a function of temperature for specimens of tin containing 0·04 to 2·0 at. per cent of various impurities we have obtained the superconductive critical temperature, T_c, of these samples, as well as the temperature coefficient, γ, of the electronic specific heat of the normal phase. We find that the change in T_c produced by the impurities consists of two parts. There is a decrease which is linearly proportional to the increase in residual resistance ratio and hence to the decrease in electronic mean free path. Superimposed on this decrease there is an increase in T_c. Our results also show that the measurable changes in γ are positive for all solutes, indicating a minimum in the density of states at or near the Fermi energy. We believe that the second, positive part of the change in T_c is due to the increase in γ, and find that the correlation between these quantities is in reasonable agreement with the recent theory of BARDEEN, COOPER, and SCHRIEFFER.[19] During the course of our work we also obtained a value of γ for pure tin which agrees well with a recent calorimetric result. Measurements of the residual resistance ratio of our samples show, as expected, that below the solubility limit this ratio increases linearly with impurity concentration with a slope which depends on the atomic radius of the impurity as well as on its valence.

1. INTRODUCTION

EXTENDING and improving on previous work at this laboratory,[1,2] we have measured the threshold magnetic field as a function of temperature for pure tin as well as for specimens of tin containing various low concentrations of antimony, bismuth, cadmium, indium, lead, mercury, or zinc. From these magnetic field values we have obtained the superconductive critical temperature in zero field, T_c, for each of the samples. We have also evaluated the temperature coefficient γ of the electronic specific heat of the normal state, γT, where T is the absolute temperature.

T_c was calculated from threshold field measurements in the temperature region $0{\cdot}9\ T_c < T < T_c$. In this region the threshold field H_c is, to a very good approximation, a linear function of the temperature, so that T_c could be found by extrapolating H_c as a function of T to $H_c = 0$, using the method of least squares.

The value of γ was determined from measurements of H_c in the range $0{\cdot}4\ T_c < T < 0{\cdot}6\ T_c$. According to the thermodynamic theory of the phase transition,[3] one can show that

$$c_n(T) - c_s(T) = -\frac{VT}{4\pi}\frac{d}{dT}\left(H_c\frac{dH_c}{dT}\right), \qquad (1)$$

where $c_n(T)$ and $c_s(T)$ are, respectively, the specific heats in the normal and in the superconductive phase. The lattice contribution to the specific heat is presumably the same in both phases, so that this difference is in turn equal to the difference between the electronic contributions to the specific heats of the two phases. We know that[4]

$$c_{ne}(T) = \gamma T, \qquad (2)$$

* This work has been supported in part by the Office of Naval Research and by the Rutgers University Research Council.

† This work formed part of a dissertation submitted by M. ZUCKER to the Graduate Faculty of Rutgers University in partial fulfillment of the requirements for the Ph.D. degree.

‡ Present address: Airborne Instruments Laboratories, Mineola, Long Island, N.Y.

where the subscript e refers to the electrons, and recent calorimetric measurements on pure tin[5] have shown that at temperatures well below the critical temperature in zero field

$$c_{se}(T) = a\gamma T_c \exp[-bT_c/T]. \qquad (3)$$

Substituting these into equation (1), and integrating from 0°K gives

$$\gamma T - a\gamma T_c[-Ei(-bT_c/T)] = -\frac{V}{8\pi}\frac{d}{dT}(H_c^2),$$

where

$$-Ei(-x) \equiv \int_x^\infty \frac{e^{-v}}{v}\,dv.$$

A further integration and rearrangement of terms finally yields

$$H_0^2 - H_c^2 = \frac{2\pi\gamma T^2}{V}[1-f(t)], \qquad (4)$$

where

$$f(t) \equiv \frac{2a}{t^2}\int_0^t Ei(-b/x)\,dx, \quad t \equiv T/T_c,$$

and H_0 is the threshold field at 0°K. The function $f(t)$ was evaluated by numerical integration. In order to use equation (4) to evaluate γ, the threshold field measurements at low temperatures were extrapolated to find H_0 for each of the specimens. On the assumptions that the electronic specific heat in the superconductive state of all samples obeys equation (3) with the same values of a and b, but different values of γ and T_c, equation (4) was then used to obtain values of γ for each set of values of T and $H_c(T)$. This procedure is further discussed in a later section.

At the conclusion of the magnetic measurements, the electrical resistance of each of our specimens was measured both at 4·2°K and at room temperature to determine whether the impurity had dissolved and had formed a homogeneous alloy, and to obtain a measure of the electronic mean free path in the normal phase. From these values of the resistance we obtain, for each sample, the ratio

$$\rho = R_0/[(R-R_0)(1-\alpha t_c)], \qquad (5)$$

which we will call the residual resistance ratio. R_0 is the resistance measured at 4·2°K, R that at room temperature, $T = 273+t_c$. R_0 is the residual resistance which arises entirely from impurity scattering. $(R-R_0)$, according to MATTHIESSEN's rule, is the high temperature resistance due to lattice scattering,[6] reduced to 0°C by means of the term $(1-\alpha t_c)$, where α is the known temperature coefficient of resistance for pure tin at room temperature. Thus the denominator in the above equation is presumably a property of pure tin, and independent, at least to a first approximation, of the impurity content of the specimen. The effect of the impurities is thus contained to the same approximation in the numerator only, and the purpose of dividing this by the denominator is to obtain a quantity inversely proportional to the low temperature electronic mean free path without having to make absolute resistivity measurements.

2. EXPERIMENTAL DETAILS

(a) *Preparation of samples*

The series of samples of any given impurity was prepared by adding the solute to Johnson-Matthey 99·998 per cent pure tin in sufficient quantities to make a large ingot of the highest impurity concentration desired. Before cooling, this mixture was kept molten *in vacuo* for 24 hours to ensure a uniform distribution of impurity. To a part of this ingot more pure tin was then added to yield a more dilute mixture, and the same procedure was repeated for each lower concentration. In this way we always dealt with large quantities of material, which could be weighed accurately and handled easily.

Several precautions were taken to prevent contamination of the samples by unwanted impurities. Each ingot was washed in a solution of 50 per cent concentrated HCl and 50 per cent distilled water to dissolve any iron which might have been left by the cutting instruments. All Pyrex tubes in which the samples were melted and cast were washed in HNO_3, rinsed repeatedly with distilled water, and finally heated to drive off any remaining moisture.

The final samples were made by vacuum casting the crude ingots into Pyrex tubes, 1 mm in diameter, and about 60 mm long. The samples were cooled slowly under a slight temperature gradient which caused the bottom of the specimen to solidify first. Before being used the specimens were annealed *in vacuo* for at least 30 days.

(b) *Determination of the threshold field values*

The threshold field value of a specimen at any given temperature was determined from the fact that the magnetic induction in a metal in the superconductive phase is zero. Each sample was closely surrounded by a detection coil of many turns of wire connected to a galvanometer. Hence with the sample superconductive, very little flux threaded through the coil, and a change in the external field under these conditions did not induce an appreciable e.m.f. across the ends of the coil. However, when the external field was increased from a value just below threshold to a value just above it, the sample became normal, and the magnetic induction in the sample increased from zero to the full applied field value, resulting in a large change in the flux threading the coil.

VOL. 3 1957

Thus a large e.m.f. was induced in the coil, giving an appreciable deflection of the galvanometer.

The external magnetic fields were provided by a combination of a Helmholtz coil outside the Dewar assembly, and a solenoid placed around the helium Dewar in the liquid nitrogen bath. The coil produced a field which was uniform to one part in 10^3 in its median plane across the sample site, and to one part in 10^2 over the length of the samples. The solenoid field was uniform to one part in 10^3 over the entire volume occupied by the specimens. This uniformity was achieved by overwinding the ends according to a design recommended by GARRETT.[7]

The procedure used at each temperature was to bring the total external field produced by both the Helmholtz coil and the solenoid to a value a few oersteds below the estimated threshold field value. Most of this field was produced by the current in the Helmholtz coil, which was measured to one part in 10^4 by determining the potential drop across a standard resistor with a potentiometer. After this, the resistance of a decade box in series with the solenoid was reduced step by step, which correspondingly raised the current through the solenoid and increased its field by about 0·3 oersted/step. At each step we observed the deflection of the galvanometer connected across the detection coil surrounding the sample under investigation. Ideally there should be one step with a quite large deflection, preceded and followed by steps with small deflection. Actually, at times, the transition from the superconductive to the normal phase, especially at the lower temperatures, took place over a range of fields corresponding to several steps. The threshold field was then estimated to lie at the point of greatest deflection.

In the low-temperature region, between about 1·5°K and 2·1°K, where the threshold field is close to 300 oersted, the transition widths for both the pure and the impure samples were of the order of 2 oersteds, or less than 1 per cent of the total field. This is about what one would expect as a result of the non-uniformity of the applied fields, and a possible slight deviation from the vertical of the samples. However, at temperatures between about 3·3°K and 3·8°K, where the threshold field is of the order of 10 oersted, the transition width of some of the more impure samples was as large as 0·5 oersted. This must be ascribed to minor imperfections in the samples themselves. Because of the rapid variation of the threshold field with temperature near T_c, even the widest transitions observed only introduced an uncertainty of two to three millidegrees in the evaluation of T_c. This is appreciably less than the smallest change in critical temperature which we obtain for any of the impure samples.

The temperatures in both regions were determined by measuring the vapor pressure of the helium bath, and using the 1948 temperature scale.[8]

(c) Sample holder

The sample holder consisted of six similar detection coils, each coil having 962 turns of 36 wire bank wound in three nearly equal layers on a thin fiber tube which was just large enough to slip over the sample tubes. The coils were arranged in a circle, 4·6 cm in diameter, which was large enough so that the magnetic field at the position of one sample was unaffected by the distorting effects of all other samples. To avoid further field distortions, all solder connections in the liquid helium bath were made with a non-superconductive solder consisting of 17 per cent Zn and 83 per cent Cd.

One detection coil was kept empty, and connected in turn in opposition to one of the other five. Of these five, one contained a pure tin specimen kept as a standard for all runs, so that four impure specimens could be measured in one experimental run. The entire coil assembly was suspended from the flask top by a thin string, and the leads from the coils passed through the Dewar cap continuously in order to avoid thermal e.m.f.'s. A small, non-inductively wound constantan heater was attached to the bottom of the sample holder. Some current was passed through this heater during all measurements above the λ-point in order to stir the liquid and thus to maintain a uniform temperature in the helium bath.

(d) Resistance measurements

The resistance of each sample was measured both at 4·2°K and at room temperature by mounting the specimen in four clamps, two at each end. The two inner clamps were used to connect the potential leads, the others to connect the current leads. A known current was sent through the sample, and the potential drop across it measured with a potentiometer. The calculated resistance values were substituted into equation (5) to yield the resistance ratio ρ to within 1 per cent.

3. RESULTS

(a) Transition temperature

Fig. 1(a) is a plot of the change in the transition temperature in zero magnetic field, ΔT_c, against the residual resistance ratio, ρ, for all the impure tin samples investigated. ΔT_c is negative for all samples. This effect was first noticed qualitatively by MANN *et al.*[9] for three samples of tin containing, respectively, 0·5 per cent Bi, 0·5 per cent Pb, and 0·7 per cent Tl. The details of Fig. 1(a) lead us to believe that the change in T_c is a superposition of two parts. There is an initial decrease in the transition temperature which varies linearly with ρ, and is independent of the type of impurity. Superimposed on this there is an increase in the transition temperature which is initially very small, but which gradually dominates the first part. The magnitude of this increase depends not only on ρ but also on the valence group of the impurity.

One can represent these conflicting effects by the empirical relation

$$\Delta T_c = A\rho + \Delta T_c'(\rho, Z), \qquad (6)$$

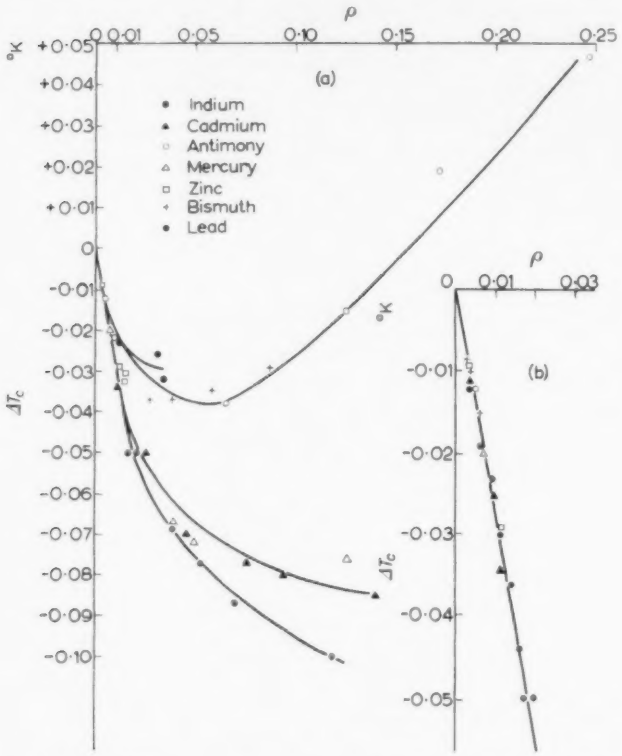

FIG. 1 (a, b). The change in the superconductive critical temperature of impure tin samples is shown as a function of their residual resistance ratio ρ.

where A is a negative constant, independent of the type of impurity, and where $\Delta T_c'$ seems to depend both on ρ and on Z, the difference in the valence of the impurity and of pure tin. For all impurities it appears that there is a region of small ρ in which $\Delta T_c'$ is negligible. This is illustrated in Fig. 1(b), which shows all those values of ΔT_c which are linear in ρ with a common slope. Since $\Delta T_c'$ becomes appreciable at fairly low values of ρ ($\sim$ ·007) for antimony, bismuth, and lead, Fig. 1(b) contains only a few points for these impurities. However, we note that for each impurity at least one point does fall on this linear curve, and that for bismuth there are indeed three. From the shapes of the curves in Fig. 1(a) there is every reason to believe that specimens containing impurities of even lower concentrations than those measured would also have values of ΔT_c falling on the linear curve of Fig. 1(b).

If, then, one accepts the premise that a part of the change in transition temperature of all specimens is a decrease which varies linearly with ρ, he could argue that this merely implies a linear dependence of this part on the concentration of impurity since, as will be shown subsequently, the residual resistance ratio is a linear function of the atomic impurity concentration for all our samples. In order to determine whether the fundamental parameter is indeed ρ and not atomic concentration, additional low concentration samples containing indium and cadmium were prepared and measured, since the resistance ratio increases most rapidly with concentration of cadmium, and least rapidly with concentration of indium. Fig. 2 shows plots of the change in transition temperature for these samples both against atomic concentration and against ρ. It is obvious that while all the curves are, as expected, linear, separate curves are

obtained for indium and cadmium when ΔT_c is plotted against concentration, while we again get a single curve when it is plotted against ρ. If ΔT_c were plotted against atomic concentration for the other impurities, the resulting curves would lie between those for indium and for cadmium. Clearly, then, the initial decrease in transition temperature is indeed a linear function of the residual resistance ratio, ρ.

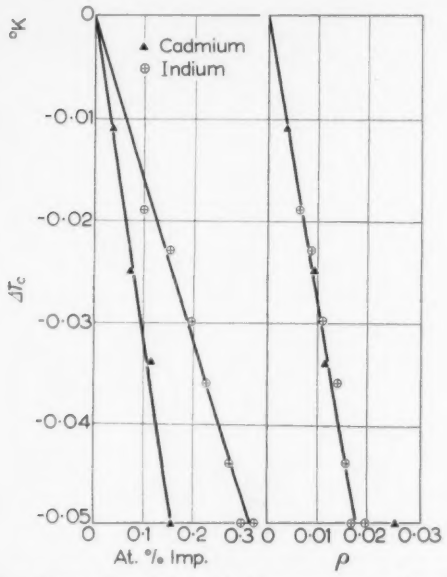

FIG. 2. The change in critical temperature of tin samples containing cadmium or indium is plotted as a function of at. per cent of impurity and by comparison as a function of the residual resistance ratio.

(b) The coefficient of the electronic specific heat

For our specimen of pure tin we calculated H_0, the threshold field at absolute zero, by extrapolation on the assumption that at sufficiently low temperatures the threshold field is a linear function of $(T-T_c)^2$ for all superconductors. The validity of this assumption will be discussed presently. The values of the threshold field used for this extrapolation were measured in the temperature range $1{\cdot}5°\text{K} < T < 2{\cdot}1°\text{K}$.

With the resulting values of H_0, equation (4) was used to calculate values of γ, the coefficient of the electronic specific heat in the normal phase, at each of the seven experimental temperatures of every run. Since the same pure sample was used in all runs, the final value is an average of about fifty individual determinations. Table 1 shows this value of γ, together with our determinations of T_c and of H_0 for the same specimen, and values for the various parameters obtained by other investigators. Our value for γ is in good agreement with that obtained by CORAK and SATTERTHWAITE[5] by a direct calorimetric method. Their result is generally regarded as considerably more accurate than that of any previous calorimetric determination. Table 1 also shows that the values of γ obtained some years ago by LOCK *et al.*,[10] MAXWELL,[11] and SERIN *et al.*[12] from their various determinations of the threshold field curve, though in good agreement with each other, are systematically larger than that of CORAK and SATTERTHWAITE and our present result.

This discrepancy, and the fact that ours is the first calculation of γ for tin from magnetic measurements which yields a somewhat smaller value than the calori-

Table 1. *Comparison of the values of T_c, H_0, and γ for pure tin obtained in this work with those of other investigations*

Reference	Method	T_c (°K)	H_0 (oersted)	γ (10^{-4}cal-deg^{-2}mole^{-1})
This work	Magnetic-corrected for exponential dependence of c_{es}	3·734	302·9	4·11
This work	Magnetic-uncorrected			4·33
CORAK and SATTERTHWAITE[5]	Calorimetric	3·722	303·2	4·18
LOCK *et al.*[10]	Magnetic-uncorrected	3·726	304·5	4·46
MAXWELL[11]	Magnetic-uncorrected	3·742	306·9	4·43
SERIN *et al.*[12]	Magnetic-uncorrected	3·752	304	4·40

metric data, can be explained as follows: In the previous magnetic work, the value of γ was calculated by means of the exact expression[10]

$$\gamma = \frac{V}{4\pi}\frac{H_0^2}{T_c^2}[h(t)h''(t)]_{t=0}, \qquad (7)$$

where $t \equiv T/T_c$, and $h(t) \equiv H(t)/H_0$. For $h(t)$ each group used an empirical polynomial in powers of t of the form

$$h(t) = 1+a_1t^2+a_2t^3+a_3t^4+ \ldots, \qquad (8)$$

choosing coefficients which gave the best fit to their direct measurements of the threshold field. However, these measurements went no lower than $t \geqslant 0{\cdot}3$, and it was assumed that a polynomial determined in this higher temperature region could be extrapolated down to $T = 0°K$. In calculating γ from equation (7), the only coefficient which enters is a_1, and we conclude that by fitting only at $t > 0{\cdot}3$, too high a value of a_1 was obtained. In other words, by only fitting the threshold field polynomial at higher temperatures one does not take fully into account the deviation of the threshold field curve from a parabola.

In order to confirm this we calculated γ from our data using the slopes of the curve of H_c vs. T^2 instead of using equation (4), and obtained a value of 4·33 cal/mole-deg². This is significantly larger than the calorimetric value, and quite close to the values obtained from earlier magnetic measurements. It appears, therefore, that short of measuring the threshold field down to very low temperatures, the only way to obtain reliable values of γ from magnetic measurements at $T > 1°K$ is to take explicit account of the exponential dependence of the electronic specific heat in the superconducting phase, as is done in the determination of γ by means of equation (4).

Since using the slope of a H_c vs. T^2 curve, *i.e.* assuming a parabolic threshold field curve, gives incorrect values for γ, the question arises whether one is justified in obtaining H_0 by linear extrapolation of such a quadratic curve. We investigated this question empirically by starting with some definite values of H_0 and γ, and using equation (4) to calculate H_c as a function of T for $1{\cdot}5°K < T < 2{\cdot}1°K$. These fields were then assumed to vary parabolically with temperature, and were extrapolated back to $T = 0°K$ by the method of least squares. The resulting value of H_0 differed from the initially assumed value by less than one oersted, which is less than our experimental error. This indicates that our simple procedure of obtaining H_0 for each of the various specimens was adequate. However, as might be expected, we found that the slope obtained from this least squares fit of the calculated field values to a T^2-dependence resulted in a value of γ which was too high by an amount comparable to the excess obtained when the experimental field values were treated in the same way.

Having thus satisfied ourselves of its validity, we used the same procedure to find H_0 for each of our impure samples, and used these numbers and equation (4) to calculate γ for these specimens at each experimental temperature. Table 2 lists the averages of these determinations of γ for each specimen, together with the nominal concentration of impurity, the residual resistance ratio, and the ratio of γ to the value determined for pure tin. Although the scatter in the data is appreciable, it is clear that with the exception of two low concentration samples, all specimens have an electronic specific heat coefficient greater than that of pure tin. We estimate the accuracy of our γ determinations to be about one half per cent, so that the two exceptions to the general pattern of the results probably are not significant. It would appear, therefore, that the addition of all the impurities used increases the electronic specific heat in the normal phase, in spite of the fact that some of these impurities (Cd, In, Hg, Zn) have a lower

Table 2. Values of γ, γ/γ_{pure}, of T_c, and of ρ for impure tin samples

Impurity	Concentration (at. %)	ρ	γ (10^{-4}cal-deg^{-2}mole^{-1})	γ/γ_{pure}
Antimony	0·09	0·005	4·124	1·003
	0·16	0·010	4·142	1·008
	1·2	0·066	4·294	1·043
	2·7	0·172	4·480	1·090
Bismuth	0·3	0·028	4·135	1·006
	0·5	0·039	4·150	1·010
	0·7	0·059	4·172	1·015
	1·0	0·087	4·175	1·016
Cadmium	0·32	0·046	4·185	1·018
	0·54	0·076	4·218	1·026
	0·66	0·094	4·223	1·028
	0·99	0·139	4·244	1·033
Indium	0·3	0·017	4·076	0·992
	1·2	0·070	4·183	1·018
Lead	0·1	0·005	4·135	1·006
	0·3	0·012	4·148	1·009
	0·7	0·034	4·160	1·012
	1·0	0·030	4·205	1·023
Mercury	0·1	0·007	4·108	1·000
	0·3	0·041	4·175	1·016
	1·0	0·049	4·161	1·012
	0·7	0·126	4·172	1·015
Zinc	0·06	0·003	4·101	0·998
	0·2	0·012	4·125	1·004
	0·5	0·014	4·144	1·008
	1·0	0·015	4·122	1·003

valence than tin, lead has the same, and some (Sb, Bi) have a larger one. LOVE[13] also found an increase in γ when higher concentrations of 2–10 per cent of Sb and Bi are added to tin.

(*c*) *Residual resistance ratio*

The residual resistance ratio of each of our specimens was measured within a few days of the magnetic measurements. The results for samples containing indium, cadmium, bismuth, and antimony show clearly a linear variation of ρ with atomic concentration of impurity, with slopes which are listed in Table 3. No slope was obtained for samples containing zinc and lead because of the lack of reproducibility in the results

*Table 3. Values of the change of ρ per at. per cent of impurity for different solutes in tin, the valence difference of the impurity, and its atomic diameter**

Impurity	Z	Diameter (Å)	ρ/at. %
Antimony	+1	3·23	0·063
Bismuth	+1	3·64	0·087
Cadmium	−2	3·04	0·142
Indium	−1	3·14	0·058

* Values taken from Metallurgical Data Sheet No. 1, American Society for Metals, Cleveland, 1950.

when measurements were made on specimens which were prepared at different times from different initial melts, but which were supposed to contain the same amount of impurity. The reason for this is probably the loss of impurity in preparing the samples. Probably for the same reason, the values of ρ for the different mercury specimens were too scattered to allow us to calculate a slope. It must be stressed, however, that these uncertainties in no way invalidate or even affect the results of the T_c and the γ measurements, since in all cases the changes in these quantities were discussed in terms of the actual value of the resistance ratio determined for the same specimen.

4. DISCUSSION

(*a*) *The critical temperature, and the electronic specific heat*

Our results indicate that the addition to tin of impurities of lower, equal, and higher valence increases the electronic specific heat coefficient, γ, of the normal phase. Since it is well known that[4]

$$\gamma = \tfrac{2}{3}\pi^2 k^2 N(E_F), \tag{9}$$

this means that the addition of these impurities raises $N(E_F)$, the density of the electronic energy states at the Fermi level. The only way this would seem possible is that in pure tin the Fermi level is at or near a minimum in the density of states curve, so that both an increase and a decrease in the Fermi energy results in an increase in $N(E_F)$ and therefore of γ. While extrema in the density of states curve are known to exist for some transition metals[14] and, moreover, while the calculations of HERRING and HILL[15] suggest that the Fermi energy in beryllium falls near a minimum of the curve, such a minimum has not previously been predicted for tin.

The scatter of our data makes it difficult to obtain more than a qualitative conclusion about the variation of γ with increasing impurity concentration. However, we feel that there is some indication that γ initially changes very slowly, with a small or vanishing slope in the limit of zero concentration, and we believe that this inference is supported by the observed changes in the critical temperature.

As mentioned previously, we have found that initially the change in transition temperature varies linearly with the residual resistance ratio. This ratio is in turn inversely proportional to the electronic mean free path in the normal state. Hence it would appear that in the region of very low impurity concentration, where γ is not yet appreciably different from pure tin and one is still working with essentially the same metal, the change in transition temperature is inversely proportional to this mean free path. In substantiation of this idea it must be noted that the change in T_c cannot be due either to changes in atomic volume or to changes in the average mass produced by the impurities. Some of the impurities we use have an atomic mass higher than that of tin, others a lower one; some of the impurities increase the atomic volume, others decrease it,[16] while we find ΔT_c to be always negative. In addition, the changes which we observe are one to two orders of absolute magnitude larger than those produced by the volume changes and by the mass changes. We are, therefore, convinced that for very small impurity concentrations the transition temperature of tin varies

inversely with the electronic mean free path in the normal state. We return to the discussion of this effect in a subsequent paragraph.

If, then, we assume that for all our samples a portion of the change in the transition temperature is due to the shortening of the mean free path of the normal electrons, we can express ΔT_c as the sum of two parts, as shown in equation (6). The first term, $A\rho$, represents the mean free path effect, with A equal to the slope of the curve shown in Fig. 1(b). The second term, which we call $\Delta T_c'$, then turns out to be positive for all those of our samples for which it differs appreciably from zero. Since the concentrations at which $\Delta T_c'$ becomes appreciable are just those for which we begin to find a measurable increase in the density of states, and since we also find that both the change in this density and $\Delta T_c'$ are positive for samples of all impurities, we believe that these two quantities are correlated. In other words, we infer from our results that the addition of small amounts of impurities to tin has two simultaneous effects which, to a first approximation, can be considered separately. There is, in the first place, a decrease in the mean free path of the normal electrons of what can essentially still be considered pure tin, and secondly there occurs, concurrently though at first negligibly, the creation of a new metal, with a different Fermi energy and hence a different density of states at E_F and a different electronic specific heat. The decrease in the mean free path results in a decrease in the transition temperature; at the same time the increase in the density of states brings about an increase in T_c.

Our assertion that the addition of small but appreciable amounts of impurities to tin creates new but still well-behaved superconductors is substantiated by the fact that all our samples have the same threshold field curve when expressed in the reduced co-ordinates $h \equiv H_c/H_0$, and $t \equiv T/T_c$. There is increasing evidence[17] that very different metals, with widely varying values of T_c and H_0, such as tin and aluminum, satisfy this "similarity principle" quite closely, although it is also recognized that mercury is an exception, as yet unexplained, to this rule.

For all of our samples, without exception, plots of h versus t coincide completely with each other and with the reduced threshold field curve for pure tin over the entire temperature range of our measurements. In addition to removing any doubts about the validity of applying equations (3) and (4) with the same constants a and b to all our samples, this immediately suggests another check on our calculated values of γ. It follows from equation (7) that since $[h(t)h''(t)]_{t=0}$ is the same for all our samples, γ is proportional to $(H_0/T_c)^2$. Calculating the changes in γ on this basis we obtain values for all our specimens which are in close agreement with those listed in Table 2.

Our view that the observed changes in critical temperature can be considered as being the result of two conflicting mechanisms receives further support when the data are compared with the empirical correlations which have been found to exist between the transition temperatures of different superconductors and their γ values. DAUNT[18] has found that $T_c \propto \gamma$, whereas LEWIS[19] suggests that $T_c \propto \gamma^{1.35}$. It is clear that both these variations predict a positive change in T_c with an increase in γ. Since our measured values of ΔT_c are always negative, they, of course, do not agree with this prediction. However, the values of $\Delta T_c'$ which we infer from the data are positive and so have the correct sign; in magnitude they are somewhat larger than the changes predicted by either empirical expression.

We obtain even stronger support for our conclusion that changes in the density of states are responsible for $\Delta T_c'$ from the theory of superconductivity proposed very recently by BARDEEN *et al.*[20] These authors have been able to show that for a sufficiently strong electron-electron interaction due to phonon exchange, there is a superconductive state, the volume energy of which at 0°K is less than the energy of the normal metal by an amount

$$W = -\frac{2N(E_F)\langle\hbar\omega\rangle^2}{\exp[2/N(E_F)V]-1}. \qquad (10)$$

In this expression $\langle\hbar\omega\rangle$ is the average zero point phonon energy, which is about equal to $(3/5)k\Theta_D$ where Θ_D is the Debye temperature. $-V$ is an average matrix element arising from the electron-phonon and the Coulomb interactions.

Since the energy difference between a unit volume of metal in the superconductive and in the normal phase at 0°K must equal $H_0^2/8\pi$[3], one can combine equations (7) through (10) to show that

$$T_c^2 = \frac{36a_1}{5\pi^2}\Theta^2{}_D/[\exp\{2/N(E_F)\mathrm{V}\}-1], \quad (11)$$

where a_1 is the first coefficient in equation (8). From the known values of T_c, Θ_D, and a_1 one finds that for tin

$$[N(E_F)\mathrm{V}]^{-1} \simeq 3{\cdot}8.$$

As, therefore, the exponential term in (11) is much larger than unity, differentiation of the equation yields for small changes in $N(E_F)$ and T_c, and constant V, the relation

$$\Delta T_c/T_c = [N(E_F)\mathrm{V}]^{-1}\Delta N(E_F)/N(E_F) \approx 3{\cdot}8\Delta\gamma/\gamma. \quad (12)$$

In line with our belief that the change in the critical temperature which is related to the change in the electronic density of states is only that part of the total change which we call $\Delta T_c'$, we have in Fig. 3 plotted $\Delta T_c'/T_c$ as a function of $\Delta\gamma/\gamma$ for all our samples for which $\Delta T_c'$ and $\Delta\gamma$ were measurable. In view of the scatter of the measured values of $\Delta\gamma$, and of the fact that especially for samples of low impurity concentration $\Delta T_c'$ is a small difference between two nearly equal quantities, it is difficult to draw very definite quantitative conclusions from this plot. It is clear, however, that

$$\Delta T_c'/T_c \approx 3\Delta\gamma/\gamma,$$

which is surprisingly close to the relation (12) predicted by the theory.

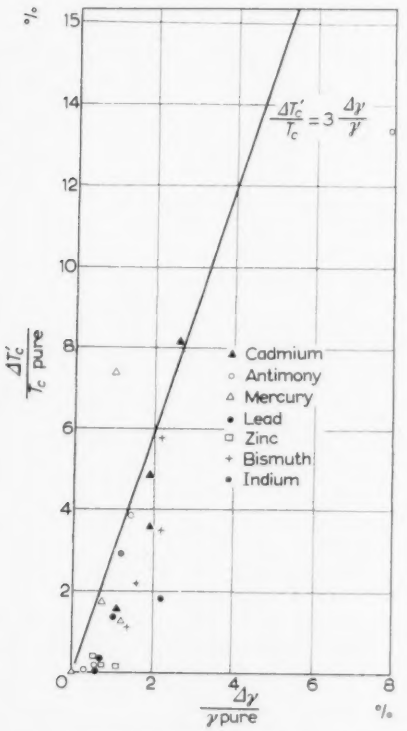

FIG. 3. The positive part of the change in critical temperature, expressed as percentage of the critical temperature of pure tin, is shown as a function of the per cent change in the temperature coefficient of the normal electronic specific heat.

We return to the initial change of the critical temperature. Since we have made extensive measurements only on tin, we cannot dismiss the possibility that the initial linear decrease of T_c with residual resistance ratio merely reflects some other property of tin which we do not at present appreciate. We believe, however, that this is a real electronic mean free path effect common to all superconductors, although it might be difficult to observe in some cases because of competition with factors tending to change the nature of the metal. We have obtained tentative support for this conclusion from some preliminary measurements on indium which have shown that the addition of small amounts of either tin or cadmium does in both cases result in a decrease in the critical temperature. STOUT and GUTTMAN[21] also observed that the addition of 5–20 per cent of thallium to indium decreased T_c.

The effect of electronic mean free path on superconducting properties has been discussed in another connection by PIPPARD,[22] who has shown that at mean free paths, small compared to those used in this investigation, the law of penetration of a magnetic field into an impure superconductor is changed appreciably from its form in the pure metal. In this theory, however, the critical temperature is an independent parameter; and, in fact, any dependence of T_c on mean free path is explicitly neglected.[23] We do not think that our results affect PIPPARD's conclusions in any essential way, since the magnitudes of the effects we observe are so small as to have negligible influence on his treatment of the problem. It may be true, nevertheless, that both effects—the decrease in T_c at

relatively long free paths and the observed change in magnetic field penetration at shorter free path—are different manifestations of the same fundamental mechanism. However, in the absence of a theory of how electronic mean free path can affect the superconductive critical temperature,* the answer to the question of whether our conclusion is appropriate to all superconductors or just to tin can come only from measurements on other metals.

(b) Residual resistance ratio

Our determinations of the residual resistance ratios ρ, as defined by equation (5), were subsidiary to our other measurements, and hardly constitute a complete study. A few conclusions emerge, however, even from this limited accumulation of data. In the first place, our results indicate once again that below the solubility limit the resistance ratio is a linear function of impurity concentration, and that it therefore provides a reliable and very simple means of determining relative concentrations of impure samples. While such a linear variation can be explained by a simple free electron theory of metals, this theory also predicts that the increase of the resistivity ratio per atomic per cent of impurity concentration should vary as Z^2, where Z is the difference in the valence between the solvent and the solute atoms.[24] As the theory ignores the possibility of two-band conduction, and neglects the scattering effects of the distortion of the lattice near the foreign atoms, it is not surprising that our results do not agree with its prediction. Antimony, bismuth, and indium all have $Z^2 = 1$, and the values listed in Table 3 show not only that the changes in ρ per atomic per cent of impurity for these three solutes are very different, but that they vary proportionately to the atomic diameter of the impurity. This indicates that the distortion of the lattice does indeed contribute appreciably to the scattering of the conduction electrons in these cases.

* *Note added in proof:* PIPPARD has recently suggested (*cf.* page 175 of this issue) that since the scattering of phonons by electrons is affected by the electronic mean free path, one might expect that the electron-lattice interaction is changed in a similar way. He obtains reasonable agreement with our results.

Acknowledgements—In the analysis of our results we have been greatly helped by many discussions with Professors E. ABRAHAMS and P. WEISS. We are also grateful to Professor J. BARDEEN for sending us a preprint of his paper before its publication.

Mr. A. SIEMENS assisted in the design of our apparatus and was largely responsible for its construction.

REFERENCES

1. LOHMAN C. Thesis, Rutgers University, New Brunswick, N.J. (1953).
2. SERIN B. *Progress in Low Temp. Physics* (Edited by C. J. GORTER) Vol. I, Chap. VII, pp. 148 *et seq.* Interscience, New York (1955).
3. GORTER C. J. and CASIMIR H. *Physica* **1,** 306 (1934).
4. WILSON A. H. *The Theory of Metals* (Second Edition) p. 144. University Press, Cambridge (1953).
5. CORAK W. S. and SATTERTHWAITE C. B. *Phys. Rev.* **102,** 662 (1956).
6. WILSON A. H. *op. cit.* pp. 310 *et seq.*
7. GARRETT M. W. *J. Appl. Phys.* **22,** 1091 (1951).
8. VAN DIJK H. and SHOENBERG D. *Nature, Lond.* **164,** 151 (1949).
9. MANN K. C., GRAYSON-SMITH H., and WILHELM J. O. *Phys. Rev.* **54,** 758 (1938).
10. LOCK J. M., PIPPARD A. B., and SHOENBERG D. *Proc. Camb. Phil. Soc.* **47,** 811 (1951).
11. MAXWELL E. *Phys. Rev.* **86,** 235 (1952).
12. SERIN B., REYNOLDS C. R., and LOHMAN C. *Phys. Rev.* **86,** 162 (1952).
13. LOVE W. F. *Phys. Rev.* **92,** 238 (1953).
14. KRIESSMAN C. J. and CALLEN H. B. *Phys. Rev.* **94,** 837 (1954).
15. HERRING C. and HILL A. G. *Phys. Rev.* **58,** 132 (1940).
16. LEE J. A. and RAYNOR G. V. *Proc. Phys. Soc.* **67,** 737 (1954).
17. FABER T. E. and PIPPARD A. B. *Proc. Roy. Soc.* A**231,** 336 (1953).
18. DAUNT J. G. *Progress in Low Temp. Physics* (Edited by C. J. GORTER) Vol. I, Chap. XI. Interscience, New York (1955).
19. LEWIS H. W. *Phys. Rev.* **101,** 939 (1956).
20. BARDEEN J., COOPER L. N., and SCHRIEFFER J. R. *Phys. Rev.* **106,** 162 (1957).
21. STOUT J. W. and GUTTMAN L. *Phys. Rev.* **88,** 703 (1952).
22. PIPPARD A. B. *Proc. Roy. Soc.* A**216,** 547 (1953).
23. FABER T. E. and PIPPARD A. B. *loc. cit.* footnote p. 346.
24. FRIEDEL J. *Adv. Phys.* **3,** 446 (1954).

J. Phys. Chem. Solids Pergamon Press 1957. Vol. 3. pp. 175–177.

THE EFFECT OF ALLOYING ON THE SUPERCONDUCTING TRANSITION TEMPERATURE OF TIN

A. B. PIPPARD

Royal Society Mond Laboratory, University of Cambridge, England

(*Received* 30 *April* 1957)

Abstract—A semi-classical treatment of electron-phonon interaction suggests that the interaction is reduced if the electrons are appreciably scattered by impurities, the reduction being expressible in terms of the ratio of phonon wavelength to electronic free path. This may account for the reduction in the transition temperature of superconducting tin caused by alloying, as investigated by LYNTON, SERIN and ZUCKER. Rough analysis of two models yields the correct order of magnitude of the effect in both. It is further suggested that the proposed effect may appear in the thermal conductivity of highly resistive alloys at low temperatures as an extra term proportional to temperature contributed by the lattice conduction.

VOL. 3 1957

THE interesting result, reported by LYNTON, SERIN, and ZUCKER,[1] that the superconducting transition temperature of tin is lowered when small quantities of other metals are added, by an amount proportional to the residual resistivity but independent of the actual metal added, may possibly be interpreted as due to a change in electron-phonon interaction when there is appreciable impurity-scattering of the electrons. In connection with the absorption of ultrasonic waves in metals by interaction with the conduction electrons an expression has been derived[2] for the attenuation coefficient of a longitudinal wave of wave-number κ

$$\alpha = \frac{Nmv_0}{\rho v_s l}\left\{\frac{1}{3}\frac{\kappa^2 l^2 \tan^{-1}(\kappa l)}{\kappa l - \tan^{-1}(\kappa l)} - 1\right\}, \qquad (1)$$

in which N is the number of electrons per unit volume, m the electronic mass, ρ the density of the metal, v_s the velocity of sound, v_0 the Fermi velocity and l the electronic mean free path. Now this expression was derived for a simple model by rather "classical" methods, and it is perhaps satisfying that if we interpret α^{-1} as equal to λ, the mean free path of a phonon of wave number κ, and let κl tend to infinity, we have

$$\lambda_\infty = \lim_{\kappa l \to \infty} (\lambda) = \frac{6\rho v_s}{\pi N m v_0 \kappa}, \qquad (2)$$

which is the same result as is obtained by the conventional quantum mechanical treatment of the same problem.* It is therefore arguable that an expression similar to (1) may be used in real metals (if we neglect umklapp-processes) to express the influence of finite electronic free paths on the absorption of phonons. For although the coefficient in (1) is certainly determined by the details of the model, the term in brackets may well be far less influenced by the model, depending as it does only on κl, the ratio of free path to wavelength. Perhaps the simplest physical argument to show why this dependence on κl exists at all is based on the uncertainty principle. When l is infinite the energy and momentum of an electron may be defined precisely; now if a phonon, also of well-defined energy and momentum, is to be absorbed by collision with an electron, conservation of energy and momentum specifies rather closely what electron can take part. The effect of electronic collisions is to render the electronic momentum uncertain to the extent of approximately $\hbar/l$, and the parameter κl, representing the ratio of phonon momentum to uncertainty in electron momentum, expresses the degree to which momentum may be seen to be conserved in the collision. The smaller the value of κl the greater the range of electrons which may interact with a

* I am grateful to Prof. J. BARDEEN for helping to verify this point.

given phonon. The bracketed term in (1) is thus not fundamentally related to the strength of the phonon-electron interaction, but only to its modification by what may be termed diffraction effects.

On the assumption that this bracketed term is indeed applicable in real metals, we may expand it as a series in $(\kappa l)^{-1}$, when $\kappa l > 1$, and write for the phonon free path,

$$\lambda = \lambda_\infty \left\{1 + \left(\frac{8}{\pi} - \frac{\pi}{2}\right)\frac{1}{\kappa l} + \ldots\right\}. \qquad (3)$$

Alternatively we may express this result as a modification of the coupling between two electronic states by way of the emission or absorption of a phonon of wave number κ

$$|M(\kappa)|^2 = |M(\kappa)|_\infty^2 \left\{1 - \left(\frac{8}{\pi} - \frac{\pi}{2}\right)\frac{1}{\kappa l} + \ldots\right\}. \quad (4)$$

We shall now assume that (4) can be applied to any expression for the transition temperature of a superconductor which involves $M(\kappa)^2$. In the recent theory of BARDEEN, COOPER, and SCHRIEFFER[3] the transition temperature is found to be of the order of $\Theta e^{-1/N(0)V}$, where Θ is the Debye temperature, $N(0)$ the density of states at the Fermi surface, and V an electronic interaction energy which is the difference between the attractive potential due to phonon exchange, proportional to $|M(\kappa)|^2$, and the repulsive screened Coulomb potential. For tin, with $T_c/\Theta \sim 1/70$, $N(0)V$ must be about 0·24, which may be interpreted roughly as the difference between two terms, each of magnitude about 2. If we consider an alloy whose residual resistivity is 1 per cent of the room temperature resistivity, $l \sim 10^{-4}$ cm and κl for the average phonon responsible for the interaction (corresponding to a frequency about $\frac{2}{3}k\Theta/\hbar$) is about 10^4. Thus $N(0)V$ is decreased by about 2×10^{-4} from its value when l is infinite and correspondingly T_c is decreased by about 0·3 per cent, or 0·011°K. This is about one-half of what is found experimentally, which can be regarded as satisfactory agreement.

It may be, however, that the theory of BARDEEN, COOPER, and SCHRIEFFER[3] is mistaken in supposing the superconducting interaction to be a weak interaction embracing electrons over an energy range $k\Theta$ by means of an interaction with all phonons, particularly those near the Debye limit. We therefore consider an alternative view, that only electrons in an energy range of about kT_c are affected, and that the dominant phonons in the interaction are those of energy about kT_c. We further suppose that the transition temperature is not the very sensitive exponential function of $|M(\kappa)|^2$ that BARDEEN, COOPER and SCHRIEFFER derive, but is simply proportional to $|M(\kappa)|^2$. For the same value of l as before, the effective value of κl is now only about 200, but because we suppose T_c not to be so highly sensitive to $|M(\kappa)|^2$ the estimated change in transition temperature is still about $\frac{1}{2}$ per cent, very much the same as for the other theory. Of course this view, that only rather low-energy phonons are involved, does not correspond to any theory of superconductivity which has been worked out in detail, but it is by no means an untenable view. It is clear that the observations on the change of T_c with addition of impurity do not serve to decide which type of theory, if either, is correct.

It is possible that the validity of (3) may be tested by measurements of the thermal conductivity of highly resistive alloys at low temperatures. If the lattice contribution to thermal conductivity, K_g, be written $\frac{1}{3}C_g v_s \lambda$, where C_g is the lattice specific heat per unit volume, proportional to T^3 at low temperatures, then on substituting for κ in (2) and (3) the mean wave number of the phonons present at temperature T, we find, since now $\kappa \propto T$,

$$K_g \propto T^2\left(1 + \frac{A}{T} + \ldots\right) \quad \text{where } A \doteq \frac{\hbar v_s}{3kl}.$$

There should thus appear a contribution to K_g proportional to T, which experimentally will be confused with the electronic thermal conductivity. We may expect then that the term proportional to T in the measured thermal conductivity will be greater than what would be calculated from the electrical conductivity by use of the Wiedemann-Franz Law. The effect should only be noticeable in alloys with electrical resistivities of 10^{-5} Ω cm or more at a few degrees absolute. There are fugitive scraps of evidence[4] that something of this sort has been observed, but it is customary to attribute the effect to

experimental error. More information would clearly be desirable.

Acknowledgements—I am indebted to Drs. BARDEEN, COOPER, SCHRIEFFER, LYNTON, SERIN, and ZUCKER for telling me of their work before publication.

VOL.
3
1957

REFERENCES

1. LYNTON E. A., SERIN B. and ZUCKER M. *J. Phys. Chem. Solids* **3,** 165 (1957).
2. PIPPARD A. B. *Phil. Mag.* **46,** 1104 (1955).
3. BARDEEN J., COOPER L. N., and SCHRIEFFER J. R. *Phys. Rev.* **106,** 162 (1957).
4. KEMP W. R. G., KLEMENS P. G., SREEDHAR A. K., and WHITE G. K. *Proc. Roy. Soc.* A **233,** 480 (1956).

SLADEK R. J. *Phys. Rev.* **97,** 902 (1955).

J. Phys. Chem. Solids Pergamon Press 1957. Vol. 3. pp. 178–195.

THE ELECTRONIC STRUCTURE OF *V*-CENTERS

THEODORE G. CASTNER* and WERNER KÄNZIG

Department of Physics, University of Illinois, Urbana, Illinois;
General Electric Research Laboratory Schenectady, N.Y.

(*Received* 15 *April* 1957)

Abstract—By X-irradiation of alkali halides (LiF, NaCl, KCl and KBr) at liquid nitrogen temperature electron defect centers are created which can be described as halogen$_2^-$ molecule-ions oriented along the [110]-axes of the crystal. The electronic structure of this defect has been deduced from the hyperfine interaction studied by means of electron spin resonance. The detailed analysis of the electron spin resonance spectra together with experiments on alkali halides containing Tl^+-ions suggests that the halogen$_2^-$ molecule-ion is not associated with any other imperfection. Thus, the defect might be regarded as a self-trapped hole.

VOL
3
195

1. INTRODUCTION

1.1. *F-centers and V-centers*

For a long time there was only one color center in the alkali halides with a well-known structure. It is the *F*-center, an electron trapped near an alkali vacancy. Electron spin resonance experiments have shown that the trapped electron is shared as a valence electron between the six alkali ions surrounding the vacancy.[1] The hyperfine interaction of this valence electron with the six alkali nuclei is relatively small and at best only partially resolvable with conventional paramagnetic resonance techniques.[2] The situation is entirely different for the *V*-centers that we have investigated. *V*-centers are holes trapped in the otherwise filled electron shells of the halogen ions. There is a large hyperfine interaction between the incomplete electron shell and the nucleus of the ion. Since in addition the hole is much more localized than is the *F*-center electron, the hyperfine interaction is easily resolvable.

In a previous paper[3] we gave the results of a preliminary analysis of the electron spin resonance spectrum of a *V*-center, which turned out to be a halogen$_2^-$ molecule-ion oriented along a [110]-axis of the crystal. The present paper contains a detailed study of the paramagnetic resonance spectra and of the electronic structure of this defect in KCl, NaCl, KBr and LiF, as well as in KCl doped with TlC .

The most important conclusions that can be drawn from this work are the following:

(1) If an electron is removed (e.g. by X-ray bombardment) from a halide ion in an alkali halide a molecular bond can be formed in that the electron deficiency is shared with a neighboring halide ion.

(2) The resulting halogen$_2^-$ molecule-ion is not associated with vacancies. Also, the experiments suggest that it probably is not associated with impurities, but may be regarded as a kind of a self-trapped hole. The self-trapping arises from the formation of a molecular bond rather than from the polarization field around the hole.

The objective of this paper is to elucidate the electronic structure of this defect, and no efforts will be made here to consider the serious implications its existence may have for the interpretation of other color center experiments.

2. PRODUCTION AND BLEACHING OF THE *V*-CENTER

2.1. *Pure alkali halides*

The electron spin resonance spectra to be described appeared upon irradiation of pure alkali halide single crystals (obtained from the Harshaw Chemical Company) with X-rays at liquid nitrogen

* Gulf Research Fellow 1955–1956 and Texas Instrument Fellow 1956–1957.

temperature. The crystals were kept at this temperature after irradiation. The spectra do not appear if, for example, the crystals are irradiated at room temperature and then cooled to liquid nitrogen temperature.* Therefore, the observed paramagnetic resonance definitely is not due to the centers that give rise to the optical V_2 and V_3 absorption bands, because these bands are the predominant V-bands produced by X-irradiation at room temperature.[4] Thus, the as ignment proposed by COHEN[5a] (V_3-band) is ruled out.

Tentatively we might associate our magnetic resonance spectra with the optical V_1-band in KCl and KBr (or possibly with a band superposed to the V_1-band) for the following reasons:

(1) The V_1-band is the predominant V-band produced by X-irradiation at liquid nitrogen temperature.

(2) If the irradiated crystal is warmed up the magnetic resonance spectrum disappears irreversibly in the same temperature range where the V_1-band bleaches thermally (roughly around 130°K for KCl and 120°K for KBr).†

(3) An upper and a lower limit for the wavelength of the optical absorption of the paramagnetic center can be calculated on the basis of the paramagnetic resonance spectra. The V_1 is the only *predominant* V-band that falls within these limits (see sec. 4.3).‡

For NaCl no optical investigations of the thermal bleaching temperature of the V_1-band are available.

For LiF the disappearance of the V-center resonance appears to coincide with the bleaching of the 3450 Å absorption band reported by PRINGSHEIM *et al.*[6]

2.2. *Alkali halides doped with TlCl*

In KCl doped with TlCl and X-rayed at liquid nitrogen temperature SMALLER, DELBECQ, and YUSTER[7] observed a paramagnetic resonance similar to the one we observed in pure KCl. Thermal bleaching, however, occurred at 205°K instead of around 130°K. Prompted by this work, we investigated a KCl : Tl crystal (containing about 0·1 mole per cent Tl)§ and found that the spin resonance spectrum is *exactly* the same as in pure KCl. (The hyperfine splittings agree within less than one part in 10^4.) However, the production rate of V-centers for a given X-ray intensity is about 10^3 times larger in KCl : Tl than in pure (Harshaw) KCl. *It is this tremendous production rate which suggests that the formation of these V-centers does not involve vacancy production.* We conclude that the trapped hole is very probably not associated with vacancies. In KCl : Tl the Tl^+-ions act as electron traps and thus prevent the recombination of the electrons and holes produced by X-rays, whereas in pure KCl the recombination prevents the rapid production of V-centers, and the X-rays first have to create electron traps such as, for example, halide vacancies.

Also association of the trapped hole with Tl is unlikely because of the identity of the spectra in pure KCl and KCl : Tl. However, this statement requires further investigation, because the Tl^+-ion may be rather similar to the K^+-ion. An optical test of the pure Harshaw crystals made by P. D. JOHNSON showed that the TlCl content was less than 5×10^{-7} mole, and this is less than the concentration of V-centers present after prolonged irradiation.

The higher bleaching temperature in KCl : Tl (205°K) indicates that the bleaching of the V-center in pure KCl (around 130°K) is not due to thermal instability of the V-center itself but rather to annihilation of the hole by an electron released from some electron trap that becomes unstable. In fact, at this temperature DUTTON and

* Other spectra with resolved hyperfine splitting appear under these conditions. They will not be discussed in this paper.

† *Note added in proof:* Recently, DELBECQ and YUSTER (private communication) were able to show that the center that gives rise to the paramagnetic resonances described in this paper is not associated with the optical V_1-band. The halogen$_3^-$-center is a *new center*. Its principal optical absorption, however, is almost superposed to the V_1-band. It has been overlooked in optical work for a long time because of the small oscillator strength. A second absorption band of the halogen$_3^-$-center is in the far red part of the spectrum, also in agreement with the predictions of this paper (see section 4.3). Also, DELBECQ and YUSTER find that the temperature of fast thermal bleaching of the halogen$_3^-$-center is about 20° higher than the temperature at which the V_1-band bleaches.

‡ The weak V_6- and V_7-bands observed by DORENDORF[5b] also fall within these limits.

§ This crystal was given to us by C. J. DELBECQ and P. H. YUSTER, and we wish to acknowledge their friendly co-operation.

MAURER[8] observed a release of charge and, simultaneously, bleaching of the optical V_1-band. This suggests again that the optical absorption of our paramagnetic centers might coincide with the V_1-band.* The temperature 205°K is a lower limit for the thermal instability of the paramagnetic center in KCl.

Finally, it is interesting to note that the I_2^- molecule-ion was observed in X-rayed KI : Tl, whereas in pure KI these defects could not be observed, even after prolonged X-irradiation.

3. DESCRIPTION AND QUALITATIVE INTERPRETATION OF THE ELECTRON SPIN RESONANCE SPECTRA

3.1. *Isotope effects*

Fig. 1a shows the electron spin resonance spectrum of the V-center in pure KCl, taken with the d.c. magnetic field along the [100]-axis. The most striking feature of the spectrum is the seven almost equally spaced lines with the intensity ratio 1 : 2 : 3 : 4 : 3 : 2 : 1. This is readily explained by the assumption that an electron or hole interacts equally with two equivalent nuclei of the spin 3/2, since the total magnetic spin quantum number m_I of the two nuclei together can then take each of the values 3, 2, 1, 0, −1, −2, −3 with the probability corresponding to the above intensity ratio. Both Cl isotopes, ^{35}Cl and ^{37}Cl, as well as both K isotopes, ^{39}K and ^{41}K, have the spin 3/2. One way to decide whether the two nuclei are alkali or halogen nuclei is to repeat the experiment with NaCl and with KBr. Fig. 1b demonstrates that the spectrum is almost the same for NaCl as for KCl, the only essential difference being the line width. Since the magnetic moment of ^{23}Na is much larger than the magnetic moment of the K nuclei we conclude from the very close similarity of the spectra that the electron or hole is shared between two halogen nuclei and not between two alkali nuclei. This in turn indicates that the spectrum arises from an electron deficiency (hole), since an excess electron is unlikely to be at a negative halide ion. That an electron deficiency is responsible for the spin resonance is also confirmed by the positive g-shift (see sec. 3.3). An electron deficiency shared by two halide ions is roughly equivalent to a halogen$_2^-$ molecule-ion. Such molecule-ions also appear to exist in the free state.[9]

If we switch from a chloride to a bromide the electron spin resonance spectrum of the V-center changes rather drastically as now expected (see Fig. 1c). Both Br isotopes, ^{79}Br and ^{81}Br, have the spin 3/2, but their nuclear magnetic moments are much larger than the magnetic moments of the Cl nuclei and thus produce a much larger hyperfine splitting. Moreover, second-order hyperfine and quadrupole effects cause additional splittings (see sec. 4.4). Seven groups of lines with roughly the above-mentioned intensity ratio are, however, still recognizable.

The existence of two halogen isotopes of comparable abundance complicates the spectra of the chlorides as well as of the bromides. In fact, this complication is another way to recognize immediately that the two nuclei are halogens. As an illustration the case of the chlorides will be discussed briefly. ^{35}Cl is about 3/4 abundant and has a somewhat larger nuclear magnetic moment than ^{37}Cl which is 1/4 abundant. Therefore, there are 3 types of molecule-ions ^{35}Cl–^{35}Cl, ^{35}Cl–^{37}Cl and ^{37}Cl–^{37}Cl with the abundance 9/16, 6/16 and 1/16 respectively. The seven main lines in Fig. 1a are due to the ^{35}Cl–^{35}Cl molecule-ions. The spectrum of the ^{35}Cl–^{37}Cl molecule-ions is different. The non-equivalence of the two nuclei lifts the degeneracies that lead to the intensity ratio 1 : 2 : 3 : 4 : 3 : 2 : 1, and instead of a single line with the relative intensity n one observes n lines of equal intensity. The spectrum of the ^{37}Cl–^{37}Cl molecule-ions is again similar to the ^{35}Cl–^{35}Cl spectrum. The position of all the isotope lines is consistent with the magnetic moments, and the intensity is consistent with the isotope abundance (compare Fig. 2 with Fig. 1a).

A simple case from the standpoint of nuclear moments is LiF, because there is only one isotope, ^{19}F, with the spin 1/2. Therefore, the basic spin

* *Note added in proof:* CHIAROTTI and INCHAUSPE (private communication) found in pure KBr, X-rayed at liquid nitrogen temperature, two charge bursts during warming up in this temperature region. The first burst at 120°K is associated with the destruction of V_1-centers (as found by DUTTON and MAURER[8]), but it leaves the halogen$_2^-$-centers unharmed. The second burst at 143°K is probably associated with the destruction of F'-centers and the annihilation of the halogen$_2^-$-centers. Thus it appears that in pure KBr (and probably also in pure KCl) electrons released from F'-centers annihilate the halogen$_2^-$-center.

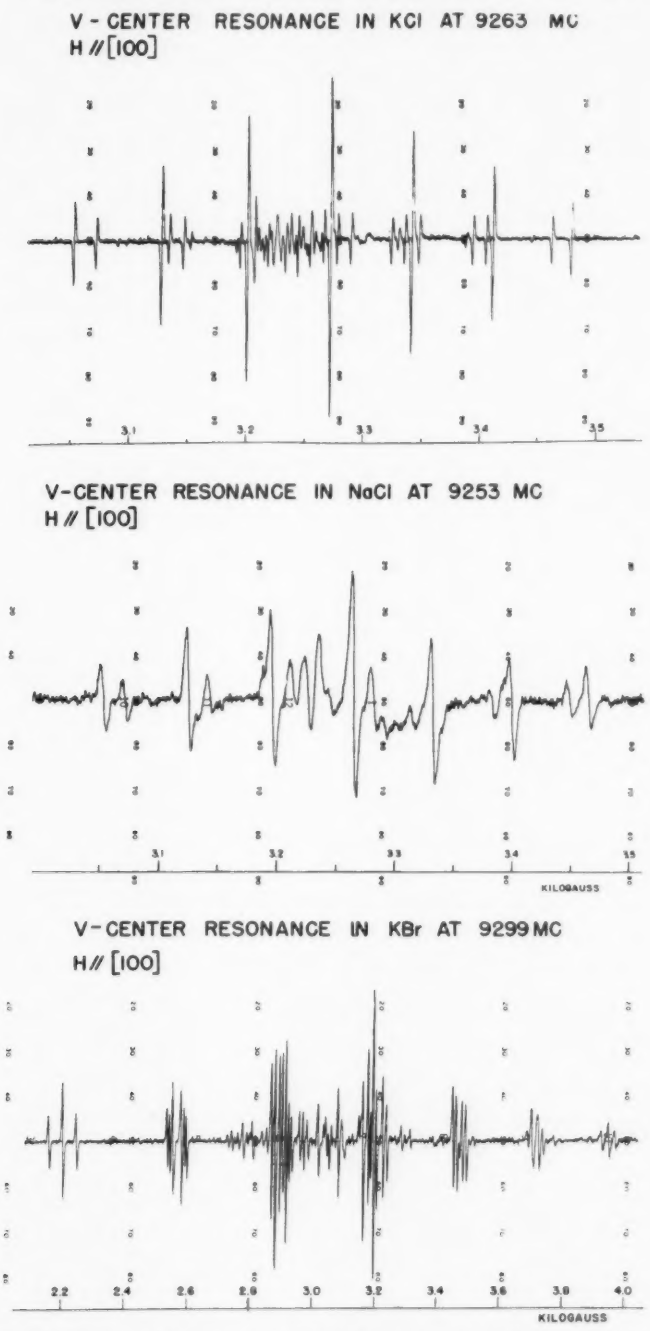

FIG. 1. Electron spin resonance absorption spectrum of the V-center in KCl, NaCl and KBr, taken with the d.c. magnetic field along the [100]-axis. Note that the magnetic field scale is the same for KCl and NaCl, but compressed for KBr. The first derivative of the absorption is recorded.

VOL. 3 1957

M

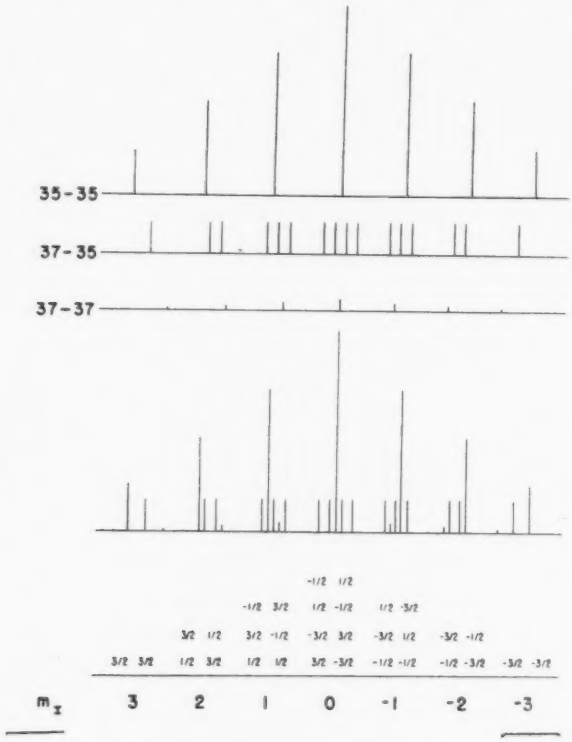

FIG. 2. Isotope effects in KCl, schematic.

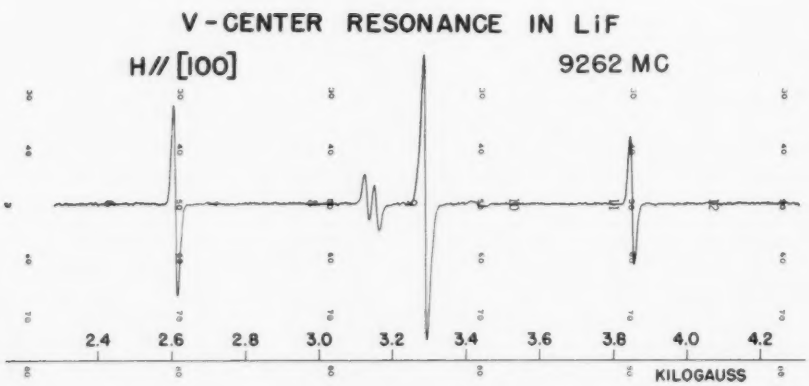

FIG. 3. Electron spin resonance absorption of the *V*-center in LiF, taken with the d.c. magnetic field along the [100]-axis.

resonance spectrum of the F_2^- molecule-ion consists of three lines with the intensity ratio 1 : 2 : 1 as is shown in Fig. 3. Note the large splitting which reflects the large magnetic moment of the ^{19}F nucleus and the small size of the fluoride ion.

3.2. *The orientation of the halogen$_2^-$ molecule-ions and the anisotropy of the hyperfine interaction*

Comparison of Fig. 2 with the actually observed spectrum Fig. 1(a) reveals that only about half of all the observed lines are explained at this point. In order to understand the rest of the lines we have to consider the orientation of the molecule-ion in the crystal and the anisotropy of the hyperfine splitting.

(a) *The orientation of the molecular axis.* To a very good approximation the diatomic molecule-ion turns out to be axially symmetric. The crystal structure suggests that the axis of the molecule may coincide with a [110]-axis of the crystal, and this is confirmed by the analysis of the spectra, as will be discussed below. The six equivalent [110]-axes of the crystal are equally populated with molecule-ions, which can be regarded as "frozen in" according to the following considerations: the internuclear distance of the halogen$_2^-$ molecule-ion is somewhere between the internuclear distance of the halogens in the unperturbed crystal (2·84 Å, 3·98 Å, 4·44 Å and 4·51 Å for LiF, NaCl, KCl and KBr respectively), and of the free halogen$_2$ molecule (1·46 Å, 2·00 Å and 2·28 Å for F_2, Cl_2 and Br_2 respectively). Thus the two halide ions involved in the formation of the molecule-ion are expected to pull together considerably. Since the spectra clearly show that the nuclei are equivalent (disregarding isotope effects and second-order hyperfine and quadrupole effects) this relaxation is symmetrical with respect to the center of gravity of the two nuclei in the unperturbed crystal. A significant rearrangement of the nuclear positions would have to occur for the molecular bond to "resonate" between the different equivalent [110]-axes. Therefore, it is the *nuclear* mass and not the electron mass that determines the frequency of such "jumps". The activation energy is of the order of 1 eV since the jump involves desintegration of the molecule-ion. The resulting jump frequency is of the order 10^{-50} sec^{-1}.

A "bending" of the molecular bond which would result if the molecule-ion were, for example, near a single vacancy can also be ruled out, because such bending would lead to a splitting of degenerate levels since the two nuclei in the "bent bond" molecule-ions are no longer equivalent with respect to an arbitrary direction of the d.c. magnetic field. We estimated that the "bending" of the bond in KCl due to a vacancy on one side would split the center line ($m_I = 0$) by about 20 gauss and thus would easily be observable. Moreover, spectra corresponding to bent bond molecule-ions were observed after proper treatment of the crystals.* Thus, at this stage the electron spin resonance spectra permit the conclusion that there are either two equivalent imperfections, one on each side of the molecule-ion, or that there is no imperfection associated with it. The experiments with KCl : Tl suggest the second possibility.

(b) *The anisotropy of the hyperfine interaction.* The unpaired electron giving rise to the spin resonance is essentially a p-electron ($2p$, $3p$ and $4p$ for the fluorides, chlorides and bromides respectively). Therefore, its wave function in the molecular orbital ground state contains a linear combination of two p-functions each centered on one of the two halogen nuclei.† The orbital moment is almost completely quenched through the formation of the molecular bond as is indicated by the small g-shifts. Hence it is quite accurate to use for the atomic orbitals making up the ground state p-functions with their rotational symmetry axis along the line joining the two nuclei. Thus, the hyperfine splitting (which for a p-function arises from magnetic dipole-dipole interaction) strongly depends upon the angle θ between the molecular axis and the d.c. magnetic field. The splitting decreases with increasing angle θ. Therefore, for any orientation of the crystal in the d.c. magnetic field at least two spectra are simultaneously observed. If, for example, the d.c. magnetic field is parallel to [100] the axes of 2/3 of the molecule-ions form an angle $\theta = 45°$ with the field and 1/3 an angle $\theta = 90°$. Table 1 gives the angles θ and the corresponding relative abundance of the molecule ion for 3 simple orientations of the crystal and Fig. 4 illustrates that the expected spectra are observed. The relative intensities are in satisfactory

* A discussion of these spectra will be deferred to a forthcoming paper.

† The admixture of s-functions will be discussed in sec. 4.2.

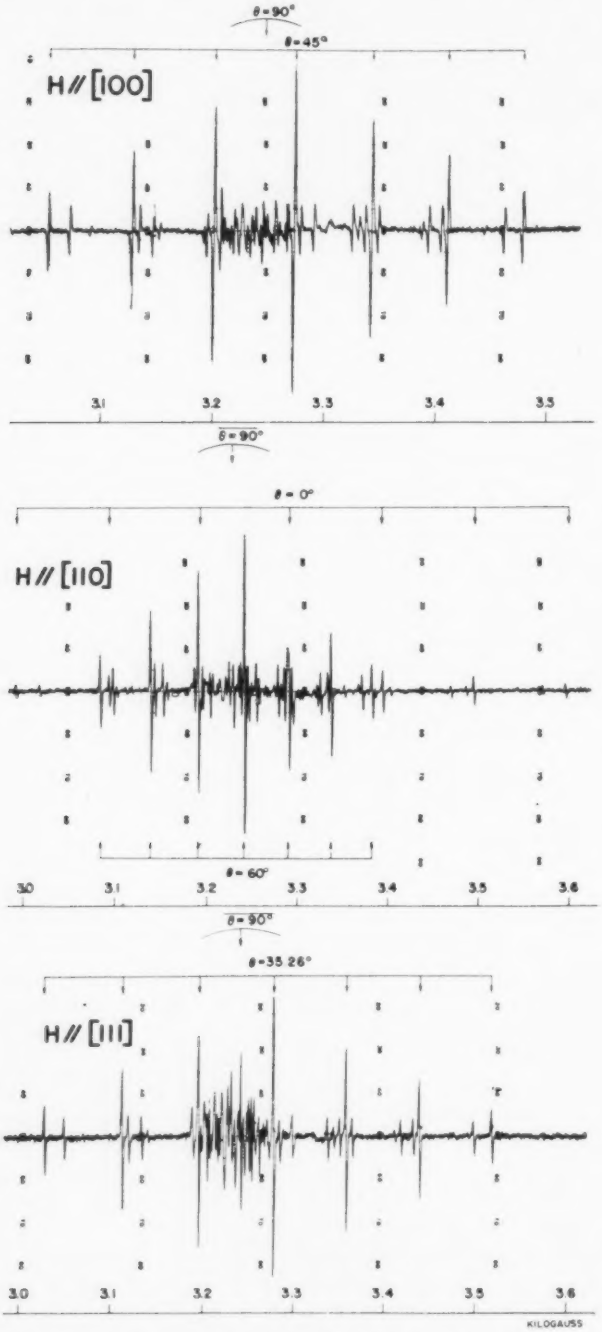

FIG. 4. Illustration of the anisotropy of the hyperfine interaction in the V-center in KCl. Frequency 9·3 kMc/s. The arrows mark the $^{35}Cl_2$ spectra.

Table 1. *Classification of molecule-ions for simple orientations of the crystal in the d.c. magnetic field*

Direction of d.c. field	Angle θ	Abundance
[100]	45°	4
	90°	2
[110]	0°	1
	60°	4
	90°	1
[111]	35·26°	3
	90°	3

agreement with the abundance numbers listed in Table 1. For $H_{\parallel}$[111] the relative intensity of the $\theta = 90°$ spectrum is largest, and it is easy to see that this spectrum is not simply a "compressed version" of the spectra for lower angles. This is due to second-order effects, which become important when the angle θ between the d.c. magnetic field and the axis of the hyperfine interaction, the molecular axis, approaches a right angle (see sec. 4.4). In LiF, for example, the 90°-spectrum consists of four lines two of which are on the low field side of the center of the spectrum, the other two merging with the center of the 45°-spectrum (see Fig. 3).

For KCl and NaCl the $^{35}Cl-^{35}Cl$ spectra for $\theta \lesssim 75°$ can be described within about 0·04 gauss by the following empirical formula

$$H-H_0 = A_1(\theta)m_I + A_2(\theta)m_I^2 + A_3(\theta)m_I^3 + A_4(\theta)m_I^4 \quad (1)$$

where $m_I = m_{I_1} + m_{I_2}$ is the nuclear magnetic quantum number of the molecule ion (-3, -2, ..., $+3$) and H_0 is the position of the center line. The A_i values are listed in Table 2 for KCl.

Table 2. *Coefficients of equation* (1) *for* $^{35}Cl-^{35}Cl$ *molecule-ions in* KCl *measured at* 9·26 kMc/s

(A_1* and A_2* were calculated by means of equation (6) using the numbers in Table 5 (see Section 4.1))

Orientation of H	Angle θ	A_1 ±0·03 Gauss	A_2 ±0·01 Gauss	A_3 ±0·003 Gauss	A_4 ±0·001 Gauss	Calculated by means of perturbation formula (6)	
						A_1*	A_2*
[110]	0°	101·39	0·00	0·000	0·000	101·39†	0·000†
[111]	35·26°	81·79	0·527	0·013	—0·004	82·34	0·505
[100]	45°	70·67	0·751	0·008	—0·002	71·23	0·751
[110]	60°	49·91	1·163	0·048	—0·015	50·47	1·104

† Fitted.

3.3. *The anisotropy of the spectroscopic splitting factor*

The orbital moment is not fully quenched, and the admixture of p-functions with axes perpendicular to the molecular axis produces a first-order shift of the spectroscopic splitting factor when the direction of the d.c. magnetic field deviates from the molecular axis. As the spin resonance is due to an *electron deficiency* this g-shift is *positive*. For axial symmetry the g-tensor would be determined by $g_{\parallel}$ and $g_{\perp}$. However, the crystalline field has *orthorhombic symmetry* about the molecular axis and three axes x', y' and z' of the molecule have to be distinguished (see Fig. 5).* The three components $g_{x'}$, $g_{y'}$, and $g_{z'}$ of the measured spectroscopic splitting factors are listed in Table 3. The shifts of $g_{x'}$ and $g_{y'}$ increase with increasing atomic number of the halogens, as is to be expected on the basis of the spin orbit coupling

* Note that the classification given in Table 1 remains valid for the orthorhombic molecule-ions.

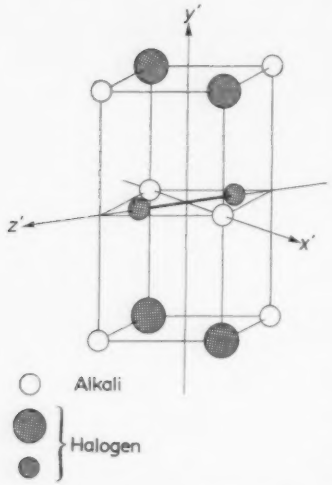

FIG. 5. Orientation and principal axes of the halogen$_2^-$ molecule-ion in the crystal.

Table 3. *Components of the g-tensor, measured at* 9·3 kMc/s

(Polycrystalline α,α-diphenyl β-picryl hydrazyl (DPPH) served as a standard. The *g*-factor corresponding to the point of zero slope of the absorption curve was given to us as 2·0034. The experimental error in this table does not include a possible error in the *g*-factor of the reference standard. For LiF and KBr the uncertainty in the *g*-factor is mainly due to overlapping lines.)

Crystal	$g_{x'}$	$g_{y'}$	$g_{z'}$	Maximum error
LiF	2·0227	2·0234	2·0031	±0·0010
KCl	2·0428	2·0447	2·0010	±0·0001
NaCl	2·0489	2·0425	2·0010	±0·0001
KBr	2·179	2·175	1·980	±0·001

constants of the halogen atoms. $g_{z'}$ is close to the free electron value $g_0 = 2{\cdot}0023$.

Since $|g_{x'} - g_{y'}| \ll g_{x'} - g_0$ we may conclude that the influence of the crystalline field on the molecule-ion is not large. Consequently, axial symmetry is a very good approximation. The sign of $g_{x'} - g_{y'}$ depends upon the substance and is not fully understood at the present time.

3.4. *Line shape, line width and saturation*

For the determination of the line width and of the line shape lines were chosen which are sufficiently isolated and not affected by second-order hyperfine and quadrupole effects that may cause unresolved splittings. It was found that the lines are very closely gaussian at liquid nitrogen temperature.* The line widths are listed in Table 4.

Table 4. *Line width in gauss, corrected for mosaic effects and orientation errors*

(The numbers represent the distance between points of maximum slope of the absorption line.)

LiF	KCl	KCl : Tl	NaCl	KBr
12·3±0·3	1·34±0·03	1·35±0·1	4·5±0·1	2·8±0·1

The major contribution to the line width is due to hyperfine interaction with the nuclei surrounding the *V*-center. This becomes clear when we compare KCl and NaCl. The *V*-center wave functions are almost the same in these two substances. The larger line width for NaCl can be explained by the larger magnetic moment of the Na nuclei compared with the K nuclei and by the somewhat smaller lattice spacing for NaCl. Simple considerations based on magnetic dipolar interaction suggest that the contribution to the line width from the surrounding alkali nuclei is comparable to the contribution from the surrounding halogen nuclei.

A small contribution results from imperfection of the crystal (mosaic structure) because the hyperfine splitting depends very sensitively upon the orientation of the crystal in the d.c. magnetic field. The angular spread of the "mosaics" does not affect all the lines equally. In the chlorides, for example, the lines $m_I = +2$, $+1$ and 0 are least affected, an angular spread of 0·1° giving a broadening of the order 0·05 gauss. On the other hand, the same angular spread broadens the lines $m_I = -2$, -3 by about 0·3 gauss. This "selectivity" of the effect enables us to estimate the small correction that has to be applied in order to arrive at the true line width. The values in Table 4 are corrected. This correction automatically also includes the

* The interesting changes that occur at very low temperatures will be discussed in a forthcoming paper.

effect of the orientation error of the crystal in the magnetic field, which is about 0·05° (the exact orientation of the crystals was accomplished by minimizing the width of those lines that split most for small angular variations). It is important to note that the axis of the V-center coincides within the same small angular error with the [110]-axes of the crystal. This indicates that *the centers are not located in the strain fields of imperfections such as dislocations.*

No line width difference was found between ^{35}Cl–^{35}Cl, ^{35}Cl–^{37}Cl and ^{37}Cl–^{37}Cl molecule ions.* Therefore, relaxation through hyperfine interaction does not give a measurable contribution to the line width at liquid nitrogen temperature.

There is a small broadening due to the interaction between the paramagnetic centers in the crystal. The total concentration of paramagnetic centers of all kinds contained in the X-rayed crystal was roughly 10^{17} cm^{-3}. Assuming a random distribution their mutual interaction leads to a line width of less than 0·1 gauss. The identity of the spectra observed with KCl : Tl and pure KCl suggests that the concentration *is* uniform.

The temperature dependence of the line width was investigated for LiF between 50°K and 80°K and found to be less than the experimental error, which indicates that the broadening due to relaxation processes can be neglected in this temperature range.

Since the magnetic resonance lines of the V-center are packages of unresolved lines the absorption signal saturates more easily than the dispersion signal.[1] The relaxation processes are at present under careful investigation.

4. ANALYSIS OF THE SPIN RESONANCE SPECTRA

4.1. *The spin Hamiltonian*

In this section we will show that the main features of the electron spin resonance spectra are adequately described by a spin Hamiltonian of the form

$$\mathcal{H}/g_0\beta_0 = \frac{g}{g_0}HS_z + a\boldsymbol{I}\cdot\boldsymbol{S} + bI_{z'}S_{z'} \qquad (2)$$

where g_0 and g are the spectroscopic splitting factors of the free electron and of the molecule-ion (for the orientation visualized) respectively. The axis of the d.c. magnetic field H is designated by z and the axis of the molecule ion by z'. Deviations from axial symmetry are neglected. β_0 is the Bohr magneton.

Using perturbation theory† we will now calculate the electronic transitions resulting from this spin Hamiltonian. The constants a and b will then be determined to fit the experimental data.

Writing

$$I_{z'} = I_z\cos\theta + I_x\sin\theta$$

and

$$S_{z'} = S_z\cos\theta + S_x\sin\theta$$

we have

$$\mathcal{H}/g_0\beta_0 =$$
$$= [(gH/g_0) + (a + b\cos^2\theta)I_z + (b\sin\theta\cos\theta)I_x]S_z +$$
$$+ [(b\sin\theta\cos\theta)I_z + (a + b\sin^2\theta)I_x]S_x + aI_yS_y$$

where θ is the angle between the molecular axis z' and the direction z of the d.c. magnetic field H. Now if we choose as our basis functions the eigenfunctions of I_z

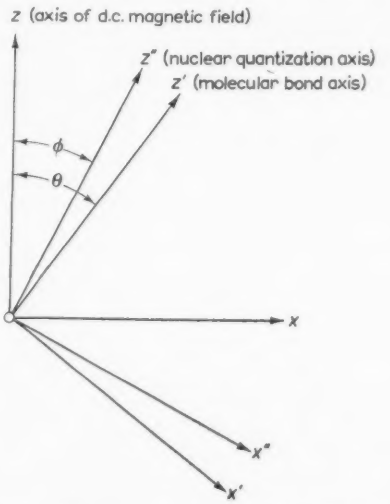

FIG. 6. Co-ordinate systems used for the analysis of the spin Hamiltonian.

* The difference reported in the preliminary paper[3] was mainly due to inaccurate orientation of the crystal and to comparison of lines with different sensitivity to angular variations.

† A treatment similar to the one given here was first given by BLEANEY[11] who in addition took into account the anisotropy of the g-factor. A rigorous treatment has been worked out for LiF by WOODRUFF and KÄNZIG.[10]

and S_z there are terms diagonal in m_s that are off-diagonal in m_I. Since these off-diagonal elements cannot be neglected it is convenient to introduce a new co-ordinate system x'', y'', z'' for the nuclear operators, such that the dominant S_z term is also diagonal in the nuclear co-ordinates (see Fig. 6). With

$$I_x = I_{z''} \sin\phi + I_{x''} \cos\phi$$

$$I_y = I_{y''}$$

and

$$I_z = I_{z''} \cos\phi - I_{x''} \sin\phi$$

we obtain

$$\begin{aligned}\mathcal{H}/g_0\beta_0 = (g/g_0)HS_z &+ [(a\sin\phi + b\sin^2\theta\sin\phi + b\sin\theta\cos\theta\cos\phi)I_{z''} + \\ &+ (a\cos\phi + b\sin^2\theta\cos\phi - b\sin\theta\cos\theta\sin\phi)I_{x''}]S_x + \\ &+ aI_{y''}S_y + [(a\cos\phi + b\cos^2\theta\cos\phi + b\sin\theta\cos\theta\sin\phi)I_{z''} + \\ &+ (-a\sin\phi - b\cos^2\theta\sin\phi + b\sin\theta\cos\theta\cos\phi)I_{x''}]S_z.\end{aligned} \tag{3}$$

In order to get rid of the major off-diagonal term $I_{z''}S_z$ we choose

$$\tan\phi = \frac{b\sin\theta\cos\theta}{a + b\cos^2\theta}$$

and obtain

$$\begin{aligned}\mathcal{H}/g_0\beta_0 = &\left[\frac{g}{g_0}H + (p^2+q^2)^{1/2}\right]S_z + \\ &+ \frac{(2a+b)q}{(p^2+q^2)^{\frac{1}{2}}}I_{z''}S_x + \\ &+ \frac{a(a+b)}{(p^2+q^2)^{\frac{1}{2}}}I_{x''}S_x + aI_{y''}S_y\end{aligned} \tag{4}$$

where

$$p = a + b\cos^2\theta$$

$$q = b\sin\theta\cos\theta$$

The term $aI_{y''}S_y$ is negligible for all angles θ, and

$$\frac{a(a+b)}{(p^2+q^2)^{\frac{1}{2}}}I_{x''}S_x$$

is very small except for $\theta \to \pi/2$. Neglecting these two terms one finds from second-order perturbation theory the following energy levels

$$\begin{aligned}E_{m_I m_s} = &(g\beta_0 H + g_0\beta_0(p^2+q^2)^{\frac{1}{2}}m_I)m_s + \\ &+ \frac{g_0^2\beta_0(2a+b)^2q^2m_I^2m_s}{2g(p^2+q^2)[H + (p^2+q^2)^{\frac{1}{2}}m_I]}\end{aligned} \tag{5}$$

where

$$m_s = \pm\tfrac{1}{2} \text{ and } m_I = m_{I_1} + m_{I_2}.$$

In the experiment the frequency is held constant and the magnetic field H is varied. Solving for H and observing the selection rules $|\Delta m_s| = 1$ and $\Delta m_I = 0$ one finds

$$H - H_0 \cong \frac{g_0}{g}(p^2+q^2)^{\frac{1}{2}}m_I + \frac{g_0(2a+b)^2q^2m_I^2}{g^2(p^2+q^2)H_0} \tag{6}$$

where H_0 corresponds to the center line $m_I = 0$. The angular dependence of these terms is shown in Fig. 7 for KCl. The anisotropy is very large. The first order splitting ranges from $(a+b)$ at $\theta = 0$ to $|a|$ at $\theta = \pi/2$. Since the second order term vanishes at $\theta = 0$ the corresponding spectrum (which is contained in the $H_{\|}$ [110] pattern) immediately yields $(a+b)$. The determination of a is much more problematic. First we notice that the sign of a in principle cannot be determined using the expression (6). Also we were unable to determine this sign in a more rigorous treatment.[10] Second, it will turn out that $|a| \ll (a+b)$, which makes the expression (6) very insensitive to the value of a except for $\theta \to \pi/2$, where $(H - H_0) \to (g_0/g)(a^2)^{1/2}m_I$. Our approximations do not permit us to determine $|a|$ from the spectra at $\theta < 75°$. Therefore, we take $|a|$ from the $\theta = \pi/2$ spectrum. This procedure is not very accurate because of higher order and quadrupole effects to be discussed below. Table 5 summarizes the values of a and $(a+b)$ that agree best with our measurements, and Table 2 shows for KCl, as an example, that the measured angular dependence of the m_I and m_I^2 terms is in satisfactory agreement with the calculations. The discrepancies are somewhat larger than the experimental errors, which is not surprising in view of the approximations made in the analysis.

4.2 *Derivation of the spin Hamiltonian from a molecular model*

In this section we try to obtain information about the electronic structure of the molecule-ion by correlating the spin Hamiltonian with a molecular model.

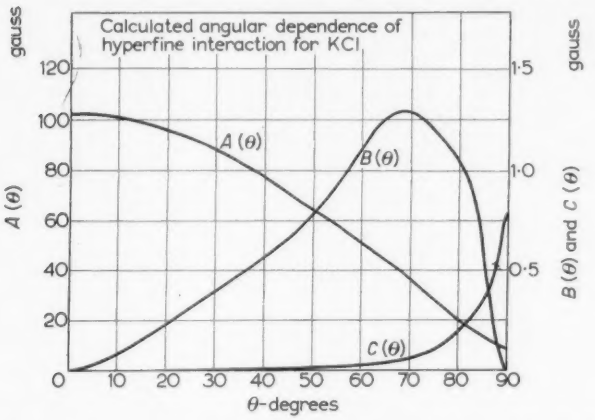

FIG. 7. Angular dependence of the terms $I_{z'}S_z$, $I_{z'}S_x$ and $I_{x'}S_x$ for KCl. Note the different scale used for the second-order terms. Frequency 9·3 kMc/s.

$$I_{z'}S_z \text{ term } A(\theta) = \frac{g_0}{g}\sqrt{(p^2+q^2)}$$

$$I_{z'}S_x \text{ term } B(\theta) = \frac{g_0(2a+b)^2q^2}{g^2(p^2+q^2)H_0}$$

$$I_{x'}S_x \text{ term } C(\theta) = \frac{a^2(a+b)^2}{4(p^2+q^2)H_0}$$

We consider a Hamiltonian of the form[11]

$$\mathcal{H} = \mathcal{H}_{\text{atom}} + V_{\substack{\text{crystalline}\\\text{field}}} + \lambda \boldsymbol{L}\cdot\boldsymbol{S} - \boldsymbol{\mu}_L\cdot\boldsymbol{H} - \boldsymbol{\mu}_s\cdot\boldsymbol{H}$$
$$+\sum_{j=1}^{2}\left(\frac{\boldsymbol{\mu}_s\cdot\boldsymbol{\mu}_I}{r_j^3} - \frac{3(\boldsymbol{\mu}_s\cdot\boldsymbol{r}_j)(\boldsymbol{\mu}_{I_j}\cdot\boldsymbol{r}_j)}{r_j^5} - \right.$$
$$\left. -\frac{8\pi}{3}\delta(r_j)\,\boldsymbol{\mu}_s\cdot\boldsymbol{\mu}_{I_j}\right) + \qquad (7)$$
$$+\sum_{j=1}^{2}\left(-\boldsymbol{\mu}_{I_j}\cdot\boldsymbol{H} + \xi\boldsymbol{L}\cdot\boldsymbol{I}_j + \mathcal{H}_{j\text{ quadrupole}}\right)$$

The sum is to be taken over the two halogen nuclei between which the electrons of the molecule-ion resonate. The interaction of the electrons with other nuclei and other paramagnetic centers is neglected.

The spin Hamiltonian is obtained by averaging the Hamiltonian (7) over the wave function of the unpaired electron of the molecule-ion. Since information about halogen$_2^-$ molecule-ions is very meager we have to construct a reasonable wave function.

The V-center is created by removing a p-electron from a negative halogen ion, and the electron deficiency is shared with a neighboring halide ion through the formation of a diatomic

Table 5. Constants of the spin Hamiltonian

(For KCl, NaCl and KBr the values were obtained using the perturbation formula (6), whereas, the values for LiF are the result of a more rigorous treatment.[10])

Crystal	Isotope	$(a+b)$ gauss	$\lvert a\rvert$ gauss
LiF	^{19}F–^{19}F	887	59
KCl	^{35}Cl–^{35}Cl	101	9
NaCl	^{35}Cl–^{35}Cl	98	9
KBr	^{81}Br–^{81}Br	455	80

molecule-ion. It is reasonable to approximate the orbital ground state of the unpaired electron by a linear combination of two atomic wave functions φ_1 and φ_2 having primarily p-character. A considerable s-admixture has to be expected because of mutual dielectric polarization of the two atoms involved in the formation of the molecule-ion.

Thus we approximate the orbital ground state eigenfunctions of $\mathcal{H}_{\text{atomic}}+V_{\text{crystalline field}}$ by

$$\psi = \frac{1}{\sqrt{2}}\left[\varphi_1(x',y',z') \pm \varphi_2(x',y',z')\right] \tag{8}$$

with

$$\varphi_j = f(r_j)\alpha\left(\frac{3}{4\pi}\right)^{\frac{1}{2}}\cos\theta_j' \pm g(r_j)\beta\left(\frac{1}{4\pi}\right)^{\frac{1}{2}}$$

where α^2 and β^2 designate the fraction of p and s-function respectively ($\beta^2 = 1-\alpha^2$), and θ_j' is the angle between r_j and the z' axis. The radial functions are normalized so that

$$\int |f(r_j)|^2 r^2\, dr = \int |g(r_j)|^2 r^2\, dr = 1$$

The degeneracy of the p-type function is lifted through the formation of the molecular bond. Therefore $\langle 0|\boldsymbol{L}|0\rangle = 0$, and to first order all the terms in the Hamiltonian (7) involving orbital angular momentum and its associated magnetic moment μ_L are zero. Also in higher order these terms will be neglected except for the interaction of the term $\lambda \boldsymbol{L}\cdot\boldsymbol{S}$ with $\mu_L \cdot \boldsymbol{H}$, which can be taken into account by introducing a shifted g-factor.[12]

The direct interaction of the external magnetic field with the nuclei will be omitted since it alters the electron spin levels at most through small off-diagonal terms. Similarly the quadrupole terms are small and influence the electronic resonance only in second order. (These interactions become, however, important for $\theta \to \pi/2$). The remaining Hamiltonian contains only the interaction of the electron spin with the d.c. magnetic field H and the magnetic moment μ_I of the nuclei. Averaging now over the molecular orbital wave function (8), neglecting overlap of the wave function φ_1 with the wave function φ_2 and nucleus 2 and vice versa, the resulting spin Hamiltonian in fact takes the form

$$\mathcal{H}/g_0\beta_0 = (g/g_0)HS_z + a\boldsymbol{I}\cdot\boldsymbol{S} + bI_{z'}S_{z'} \tag{1}$$

with

$$a = \frac{\mu_I}{2}\left[\frac{8\pi}{3}\beta^2|\psi(0)|^2 - \frac{2}{5}\alpha^2\overline{\left(\frac{1}{r^3}\right)}\right] \tag{9}$$

$$b = \frac{\mu_I}{2}\left[\frac{6}{5}\alpha^2\overline{\left(\frac{1}{r^3}\right)}\right] \tag{10}$$

where μ_I is the magnetic moment of the halogen nucleus, and $|\psi(0)|$ is the amplitude of an s-function at the nucleus. $\overline{(1/r^3)}$ has to be taken over the p-function centered on the nucleus. Equations (9) and (10) permit a good estimate of β^2 (or $\alpha^2 = 1-\beta^2$), particularly if one uses the ratio a/b only, such that overlap effects cancel to a certain extent. Solving for β^2 one has

$$\beta^2 = \frac{(a/b+1/3)}{(a/b+1/3)+\dfrac{2\pi|\psi(0)|^2}{9\overline{\left(\frac{1}{r^3}\right)}}} = 1-\alpha^2 \tag{11}$$

For $\overline{(1/r^3)}$ we may insert the values computed by STERNHEIMER[13] for the np-functions of halogen atoms. The value for $|\psi(0)|^2$ to be used is more problematic. It seems reasonable to admix a $(n+1)s$ function to the np-function. Unfortunately, no hyperfine data for halogens are available that permit a determination of $|\psi(0)|^2$. However, the hyperfine-structure separation[14]

$$\Delta = \frac{16\pi}{3h}\frac{\mu_0\mu_I}{I}|\psi_{n0}(0)|^2(I+\tfrac{1}{2})$$

is known for the alkali atoms[15] and a reasonable "interpolation formula" can be found to make possible an estimate of $|\psi(0)|^2$ for the halogens. We used for the interpolation the relation $|\psi_{n0}(0)|^2 \cong Z^k/\pi n^3 a_0{}^3$, where Z is the atomic number, a_0 the Bohr radius, and k was determined using the experimental Δ-values[15] for alkali atoms.

A further complication arises from the fact that the sign of a is not known. We cannot even expect that this sign is the same for all the alkali halides, because a minor change of the s-admixture may change it. Table 6 summarizes the numerical data of the computation of β^2. The values of β^2 for the $(n+1)$ s-function are rather on the high side, because a slight admixture of a ns-function cannot be excluded for the molecule-ion. An admixture of this kind would have a rather large effect because $|\psi_{n0}(0)|^2 \propto 1/n^3$.

Table 6. Computation of the fraction β^2 of s-character by means of formula (11)

(The fraction of p-character is $\alpha^2 = 1-\beta^2$. The calculations are given for both signs of a)

Substance	np function	$\overline{(1/r^3)}$ (Sternheimer)	$(n+1)s$ function	$\lvert\psi_{(n+1)_0}(0)\rvert^2$ (estimated)	β^2	
					$a>0$	$a<0$
LiF	$2p$	$60{\cdot}0\times10^{24}$	$3s$	$3{\cdot}32\times10^{24}$	0·51	0·41
KCl	$3p$	$55{\cdot}6\times10^{24}$	$4s$	$5{\cdot}72\times10^{24}$	0·38	0·26
NaCl					0·38	0·25
KBr	$4p$	163×10^{24}	$5s$	$14{\cdot}16\times10^{24}$	0·43	0·28

VOL. 3 1957

4.3. *The g-shifts and the excited states*

The g-shifts arise from the admixture of excited states with the ground orbital state of the molecule-ion. An interpretation of the g-shifts based on our preliminary data[3] for KCl was given by COHEN[5a] and, independently, by INUI, HARASAWA, and OBATA.[16] We follow here the treatments of these authors and incorporate our results for LiF, NaCl and KBr.

Consider first two negative halogen ions that are brought together to form a pseudomolecule-ion. There are 2×6 np-electrons to be accommodated in the levels $np\sigma_g$, $np\pi_u$, $np\pi_g$ and $np\sigma_u$ of the pseudomolecule.[17] In its ground state the hole is in the $np\sigma_u$ level, and the configuration of the halogen$_2^-$ molecule-ion is $(np\sigma_g)^2\,(np\pi_u)^4\,(np\pi_g)^4\,(np\sigma_u)$. In free space the molecule-ion is axially symmetric and the $np\pi_u$ level and the $np\pi_g$ level are both doubly degenerate. In the crystal, however, this degeneracy is lifted by the crystalline field having orthorhombic symmetry about the molecular axis (see Fig. 5 and Fig. 8). This lifting is a very subtle effect as is indicated by the small difference $g_{x'}-g_{y'}$ the sign of which depends upon the substance.*

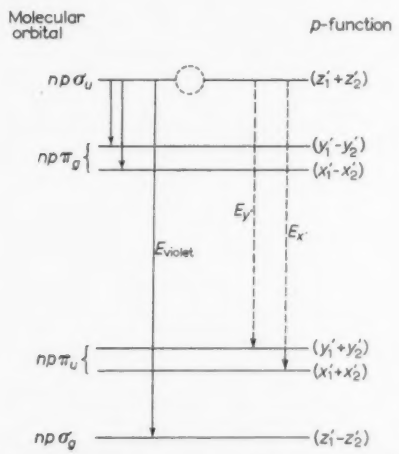

FIG. 8. Energy levels of the halogen$_2^-$ molecule-ion (schematic). Full arrows represent allowed optical transitions, broken arrows represent the optically forbidden transitions that produce the g-shifts.

The allowed optical transitions are indicated in Fig. 8 by full arrows whereas the broken arrows represent the transitions that produce the g-shifts, but are optically forbidden. INUI, HARASAWA and OBATA derived the following relations for the g-shifts[16]

$$g_{z'}-g_0 = -\alpha^2\lambda^2\left[\frac{g_0}{2}\left(\frac{1}{E_{x'}{}^2}+\frac{1}{E_{y'}{}^2}\right)-\frac{1}{E_{x'}E_{y'}}\right] \tag{12}$$

$$g_{x'}-g_0 = -\frac{2\alpha^2\lambda}{E_{y'}}-\alpha^2\lambda^2\left[\frac{g_0}{2}\left(\frac{1}{E_{x'}{}^2}+\frac{1}{E_{x'}E_{y'}}\right)\right] \tag{13}$$

* Attempts were made to decide whether there are two alkali vacancies associated with the molecule-ion (one on each side), or whether there is no vacancy, by calculating the effect of the crystalline field on the g-shifts. The calculations predict $g_{x'}<g_{y'}$ for two vacancies and $g_{x'}>g_{y'}$ for no vacancy. This is not in agreement with the experiments except for NaCl and KBr.

Table 7. Excited states of the halogen$_2^-$ molecule-ions computed from the g-shifts
(Comparison with the optically observed V-bands.[4,5b])

Crystal	Sign a	From spin resonance experiment			λ From atomic spectra cm^{-1}	Computed by means of equations (13) and (14) 10^4 cm^{-1}			Observed optical bands 10^4 cm^{-1}			
		$g_{x'}-g_0$	$g_{y'}-g_0$	α^2		$E_{x'}$	$E_{y'}$	limits for E_{violet}	V_1	V_2	V_3	V_4
LiF	+	0·0204	0·0211	0·49	−271	1·23	1·28	$1{\cdot}23 < E_v < 2{\cdot}56$				
	−			0·59		1·49	1·54	$1{\cdot}49 < E_v < 3{\cdot}08$				
KCl	+	0·0405	0·0424	0·62	−587	1·66	1·74	$1{\cdot}66 < E_v < 3{\cdot}48$	2·81	4·35	4·72	3·94
	−			0·74		2·00	2·08	$2{\cdot}00 < E_v < 4{\cdot}16$				
NaCl	+	0·0466	0·0422	0·62	−587	1·74	1·52	$1{\cdot}52 < E_v < 3{\cdot}48$	2·90	4·48	4·75	
	−			0·75		2·12	1·84	$1{\cdot}84 < E_v < 4{\cdot}24$				
KBr	+	0·153	0·142	0·57	−2456	1·73	1·64	$1{\cdot}64 < E_v < 3{\cdot}46$	2·44	3·77	4·33	3·64
	−			0·72		2·24	2·11	$2{\cdot}11 < E_v < 4{\cdot}48$				

$$g_{y'}-g_0 = -\frac{2\alpha^2\lambda}{E_{x'}} - \alpha^2\lambda^2\left[\frac{g_0}{2}\left(\frac{1}{E_{y'}^2}+\frac{1}{E_{x'}E_{y'}}\right)\right] \tag{14}$$

λ is the spin orbit coupling constant and a^2 the fraction of the wave function of p-character. The co-ordinate system is labeled as in Fig. 5. The energies $E_{x'}$ and $E_{y'}$ are labeled as in Fig. 8. Since we approximated the molecular orbital by a linear combination of two atomic orbitals it is reasonable to insert for λ the value for halogen atoms, which is 2/3 of the doublet separation of the $(ns)^2\,(np)^5$ state. $E_{x'}$ and $E_{y'}$ can now be computed by inserting in equations (13) and (14) the observed g-shifts (Table 3) and a^2-values (Table 6). Since the level scheme depicted in Fig. 8 is expected to be roughly symmetrical with respect to a virtual center level $E_{\text{violet}}/2$ it is possible to give an upper limit ($2E_{x'}$ or $2E_{y'}$) as well as a lower limit ($E_{x'}$ or $E_{y'}$) for the optical absorption E_{violet}. The results of these computations are summarized in Table 7. The table appears to confirm the conclusion made in sec. 2.1 that the centers giving rise to the optical V_2 or V_3 absorption are not identical with our paramagnetic centers, whereas the V_1 band falls within the calculated limits for E_{violet}.* In addition to the violet optical transition there are two red or infrared transitions (Fig. 8) probably between $0{\cdot}6\times10^4$ cm^{-1} and $1{\cdot}2\times10^4$ cm^{-1}. In fact, DELBECQ and YUSTER[18] observed in X-rayed KCl : Tl stimulated emission when irradiating in the infrared, which implies the existence of an absorption in this range.

The second-order terms in the expressions (12)–(14) for the g-shifts are a few percent of the first-order terms and thus cannot be neglected. The shift of $g_{z'}$ is entirely second order and *negative*. It is outside experimental error for KCl, NaCl and KBr. Table 8 compares the observed $(g_{z'}-g_0)$ values with the result of the calculation. The agreement is satisfactory if a positive sign is assumed for the constant a in the spin Hamiltonian.

4.4. *Second-order hyperfine and quadrupole effects*

The quadrupole interaction in the Hamiltonian (7) can be represented by

* COHEN[5a] arrived at a different conclusion because of an error by a factor of 2 in his calculation of the energy of the excited states.

Table 8. Measured and calculated second-order shift of $g_{z'}$

(Note that the experimental error does not include the error in the g-factor of the reference substance DPPH $g = 2{\cdot}0034$)

Crystal	sign a	$g_{z'}-g_0$ calculated	$g_{z'}-g_0$ observed $\pm 0{\cdot}0001$
KCl	+	−0·0007	−0·0013
	−	−0·0006	
NaCl	+	−0·0008	−0·0013
	−	−0·0006	
KBr	+	−0·0219	−0·0219
	−	−0·0129	

$$\mathcal{H}_{\text{quadrupole}} = \sum_{j=1}^{2} \frac{e^2Q}{2I_j(2I_j-1)} \times$$

$$\times \left[\frac{I_j(I_j+1)}{r_j^3} - \frac{3(\boldsymbol{r}_j \cdot \boldsymbol{I}_j)}{r_j^5} \right] \qquad (15)$$

Averaging over the wave function of the ground orbital state (8) one obtains

$$\mathcal{H}_{\text{quadrupole}} = \sum_{j=1}^{2} \frac{e^2Q}{2I_j(2I_j-1)} \times$$

$$\times \frac{2\alpha^2}{5} \overline{\left(\frac{1}{r^3}\right)} [I_j(I_j+1) - 3I_{jz'}^2] \qquad (16)$$

where z' is the molecular axis. Introducing again the co-ordinate system x'', y'', z'' (see sec. 4.1) one finds that the diagonal terms $I_j(I_j+1)$ and $I_{jz''}^2$ alter the electron spin levels $m_s = \pm\frac{1}{2}$ by the same amount and thus do not change the magnetic resonance spectrum. However, the terms $I_{jz''}I_{jx''}$ and $I_{jx''}^2$ contribute in second order. Therefore, the eigenvalues depend upon $m_{I_j}^2$ and this breaks down the equivalence of the two nuclei ($m_{I_1}^2 + m_{I_2}^2 \neq (m_{I_1}+m_{I_2})^2 = m_I^2$). This produces a splitting of the degenerate m_I levels, similar to the isotope effect in ^{35}Cl–^{37}Cl molecule-ions (see e.g. Fig. 2).

A similar effect arises from the second-order hyperfine term $I_{x''}S_x$ which has been neglected so far (see Section 4.1). All these second-order terms have strongly anisotropic coefficients which are peaked for $\theta \to \pi/2$, and thus explain the different appearance of the high angle spectra as compared with the spectra for $\theta < 75°$.

The second-order hyperfine effects are best observed for LiF because of the large magnetic moment of ^{19}F and the absence of quadrupole effects. The center line which is doubly degenerate at $\theta = 0°$ is split by about 120 gauss at $\theta = \pi/2$[10]. For the chlorides second order quadrupole and hyperfine effects are almost unobservable except for $\theta \to \pi/2$. For KBr, on the other hand, these

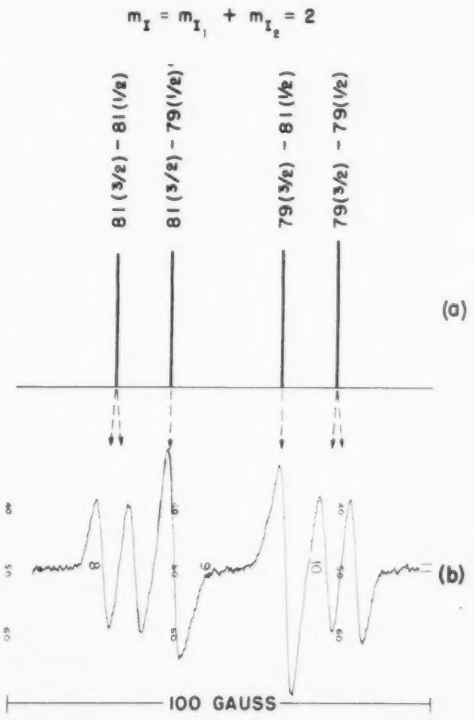

FIG. 9. Illustration for second-order hyperfine and quadrupole splitting in KBr. Lines $m_I = +2$, $\theta = 45°$.

(a) Hypothetical pattern for absence of second-order hyperfine and quadrupole effects.

(b) observed pattern: The double degeneracy of the lines, due to $^{81}Br_2$ and to $^{79}Br_2$ molecule ions is lifted. The two lines due to ^{81}Br ^{79}Br molecule ions do not split since the two nuclei are a *priori* non-equivalent. Frequency 9·3 kMc/s.

Table 9. Lifting of the degeneracy of the nuclear wave functions due to second-order hyperfine and quadrupole effects

m_I	Original degeneracy	Nuclear wave function	Symmetry	Estimated total splitting of lines for $\theta = 45°$ (gauss)	
				KCl ^{35}Cl–^{35}Cl	KBr ^{81}Br–^{81}Br
3	1	$\varphi_{3/2}^{(1)}\,\varphi_{3/2}^{(2)}$ + second order	S	none	none
2	2	$\frac{1}{\sqrt{2}}[\varphi_{3/2}^{(1)}\,\varphi_{1/2}^{(2)} + \varphi_{1/2}^{(1)}\,\varphi_{3/2}^{(2)}]$ + second order	S	0·04	7·00
		$\frac{1}{\sqrt{2}}[\varphi_{3/2}^{(1)}\,\varphi_{1/2}^{(2)} - \varphi_{1/2}^{(1)}\,\varphi_{3/2}^{(2)}]$ + second order	A		
1	3	$\frac{1}{\sqrt{3}}[c_1\varphi_{1/2}^{(1)}\,\varphi_{1/2}^{(2)} + c_2(\varphi_{3/2}^{(1)}\,\varphi_{-1/2}^{(2)} + \varphi_{-1/2}^{(1)}\,\varphi_{3/2}^{(2)})]$ + second order	S_1	0·08	
		$\frac{1}{\sqrt{3}}[d_1\varphi_{1/2}^{(1)}\,\varphi_{1/2}^{(2)} - d_2(\varphi_{3/2}^{(1)}\,\varphi_{-1/2}^{(2)} + \varphi_{-1/2}^{(1)}\,\varphi_{3/2}^{(2)})]$ + second order	S_2		
		$\frac{1}{\sqrt{2}}[\varphi_{3/2}^{(1)}\,\varphi_{-1/2}^{(2)} - \varphi_{-1/2}^{(1)}\,\varphi_{3/2}^{(2)}]$ + second order	A		
0	4	$\frac{1}{\sqrt{4}}[c_1(\varphi_{3/2}^{(1)}\,\varphi_{-3/2}^{(2)} - \varphi_{-3/2}^{(1)}\,\varphi_{3/2}^{(2)}) + c_2(\varphi_{1/2}^{(1)}\,\varphi_{-1/2}^{(2)} - \varphi_{-1/2}^{(1)}\,\varphi_{1/2}^{(2)})]$ + second order	A_1	0·19	
		$\frac{1}{\sqrt{4}}[c_1(\varphi_{3/2}^{(1)}\,\varphi_{-3/2}^{(2)} + \varphi_{-3/2}^{(1)}\,\varphi_{3/2}^{(2)}) + c_2(\varphi_{1/2}^{(1)}\,\varphi_{-1/2}^{(2)} + \varphi_{-1/2}^{(1)}\,\varphi_{1/2}^{(2)})]$ + second order	S_1		
		$\frac{1}{\sqrt{4}}[d_1(\varphi_{3/2}^{(1)}\,\varphi_{-3/2}^{(2)} + \varphi_{-3/2}^{(1)}\,\varphi_{3/2}^{(2)}) + d_2(\varphi_{1/2}^{(1)}\,\varphi_{-1/2}^{(2)} + \varphi_{-1/2}^{(1)}\,\varphi_{1/2}^{(2)})]$ + second order	S_2		
		$\frac{1}{\sqrt{4}}[d_1(\varphi_{3/2}^{(1)}\,\varphi_{-3/2}^{(2)} - \varphi_{-3/2}^{(1)}\,\varphi_{3/2}^{(2)}) + d_2(\varphi_{1/2}^{(1)}\,\varphi_{-1/2}^{(2)} - \varphi_{-1/2}^{(1)}\,\varphi_{1/2}^{(2)})]$ + second order	A_2		
−1	3	similar wave functions as for positive m_I values, but larger second-order terms.	S_1 S_2 A	0·24	
−2	2		S A	0·08	11·50
−3	1		S	none	none

effects are readily observable at any angle θ (inc'uding 0°) because of the large magnetic moment and the large quadrupole moment of the Br nuclei. As an illustration the splitting of the line $m_I = +2$ is discussed in Fig. 9.

For a quantitative treatment we consider the nuclear wave function

$$\varphi_{m_I m_s} = \frac{1}{N^{\frac{1}{2}}} \sum a_{m_I m_{I_1} m_{I_2}}{}^{(m_s)} \varphi_{m_{I_1}}{}^{(1)} \varphi_{m_{I_2}}{}^{(2)}$$

where $m_I = m_{I_1} + m_{I_2}$, and the subscripts and superscripts 1 and 2 label the two nuclei. $1/N^{\frac{1}{2}}$ is a normalization factor. Because the matrix is almost diagonal m_I is a good quantum number and the admixture of other m_I states is small. The wave functions that result are listed in Table 9. The admixture of other m_I states splits the originally degenerate states into their symmetric and antisymmetric components. The resulting total line splittings have been computed for the 45°-spectra of KCl and KBr. The predominant contribution to the splitting arises from second-order hyperfine terms; the quadrupole terms are almost negligible. Note that these splittings are not symmetrical with respect to the center line. They are larger for $-m_I$ than for $+m_I$. The results of these calculations are qualitatively consistent with the observations.

Acknowledgements—The authors thank C. P. SLICHTER and T. O. WOODRUFF for active help in the interpretation of the spectra. They have profited from stimulating discussions with F. SEITZ and R. J. MAURER. They are also indebted to P. D. JOHNSON and to C. J. DELBECQ and P. H. YUSTER for their valuable co-operation and to M. D. FISKE for advice in the construction of the cryogenic equipment.

REFERENCES

1. KIP A. F., KITTEL C., LEVY R. A., and PORTIS A. M. *Phys. Rev.* **91,** 1066 (1953); PORTIS A. M. *Phys. Rev.* **91,** 1071 (1953).
2. An ingenious double resonance technique which permits complete resolution has been applied by G. FEHER to the F-center problem. *Phys. Rev.* **105,** 1122 (1957).
3. KÄNZIG W. *Phys. Rev.* **99,** 1890 (1955).
4. SEITZ F. *Rev. Mod. Phys.* **26,** 7 (1954).
5a. COHEN M. H. *Phys. Rev.* **101,** 1432 (1956).
5b. DORENDORF H. *Z. Phys.* **129,** 317 (1951).
6. PRINGSHEIM P. *Z. Phys.* **136,** 573 (1954); DELBECQ C. J., PRINGSHEIM P., and YUSTER P. H. *Z. Phys.* **138,** 266 (1954).
7. SMALLER B., DELBECQ C. J., and YUSTER P. H. Color Center Symposium at Argonne National Laboratory (1956); see also *Bull. Amer. Phys. Soc.* II, **1,** 324 (1956).
8. DUTTON D. and MAURER R. *Phys. Rev.* **90,** 126 (1953).
9. MASSEY H. S. W. and BURHOP E. H. S. *Electronic and Ionic Impact Phenomena.* Oxford (1952).
10. WOODRUFF T. O. and KÄNZIG W. To be published.
11. BLEANEY B. and STEVENS K. W. H. *Rep. Prog. Phys.* **16,** 108 (1953); BLEANEY B. *Phil. Mag.* **42,** 441 (1951).
12. PRYCE M. H. L. *Proc. Phys. Soc.* A**63,** 25 (1950).
13. STERNHEIMER R. *Phys. Rev.* **84,** 244 (1953).
14. RAMSEY N. F. *Moleculer Beams* p. 74–76. Oxford (1956).
15. KUSCH P. and TAUB H. *Phys. Rev.* **75,** 1477 (1949).
16. INUI T., HARASAWA S., and OBATA Y. *J. Phys. Soc. Japan* **11,** 612 (1956).
17. HERZBERG G. *Molecular Spectra and Molecular Structure* p. 329 New York (1950).
18. DELBECQ C. J. and YUSTER P. H. Private communication.

J. Phys. Chem. Solids Pergamon Press 1957. Vol. 3. pp. 196–209.

PRECIPITATION OF LITHIUM IN GERMANIUM

F. J. MORIN and HOWARD REISS

Bell Telephone Laboratories, Inc. Murray Hill, N.J.

(*Received* 19 *April* 1957)

Abstract—The precipitation of lithium in germanium has been studied by resistivity methods. The kinetics of precipitation follow an exponential $(\text{time})^{3/2}$ law with constants predicted by theory. This indicates that the precipitate particles are approximately spherical. Considerable evidence is found that nucleation centers are vacant germanium lattice sites.

VOL
3
195

1. INTRODUCTION

PRECIPITATION in solids, especially in metals,[1] has been studied for many years, because of the important effect of precipitation processes on many of the properties of solids. Investigations have been handicapped by the lack of easily measurable parameters simply related to the nature and distribution of the precipitate. Techniques like X-ray analysis,[2] resistivity measurements,[3] and direct counting of particles[4] have been used with varying degrees of success. These tools possess marginal accuracy. X-rays are unsuited for exceedingly small particles, and resistivity measurements are clumsy because metal specimens must be cooled to low enough temperatures for the effect of the precipitate on the carrier mobility to be detectable. Not only is this an intermittent measuring process, but the relation between extent of precipitation and mobility is not clearly understood. On the other hand, the direct counting of particles requires sectioning of the specimen so that only one determination can be made on a sample. Also, the rate of growth of small particles can only be inferred by this method.

In the present article certain precipitation phenomena in *semiconductors* are described. Germanium and silicon are proving excellent media in which to study phenomena widely important in other substances. Examples of this are their use in the study of dislocations[5,6,7] and in the study of interactions among defects.[8,9] An identical service is performed in the study of precipitation. Although precipitation is of paramount interest in metals it is conveniently studied in semiconductors, where the process is expected to resemble that in metals in many ways.

Reference 8 draws an analogy between solid solutions in germanium and silicon, and aqueous solutions, especially solutions of electrolytes. Continuing this analogy suggests interesting precipitation experiments. Many careful studies of precipitation in aqueous solution appear in the literature. We may cite the work of LA MER and coworkers on the formation of sulfur hydrosols,[10] to the work of TURNBULL[11] on barium sulfate solutions, and that of COLLINS and LEINWEBER,[12] also on barium sulfate. In these studies the course of precipitation is followed either by light scattering methods,[13] which measure the size of a growing particle, or by resistivity techniques, in which the quantity of unprecipitated solute is determined through its electrical effect on the solution. It is important to distinguish this resistivity measurement from that mentioned above in connection with metals. In metals changes in resistivity are due to changes in mobility whereas in solutions they are the result of changes in carrier concentration. The latter measurement is not only more sensitive but it is related more simply to the progress of precipitation.

Measurements in aqueous solution have the distinct advantage that the kinetics of precipitation can be followed *in situ* continuously, thus eliminating the intermittent type of procedure.

Now it happens that both light scattering and resistivity techniques can be applied effectively to certain precipitations in germanium—in particular to the precipitation of lithium. In this article an

application of the resistivity (or more accurately the carrier concentration) technique to this system is described.

The unique properties of lithium in both germanium and silicon have been discussed in a number of papers. References 8 and 9 furnish the most complete picture in this respect, and some additional general facts can be found in a paper by FULLER.[14] For understanding the present article some of the information in these papers is pertinent. A very important piece of information is the solubility of lithium in pure germanium. This solubility depends upon the nature (thermodynamic activity) of the lithium-rich phase in equilibrium with germanium. In Fig. 1 we show a plot of lithium solubility in pure germanium versus temperature when the lithium phase is formed by alloying lithium to the germanium surface. The solubility is given in atoms of lithium per cubic centimeter.

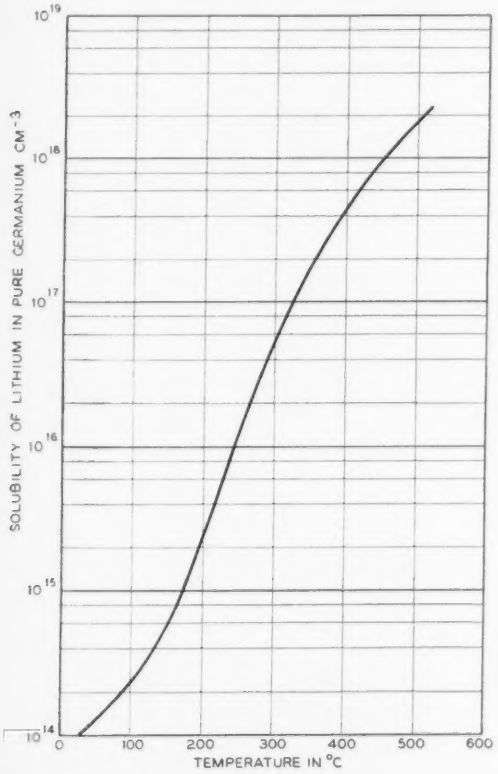

FIG. 1. The solubility of lithium in pure germanium as a function of temperature.

The composition of the lithium-rich phase is unknown, although it can be formed with a reproducible lithium activity at any temperature. The meager evidence which exists[15] indicates it to be composed of comparable amounts of lithium and germanium. Whether it is a compound or a solid solution has not been established. The important thing to note in Fig. 1 is that the solubility of lithium increases with temperature in the range shown.

Being interstitial in germanium (see reference 8) lithium can diffuse at very low temperatures. It is this mobility which permits equilibration to occur and the solubility data of Fig. 1 to be obtained. If lithium is diffused from the external phase into a germanium crystal until equilibrium is established at some elevated temperature, the solution so formed will be supersaturated when the crystal is cooled. At any temperature above 0°C the excess lithium has been found to have sufficient mobility to precipitate.

Since lithium is a donor[16] in germanium and silicon it confers *n*-type conductivity on these crystals. Each lithium donates one current-carrying electron to the conduction band[17] and therefore any measurement of carrier concentration measures the concentration of dissolved lithium atoms. In semiconductors carrier concentration can be measured by resistivity and HALL[18] methods. We have used these to follow the kinetics of lithium precipitation.

One fact which should be mentioned at the outset is that the quantity of lithium remaining in solution at a given temperature when precipitation is complete appears equal to the solubility shown in Fig. 1, where the lithium phase is formed externally by alloying lithium to germanium. This shows that the thermodynamic activity of lithium in the precipitate is identical with that of the external phase of Fig. 1, and constitutes presumptive evidence that the precipitate is identical with that phase.

2. THEORY OF DIFFUSION CONTROLLED PRECIPITATION

Before considering the experiments it is convenient to introduce some discussion of the theory of precipitation rates. There are two principal aspects to the problem. The first deals with nucleation or the inception of precipitation, and the

second with growth as the nuclei develop into precipitate particles. Two kinds of nucleation are possible—homogeneous or spontaneous, and heterogeneous or foreign nucleation. In the former, nuclei appear as a result of homophase fluctuations[19,20,21] within the original solution, and in the latter they are formed on local defects or impurities within the solution. Evidence to be presented later will demonstrate that our process involves foreign nucleation, and that in fact during the growth stage the number of nuclei and therefore the number of growing particles remains constant. The nature of these foreign nucleation sites forms an important part of the present investigation and will be considered later in detail.

For the moment it is sufficient to focus attention on the growth stage of the phenomenon. The picture is one of a constant number of growing precipitates competing for the same diffusing growth material, in this case lithium. Such competitive diffusion assemblies have been considered in the past by several authors.[22,23,24,25,26] Aside from the competition, the diffusion problem is complicated because the surface of each particle is growing and therefore one of the boundaries of the boundary value problem is moving with time. Methods for handling this difficulty have been discussed by several authors,[22,26,27,28,29] although in most cases, isolated rather than competitive particles have been dealt with. Recently WAITE[30,31] has performed a careful analysis of the competition problem in discussing the fundamentals of diffusion controlled reactions.

Since the entire problem has been treated in one form or another in the literature and is necessarily involved we will content ourselves with a very simple derivation designed for plausibility rather than rigor, and specialized to the case at hand.

Let us begin by considering an isolated spherical particle of radius x, growing by diffusion of some species from an infinite solution. Suppose that the concentration of the diffusing species at infinite distance from the particle is C_0 and that the concentration on the boundary at x is maintained at C_s, the solubility of the diffusing species corresponding to its thermodynamic activity in the precipitate particle. Obviously the problem has spherical symmetry, and after sufficient time a steady state will be reached in which the concentration C of diffusant depends on r, the radial distance from the center of the particle, in the following manner[32]

$$C = A+B/r \tag{2.1}$$

where A and B are constants. Now the boundary conditions are

$$\begin{aligned} C &= C_s, \qquad r = x \\ C &= C_0, \qquad r = \infty \end{aligned} \tag{2.2}$$

and these determine A and B in (2·1) so that

$$C = C_0-(C_0-C_s)x/r. \tag{2.3}$$

The flux of growth material into the particle will be determined by Fick's law[33] as

$$4\pi x^2 D\left(\frac{\partial C}{\partial r}\right)_{r=x} \tag{2.4}$$

where D is the diffusivity of the diffusant and $4\pi x^2$ is the surface area of the particle. Each molecule of diffusant brings to the particle an increment of volume, v, so that the rate of change of volume of the particle is

$$\frac{d}{dt}\left(\frac{4\pi x^3}{3}\right) = 4\pi x^2 Dv\left(\frac{\partial C}{\partial r}\right)_{r=x} \tag{2.5}$$

where t is time.
Substitution of (2.3) into (2.5) leads to the differential equation.

$$\frac{d(x^2)}{dt} = 2Dv(C_0-C_s) \tag{2.6}$$

whose solution is

$$x^2 = 2Dv(C_0-C_s)t, \tag{2.7}$$

under the assumption that

$$x = 0, \quad t = 0. \tag{2.8}$$

At any time the volume of the particle is

$$\frac{4\pi x^3}{3} = \frac{4\pi}{3}[2Dv(C_0-C_s]^{3/2}t^{3/2}. \tag{2.9}$$

This equation has been derived by assuming that equation (2.1) for the steady state applies down to time zero. Obviously this is untrue.* A more care-

* For x varying with time a real steady state can never be achieved even at infinite time. The departure from such a state will, however, be small at early times.

ful analysis[27,28] shows, however, that (2.9) is valid down to zero times.

Next suppose that instead of an isolated particle the solution is populated with identical growing particles at a density N, and that these are randomly distributed. At very early times the region of depleted diffusant around a given particle will not have overlapped a similar region about some other particle. For practical purposes the individual particles remain isolated. During this time the aggregate volume of precipitate within a cubic centimeter can therefore be obtained by multiplying the right member of (2.9) by N, i.e.,

$$\frac{4\pi N}{3}[2Dv(C_0-C_s)]^{3/2}t^{3/2}. \qquad (2.10)$$

This, when divided by v the volume per molecule, represents the quantity of solute which has precipitated in one cubic centimeter. The amount remaining unprecipitated, $\bar{C}$, is then

$$\bar{C} = C_0-\frac{4\pi N}{3}(v)^{1/2}[2D(C_0-C_s)]^{3/2}t^{3/2}. \qquad (2.11)$$

This can be rearranged to the form

$$\frac{\bar{C}-C_s}{C_0-C_s} = 1-\frac{4\pi N}{3}[(C_0-C_s)v]^{1/2}(2D)^{3/2}t^{3/2}. \qquad (2.12)$$

For small values of the second term on the right of (2.12) (small values of t) one can write

$$\frac{\bar{C}-C_s}{C_0-C_s} = \exp\{-\tfrac{4}{3}\pi N[(C_0-C_s)v]^{1/2}(2D)^{3/2}t^{3/2}\}$$

$$= \exp(-\alpha t^{3/2}). \qquad (2.13)$$

It can be shown[24,25,26] that (2.13), which reduces to (2.12) at early times, remains valid at all times, i.e., even after the depletion layers about individual particles overlap. There are some restrictions on this, but provided that

$$vC_0 \ll 1 \qquad (2.14)$$

(2.13) may be considered exact. Equation (2.14) is satisfied very well in the experiments to be described later.

The $t^{3/2}$ dependence exhibited in the exponent of (2.13) is a special consequence of the restriction to spherical symmetry. If the growing precipitate were cylindrical, for example if it were growing around a dislocation, a different time dependence would be expected. In fact, for cylindrical precipitates the dependence becomes t, provided that the length of the cylinder remains constant. For growing flat disks the dependence is $t^{5/2}$. These statements can be proved by considerations very similar to those advanced above.[27,34]

3. EXPERIMENTAL

The general technique for precipitating lithium in germanium was described in section 1. Briefly, a germanium crystal is saturated with lithium at an elevated temperature, the external phase having been alloyed to the crystal. Upon cooling the lithium enters a supersaturated state and precipitates.

In order to maintain the properties of the solvent, germanium, as constant as possible throughout a series of runs zone grown crystals 5 to 10 cm long were used. They were uniform to within 10 per cent along their lengths in concentrations of both dislocations and ionized impurities. Most runs were carried out on germanium, nearly intrinsic at room temperature (before the addition of lithium) and containing about 2800 dislocations per square centimeter. In certain cases these conditions were altered purposely.

Bridge-shape samples[35] were cut normal to the direction of crystal growth, i.e., the [111] direction. After etching to remove surface damage an etch pit count[36] was made to determine dislocation densities. Specimens were cleaned in KCN solution to minimize copper contamination, rinsed in de-ionized water, and dried.

In saturating the bridges with lithium the data of Fig. 1 were utilized as a guide. The external phase was formed by painting a thin film of lithium dispersed in mineral oil* on all surfaces after which the sample was heated for 30 sec in dry helium at 375°C. This treatment evaporated the oil and alloyed the lithium to the surface of the bridge. Following this the specimen was enclosed in an evacuated pyrex capsule and heated for a time, sufficient to diffuse lithium uniformly throughout it. In most cases, for reasons to be advanced later, the time of heating exceeded that required to saturate the bridge with lithium.

After heating, the pyrex capsule and the specimen were cooled to room temperature in a few seconds, and the capsule opened so that the lithium-rich phase could be etched from the sample. The bridge (with gold lead wires spot welded to its contact areas) was mounted in a holder and placed in a constant temperature bath where precipitation was followed by the measurement of electrical resistivity. Hall measurements showed that the precipitate itself did not change the electron mobility appreciably at room temperature. This mobility is known and can be used to determine carrier concentration from resistivity. Since dissolved lithium atoms and

* Obtained from the Foote Mineral Co.

carriers stand in one to one correspondence, this amounts to a determination of the lithium remaining unprecipitated.

In most of the experiments simultaneous precipitations in two bridges were carried out, one bridge acting as a control. The following describes a typical run. Two samples were cut from adjacent regions of a nearly intrinsic crystal having an etch pit count of 2800 cm^{-2}. These samples were prepared as described above and equilibrated together in the same capsule at 425°C, for 16 hr. They were then allowed to precipitate simultaneously at 59°C.

According to Fig. 1 the solubility of lithium at 425°C is $6{\cdot}5\times10^{17}$ cm^{-3}, while at 59°C it is only 2×10^{14} cm^{-3}. Thus, when cooled to 59°C the above specimens were supersaturated by a factor of about 3×10^{3}. In the notation of section 2 this factor is C_0/C_s, where C_0 is $6{\cdot}5\times10^{17}$ cm^{-3} and C_s is 2×10^{14} cm^{-3}. In Fig. 2 $\log(\bar{C}-C_s)$ is plotted against time t for two typical cases. The zero of time in this plot has been taken as the moment of removal of the capsule from the equilibration furnace. This need not be a true zero. Some precipitation occurred while the samples cooled and while the external phase was removed and electrical contacts attached. This is evident from Fig. 2 where the first recorded data are at $t = 20$ min and $\bar{C}-C_s$ is 4×10^{17} cm^{-3} rather than the $6{\cdot}5\times10^{17}$ cm^{-3} to be expected for C_0-C_s. More concerning the choice of zero conditions will be said later.

The agreement between the two curves in Fig. 2 demonstrates the reproducibility possible through control of external conditions. As we shall see later this, among other things, rules out the possibility of nucleation proceeding from random homophase fluctuations.

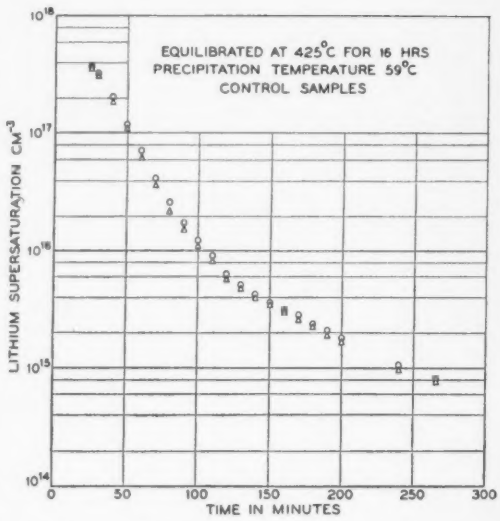

FIG. 2. Showing the decrease in lithium supersaturation with time during a typical precipitation experiment.

4. DISCUSSION OF THE KINETICS

The curves of Fig. 2 suggest the presence of two fairly distinct stages in the process. These are delineated roughly by the break in the curve occurring in the vicinity of 115 min where $\bar{C}-C_s$ has been reduced from C_0-C_s equal to $6{\cdot}5\times10^{17}$ cm^{-3} to about 6×10^{15} cm^{-3}. By this time 99 per cent of precipitation is complete so that the second stage, though measurable, is a very small part of the overall phenomenon. As we shall see the first stage can be described quantitatively by a simple theory while the second is less clearly understood, although amenable to fairly reasonable speculation.

We now turn to the question of how precipitation actually occurs. The reproducibility exhibited in Fig. 2, when external conditions are controlled is evidence against the possibility of random homophase nucleation, and in particular against the continuance of nucleation during the major time of precipitation. In other words, we are led to consider the competitive growth by diffusion of an assembly consisting of a fixed number of precipitate particles of the sort discussed in section 2. In this section we shall merely assume that the fixed number of nuclei is available. The next section will be devoted to the nature and origin of the nuclei.

It is natural to examine the possibility that the particles are approximately spherical. In this case equation (2.13) would apply. Inverting both sides of (2.13) and taking logarithms yields

$$(2{\cdot}303)\log\left(\frac{C_0-C_s}{\bar{C}-C_s}\right)=\alpha t^{3/2} \tag{4.1}$$

with

$$\alpha=\frac{4\pi N}{3}[(C_0-C_s)v]^{1/2}(2D)^{3/2}. \tag{4.2}$$

A plot of the logarithm of $(C_0-C_s)/(\bar{C}-C_s)$ against $t^{3/2}$ should thus be a straight line of slope $\alpha/2{\cdot}303$.

Plots of this kind for some typical runs are shown in Fig. 3. The results are perfect straight lines over at least 99 per cent of the processes after which a break occurs and the second stage mentioned in section 3 sets in. The curves in Fig. 3 have had their time scales adjusted slightly to make them

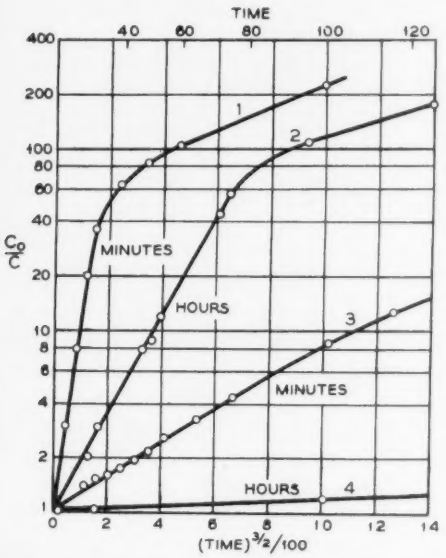

FIG. 3. Results of four precipitation experiments to show the linear dependence of the lithium supersaturation upon (time)$^{3/2}$. The time scale for samples 1 and 3 is in minutes and for samples 2 and 4 in hours.

pass through the origin. This adjustment is so small as to be almost negligible.

If attention is confined to the first and certainly the major stage of the process, equation (2.13) must be considered applicable. All our other data confirm (2.13) with the same precision as the four sets treated in Fig. 3. The confirmation of (2.13) is evidence that precipitation does not occur at dislocations, for then we would be dealing with cylindrical diffusion and $\log[(C_0-C_s)/(\bar{C}-C_s)]$ would plot linearly against t rather than as $t^{3/2}$. Furthermore the observed $t^{3/2}$ dependence confirms the idea that the particles are spherical.

In Fig. 2 precipitation is complete substantially in times of the order of 10^2 min. This constitutes additional evidence which rules out dislocations as nucleation centers surrounded by cylindrical growing precipitates. The time for precipitation in the latter case would be the time required for the lithium to diffuse to the dislocations from the bulk of the solid. This times is characterized by

$$\tau = L^2/D \qquad (4.3)$$

where L is the average separation of dislocations and D is the diffusivity of lithium in germanium. The latter is available in the data of FULLER and SEVERIENS[37] for higher temperatures and is extended to lower temperatures in reference 8. For the experiment of Fig. 2, $L = 1{\cdot}9\times10^{-2}$ cm and $D = 5{\cdot}75\times10^{-11}$ cm^2/sec. This leads to a value of τ equal to about 10^5 min, incompatible with the 10^2 min of our experiment.

Some speculation concerning the break in the curve and the onset of the second stage is possible. It can be shown that slight inhomogeneities in the distribution of nuclei, such that certain regions have densities of nuclei one per cent or so less than others, could lead to a break. Precipitation in regions of higher nuclei density would be completed before that in regions of low density. In the final stages precipitation in the latter regions alone would be observed, and since this would be averaged by the electrical measurement over the entire crystal it would appear as though the process had slowed abruptly. More will be said on this point in the next section.

Further confirmation of equation (2.13) can be achieved through investigation of the form of α obtained from the slopes of curves such as appear in Fig. 3. The easiest factor in α to test is $D^{3/2}$ as it appears in (4.2). This can be accomplished by preparing two specimens identically and allowing them to precipitate at two different temperatures, both of which are low enough so that N, the number of nuclei, does not change during precipitation. This would insure that N is the same in both specimens. Experiments along these lines were performed as follows:

Two samples were cut from adjacent regions of a nearly intrinsic crystal having 2800 cm^{-2} dislocations. They were carried through the process together except that one precipitated at 66°C, and the other at 25°C. The diffusivity of lithium at 60°C is ten times larger than at 25°C. The results are plotted in Fig. 4; curve 1 applies to the 25°C sample and curve 2 to the 60°C sample. Using the known diffusivity of lithium at 25°C, and assuming v to be the volume per atom, $2{\cdot}3\times10^{-23}$ cm^{-3}, in a perfect germanium lattice, the value of N was computed using (4.2) and the slope of curve 1. Assuming that the same value of N applied to the 60°C case, the value of D for that temperature was used in (4.2) and 4.1) to calculate curve 2. It passes *exactly* through the measured points, thus

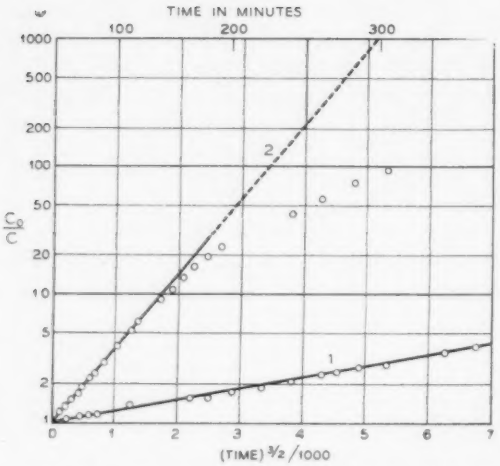

FIG. 4. Showing the dependence of α on lithium diffusivity. Sample 1 precipitated at 25°C and sample 2 at 60°C.

the validity of (2.13) is further confirmed. The fact that the assumption of identical N values for curves 1 and 2 leads to agreement with the theory is evidence that the N values are indeed the same. The fact that N does not change *during* precipitation at any *one* temperature (provided it is low enough) follows from the applicability of (2.13), which is based on a model having constant N.

The choice we have made for v as the volume per atom in germanium is based upon the consideration that were the volume very different from this value sizeable strains would exist.

Since lithium is contained interstitially, and germanium atoms cannot be moved large distances at room temperature, the precipitate must contain about as much or more germanium as lithium. That is the germanium atoms cannot get out of the way. All they can do is take part in some local rearrangement. This idea is consistent with our earlier remark that the precipitate was identical with the external lithium phase and that the latter contained comparable amounts of lithium and germanium.

Having confirmed (2.13) within reasonable limits, it is possible to use it in conjunction with experimental data, to determine N. With this tool at our disposal it becomes possible to investigate the nature and origin of the nuclei. This is done in the next section. If the use of (2.13) as a tool for determining N leads to a consistent story of nucleation, this fact would provide additional evidence as to the equation's validity.

5. THE ORIGIN AND NATURE OF THE NUCLEI

At the outset, we shall state what we believe to be the origin and nature of the precipitation nuclei. A nucleation center is thought to be a vacant germanium lattice site occupied by a lithium atom. Exactly why this configuration should behave as a nucleation center is still open to speculation.* In this paper we shall only try to show that a model of this sort is consistent with all the facts.

At a given temperature, in the absence of lithium a characteristic density, V_0, of vacancies will be established within a piece of germanium. In the absence of dislocations vacancies can only be produced at the surface of the crystal and if the diffusivity of a vacancy is small, exceedingly long periods of time will be required before the bulk of the crystal can be supplied to the level V_0 by diffusion. On the other hand, in the presence of large numbers of dislocations vacancies can be supplied internally as edge dislocations descend below their slip planes.[38] Thus, although precipitation does not occur on dislocations we should expect the presence of dislocations to exert profound influence on the rate at which precipitation centers are generated.

There is very little doubt that vacancies have an affinity for lithium ions. Evidence[39] indicates that vacancies in germanium behave as acceptors and should therefore be negatively charged. Ion pairing between positive and negative impurities in germanium is now a well established fact[8] and it should occur between a negative vacancy and a positive lithium ion. However, when the lithium approaches the vacancy closely it finds not only a negative charge but a multiplicity of uncoupled electrons and probably forms covalent bonds which are apt to be much firmer than the coulomb bond implicit in ion pairing alone.

There exists also the possibility that lithium,

* The region surrounding a vacancy may be "soft" in the sense that local rearrangements of atoms may occur there with greater ease than elsewhere. Since, as pointed out at the end of section 4, germanium atoms must rearrange in order for precipitation to occur, such movements may take place with the least expenditure of energy near a vacancy, and thus account for the latter's nucleating ability.

when it can, will enter other kinds of vacancies. For example if vacancies are formed next to substitutional boron atoms and become occupied by lithium atoms so that a lithium-boron complexion, $Li\square B^-$ is formed, the total reaction might be represented as

$$Li^+ + e^- + \square + B^- = Li\square B^- \qquad (5.1)$$

where $\square$ stands for a vacancy and e^- for a conduction band electron.*

The following experiment first gave strong support to the vacancy model of nucleation. A crystal of germanium was saturated with lithium, by heating at 295°C for 40 hr. (At this low temperature the characteristic equilibrium density of vacancies is very low.) The C_0 value at 295°C is 5×10^{16} cm^{-3}. Upon standing at 25°C for 168 hr this sample failed to evidence any precipitation. The crystal was then subjected to high energy electron bombardments, a technique known to produce lattice vacancies.[41] Immediately after bombardment precipitation was observed and in fact the rate law proved to be exactly (2.13). Curve 2 in Fig. 3 shows these data.

If the vacancy model is correct certain gross qualitative features should be expected in the precipitation data. For example, if vacancy equilibrium is established in times long compared to the times required to saturate a crystal with lithium, then longer heatings at the equilibration temperature (beyond the time required for lithium saturation) should give rise to more vacancies and thus more nuclei. As a result the rates of precipitation in samples which differ only in the times of heating should be ordered such that the highest rate corresponds to the longest heating. Alternatively, since vacancies can be produced at dislocations, samples which are heated for equal periods of time but containing different densities of dislocations should show rates in the order of increasing densities. Furthermore, at very long times the equilibrium density of nuclei should be established so that for long enough heatings the rate should depend on neither the time of heating nor the dislocation count. Finally, although vacancies can be produced at the surface, the surface is so far removed from the bulk of the crystal that different treatments of the surface should not lead to different rates. Exceptions to this rule should only occur when surface treatments differ drastically and the times of heating are long enough for surface events to affect the interior of crystal.

Figs. 5 and 6 demonstrate some of these qualitative features. Fig. 5 shows the data for samples cut from three crystals having different dislocation counts 800 cm^{-2}, 2800 cm^{-2}, and 90,000 cm^{-2}, respectively. They were equilibrated with lithium at 425°C for 16 hr and allowed to precipitate at 59°C. It is seen in Fig. 5 that the

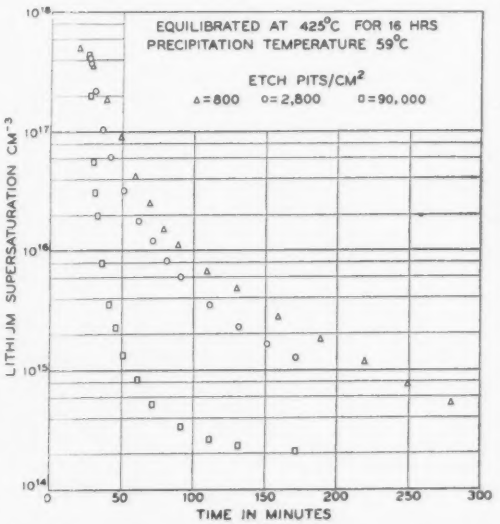

FIG. 5. Dependence of precipitation rate on dislocation concentration.

* The peculiarity of boron has been observed in germanium. For example its uniqueness in ion pairing due to the large lattice strain it produces is discussed in reference 8. Indeed the ease of formation of a vacancy near a substitutional boron ion is thought to be connected with this large strain.

Possible evidence, as yet unpublished has been obtained by the authors for the existence of $Li\square B^-$ in germanium, the $Li\square B^-$ being a configuration in which lithium occupies a vacancy. $Li\square B^-$ represents a charged acceptor and should reveal an electron energy level in the forbidden energy gap of the energy band diagram of the crystal. Upon diffusing lithium into boron doped germanium under suitable conditions, Hall measurements as a function of temperature[40] reveal the existence of a deep energy level above the valence band. This level decays away with time (after a few days) upon standing at room temperature, corresponding to the reversal of the reaction shown in (5.1). Furthermore, the level can only be formed easily in crystals with high dislocation densities, i.e. with ready sources of vacancies.

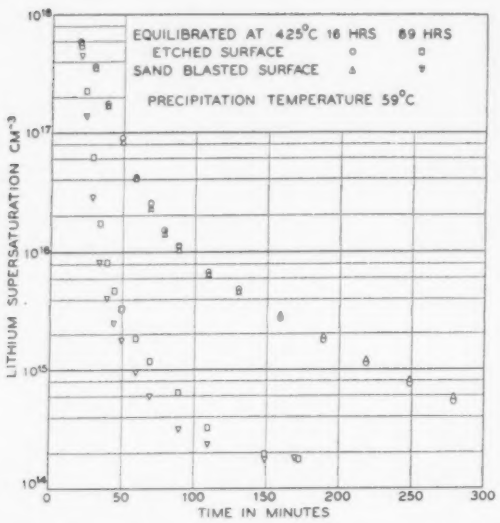

FIG. 6. Dependence of precipitation rate on equilibration time and surface treatment.

rate of precipitation increases with increasing etch pit count as expected from the above discussion.

In another set of experiments shown in Fig. 6 the effect of time of heating is demonstrated, as well as that of surface treatment. Four samples were cut from adjacent regions of a nearly intrinsic crystal having 2800 cm^{-2} dislocations. Two of the samples were prepared with etched surfaces, and two with sandblasted surfaces prior to application of the lithium emulsion. One pair of samples (etched and sandblasted) was heated at 425°C for 16 hr, and another set was heated at the same temperature for 89 hr. All were precipitated at 59°C. Fig. 6 shows, in accordance with expectation, that increasing the heating time increases the rate of precipitation, and also that a significant difference between the rates for etched and sandblasted samples is only apparent in the set heated for a long time—also in accordance with expectation—i.e. the surface is far from the body of the crystal.

The results in Fig. 5 exhibit another significant fact. This is, that increasing the dislocation count or the heating time reduces the length of that part of the process which has been termed the second stage. This accords with the idea advanced above that the second stage is a result of inhomogeneity in the distribution of nuclei. Since they are being generated at line sources (dislocations) the vacancies need to diffuse to the body of the crystal. An inhomogeneous distribution of nuclei will therefore result as long as the diffusion process is not absolutely complete. The nearer to completion, the less will be the inhomogeneity, and in consequence the less will be the fraction of the process consumed by the second stage. The higher the dislocation count or the longer the time of heating the more nearly complete will be the vacancy generation process.

In other experiments to be described later it is shown that changing the equilibration temperature changes the rate of precipitation. This is to be expected because changing the C_0 value (saturation value of lithium) changes the rate. Furthermore, changing the temperature changes the saturation value as well as the rate of production of nuclei.

We now proceed to some quantitative considerations. The fundamental tool in this endeavor is equation (2.13) from which N the density of nuclei can be determined through use of the experimental data. We assume that every vacancy occupied by a lithium atom (indicated by the symbol Li□) behaves as a nucleation center. It is important to emphasize the fact that a nucleation center *is no longer a simple vacancy*. Thus we might write the following equilibrium reaction

$$Li^+ + e^- + \square = Li\square \qquad (5.2)$$

where the entity on the right represents a nucleation center. In the presence or absence of lithium the concentration of vacancies (symbol □) will attain the equilibrium value V_0 dependent only upon temperature. The equilibrium value of Li□ on the other hand, depends on the concentration of lithium. It is zero in case no lithium is present, and far exceeds V_0 in the presence of large amounts of lithium. In general, however, the concentration, N, of Li□ will be orders of magnitude less than that of lithium so that an inappreciable amount of lithium is consumed by the reaction (5.2).

Some typical results involving values of N measured by use of (2.13) are shown in Table 1, which includes results on a number of different crystals. In some cases several different samples from the same crystal are involved. The table lists dislocation densities, ρ, and equilibration times, t^*. The next to the last column gives values of N, obtained through use of (2.13) which correspond to

Table 1. *Rate of generation and solubility of nuclei at equilibration temperature* = 425°C

Crystal No.	Sample No.	ρ Dislocations (cm^{-2})	t^* Equilibration time (hr)	N (cm^{-3})	G per cm of dislocation per hour
I	*a*	800	16	$7{\cdot}9\times10^{11}$	$6{\cdot}2\times10^{7}$
I	*b*	800	89	$3{\cdot}8\times10^{12}$	$5{\cdot}3\times10^{7}$
II	*a*	2800	16	$2{\cdot}5\times10^{12}$	$5{\cdot}6\times10^{7}$
II	*b*	2800	64	$2{\cdot}6\times10^{12}$	
III	*a*	2800	16	$2{\cdot}0\times10^{11}$	$4{\cdot}5\times10^{6}$
III	*b*	2800	40	$2{\cdot}2\times10^{11}$	
III	*c*	2800	66	$3{\cdot}3\times10^{11}$	
IV(†)	*a*	4000	16	$5{\cdot}8\times10^{11}$	$9{\cdot}1\times10^{6}$
V	*a*	40,000	16	$3{\cdot}2\times10^{12}$	$5{\cdot}0\times10^{6}$
VI	*a*	90,000	16	$7{\cdot}5\times10^{12}$	$5{\cdot}2\times10^{6}$
VII(‡)	*a*	25,000	16	$4{\cdot}4\times10^{10}$	

† Doped with $1{\cdot}0\times10^{15}$ cm^3 gallium.
‡ Doped with $2{\cdot}2\times10^{14}$ cm^3 boron.

the equilibration times listed in the preceding column. The temperature of equilibration for all cases included in Table 1 was 425°C. It will be noticed that a considerable spread exists in both equilibration times and dislocation densities.

Crystal I contains 800 cm^{-2} dislocations and for sample *a*, equilibrated for 16 hr, $7{\cdot}9\times10^{11}$ cm^{-3} nuclei were generated. The number G of sites generated per centimeter of dislocation per hour is obtained through use of the formula

$$G = \frac{N}{pt^*}. \tag{5.3}$$

This is seen to be $6{\cdot}2\times10^{7}$ cm^{-1} hr^{-1} for sample *a*. For sample *b*, equilibrated for 89 hr, G turns out to be $5{\cdot}3\times10^{7}$ cm^{-1} hr^{-1}. This value is less than that for *a* and shows that the Li□ concentration is approaching its saturation value.

Proceeding to crystal II, sample *a* leads to a value of G equal to $5{\cdot}6\times10^{7}$ cm^{-1} hr^{-1}, which compares favorably with crystal I even though now 2800 dislocations per square centimeter are involved rather than 800 cm^{-2}. Sample *b* for the same crystal yields an N value of $2{\cdot}6\times10^{12}$ cm^{-3} which is practically identical with the value for sample *a* even though the latter was only equilibrated for 16 hr as compared with the 64 hr in the case of *b*. This shows that saturation set in after only 16 hr in the case of crystal II whereas a much longer time was required for I. This is reasonable since the former crystal had 3·5 times as many dislocations as the latter.

The next crystal, III, is peculiar in that the rate of generation, G, appears to be down by an order of magnitude, and what is more important the saturation value of N appears to be 2 to 3×10^{11} cm^{-3} which is also down by an order of magnitude. Since the saturation density of Li□ depends only on temperature and not on the past history of the crystal this is an unexpected result. Some very definite indications of the source of difficulty can be had however from crystal VII which contained $2{\cdot}2\times10^{14}$ cm^{-3} boron atoms. This crystal contained 25000 cm^{-2} dislocations and 16 hr should have been enough to reach the saturation density of Li□. Yet N is only $4{\cdot}4\times10^{10}$ cm^{-3}, down by about two orders of magnitude from the saturation N's for crystals I and II.

To understand how boron can change the equilibrium value of N consider a combination of the reactions (5.1) and (5.2)

$$\mathrm{Li^+ + e^- + \square = Li\square} \qquad (5.4)$$

$$+$$

$$\mathrm{B^-}$$

$$\|$$

$$\mathrm{Li\square B^-}.$$

At the temperature of equilibration the entire system comes to equilibrium and since there is effectively an infinite supply of Li^+ and $\square$ the equilibrium density of $Li\square$ is unaffected by the vertical equilibrium (process (5.1)) which consumes vacancies to produce $Li\square B^-$. However after equilibration and cooling the supply of vacancies is cut off (because of the low diffusivity of vacancies at room temperature the dislocations are very far from the body of the crystal) and a constant number of vacancies is apportioned to the species $\square$, $Li\square B^-$, and $Li\square$. The readjustment of the equilibria in (5.4) upon reduction of temperature redistributes the vacancies in favor of $Li\square B^-$ and lowers the concentration of the nucleation centers, $Li\square$. This accounts for the reduction in the value of saturation N for crystal VII.

Of course, different crystals contain traces of boron in small amounts (less than 10^{13} cm^{-3}). These amounts though small may be equal to or greater than the saturation N values which at the most have been of the order of 10^{12} cm^{-3} at 425°C. Variation in saturation N values with boron content for several crystals is shown in Fig. 7.

Gallium exerts no effect upon the equilibrium value of N. This is evident from the data for crystal IV which contained 1×10^{15} cm^{-3} gallium, almost ten times the boron content in VII. The equilibrium N is still seen to be of the order of 10^{12} cm^{-3}. This is not surprising since nowhere does evidence exist for the formation of $Li\square Ga^-$.

Some other typical data (crystals V and VI) appear in Table 1. Internally consistent results may be obtained with crystals containing different amounts of boron. A large amount of data has now been collected not only on different crystals but also for different equilibration temperatures. It is found that each crystal is internally consistent, i.e., smooth and reproducible curves, of the form expected theoretically, are found *for a given crystal*. The internal consistency within a single crystal is to be expected on the basis of the boron mechanism discussed above, i.e., the differences between crystals are due only to different boron contents.

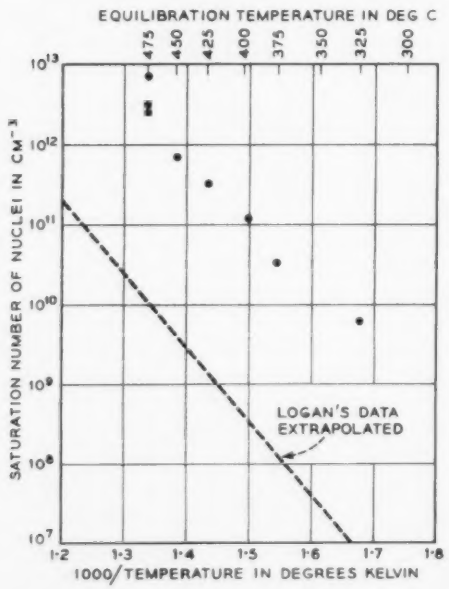

FIG. 7. Dependence of the saturation concentration of precipitation nuclei upon the concentration of boron in the sample for equilibrium temperature = 425°C.

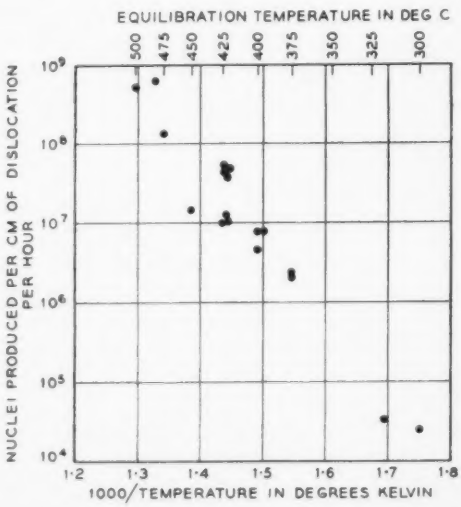

FIG. 8. Initial rate of production of precipitation nuclei as a function of reciprocal equilibration temperature.

Fig. 8 is a plot of log G_0 against the reciprocal of temperature for a typical crystal* where G_0 is the initial rate of generation of nuclei in $cm^{-1}\,hr^{-1}$. The data for Fig. 8 were obtained in the same fashion as those appearing in Table 1. The spread in points is probably due mainly to difficulty in determining the initial rate since the rate itself is a function of time, passing to zero at infinite time. Despite the spread one notices that the data follow a fairly good straight line from which an activation energy of 2·0 eV is obtained. This is the energy barrier involved in the rate process associated with the motion of the dislocation to produce vacancies.

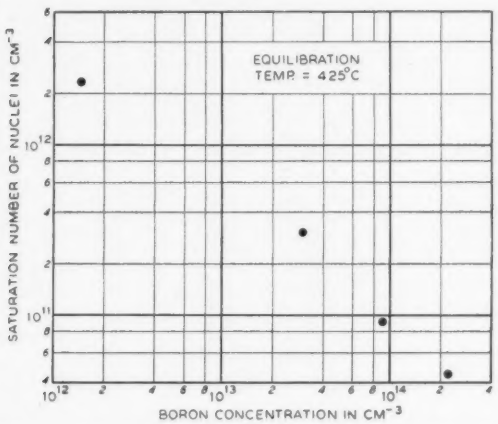

FIG. 9. Saturation number of nuclei as a function of reciprocal equilibration temperature.

An even more interesting quantity is the saturation value of N in its dependence on temperature. In Fig. 9 log N is plotted versus inverse temperature for crystal III. A good straight line is obtained, LOGAN[42] has measured the equilibrium density V_0, of vacancies in germanium at much higher temperatures than we are dealing with here. His data for log V_0 plot against inverse temperature, are given as a straight line. The extrapolation of that line to our temperature range is shown as the dashed line in Fig. 9. The slope of the curve for N in Fig. 9 yields for the heat of formation, ΔH, the value 1·6 eV. Our model permits the computation of ΔH by independent means. We proceed as follows: equation (5.2) can be rewritten as

$$Li^+ + \square^- = Li\square \qquad (5.5)$$

where $\square^-$ stands for a vacancy which has captured an electron. As a matter of fact this equation is more realistic than (5.2) in that at high Li^+ densities almost all the vacancies will be ionized. The density V_0 thus applies to $\square^-$. However, both (5.2) and (5.5) are *mathematically* equivalent in that they lead to identical results upon proper application of the law of mass action.

Now (5.5) may be viewed as a process in which the entity $\square^-$ is distributed between two energy states, i.e., between states on Li^+ ions ($Li\square$) and states on normal lattice sites ($\square^-$). There are $\Gamma = 4{\cdot}4\times10^{22}$ cm^{-3} normal lattice sites in germanium, and at any temperature the number of Li^+ sites is simply C_0, the solubility of lithium. Suppose that an energy ϵ is evolved when a Li^+ falls into a charged vacancy to produce $Li\square$, or to put it another way, when a charged vacancy falls from a normal lattice site onto a Li^+. If V_0 represents the concentration of $\square^-$, and N, the concentration of $Li\square$, then the Boltzmann distribution law yields

$$\frac{V_0}{N} = \frac{\Gamma e^{-\epsilon/kT}}{C_0} \qquad (5.6)$$

i.e., the ratio of the population of two states by an entity, is simply the ratio of the densities of the two states modified by a Boltzmann energy factor. Referring to Fig. 9 we see that V_0/N (V_0 from the LOGAN curve and N from our curve) is of the order of 10^{-2} at 425°C(698°K). Furthermore, from Fig. 1, C_0 is about $6{\cdot}5\times10^{17}$ cm^{-3}. Substituting these data (*at one temperature*), and the value of Γ, into (5.6) we obtain for ϵ

$$\epsilon \approx 1{\cdot}0 \text{ eV}. \qquad (5.7)$$

Now (5.6) can be solved for N. The result is

$$N = \frac{C_0 V_0}{\Gamma} e^{\epsilon/dT}. \qquad (5.8)$$

Below 500°C log C_0 plots as a good straight line against inverse temperature, from which we can compute λ in the formula

$$C_0 = Ae^{-\lambda/kT}. \qquad (5.9)$$

The result is

$$\lambda = 0{\cdot}64 \text{ eV}. \qquad (5.10)$$

* Containing $\sim 10^{12}$ cm^{-3} boron.

We already have the constants in

$$V_0 = K \exp(-\lambda_v/kT) \tag{5.11}$$

where λ_v is the heat of formation of a vacancy. These are available from LOGAN's curve which gives

$$\lambda_v = 2{\cdot}1 \text{ eV}. \tag{5.12}$$

Substitution of (5.9) and (5.11) into (5.8) yields

$$N = \frac{AK}{\Gamma} \exp[-(\lambda+\lambda_v-\epsilon)/kT]. \tag{5.13}$$

ΔH, obtained from the slope of a plot of log N vs. $1/T$, should be given by

$$\Delta H = \lambda+\lambda_v-\epsilon. \tag{5.14}$$

According to (5.7), (5.10), and (5.12) the expected value is then

$$\Delta H \approx 1{\cdot}6.* \tag{5.15}$$

in good agreement with the value determined from Fig. 9.

Acknowledgement—The authors wish to express their appreciation to HOWARD GUGGENHEIM and JOHN MAITA for help with the experimental work, and to WALTER BROWN for the electron bombardment experiment. Discussions of great value were had with Drs. H. L. FRISCH, C. S. FULLER, and N. B. HANNAY, all of Bell Laboratories. We are much indebted for this assistance.

REFERENCES

1. GEISLER A. H. *Symposium on Phase Transitions in Solids* p. 387. John Wiley, New York (1951).
2. GEISLER A. H. and HILL J. K. *Acta Cryst.*, Camb. **1,** 238 (1948).
3. JOHANSSEN C. K. and HAGSTEN G. *Ann. Phys. Lpz.* **28,** 520 (1937).
4. HARKER D. and MURPHY M. J. *Trans. Amer. Inst. Min. (Metall.) Engrs.* **161,** 75 (1945).
5. PEARSON G. L., READ W. T., and MORIN F. J. *Phys. Rev.* **93,** 666 (1954).
6. READ W. T. *Phil. Mag.* **45,** 775, 1119 (1954); **46,** 111 (1955).
7. DASH W. C. *J. Appl. Phys.* **27,** 1193 (1956).
8. REISS H., FULLER C. S. and MORIN F. J. *Bell Syst. Tech. J.* **35,** 535 (1956).
9. MORIN F. J. and REISS H. *Phys. Rev.* **105,** 384 (1957).
10. LA MER and BARNES *J. Colloid Sci.* **1,** 71, 79 (1946).
    LA MER and KENYON *J. Colloid Sci.* **2,** 251 (1947).
    JOHNSON and LA MER *J. Amer. Chem. Soc.* **69,** 1184 (1947).
    BARNES, KENYON, ZAISER and LA MER *J. Colloid Sci.* **2,** 349 (1947).
    ZAISER and LA MER *J. Colloid Sci.* **3,** 571 (1948).
    REISS and LA MER *J. Chem. Phys.* **18,** 1 (1950).
11. TURNBULL D. *Acta Met.* **1,** 684 (1953).
12. COLLINS F. C. and LEINWEBER J. P. *J. Phys. Chem.* **60,** 389 (1956).
13. LA MER V. K. and SINCLAIR D. *Chem. Rev.* **44,** 245 (1949).
14. FULLER C. S. *Rec. Chem. Progr.* **17,** No. 2 (1956).
15. FULLER C. S. Private communication.
16. SHOCKLEY W. *Electrons and Holes in Semiconductors.* Van Nostrand (1950).
17. SHOCKLEY W. *Electrons and Holes in Semiconductors.* Van Nostrand (1950).
18. SHOCKLEY W. *Electrons and Holes in Semiconductors.* Van Nostrand (1950).
19. FRENKEL J. *Kinetic Theory of Liquids* Chapter VIII. Oxford (1946).
20. REISS H. *J. Chem. Phys.* **18,** 840 (1950).
21. SMOLUCHOWSKI R. *Symposium on Phase Transitions in Solids* p. 149. John Wiley, New York (1951).
22. REISS H. and LA MER V. K. *J. Chem. Phys.* **18,** 1 (1950).
23. REISS H. *J. Chem. Phys.* **19,** 482 (1951).
24. FRISCH H. L. and COLLINS F. C. *J. Chem. Phys.* **20,** 1797 (1952).
25. COLLINS F. C. and FRISCH H. L. *J. Chem. Phys.* **21,** 1116 (1953).
26. FRISCH H. L. and COLLINS F. C. *J. Chem. Phys.* **21,** 2158 (1953).
27. ZENER C. *J. Appl. Phys.* **20,** 950 (1949).
28. FRANK F. C. *Proc. Roy. Soc.* A**201,** 586 (1950).
29. FRISCH H. L. *Z. Electrochem.* **56,** 324 (1952).
30. WAITE T. R. *Phys. Rev.* (to be published).
31. WAITE T. R. *Phys. Rev.* (to be published).
32. CARSLOW H. S. and JAEGER J. C. *Conduction of Heat in Solids* p. 210 Oxford (1948).
33. Le CLAIRE A. D. *Progress in Metal Physics* Vol. 1, p. 306. Interscience, New York (1949).
34. HARDY H. K. and HEAL T. J. *Progress in Metal Physics* Vol. 5. p. 143. Interscience, New York (1954).
35. MORIN F. J., GEBALLE T. H. and HERRING C. *Phys. Rev.* **105,** 525 (1957).

* This calculation has not taken into account the possible effect of the vertical equilibrium in (5.4). A more detailed analysis shows that the major effect of this equilibrium is to shift the log N versus $1/T$ curve parallel to itself, moving it to a lower position in the presence of more boron. The slope, however, can be computed fairly accurately in the manner above (ignoring the boron equilibrium) provided that the ratio V_0/N used in (5.6) is taken from the particular curve under investigation.

36. Vogel F. L., Pfann W. G., Corey H. E., and Thomas E. E. *Phys. Rev.* **90,** 489 (1953).
37. Fuller C. S. and Severiens J. C. *Phys. Rev.* **95,** 21 (1954).
38. Read W. T. *Dislocations in Crystals* p. 49. McCraw-Hill, New York (1953).
39. Logan R. A. *Phys. Rev.* **101,** 1455 (1956).
40. *Procedures in Experimental Physics* Vol. 6. Academic Press, New York.
41. James H. M. and Lark-Horowitz K. *Z. Phys. Chem.* **198,** 107 (1951).
42. Logan R. A. *Phys. Rev.* **101,** 1455 (1956).

VOL.
3
1957

J. Phys. Chem. Solids Pergamon Press 1957. Vol. 3. pp. 210–222.

DISTORTION AROUND POINT IMPERFECTIONS IN SIMPLE CRYSTALS

GEORGE L. HALL*

University of Virginia, Charlottesville, Virginia

(*Received* 9 *November* 1956)

Abstract—Point imperfections in crystals with central forces at 0°K, and under arbitrary pressure are considered theoretically. Two approaches are presented with applications to the cases of a vacancy and an interstitial in an f.c.c. Lennard-Jones crystal. The first, an atomic theory, gives a description of the relaxation of the lattice near the site of the defect; the second, which utilizes linear elasticity, gives a spherically symmetric average of the relaxation everywhere. For both defects, it is found that the energy of distortion is mainly core energy and that the distortion has a high degree of anisotropy. In fact, the displacement near either defect is outward along the cubic axes and inward elsewhere. The results of this paper are compared with those resulting from several methods of fitting an asymptotic r^{-2} law of displacement.

1. INTRODUCTION

THE relaxation around a point imperfection can be separated into two types: (1) the core relaxation, which occurs in the immediate neighborhood of the imperfection, and (2) the elastic relaxation which extends over the remainder of the crystal. The first can be calculated only in terms of an atomic theory; it is of importance in estimating the total energy of relaxation and in considering both the motion of the imperfection and the short-range interactions between two imperfections. The second type can be calculated, at least approximately, by using elasticity theory; its absolute value depends, of course, on the core relaxation of which some knowledge is always necessary. The elastic relaxation is of interest mainly in connexion with the problem of long-range interactions between imperfections.

Most of the work in this field has been associated with the elastic relaxation. In the simplest case of an elastically isotropic body, the asymptotic law of displacement becomes of the form C/r^2, where C is a parameter depending on the core relaxation. This elastic treatment can be extended to anisotropic bodies yielding an asymptotic law of displacement with the proper symmetry of the crystal.[1] In both cases, the constants have been estimated in very unsatisfactory ways.[1,2,3]

In order to obtain further insight into the nature of the core relaxation, this paper presents a calculation of the core relaxation in the simplest possible case, namely a crystal obeying central forces and at the absolute zero of temperature. The calculations are made for a vacancy and an interstitial in an f.c.c. crystal with interatomic forces derivable from a Lennard-Jones 6–12 potential. The results show that the core relaxation has an unexpectedly high cubic anisotropy. Most of the total energy of relaxation is core energy, so that the parameters determining the absolute value of the asymptotic elastic law of displacement are smaller than previously expected.

Section 2 discusses the type of distortion around a point imperfection (particularly a substitutional impurity) and shows that provided the displacements are so small that the so-called "harmonic approximation" is sufficient, the displacements should have the symmetry of the crystallographic point-group around the point where the fault is located. This simplifies greatly the calculations in the case of a f.c.c. crystal by imposing many of the

* Presently at Westinghouse Research Laboratories, Pittsburgh 35, Pennsylvania.

displacements to be radial. Sections 3 and 4 are devoted to the calculations of the distortion around a vacancy and an interstitial respectively.

In section 5 there is presented a second theory which is obtained by the additions of several approximations to those necessary for the development of the atomic theory of point defects. Although it is more approximate than the atomic theory, the elastic method has the advantage of yielding both the core and the elastic relaxation. It is a quantitative theory which can be compared with several ways of fitting a C/r^2 law of displacement.

An essential feature of both procedures is that the problem of describing the distortion around a point defect is transformed into the problem of finding the relaxation of a homogeneous crystal acted upon by a known body force. As an illustration, consider the case of a vacancy in a Lennard-Jones 6–12 crystal under zero external pressure. Removing an atom from such a crystal is equivalent to applying a body force that exactly cancels the interactions between the atom in question and all other atoms of the crystal. An atom may be removed, *or* a body force applied. At zero pressure, the body force acting on the first nearest neighbors is directed toward the vacancy, but on all other neighbors it is directed away from the fault. The consideration of both the body force and the geometry of a point defect will be shown to produce an anisotropy in the displacement. For the particular cases of the vacancy and the interstitial in Lennard-Jones crystals, the displacement is outward along the cubic axes and inward elsewhere. For example, consider an interstitial in an f.c.c. crystal of the Lennard-Jones type, where the outward body force on the first neighbors is several times larger than the inward body force on the second neighbors. An examination of the geometry of the defect shows that the outward displacement of the first neighbors makes easier an inward motion of the second neighbors.

2. GENERAL DISCUSSION OF THE DISTORTION DUE TO SUBSTITUTIONAL IMPURITIES

If the equilibrium position of the ith atom in the perfect crystal is $\boldsymbol{R}_i$, and the potential energy between two atoms separated by $\boldsymbol{r}$ is $\varphi(\boldsymbol{r})$ then the energy required to displace every ith atom by $\boldsymbol{r}_i$ is

$$\Delta E = \tfrac{1}{2} \sum_{ij}{}' \{\phi(\boldsymbol{R}_{ij}+\boldsymbol{r}_j-\boldsymbol{r}_i)-\phi(\boldsymbol{R}_{ij})\},$$
$$\boldsymbol{R}_{ij} = \boldsymbol{R}_j-\boldsymbol{R}_i.$$

ΔE will clearly be zero if the $\boldsymbol{r}_i$ corresponds to a rigid body motion of the crystal. To avoid discussion of this case we shall suppose that three atoms of the crystal are undisplaced, one at the origin, say $i = 0$, and two others at great distances from the origin. Since the atom positions $\boldsymbol{R}_i$ are supposed to be equilibrium positions and we assume $\boldsymbol{r}_i$ to be small, an expansion of ΔE will be quadratic in the $\boldsymbol{r}_i$, say

$$\Delta E = \tfrac{1}{2} \sum_{ji} \mathbf{A}_{ij} : \boldsymbol{r}_i \boldsymbol{r}_j,$$

where the $\mathbf{A}_{ij}$ are second-rank tensors:

$$\mathbf{A}_{ij} = -\frac{\partial^2}{\partial \boldsymbol{R} \partial \boldsymbol{R}} \phi(\boldsymbol{R}_{ij}), \quad i \neq j;$$

$$\mathbf{A}_{ii} = \sum_{j \neq i} \frac{\partial^2}{\partial \boldsymbol{R} \partial \boldsymbol{R}} \phi(\boldsymbol{R}_{ij})$$

invariants under the symmetry operations of the perfect lattice. Again from the assumed equilibrium and also the fact that three atoms (not on a line) are undisplaced it follows that the quadratic form for ΔE is positive definite; any small displacement raises the energy.

Now substitute for the atom at the origin, $i = 0$, another atom which has an interaction energy of $\chi(\boldsymbol{R})$ with an atom of the crystal at the point $\boldsymbol{R}$. The energy required to displace every ith atom of the crystal by $\boldsymbol{r}_i$, from its original unperturbed position $\boldsymbol{R}_i$, is

$$\Delta \mathscr{E} = \Delta E - Q,$$

where

$$Q = \sum_{i \neq 0} \{[\phi(\boldsymbol{R}_i+\boldsymbol{r}_i)-\phi(\boldsymbol{R}_i)]-$$
$$-[\chi(\boldsymbol{R}_i+\boldsymbol{r}_i)-\chi(\boldsymbol{R}_i)]\}.$$

We do not need to exclude the two fixed lattice points from the sum defining Q since they are supposed to be so far away from the origin that $Q(R_i)$ and $\chi(R_i)$ are zero for them.

Let us expand Q about $\boldsymbol{r}_i = 0$:

$$Q = \sum_i \boldsymbol{F}_i \cdot \boldsymbol{r}_i + \tfrac{1}{2} \sum_{ij} \mathbf{G}_{ij} : \boldsymbol{r}_i \boldsymbol{r}_i,$$

with

$$\boldsymbol{F}_i = -\frac{\partial}{\partial \boldsymbol{R}}\chi(\boldsymbol{R}_i)+\frac{\partial}{\partial \boldsymbol{R}}\phi(\boldsymbol{R}_i),$$

$$\mathbf{G}_{ii} = -\frac{\partial^2}{\partial \boldsymbol{R}\partial \boldsymbol{R}}\chi(\boldsymbol{R}_i)+\frac{\partial^2}{\partial \boldsymbol{R}\partial \boldsymbol{R}}\phi(\boldsymbol{R}_i).$$

$\boldsymbol{F}_i$ is, of course, the force on an atom at the point $\boldsymbol{R}_i$ due to the substitution of an impurity atom at the origin.

If we assume that the new equilibrium configuration is sufficiently close to that for the original crystal we shall have the following equation for the displacement of the ith atom

$$\sum_j \mathbf{A}_{ij} \cdot \boldsymbol{r}_j - \mathbf{G}_{ii} \cdot \boldsymbol{r}_i = \boldsymbol{F}_i.$$

Were it not for the term $\mathbf{G}_{ii} \cdot \boldsymbol{r}_i$ in this equation we could claim the existence and uniqueness of a solution. The determinant of these linear equations would be the product of the eigen values of the matrix $\boldsymbol{A}_{ij}$ all of which are known to be greater than zero. Now in fact all the $\mathbf{G}_{ii}$ which are second derivatives of the interaction energy, are very small. It is reasonable to suppose therefore that the complete matrix still has positive eigen values and a non-zero determinant. It is then easy to prove that small displacements from this solution raise the energy so that the solution is stable. If the $\mathbf{G}_{ii}$ were so large and had just the right values to make the determinant nearly zero then clearly the linear approximation would not be good enough and the $\boldsymbol{r}_i$'s would be large and not necessarily unique. It is obviously impossible even for small $\mathbf{G}_{ii}$ to state categorically that there are no stable configurations that involve large displacements since the linear equations are useless. For example, there might exist a configuration of the unsubstituted crystal that had an energy not much larger than the true periodic configuration and which would be stabilized by the substitution, however a few preliminary calculations have indicated that the icosahedral arrangement of nearest-neighbor atoms round a vacancy ($\chi(r) \equiv 0$) is not stable and it is difficult to think of other likely geometrical arrangements.

The reason for stressing the uniqueness of the solution is that it implies that the solution must have the symmetry of the crystallographic point-group about the origin. This will greatly reduce the number of independent $\boldsymbol{r}_i$'s with a consequent simplification of the problem.

It may be remarked in passing, that all these considerations equally apply to an interstitial impurity. There is, however, an important difference: due to the closeness of the nearest neighbors of the interstitial the $\mathbf{G}_{ii}$ for these neighbors is very large and the $\boldsymbol{r}_i$ cannot be asserted to be small with the same assurance. There is then a better chance for non-unique and non-symmetric solutions.

3. VACANCIES BY THE ATOMIC METHOD IN A FACE-CENTRED CUBIC CRYSTAL

The energy of formation of a vacancy at constant pressure is the sum of two quantities, an upper limit and a correction due to relaxation which is always negative. The upper limit is given by the energy to form a vacancy without distortion. It is easily calculated and is given by

$$W^0 = pv - \epsilon,$$

where v is the volume per atom and $-\epsilon$ is the sublimation energy per atom. To this must be added the $\Delta\mathscr{E}$ discussed in 2.

The symmetry requirements on the actual displacements are most easily described by considering fictitious concentric spheres, "shells", with radii $d\sqrt{k}$, $k = 1, 2, 3, \ldots$, centred about the origin with d being the distance between nearest neighbors. The unperturbed position of every atom is on one of these shells. Furthermore, it can easily be shown by WARING's theorem[4] that there is an atom on every shell except those for which $k = 2^{2a+1}(8b+7)$ with $a, b = 0, 1, 2, \ldots$. The fourteenth shell is the first empty one. The atoms on any given shell are distributed on it with cubic symmetry. On the first eight shells, application of the cubic point-group takes each atom at least once into all atomic positions in the same shell; i.e., there is only one "type" of atomic position in the first eight shells. The ninth shell has two types.

The results of the requirement of cubic symmetry of the displacement can be stated as follows: The atoms that lie on any of the three rotation vectors [100], [110], and [111], can undergo only radial displacements, and all atoms of any one "type" in a given shell must have the same displacement. More explicitly, the first eight shells are characterized by one magnitude of displacement for all atoms in each shell; the first, second,

fourth, sixth, and eighth shells are restricted to radial displacements; and the third, fifth, and seventh are restricted to motion in only a few planes.

On the basis of these considerations and the expected rapid decay of the distortion away from the vacant site, it has been assumed that all displacements are radial and that all atoms in a given shell are displaced by the same amount. These conditions are imposed in both the atomic and the elastic methods.

The atomic theory and the elastic methods are identical up to this point. From this point on the two will differ in the approximations made to ΔE and Q in order to minimize $\Delta\mathscr{E}$. The atomic theory is now continued by specializing to particular central forces.

(a) *The vacancy in Lennard-Jones crystals.* The atomic theory is now completed for the particular case of Lennard-Jones crystals for which the potential energy of interaction of two atoms at a distance r is

$$\phi(r) = \gamma[(r_0/r)^{12} - 2(r_0/r)^6].$$

The equilibrium distance between two isolated atoms is r_0 and their dissociation energy is γ.

If terms higher than those quadratic in the displacements are neglected, and all displacements are assumed radial with respect to the fault, ΔE and Q are respectively given by.

$$\Delta E = \tfrac{1}{2} \sum_k n_k \delta_k \{A_k \delta_k + \sum_{l \neq k} \delta_l A_{kl}\}, \qquad (1)$$

$$Q = -\sum_k n_k \delta_k \{\sigma_k - \eta_k \delta_k\}. \qquad (2)$$

The subscript k refers to the kth shell, n_k giving the number of atoms in it and $\delta_k = r_k/d$ giving its reduced displacement. The other symbols are defined in the appendices, but it is immediately obvious that A_{kl} is a type of coupling constant, and that σ_k and η are directly proportional to the first and second derivatives, respectively, of $\phi(r)$ evaluated at the kth shell. For $k, l < 9$, $n_k A_{kl} = n_l A_{lk}$. Setting B_k equal to $(A_k - 2\eta_k)$ gives

$$\Delta\mathscr{E} = \tfrac{1}{2} \sum_k n_k \delta_k \{B_k \delta_k + 2\sigma_k + \sum_{l \neq k} \delta_l A_{kl}\}.$$

The minimization of $\Delta\mathscr{E}$ yields an infinite set of linear algebraic equations for the equilibrium δ_k. Thus

$$\delta_k B_k + \sum_{l \neq k} \delta_l A_{kl} = -\sigma_k. \qquad (3)$$

Also, at equilibrium,

$$\Delta\mathscr{E} \to \Delta\mathscr{E}^0 = -\tfrac{1}{2} \sum_k n_k \sigma_k \delta_k. \qquad (4)$$

Expressions for p, pv, $\mathscr{E}$, and W^0 for these particular force laws are easily derived and hence not given here.

(b) *Solution of the equilibrium equations for zero pressure.* A relaxation method is used to solve equation (3); the convergence is rapid thereby making the method feasible.

As a first approximation each shell may be supposed to relax independently, i.e. the coupling constants may be set equal to zero. Then,

$$\delta_k \cong -\sigma_k / B_k. \qquad (5)$$

Equation (5) gives the reduced displacement of each shell when each atom in a given shell is considered to interact with others in the same shell at displaced positions but to interact with atoms in different shells at their undisplaced positions. Numerical results for the case of zero external

Table 1. *Reduced displacement,* times* 10^3

δ_1	δ_2	δ_3	δ_4	δ_5	δ_6	δ_7
−8·13	—	—	—	—	—	—
—	2·38	—	—	—	—	—
—	—	0·65	—	—	—	—
—	—	—	0·23	—	—	—
—	—	—	—	0·11	—	—
—	—	—	—	—	0·06	—
—	—	—	—	—	—	0·04
−8·13	2·42	—	—	—	—	—
−8·23	2·42	−0·31	—	—	—	—
−8·38	2·42	−0·33	−0·83	—	—	—
−8·39	2·54	−0·31	−0·83	0·33	—	—
−8·39	2·54	−0·31	−0·83	0·33	0·02	—
−8·39	2·54	−0·31	−0·83	0·33	0·02	−0·02

* Dashes denote fixed shells.

(The reduced displacement of the kth "shell" of atoms surrounding a vacant site are given for the case of zero external pressure; dashes denote fixed shells. The displacement of the first and second shells changes little as further shells are relaxed.)

pressure are given in the upper part of Table 1. It is interesting to note that, to this first approximation, the displacement is inward at the first shell but outward at all other shells.

One, two, etc., to seven successive shells were permitted to relax simultaneously taking into account the coupling constants, and equation (3) was solved for each case. The results are given in the lower part of Table 1. The signs of the displacements, the shells that interact strongly, and the rapid convergence of the method should be noted. For a thorough understanding of the equilibrium configuration of displacement, it is necessary to examine the geometrical arrangement of atoms in each shell. It is seen that the displacement is positive (outward) along the cubic axes and negative elsewhere (the sixth shell [111] is an exception).

The three-dimensional configuration of distortion is not easily displayed graphically, but there is some merit to presenting the results as in Fig. 1.

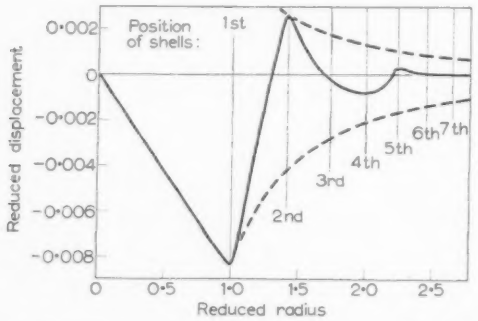

FIG. 1. The distortion around a vacancy for the case of zero external pressure. The reduced displacement of each shell is plotted as a function of its reduced distance from the vacant site; then these points are connected with the otherwise arbitrary solid curve. The two dashed curves vary as the inverse square of the reduced radius. All distances are reduced by the first-nearest-neighbor distance in a perfect crystal.

The two dashed curves are drawn to indicate that the positive displacement of atoms along (second and eighth shells) or near (fifth shell) the cubic axes falls off faster than r^{-2}, as also does the negative displacement in any other direction. (The vectors of the second, fifth, and eighth shells are [100], [3/2, 1·2, 0], and [200], respectively.)

Equation (4) is used to calculate the value of $\Delta\mathscr{E}$ for each stage in the relaxation process. Fig. 2

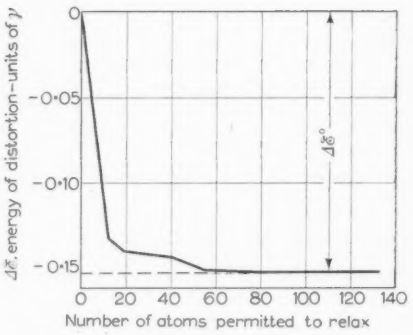

FIG. 2. The dependence of the energy of distortion around a vacancy on the number of atoms permitted to relax for the case of zero external pressure. Most of the energy of distortion is derived from the relaxation of the first few shells.

gives the results. At zero pressure, the major portion of $\Delta\mathscr{E}^0$ results from the relaxation of the first few shells where the displacement is varying rapidly. This graph gives further evidence of the rapid convergence of the relaxation technique. From the limiting value of $\Delta\mathscr{E}$, it is seen that $\Delta\mathscr{E}^0$ is equal to 1·78 per cent of the energy of formation of a vacancy without distortion under zero pressure (at $p = 0$, $W^0 = -\epsilon = 8{\cdot}6102\ \gamma$, where use is made of the Lennard-Jones potential constants[5]).

(c) *Solution of the equilibrium equations for non-zero pressure.* Since the relaxation technique converged quite rapidly for the case of zero pressure (94 per cent of $\Delta\mathscr{E}^0$ was attained in three steps), only three steps in the process have been carried out for non-zero pressures.

Fig. 3 gives the reduced displacement of the first three shells as a function of the volume reduced by the volume at zero external pressure. The solid curves extend to reduce volumes that correspond to extremely high pressures—of the order of 10^6 atmospheres for argon. Even at such high pressures, the second shell is still displaced outwards. The point at which δ_1 equals zero corresponds to a negative pressure of about eight thousand atmospheres for argon.

A measure of the importance of accounting for distortion is given by $\Delta\mathscr{E}^0/W^0$. This is plotted as a function of reduced volume in Fig. 4. It is seen that $\Delta\mathscr{E}^0$ varies from 1·78 per cent to about 12 per cent of W^0 as the reduced volume decreases from 1 to 0·4.

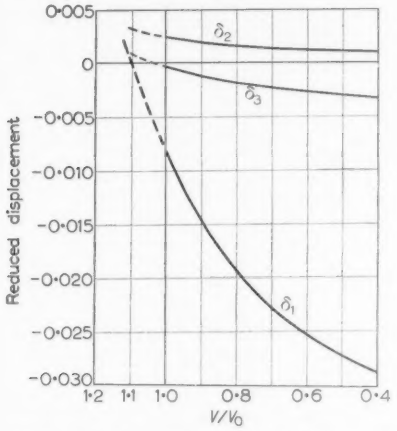

FIG. 3. The reduced displacement of the first three shells around a vacancy as a function of the volume reduced by the volume at zero external pressure. The solid portions of the curves represent calculated values; the dashed portions represent extrapolations.

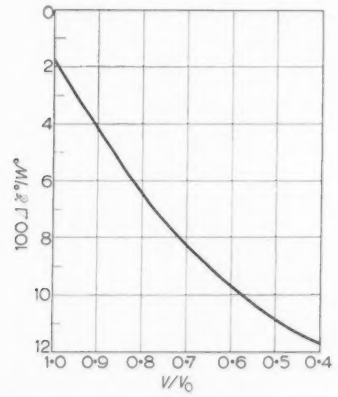

FIG. 4. The ratio of the energy of distortion $\Delta\mathscr{E}$ to the energy to form a vacancy without distortion W^0 as a function of the volume reduced by the volume at zero external pressure.

4. THE INTERSTITIAL BY THE ATOMIC METHOD

The most probable position for an interstitial atom in an f.c.c. crystal is at the center of an octahedron defined by six atoms at its verticies. Each group of neighbors, or each shell, has cubic symmetry about the interstitial position, and it is required that the equilibrium configuration of displacement satisfy the cubic crystallographic point-group about the interstitial position. As in the case of the vacancy, the latter requirement forces all atoms in a given shell for the first eight shells to have the same magnitude of displacement, and it restricts the first two, and many other, shells to radial displacements. The radii of the various shells about the interstitial are given by $d\sqrt{(k-\frac{1}{2})}$, $k = 1, 2, 3, \ldots$, with every fourth shell being empty.

In a manner similar to that utilized for the vacancy, it can be shown that the problem of an interstitial atom is equivalent to the problem of a perfect crystal in a known field of force. The special case in which the interstitial atom is identical with the atoms of the regular lattice is treated here.

Let $\boldsymbol{u}_i$ be a vector drawn from the interstitial site as origin to the ith atom; then the energy of interaction of an interstitial atom with an undistorted crystal is given by,

$$\epsilon_I \equiv \sum_i \phi(\boldsymbol{u}_i).$$

The energy to form an interstitial at constant pressure without distortion of the lattice is

$$W_I{}^0 = \epsilon_I + \epsilon - pv.$$

Let ΔE be defined as previously, but define a new quantity Q_I by,

$$Q_I = -\sum_i \{\phi(\boldsymbol{u}_i+\boldsymbol{r}_i)-\phi(\boldsymbol{u}_i)\},$$

which is somewhat analogous to the negative of Q for the vacancy. Also let,

$$\Delta\mathscr{E}_I = \Delta E - Q_I,$$

where at equilibrium $\Delta\mathscr{E}_I \to \Delta\mathscr{E}_I{}^0$, the energy of distortion associated with an interstitial. The problem reduces to one of minimizing $\Delta\mathscr{E}_I$.

(a) *The interstitial in Lennard-Jones crystals.* The law of potential for these crystals has been given in 3(a). Again both ΔE and Q_I are expanded to quadratic terms in the displacement about the undistorted lattice points. The expression for ΔE is given by equation (1) but it must be understood that the shells are different from those for the vacancy; hence the n_k, A_k, and A_{kl} have different values from those for the kth shell of the vacancy. In the appendices, it is shown that

$$Q_I = \sum_k n_k\delta_k\{\sigma_k{}^I - \eta_k{}^I\delta_k\}.$$

Defining $B_k{}^I = A_k + 2\eta_k{}^I$, we have

$$\Delta\mathscr{E}_I = \tfrac{1}{2}\sum_k n_k\delta_k\{B_k{}^I\delta_k - 2\sigma_k{}^I + \sum_{l\neq k}\delta_l A_{kl}\},$$

and at equilibrium

$$\delta_k B_k{}^I + \sum_{l \neq k} \delta_l A_{kl} = \sigma_k{}^I, \tag{6}$$

$$\Delta \mathscr{E}_I{}^0 = \tfrac{1}{2} \sum_k n_k \sigma_k{}^I \delta_k. \tag{7}$$

(b) *Solution of the equilibrium equations for zero pressure.* The solutions of (6) and (7) yield a description of the distortion around an interstitial in Lennard-Jones crystals under arbitrary external pressure. The numerical calculations have been carried out only to the first two stages in the relaxation technique for the special case of zero external pressure. This is sufficient to indicate the qualitative nature of the configuration of distortion and to give a fairly good estimate of δ_1, δ_2, and $\Delta \mathscr{E}_I{}^0$.

The simultaneous relaxation of the first and second shells yield δ_1 equal to $5{\cdot}07 \times 10^{-2}$ and δ_2 equal to $-5{\cdot}20 \times 10^{-3}$. Note that δ_1 for the interstitial is about six times larger than, and opposite in sign to, δ_1 for the vacancy.

The displacement is again outward along the cubic axes and inward elsewhere, at least near the interstitial. An examination of the geometrical arrangement of the atoms in the first and second shells is essential. It should be observed that as an atom in the first shell around an interstitial moves away from the interstitial, it also moves *farther away* from the atoms in the second shell. An atom moving radially outward in the first shell does not " push " against atoms in the second shell! Thus, the results here reported should be expected from simple geometrical arguments. This odd result does not obtain for linear chains.

To the second order in the relaxation process, $\Delta \mathscr{E}_I{}^0$ for the interstitial is about 60 per cent of the energy to form the fault without distortion. Consequently, distortion is of much more significance for the interstitial than for the vacancy.

There is one further point, which is obscured in the numerical calculations, namely the importance of $\eta_k{}^I$. This quantity appears in the second-order term in Q_I as does η_k in Q. The important point is that, at zero external pressure, the η_k are practically negligible whereas the $\eta_k{}^I$ are not.

5. APPLICATION OF ELASTICITY TO VACANCIES AND INTERSTITIALS

The elastic method is identical with the atomic approach in that an energy of distortion is defined by,

$$\Delta \mathscr{E} = \Delta E - Q,$$

where ΔE and Q have been defined and discussed in sections 2 and 3. The procedure used in this section differs from the atomic approach in that more approximate expressions for ΔE and Q are now to be used. However, the elastic approximation presented here differs from previous treatments in so far as the body force is examined in detail.

(a) *The elastic approximation to* Q. Terms in Q of the order of $\delta_k{}^3$ were neglected in the atomic theory; in the elastic method, terms of the order of $\delta_k{}^2$ are also to be neglected. Thus,

$$Q \cong - \sum_k n_k \sigma_k \delta_k.$$

This quantity can be considered as the work done by a body force which is radial with respect to the fault and is of equal magnitude for all atoms in a given shell. Since the perfect crystal is to be represented by a continuum, the body force may be further considered as smeared over each shell. Then for uniform smearing, the body force per unit volume is imagined to be,

$$P(r) = -(4\pi d^3)^{-1} \sum_k n_k \sigma_k k^{-1} \delta(r - d\sqrt{k}), \tag{8}$$

as could have been anticipated by observing that σ_k is directly proportional to $\phi'(r)$ evaluated at the kth shell.

By starting with Q_I instead of Q and proceeding similarly, it is found that the body force per unit volume for the interstitial is given by,

$$P^I(r) = (4\pi d^3)^{-1} \sum_k (k - \tfrac{1}{2})^{-1} n_k \sigma_k{}^I \delta \times \\ \times [r - d\sqrt{(k - \tfrac{1}{2})}]. \tag{9}$$

Generally, the latter expression constitutes a worse approximation than equation (8). For example, at zero external pressure, the second-order terms in Q are quite negligible, whereas Q_I has one appreciable second-order term, namely $n_1 \sigma_1{}^I \delta_1{}^2$. Consequently, in the following paragraphs application of the elastic method is made only to the problem of the vacancy.

(b) *The elastic approximation to* ΔE. By definition,

$$\Delta E = \tfrac{1}{2} \sum_{ij}{}' \{\phi(\boldsymbol{R}_{ij} + \boldsymbol{r}_j - \boldsymbol{r}_i) - \phi(\boldsymbol{R}_{ij})\},$$

which is that strain energy of a perfect crystal that arises when the crystal is subjected to an arbitrary deformation defined by the $\boldsymbol{r}_i$. This quantity is now to be approximated by a strain in a homogeneous elastic continuum.

Certain approximations are necessary in order to effect a correspondence between the crystal and the continuum. The first of these, the assumption of small displacements, was also made in the atomic theory; hence, both theories are linear. The additional approximations necessary to establish elasticity are too well known to reproduce here. However, it is worth pointing out the most drastic of these, from the viewpoint of the intended application to the problem of the vacancy, is that the derivative of the displacement is constant over volumes that are large in proportion to the range of interatomic forces—sometimes termed "the assumption of homogeneous strain over small volumes". This condition is not satisfied as is clearly demonstrated by the atomic solution of Section 3; there it was found that the displacement around a vacancy varies rapidly within a few atomic spacings. Nevertheless, it is worthwhile to discover what can be achieved by linear elasticity theory in a particular case for which an atomic solution is reported.

A table of the strain-energy functions for the principal classes of crystals are given in LOVE's book.[6] For many crystals, literature exists relating the elastic constants of the continuum to the appropriate molecular constants; for the frozen rare-gases, we refer to the work of BORN and his collaborators.[7]

Once the strain-energy function and the body force are known, the differential equations for the equilibrium displacement are found by equating to zero the variation of the strain-energy plus the energy of the crystal in the field of force. The most general variation for the case of cubic symmetry leads to three, simultaneous, inhomogeneous, partial, differential equations in the displacement. These are usually difficult to solve exactly, and other approximations become necessary.

The approximation (8) to the body force of a vacancy is spherically symmetric, but the continuum representation of the crystal has cubic symmetry. We can effectively average the cubic continuum and obtain an isotropic representation of it by imposing *before* taking the variation that,

$$u_k = x_k r^{-1} U(r),$$

where u_k and x_k are the kth components of the displacement and the radius vector, respectively. The Euler equation becomes,

$$b\frac{d}{dr}\left(\frac{dU}{dr}+\frac{2U}{r}\right) = -P(r), \tag{10}$$

$$b \equiv \tfrac{1}{5}(3C_{11}+2C_{12}+4C_{44}). \tag{11}$$

For isotropy, $C_{11} = C_{12}+2C_{44}$, and then $b \to C_{11}$. Equation (10) then reduces to that given in LOVE[8] for isotropic solids; $P(r)$ is a body force per unit volume and is equal to LOVE's $\rho R(r)$. The method thus outlined gives the proper combination of the cubic constants that is to be used as the C_{11} of the approximating isotropic continuum.

A better approximation to the atomic solution is obtained by imposing that,

$$u_k = x_k r^{-1}[F(r)+G(r)\sum_i x_i{}^4 r^{-4}]$$

which has the required cubic symmetry. Two simultaneous differential equations for $F(r)$ and $G(r)$ result, but we shall limit the present treatment to the isotropic approximation.

(c) *Solution of the differential equation.* Substituting (8) into (10) yields,

$$1/d\ U(r) = -(12\pi b d^3)^{-1} \times$$

$$\times\left[\left(\frac{d}{r}\right)^2 \sum_{k=1}^{l} n_k \sigma_k \sqrt{k} + \left(\frac{r}{d}\right) \sum_{k=l+1}^{\infty} n_k k^{-1} \sigma_k\right],$$

for $d\sqrt{l} \leqslant r \leqslant d\sqrt{(l+1)}$. Equation (11) together with GOW's[7] results give,

$$b = 175\gamma/d^3.$$

The elastic solution for the reduced displacement U/d is given by Curve A of Fig. 5 as a function of r/d, the reduced radius. Since a comparison with the atomic solution was desired, only the first seven terms in the body-force were used, that is k was permitted the values 1, 2, ..., 7. Curve C of Fig. 5 is reproduced from Fig. 1 for comparison. Note that the elastic solution gives a surprisingly good spherically symmetric average of the atomic solution.

Curve B of Fig. 5 results from permitting k to assume only the value 1, that is to say all parts of

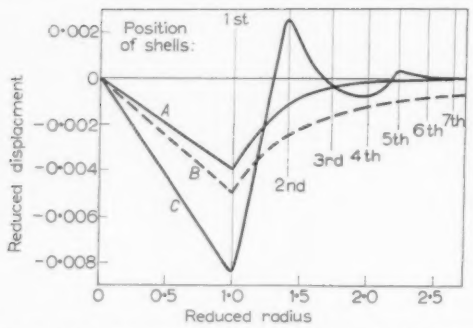

FIG. 5. (A) The elastic solution when body forces are applied on the first seven shells surrounding a vacant site. (B) The elastic solution when a body force is applied to the first shell only. (C) The atomic solution reproduced from Fig. 1. All curves are for the case of zero external pressure.

the body force are neglected except that on the first shell. From the first shell outward, the displacement varies as r^{-2}. It predicts poorly the displacement far from the defect. This lowest-order approximation to the elastic solution represents the logical method of fitting an r^{-2} law of displacement.

It is interesting to compare two other methods of fitting an r^{-2} law of displacement. Firstly, an r^{-2} law may be fitted to the atomic solution for the displacement of the seventh shell. This procedure yields negligible displacement everywhere and gives for the relaxation energy a value less than 1 per cent of the proper $\Delta\mathscr{E}^0$ calculated in 3(b). secondly, an r^{-2} law may be fitted so as to give the correct $\Delta\mathscr{E}^0$; this yields a displacement that is only slightly too large at the first shell, but which is about a hundred times too large at the seventh shell.

The atomic and the elastic solutions can be further compared by examining the value of $\Delta\mathscr{E}^0$ obtained by the elastic method. According to the approximations of this section,

$$Q = -\sum_k n_k\sigma_k\delta_k,$$

and it is easily shown that at equilibrium in the case of the vacancy,

$$\Delta E = 6\pi bd^3 \sum_k \sqrt{k}\delta_k^2.$$

So,

$$\Delta\mathscr{E}^0 = \sum_k \delta_k\{6\pi bd^3\sqrt{k}\delta_k - n_k\sigma_k\}.$$

If the general differential equations of elasticity had been solved instead of the restricted equation (10), use could be made of the theorem[9] that at static equilibrium,

$$\Delta E = \tfrac{1}{2}Q, \quad \text{or} \quad \Delta\mathscr{E}^0 = -\Delta E = -\tfrac{1}{2}Q.$$

Actually, these relations hold true within the significant figures reported here. Therefore

$$\Delta\mathscr{E}^0 \cong \tfrac{1}{2}\sum_k n_k\sigma_k\delta_k \cong -6\pi bd^3 \sum_k \sqrt{k}\delta_k^2.$$

With body forces applied to the first seven shells, $\Delta\mathscr{E}^0$ is equal to minus $0{\cdot}061\gamma$, about half of the energy of distortion as given by the atomic method. It should be mentioned, however, that a larger negative number obtains for $\Delta\mathscr{E}^0$ if fewer body forces are applied. This fact is easily interpreted in terms of the results of the atomic theory. In Section 3(b) it was seen that most of $\Delta\mathscr{E}^0$ resulted from the displacement of the first shell, and the elastic method gives a more accurate value for δ_1 when only the first body force is applied than when several body forces are applied. The requirement that a theory of point defects predicts simultaneously the energy of distortion and the long-range interactions is best met by the application of the entire body force.

6. DISCUSSION

The high degree of anisotropy found for point imperfections in central-force crystals can be qualitatively understood by a simple physical argument based on the law of interatomic forces and the geometry of the crystal: (1) To every point imperfection in these crystals there corresponds a body force which usually varies rapidly and changes sign at least once. In most cases, the body force (at zero external pressure) tends to displace in opposite directions the first and second neighbors to the fault. These two shells of atoms should determine the qualitative nature of the distortion. (2) The *magnitude* of the effect of the first-neighbor displacement on the second neighbor is of the second order when it is in a direction perpendicular to the line joining the first and the adjacent second neighbors, e.g. (a), (b), and (d) of Fig. 6. (3) A small displacement of the first neighbor in the indicated direction may *aid* [(b) and (c)] or slightly hinder [(a) and (d)] the indicated motion of the second neighbors—an entirely

different situation from that existing for a defect in a linear chain of atoms.

One expects a relatively large displacement of the first neighbors in the case of an interstitial in an f.c.c. crystal (large body force on first neighbors), and in the case of a vacancy in a b.c.c. crystal (a small number of first neighbors), but in these very cases the indicated (Fig. 6) motion of the first

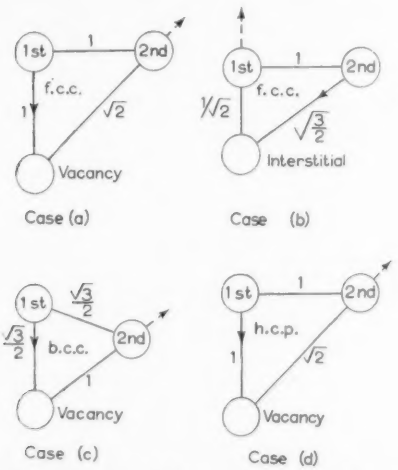

FIG. 6. Various point defects with a first and a second neighbor. The arrows indicate the direction of the body force at zero external pressure. The magnitude of the effect of a displacement of the first neighbor on the second neighbor is of the second order in (a), (b), and (d), but of the first order in (c). A small displacement of the first neighbor in the indicated direction *aids* in (b) and (c) and slightly hinders in (a) and (d) the indicated motion of the second neighbor.

neighbor *aids* the indicated motion of the second neighbors. Thus the second neighbors are less likely to "follow" a small displacement of the first neighbors in these two cases than in the case of a vacancy in an f.c.c. crystal. Accordingly, the distortion around the point imperfection of (b) or (c) is probably more anisotropic than in case (a) for which detailed calculations are presented in this paper. In addition it is concluded that calculations concerning the distortion around imperfections in linear chains of atoms are generally irrelevant, or misleading, with respect to point imperfections in three-dimensional crystals.

Apparently the inward displacement of some atoms about a point defect with the simultaneous outward displacement of others is a mechanism by which the crystal can readily readjust itself to perfect lattice in spite of large displacements of the first neighbors to the defect. On this basis it can be stated that in an f.c.c. crystal an interstitial has a greater "readjustment capacity" than a vacancy. These principles may hold true to a certain extent for crystals in which the body force is not radial (interatomic forces not central).

In the atomic solution for the vacancy, the displacement beyond the eighth shell has been shown to have a negligible effect on the energy of formation of the defect and the configuration of distortion near the defect; hence it was neglected. The elastic method gives a solution everywhere, but, being a spherically symmetric average, it gives no clue to the anisotropic nature of the distortion far from the defect. Until one of the two methods is extended as discussed in the sequel, one can only speculate on the asymptotic form of the atomic solution or on the nature of the anisotropic elastic solution. The latter would be of great interest in describing that portion of the long-range interaction between defects which results from the static distortion. It is well known[10] that two centers of dilation in an isotropic elastic medium do not interact except through their image field. On the other hand, ESHELBY[11] has pointed out that this is not the case either for a non-symmetrical center in an isotropic medium or a symmetrical center in an anisotropic medium. Therefore, an extension of the anisotropic atomic solution for the vacancy and the interstitial would be of great interest, particularly since both defects have a displacement which is initially outward along the cubic axes and inward elsewhere.

The calculations presented here are for a classical model at arbitrary pressure but at 0°K. The neglect of the zero-point fluctuations is probably justifiable for the relatively high pressures. For zero external pressure, it would be interesting to go a stage further and account for the changes in the vibrational spectrum, but the author feels that it is very important to take into account the distortion of the lattice in such calculations. In most of the published literature on the subject, the relaxation has been neglected entirely[12,13] or an estimate[14,15] has been made of the relaxation of the first neighbors. MONTROLL's[16] work is not particularly useful to us here because he applied his theory only to a linear chain of atoms and to a

simple cubic crystal where only nearest neighbor forces were considered operative. The limitations of the latter model are obvious from the following statement: *No* relaxation of the simple cubic lattice will occur upon the removal of an atom if the crystal obeys nearest-neighbor central forces, is at zero external pressure, and zero-point fluctuations are neglected.

The elastic method, in the simple form presented here, does not give the anisotropic strain around point imperfections, but it is easily extended as follows: (1) It is necessary to use non-uniform smearing of the body forces on the first few, say two, shells. For example, along the cubic axes in the case of the vacancy, the body force on the first shell should reduce to zero and that on the second shell should attain its maximum value. (2) In using the variational principle, the displacement should be permitted to have a certain amount of cubic symmetry as outlined in the last paragraph of Section 5(b).

The atomic method could be extended to give the long-range distortion as well as the core relaxation by treating the crystal as a discrete structure at the core and as a continuum outside the core. The extension is straightforward except in the calculation of the coupling constants between those atoms and that portion of the continuum which are both near the boundary. A solution of this problem would be quite useful in other fields and is being considered further.

It is to be expected that elasticity theory is more nearly valid in the description of dislocations than in the description of point defects. In this connexion, it is usually assumed that the core energy of a dislocation is a small fraction of the total energy of distortion. Neither the atomic theory nor the elastic method is easily applied to dislocations, however the fact that the energy of distortion of point defects treated here is almost entirely core energy might suggest that the core energy of a dislocation may be more significant than previously thought.

The atomic method is applicable to the problem of the distortion at the "saddle-point configuration" of diffusion by vacancies. A theoretical dependence of the activation energy for diffusion may prove to be accessible to experimental verification. The simple case of Lennard-Jones crystals is being considered.

Extremely high pressures do not "mix" the atoms that move away from a vacant site (Section 3(d)) with those that move toward it. This might suggest that non-zero temperatures may also be very ineffective in mixing the two groups.

Acknowledgements—The author wishes to thank PROF. NICOLAS CABRERA and JOHN PLASKETT for giving valuable suggestions and criticisms during many discussions.

The work was supported in part by Union Carbide and Carbon Company, the United States Steel Corporation, and the Office of Naval Research.

REFERENCES

1. *Handbuck der Physik.* Band VII. Teil1; *Crystal Physics* Vol. 1, p. 529.
2. MACHLUP S. Baltimore Meeting of A.P.S., March 1955.
3. HUNTINGTON H. B. *Acta Met.* **2,** 554 (1954).
4. HARDY G. H. and WRIGHT E. M. *Theory of Number* (3rd Ed.) p. 310. Oxford Press (1954).
5. JONES J. E. and INGHAM A. E. *Proc. Roy. Soc.* **A107,** 636 (1925).
6. LOVE A. E. H. *Mathematical Theory of Elasticity* (4th Ed.) p. 159. Cambridge Press (1934).
7. GOW M. M. *Proc. Camb. Phil. Soc.* **40,** 151 (1944).
8. LOVE A. E. H. *Op. cit.* p. 142.
9. LOVE A. E. H. *Op cit.* p. 173.
10. BITTER F. *Phys. Rev.* **37,** 1526 (1931).
11. ESHELBY J. D. *Acta Met.* **3,** 487 (1955); *Solid State Physics* Vol. 3. Academic Press (1956).
12. STRIPP K. F. and KIRKWOOD J. G. *J. Chem. Phys.* **22,** No. 9, 1579 (1954).
13. MONTROLL E. W. and POTTS R. B. *Phys. Rev.* **100,** 525 (1955); *Phys. Rev.* **102,** 72 (1956).
14. FUMI F. G. *Phil. Mag.* **46,** 1007 (1955).
15. HUNTINGTON H. B. *Phys. Rev.* **61,** 325 (1942).
16. MONTROLL *Op. cit.*
17. JONES J. E. and INGHAM A. E. *Op. cit.*

APPENDIX 1: DERIVATION OF Q AND Q_I FOR LENNARD-JONES CRYSTALS

After a radial distortion about a lattice site, the distance from the site to an atom in the kth shell is $d(\sqrt{k}+\delta_k)$ if all atoms in a given shell have the same radial displacement. Thus, for the vacancy,

$$Q = \gamma \sum_k n_k\{a^p[(\sqrt{k}+\delta_k)^{-p}-k^{-p/2}]-$$

$$-2a^q[(\sqrt{k}+\delta_k)^{-q}-k^{-q/2}],$$

where p is equal to 12 and q is equal to 6 for Lennard-Jones crystals. A Taylor's expansion gives

$$Q = -\sum_k n_k\{\sigma_k\delta_k - \eta_k\delta_k^2 + \dots\},$$

where,

$$\sigma_k = \gamma\{pa^p k^{-(p+1)/2} - 2qa^q k^{-(q+1)/2}\},$$

and,

$$\eta_k = \gamma\{\tfrac{1}{2}p(p+1)a^p k^{-(p+2)/2} - q(q+1)a^q k^{-(q+2)/2}\}.$$

In the case of an interstitial, the procedure is the same, giving,

$$Q_I = \sum_k n_k\{\sigma_k\delta_k - \eta_k\delta_k^2 + \dots\}.$$

The definitions of $\sigma_k{}^I$ and $\eta_k{}^I$ differ, respectively, from those for σ_k and η_k in that k is replaced by $(k-\frac{1}{2})$. The n_k for the interstitial differ, of course, from the n_k for the vacancy.

VOL. 3 1957

APPENDIX II. DERIVATION OF ΔE FOR LENNARD-JONES CRYSTALS

By definition,

$$\Delta E = \tfrac{1}{2}\sum_{i,j}{}' \{\phi(\boldsymbol{R}_{ij} + \boldsymbol{r}_j - \boldsymbol{r}_i) - \phi(\boldsymbol{R}_{ij})\}, \quad (12)$$

where all symbols have been defined in section 3. The potential energy of interaction of two isolated atoms separated by a distance r is taken to be

$$\phi(r) = \gamma\left\{a^p\left(\frac{d}{r}\right)^p - 2a^q\left(\frac{d}{r}\right)^q\right\},$$

where $a = r_0/d$. This expression reduces to that given in 3(a) when p is set equal to 12 and q is equated to 6.

Let us now expand ΔE in the displacements about the undistorted lattice points. For this purpose, it is convenient to first evaluate a quantity L^p defined by

$$L^p \equiv \sum_{i\,j}{}' \left\{\left(\frac{d^2}{\mathcal{R}_{ij}\cdot\mathcal{R}_{ij}}\right)^{p/2} - \left(\frac{d}{\boldsymbol{R}_{ij}}\right)^p\right\}, \quad (13)$$

where,

$$\mathcal{R}_{ij} \equiv \boldsymbol{R}_{ij} + \boldsymbol{r}_j - \boldsymbol{r}_i.$$

To second-order terms in r_i/R_{ij}, we have

$$L^p = \tfrac{1}{2}p(p-1)C_{p+2}\sum_i\left(\frac{r_i}{d}\right)^2 + p\sum_{i,j}{}'\left(\frac{r_i r_j}{d^2}\right)\left(\frac{d}{R_{ij}}\right)^{p+2} D_{ij}(p), \quad (14)$$

where the LENNARD-JONES[17] potential constants are given by,

$$C_p \equiv \sum_{j\neq i}\left(\frac{d}{R_{ij}}\right)^p,$$

and where,

$$D_{ij}(P) \equiv \sin\theta_i \sin\theta_j \cos\Psi_{ij} - (p+1)\cos\theta_i\cos\theta_j.$$

The angles θ_i and θ_j are the angles that $\boldsymbol{r}_i$ and $\boldsymbol{r}_j$ respectively make with $\boldsymbol{R}_{ij}$; the angle ψ_{ij} is the angle between the planes defined by $(\boldsymbol{r}_i \wedge \boldsymbol{R}_{ij})$ and $(\boldsymbol{r}_j \wedge \boldsymbol{R}_{ij})$. Note that for p equal to one, the second term in equation (14) reduces to the electrostatic dipole-dipole interaction. A reduced displacement $\delta_i = r_i/d$ is now introduced yielding,

$$L^p = \tfrac{1}{3}p(p-1)C_{p+2}\sum_i \delta_i^2 + p\sum_{i\,j}{}'\delta_i\delta_j T(i,j,p), \quad (15)$$

where,

$$T(i,j,p) \equiv \left(\frac{d}{R_{ij}}\right)^{p+2} D_{ij}(p).$$

Since applications to point imperfections are anticipated, it is convenient to group the atoms of the crystal into shells (section 3). Accordingly, each summation index in (15) is replaced by two indices, a subscript which labels the shell concerned and a superscript which locates a particular atom in a given shell. Thus, (15) is rewritten as,

$$L^p = \tfrac{1}{3}p(p-1)C_{p+2}\sum_{k,s}(\delta_k{}^s)^2 + p\sum_{k,l,s,t}{}'\delta_k{}^s\delta_l{}^t T(k,l,s,t,p), \quad (16)$$

where the prime indicates that $s \neq t$ if $k = l$.

The second term in (16) can be written,

$$p\sum_{k\,s}\delta_k{}^s\{\sum_{t\neq s}\delta_k{}^t T(k,k,s,t,p) + \sum_{l\neq k}\sum_t \delta_l{}^t T(k,l,s,t,p)\}.$$

If it is assumed that all atoms in a given shell have the same magnitude of displacement, the superscript on the reduced displacement can be dropped giving,

$$p\sum_k \delta_k\{\delta_k \sum_{s\,t}\sum_{\neq s} T(k,k,s,t,p) + \sum_{l\neq k}\delta_l\sum_s\sum_t T(k,l,s,t,p)\}.$$

In both the case of the vacancy and that of the interstitial, there is only one "type" (Section 3) of atom in each of the first eight shells. For those,

$$\sum_s \sum_{t\neq s} T(k,k,s,t,p) = n_k \sum_{t\neq 1} T(k,k,l,t,p) \equiv n_k S_{kk}{}^p,$$

$$\sum_s \sum_t T(k,l,s,t,p) = n_k \sum_t T(k,l,1,t,p) \equiv n_k S_{kl}{}^p,$$

$$n_k S_{kl}{}^p = n_l S_{lk}{}^p,$$

where n_k is the number of atoms in the kth shell. Therefore we write,

$$L^p = \sum_k \delta_k p n_k \{\delta_k \times \times [\tfrac{1}{3}(p-1)C_{p+2} + S_{kk}{}^p] + \sum_{l\neq k} \delta_l S_{kl}{}^p\}. \quad (17)$$

Substituting (17) into (12) gives

$$\Delta E \cong \tfrac{1}{2} \sum_k n_k \delta_k \{A_k \delta_k + \sum_{l\neq k} \delta_l A_{kl}\}, \quad (18)$$

where,

$$A_k = \gamma\{\tfrac{1}{3}p(p-1)C_{p+2}a^p - \tfrac{2}{3}q(q-1)C_{q+2}a^q + + pa^p S_{kk}{}^p - 2qa^q S_{kk}{}^q\}$$

$$A_{kl} = \gamma[pa^p S_{kl}{}^p - 2qa^q S_{kl}{}^q].$$

Equation (18) expresses the atomic approximation to ΔE.

VOL 3 195

J. Phys. Chem. Solids Pergamon Press 1957. Vol. 3. pp. 223–228.

THE IONIC CHARACTER AND ELASTIC MODULI OF ZINC BLENDE LATTICES*

ROY F. POTTER†

National Bureau of Standards, Washington, D.C.

(*Received* 7 *February* 1957)

Abstract—The elastic moduli for a number of materials with the diamond or zinc blende (sphalerite) crystal structure are available in the literature. It has been noticed that the ratio C_{11}/C_{12} has values between 2·6 and 2·7 for Si and Ge, respectively, and 1·65 or 1·50 in the case of ZnS. InSb and GaSb have elastic moduli that give intermediate values for this ratio. A scale which gives the ionic character as a function of the ratio C_{11}/C_{12} has been constructed based on the Born diamond lattice theory and the relationship between the longitudinal optical mode and transverse optical modes when the lattice has some ionic character. This scale indicates that InSb has the ionic character that corresponds to an ionic charge of 0·65 electron. GaSb has an ionic character approximately two-thirds of that for InSb. Conversely, the elastic moduli may be estimated for crystals of this type if the optical data are available.

INTRODUCTION

THE steadily increasing interest in the physical properties of the intermetallic semiconductors having the zinc blende (sphalerite) structure makes it desirable to have some estimate of the ionic character of the lattice. The effect that any polar character of the lattice may have on electron scattering mechanisms in these compounds is currently being considered by several investigators.

If one considers the covalent diamond crystals Si and Ge as special cases of the zinc blende lattice having a higher order of symmetry, he will find that the elastic moduli of a number of these compounds have been measured, many by modern techniques. Table 1 comprises a list of such values and the investigators who reported them.

The ratio C_{11}/C_{12} shows a definite variation between such covalent crystals as Si and Ge (2·65) and the partially ionic zinc blende (1·65, 1·49). The materials InSb and GaSb have intermediate values. On the other hand, the ratio C_{11}/C_{44} shows no large deviation from the value 2.

* This research was supported by the United States Air Force through the Air Force Office of Scientific Research of the Air Research and Development Command under Contract No. CSO 670–53–12.

† Present Address—U.S. Naval Ordnance Laboratory, Corona, California.

The manner in which the value of C_{11}/C_{12} varies from the covalent compounds to the partially ionic compounds suggests that the ratio could be related to the ionic character of the bond.

SPITZER and FAN[1] have given what they believe to be an upper limit for the value of the ionic charge of InSb. Based on an estimate of the difference between the static and high frequency dielectric constants the value given is 0·34 electron charge.

LATTICE VIBRATION THEORIES

Lattices with tetrahedral symmetry about each site have been considered by MOTT and FRÖHLICH,[2] SZIGETI[3] and others.[4] This work has been summarized by BORN and HUANG[4] and their notation will be used here in presenting the resulting equations.

It is shown that the transverse optical frequency (corresponding to the reststrahlen frequency) is related to the longitudinal mode frequency, the ionic charge, Ze, and the static and high-frequency dielectric constants, ϵ_0 and ϵ_∞ by the following expression:

$$\omega_0^2 = \omega_l^2\left(\frac{\epsilon_\infty}{\epsilon_0}\right)\left(\frac{\epsilon_0+2}{\epsilon_\infty+2}\right) - \frac{4\pi(Ze)^2}{3\bar{m}v_a}\left(\frac{\epsilon_\infty+2}{3}\right) \quad (1)$$

where $\bar{m}$ is the reduced mass of the primitive cell and v_a is its volume, i.e. $a_0^3/4$ for zinc blende structures.

By considering ionic overlap potentials SZIGETI[3] derived a relation between the bulk modulus $[K=(C_{11}+2C_{12})/3]$ and the optical modes which can be written

$$\omega_l^2 = (4Ka_0)/\bar{m}\left(\frac{\epsilon_\infty+2}{\epsilon_0+2}\right)\left(\frac{\epsilon_0}{\epsilon_\infty}\right) \approx \frac{4Ka_0}{\bar{m}}. \quad (2)$$

The bulk moduli of InSb and ZnS give values for frequency that are too low compared to the values obtained from measured reststrahlen frequencies, although in the case of ZnS the agreement is somewhat better. This discrepancy is not surprising in that a large amount of covalent bonding exists in these lattices.

One may eliminate ω_l from equation (1) by writing $\omega_0^2 = \omega_l^2(\epsilon_\infty/\epsilon_0)$[5]. This gives the equivalent expression

$$\omega_0^2(\epsilon_0-\epsilon_\infty) = \frac{4\pi(Ze)^2}{\bar{m}v_a}\left(\frac{\epsilon_\infty+2}{3}\right)^2 \quad (3)$$

which was used by SPITZER and FAN[1] in estimating the effective charge for InSb.

Instead of using the estimated dielectric constant difference, it is the purpose here to investigate the possibilities of getting values for ω_l from the elastic moduli. Once this is obtained, a value for Z can be determined from equation (1).

BORN[6] and SMITH[7] have investigated the diamond lattice. Only the nearest neighbor lattice theory will be considered here. The results of this theory predict that only two independent elastic constants for the diamond lattice exist,

$$[4C_{11}(C_{11}-C_{44})]/(C_{11}+C_{12})^2 = 1 \quad (4)$$

and that the fundamental frequency ω for the optical mode of vibration with lattice wave vector $\boldsymbol{q}=0$ is given by

$$\omega^2 = (4C_{11}a_0)/\bar{m}. \quad (5)$$

The last column of Table 1 gives values for the left side of equation (4). It can be seen that they become markedly less than unity for the more ionic crystals.

The ratio C_{11}/C_{12} decreases in value as the lattices become more ionic (see Table 1), however, this ratio must have unity as a lower bound. This limit results from the critical conditions for lattice stability,[8]

$$C_{11}-C_{12}>0, \qquad C_{44}>0, \qquad C_{11}+2C_{12}>0. \quad (6)$$

This would indicate that lattices for which $C_{11}-C_{12}=0$ are unstable in that they approach what BORN refers to as a gel state. Furthermore, the bulk modulus for such a lattice would be equal to either C_{11} or C_{12}.

Table 1. Room temperature values of the elastic constants (units are 10^{11} dyn/cm^2)

Crystal	C_{11}	C_{12}	C_{44}	C_{11}/C_{12}	C_{12}/C_{44}	C_{11}/C_{44}	$\frac{4C_{11}(C_{11}-C_{44})}{(C_{11}+C_{12})^2}$
Si[a]	16·57	6·392	7·957	2·6	0·8	2·08	1·07
Ge[a]	12·89	4·832	6·712	2·7	0·72	1·93	1·015
GaSb[b]	8·849	4·037	4·325	2·2	0·93	2·04	0·965
InSb[b]	6·717	3·665	3·018	1·83	1·21	2·22	0·90
InSb[c]	6·472	3·265	3·071	1·98	1·06	2·11	0·91
ZnS[d]	9·45	5·70	4·36	1·65	1·76	2·16	0·85
ZnS[e]	10·7	7·22	4·12	1·49		2·50	0·89

(*a*) McSKIMIN H. J. *J. Appl. Phys.* **24,** 988 (1953).
(*b*) McSKIMIN H. J., BOND W. L., PEARSON G. L. and HROSTOWSKI H. J. *Bull Amer. Phys. Soc.* **1,** (1956).
(*c*) POTTER R. F. *Phys. Rev.* **103,** 42 (1956).
(*d*) VOIGHT W. see HEARMAN R. F. S. *Rev. Mod. Phys.* **18,** 409 (1946).
(*e*) BHAGAVANTAM S. *Proc. Indian Acad. Sci.* **41,** 72 (1955).

Table 2. Data used for determining the values of Z in Fig. 1

Crystal	$\bar{m}$	$a_0(A)$	$\omega_l^{2(e)}$	$\lambda_l^{(e)}(\mu)$	$\lambda_t(\mu)$	ε_∞	$Z^{(j)}$
Si	2·32	5·43[a]	155×10^{26}	15	16·5[f]		0
Ge	6·02	5·66[b]	48·6	27	29[f]	16	0
GaSb	7·36	6·10[c]	29·3	35	41[k]	14	—
InSb	9·81	6·48[d]	17·75	45	52[g]	16	0·71
InSb		6·48	17·10	46	52[h]	16	0·65
ZnS	3·57	5·40[a]	59·5	24·5	33[i]	5	1·29
ZnS		5·40	64·8	23·5	26[h]	5	0·9

(*a*) SWANSON H. and FUYAT R. NBS Circular 539 II, 6 (1953).
(*b*) SWANSON H. and TATGE E. NBS Circular 539 I, 19 (1953).
(*c*) MCSKIMIN H., BOND W., PEARSON G., and HROSTOWSKI H. *Bull. Amer. Phys. Soc.* II **1,** 111 (1956).
(*d*) SWANSON H., FUYAT R., and UGRINIC G. NBS Circular 539 IV, 73 (1955).
(*e*) Calculated from equation (2a).
(*f*) COLLINS R. J. and FAN H. Y. *Phys. Rev.* **93,** 676 (1954).
(*g*) SPITZER W. and FAN H. *Phys. Rev.* **99,** 1893 (1955).
(*h*) YOSHINADA H. *Phys. Rev.* **100,** 753 (1955).
(*i*) PARADI M. *C.R. Acad. Sci., Paris* **205,** 1224 (1937).
(*j*) Calculated from equation (1).
(*k*) See ref. 9.

VOL. 3 1957

APPLICATION TO MIXED IONIC AND COVALENT BONDS

It is assumed here that the case for $C_{11}/C_{12} = 1$ corresponds to the completely ionic zinc blende lattice. This does not appear unreasonable from the characteristics of the compounds in Table 1. This assumption further implies that any stable sphalerite form must have some covalent bonding.

Equation (2) based on ionic overlap potentials is now written as

$$\omega_l^2 = 4C_{11}a_0/m. \qquad (2a)$$

Thus the relationship between the modulus C_{11} and the longitudinal optical mode has nearly the identical form for the extreme covalent bond (equation 5) and the completely ionic bond (equation 2a).

The crystals of interest, of course, are those with mixed ionic and covalent bonding. The above conclusions would indicate that a reasonable estimate for ω_l can be made for all zinc blende lattices by using equation (5). With ω_l, the reststrahlen frequency ω_0, the high frequency dielectric constant, the reduced cell mass, and the cell volume, one may estimate the effective charge of the lattice from equation (1). In Table 2 are shown the results for the several zinc blende lattices for which data are available.

The upper curve, Fig. 1, shows a scale based on the assumptions of this section using equations

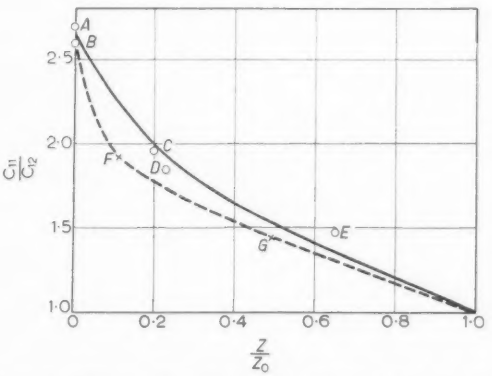

FIG. 1. The relationship between the ratio C_{11}/C_{12} and the ionic charge of zinc blende lattices. The solid curve is based on equations (1) and (5) using data for

A Ge MCSKIMIN
B Si MCSKIMIN
C Insb MCSKIMIN *et al.*
D InSb POTTER
E ZnS VOIGHT.

The broken curve is based on values for Z determined from equation (3) with data from

F InSb SPITZER and FAN
G ZnS SZIGETI.

Table 3. Data used for estimating elastic moduli of copper halide crystals

Crystal	$K^{(a)}$ $\times 10^{-11}$	ω_t^2 $\times 10^{-26}$	$\lambda_t(\mu)^{(b)}$	$a_0(A)^{(c)}$	ϵ_∞	$\overline{m}$ $\times 10^{23}$	C_{11} $\times 10^{-11}$	C_{12} $\times 10^{-11}$	C_{44} $\times 10^{-11}$
CuCl	4·00	12·6	53	5·42	3·0	3·95	4·25	3·9	2·1
CuBr	3·48	10·9	57	5·69	4·08	5·90	3·91	3·26	1·95
CuI		10·5	58	6·05		7·05			

(*a*) SZIGETI B. *Proc. Roy. Soc.* **204,** 51 (1950).
(*b*) PARADI M. *C.R. Acad. Sci., Paris* **205,** 1224 (1937).
(*c*) SWANSON H., FUYAT R., and UGRINIC G. NBS Circular 539 IV, 35 (1955).

(1) and (2a). This curve is given approximately by $Z/Z_0 = [(1/1{\cdot}65)(\alpha - 2{\cdot}65)]^2$, where $\alpha = C_{11}/C_{12}$.

When the elastic constants for GaSb are used with this curve the charge Z is estimated to be 0·39. This value of Z with the application of equations (1) and (2a) determines the reststrahlen wavelength to be $\lambda_t = 37\ \mu$. PICUS[9] has recently determined the reststrahlen wavelength for GaSb to be 41μ.

The lower curve in Fig. 1 is based on values of Z/Z_0 based on the SPITZER and FAN estimate for $\Delta\epsilon < 1{\cdot}5$ in the case of InSb[1] and that $\Delta\epsilon = 3$ for ZnS.[3] This gives an alternative scale for Z based on the elastic constants. The discrepancy between the two curves in the low Z/Z_0 region may be due to the fact that equation (2a) is not rigorously true.

TWO METHODS FOR ESTIMATING THE ELASTIC CONSTANTS

(a) *If the bulk modulus, high frequency dielectric constant, and reststrahlen frequency are known*

In the case of the copper halides, the bulk modulus, the dielectric constants, and the reststrahlen frequencies have been determined experimentally.[3] The present scheme for relating the elastic constants and the optical modes then allows an estimate for the elastic constants. It follows from equations (1) and (5) that

$$\frac{1{\cdot}285 \times 10^3 Z^2(\epsilon_\infty + 2)}{\overline{m} a_0^3 \omega_0^2} = \frac{[3\alpha/(\alpha+2)]K4a_0}{\omega_0^2 \overline{m}} - 1. \qquad (7)$$

The values of Z/Z_0 and $\alpha = C_{11}/C_{12}$ which satisfy equation (7) are determined from the curve of Fig. 1.

In Table 3 are shown the resulting C_{11} and C_{12} for the copper halides. The values for C_{44} were arbitrarily taken as one-half the values of C_{11}. This seems to be a reasonable procedure suggested by experimental values in Table 1. The coefficient of linear expansion of CuCl and CuBr have been measured by X-ray techniques.[10,11] The fact that two phase transformations are observed at elevated temperatures indicates the relative instability of these compounds. The crystals exhibit transitions from the sphalerite form to the hexagonal wurtzite form and back to a final form with cubic symmetry.

(b) *If the characteristic Debye temperature is known*

Early in the century there were derivations for isotropic materials relating θ_D to the bulk modulus K.[12] However, a general expression for lattices with cubic symmetry is given by[13]

$$\theta = (2h/k)(9/Y_R 4\pi)^{1/3}(1/a_0)[(C_{11} - C_{44})/\rho]^{1/2}. \qquad (8)$$

Several schemes for evaluating Y_R, which is a function of the elastic constants, have been developed. The method of QUIMBY and SUTTON,[14] which has been simplified in application by SUTTON,[15] seems to be the most facile.

With the assumption that $C_{11}/C_{44} = 2$, then equation (8) becomes, for the case of zinc blende structure,

$$\theta_D = (h/k)(9/Y_R 4\pi)^{1/3}(2C_{11}/\rho a_0^2)^{1/2} \qquad (8')$$

and

$$3{\cdot}0 < Y_R < 8$$
$$0{\cdot}7 > Y_R^{-1/3} > 0{\cdot}5. \qquad (9)$$

The lower limit of Y_R is evaluated from the

constants for Ge and Si while the upper limit is based on the estimate for the copper halides.

The elastic constants for α Sn (gray tin) have been worked out from the θ_D ($\theta_D = 260°K$) given by HILL and PARKINSON.[16] The values for ρ and a_0 are the same as those for InSb. The elastic constants evaluated from equation (8′) are: $C_{11} = 9{\cdot}6$, $C_{12} = C_{11}/2{\cdot}7 = 3{\cdot}5$, and $C_{44} = 4{\cdot}8$, all in units of 10^{11} dynes/cm^2.

From equation (5) the optical mode wavelength for α Sn is given as $\lambda = 38\,\mu$.

CONCLUSIONS

This hybrid method for determining the relationship between the optical modes of the zinc blende lattice and the elastic constants is not as satisfactory as a more sophisticated approach might be. It does, however, offer a better approximation than existing theories in their application to the intermetallic compounds. The entire structure rests on three assumptions: (1) that equation (5) holds, (2) that the 100 per cent ionic zinc blende lattice is non-existent because $C_{11} = C_{12}$, and (3) that the theory for polar lattices holds.

It does provide an estimate for ionic character and the reststrahlen frequency if the elastic moduli are known. Conversely, the elastic moduli and ionic character can be determined under this scheme if the bulk modulus and reststrahlen frequency are known. Examples of both applications have been given.

Table 4.[a] *Electronegativities*

Element	Compound	X	$(X_A - X_B)$
Zn		1·5	
S		2·5	
	ZnS		1·0
In		1·5	
Sb		1·8	
	InSb		0·3
Ga		1·5	
Sb		1·8	
	GaSb		0·3
Cu		1·8	
Cl		3·0	
Br		2·8	
I		2·5	
Ag		1·8	
	CuCl		1·2
	CuBr		1·0
	CuI		0·7
	AgI		0·7

(*a*) GORDY W. and THOMAS W. J. O. *J. Chem. Phys.* **24,** 439 (1956).

The ionic character estimated by this method can be compared to that given from the electronegativity scale of PAULING.[17] GORDY and THOMAS[18] have published a list of electronegativities (X) for the elements. The electronegativities of the elements of particular interest are shown in Table 4. It can be seen that the ionic character of a molecule AB (a monotonic function of $(X_A - X_B)$ generally follows in the order shown in the last column of Table 1. The exceptions are that in Table 4 GaSb and InSb have the same electronegativity character as do ZnS and CuBr The scheme outlined here predicts a difference. PAULING[17] shows a scale of ionic character based on the ionic character and electronegativity of hydrogen halide molecules. The values for Z/Z_0 based on his scale are lower than those shown in Fig. 1 except in the case of GaSb. GOODMAN[19] has discussed the electronegativity scale of these semiconducting compounds and the ionic character to be expected.

The scheme outlined above for determining the optical modes of zinc blende type crystals from a knowledge of elastic moduli undoubtedly has serious shortcomings; nevertheless, in view of the present state of dynamic lattice theory it may provide a rough tool where none existed.

REFERENCES

1. SPITZER W. G. and FAN H. Y. *Phys. Rev.* **99,** 1893 (1955).
2. FRÖHLICH H. and MOTT N. F. *Proc. Roy. Soc.* A **171,** 496 (1939).
3. SZIGETI B. *Proc. Roy. Soc.* A **204,** 51 (1950).
4. BORN M. and HUANG K. *Dynamical Theory of Crystal Lattices.* Oxford University Press, Oxford (1954).
5. LYDDANE R. H., SACHS R. G. and TELLER E. *Phys. Rev.* **59,** 673 (1941).
6. BORN M. *Ann. Physik* **44,** 605 (1914).
7. SMITH H. M. J. *Trans. Roy. Soc.* **241,** 105 (1948).
8. See reference 4, p. 142.
9. PICUS G. Private correspondence.
10. MIYAKE S., HOSHINA S., and TAKENAKA T. *J. Phys. Soc. Japan* **7,** 19 (1952).

11. HOSHINA S. *J. Phys. Soc. Japan* **7,** 560 (1952).
12. BLACKMAN M. *Crystal Physics I Encyclopedia of Physics* p. 376. Springer-Verlag, Berlin (1955).
13. LEIBFRIED G. *Ibid.* p. 247 ff.
14. QUIMBY S. L. and SUTTON P. M. *Phys. Rev.* **91,** 1122 (1953).
15. SUTTON P. M. *Phys. Rev.* **99,** 1826 (1955).
16. HILL R. W. and PARKINSON D. H. *Phil. Mag.* **43,** 309 (1952).
17. PAULING L. *Nature of the Chemical Bond.* Cornell University Press, Ithaca (1948).
18. GORDY W. and THOMAS W. J. O. *J. Chem. Phys.* **24,** 439 (1956).
19. GOODMAN C. H L. *Proc. Phys. Soc.* B **67,** 258 (1954).

VOL
3
195

J. Phys. Chem. Solids Pergamon Press 1957. Vol. 3. pp. 229–237.

INTERSTITIAL ZINC IN ZINC OXIDE

D. G. THOMAS

Bell Telephone Laboratories, Inc., Murray Hill, New Jersey

(*Received* 8 *March* 1957)

Abstract—Methods of introducing interstitial zinc into single crystals of zinc oxide are described which involve heating the crystals in zinc vapor followed by rapid quenching. The interstitial zinc atoms act as donors with a low ionization energy and they are observed by the extra conductivity which they impart to the crystals. The solubility in atoms/cm³ from saturated zinc vapor is:

$$n = 3{\cdot}4 \times 10^{20} \exp(-0{\cdot}65e/kT).$$

This solubility leads to a reasonable value for the vibrational entropy of the interstitial atom. In the range 180–350°C the diffusion coefficient of the donor obeys:

$$2D_i = 5{\cdot}3 \times 10^{-4} \exp(-0{\cdot}55e/kT).$$

From these results the parabolic rate constant for the oxidation of metallic zinc may be calculated and the results are in good agreement with previous observations. The results of the high temperature diffusion of radioactive zinc into zinc oxide are less easy to understand and it may be that interstitial zinc is not involved in this process.

Evidence is advanced that the defects are interstitial zinc atoms and not oxygen vacancies. The donors normally present in zinc oxide are not interstitial zinc atoms, but may be chemical impurities.

INTRODUCTION

ZINC oxide is an *n*-type semiconductor, and is usually considered to have a stoichiometric excess of zinc which is responsible for the conductance electrons in the crystal. It should however be emphasized that the methods used for determining this excess of zinc are usually not specific for zinc. Thus the crystals are dissolved in the presence of an oxidizing agent such as potassium permanganate or iodine, and the amount of this oxidizing agent which reacts with the reducing agent in the crystals is determined by back titration. Clearly this method will detect almost any reducing agent including interstitial zinc, oxygen vacancies, or impurities such as interstitial lithium or substitutional aluminum. Thus these experiments do not prove the existence of interstitial zinc.

Interstitial zinc has also been invoked to account for the oxidation of metallic zinc, and the exchange of radioactive zinc with lattice zinc ions in zinc oxide.

The oxidation of zinc has been observed over a wide temperature range both above and below the melting point at 419°C. The oxide has a higher molecular volume than that of the metal and so forms a protective skin. Below 370° the kinetics of oxidation are not simple and may be controlled by rate processes at the oxide-gas interface. Also when the film is very thin complications arise but this is expected. But above 370°C it is generally agreed that the oxidation follows a parabolic time law and is independent of oxygen pressure at high enough pressures. At 400°C MOORE and LEE[1] give the parabolic rate constant as $1{\cdot}8 \times 10^{-16}$ cm² sec^{-1}, whilst GRUNEWALD and WAGNER[2] give $0{\cdot}8 \times 10^{-14}$ cm² sec^{-1}. The rate of oxidation varies exponentially with temperature and MOORE and LEE give as the energy of activation 28·5 kcal/g = 1·24 eV. Other values in the literature[3] for liquid zinc vary from 1·0 to 1·5 eV over a temperature range 430–1000°C. The parabolic behavior is of course readily explained by WAGNER's theory in which either interstitial zinc atoms or oxygen vacancies diffuse across the oxide layer, and their concentration is kept at a constant value at the zinc interface and at a very low value at the oxygen interface.

Using radioactive zinc and following the diffusion onto lattice sites, LINDNER[4] found over the temperature range 700–1350°C.

$$D = 3{\cdot}5 \exp(-3{\cdot}22e/kT) \text{ cm}^2 \text{ sec}^{-1}.$$

These experiments were done with sintered samples in air which had a radioactive layer of zinc oxide on the surface.

MOORE and SECCO[5] worked with radioactive crystals which exchanged with an inactive zinc atmosphere. In the range 900–1025°C and in one atmosphere of zinc vapor they found:

$$D = 4{\cdot}8 \exp(-3{\cdot}17e/kT) \text{ cm}^2 \text{ sec}^{-1}$$

At 1000°C this gives a value of D of $1{\cdot}58\times10^{-12}$ cm^2 sec^{-1}. Variation of zinc pressure from 0·2–2·9 atmospheres indicated that D varied as $P_{Zn}^{0{\cdot}65}$. They concluded from this that the diffusing species was the singly dissociated interstitial zinc ion, Zn_i^+. The close agreement between the results of LINDNER, and of MOORE and SECCO[5] is curious if the diffusion of interstitial zinc is the rate determining step, since the concentration of interstitial zinc should be very different when the zinc oxide is in zinc or air atmospheres. Indeed MOORE and SECCO[5] stated that there was rough agreement between the diffusion results whether done in zinc or in air. MOORE and SECCO[5] also used a chemical method to determine the excess zinc in the crystals, and these data, in conjunction with the diffusion data, enable a calculation to be made of the rate of oxidation of metallic zinc. The rate so calculated was far removed from the observed value; no satisfactory explanation was offered to account for this.

MUNNICH[6] studied the exchange between radioactive zinc vapor and zinc oxide crystals. His results did not fit a simple diffusion equation, and at 1000°C he quotes values of D from 4×10^{-11} to 2×10^{-10}, the value being larger the lower the concentration of radio zinc in the crystal. These values are considerably larger than those reported by MOORE and SECCO.[5]

Some of the difficulties in the results just summarized might be resolved if the properties of interstitial zinc in zinc oxide were known, and it is the object of the present paper to describe these properties. The electrical conductivity of crystals of zinc oxide has been the chief method used to follow the interstitial zinc.

EXPERIMENTAL

Crystals. Needle-like crystals of zinc oxide were grown by the SCHAROWSKY[7] method in all alumina furnaces. Most of the crystals used had diameters of 0·005–0·010 in. Some of the batches from the furnace consisted of quite pure crystals with room temperature conductivities of 0·05 $(\Omega \text{ cm})^{-1}$ or less, and the conductivities fell as the temperature rose. Such crystals were selected and used in these experiments.

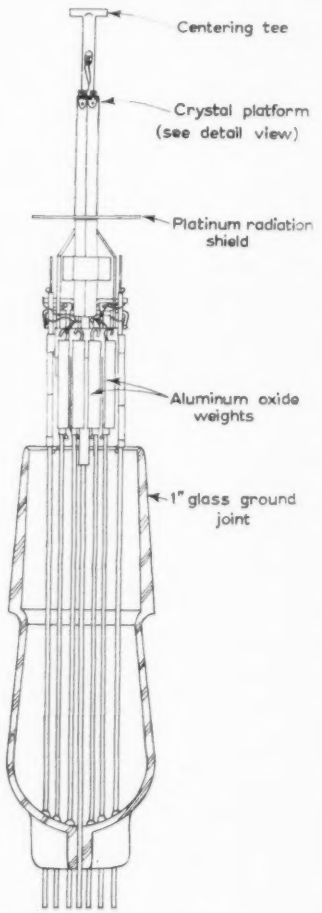

FIG. 1. Crystal holder, general view.

Measurement of crystal conductivity. In air the conductivity of the crystals was measured from room temperature up to 700°C in the apparatus shown in Fig. 1. Fig. 2 shows the detail where the

crystal is held. In effect four platinum wires loop over the crystals and these four loops are held tight by weights in the cold part of the holder. The loops act as current and probe contacts so avoiding

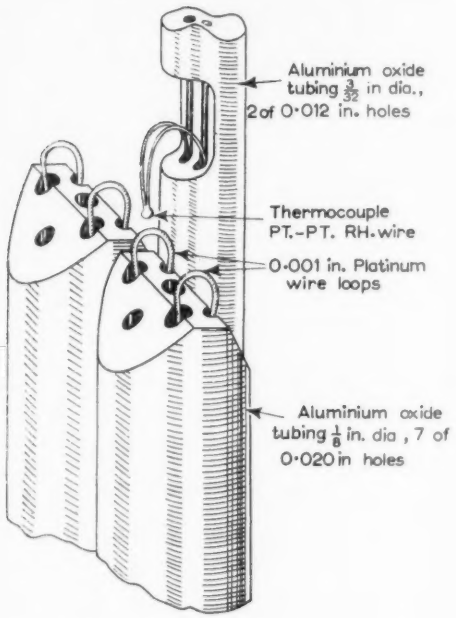
Aluminium oxide tubing 3/32 in dia., 2 of 0·012 in. holes
Thermocouple PT.-PT. RH. wire
0·001 in. Platinum wire loops
Aluminium oxide tubing 1/8 in. dia, 7 of 0·020 in holes

FIG. 2. Crystal holder, detail of crystal platform.

trouble from rectification. Usually it was necessary to discharge a condenser at about 300 V through the contacts in order to obtain noise free readings. A platinum wound ceramic oven surrounds the crystal area and is held inside a glass tube which slides onto the ground joint. A bare thermocouple near the crystal measured the temperature. This holder* was very convenient for making measurements in oxygen or nitrogen, and all diffusion work was done in it by bringing the temperature rapidly to the desired value and holding it there and then observing the conductivity change as a function of time.

Measurements in zinc vapor were made by holding the crystal in four small 0·005 in. tungsten wire loops by friction. The wires were led out through a ceramic tube and the whole assembly together with a thermocouple encased in thin quartz tubing was put into a vertical quartz tube. This tube contained some metallic zinc, was filled with helium at one atmosphere and was surrounded by an external oven. In this way the crystal could be measured in saturated zinc vapor over a range of temperatures limited by the temperatures at which the vapor pressure of zinc was less than about 1 mm, or greater than about 1/2 atmosphere. The helium served to prevent excessive distillation of the zinc onto cold parts of the apparatus and also obviated the need of a vacuum system.

When a crystal was dipped in liquid zinc in order to introduce interstitial zinc it was held at one end in a small ceramic clamp with tungsten wires serving as a spring. The ceramic clamp slid in a cork inside a quartz tube which held the molten metal. The surface film on the metal was usually removed by dipping a quartz rod in and out of the melt before the crystal was dipped. Again helium served as an inert atmosphere. The crystals could be quenched by pulling rapidly from the melt, however the heat capacity of the holder prevented rapid cooling of the whole crystal.

A simpler way to dope crystals with zinc was found to be by dipping them into zinc vapor rather than liquid zinc. The crystals were held in a fine upturned quartz capillary which had a very low heat capacity. The capillary was attached to a rod which slid in a cork. Some zinc in a quartz tube was heated, again in one atmosphere of helium, and the crystal dipped in and out of this vapor, thus allowing very rapid quenching.

The results described below were the same whether the crystals had been doped in zinc vapor or in liquid zinc, and it was likewise immaterial whether the liquid zinc was especially pure or whether it contained 1 per cent gallium as an impurity. These results show quite clearly that the effects produced are to be ascribed to zinc and not to some impurity in the zinc.

RESULTS

Solubility of interstitial zinc. If crystals were dipped in liquid zinc or zinc vapor at 450°C the room temperature conductivity rose to about 0·2 $(\Omega\ \mathrm{cm})^{-1}$. Higher doping temperatures resulted in

* The holder was developed in conjunction with J. J. LANDER.

higher conductivities provided the crystals were rapidly quenched. Fig. 3 shows the logarithm of the conductivity in air as a function of $1/T$ for a crystal before and after doping in zinc vapor at 650°C for 30 sec. Also shown is a curve obeying the relation

$$\sigma \propto T^{-3/2}. \qquad (1)$$

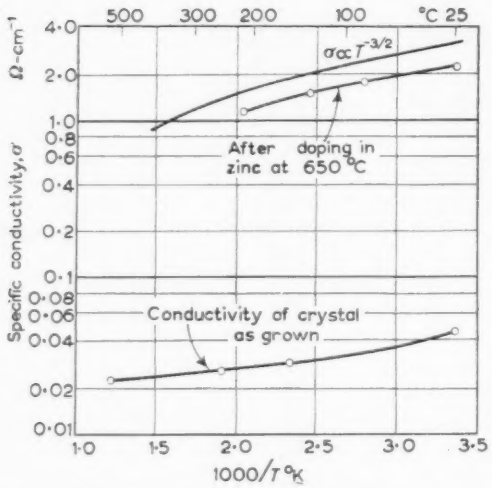

FIG. 3. Conductivity of ZnO crystal before and after doping.

The conductivity of the doped crystal is seen to follow this curve quite closely up to about 200°C. At this point the donor atoms start to diffuse out and ultimately the base conductivity of the crystal can be regained. By quenching from a series of different temperatures after allowing sufficient time for equilibrium to be attained and then measuring the conductivity at room temperature, the solubility of interstitial zinc at the high temperatures may be calculated if the quenching process is efficient. A small correction is made for the base conductivity of the crystal, and a value of 180 cm²/V sec for the room temperature mobility, supplied by A. R. HUTSON of these laboratories, is used to obtain the solubility in atoms/cm³ from the saturated zinc vapor. These values are the crosses in Fig. 4. It has been assumed that each interstitial atom ionizes once:

$$Zn_i \leftrightharpoons Zn_i^+ + \epsilon. \qquad (2)$$

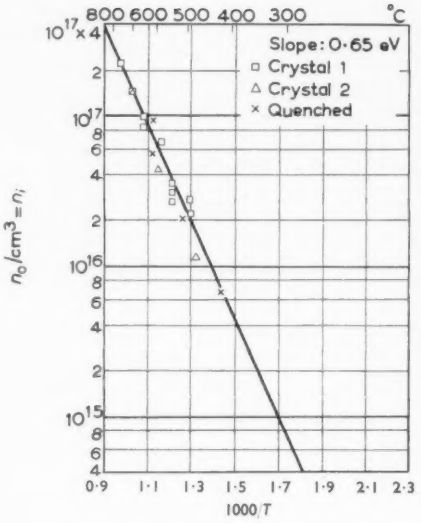

FIG. 4. Solubility of Zn_i in ZnO from saturated vapor.

Slope: 0·65 eV
□ crystal 1
△ crystal 2
X quenched

A second method gave the squares and triangles in Fig. 4. This involved the direct measurement of the conductivity in saturated zinc vapor. A correction was made for the base conductivity and also for the contribution made to the conductivity by the adsorption of zinc, this being determined by measuring the conductivity in zinc vapor but at a temperature low enough that the contribution from interstitial zinc was negligible. This correction was always less than 10 per cent of the conductivity increase. The interstitial zinc conductivity was then corrected to room temperature assuming the $T^{-3/2}$ relation, and the same mobility figure was used.

The good agreement between the two methods is unlikely to result from a cancellation of errors. Consequently we may assume that the quenching is efficient, that there is no further ionization of the donors above room temperature and that the $T^{-3/2}$ relation is a useful one even to quite high temperatures. Since, from low temperature measurements A. R. HUTSON has shown that the first ionization of Zn_i is complete below room temperature (the

donor ionization energy is about 0·05 eV) we conclude that up to 750°C at least, second ionization is not appreciable. This is not surprising if after the first ionization the outer electron orbit contracts so that the electron is now in a dielectric medium of one, rather than that of the crystal.

The solubility may be expressed:

$$n_i = 3{\cdot}4 \times 10^{20} \exp(-0{\cdot}65e/kT) \qquad (3)$$

where n_i is in atoms/cm³, and the system is in equilibrium with condensed zinc. Using equation (2), the heat of solution of one atom of liquid zinc in zinc oxide is $2 \times 0{\cdot}65 = 1{\cdot}3$ eV (heat being absorbed). Since the heat of vaporization of liquid zinc is 1·23 eV[8] the heat of solution of a gaseous zinc atom in ZnO is approximately zero.

In these experiments in which doping temperatures up to 750°C were used, the crystals never became colored.

Diffusion of interstitial zinc. It was found that at temperatures at which interstitial zinc had an appreciable solubility the diffusion was too rapid to follow. Consequently crystals were doped by quenching, and then they were rapidly heated to the desired temperature in air in the apparatus illustrated in Fig. 1. The slightly uneven distribution of donors in the crystal resulting from imperfect quenching, and the uncertainty in the zero of time for a diffusion run resulting from the finite time required to heat the crystals, introduced an error of perhaps 10 per cent in the diffusion coefficients. The crystals were usually doped in zinc vapor at 650°C giving a room temperature conductivity near 2 $(\Omega\ \text{cm})^{-1}$. After a diffusion run the crystals were heated to about 550°C for a few minutes in air, thus removing practically all the interstitial zinc and re-establishing the base conductivity.

The diffusion coefficient, D' was obtained by observing the conductivity as a function of time. The fraction of the total diffused could then be calculated at any instant, and using the standard equations for diffusion into an infinite cylinder, D' could be calculated. The radius used in these calculations was 90 per cent of the greatest radius of

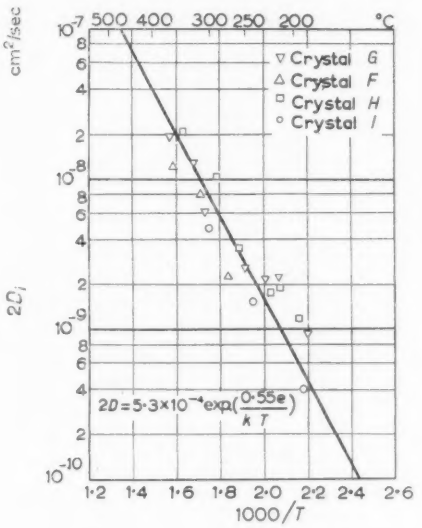

FIG. 5. Diffusion of Zn_i in ZnO.
▽ crystal *G*
△ crystal *F*
□ crystal *H*
○ crystal *I*

Table 1. *Diffusion of interstitial Zn at* 240°C 0·0047 in. *diameter crystal*

t(sec)	σ	% diffused	Dt/r^2(calc.)	D (cm²/sec)
0	(0·52)	0		
170	0·42	20	0·0085	$1{\cdot}39 \times 10^{-9}$
510	0·34	35	0·028	$1{\cdot}55 \times 10^{-9}$
1080	0·26	50	0·064	$1{\cdot}68 \times 10^{-9}$
1910	0·20	62	0·107	$1{\cdot}59 \times 10^{-9}$
∞	0·002	100		
			Mean	$1{\cdot}5 \times 10^{-9}$

the crystal, as the crystals were hexagonal in cross section rather than circular. Some typical figures are shown in Table 1. The observed value of D' is twice that of D_i, the diffusion coefficient of the interstitial ions, since ionization is complete, and the crystals remain extrinsic.[9]

Log $2D_i$ is plotted against $1/T$ in Fig. 5, for a number of crystals. The straight line may be represented by:

$$2D_i = 5{\cdot}3 \times 10^{-4} \exp(-0{\cdot}55e/kT) \ldots . \quad (4)$$

There is some scatter of the points about this line, sometimes even between runs on the same crystal. The reason for this is not known, although it may be connected with some sort of crystal imperfection. It is to be noticed that for these crystals of about 0·007 in. diameter diffusion could be conveniently observed (periods of a few minutes to a few hours being involved), in the surprisingly low temperature range of 180–350°C.

DISCUSSION

1. *Oxidation of metallic zinc.* On the basis of WAGNER's theory for the growth of a thick oxide film it may be shown that the parabolic rate constant k' is given by:

$$k' = 2D_i f_i \text{ cm}^2 \text{ sec}^{-1} \ldots \quad (5)$$

where f_i is the mole fraction of defects at the metal-oxide interface* and it is assumed that the mole fraction at the oxide-gas interface is negligible.[10] D_i is the defect diffusion coefficient. We have measured values of 2 D_i and f_i and found them to vary exponentially with temperature. We may therefore calculate values of k' and obtain its exponential temperature coefficient by adding the coefficients of f_i and D_i. k' has been calculated from extrapolated values of 2 D_i and f_i at 400°C, and in Table 2 it is compared with the observed values quoted in the introduction. There is fair agreement with the value of GRUNEWALD and WAGNER[2] and fair agreement with the high oxygen pressure value of MOORE and LEE.[1] The latter's value for the temperature coefficient is however in good agreement with ours. It seems clear that the oxidation of zinc and the phenomena described in this work may both be attributed to the same defect. The lack of more precise agreement may arise from experimental errors. But it must be remembered that our measurements of diffusion have been made in one crystal direction (normal to the C axis), whereas oxidation may involve diffusion down the C axis as well.

2. *Entropy of interstitial zinc.* It has been mentioned above that the heat of solution of a gaseous zinc atom in zinc oxide is approximately zero,

* The growth law is: $dx/dt = k'/x$ where x is in cm and t in seconds.

Table 2. Oxidation of zinc

$$k' = 2D_i f_i$$

At 400°C: $2D_i = 4 \times 10^{-8}$, $f_i = \dfrac{n_i}{4{\cdot}1 \times 10^{22}} = 1{\cdot}2 \times 10^{-7}$

therefore $k' = 4{\cdot}7 \times 10^{-15}$ cm^2 sec^{-1}.

At 400°C: k' observed $\begin{cases} 0{\cdot}8 \times 10^{-14} \text{ cm}^2 \text{ sec}^{-1} \text{ (1938)} \\ 1{\cdot}8 \times 10^{-16} \text{ cm}^2 \text{ sec}^{-1} \text{ (1951)} \end{cases}$

E for $D_i = 0{\cdot}55$ eV

E for $f_i = 0{\cdot}65$ eV

Therefore E for $k' = 1{\cdot}20$ eV

E_{obs} for $k' = 1{\cdot}24$ eV (1951).

showing that the attractive Van der Waals and polarization forces, just balance the repulsive forces. This is perhaps not surprising if the donor is an interstitial atom since it is being forced into a small space. It means however that it is the entropy increase which is responsible for the solubility of the excess zinc. We may see if the entropy contribution is a reasonable one as follows.

At 800°K = 527°C the solubility of interstitial zinc in zinc oxide in equilibrium with liquid zinc is 3×10^{16} atoms/cm^3. It is assumed that the reaction is

$$Zn_l \leftrightharpoons Zn_i^+ + \epsilon.$$

The entropy of one mole of liquid zinc at 800°K may be obtained from BARROW *et al.* (*loc. cit.*) and is $S_{Zn_l} = 19{\cdot}0$ cal/g atom deg, where the third law of thermodynamics has been used.

The partial molar entropy of the electron gas which is non degenerate, at the temperature and concentration under consideration, is obtained from the Sackur-Tetrode equation allowing for the spin of the electron:

$$\overline{S_\epsilon} = R\left\{\ln\left[\left(\frac{2\pi m^* kT}{h^2}\right)^{3/2}\frac{V}{N}\right]+5/2+\ln 2\right\}$$

V/N is the volume occupied per electron and m^* is the effective electron mass, for which a value of 0·54 m has been taken (private communication from A. R. HUTSON). $\overline{S_\epsilon}$ is thus found to be 19·5 cal/g atom deg.

The heat of the reaction is 1·30 eV = 29·9 kcal/mole. The entropy change is therefore $\Delta S = 29900/800 = +37{\cdot}4$ cal/mole deg. Hence the partial molar entropy of the interstitial zinc is:

$$\overline{S_{Zn_i^+}} = \Delta S - \overline{S_\epsilon} + S_{Zn_l} = 37{\cdot}4 - 19{\cdot}5 + 19{\cdot}0$$

$$= 36{\cdot}9 \text{ cal/g atom deg.}$$

Some of this entropy is the entropy of mixing: $-kn\ln(n/N)$ where n atoms are distributed among the N sites.

This contribution is 28·2 cal/g atom deg. This leaves $36{\cdot}9-28{\cdot}2 = 8{\cdot}7$ units which must be ascribed to the vibrational modes of the interstitial zinc. Now for the Einstein model of a solid the vibrational entropy is given by:

$$S_{vib} = -3R\frac{\partial}{\partial T}\left[T\ln(1-e^{-h\nu/kT})\right]$$

$$= -3R\left[\ln(1-e^{-u})-u\left(\frac{e^{-u}}{1-e^{-u}}\right)\right]$$

where $u = h_\nu/kT$.

It has been assumed that the atoms have three degrees of freedom.

S_{vib} has been calculated for different values of ν at 800°K with the following results:

ν	10^{12}	10^{13}	10^{14}
S_{vib}	22·7	9·1	0·1

Interpolation shows that if $S_{vib} = 8{\cdot}7$, $\nu = 1{\cdot}1\times10^{13}$. Estimates made from optical absorption give for the lattice vibrational frequencies $1{\cdot}65\times10^{13}$ and $9{\cdot}4\times10^{12}$, along and perpendicular to the C axis respectively.[11] We conclude therefore that the interstitial atoms vibrate in phase with the lattice atoms, which is not surprising as the repulsive forces must exert a powerful effect.

3. *Nature of donor center.* We have been referring to the donor described in this work as interstitial zinc. It is also possible that a zinc atmosphere could produce oxygen vacancies which might also act as donors. However we believe this not to be the case for the following reasons.

(a) We have seen that the diffusion coefficient obeys:

$$2D_i = 5{\cdot}3\times10^{-4}\exp(-0{\cdot}55e/kT).$$

FULLER and SEVERIENS[12] have observed the diffusion of interstitial lithium in germanium and silicon and find:

$$D = 25\times10^{-4}\exp(-0{\cdot}51e/kT) \text{ for Ge}$$

and

$$D = 23\times10^{-4}\exp(-0{\cdot}66e/kT) \text{ for Si.}$$

Germanium, silicon and zinc oxide all have tetrahedral co-ordination of the lattice atoms and interatomic distances that are not very different.

The similarity between the three expressions strongly suggests that they refer to similar processes and so we conclude that in zinc oxide we have interstitial zinc.

The reason for the rather small D_0 values, which

are normally near unity, is not known. It may be characteristic of interstitial diffusion in these lattice types since the entropy requirements for this diffusion may be more severe than for normal lattice site diffusion. It is considered unlikely that in the very small zinc oxide crystals grain boundaries or dislocation lines play an important part.

(b) It is most unlikely that an oxygen vacancy could move with an energy of activation as low as 0·55 eV, since for it to do so an oxygen atom has to move, and this involves the rupture of several chemical bonds in the crystal, a process which would require a large energy of activation.

(c) Lithium has been observed as a donor in zinc oxide[13] and its diffusional properties are essentially the same as those described here. Now if the lithium were substituted for zinc it would be an acceptor since it has only one valence electron whereas zinc has two, and the introduction of lithium does in fact introduce a small fraction of acceptors. But as a donor, lithium must be interstitial and so we conclude that we are dealing with interstitial zinc also.

4. *Nature of defects in "ordinary" zinc oxide.* Although it has often been suggested that the conductivity of zinc oxide crystals as grown, and of sintered zinc oxide, is due to interstitial zinc, this work shows that unless the oxide has been treated in a special way, viz. rapid quenching from an atmosphere of nearly saturated zinc vapor, it will contain very little interstitial zinc. Furthermore any such interstitial zinc will largely disappear on heating in air at 500°C or above for a short time. Such conditions are seldom fulfilled so that interstitial zinc is certainly not the usual donor in zinc oxide.

There remain oxygen vacancies or some more complicated donor, or chemical impurities. At present we think that chemical impurities acting as both donors and acceptors are most likely to explain the rather complicated behavior usually encountered.

In the light of these remarks some results of SCHAROWSKY[14] may be mentioned. He treated crystals in zinc vapor from 920–1220° and obtained a yellow color and an increase of conductivity. He connected the two, but had he heated the crystals to about 550°C in air we believe that some of the extra conductivity would have gone, but not the color. The color bleaches at higher temperatures. The scatter he obtained in the increase of conductivity probably arose from ill-defined quenching. The "Meyer's Rule" which he quotes and which states that the ionization energy of the donor appears to increase as the donor concentration decreases is clearly wrong as A. R. HUTSON has found. It may arise from the incorrect supposition that the donors in an as grown crystal are the same as those produced by zinc treatment. In fact it often happens that the former are not completely ionized at room temperature, whereas interstitial zinc always is. This situation could give results in accordance with "Meyer's Rule".

5. *The diffusion of radioactive zinc in zinc oxide* remains to be discussed. Suppose that the exchange probability between lattice and interstitial zinc atoms is large enough not to influence the overall rate of the process. REDINGTON[15] has shown that this probability need be only 10^{-10} per jump. Suppose also that the process is governed by the diffusion rate of interstitial zinc. The observed diffusion coefficient D for diffusion onto lattice sites is then[16]

$$D = 2D_i f_i \text{ cm}^2/\text{sec}.$$

At 1000°C the extrapolated value of $2D_i$ is $1{\cdot}8\times10^{-6}$. Similarly the value of f_i for saturated zinc at 1000°C is $2{\cdot}7\times10^{-5}$. At 1000°C zinc has a vapor pressure of 5·8 atm. If f_i varies as $\sqrt{P_{Zn}}$ as is to be expected for single ionization and for the interstitial zinc being present in excess of other defects, then in one atmosphere of zinc at 1000°C,

$$f_i = 2{\cdot}7\times10^{-5}\times\sqrt{(1/5{\cdot}8)} = 1{\cdot}1\times10^{-5}.$$

Thus D is calculated to be 2×10^{-11}. If the zinc pressure is maintained constant f_i should be nearly independent of temperature, and so D should vary with an exponential coefficient of 0·55 eV. Now we have seen that MOORE and LEE[1] found $D = 4{\cdot}8\exp(-3{\cdot}2e/kT)$, which gives a value of D at 1000°C of $1{\cdot}6\times10^{-12}$ cm^2 sec^{-1}. It happens that this value of D is not far off the calculated value, but the exponential factor is very far removed from the calculated value. If now the diffusion is studied in air instead of in one atmosphere of zinc we may calculate f_i as follows. Zinc oxide dissociates:*

$$\text{ZnO} \leftrightharpoons \text{Zn}+\tfrac{1}{2}\text{O}_2.$$

* These data are taken from Bulletin of Bureau of Mines, No. 542, 1954.

At 1000°C. $K = P_{Zn}P_{O_2}^{1/2} = 2{\cdot}6\times10^{-9}(\text{atm})^{3/2}$.

If $P_{O_2} = 1/5$ atm, then

$$P_{Zn} = \frac{2{\cdot}6\times10^{-9}}{(0{\cdot}2)^{1/2}} = 5{\cdot}8\times10^{-8}\text{ atm.}$$

Thus assuming the square root pressure dependence again,

$$f_i = 1{\cdot}1\times10^{-5}\times(5{\cdot}8\times10^{-8})^{1/2} = 2{\cdot}7\times10^{-9}.$$

(Actually the concentration of interstitial zinc will fall below the concentration of electrons present in the crystal from other sources, whereupon f_i will vary directly with zinc pressure so that f_i will be even smaller than the value indicated.) We now have for D at 1000°C, $1{\cdot}8\times10^{-6}\times2{\cdot}7\times10^{-9} = 4{\cdot}9\times10^{-15}$. This maximum value is 2–3 orders of magnitude less than the figures given for the rather approximate measurements made of the diffusion into zinc oxide in air. In a constant oxygen pressure, the zinc pressure over zinc oxide varies with an exponential coefficient of 4·8 eV. Hence the Zn_i^+ concentration would have a coefficient of $4{\cdot}8/2 = 2{\cdot}4$ eV, and adding the coefficient for D_i we get for the exponential coefficient of D, about 3 eV. This may be compared with the observed value of 3·2 eV given by LINDNER.

The position is thus not clear. In zinc at 1000°C the predicted value is slightly larger than the observed value, but the predicted temperature coefficient is quite wrong. In air the predicted value is considerably smaller than the observed value although for the temperature coefficient there is approximate agreement.

It may be that other donors in the crystal at high temperature suppress the interstitial zinc concentration below the calculated values so that the calculated diffusion coefficient could be below the observed value even for experiments done in zinc vapor. If this were so interstitial zinc might be expected to play an unimportant part in the radioactive diffusion. It would then seem likely that a simple place exchange or ring mechanism accounts for the diffusion, and this would explain the tentative observation that diffusion is independent of the atmosphere at least in the regions so far examined. However, definite conclusions must await further experiments.

Acknowledgement—Thanks are due to Mr. E. A. SADOWSKI for his competent assistance in this work.

VOL. 3 1957

REFERENCES

1. MOORE W. J. and LEE J. K. *Trans. Faraday Soc.* **47,** 501 (1951).
2. WAGNER C. and GRUNEWALD K. *Z. Phys. Chem.* B**40,** 455 (1938).
3. KRUPKOWSKI A. and BALICKI S. *Metaux et Corros.* **12,** 89 (1937); TEREM H. N. *Rev. Fac. Sci. Univ. Istanbul* **16A**, 226 (1951); GEBHARDT E. *Z. Metallk.* **37,** 87 (1946).
4. LINDNER R. *Acta. Chem. Scand.* **6,** 457 (1952).
5. MOORE W. J. and SECCO E. A. *Diffusion and Exchange of Zinc in Crystalline Zinc Oxide* August 1955. Report on AEC Contract No. AT(11–1)–250 Bloomington, Indiana.
   MOORE, W. J. *J. Chem. Phys.* **53,** 845 (1956).
6. MUNNICH F. *Naturwissenschaften* **42,** 340 (1955).
7. SCHAROWSKY E. *Z. Phys.* **135,** 318 (1953).
8. BARROW R. F. *et al. Trans Faraday Soc.* **51,** 1354, (1955).
9. BARDEEN J., BRATTAIN W. H. and SHOCKLEY W. *J. Chem. Phys.* **14,** 714 (1946).
10. MOTT N. F. and GURNEY R. W. *Electronic Process in Ionic Crystals* O.U.P. Chap. VIII (1950).
11. KRÖGER F. A. and MEYER H. J. G. *Physica* **20,** 1149 (1954).
12. FULLER C. S. and SEVERIENS J. C. *Phys. Rev.* **96,** 21 (1954).
13. LANDER J. J. Private communication.
14. SCHAROWSKY E. *Z. Phys.* **135,** 318 (1953).
15. REDINGTON R. W. *Phys. Rev.* **87,** 1066 (1952).
16. MOTT N. F. and GURNEY R. W. *Op. Cit.* p. 34.

J. Phys. Chem. Solids Pergamon Press 1957. Vol. 3. pp. 238–249.

SOLID SOLUTIONS BETWEEN FERROMAGNETIC AND ANTIFERROMAGNETIC COMPOUNDS WITH NiAs STRUCTURE

F. K. LOTGERING and E. W. GORTER

Philips Research Laboratories, N. V. Philips' Gloeilampenfabrieken, Eindhoven-Netherlands

(*Received* 22 *February* 1957)

Abstract—Several solid solution series with NiAs structure (Fig. 1) have been prepared between a ferromagnetic ($x = 0$) and an antiferromagnetic ($x = 1$), viz. (a) $CrTe_{1-x}Se_x$, (b) $Mn_{1-x}Cr_xSb$ and (c) $CrTe_{1-x}Sb_x$. The system $Cr_{1-x}Mn_xTe$ shows a miscibility gap.

Saturation magnetizations have been measured between 20°K and the Curie temperatures, and susceptibilities between the Curie temperatures and 850–1100°K. In (b) and (c) the Curie and Néel temperatures decrease on addition of the other component, but do not simultaneously drop to zero. Notably in (b) compositions occur for which a Néel temperature is present above a Curie temperature. The saturation magnetization decreases with x in both systems, but in a different way. The magnetic properties found can be accounted for by assuming that the dominant exchange interaction is not a direct M–M interaction, but a superexchange interaction via the metalloid atom, via the largest of the three angles M–X–M that occur for nearest neighbours M–X. These interactions are supposed to be strong and positive for Mn–Sb–Mn and Cr–Te–Cr configurations, strong and negative for Cr–Sb–Cr and weak for Mn–Sb–Cr configurations.

INTRODUCTION

MANY binary compounds of the transition metals have the crystal structure of nickel arsenide (Fig. 1) or a closely related one. This is for example the case for the compounds MX with M = Cr, Mn, Fe, Co and Ni and X = S, Se, Te, As and Sb, with a few exceptions, like MnS, MnSe and FeAs. Depending on the position in the periodic table of the metalloid a great variety in the chemical bond character of these compounds is expected. Because sulphur is chemically closely related to oxygen, it may be expected that sulphides (especially CrS and FeS[1]), like oxides, have a more or less ionic structure. The occurrence of an electrostatic bond in arsenides and antimonides (e.g. MnAs and CrSb) is, however, not probable.

Some of these compounds are antiferromagnetic (e.g. CrS, FeS, MnTe and CrSb), others are ferromagnetic (e.g. CrTe, MnAs and MnSb). From this fact it appears that the metal atoms possess a magnetic moment, that strong interactions between these magnetic dipoles exist and that positive as well as negative interactions may occur.

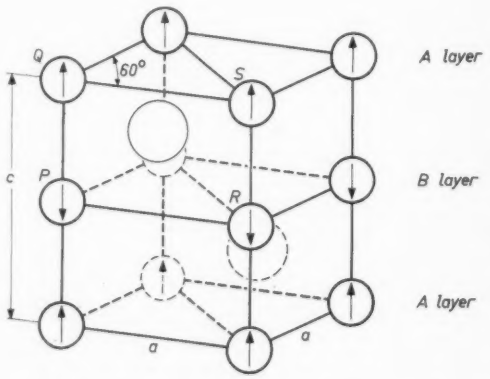

FIG. 1. The NiAs structure. Small circles: metal, e.g. Ni, large circles: metalloid, e.g. As.

The arrows symbolize the antiferromagnetic order of the Cr spins in CrSb found by SNOW. The spins are ordered according to two equivalent sublattices A and B. Each sublattice, in which the spins are aligned parallel, consist of a series of layers perpendicular to the c-axis, arranged in such a way that the A and B layers alternate in the c direction.

VOL. 3 1957

The above-mentioned differences in bond character reveal themselves in certain magnetic properties. As an example the paramagnetic behaviour of FeS and MnSb may be compared. For both substances at sufficiently high temperatures the susceptibility obeys a Curie-Weiss law from which the magnetic moments per metal atom can be calculated. For FeS[1] the moment found ($5{\cdot}2\mu_B$) is slightly larger than the theoretical moment for the ferrous ion ($4{\cdot}9\mu_B$), whereas for MnSb[2] the experimental value ($4{\cdot}1\mu_B$) is considerably lower than the spin-only values of manganous ($5{\cdot}92\mu_B$) and manganic $4{\cdot}90\mu_B$) ions.

The interaction mechanism in the compounds with NiAs structure have not so far been discussed except for FeS. According to current ideas two types of interactions may exist, both of which may be either positive or negative.

(a) A "direct" exchange interaction[3] between the 3*d* electrons of two neighbouring magnetic atoms. This type of interaction is assumed to exist in metals and alloys.

(b) An "indirect" exchange interaction, e.g. the superexchange interaction according to KRAMERS-ANDERSON,[4] between two magnetic cations via an intermediate anion. This mechanism has been proposed for substances with essentially ionic structures, like e.g. oxides.

Since in the compounds with NiAs structure the bond character is neither clearly metallic, as in (a), nor clearly ionic, as in (b) either type of interaction, or both, may be present.

The purpose of the present investigation was to see whether continuous series of mixed crystals between a ferromagnetic and an antiferromagnetic binary compound with NiAs structure exist and, if so, to study the magnetic properties.

PREPARATION, IDENTIFICATION AND MEASURING TECHNIQUE

Preparation of solid solutions between ferromagnetic CrTe and antiferromagnetic CrSe, CrSb or MnTe, and between ferromagnetic MnSb and antiferromagnetic CrSb was attempted.

The elements were finely ground in an agate mortar, weighed and mixed. The following procedure was then used: the mixture of the elements was pressed to a pellet, which was sealed into an evacuated silica tube. This was heated for 24 hr at a constant temperature and cooled slowly. The highest sintering temperature used was 1000°C. When melting occurred at a lower temperature, the sintering temperature was chosen below that temperature. Melting occurred at the lowest temperatures for some antimony-rich mixtures, in which cases the samples were fired at 700°C. The reaction product was again ground in a mortar and the procedure repeated once or, in most cases, twice. A part of the slowly cooled material was then sealed into a thin-walled silica tube, heated for 2 hr at the temperature at which it was prepared, and quenched by plunging the tube in ice water.

An X-ray investigation was carried out with the aid of a Norelco 90° Diffractometer on both slowly cooled and quenched samples in order to identify the phases obtained and to determine the unit cell dimensions *a* and *c* of the NiAs structure. The errors in *a* and *c* are of the order of a few hundredths of an Ångstrom.

The results are given in Table 1, from which it is seen that in the system

$$CrTe_{1-x}Se_x,\ CrTe_{1-x}Sb_x \text{ and } Mn_{1-x}Cr_xSb$$

the X-ray diagrams are consistent with the formation of a continuous series of mixed crystals with the NiAs structure. In the slowly cooled samples the NiAs phase was often contaminated by small amounts of one of the elements. For the materials $CrTe_{1-x}Se_x$ and $CrTe_{1-x}Sb_x$ this contamination could not be observed any more after quenching the samples; for the $Mn_{1-x}Cr_xSb$ samples the NiAs phase could not be obtained free from small amounts of free antimony. The X-ray diagrams of the slowly cooled $Cr_{1-x}Mn_xTe$ preparations were not consistent with the presence of a single NiAs phase; the quenched samples contained one NiAs phase only for $x \leqslant 0{\cdot}35$.

The magnetic measurements were performed on the samples indicated by an asterisk in Table 1.

The paramagnetic susceptibilities χ per gram (units cm^3g^1) were measured with the aid of a magnetic balance constructed by Dr. VOLGER (see [5]). The field was of the order of 1500 oersteds. The samples were enclosed in evacuated silica tubes. The ferromagnetic magnetization σ per gram (units gauss cm^3g^{-1}) was measured at temperatures down to −180°C using a method described by RATHENAU and SNOEK.[6] Measurements of σ for increasing fields up to 28000 oersted were carried out by Ir. P. JONGENBURGER with the aid of an apparatus based on a method described by DOMENICALI.[7]

LITERATURE DATA ON THE MAGNETIC PROPERTIES OF CrTe, MnSb, CrSb, CrSe AND MnTe AND A COMPARISON WITH OWN MEASUREMENTS

Table 2 gives data obtained from literature and from our own measurements on the pure compounds that form the limiting compositions of the series of solid solutions investigated. The tabulated quantities T_a, T_C, T_N, μ_p and μ_f are defined and determined as follows.

For each of the substances the paramagnetic behaviour at sufficiently high temperatures can be described by a Curie-Weiss law $\chi^{-1} = C^{-1}(T - T_a)$. From the straight χ^{-1}–T lines found experimentally the asymptotic Curie temperature

Table 1. *Lattice constants a and c of the* NiAs *phase and impurities found in the slowly cooled and quenched samples (samples indicated by an asterisk were used for the magnetic measurements)*

Composition	x	Cooled slowly			Quenched		
		a (Ångstrom)	c (Ångstrom)	Impurity	a (Ångstrom)	c (Ångstrom)	Impurity
CrSe	—	3·71	6·03*	not obs.			
CrTe	—	4·01	6·29	trace Cr	4·01	6·25*	not obs.
CrSb	—	4·13	5·51*	not obs.			
MnSb	—	4·15	5·78	not obs.			
$CrTe_{1-x}Se_x$	0·1	3·98	6·22	small amount Cr	3·99	6·25*	not obs.
	0·25	3·91	6·18	trace Cr	3·92	6·22*	not obs.
	0·5	3·87	6·15	trace Cr	3·86	6·19*	lines unsharp
	0·75	3·78	6·11	trace Cr	3·78	6·13*	not obs.
	0·9				3·74	6·11*	not obs.
$CrTe_{1-x}Sb_x$	0·1	4·01	6·21	trace unident.	4·02	6·25*	trace unident.
	0·25	4·01	6·10	trace Cr	4·02	6·10*	not obs.
	0·5	4·05	5·94	not obs.	4·05	5·94*	not obs.
	0·6				4·07	5·72*	not obs.
	0·75	4·10	5·68	not obs.	4·09	5·67*	not obs.
	0·9	4·13	5·53	not obs.	4·13	5·54*	not obs.
$Mn_{1-x}Cr_xSb$	0·1	4·15	5·80	trace Sb	4·14	5·76	small amount Sb
	0·15	4·15	5·78*	not obs.			
	0·25	4·10	5·80*	small amount Sb			
	0·50	4·08	5·72*	small amount Sb			
	0·75	4·14	5·60*	not obs.			
$Cr_{1-x}Mn_xTe$	0·05				4·03	6·29*	not obs.
	0·1			two NiAs phases	4·04	6·32*	not obs.
	0·15			two NiAs phases	4·04	6·35*	not obs.
	0·25			two NiAs phases	4·06	6·40*	not obs.
	0·35				4·08	6·39*	not obs.
	0·50			second phase			second phase
	0·75			second phase			second phase
	0·1						second phase

Table 2. The cell edges a and c, the asymptotic Curie temperature T_a, the Curie temperature T_C, the Néel temperature T_N, the effective moments μ_p and μ_f deduced from the Curie-Weiss law and the ferromagnetic saturation respectively for some ferromagnetic and antiferromagnetic compounds with NiAs structure

Substance	a(Å)	c(Å)	T_a(°K)	T_C(°K)	T_N(°K)	$\mu_p(\mu_B)$	$\mu_f(\mu_B)$
CrTe	3·96[a]	6·15[a]	≈ 340[a]	≈ 340[a] 339[b]		4·0[a]	2·39[b]
	3·94[c]	6·15[c]	327[c]	327[c]		4·08[c]	
	4·01[i]	6·29[i]	366 ± 3[i]	350–360[i]		3·99 ± 0·06[i]	2·45 ± 0·05[i]
MnSb	4·12[d]	5·78[d]	608[e]	587[d]		4·10[e]	3·53[d]
CrSb	4·12[f]	5·47[f]			725[g]		2·7[f]*
	4·13[i]	5·51[i]	−400 ± 130[i]		≈ 720[i]	4·3 ± 0·2[i]	
CrSe	3·71[i]	6·03[i]	−185 ± 20[i]			4·50 ± 0·06[i]	
MnTe	4·143[h]	6·703[h]	−690[e]		323[e]	6·1[e]	

* Moment per Cr deduced from neutron diffraction.

[a] See reference 8.
[b] GUILLAUD C. and BERBEZAT S. *C.R. Acad. Sci., Paris* **222,** 386, 1224 (1946).
[c] See reference 9.
[d] GUILLAUD C. *Ann. Phys., Paris* (12) **4,** 671 (1949).
[e] See reference 2.
[f] See reference 12.
[g] See reference 10.
[h] GREENWALD S. *Acta. Cryst.* **6,** 396 (1953).
[i] Own measurements.

T_a and the Curie constant C (per gram) are found and an effective moment μ_p per metal atom is calculated using the equation $\mu_p = 2{\cdot}83_B\sqrt{(MC)}$ Bohr magnetons, in which M is the molecular weight.

The substances CrTe and MnSb become ferromagnetic below a Curie temperature T_C. From the saturation magnetization σ_0 at $T = 0$, estimated from σ measurements at low temperatures, an effective moment μ_f per metal atom is calculated using the equation $\mu_f = \sigma \times M/5585$ Bohr magnetons.

The compounds CrSb and MnTe are antiferromagnetic, which is deduced from the occurrence of a minimum in the χ^{-1}–T curves at temperatures T_N, the Néel temperatures.

We carried out measurements on CrTe, CrSb and CrSe and shall now compare the results with literature data.

CrSe. The χ^{-1}–T curve (Fig. 4) shows that at high temperature a Curie-Weiss law holds with a negative T_a and that at temperatures below 235°K a deviation from the Curie-Weiss law occurs in such a way that the susceptibility is lower. Such a deviation and the negative value of T_a suggest that the transition temperature is a Néel temperature below which an antiferromagnetic ordering of spins occurs.

The χ^{-1}–T curve, however, does not have the shape characteristic for a classical antiferromagnetic, which shows a minimum at T_N.

Susceptibility values of CrSe, found by HARALDSEN *et al.*[8] are slightly lower than those given by the authors, but a curve drawn through HARALDSEN's experimental points has essentially the same shape (Fig. 4). More recently TSUBOKAWA[9] published a χ^{-1}–T curve for CrSe. He interprets his measurements by assuming that a transition occurs at 150°K. His experimental points, however, do not seem to us to exclude the possibility of a magnetic transition between 200° and 300°K.

CrTe. The σ–T, $\sigma_{20°K}$–H and χ^{-1}–T curves are

shown in Figs. 2, 3, 4 respectively. It is seen from Table 2 that our values for μ_p and μ_f are in agreement with the values given by the other authors and that T_C is slightly higher than the published values.

CrSb. For temperatures above 830°K a Curie-Weiss law is found (Fig. 12) from which T_a and μ_p are obtained. These values are, however, not very accurate because they are deduced from low susceptibility values in a small temperature range. T_N was determined by an extrapolation of the χ^{-1}–T curves below and above the transition temperature (as indicated in Fig. 12). The measurements in the antiferromagnetic region were not completely reproducible. When we started the measurements at room temperature and increased the temperature to 1100°K, we found after cooling below 650°K values that were different from those originally measured.

Our χ^{-1}–T curve is in agreement with that of HARALDSEN *et al.*[10] FOËX and GRAFF[11] published a χ^{-1}–T curve of an analogous type but with susceptibilities about three times larger.

A neutron-diffraction investigation by SNOW[12] showed that CrSb is indeed an antiferromagnetic, that the ordering of the Cr spins is that shown in Fig. 1 and that the value of the Cr moment is approximately $\mu_f = 2{\cdot}7\mu_B$.

The observed values of μ_p and μ_f (Table 2), except that for MnTe, are not consistent with the presence of metal ions like Mn^{2+}, Mn^{3+}, Cr^{2+} or Cr^{3+} in which the orbital moments are almost completely quenched, as is usually found for oxides. CrTe is known to show metallic conductivity,[13] which is another indication for a deviation from ionic bonding.

MAGNETIC PROPERTIES OF THE SOLID SOLUTIONS CrTe–CrSe, MnSb–CrSb, CrTe-CrSb AND CrTe-MnTe

$CrTe_{1-x}Se_x$ (Figs. 2–5). For increasing values of x the σ–T curves (Fig. 2) show that T_C decreases and becomes less sharply defined, due to a more gradual decline of the magnetization with temperature. From the σ–H curves at 20°K (Fig. 3) it is seen that as x increases higher fields are necessary to reach saturation. For $x = 0{\cdot}75$ no indication of approaching saturation is found even for a field of 26000 oersted. For the other compositions the saturation magnetization σ_s can be estimated.

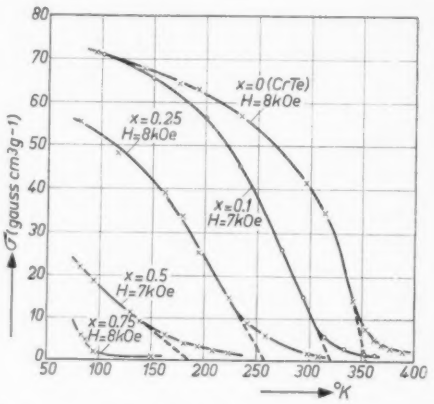

FIG. 2. $CrTe_{1-x}Se_x$. The ferromagnetic magnetization σ (per gram), measured in a field H, as a function of the temperature.

The x^{-1}–T curves for $x = 0{\cdot}9$ and $x = 0{\cdot}75$ (Fig. 4) show that at high temperatures a Curie-Weiss law holds and that at temperatures below a fairly sharply defined transition temperature deviations from the Curie-Weiss law occur.

In Fig. 5 the unit cell edges a and c, the saturation magnetization σ_s per gram at 20°K and the Curie temperature T_C are shown as a function of the composition.

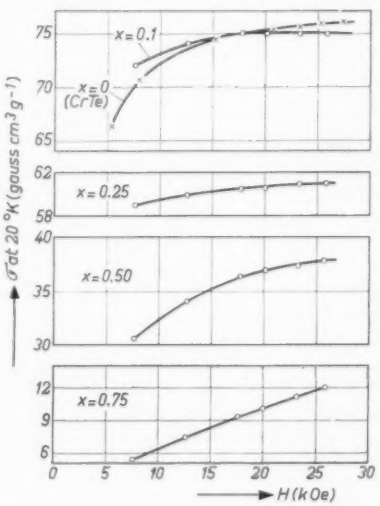

FIG. 3. $CrTe_{1-x}Se_x$. The ferromagnetic magnetization σ (per gram) as a function of the applied field H at 20° K.

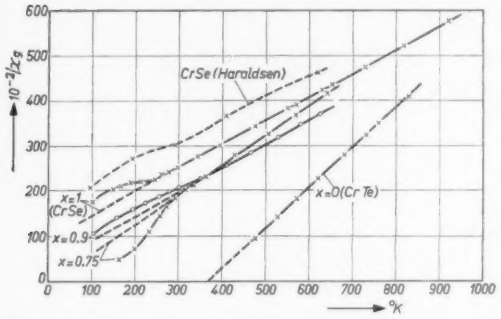

FIG. 4. $CrTe_{1-x}Se_x$. The reciprocal paramagnetic susceptibility χ^{-1} (per gram) as a function of the temperature.

A magnetic investigation of the $CrTe_{1-x}Se_x$ system has recently been published by TSUBOKAWA.[9] The results given by the authors in general agree with those given by TSUBOKAWA.

$Mn_{1-x}Cr_xSb$ (Figs. 6–9). Figs. 6 and 7 show that T_C decreases for increasing x, that from all σ–T curves a fairly sharply defined Curie temperature can be found, and that from all σ–H curves at 20°K the saturation magnetization is approached for the highest fields.

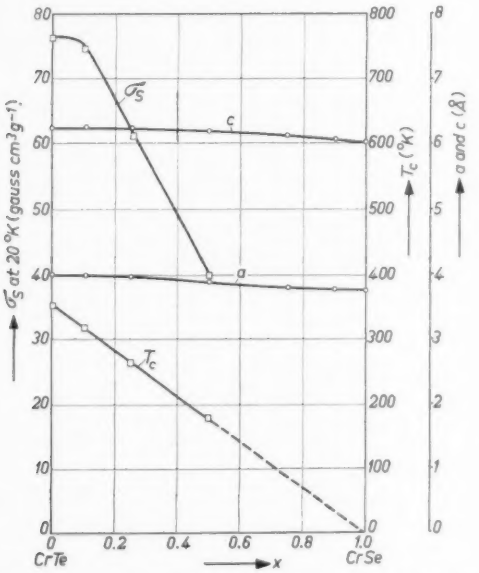

FIG. 5. $CrTe_{1-x}Se_x$. The lattice constants a and c, the Curie temperature T_C (estimated from the σ–T curves) and the saturation magnetization σ_s at 20°K (estimated from the σ–H curves at 20°K) as a function of the composition.

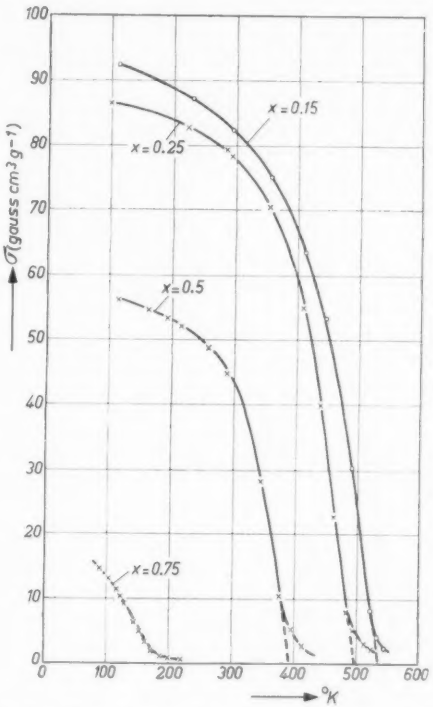

FIG. 6. $Mn_{1-x}Cr_xSb$. For meaning of symbols see Fig. 2. (H = 8000 oersted).

As was mentioned above, the minimum of the χ^{-1}–T curve for CrSb (Fig. 12) has been shown to be due to the fact that this substance is antiferromagnetic. The minimum in the χ^{-1}–T curve for

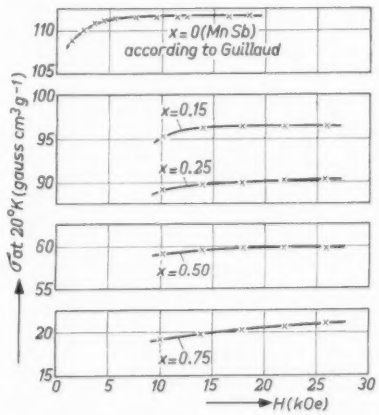

FIG. 7. $Mn_{1-x}Cr_xSb$. For meaning of symbols see Fig. 3. See Table 2, reference (d).

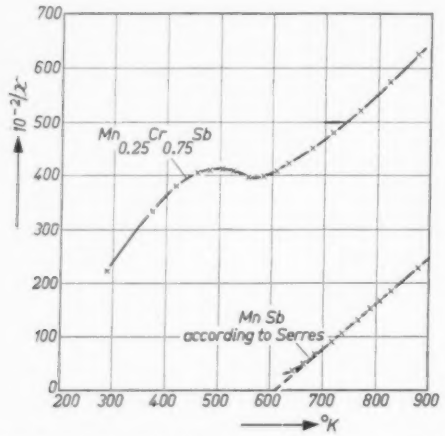

FIG. 8. MnSb and $Mn_{0.25}$-$Cr_{0.75}Sb$. For meaning of symbols see Fig. 4. See Table 2, reference (e).

$Mn_{0.25}Cr_{0.75}Sb$ (Fig. 8) suggests a similar interpretation. Therefore, we assume that in this substance an antiferromagnetic ordering of spins (as shown in Fig. 1) occurs at temperatures below a temperature T_N that corresponds approximately to the minimum in the x^{-1}–T curve.

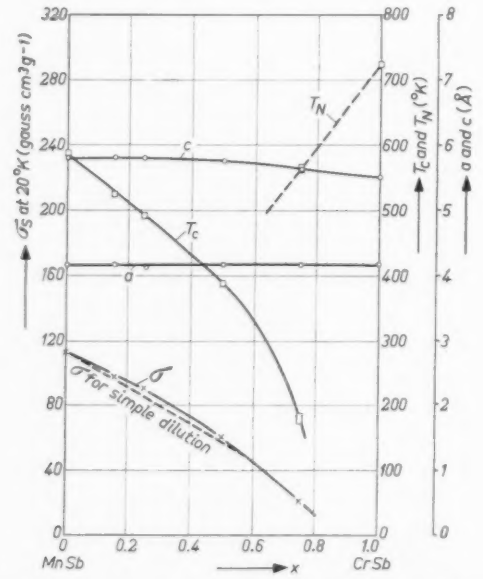

FIG. 9. $Mn_{1-x}Cr_xSb$. The Néel temperature T_N, estimated from the temperature at which the minimum in the χ^{-1}–T curve occurs, as a function of the composition. For meaning of the other symbols see Fig. 5.

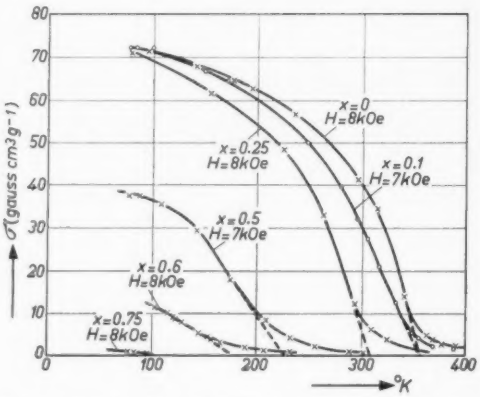

FIG. 10. $CrTe_{1-x}Sb_x$. For meaning of symbols see Fig. 2.

In Fig. 9 σ_s, T_C and T_N are plotted as functions of the composition.

After completion of the manuscript the authors saw the recent publication of HIRONE *et al.** The experimental results of the Japanese workers,

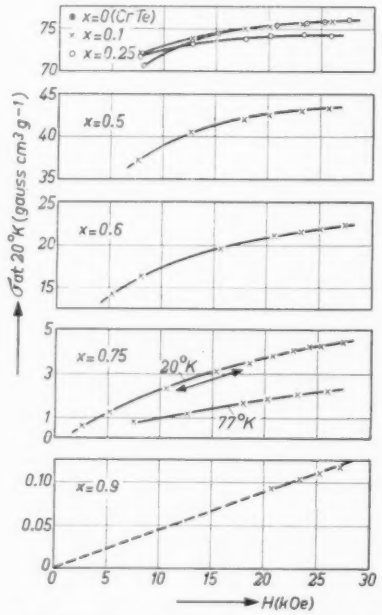

FIG. 11. $CrTe_{1-x}Sb_x$. For meaning of symbols see Fig. 3.

* HIRONE T., MAEDA S. and TSUBOKAWA I. On the magnetic properties of the system MnSb–CrSb. *J. Phys. Soc. Japan* **11**, 1083 (1956).

obtained on many more compositions, but in fields up to 7000 oersteds and down to temperatures of 77°K, are in general agreement with those of the present authors. The discussion and conclusions are different.

$CrTe_{1-x}Sb_x$ (Figs. 10–13). Figs. 10 and 11 show that the ferromagnetic behaviour is analogous to that found for $CrTe_{1-x}Se_x$. The χ^{-1}–T curves (Fig. 12) for $x = 0{\cdot}9$ and $x = 0{\cdot}75$ have minima.

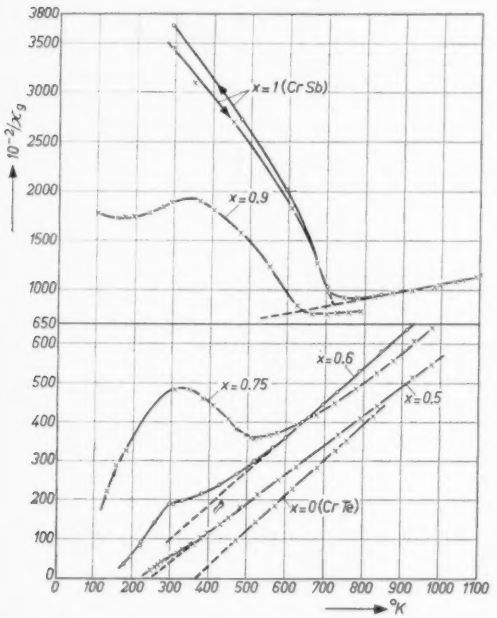

FIG. 12. $CrTe_{1-x}Sb_x$. For meaning of symbols see Fig. 4.

As was discussed above, we assume that the temperatures that correspond approximately with these minima are Néel temperatures.

In Fig. 13 σ_s, T_C and T_N are plotted as functions of the composition.

The compositions $CrTe_{0.4}Sb_{0.6}$ and $CrTe_{0.25}Sb_{0.75}$ are especially interesting.

$CrTe_{0.4}Sb_{0.6}$ is paramagnetic at high temperatures and follows a Curie-Weiss law. For decreasing temperatures deviations from the Curie-Weiss law start below approximately 550°K in such a way that χ is lower (just as found for CrSe) and at 300°K the χ^{-1}–T curve shows a kink. On further lowering of the temperature, the substance becomes ferromagnetic below a fairly uncertain Curie temperature at approximately 180°K.* Thus $CrTe_{0.4}Sb_{0.6}$ may be considered as a ferromagnetic that shows deviations from the paramagnetic behaviour of a normal ferromagnetic in the same sense as that of an antiferromagnetic below the Néel temperature (Fig. 12).

The χ^{-1}–T curves for $CrTe_{0.25}Sb_{0.75}$ and $Mn_{0.25}Cr_{0.75}Sb$ have essentially the same shape. By extrapolation of these curves to lower tempera-

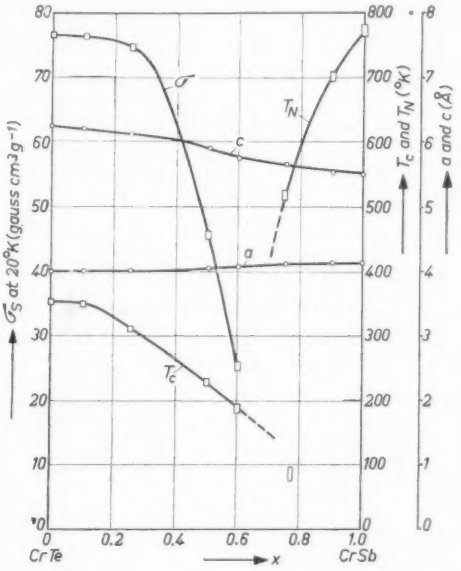

FIG. 13. $CrTe_{1-x}Sb_x$. For meaning of symbols see Figs. 5 and 9.

tures paramagnetic Curie temperatures are found approximately at +90°K for $CrTe_{0.25}Sb_{0.75}$ and at +190°K for $Mn_{0.25}Cr_{0.75}Sb$. The latter substance becomes ferromagnetic, as expected, below a temperature equal to this paramagnetic Curie temperature. From the magnetic properties at low temperature, it is, however, not obvious whether $CrTe_{0.25}Sb_{0.75}$ becomes ferromagnetic below 90°K. At 20°K σ changes reversibly with H without any hysteresis, and from the σ–H curve (Fig. 11) it is seen that the remanence is zero within the error of the measurements.

* Dr. VOLGER of this laboratory has kindly measured the specific heat on $CrTe_{0.4}Sb_{0.6}$ for temperatures running from 77°K to room temperature. He did not observe any indication of a peak in the specific heat vs. temperature curve.

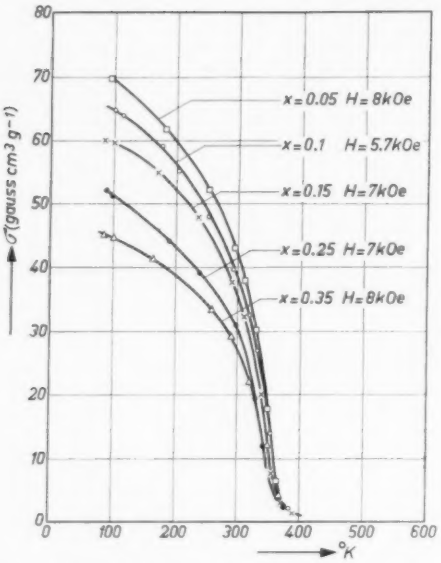

FIG. 14. $Cr_{1-x}Mn_xSb$. For meaning of symbols see Fig. 2.

$Cr_{1-x}Mn_xTe$ (Figs. 14–16). The preparations, which contained a single NiAs phase according to X-ray analysis, had Curie temperatures that were practically independent of the composition, and saturation magnetizations that decrease linearly with the Mn content. Such a behaviour is generally characteristic for a two-phase region.

The rise in the cell height c from 6·29 for $x = 0$ to 6·39 Å for $x = 0{\cdot}35$, which indicates a one-phase region, seems to be outside the errors introduced by measurement and non-stoicheiometry, but from the data so far available the authors cannot with certainty exclude the possibility of a two-phase region extending to a lower x-value than $x = 0{\cdot}35$. The results will not, therefore, be discussed in the next section.

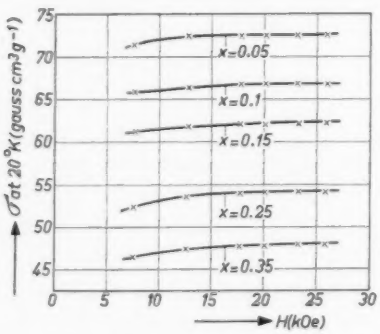

FIG. 15. $Cr_{1-x}Mn_xSb$. For meaning of symbols see Fig. 3.

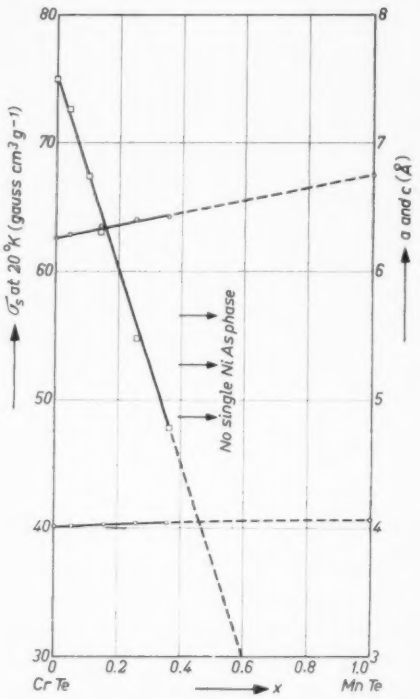

FIG. 16. $Cr_{1-x}Mn_xSb$. For meaning of symbols see Fig. 5.

DISCUSSION

Although the authors are aware that the experimental results reported are in several respects inadequate for a full description of the magnetic properties of the mixed-crystal systems concerned, an attempt will be made at a discussion of the data so far obtained, in particular those concerning CrSb and its mixed-crystal series with MnSb and CrTe.

CrSb. The question arises whether the observed antiferromagnetic ordering according to the simple two-lattice model, shown in Fig. 1 and symbolized by *AB*, is caused by direct or by indirect exchange interactions.

Arranged in the order of increasing distances the

Cr–Cr pairs *PQ*, *PR*, *PS* ... (Fig. 1) occur in CrSb. According to the Slater-Néel curve[3] a direct Cr–Cr exchange interaction is appreciable only for the distance $PQ = 2{\cdot}75$ Å (which is comparable to distances that occur in ferromagnetic metals). For the much larger distances $PR = 4{\cdot}13$ Å and $PS = 4{\cdot}96$ Å the overlap of the wave functions of the two atoms must be vanishingly small. Therefore a direct interaction mechanism can explain only a strong *PQ* interaction. The assumption of a strong negative *PQ* interaction is, however, not sufficient to explain the antiferromagnetic order found, since it fails to explain the coupling between the spins of magnetic atoms lying on different vertical axes (Fig. 1). Even in the case that, to account for this coupling, an additional much weaker interaction is assumed to exist, the high Néel temperature is not explained.

If, on the other hand, we assume that the interactions are caused by the superexchange mechanism[4] the *AB* ordering can be easily explained. The strengths of the relevant three types of interactions *P*–Sb–*Q*, *P*–Sb–*R* and *P*–Sb–*S* are then determined by the angles Cr–Sb–Cr (since all Cr–Sb distances are equal) and the interaction is the stronger the more obtuse this angle is. The angles *P*–Sb–*Q*, *P*–Sb–*R* and *P*–Sb–*S* are equal to 60, 97 and 139° respectively which implies that the *P*–Sb–*S* interaction predominates. When this interaction is assumed to be negative, the occurrence of *PS* interactions only is sufficient to explain the *AB* spin order since every Cr atom has 12 neighbours of the type *PS*.

The possibility cannot be excluded that apart from this indirect interaction, a direct *PQ* interaction is active as well. An estimation of the magnitude and even of the sign of this direct interaction, based on the Néel-Slater curve, is difficult because the state in which the Cr occurs (i.e. the diameter of the 3*d* orbital) is not known.

$Mn_{1-x}Cr_xSb$. The $\sigma_{s(20°K)}$–x curve (Fig. 9) is roughly a straight line through the point $\sigma_s = 0$, $x = 1$, i.e., the curve that would be expected for simple dilution of Mn by a diamagnetic metal. The substance $Mn_{0{\cdot}25}Cr_{0{\cdot}75}Sb$ shows an antiferromagnetic ordering below 560°K and becomes ferromagnetic below 175°K. Such a behaviour can be explained in a first approximation by the assumption that the Mn–Cr interaction is vanishingly weak in comparison with the (positive) Mn–Mn and (negative) Cr–Cr interactions. A ferromagnetic order of Mn spins and an antiferromagnetic order of Cr spins then occur practically independently of each other and the Cr spins do not contribute to the ferromagnetic magnetization.

If the Mn–Cr interaction were not small, a strong deviation from the straight σ_s–x line would be expected. For small values of x the number of Cr–Mn neighbours is much larger than the number of Cr–Cr neighbours and, e.g. in the case of positive Mn–Cr interaction, the Cr spins would be ordered parallel to the surrounding Mn spins in the ferromagnetic state. Since Mn and Cr have moments of equal order of magnitude (as deduced from the properties of MnSb and CrSb), the tangent to the σ_s–x curve for $x = 0$ would be approximately horizontal.

$CrTe_{1-x}Sb_x$. In the narrow range of compositions between $x = 0{\cdot}6$ and $x = 0{\cdot}75$ the materials change from a clearly ferromagnetic ($T_c = 190$°K) into a clearly antiferromagnetic substance ($T_N = 520$°K). The temperatures below which the χ^{-1}–T curves start to deviate from Curie-Weiss laws, are roughly equal to 350°, 500°, 600° and 750°K for $x = 0{\cdot}5$, $0{\cdot}6$, $0{\cdot}75$ and $1{\cdot}0$ respectively (Fig. 12). For the range $0{\cdot}6 < x < 0{\cdot}75$ this temperature is thus 500–600°K.

In the substances $CrTe_{1-x}Sb_x$ chromium is obviously the only magnetic atom present. If the interactions for all Cr–Cr pairs of a similar type (e.g. the type *PS* shown in Fig. 1) were equal, then the change with increasing x from ferromagnetism, i.e. with positive *AB* interaction, to antiferromagnetism, i.e. with negative *AB* interaction, would take place via materials with small AB interaction, i.e. materials for which a Curie-Weiss law holds down to low temperatures. We have seen that such a behaviour is not observed, i.e., the experimental results are not compatible with a gradual change from a positive to a negative interaction for increasing x but can be accounted for only by assuming the presence of a mixture of Cr–Cr pairs with pronounced positive and negative interactions, e.g. strongly positive Cr–Te–Cr and strongly negative Cr–Sb–Cr interactions.

This assumption is strongly supported by the above-mentioned deviations from the normal ferromagnetic and antiferromagnetic behaviour of the materials $CrTe_{0{\cdot}4}Sb_{0{\cdot}6}$ and $CrTe_{0{\cdot}25}Sb_{0{\cdot}75}$ respectively. For example, the curvature of the χ^{-1}–T curve for $CrTe_{0{\cdot}25}Sb_{0{\cdot}75}$ at temperatures

below 300°K is inconceivable without the assumption that strong positive interactions occur as well as strong negative interactions, which are responsible for the high Néel temperature.

On the other hand we are not able to develop a theory to account in detail for the shapes of the χ^{-1}–T curves of $CrTe_{0.4}Sb_{0.6}$ and $CrTe_{0.25}Sb_{0.75}$ with the model of a mixture of positive and negative Cr–Cr interactions. A theoretical treatment of the order-disorder problem of a system of spins, which are coupled partly by positive and partly by negative interactions in a statistical way* cannot be given with the aid of elementary methods (like e.g. the Weiss-field approximation) and will be very complicated.

As in $CrTe_{0.25}Sb_{0.75}$ an ordering of spins sets in at $T_N = 520°K$, it is very likely that in the state present at low temperatures an ordering of spins is also present. Our experiments are not sufficient to decide whether this state is "ferromagnetic" or "anti-ferromagnetic", by which terms is meant an ordering with or without a resulting moment. It seems likely that this state is closely related to the "ferromagnetic" state of the samples $x < 0{\cdot}6$, because the paramagnetic Curie temperature of $CrTe_{0.25}Sb_{0.75}$ (approx. 90°K) fits very well on the extrapolated T_C–x curve (Fig. 13).

We shall now show that the occurrence of a mixture of Cr–Cr pairs with positive and negative interactions is difficult to explain by direct interactions but easily understood for superexchange interactions.

If the interactions were supposed to be direct, then their different signs for CrSb and CrTe must be explained by the difference in distance (e.g. $PQ = 3{\cdot}15$ Å for CrTe and $PQ = 2{\cdot}75$ Å for CrSb) or by an influence of the metalloid atoms on the state of the Cr atoms (e.g. on the diameter of the 3*d* orbitals). The magnitude and sign of the interaction would be determined by the numbers of Te and Sb neighbours of the two atoms. As each Cr is surrounded by 6 metalloid atoms, a practically continuous variation of the interaction is expected and, for a certain value of x, the interactions would fluctuate around zero.

If, however, superexchange interaction is supposed to occur, then the *PS* interactions (Fig. 1), in this case *P*–Te–*S* and *P*–Sb–*S*, dominate, as was discussed above. From the properties of CrTe and CrSb it follows that the *P*–Te–*S* and *P*–Sb–*S* interactions are positive and negative respectively. Since a Cr–Cr pair of the *PS* type is coupled by only one metalloid atom, the superexchange interaction cannot be weak, but is strongly positive or strongly negative when this metalloid atom is a Te or a Sb atom respectively.

A striking difference between the $CrTe_{1-x}Sb_x$ and $Mn_{1-x}Cr_xSb$ systems is the initial slope of the σ_s–x curves, which is zero and negative respectively. In $CrTe_{1-x}Sb_x$ interactions exist between all Cr–Cr pairs so that all Cr spins will contribute to the saturation magnetization either with positive or negative sign. Therefore the σ_s–x curve will in general deviate from the straight line expected for simple dilution, such as was found for $Mn_{1-x}Cr_xSb$. We will show that the sense of this deviation of the slope of the σ_s–x curve for $CrTe_{1-x}Sb_x$ does not contradict the assumption of a mixture of pronounced positive and negative interactions.

For small values of x, where isolated Sb atoms occur among an excess of Te atoms, the Cr–Sb–Cr interactions of the type *PS* give an antiparallel coupling of the spins of the six Cr neighbours of an Sb atom, tending to give an arrangement as observed in CrSb. The six spins are, however, ferromagnetically coupled via neighbouring Te atoms, and the number of positive Cr–Te–Cr interactions of the type *PS* is much greater than the number of negative Cr–Sb–Cr interactions between the six Cr atoms considered. The order of magnitude of the positive and negative interactions can be estimated from the Curie and Néel temperatures of CrTe and CrSb. A simple calculation shows that the energy of the ferromagnetic state is considerably lower for all spins parallel than for some spins antiparallel to the resulting moment. An approximately horizontal tangent to the σ_s–x curve for $x = 0$ is, therefore, expected.

* Due to the small difference in scattering power of Te and Sb it is difficult to detect an ordering of Te and Sb in $CrTe_{1-x}Sb_x$ by X-ray analysis. The absence of discontinuities in the curves in Fig. 13 makes the occurrence of such an ordering seem unlikely.

Acknowledgements—The authors are much indebted to Messrs. M. VROLIJKS and F. LAURIJSEN who prepared the compounds and carried out part of the measurements. Thanks are likewise due to

IR. P. JONGENBURGER for performing the measurements at 20°K.

REFERENCES

1. LOTGERING F. K. *Philips Res. Rep.* **11,** 190, 337 (1956).
2. SERRES A. *J. Phys. Radium* **8,** 146 (1947).
3. NÉEL L. *Ann. Phys., Paris* **5,** No. 11, 232 (1936).
4. ANDERSON P. W. *Phys. Rev.* **79,** 350, 705 (1950).
5. VOLGER J., DE VRIJER F. W. and GORTER C. J. *Physica* **13,** 621 (1947).
6. RATHENAU G. W. and SNOEK J. L. *Philips Res. Rep.* **1,** 239 (1946).
7. DOMENICALI C. A. *Rev. Sci. Instrum.* **21,** 327 (1950).
8. HARALDSEN H. and NEUBER A. *Z. Anorg. Chem.* **234,** 353 (1937).
9. TSUBOKAWA I. *J. Phys. Soc. Japan* **11,** 662 (1956).
10. HARALDSEN H., ROSENQVIST T., and GRØNVOLD F. *Arch. Math. Naturv.* B.L. Nr. 4.
11. FOËX G. and GRAFF M. *C.R. Acad. Sci., Paris* **209,** 160 (1939).
12. SNOW A. I. *Phys. Rev.* **85,** 365 (1952); *Rev. Mod. Phys.* **25,** 127 (1953).
13. FAKIDOF J. G., GRAZJDANKINA N. P. and KIKOIN A. K. *Dokl. Akad. Nauk SSSR.* **68,** 491 (1949).

VOL. 3 1957

J. Phys. Chem. Solids Pergamon Press 1957. Vol. 3. pp. 250–252.

CORRELATION OF $\Delta S^{\ddagger}$ AND $\Delta V^{\ddagger}$ IN SIMPLE ACTIVATED PROCESSES IN SOLIDS

A. W. LAWSON

Institute for the Study of Metals University of Chicago, Chicago 37, Ill.

(*Received* 24 *April* 1957; *in revised form* 13 *May* 1957)

Abstract—It is shown $\Delta S^{\ddagger}/\Delta V^{\ddagger} \cong \alpha/\beta$, where α is the volume coefficient of expansion and β is the isothermal compressibility. A comparison with experimental results is given.

ZENER[1] has reviewed and elucidated the Arrhenius rate equation as applied to diffusion in solids in terms of absolute reaction rate theory. In particular, he shows that for temperatures above the Debye temperature of the solid, the diffusion coefficient D may be written as

$$D = \gamma a^2 \nu e^{-\Delta G^{\ddagger}/RT} = \gamma a^2 \nu e^{\Delta S^{\ddagger}} R e^{-\Delta U_0^{\ddagger}/RT} \times \times e^{-p\Delta V^{\ddagger}/RT} \quad (1)$$

where γ is a dimensionless quantity of the order of unity which depends on the diffusion mechanism, a is the lattice constant, ν a frequency of the order of the Debye frequency, and $\Delta G^{\ddagger}$ is the isothermal work required to move one gram atom of diffusing atoms reversibly from equilibrium lattice sites to positions corresponding to the saddle configuration in an elementary diffusion process. $\Delta G^{\ddagger}$ may be written in terms of $\Delta S^{\ddagger}$ the associated entropy of activation, $\Delta V^{\ddagger}$ the associated volume of activation, $\Delta U_0^{\ddagger}$ the work required at absolute zero and zero pressure, and P the external hydrostatic pressure. R is the universal gas constant.

At any finite temperature T above 0°K, at zero pressure

$$\Delta G^{\ddagger}(T) = \Delta G^{\ddagger}(0) - T\Delta S^{\ddagger} = \Delta U_0^{\ddagger} - T\Delta S^{\ddagger}. \quad (2)$$

If we assume that $\Delta G^{\ddagger}$ is a function only of the volume and hence only changes with temperature because of thermal expansion, then

$$\Delta G^{\ddagger} = \Delta U_0^{\ddagger} - P(T)\Delta V^{\ddagger} \quad (3)$$

where P is the pressure required to compress the lattice from its volume $V(T)$ at temperature T to $V(0)$ its volume at absolute zero. But

$$P(T) = -\int_0^T \frac{\partial P}{\partial \ln V}\Big)_T \frac{\partial \ln V}{\partial T}\Big)_p dT = \int_0^T \alpha/\beta \, dT \quad (4)$$

where α is the isobaric coefficient of thermal expansion and β is the isothermal compressibility. Hence $P(T) \cong (\alpha/\beta)T$.

From a comparison of equations (3) and (4) with equation (2), we obtain

$$\frac{\Delta S^{\ddagger}}{\Delta V^{\ddagger}} \cong \frac{\alpha}{\beta}. \quad (5)$$

The approximate equation (5) does not appear to have been spelled out explicitly before although it may be obtained from an equivalent treatment of FRENKEL[2] following his equation (40). MOTT and GURNEY[3] also give related arguments. Strictly speaking, the derivation of equation (5) has been carried out only for unimolecular processes such as the formation of a vacancy in a simple metal and its motion through the lattice. In addition, equation (5) should also hold separately for each part of the process, i.e. for the formation of the vacancy, and in addition for the activated motion of the vacancy. Further, it is easy to show that it is also applicable

VOL. 3 1957

to processes involving bimolecular reactions of the type encountered in certain ionic crystals between interstitial and vacancies. It is possible to give a more rigorous formula by recourse to thermodynamics. The argument is as follows: Since

$$\Delta S^{\ddagger} = -\frac{\partial \Delta G^{\ddagger}}{\partial T}\Big)_{P} \tag{6}$$

and

$$\Delta V^{\ddagger} = \frac{\partial \Delta G^{\ddagger}}{\partial P}\Big)_{T} \tag{7}$$

we have

$$\frac{\Delta S^{\ddagger}}{\Delta V^{\ddagger}} = \frac{\partial P}{\partial T}\Big)_{\Delta G^{\ddagger}} \tag{8}$$

But

$$\frac{\partial P}{\partial T}\Big)_{\Delta G^{\ddagger}} = \frac{\partial P}{\partial T}\Big)_{V} + \frac{\partial P}{\partial V}\Big)_{T}\frac{\partial V}{\partial T}\Big)_{\Delta G^{\ddagger}} \tag{9}$$

So

$$\frac{\Delta S^{\ddagger}}{\Delta V^{\ddagger}} = \frac{\alpha}{\beta}\left(1-\frac{\alpha_{\Delta G^{\ddagger}}}{\alpha_{P}}\right) \tag{10}$$

where $\alpha\Delta G^{\ddagger}$ is the change in volume with temperature at constant $\Delta G^{\ddagger}$. This is certainly less than α_P since such a process requires the application of a positive pressure to the system if $\Delta S^{\ddagger}$ is positive.

The approximations involved in equation (5) are considerably less than the uncertainty in the values of $\Delta S^{\ddagger}$ arising from experimental error and the uncertainty in γ and ν in equation (1). All in all, the relation should be good to about a factor of two.

If we consider the case of mobility activation, an argument may be made from fluctuation theory. According to the theory of absolute activation rates, when an atom, for instance, diffuses over a barrier into a neighboring site, the time involved is of the order of a reciprocal Debye frequency, i.e. 10^{-12} to 10^{-13} sec. In such a time, the strain in the lattice produced by the diffusing atom does not propagate more than a few interatomic distances. If we imagine a subvolume surrounding the diffusing atom cut out of the surrounding material (such that it encompasses all the local strain associated with the diffusion), then a local fluctuation in energy must occur within this volume sufficient to activate the diffusing atom. Associated with this fluctuation energy must be a corresponding local increase in volume and entropy. If we assume further, in agreement with the equilibrium hypothesis of absolute reaction rate theory, that the activation process proceeds locally on an isothermal basis, then we may write

$$\Delta T = \frac{\partial T}{\partial S}\Big)_{V}\Delta S + \frac{\partial T}{\partial V}\Big)_{S}\Delta V = 0 \tag{11}$$

or

$$\frac{\Delta S}{\Delta V} = \frac{C_V}{TV\alpha_S} = \frac{\partial S}{\partial V}\Big)_{T} = \frac{\partial P}{\partial T}\Big)_{V} = \alpha/\beta. \tag{12}$$

The approximation involved in equation (12) is that a linear expansion of ΔT is sufficient. This argument is not readily applicable to the case of the formation of an equilibrium number of imperfections (which make possible the diffusion process) owing to the ensuing relaxation phenomena.

Over the past few years, the effect of pressure[4–7] on a number of activated processes has been studied in the author's laboratory. These data provide an estimate of $\Delta S^{\ddagger}$ (limited as described above) and a determination of $\Delta V^{\ddagger}$. These quantities are listed in Table 1 as $\Delta S^{\ddagger}_{\text{obs.}}$ and $\Delta V^{\ddagger}_{\text{obs.}}$ respectively. $\Delta S^{\ddagger}$ calc. is obtained from $\Delta V^{\ddagger}_{\text{obs.}}$ by use of equation (5). The agreement obtained in Table 1 between $\Delta S^{\ddagger}_{\text{obs.}}$ and $\Delta S^{\ddagger}_{\text{calc.}}$ is within the limits of error to be expected, except for the low temperature observations on white phosphorous. In the latter case, the diffusion observed may be grain boundary diffusion.

The difference between $\Delta S^{\ddagger}_{\text{calc.}}$ and $\Delta S^{\ddagger}_{\text{obs.}}$ arises from three sources: (a) the uncertainty in the quantity γ of equation (1); (b) the approximations used in the calculation of $\Delta S^{\ddagger}_{\text{obs.}}$ from the use of a Debye θ in estimating ν of equation (1); (c) the approximations involved in equation (5). The last will be discussed below. The estimate of ν from a Debye θ involves the concept of an average frequency which is well established in solid state physics through the use of a Gruneisen equation of state. In the calculations used in preparing Table 1, the Debye θ was estimated from specific heat data where this was available; otherwise, it was estimated by use of the Lindemann formula. In general, the author feels the uncertainty in γ is greater than the uncertainty in ν.

Table 1. Comparison of $\Delta S^{\ddagger}_{exp.}$, $\Delta V^{\ddagger}_{exp.}$ *and* $\Delta S^{\ddagger}_{calc.}$ *from equation* (5) *for known simple activated processes in solids*

Process	$\Delta S^{\ddagger}_{exp.}$ cal/mole/°C	$\Delta S^{\ddagger}_{calc.}$ cal/mole/°C	$\Delta V^{\ddagger}_{exp.}$ cc/mole	Ref.
Mobility of Ag vacancies in AgBr	8·6	8·1	7·4	(4,8)
Mobility of Ag interstitials in AgBr	−0·6 to 4	4·2	2·6	(4,8)
Formation of Frenkel defects in AgBr	15 to 25	15	16	(4,8)
Overall diffusion rate of Br^- ions in AgBr	41·4	36	38	(7)
Self diffusion in Na	7·3	4	12·4	(5)
Self diffusion in White Phosphorous (low temperature)	negative	13	30	(6)
Self diffusion in White Phosphorous (high temperature)	224	90	210	(6)

CONCLUSIONS

The most delicate problem involved in this discussion is that of estimating the errors involved in writing equation (5). Some idea of the nature of the approximations involved may be obtained in the following way. Since the change in entropy between the normal and activated states arises from changes in vibrational frequency of the various normal modes, we may write

$$\Delta S^{\ddagger} = -3R \ln \frac{\bar{\nu}^{\ddagger}}{\bar{\nu}} \tag{13}$$

where $\bar{\nu}^{\ddagger}$ and $\bar{\nu}$ are appropriate geometric means of all frequencies in the activated and normal states respectively. From equation (13), we find

$$\frac{\Delta S^{\ddagger}}{\Delta V^{\ddagger}} = -\frac{C\nu \Delta \bar{\nu}}{\bar{\nu} \Delta V^{\ddagger}} = -\frac{C\nu}{V} \frac{\partial \ln \theta}{\partial \ln V} \tag{14}$$

where the logarithm of equation (13) has been expanded and the resulting terms collected in differential form. This requires that $\Delta\nu \ll \bar{\nu}$. It follows without further manipulation from Gruneisen's law that

$$\frac{\Delta S^{\ddagger}}{\Delta V^{\ddagger}} = \alpha/\beta. \tag{15}$$

Hence equation (5) should be more accurate for activated processes in which $\Delta V^{\ddagger}$ and $\Delta\bar{\nu}$ are not too large. This conclusion jibes with the fact that equation (12) was derived on the assumption that ΔT could be expressed by the first terms in a Taylor's series expansion of ΔT in terms of ΔS and ΔV.

Despite the approximate nature of equation (5), its usefulness is apparent. For example, consider the creep of a polymer, for which, let us say, $\Delta S^{\ddagger} = 500$ cal/mole °C. Then $\Delta V^{\ddagger} \cong 500$ cm^3/mole, for reasonable values of α and β, and the volume of the rate controlling segment is known approximately without the necessity of performing a high pressure experiment. This calculation presumes, of course, that a single (or approximately an average) activated process is the controlling mechanism.

Acknowledgements—I am indebted to Mr. DAVID TANNHAUSER for permission to use results of his which are to be published shortly. I am also indebted to him for making calculations used in Table 1. This research was supported in part by the Office of Naval Research.

REFERENCES

1. ZENER C. *Thermodynamics in Metallurgy*. American Society of Metals (1950).
2. FRENKEL J. *Kinetic Theory of Liquids*. Oxford University Press (1946).
3. MOTT N. F. and GURNEY R. *Electronic Processes in Ionic Crystals*. Oxford University Press (1940).
4. KURNICK S. W. *J. Chem. Phys.* **20,** 218 (1952).
5. NACHTRIEB N. H. *et al. J. Chem. Phys.* **20,** 1189 (1952).
6. NACHTRIEB N. H. and LAWSON A. W. *J. Chem. Phys.* **23,** 1193 (1955).
7. TANNHAUSER D. Private communication.
8. TELTOW J. *Ann. Physik* **5,** 63 (1950).

J. Phys. Chem. Solids Pergamon Press 1957. Vol. 3. pp. 253–274.

THE ELECTRIC AND MAGNETIC PROPERTIES OF GRAPHITE

R. R. HAERING and P. R. WALLACE

Department of Mathematics, McGill University, Montreal, Quebec, Canada

(*Received* 7 *March* 1957; *revised* 30 *April* 1957)

VOL. 3 1957

Abstract—The conduction electron magnetic susceptibility has been calculated taking into account band-to-band transitions. The calculation is an extension to three dimensions of a calculation by McClure. It is shown that agreement with experiment can only be retained if the inter-layer interaction is much weaker than was previously supposed. If the Fermi energy at zero temperature is $\sim 0{\cdot}06$ eV and if the shift of the Fermi surface with temperature is taken into account, excellent agreement with experiment is obtained for all temperatures. The average value of the susceptibility at low temperatures and the average period of the de Haas-Van Alphen effect fluctuations independently determine the position of the Fermi level at low temperatures. The de Haas–Van Alphen effect fluctuations turn out to be far too large, both in a two and in a three-dimensional calculation. In order to test the values of the various parameters, the ratio of the electrical conductivities, the Hall coefficient and the transverse magneto-resistance have also been calculated.

INTRODUCTION

Several attempts have been made to explain the diamagnetic susceptibility of graphite.[1,2,3] Most of these calculations are based on the Peierls formula[4,5] which neglects band-to-band transitions.[6] McClure, however, has extended these investigations by taking the previously neglected transition terms into account. Using the equations of Luttinger and Kohn[7] and the two-dimensional band structure of Wallace,[8]* he has succeeded in solving the equations for the energy relation in the presence of a magnetic field. McClure's work presents a very satisfactory explanation of the high temperature susceptibility. It will, in fact, be seen that the same model is also capable of explaining the average value of the susceptibility at low temperatures, and the average period of the fluctuations in the de Haas–Van Alphen effect.

Agreement with the experimentally observed average low-temperature susceptibility of -30×10^{-6} e.m.u./g[1] is obtained if the Fermi surface is taken to be about 0·06 eV from the degeneracy corner. Similarly, the experimental average period of the de Haas–Van Alphen effect fluctuations[9,10] can be accounted for by choosing $\zeta_0 \simeq 0{\cdot}065$ eV. We shall see that this rather large value of ζ_0 does not imply that the high temperature susceptibility becomes vanishingly small, as McClure supposed. The apparent discrepancy is reconciled by taking account of the shift of the Fermi level with temperature.

In calculating the high temperature susceptibility from a three-dimensional model, we will be led to the conclusion that the inter-layer interactions are much smaller than was previously supposed.[11] If we are going to retain any susceptibility at all, we require $\gamma_1 \lesssim 0{\cdot}01$ eV, where γ_1 is the exchange integral between nearest neighbours in adjacent planes. Thus, we shall find that graphite is essentially two-dimensional.

An independent rough estimate of γ_1 can be obtained from the de Haas–Van Alphen effect if one uses the semi-classical (Bohr-Sommerfeld) approximation.[12] The two periods of the de Haas–Van Alphen effect[9,10] determine in this approximation both ζ_0 and γ_1. A simple calculation gives $\zeta_0 \simeq 0{\cdot}065$ eV; $\gamma_1 \simeq 0{\cdot}005$ eV.

The origin of the excess electrons implied by this value of ζ_0 is not clear. A possible source might

* This paper will hereafter be referred to as *A*.

be the incomplete valence bonds on the carbon atoms near the surface of the graphite crystal, as suggested by MROZOWSKI.[13] There are, however, objections to this interpretation, e.g. the prediction of a size effect which is not experimentally established.

Our choice of the Fermi level ζ_0 implies about 10^{-4} excess electrons per carbon atom. This value is in fair agreement with estimates based on additive compound and radiation damage studies.[2,14,15] In particular, bromination experiments seem to indicate a variation of the susceptibility with ζ which is consistent with our model. This point will be further discussed in Section 5.

In order to test our explanation of the susceptibility and the de Haas–Van Alphen effect, it is desirable to investigate the consequences of our small value of γ_1 and large value of ζ_0 on other properties of graphite. Unfortunately, the usual difficulties with the relaxation time prevent one from doing this satisfactorily. However, it should still be possible to decide whether a compatible explanation is possible, or whether a completely different choice of parameters is required. Using standard formulae for the electrical conductivities, the Hall coefficient and the transverse magneto-resistance, we will show, using the three-dimensional band structure of *A*, that satisfactory agreement is obtained with the following choice of parameters:

γ_0 = nearest "in-plane" neighbour exchange integral $\simeq -2{\cdot}5$ to $-2{\cdot}6$ eV.
γ_1 = nearest "out-of-plane" neighbour exchange integral $\simeq 0{\cdot}005$ eV.
ζ_0 = Fermi level at low temperatures $\simeq 0{\cdot}06$ eV.

We shall see that if the relaxation time τ is assumed constant or a function of energy only, the ratio of the two principal conductivities of graphite $\sigma_\parallel/\sigma_\perp$ becomes 10^5 with our choice of parameters, in fair agreement with the experimental results of KRISHNAN and GANGULI[16] and DUTTA.[17] Lower values of this ratio have also been reported, for example, by PRIMAK and FUCHS.[18] We feel, however, that the largest reported experimental value should be chosen for comparison with theory, since any slight misalignment during an experiment would greatly reduce the ratio.

The zero field Hall coefficient will also be calculated. At low temperatures, where the difficulties due to the relaxation time are least severe, the calculated Hall coefficient agrees with the measurement of KINCHIN.[30] At higher temperatures, our calculation becomes doubtful, due to the simplifying assumptions about the relaxation time, and the experiments become difficult to interpret.

At low temperatures, the mean free path cancels out in the expressions for the ratio of the conductivities and for the Hall effect, if one assumes that the relaxation time τ depends on $\boldsymbol{k}$ only through the energy. This is not true in the expression for the transverse magneto-resistance. In fact, $\Delta\rho/\rho$ is just proportional to τ^2. Comparison with experiment then yields a value for the relaxation time τ, which can be compared with the results of cyclotron resonance. Agreement with experiment is again satisfactory.

Summarizing, we shall find that a model of graphite based on excess electrons and a small interplanar interaction is in good agreement with experiment.

The position of the Fermi surface at low temperatures may be determined independently by each of the following effects:

(1) The mean period of the de Haas–Van Alphen effect.
(2) The average steady susceptibility at low temperatures.
(3) The low temperature, zero field Hall effect.
(4) The transverse magneto-resistance (only indirectly).

On the other hand, the smallness of the interplane exchange integral follows independently from:

(1) The high temperature susceptibility.
(2) The two periods of the de Haas–Van Alphen effect.
(3) The ratio of the electrical conductivities.
(4) The transverse magneto-resistance (only indirectly).

1. CALCULATION OF THE ENERGY SPECTRUM IN THE PRESENCE OF A MAGNETIC FIELD

LUTTINGER and KOHN[7] have developed a general theory of the motion of electrons and holes in perturbed periodic fields. These equations form the basis of MCCLURE's calculation of the diamagnetism of graphite.[3] MCCLURE's coupled equations (2.7a and 2.7b) are a special case of LUTTINGER and KOHN's equations after certain

terms are neglected. Since we are primarily interested in a calculation of the susceptibility, we shall make use of the fact that in graphite the susceptibility with the magnetic field parallel to the crystal c-axis is about forty times larger than the ionic susceptibility. The terms that McClure has omitted from the equations of Luttinger and Kohn are terms which would lead to contributions to the susceptibility which are of the order of the ionic susceptibility.

In the extension of the work done by McClure, we shall also make use of the fact that the diamagnetic susceptibility of graphite is large. In such a case, it is possible to derive an approximate set of equations which, upon solution, yield the energy spectrum in the presence of a magnetic field. The derivation of these equations is based on Löwdin functions[19] and is carried out in the tight binding formalism, although one could generalize this approach. The proof is based on Luttinger's[20] derivation of the "perturbed lattice equation" and is given elsewhere.[21] In particular, the derivation shows that the neglected terms are of the order of the ion core susceptibility.

A simple prescription can be given for obtaining the set of coupled equations which determine the energy spectrum in the presence of the magnetic field. One simply takes the secular determinant which determines the $E(\boldsymbol{k})$ relation in the absence of the magnetic field, and makes the elements of this determinant operators by replacing k_x by $k_x+is(\partial/\partial ky)$, $(s=eH/\hbar c)$. The elements of the resulting matrix operator are to be taken in the sense of an expansion, and the operator acts on a column vector $B_i(\boldsymbol{k})$ whose dimensionality is the multiplicity of the degeneracy in question. Let us illustrate the procedure by re-deriving McClure's equations (2.7a and 2.7b) in this manner.

The secular equation in the two dimensional approximation is given in A as:

$$\begin{vmatrix} H_{11}'-E & H_{12}' \\ H_{12}^{*\prime} & -E+H_{22}' \end{vmatrix} = 0$$

where:

$$H'_{12} = H'^{*}_{21} = -\gamma_0\left[\exp\left(\frac{-ik'_x a}{\sqrt{3}}\right)+ 2\cos\left(\frac{k'_y a}{2}\right)\exp\left(\frac{ik'_x a}{2\sqrt{3}}\right)\right]$$

$$H'_{11} = H'_{22} = E_0-2\gamma'_0\left[\cos(k'_y a)+ 2\cos\left(\frac{k'_x a\sqrt{3}}{2}\right)\cos\left(\frac{k'_y a}{2}\right)\right].$$

The notation here is the same as that used in A except that our k's are defined differently by a factor of 2π.

We now expand these elements to lowest order about the degeneracy corner. Introducing:

$$k'_x = k_x^c+k_x \qquad k_x^c = \frac{2\pi}{\sqrt{3}a}$$

$$k'_y = k_y^c+k_y \qquad k_y^c = \frac{2\pi}{3a}$$

we find:

$$H'_{11} = H'_{22} \simeq E_0+3\gamma'_0$$

$$H'_{12} = \frac{\sqrt{3}}{2}\gamma_0 a e^{i\pi/3}(k_y-ik_x) = \hbar v e^{i\pi/3}(k_y-ik_x).$$

The notation $\hbar v = (\sqrt{3}/2)\gamma_0 a$ was introduced by McClure[3] and will be used throughout this paper. Furthermore, we shall from here on measure energy from the degeneracy corner; we shall put $H_{11}' = H_{22}' = 0$.

Thus, in the absence of a field H, the energy spectrum in the vicinity of the corner of the zone is:

$$E(\boldsymbol{k}) = \pm\hbar v(k_x^2+k_y^2)^{\frac{1}{2}} = \pm\hbar vK.$$

Let us now apply a magnetic field H along the z direction. Following our prescription, our set of coupled equations is:

$$\begin{bmatrix} -E & \hbar v e^{i\pi/3}\left(k_y-ik_x+s\dfrac{\partial}{\partial k_y}\right) \\ \hbar v e^{-i\pi/3}\left(k_y+ik_x-s\dfrac{\partial}{\partial k_y}\right) & -E \end{bmatrix}\begin{bmatrix} B_1 \\ B_2 \end{bmatrix} = 0$$

or:

$$\hbar v e^{i\pi/3}\left[k_y - ik_x + s\frac{\partial}{\partial k_y}\right]B_2 = EB_1$$

$$\hbar v e^{-i\pi/3}\left[k_y + ik_x - s\frac{\partial}{\partial k_y}\right]B_1 = EB_2.$$

These equations are completely equivalent to McCLURE's equations (2.7a and 2.7b) (the sign of s is unimportant) and predict the following energy spectrum:

$$E = \pm\hbar v(2ns)^{\frac{1}{2}} = \pm v(ns)^{\frac{1}{2}}.$$

It should be pointed out that the secular determinant used here neglects overlap. COULSON and TAYLOR[11] have estimated the various overlap integrals, and have shown that only nearest neighbour overlap is important. If this overlap, which we shall call σ is considered, it can be easily shown that the above energy spectrum is replaced by:

$$\frac{E}{1-\dfrac{E\sigma}{\gamma_0}} = \pm v(ns)^{\frac{1}{2}}.$$

Now $\sigma \simeq 0{\cdot}25$. Since we are interested in energies near the degeneracy corner $0 \leqslant E \leqslant \zeta_0$ and since $\gamma_0 \simeq 2{\cdot}6$ eV, it is clear that overlap contributions are completely unimportant.

It may be similarly verified that inclusion of exchange integrals with second nearest neighbours in the graphite plane, as investigated by HOVE,[22] has no appreciable effect in the region of k-space which is of interest in our model.

Let us now extend this treatment to three dimensions. We shall consider only nearest neighbour exchanges within the plane and nearest out-of-plane exchange integrals. Second nearest-neighbour interactions in the plane are again unimportant. The introduction of the out-of-plane interaction on the other hand, changes the spectrum completely, since it is this term which introduces the k_z-dependence through which the two-dimensional levels are spread.

In view of the small value of γ_1 required by our model, the neglect of exchange integrals between more remote neighbours in different planes seems justified.

Finally, as pointed out by CARTER and KRUMHANSL,[23] there is a small difference in the energy of two neighbouring atoms in a plane. This primarily produces a slight splitting of the $n = 0$ level, which is however too small to affect our conclusions.

In this approximation, the secular equation is:[8]

$$\begin{vmatrix} H_0-E & -\gamma_0 S & \gamma_1\Gamma & 0 \\ -\gamma_0 S^* & H_0-E & 0 & 0 \\ \gamma_1\Gamma & 0 & H_0-E & -\gamma_0 S^* \\ 0 & 0 & -\gamma_0 S & H_0-E \end{vmatrix} = 0. \quad (1.1)$$

The notation used is the same as that used in A except for the slightly different definition of $\boldsymbol{k}$. We shall measure energy from the points at which both S and Γ are zero; that is, from the corner of the Brillouin zone at the points $k_z = \pm\pi/c$. Again, we shall expand S about the corner of the zone and then replace k_x by $k_x + is(\partial/\partial k_y)$. (We are using the vector potential $A_x = -yH$, $A_y = A_z = 0$.) The resulting set of coupled equations is:

$$\beta D^- B_2 + \alpha B_3 = \epsilon B_1 \quad (1.2a)$$

$$\beta^{-1} D^+ B_1 = \epsilon B_2 \quad (1.2b)$$

$$\alpha B_1 + \beta^{-1} D^+ B_4 = \epsilon B_3 \quad (1.2c)$$

$$\beta D^- B_3 = \epsilon B_4 \quad (1.2d)$$

where:

$$\alpha = \frac{\gamma_1\Gamma}{\hbar v} = \frac{2\gamma_1}{\hbar v}\cos\left(\frac{k_z c}{2}\right)$$

$$\epsilon = \frac{E}{\hbar v}; \qquad \beta = e^{i\pi/3}$$

$$D^+ = k_y + i\left(k_x + is\frac{\partial}{\partial k_y}\right)$$

$$D^- = k_y - i\left(k_x + is\frac{\partial}{\partial k_y}\right).$$

The substitution $B_m = e^{ik_x k_y/s} b_m$ $(m = 1, 2, 3, 4)$ results in a considerable simplification. Eliminating b_2, b_3, and b_4, the equation for b_1 becomes:

$$[(\Omega^-\Omega^+ - \epsilon^2)(\Omega^+\Omega^- - \epsilon^2) - \epsilon^2\alpha^2]b_1 = 0 \quad (1.3)$$

where:

$$\Omega^+ = k_y + s\frac{\partial}{\partial k_y}$$

$$\Omega^- = k_y - s\frac{\partial}{\partial k_y}$$

But

$$\Omega^-\Omega^+ = -s^2\frac{\partial^2}{\partial k_y^2} + k_y^2 - s$$

and

$$\Omega^+\Omega^- = -s^2\frac{\partial^2}{\partial k_y^2} + k_y^2 + s.$$

Hence, putting

$$L = -s^2\frac{\partial^2}{\partial k_y^2} + k_y^2 - \epsilon^2,$$

(1.3) becomes:

$$(L^2 - \lambda^2)b_1 = 0 \qquad (1.4)$$

where:

$$\lambda^2 = s^2 + \epsilon^2\alpha^2.$$

It is easily seen that the only solutions of (1.4) which satisfy the regularity boundary conditions are φ and χ, which satisfy

$$(L-\lambda)\varphi = 0 \quad \text{and} \quad (L+\lambda)\chi = 0.$$

Now, $(L-\lambda)\varphi = 0$ leads to:

$$\epsilon^2 + (s^2+\alpha^2\epsilon^2)^{\frac{1}{2}} = (2p+1)s$$

(because of regularity of φ, $p = 0, 1, 2, \ldots$)

while $(L+\lambda)\chi = 0$ leads to:

$$\epsilon^2 - (s^2+\alpha^2\epsilon^2)^{\frac{1}{2}} = (2m+1)s$$

(because of regularity of χ, $m = 0, 1, 2, \ldots$).

It is easily checked that these two energy spectra are mutually exclusive when $\alpha \neq 0$. Solving each of these for the energy ϵ we find:

$$b_1 = \chi: \quad \epsilon^2 = \frac{\alpha^2}{2} + s(2m+1) + \left[\left(\frac{\alpha^2}{2}\right)^2 + \alpha^2 s(2m+1) + s^2\right]^{\frac{1}{2}}$$

$$b_1 = \varphi: \quad \epsilon^2 = \frac{\alpha^2}{2} + s(2p+1) - \left[\left(\frac{\alpha^2}{2}\right)^2 + \alpha^2 s(2p+1) + s^2\right]^{\frac{1}{2}}.$$

Thus, we find that the general, regular, non-trivial B_1 can be written

$$B_1 \sim \exp\left(\frac{ik_xk_y}{s}\right)\exp\left(-\frac{k_y^2}{2s}\right)H_n\left(\frac{k_y}{\sqrt{s}}\right) \times \times\delta(k_x - k'_x)\delta(k_z - k'_z).$$

The corresponding energy is:

$$\frac{E}{\hbar v} = \pm\left[\frac{\alpha^2}{2} + s(2n+1) \pm \left(\frac{\alpha^4}{4} + \alpha^2 s(2n+1) + s^2\right)^{\frac{1}{2}}\right]^{\frac{1}{2}}.$$

$$n = 0, 1, \ldots \qquad (1.5)$$

In order to determine whether or not we have missed any solutions, we have to go back to the original set of equations (1.2a, 1.2b, 1.2c, 1.2d). Making use of the fact that the various operators involved are the raising and lowering operators for oscillator functions, we find that the general solution is:

$$B_1 \sim H_n; \quad B_2 \sim H_{n-1}; \quad B_3 \sim H_n; \quad B_4 \sim H_{n+1}$$

(with the convention that $H_{-1} \equiv 0$).

The solution with $E = 0$ is:

$$B_1 \sim H_0; \quad B_2 = 0; \quad B_3 = 0; \quad B_4 \sim H_1.$$

It is, however, also possible to find another solution with energy zero, not included in the above set because in this case, $B_1 = 0$. The solution is:

$$B_1 = 0; \quad B_2 = 0; \quad B_3 = 0; \quad B_4 \sim H_0.$$

Let us now consider the limiting case of $\alpha = 0$. In this case, equation (1.5) becomes:

$$\frac{E}{\hbar v} = \pm(2ns)^{\frac{1}{2}} \qquad (1.6a)$$

or:

$$\frac{E}{\hbar v} = \pm(2(n+1)s)^{\frac{1}{2}}. \qquad (1.6b)$$

In addition to the $E = 0$ coming from $n = 0$ above, we have seen that there is also another $E = 0$ solution not included in the above relations.

We shall see that the degeneracy of each level (characterized by n and ± 1) is $2Vs/\pi c = qs/2$. Clearly, the energies arising from (1.6a) with $n \geqslant 1$ can be grouped with those from (1.6b) with $n \geqslant 0$. The result can then be written:

$$E = \pm \hbar v (2ns)^{\frac{1}{2}}. \tag{1.6c}$$

If the extra $E = 0$ level is included in (1.6c), the degeneracy of each level is just qs, in agreement with McCLURE's result.

We shall see later that we must choose a very small value of the interlayer exchange integral γ_1 if we wish to explain the experimentally observed susceptibility. The energy relation (1.5) is much too complicated for the calculation of the susceptibility, so that we want to expand equation (1.5) for small γ_1. Unfortunately, this cannot be done for an arbitrary s, since the condition for the validity of the expansion is:

$$\alpha^2 \ll s/(2n+1).$$

Our results will be meaningful only if we restrict ourselves to fields which satisfy this condition. We shall never be interested in high n values. Such an expansion can never be extrapolated to very small fields, but since susceptibility measurements usually involve a torsional technique, fields of several thousand gauss are generally employed. In this region, our expansion will be valid over the entire range of k_z.

The result for small γ_1 may be expressed in the following form:

$$E = \pm \hbar v (2ns)^{\frac{1}{2}} \left\{ 1 \pm \frac{\alpha^2}{4s} \right\}. \tag{1.7}$$

We have again grouped the levels, so that the degeneracy of each level (characterized by n and the external $\pm$ sign) is qs.

Note that the introduction of interplanar interaction has spread each level out into a narrow band of width $(\hbar v \alpha^2/2s)(2ns)^{\frac{1}{2}}$. Thus the levels become wider with increasing n values. The $n = 0$ level, however, has remained sharp. This result is independent of our approximation, and follows directly from equation (1.5). Note also, that the level width depends on the magnetic field and that all levels become sharp as the magnetic field becomes very large. This fact has an interesting consequence in the de Haas–Van Alphen effect.

Eventually, for the higher n values, the levels will overlap each other. However, the levels near the degeneracy point are discrete. For example, in a field of 10^4 gauss with $\gamma_1 \simeq 0{\cdot}005$ eV, the levels do not overlap until one reaches an energy of $0{\cdot}07$ eV. This occurs between the $n = 5$ and $n = 6$ levels.

2. APPROXIMATE CALCULATION OF THE SUSCEPTIBILITY AT HIGH TEMPERATURES

Let us now estimate the susceptibility in a manner analogous to McCLURE's estimate in the two-dimensional case. We shall simply calculate the energy gain of our system as the magnetic field is turned on. For this purpose we need only the general features of our energy spectrum as predicted by equation (1.5). In particular we note that the $n = 0$ level is sharp and that the spacing between this level and the two $n = 1$ levels is larger than the spacing between any other two adjacent levels. Furthermore, it will be shown that at high temperatures the Fermi level is very near the $n = 0$ level. It follows that most of the energy gain of the system is due to the electrons, which in the presence of the field, occupy the $n = 0$ level.

When the field is applied, there is room for qs electrons in the $n = 0$ level. The number of electrons in the $n = 0$ level is then $qsf(0)$ and the total energy of these electrons is zero. Before the field was applied, these electrons had energies between $-\Delta$ and $+\Delta$, the negative energy states being preferentially occupied. The total energy of these electrons was thus:

$$E = \int_{-\Delta}^{+\Delta} N(E) f(E) E \, dE \tag{2.1}$$

where $N(E)$ is the density of states in the absence of a magnetic field and is given by:

$$N(E) = \frac{2V}{\pi^2 c (\hbar v)^2} \left[(4\gamma_1^2 - E^2)^{\frac{1}{2}} + \right.$$

$$\left. + \pi |E| + 2E \sin^{-1}\left(\frac{E}{2\gamma_1} \right) \right] \qquad E < 2\gamma_1 \tag{2.2a}$$

$$= \frac{4V}{\pi c (\hbar v)^2} |E|. \qquad E > 2\gamma_1 \tag{2.2b}$$

Furthermore, Δ is determined by the condition:

$$\int_{-\Delta}^{+\Delta} N(E)f(E)\,dE = qsf(0). \qquad (2.3a)$$

At high temperatures, this condition simply becomes:

$$\int_{-\Delta}^{+\Delta} N(E)\,dE = qs. \qquad (2.3b)$$

We now consider two separate cases. First, let us choose a high value for γ_1, say $\gamma_1 \simeq 0{\cdot}1$ eV. Since the integrations in equations (2.1) and (2.3b) extend over an energy range of the order of the magnetic level spacing, all energies involved in the integrands will then satisfy the condition $E/\gamma_1 \ll 1$. Hence the $N(E)$ in question is given by (2.2a). In fact, we only require this relation for small E and hence we may expand in powers of E/γ_1. We find:

$$N(E) \simeq \frac{4V\gamma_1}{\pi^2 c(\hbar v)^2} + \frac{2V}{\pi c(\hbar v)^2}\cdot|E|. \qquad (2.4)$$

It is easily checked that under these circumstances

$$\Delta \simeq \frac{\pi(\hbar v)^2 s}{\gamma_1}. \qquad (2.5)$$

and that the increase in energy contains no term proportional to s^2. This result has a simple physical interpretation. We note that in the three-dimensional case the density of states in the absence of a field does not approach zero when the energy approaches zero. Instead, it approaches a value proportional to γ_1. Hence there are already some electrons whose energies are zero before the field is applied. In fact, there are too many of them. The result is that the energy of the system cannot be raised much through the application of the field since Δ becomes very small and advantage cannot be taken of the preferential occupation of the lower energy states.

It is clear what one has to do in order to retain a susceptibility in the three-dimensional case. We need to reduce the number of electrons whose energies are zero before the field is applied; that is, we need to reduce γ_1. It is easily shown that if $\gamma_1 < \hbar v\sqrt{(\pi s/2)}$, the susceptibility is just equal to that predicted by McClure for the two-dimensional case.

This simple argument does not depend on the detailed structure of the energy spectrum and is independent of any approximations. We are thus led to the conclusion that graphite is essentially two-dimensional in structure. We shall see that $\gamma_1 \simeq 0{\cdot}005$ eV is consistent with all the observed properties of graphite. An upper limit for $\gamma_1 \simeq 0{\cdot}01$ eV can be established in this way. This value is about twenty times smaller than that used in A. A theoretical estimate of γ_1 was made by Godin.[24] His value for γ_1 is 0·007 eV, but no other estimate of this order of magnitude seems to have appeared in the literature.

3. CALCULATION OF THE FREE ENERGY

In order to calculate the free energy of our system, we need to obtain the density of states in the presence of a magnetic field. We shall write:

$$g(E) = \sum_n g(E_n) \qquad (3.1)$$

where $g(E_n)$ is the density of states in the nth level and the sum extends over all levels which contribute at the energy E. For a general n, $g(E_n)$ is simply:

$$g(E_n) = \frac{8Vs}{4\pi^2}\cdot\frac{dk_z}{dE_n}. \qquad (3.2)$$

The factor of 8 accounts for the various degeneracies in graphite: spin degeneracy (a factor of 2) and site degeneracy (a factor of 4). The total number of states for each value of n and choice of sign is just:

$$\frac{8Vs}{4\pi^2}\times\frac{2\pi}{c} = \frac{4Vs}{\pi c} = qs. \qquad (3.3)$$

For the $n = 0$ level, which we have seen is always sharp, (3.2) is replaced simply by a δ-function. This level also contains qs states, exactly as in the two-dimensional case.

The above arguments are completely analogous to those made in the counting of states in the free electron case. This is a direct consequence of the form of our solutions $B_m(k)$. We note that k_x and k_z enter these solutions only parametrically. Thus the $\delta(k_x - k_x')$ and $\delta(k_z - k_z')$ factors lead to $e^{ik_x'x}$ and $e^{ik_z'z}$ in the spatial wave functions. Furthermore, the complex factor $e^{ik_xk_y/s}$ centres

the spatial wave function at $y = k_x'/s$. Thus we can apply cyclic boundary conditions in the x and z directions. Limiting y to lie within the crystal then limits k_z and hence equation (3.2) follows.

We shall now take for E_n:

$$E_n = \nu(ns)^{\frac{1}{2}}\left[1 \pm \frac{2\gamma_1^2 \cos^2(k_z c)/2}{\nu^2 s}\right]. \quad (3.4)$$

(cf. eqn. (1.7)

Evaluating dk_z/dE_n, it becomes convenient to introduce three new symbols. Let:

Minimum energy of nth level

$$= A_n = \nu(ns)^{\frac{1}{2}}[1-(2\gamma_1^2/\nu^2 s)]$$

Average energy of nth level

$$= C_n = \nu(ns)^{\frac{1}{2}}$$

Maximum energy of nth level

$$= B_n = \nu(ns)^{\frac{1}{2}}[1+(2\gamma_1^2/\nu^2 s)].$$

The resulting $g(E_n)$ may then be written:

$$g(E_n) = \frac{qs}{2\pi}[(E-A_n)(C_n-E)]^{-\frac{1}{2}} \qquad A_n \leqslant E \leqslant C_n \quad (3.5a)$$

$$= \frac{qs}{2\pi}[(B_n-E)(E-C_n)]^{\frac{1}{2}} \qquad C_n \leqslant E \leqslant B_n. \quad (3.5b)$$

We are now ready to evaluate the free energy. Following McClure, we write:

$$F = N\zeta + E_0 + \int_{-\infty}^{+\infty} dE\phi(E)\left[\frac{-\partial f}{\partial E}\right] \quad (3.6)$$

where:

$$N = N_{\text{total}} - \int_{E(0)}^{0} dx g(x) \quad (3.7)$$

$$E_0 = \int_{E(0)}^{0} dx \,.\, xg(x) \quad (3.8)$$

$$\phi(E) = \int_{0}^{E} dx(x-E)g(x). \quad (3.9)$$

Here $E(0)$ is the energy of the lowest state in the valence band and it is assumed that $\zeta - E(0) \gg kT$. We shall be primarily interested in $\phi(E)$ for $E \leqslant \zeta_0 \sim 0{\cdot}06$ eV. Since (3.4) involves the assumption that $2\gamma_1^2/\nu^2 s < 1$ it is easy to see that the magnetic energy levels corresponding to the first few n values do not overlap at all. Thus for $E < \zeta_0$ the integration in (3.9) never involves a sum over various n. Carrying out the integrals in $\phi(E)$, we find:

$$\phi(E) = qs\{-(m+\tfrac{1}{2})E + \tfrac{1}{4}\sum_{n=1}^{m}(A_n+B_n+2C_n)+\delta\}$$

$$= qs\{-(m+\tfrac{1}{2})E + \tfrac{1}{4}\sum_{n=1}^{m} 4C_n+\delta\}$$

$$= qs\{-(m+\tfrac{1}{2})E + \sum_{n=1}^{m}\nu(ns)^{\frac{1}{2}}+\delta\} \quad (3.10)$$

where: $m = \langle r^2 \rangle$ = maximum integer $\leqslant r^2 = E^2/\nu^2 s$. The term δ indicates the departure from the two-dimensional model. In general this term involves fractional contributions from several levels, but as long as the levels do not overlap ($E \lesssim 0{\cdot}07$ eV in fields $\gtrsim$ 10,000 gauss) δ will involve at most a fractional contribution from one level. In this case:

$$\delta = \frac{-1}{2\pi}\left\{[(B_m-E)(E-C_m)]^{\frac{1}{2}} + \frac{B_m+C_m-2E}{2}\left[\frac{\pi}{2}+\sin^{-1}\left(\frac{B_m+C_m-2E}{B_m-C_m}\right)\right]\right\}$$

$$C_m \leqslant E \leqslant B_m \quad (3.11a)$$

$$= 0 \qquad B_m \leqslant E \leqslant A_{m+1} \quad (3.11b)$$

$$= \frac{-1}{2\pi}\left\{[(C_{m+1}-E)(E-A_{m+1})]^{\frac{1}{2}} + \frac{A_{m+1}+C_{m+1}-2E}{2}\left[\frac{\pi}{2}+\sin^{-1}\left(\frac{A_{m+1}+C_{m+1}-2E}{A_{m+1}-C_{m+1}}\right)\right]\right\}.$$

$$A_{m+1} \leqslant E \leqslant C_{m+1} \quad (3.11c)$$

Our expression (3.10) is in agreement with McClure's result when $\delta = 0$. We shall see that δ is an unimportant correction for the high temperature susceptibility and for the average low temperature susceptibility. However, this term does play a role in the fluctuations of the susceptibility at low temperatures, where it serves to reduce the amplitudes of the oscillations and introduces an aperiodicity when plotted against the reciprocal of the magnetic field.

4. THE SHIFT OF THE FERMI LEVEL WITH TEMPERATURE

Before we go on to calculate the susceptibility at various temperatures, we will need to know the position of the Fermi surface at these temperatures. We shall now calculate this shift with temperature on the basis of a two-dimensional model. The error made in such a calculation is very small, since it is caused solely by the use of an approximate $N(E)$ relation in the region $0 \leqslant E \leqslant 2\gamma_1$. In general, we can have confidence in our result provided $\zeta(T) > 2\gamma_1$. As we shall see, this condition is satisfied up to a temperature of about 800°K.

The total number of electrons is given by:

$$N_0 = \int_{-\infty}^{+\infty} N(E) f(E)\, dE = \int_{-\infty}^{\zeta_0} N(E)\, dE \quad (4.1)$$

where

$$N(E) = \frac{4V|E|}{\pi c(\hbar v)^2}.$$

With the above density of states equation (4.1) can be re-written:

$$\int_{-\infty}^{0} E[1-f(E)]\, dE + \int_{0}^{\infty} Ef(E)\, dE = \frac{\zeta_0^2}{2}.$$

Writing $\theta = \dfrac{\zeta}{kT}$; $\theta_0 = \dfrac{\zeta_0}{kT}$, one finds:

$$\theta_0^2 = 2\theta \log\left[\frac{1+e^{\theta}}{1+e^{-\theta}}\right] - 3\theta^2 + 4\int_0^{\theta} \log(1+e^{x})\, dx. \quad (4.2)$$

This expression can be approximated for large and small θ.

$$\theta_0^2 \simeq \theta \log 16 \qquad \theta \ll 1 \quad (4.2a)$$

$$\theta_0^2 \simeq \theta^2 + \frac{\pi^2}{3}. \qquad \theta \gg 1 \quad (4.2b)$$

Choosing a value for ζ_0, one can plot ζ as a function of temperature using equation (4.2). This is done by giving θ a value and solving the equation for θ_0. If ζ_0 is assumed known, one thus finds ζ and T.

The results are plotted in Fig. 1 for two values of ζ_0. The shift of the Fermi level plays in our model an important role in the susceptibility of graphite. Without this variation with temperature one could not reconcile the high and the low temperature results.

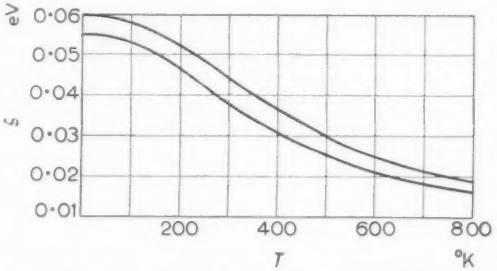

FIG. 1. The variation of the fermi level with temperature. The upper and lower curve corresponds to $\zeta_0 = 0{\cdot}06$ eV and $\zeta_0 = 0{\cdot}055$ eV respectively.

5. CALCULATION OF THE SUSCEPTIBILITY AND THE DE HAAS-VAN ALPHEN EFFECT

The magnetic moment and the susceptibility are defined in terms of the free energy by the following relations:

$$M = -\frac{\partial F}{\partial H} \quad (5.1)$$

$$\chi = -\frac{1}{H}\frac{\partial F}{\partial H} = \frac{M}{H}. \quad (5.2)$$

Our calculation of these quantities will thus be based on equation (3.6) and the additional relation (3.10). The correction term δ, which is a measure of the departure from the two-dimensional model is given by (3.11). However, this relation is far too complicated to be treated exactly.

At high temperatures this term need not be considered at all, since it does not contribute appreciably to the susceptibility. This can be seen as follows: At high temperatures the Fermi level is very near the $n = 0$ level (see Fig. 1). In this region the energy levels are very nearly sharp and the spacing between these levels is large. It follows that the correction term δ is primarily defined by (3.11b) and can be ignored completely. Thus at high temperatures the susceptibility is just equal to that calculated by McCLURE and is given by:

$$\chi = -0{\cdot}044qv^2\left(\frac{e}{hc}\right)^2\frac{1}{kT}\cdot\operatorname{sech}^2\left(\frac{\zeta}{2kT}\right). \quad (5.3)$$

Converted to e.m.u./g, (5.3) becomes ($\gamma_0 =$ 2.6 eV):

$$\chi = \frac{-0{\cdot}010}{T}\operatorname{sech}^2\left(\frac{\zeta}{2kT}\right)\text{e.m.u./g.} \quad (5.4)$$

The condition of the validity of this result is that the level splitting be small compared to the thermal energy, that is $kT > vs^{\frac{1}{2}}$. In a field of 10,000 gauss $vs^{\frac{1}{2}} \simeq 0{\cdot}03$ eV so that the relation (5.4) is valid at temperatures higher than about 400°K. McCLURE did not consider the variation of the Fermi level with temperature and simply replaced the $\operatorname{sech}^2(\zeta/2kT)$ factor by 1. Using the results of Section 4, we can now obtain the deviation of the high temperature susceptibility from a $1/T$ law. The results, together with the experimental curve are illustrated in Fig. 2.

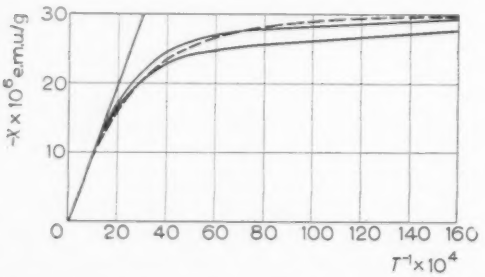

FIG. 2. The variation of the susceptibility with temperature. The dashed curve is taken from GANGULI and KRISHNAN. The two solid curves represent the theoretical variation of the susceptibility corresponding to $\zeta_0 = 0{\cdot}06$ eV and $\zeta_0 = 0{\cdot}055$ eV. The latter value results in slightly better agreement with experiment.

The dependence of the high temperature susceptibility on the Fermi level has been investigated by bromination of graphite.[15] These investigations show that as the bromine to carbon ratio is increased, the susceptibility first increases slightly and then decreases. This trend is in agreement with equation (5.4). The Br/C ratio which results in the maximum susceptibility is determined by the number of excess electrons originally in the conduction band. The number of these electrons implied by our model agrees well with the value of $1{\cdot}1\times10^{-4}$ per atom, estimated from the above experiment.[15]

At low temperatures there is no *a priori* reason why one can neglect the correction term δ. It will, however, be seen that even at low temperatures the average value of the susceptibility is not affected by this term. On the other hand, the fluctuations of the susceptibility are affected. Let us for the present deal with the two-dimensional model and consider the correction later. We thus choose for $\phi(E)$:

$$\phi(E) = qs\{\sum_{n=0}^{m} v(ns)^{\frac{1}{2}} - (m+\tfrac{1}{2})E\}. \quad (5.5)$$

Here m is the maximum integer $\leqslant E^2/v^2s$. The notation

$$\frac{E^2}{v^2s} = r^2 \qquad m = \langle r^2 \rangle$$

will be convenient. We shall now evaluate the sum involved in (5.5) by the Poisson summation formula.[25]

One form of this formula is:

$$\sum_{n=0}^{\infty} f(n) = \sum_{m=-\infty}^{+\infty} \int_0^{\infty} f(x)e^{2\pi imx}\,dx$$

where: (1) $f(x)$ is of bounded variation in the interval $(0, \infty)$ and $f(x) = 0 \qquad x < 0$

$$(2)\int_0^{\infty} f(x)\,dx \text{ exists}$$

(3) $f(x)$ is continuous at least near the points where x is an integer, i.e.

$$\tfrac{1}{2}[f(n_+)+f(n_-)] = f(n).$$

We see how we have to define $f(x)$ in our case. Let us introduce the stepfunction $P(x)$ defined by:

$$P(x) = 1 \qquad x < 0$$

$$P(x) = 0 \qquad x > 0.$$

Then we may define $f(x)$ to be:

$$f(x) = x^{\frac{1}{2}}P(-x)P(x-r^2). \tag{5.6}$$

With this definition, one clearly has:

$$\sum_{n=0}^{m} n^{\frac{1}{2}} = \sum_{n=0}^{\infty} f(n). \tag{5.7}$$

Just exactly where we "chop" the function between $\langle r^2\rangle$ and $\langle r^2\rangle+1$ is immaterial. By choosing the point to be r^2 we know that our result is exact provided r^2 is not an integer. In that case the continuity condition is not satisfied, but this clearly does not matter since these points coincide with the points of discontinuity of our original sum.

In this way we find:

$$\sum_{n=0}^{m} n^{\frac{1}{2}} = \sum_{m=-\infty}^{+\infty} \int_0^{r^2} x^{\frac{1}{2}} e^{2\pi i m x}\, dx$$

$$= \tfrac{2}{3}r^3 + r\sum_{m=1}^{\infty} \frac{\sin(2\pi m r^2)}{\pi m} -$$

$$\frac{1}{2\pi}\sum_{m=1}^{\infty} m^{-3/2} S(2rm^{\frac{1}{2}}) \tag{5.8}$$

where:

$$S(\varphi) = \int_0^{\phi} \sin\left(\frac{\pi}{2}t^2\right) dt.$$

We can now substitute (5.8) into (5.5). The result is:

$$\phi(E) = qvs^{3/2}\left(-\tfrac{1}{3}r^3 - \frac{1}{2\pi}\sum_{m=1}^{\infty} m^{-3/2} S(2rm^{\frac{1}{2}})\right). \tag{5.9}$$

We have made use of the relation

$$\sum_{m=1}^{\infty} \frac{\sin(2\pi m r^2)}{\pi m} = \langle r^2\rangle + \tfrac{1}{2} - r^2;$$

$$\langle r^2\rangle < r^2 < \langle r^2\rangle + 1.$$

Equation (5.9) is exact. For large energies $r \to \infty$, and

$$S(2rm^{\frac{1}{2}}) \to S(\infty) = \tfrac{1}{2}.$$

Thus in the limit of large energies, (5.9) becomes:

$$\phi(E) \simeq qvs^{3/2}\left[-\frac{1}{3}r^3 - \frac{1}{4\pi}\zeta\left(\frac{3}{2}\right)\right]$$

$$\simeq qvs^{3/2}\left[-\frac{1}{3}r^3 - 0{\cdot}208\right]. \tag{5.10}$$

Here ζ is the Riemann Zeta-function.

The above result agrees with McCLURE's equation (3.9). We note that of these two terms, the first is independent of the magnetic field and the second is independent of the energy. Hence the first term does not contribute to the susceptibility. One can easily verify that the term independent of the energy just cancels the part of E_0 which depends upon the magnetic field when integrated in (3.6). Again following McCLURE, we write

$$\psi(E) = \phi(E) + \tfrac{1}{3}q\frac{E^3}{v^2} + 0{\cdot}208qvs^{3/2}. \tag{5.11}$$

Neglecting the field dependence of ζ, the susceptibility is then given by:

$$\chi = -\frac{1}{H}\frac{\partial F}{\partial H} = -\frac{1}{H}\frac{\partial}{\partial H}(F - N\zeta)$$

$$= -\frac{1}{H}\frac{\partial}{\partial H}\int_{-\infty}^{+\infty} dE\,\psi(E)\left[-\frac{\partial f}{\partial E}\right]. \tag{5.12}$$

Since we are interested only in very low temperatures for the present, (5.12) simply becomes:

$$\chi = -\frac{1}{H}\frac{\partial}{\partial H}\psi(\zeta_0). \tag{5.13}$$

Here $\psi(E)$ is given by equation (5.11). We now anticipate where the Fermi surface will be at low temperatures. Thus our Hall effect results will show that $\zeta_0 \simeq 0{\cdot}06$ eV. Another estimate can be obtained from the period of the de Haas–Van Alphen effect fluctuations (cf. McCLURE). Thus in fields of the order of 10,000 gauss $r \sim 2$. We shall now expand $\psi(E)$ asymptotically for large r. This

asymptotic form of $\psi(E)$ will be completely adequate at $E = \zeta_0$. Thus

$$S(2rm^{\frac{1}{2}}) = \int_0^{2rm^{\frac{1}{2}}} \sin\left(\frac{\pi}{2}z^2\right) dz$$

$$= \frac{1}{2} - \int_{2rm^{\frac{1}{2}}}^{\infty} \sin\left(\frac{\pi}{2}z^2\right) dz$$

$$\simeq \frac{1}{2} - \frac{1}{2\pi} \frac{\cos(2\pi mr^2)}{(2\pi mr^2)^{\frac{1}{2}}}.$$

When this result is substituted into (5.11) one finds:

$$\psi(E) \simeq qvs^{3/2}\left[\frac{1}{4\pi^2 r} \sum_{m=1}^{\infty} \frac{\cos(2\pi mr^2)}{m^2}\right]. \quad (5.14)$$

It may be verified that $\psi(E)$ as given by (5.14) differs from the exact $\psi(E)$ defined by (5.11) and (5.5) by less than 1 per cent when $r \gtrsim 1/2$. Hence we are completely justified in using (5.14) at low temperatures even in large magnetic fields.

The magnetic moment and the susceptibility are now easily evaluated at low temperatures. Making use of the relation

$$\sum_{m=1}^{\infty} \frac{\cos(2\pi mr^2)}{\pi^2 m^2}$$

$$= \tfrac{1}{6} + [r^2 - \langle r^2\rangle] \cdot [r^2 - \langle r^2\rangle - 1]$$

$$\langle r^2\rangle < r^2 < \langle r^2\rangle + 1.$$

we find:

$$M = -\frac{q\zeta_0}{12}\left(\frac{e}{\hbar c}\right) r_0^{-2} - \frac{q\zeta_0}{2}\left(\frac{e}{\hbar c}\right) \times$$

$$\times \left\{\frac{\langle r_0^2\rangle}{r_0^2}\left[1 + \langle r_0^2\rangle\right] - \langle r_0^2\rangle - \tfrac{1}{2}\right\}. \quad (5.15)$$

The first factor in this relation is proportional to the magnetic field and yields the average value of the magnetic moment. The second factor, when plotted against the magnetic field, oscillates about zero. The oscillatory part of the magnetic moment is plotted against $r_0^{-2} = \nu^2 s/\zeta_0^2$ in Fig. 3. The observed behaviour is characteristic of a two-dimensional model and should be compared with the results of SEITZ[26] for free electrons. The susceptibility resulting from (5.15) is thus:

$$\chi = -\frac{qv^2}{12\zeta_0}\left(\frac{e}{\hbar c}\right)^2 - \frac{qv^2}{2\zeta_0}\left(\frac{e}{\hbar c}\right)^2 \times$$

$$\{\langle r_0^2\rangle[1 + \langle r_0^2\rangle] - r_0^2[\tfrac{1}{2} + \langle r_0^2\rangle]\}. \quad (5.16)$$

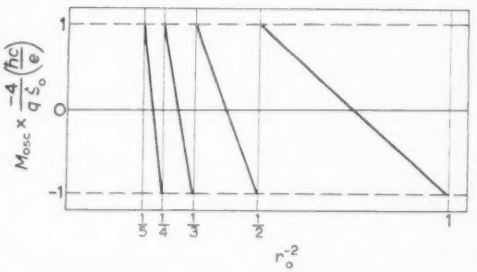

FIG. 3. Plot of the oscillatory part of the magnetic moment as a function of the magnetic field. The curve is based on a two-dimensional model.

The first factor in (5.16) is independent of the magnetic field and yields the average value of the low temperature susceptibility. The second factor is "periodic" in $1/H$ with period $(e/\hbar c) \cdot (\nu^2/\zeta_0^2)$. A plot of the oscillatory part of (5.16) is given in Fig. 4. Converting these quantities to e.m.u./g, we find:

$$\chi_{av} = -\frac{\frac{1}{6}qv^2}{12\zeta_0}\left(\frac{e}{\hbar c}\right)^2$$

$$\simeq -27{\cdot}2 \times 10^{-6} \text{ e.m.u./g.} \quad (5.17)$$

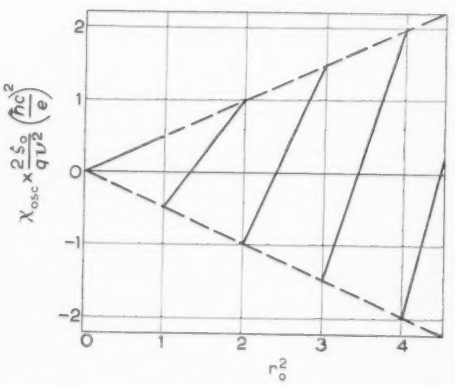

FIG. 4. The De Haas–Van Alphen effect in two-dimensional graphite.

We have chosen $\zeta_0 = 0{\cdot}06$ eV. χ_{av} would approach zero as suggested by McCLURE in the limit $r_0 \to \infty$; i.e. $\zeta_0 \to \infty$.

In order that the period of our oscillations agree with the average experimental period of $2{\cdot}15 \times 10^{-5}$ gauss^{-1}, we require $\zeta_0 \simeq 0{\cdot}065$ eV. On the other hand the theoretical amplitude of the oscillations is approximately 300×10^{-6} e.m.u./g in a field of 10^4 gauss. The experimentally observed amplitude is only $2\text{–}3 \times 10^{-6}$ e.m.u./g. [9,10] This discrepancy between theory and experiment will be discussed later.

The average value of the low temperature susceptibility is in good agreement with the reported experimental values, which range from -28×10^{-6} e.m.u./g to -34×10^{-6} e.m.u./g.[1,9,10]

LIFSHITZ and KOSEVICH[12] have developed a semi-classical theory of susceptibility. If their results are applied to two-dimensional graphite, one finds a period for the susceptibility fluctuations which is in agreement with our result. The oscillation amplitudes, however, are infinite in their approximation. We shall return to their results when we consider the introduction of the third dimension.

Before we go on to consider these three-dimensional effects, we shall calculate the temperature variation of the average susceptibility at low temperatures. We have already seen that at high temperatures the susceptibility is given by (5.4). In calculating the temperature dependence of the susceptibility at low temperatures we shall not be interested in the oscillatory part of the susceptibility. Hence we retain only that part of $\psi(E)$ which gives rise to the part of the magnetic moment which is proportional to H. In this case $\psi(E)$ simply becomes

$$\psi(E) = \frac{1}{24}\frac{qv^2s^2}{E}. \tag{5.18}$$

Actually $\psi(E)$ is a symmetric function of E, so that E should be replaced by $|E|$. (cf. McCLURE). However at low temperatures the contributions to χ from the $E < 0$ region are completely negligible because of the position of the Fermi level. Using (5.18), the expression (5.12) for the susceptibility becomes:

$$\chi \simeq -\frac{1}{48}\frac{qv^2}{kT}\left(\frac{e}{\hbar c}\right)^2 \int \frac{dE}{E}\,\mathrm{sech}^2\left(\frac{\zeta - E}{2kT}\right) \tag{5.19}$$

where the integral is taken over a range of the order of $3kT$ about $E = \zeta$.
Upon evaluation this yields:

$$\chi \simeq -\frac{1}{12}qv^2\left(\frac{e}{\hbar c}\right)^2 \frac{1}{\zeta}\left[1 - \frac{kT}{\zeta}\log 2\right]. \tag{5.20}$$

Or, converting to e.m.u./g,

$$\chi \simeq -\frac{1{\cdot}63}{\zeta} \times 10^{-6}\left[1 - \frac{kT}{\zeta}\log 2\right] \text{e.m.u./g} \tag{5.21}$$

where ζ, kT are measured in eV. The result, together with the variation at high temperatures, is plotted in Fig. 2. Expressions (5.20) and (5.21) are valid provided $kT < \zeta$. In Fig. 2, these expressions have been used between $T = 0°$K and $T = 200°$K.

We have seen that a two-dimensional model of graphite explains all the features of the susceptibility except the amplitude of the oscillations at low temperatures, which turn out to be 100–150 times too large. There are three main factors which serve to reduce this amplitude. These are:

(1) Introduction of k_z-dependence by a three-dimensional model. This clearly has the effect of broadening the energy levels in the presence of a magnetic field and hence reduces the amplitudes of the susceptibility fluctuations.

(2) Temperature damping of the oscillations at temperatures for which the thermal energy becomes greater than the level spacing.

(3) Collision damping of the levels. The effect of collisions is also to broaden the energy levels by an amount $\sim \hbar/\tau$ where τ is the relaxation time for electrons whose energies are near the Fermi energy.

The last two of these factors are unimportant at very low temperatures. We shall see later that the relaxation time in graphite at such temperatures is of the order of 10^{-11} seconds. If one uses this value for τ, and estimates the collision damping factor in the manner of DINGLE,[27] one finds that the amplitudes are only reduced by about 5 per cent by the collision process. Similarly, temperature damping can be made arbitrarily unimportant by going to sufficiently low temperatures. We will now study the three-dimensional model in order to attempt an explanation of this discrepancy.

The experiments on graphite show that the low temperature susceptibility does not display a strict

periodicity in $1/H$.[9,10] The pattern may be approximately resolved into two different periodicities, one with about 3/4 the period of the other. The period of $2{\cdot}15\times10^{-5}$ gauss^{-1} which was used in the two-dimensional model, is then interpreted as an average period.

It is interesting to apply the theory of ONSAGER[28] and of LIFSHITZ and KOSEVICH[12] to graphite. As we shall see, their theory, together with the usually assumed band structure, affords a very nice picture for the origin of the two periodicities found in graphite. Unfortunately, since this approach is based on Bohr–Sommerfeld quantization, one cannot have faith in the results when the theory is applied to graphite. We shall find important differences between such a semi-classical treatment and a treatment based on the results of Section 1 of this paper. Let us first outline the semi-classical approach.

The $E(\boldsymbol{k})$ relation near a corner of the Brillouin zone is given in A as:

$$E(\boldsymbol{k}) = -\gamma_1 \cos\left(\frac{k_z c}{2}\right) \pm \left[\gamma_1^2 \cos^2\left(\frac{k_z c}{2}\right) + (\hbar v K)^2\right]^{\frac{1}{2}}. \tag{5.22}$$

As before, $K = (k_x^2 + k_y^2)^{\frac{1}{2}}$ is measured from the corner of the zone, while k_z is measured from the half-way point on the vertical edge. The constant energy surfaces described by (5.22) are illustrated in Fig. 5. When $E < 2\gamma_1$ the surfaces are closed and capsule-shaped with the long axis parallel to the vertical edge of the zone. However, for $E > 2\gamma_1$ the surfaces become endless tubes of variable cross-section.

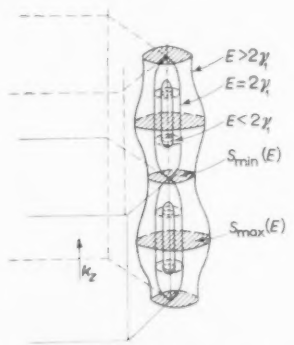

FIG. 5. The nature of the energy surfaces in graphite. Two Brillouin zones are shown. Actually 1/3 of the surfaces shown lies at each corner of the zone, resulting in a two-fold degeneracy of the illustrated surfaces, which have been pieced together for clarity.

Now consider a magnetic field to be applied along the c-axis in graphite. In the theory of LIFSHITZ and KOSEVICH[12] the periods of the susceptibility oscillations are then determined by the extreme cross-sectional areas of the planes $k_z =$ constant with the surface of constant energy for $E = \zeta$. It is clear that two different periods can only result if $\zeta > 2\gamma_1$, since otherwise the minimum cross-sectional area is zero and gives no periodicity. Applying (5.22) to the theory of LIFSHITZ and KOSEVICH we find:

$$S(E, k_z) = \frac{\pi E[E + 2\gamma_1 \cos(k_z c/2)]}{(\hbar v)^2} = 2\pi(n+\gamma)s. \qquad E \geqslant 2\gamma_1 \tag{5.23}$$

The maximum and minimum areas in question are thus:

$$S_{\text{ext}}(\zeta) = \frac{\pi\zeta[\zeta \pm 2\gamma_1]}{(\hbar v)^2}. \qquad \zeta \geq 2\gamma_1 \tag{5.24}$$

It is interesting to note what (5.23) predicts for the energy spectrum in the presence of a magnetic field. Solving for $E(n,H,k_z)$ we find:

$$E(n, H, k_z) = -\gamma_1 \cos\left(\frac{k_z c}{2}\right) \pm \left[\gamma_1^2 \cos^2\left(\frac{k_z c}{2}\right) + \nu^2 s(n+\gamma)\right]^{\frac{1}{2}}. \tag{5.25}$$

When $\gamma_1 = 0$ this relation gives the two-dimensional spectrum provided the parameter γ is chosen to be zero. However, if $\gamma_1 \neq 0$, this energy spectrum is radically different from that found in Section 1. When γ_1 is small, (5.25) predicts a width of $\sim 2\gamma_1$ for the higher n levels, independently of the magnetic field, while in our treatment the level width increases with n and depends on the magnetic field. We shall see later how this difference affects the de Haas–Van Alphen effect.

Since in the semi-classical treatment the periods of the low temperature susceptibility oscillations are completely determined by $S_{\text{ext}}(\zeta)$ a

knowledge of the two periods completely determines ζ_0 and γ_1. In this way we find:

$$\zeta_0 \simeq 0{\cdot}065 \text{ eV.} \qquad \frac{\zeta_0}{\gamma_1} \simeq 14.$$

The amplitudes of the oscillations may also be determined by an application of the formulae of LIFSHITZ and KOSEVICH. At $T = 1{\cdot}37°\text{K}$ an evaluation yields approximately 20×10^{-6} e.m.u./g for the amplitudes in a field of 10,000 gauss. This is a factor of about 10 larger than the observed amplitude.[9,10]

An exact calculation of the three-dimensional de Haas–Van Alphen effect is impractical because of the complex nature of the correction term δ in equation (3.10). We can however construct a simplified model by noting how the density of states varies within the nth level. We shall replace $g(E_n)$ defined by (3.5a) and (3.5b) by:

$$g(E_n) = qs[\tfrac{1}{4}\delta(E-A_n)+\tfrac{1}{4}\delta(E-B_n)+ +\tfrac{1}{2}\delta(E-C_n)]. \tag{5.26}$$

It is easily checked that this expression gives the correct degeneracy for the nth level, namely qs.

If (5.26) is used instead of (3.5a) and (3.5b), the correction term δ can be shown to be:

$$\delta = \frac{qs}{4}\Big[(2m-m'-m'')+ + \sum_{m}^{m'} A_n + \sum_{m''}^{m} B_n\Big] \tag{5.27}$$

where:

$$m = \langle r^2\rangle$$
$$m' = \langle r^2(1-\Delta)^{-2}\rangle \qquad \Delta = \frac{2\gamma_1^2}{\nu^2 s}$$
$$m' = \langle r^2(1+\Delta)^{-2}\rangle.$$

It is a straightforward matter to calculate the contribution of (5.27) to the low temperature susceptibility. The calculation is analogous to the two-dimensional model calculation carried out earlier. In calculating the derivative with respect to H, it is not necessary to differentiate the various $(1\pm\Delta)$ factors, since these vary very slowly with H. The result is that to the oscillatory part of χ in (5.16) one must add the following term:

$$-\frac{q\nu^2}{8\zeta_0}\left(\frac{e}{\hbar c}\right)^2\left\{r_0^2\left[2\langle r_0^2\rangle-\left\langle\frac{r_0^2}{(1+\Delta)^2}\right\rangle-\left\langle\frac{r_0^2}{(1-\Delta)^2}\right\rangle\right]-2\langle r_0^2\rangle^2+(1+\Delta)^2\left\langle\frac{r_0^2}{(1+\Delta)^2}\right\rangle^2+ +(1-\Delta)^2\left\langle\frac{r_0^2}{(1-\Delta)^2}\right\rangle^2-2\langle r_0^2\rangle+(1+\Delta)^2\left\langle\frac{r_0^2}{(1+\Delta)^2}\right\rangle+(1-\Delta)^2\left\langle\frac{r_0^2}{(1-\Delta)^2}\right\rangle\right\}. \tag{5.28}$$

Fig. 6 shows the de Haas–Van Alphen effect as calculated from this simplified three-dimensional model. In plotting the result Δ has been chosen to be $0{\cdot}014r_0^2$, which corresponds to $\gamma_1 \simeq 0{\cdot}005$ eV and $\zeta_0 \simeq 0{\cdot}06$ eV. It can be seen that the simple periodicity in $1/H$ has been destroyed. Semi-classically this pattern was interpreted in terms of two slightly different periods, both however, strictly periodic in $1/H$. The amplitudes of the oscillations have been reduced by a factor of two or so at 10,000 gauss. They are however still far too large to be in agreement with experiment.

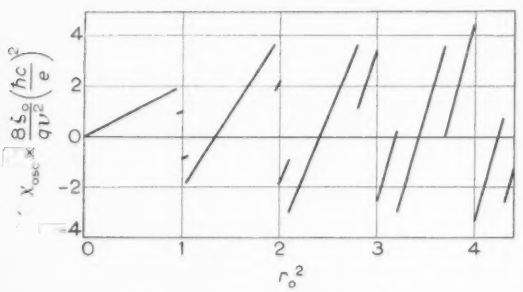

FIG. 6. The De Haas–Van Alphen effect in three-dimensional graphite.

Perhaps the most significant feature of the three-dimensional calculation is the behaviour in very large magnetic fields ($r_0^2 < 1$). Our calculation indicates that in these fields graphite will not display what looks like two periods. Instead, the oscillations will be strictly periodic in $1/H$, the period being just that predicted by the two-dimensional model. The semi-classical treatment on the other hand, predicts two periods regardless of the magnetic field. This result is independent of our simplifying assumptions and follows directly from

the fact that the energy levels become sharp in very large magnetic fields (cf. equation 1.7).

It seems possible that this difference could be investigated experimentally by the recently developed pulsed field technique. A careful analysis of the oscillations may be required, since the difference between these two predictions is not apparent on every half-cycle.

6. THE ELECTRICAL CONDUCTIVITIES OF GRAPHITE

Let us now evaluate the electrical conductivities of graphite parallel and perpendicular to the graphite planes. We shall assume that τ does not depend significantly on $\boldsymbol{k}$.

Following A, we have for the conductivity in the direction of the unit vector $\boldsymbol{u}$:

$$\sigma(\boldsymbol{u}) = -\frac{2e^2\tau}{h^2}\int \frac{df_0}{dE}\Big[\int_{E=\text{const.}} (\boldsymbol{u}\,.\,\boldsymbol{n})^2|\text{grad}_k E|\, dS_k\Big]\, dE \tag{6.1}$$

where the inner integral is taken over a surface of constant energy, and $n\, dS_k$ is the vector element of area on this surface.

For our $E(\boldsymbol{k})$ relation, we shall use equation (5.22), which is valid provided $E \ll \gamma_0 \simeq 2{\cdot}6$ eV.

The integral in (6.1) is easily transformed into an integral over K and an integral over E, by projecting the surface of constant energy onto the plane $k_z = 0$. A factor of 4 is introduced because of the equivalence of the six corners of the Brillouin zone, and because of the two projections onto the plane $k_z = 0$ coming from above and below this plane.

When u is chosen in the graphite plane and perpendicular to it, we find respectively:

$$\sigma_{\parallel} = -\frac{e^2\tau}{2\pi h^2}\int \frac{df_0}{dE}\Big[\int \frac{(\partial E/dK)^2}{(\partial E/\partial k_z)}\,.\,8\pi K\, dK\Big]\, dE \tag{6.2}$$

$$\sigma_{\perp} = -\frac{2e^2\tau}{2\pi h^2}\int \frac{df_0}{dE}\Big[\int \left(\frac{\partial E}{\partial k_z}\right) 8\pi K\, dK\Big]\, dE. \tag{6.3}$$

Let us now look at the range of the inner integral. As long as we are dealing with low temperatures, df_0/dE will be a sharply peaked function at $E = \zeta$, which is much greater than $2\gamma_1$. From (5.22), it follows that the constant energy surfaces for $E > 2\gamma_1$ are open endless tubes of variable cross-section. Hence, the range of K is:

$$\frac{1}{\hbar v}\cdot(E^2-2\gamma_1 E)^{\frac{1}{2}} \leqslant K \leqslant \frac{1}{\hbar v}\cdot(E^2+2\gamma_1 E)^{\frac{1}{2}}.$$

However, for higher temperatures df_0/dE is not sufficiently peaked to exclude the contributions to the conductivity from $E < 2\gamma_1$. We then write:

$$\frac{-2\pi h^2\sigma_{\parallel}}{e^2\tau} = \int_{-\infty}^{-2\gamma_1} f_0' C_1(E)\, dE + \int_{-2\gamma_1}^{0} f_0' C_2(E)\, dE + \int_{0}^{2\gamma_1} f_0' C_3(E)\, dE + \int_{2\gamma_1}^{\infty} f_0' C_4(E)\, dE \tag{6.4}$$

$$\frac{-2\pi h^2\sigma_{\perp}}{2e^2\tau} = \int_{-\infty}^{-2\gamma_1} f_0' D_1(E)\, dE + \int_{-2\gamma_1}^{0} f_0' D_2(E)\, dE + \int_{0}^{2\gamma_1} f_0' D_3(E)\, dE + \int_{2\gamma_1}^{\infty} f_0' D_4(E)\, dE \tag{6.5}$$

where $C_l(E)$, $D_l(E)$ stand for the inner integrals in (6.2) and (6.3) respectively, with the proper range of integration in each case.

Because of the simplification of (6.4) and (6.5) at very low temperatures, the zero temperature conductivities are easily evaluated.
We find:

$$\sigma_{\parallel}(0) = \frac{8\pi e^2\tau}{h^2 c}\cdot\zeta_0 \tag{6.6}$$

$$\sigma_{\perp}(0) = \frac{2\pi e^2\tau}{h^2}\cdot\frac{\gamma_1^2 c}{(\hbar v)^2}\cdot\zeta_0. \tag{6.7}$$

And hence:

$$\frac{\sigma_{\parallel}(0)}{\sigma_{\perp}(0)} = \frac{4(\hbar v)^2}{c^2\gamma_1^2} \tag{6.8}$$

With $a = 2{\cdot}46\text{A}^0$, $c = 6{\cdot}74\text{A}^0$, $\gamma_0 = 2{\cdot}5$ eV, $\gamma_1 = 0{\cdot}005$ eV we find:

$$\frac{\sigma_{\parallel}(0)}{\sigma_{\perp}(0)} = 10^5. \tag{6.9}$$

KRISHNAN and GANGULI[16] found a ratio of about 10^5. DUTTA[17] reports a ratio of between 10^4 and 10^5, while PRIMAK and FUCHS[18] report a considerably lower ratio. The experiment is however a difficult one, and it is easy, because of the large anisotropy, to underestimate the ratio of $\sigma_{11}/\sigma_{\perp}$, while it seems impossible to get too large a value in any experiment. This has been pointed out by MROZOWSKI.[13]

We now proceed to the evaluation of the two principal conductivities for arbitrary temperature. The inner integrals in equations (6.4) and (6.5) can all be done analytically. The final results can be written in the following form:

$$\sigma_{\parallel}(T) = \frac{4e^2\tau}{h^2}\cdot\frac{\gamma_1^2}{c(kT)}\int_{-\infty}^{+\infty}\operatorname{sech}^2\left[\frac{x-\zeta/\gamma_1}{2kT/\gamma_1}\right]F(x)\,dx \tag{6.10}$$

where

$$F(x) = x\left\{\frac{\pi}{2}+\sin^{-1}\left(\frac{x}{2}\right)-\frac{x}{2(1-x^2)^{\frac{1}{2}}}\cdot\log\left[\frac{((4-x^2)(1-x^2))^{\frac{1}{2}}+2-x^2}{x}\right]\right\} \qquad 0 \leqslant x \leqslant 1$$

$$= \frac{2\pi}{3}-\frac{\sqrt{3}}{2} \qquad x = 1$$

$$= x\left\{\frac{\pi}{2}+\sin^{-1}\left(\frac{x}{2}\right)-\frac{x}{2(x^2-1)^{\frac{1}{2}}}\cdot\left[\frac{\pi}{2}-\sin^{-1}\left(\frac{2-x^2}{x}\right)\right]\right\} \qquad 1 \leqslant x \leqslant 2$$

$$= x\left\{\pi-\frac{\pi}{2}\cdot\frac{x}{(x^2-1)^{\frac{1}{2}}}\right\} \qquad x \geqslant 2$$

($F(x)$ is symmetric about $x = 0$).

$$\sigma_{\perp}(T) = \frac{e^2\tau c}{2h^2}\cdot\frac{\gamma_1^4}{(kT)(\hbar v)^2}\int_{-\infty}^{+\infty}\operatorname{sech}^2\left[\frac{x-\zeta/\gamma_1}{2kT/\gamma_1}\right]G(x)\,dx \tag{6.11}$$

where

$$G(x) = x^2\left\{-(4-x^2)^{\frac{1}{2}}+2x\left[\frac{\pi}{2}+\sin^{-1}\left(\frac{x}{2}\right)\right]+2(1-x^2)^{\frac{1}{2}}\cdot\log\left[\frac{((4-x^2)(1-x^2))^{\frac{1}{2}}+2-x^2}{x}\right]\right\} \quad 0 \leqslant x < 1$$

$$= \frac{4\pi}{3}-\sqrt{3} \qquad x = 1$$

$$= x^2\left\{-(4-x^2)^{\frac{1}{2}}+2x\left[\frac{\pi}{2}+\sin^{-1}\left(\frac{x}{2}\right)\right]-2(x^2-1)^{\frac{1}{2}}\cdot\left[\frac{\pi}{2}-\sin^{-1}\left(\frac{2-x^2}{x}\right)\right]\right\} \qquad 1 < x < 2$$

$$= x^2\{2\pi x-2\pi(x^2-1)^{\frac{1}{2}}\}. \qquad x \geqslant 2$$

($G(x)$ is symmetric about $x = 0$).

Equations (6.10) and (6.11) can now be evaluated numerically for any temperature. This is done as follows: $F(x)$ and $G(x)$ are evaluated once and for all, for the entire range of x required. Then T, γ_1 and $\zeta(T)$ are chosen (the latter from Fig. 1) and the integral can be evaluated by any of the standard approximate methods.

A numerical evaluation shows that the ratio $\sigma_\parallel(T)/\sigma_\perp(T)$ is almost independent of temperature between 0°K and 600°K.

$$\frac{\sigma_\parallel(T)}{\sigma_\perp(T)} \simeq \frac{\sigma_\parallel(0)}{\sigma_\perp(0)} = 10^5. \qquad (6.12)$$

Experimentally, DUTTA[17] reports a variation by a factor of ~ 2 over this range.

Thus, our results show that $\sigma_\parallel$ and $\sigma_\perp$ exhibit the same temperature dependence (within about 1 or 2 per cent). Agreement with experiment could of course be obtained by attributing *different* temperature dependences to the two relaxation times parallel and perpendicular to the two graphite planes. However, such an assignment implies that τ is $\boldsymbol{k}$-dependent and thus violates our original assumption. It is reasonable to suppose that in graphite the relaxation time is indeed a markedly anisotropic function of $\boldsymbol{k}$. Until more is known about the relaxation time, it does not seem profitable to extend this simple calculation.

An approximation which is sometimes made, is that τ depends on $\boldsymbol{k}$ through the energy only. In this case, τ factors outside the inner integrals in equations (6.2) and (6.3), since these are integrals over constant energy surfaces. Then, at low temperatures, the ratio of $\sigma_\parallel/\sigma_\perp$ is independent of τ, since the outer integrations in equations (6.2) and (6.3) will involve a δ-function. At higher temperatures, the ratio $\sigma_\parallel/\sigma_\perp$ will however depend on τ even in this approximation.

We conclude that the low temperature value of $\sigma_\parallel/\sigma_\perp$ predicted by our choice of γ_0, γ_1 and ζ_0 can probably be trusted and is in fair agreement with experiment.

7. THE HALL COEFFICIENT IN GRAPHITE

Let us now evaluate the zero field Hall coefficient for graphite. To do this, we shall use the same approximation as was used in the conductivity calculation, namely that τ is independent of $\boldsymbol{k}$. Again we shall find that at low temperatures, our result will be independent of τ, if τ is a function of energy only, and not a general function of $\boldsymbol{k}$.

When the magnetic field H lies along the z-axis (in our case, the c-axis in graphite), the general formula for the zero field Hall coefficient is.[29]

$$A_{H\to 0} = \frac{-8\pi^3}{2e}\frac{\int\left[\frac{\partial E}{\partial k_y}\left(\frac{\partial^2 E}{\partial k_x^2}\right)-\frac{\partial E}{\partial k_x}\left(\frac{\partial^2 E}{\partial k_x \partial k_y}\right)\right]\cdot\frac{\partial E}{\partial k_y}\cdot\frac{df_0}{dE}\cdot d^3k}{\int\left(\frac{\partial E}{\partial k_x}\right)^2\frac{df_0}{dE}d^3k\cdot\int\left(\frac{\partial E}{\partial k_y}\right)^2\frac{df_0}{dE}d^3k} \qquad (7.1)$$

Using the $E(\mathbf{k})$ relation given by (5.22), and a procedure analagous to that used in calculating the electrical conductivities, equation (7.1) can be transformed to:

$$A_{H\to 0} = \frac{-\pi^2}{e} \frac{\int \frac{df_0}{dE}\left[\int \left(\frac{\partial E}{\partial K}\right)^3 \frac{dK}{(\partial E/\partial k_z)}\right] dE}{\left\{\int \frac{df_0}{dE}\left[\int \left(\frac{\partial E}{\partial K}\right)^2 \frac{K\,dK}{(\partial E/\partial k_z)}\right] dE\right\}^2}. \tag{7.2}$$

As in the case of the conductivity, these integrals are easily evaluated at very low temperatures, because of our assumption that $\zeta_c \simeq 0{\cdot}06$ eV $\gg \gamma_1 \simeq 0{\cdot}005$ eV. The result for the zero field Hall coefficient at absolute zero of temperature is:

$$\underset{H\to 0}{A(0)} = -\frac{\pi c(\hbar v)^2}{2e\zeta_0^2} \simeq -0{\cdot}705 \frac{\text{cm}^3}{\text{C}}. \tag{7.3}$$

The numerical value is obtained if we use:

$$a = 2{\cdot}46 \text{ Å}; \quad c = 6{\cdot}74 \text{ Å}; \quad \gamma_0 = 2{\cdot}5 \text{ eV}; \quad \zeta_0 = 0{\cdot}06 \text{ eV}.$$

KINCHIN[30] has measured the zero field Hall coefficient for a single crystal of graphite, and reports a value of $-0{\cdot}69$ cm^3/C at very low temperatures, in good agreement with that predicted by equation (7.3).

In the general case of arbitrary temperature, the outer integrals in (7.2) must again be done numerically. One can transform equation (7.2) into:

$$\underset{H\to 0}{A(T)} = -\frac{\pi^2}{2e} \cdot \frac{(\hbar v)^2 c(kT)}{\gamma_1^2} \cdot \frac{\int_{-\infty}^{+\infty} \text{sech}^2\left[\frac{x-\zeta/\gamma_1}{2kT/\gamma_1}\right] K(x)\,dx}{\left\{\int_{-\infty}^{+\infty} \text{sech}^2\left[\frac{x-\zeta/\gamma_1}{2kT/\gamma_1}\right] F(x)\,dx\right\}^2} \tag{7.4}$$

where

$$K(x) = -\frac{x(4-x^2)^{\frac{1}{2}}}{1-x^2} + \frac{x(2-x^2)}{(1-x^2)^{3/2}} \cdot \log\left[\frac{((4-x^2)(1-x^2))^{\frac{1}{2}}+2-x^2}{x}\right] \qquad 0 \leqslant x \leqslant 1$$

$$= \sqrt{3} \qquad x = 1$$

$$= \frac{+x(4-x^2)^{\frac{1}{2}}}{x^2-1} - \frac{x(2-x^2)}{(x^2-1)^{3/2}} \cdot \left[\frac{\pi}{2} - \sin^{-1}\left(\frac{2-x^2}{x}\right)\right] \qquad 1 \leqslant x \leqslant 2$$

$$= \frac{\pi x(x^2-2)}{(x^2-1)^{3/2}} \qquad x \geqslant 2$$

($K(x)$ is antisymmetric about $x = 0$).

and $F(x)$ is defined by (6.10).

A numerical evaluation of $A(T)$ yields Fig. 7. Basically, the behaviour of the Hall coefficient is

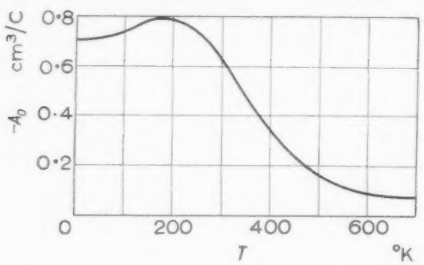

FIG. 7. The variation of the Hall coefficient with temperature.

due to the shift of the Fermi level with temperature. As the temperature is raised, the Fermi level moves towards the degeneracy point, and hence more and more positive carriers contribute. However, there will always be an excess of negative carriers, and hence the Hall coefficient approaches zero for high temperatures but remains negative. The peculiar behaviour of the Hall coefficient between 100°K and 300°K is due to the numerator of equation (7.4). This integral has a maximum value in this temperature range, which results in a Hall coefficient slightly lower than the zero temperature value.

The various experimental investigations of the Hall coefficient have led to rather widely varying results.[10,30,31] Our low temperature value agrees with a reasonable extrapolation of the results of KINCHIN, while the trend we predict at high temperatures seems in agreement with all relevant measurements. On the other hand, SOULE[31] gets very much larger values than those obtained by other investigators at low temperatures and high fields. He also gets a small *positive* Hall coefficient for fields less than one kilogauss at 4·2°K. These results are in definite disagreement with the predictions of our model.

8. THE TRANSVERSE MAGNETO-RESISTANCE IN GRAPHITE

Finally, we calculate the transverse magneto-resistance, the magnetic field being applied along the c-axis of graphite. If we again make our previous assumptions about τ, we will find that the ratio $\Delta\rho/\rho$ is proportional to τ^2. Thus, comparison with experiment will, at best, predict a relaxation time τ.

Following JONES and ZENER,[29] we write for the ratio of the change in resistivity to the resistivity:

$$\frac{\Delta\rho}{\rho} = \left(\frac{eH\tau}{\hbar^2 c}\right)^2 . \frac{I_3}{I_1 . I_2} \tag{8.1}$$

where

$$I_1 = -\int \frac{df_0}{dE}\left(\frac{\partial E}{\partial k_x}\right)^2 d^3k$$

$$I_2 = -\int \frac{df_0}{dE}\left(\frac{\partial E}{\partial k_y}\right)^2 d^3k$$

$$I_3 = \int \frac{df_0}{dE}\left(\frac{\partial E}{\partial k_y}\right)\Omega\frac{\partial E}{\partial k_x}\,d^3k \,.\int \frac{df_0}{\partial E}\left(\frac{\partial E}{\partial k_x}\right)\Omega\frac{\partial E}{\partial k_y}\,d^3k - \int \frac{df_0}{dE}\left(\frac{\partial E}{\partial k_y}\right)^2 d^3k \,.\int \frac{df_0}{dE}\left(\frac{\partial E}{\partial k_x}\right)\Omega^2\frac{\partial E}{\partial k_x}\,d^3k$$

$$\Omega = \left(\frac{\partial E}{\partial k_y}\right)\frac{\partial}{\partial k_x} - \left(\frac{\partial E}{\partial k_x}\right)\frac{\partial}{\partial k_y}.$$

The transformation of these integrals into integrals over $K = [k_x^2 + k_y^2]^{\frac{1}{2}}$ is straightforward but tedious. At low temperatures, where the derivative of the Fermi distribution is sharply peaked at $E = \zeta_0$, we find:

$$\frac{I_3}{I_1 . I_2} = \frac{-\left[\int \left(\frac{\partial E}{\partial K}\right)^3 \frac{dK}{|\partial E/\partial k_z|}\right]^2 + \int \left(\frac{\partial E}{\partial K}\right)^2 \frac{K\,dK}{|\partial E/\partial k_z|} \cdot \int \left(\frac{\partial E}{\partial K}\right)^4 \frac{dK}{K|\partial E/\partial k_z|}}{\left[\int \left(\frac{\partial E}{\partial K}\right)^2 \frac{K\,dK}{|\partial E/\partial k_z|}\right]^2}. \tag{8.2}$$

Under the assumption that $\zeta_0 > 2\gamma_1$, the integrals have the range $\hbar vK = (\zeta_0^2 - 2\gamma_1\zeta_0)^{\frac{1}{2}}$ to $\hbar vK = (\zeta_0^2 + 2\gamma_1\zeta_0)^{\frac{1}{2}}$. The integrals are easily evaluated in a power series of γ_1^2/ζ_0^2. To the lowest non-zero order we find:

$$\frac{\Delta\rho}{\rho} = \left(\frac{eH\tau}{\hbar^2 c}\right)^2 \cdot \frac{(\hbar v)^4 \gamma_1^2}{2\zeta_0^4}. \qquad (8.3)$$

This result may now be compared with the experiments of KINCHIN.[30] Using the various values of $\Delta\rho/\rho$ and H given in KINCHIN's paper and our previous choice of parameters γ_0, γ_1, ζ_0 equation (8.3) predicts:

$$\tau \simeq 4-6\times 10^{-11} \text{ sec.} \qquad (T = 4.2°\text{K})$$

GALT *et al.*[32] report a relaxation time of approximately 10^{-11} sec, using the cyclotron resonance technique. Thus, agreement seems very satisfactory. We shall discuss the cyclotron resonance result a little more fully in the conclusions.

SUMMARY AND CONCLUSIONS

The basis for our model of graphite is a small interplanar interaction plus a certain number of excess electrons. Perhaps the most striking feature of this model is its simplicity. Only three parameters are incorporated in it (γ_0, γ_1, and ζ_0), yet the basic features of most of the properties of graphite in external fields are explained. The most unsatisfactory result is obtained for the amplitudes of the de Haas–Van Alphen effect fluctuations, which turn out to be far too large even when estimated from a simplified three-dimensional model. It may be argued that if the density of states within the nth level had not been replaced by the sum of three δ-functions, the amplitudes would have been further reduced. Although some reduction of the amplitudes would occur, the major source of the trouble lies elsewhere. As long as the magnetic energy levels are narrow as compared to their spacing, large fluctuations (and discontinuities) will occur. We must conclude that there is some other source of level broadening, which we have not considered. The fact that the observed oscillations are smaller than the theoretically predicted ones is in line with what has been found to be the case in many other substances. In Li, Na, Cu, Ag and Au for example, no oscillations have yet been observed, although theoretically one has reason to expect them. These difficulties are discussed in a very illuminating article by CHAMBERS.[33]

The form of the energy relations we have used were derived within the framework of the tight binding approximation. However, SLONCZEWSKI[34] has shown that the same form for these relations can also be obtained by group theoretical methods. It therefore seems improbable that the difficulties with the susceptibility oscillations have their origin in this approximation.

We have calculated the magneto-resistance to order H^2 only. An exact calculation, which leads to a saturation factor, is possible for graphite. However, since such a calculation is based on the Boltzmann equation, one can have confidence in the results only for magnetic fields which are small enough so that quantum effects are unimportant. In graphite, the condition for the validity of the Boltzmann equation is that $sv^2\tau/2\hbar\zeta \ll 1$. At low temperatures this condition breaks down at fields between 1000 and 10,000 gauss.

Finally, we have stated that our magneto-resistance result corresponds to a value of the relaxation time which is in fair agreement with the value found by GALT *et al.*[32] by cyclotron resonance. Cyclotron resonance results seem to indicate the presence of positive carriers. In their publication GALT *et al.* state that the presence of these carriers is uncertain, since a similar effect is under certain circumstances observed due to extremely eccentric energy surfaces.[35] In a recent private communication with one of us (P.R.W.), GALT expressed the view that positive carriers are almost certainly present and that the relaxation time is probably as long as 10^{-9} seconds. If these more recent findings are correct, they are difficult to reconcile with our model because of the position of the Fermi surface.

It may be that the reduction in the absorption near $H = 0$ is a magneto-resistance effect. CHAMBERS[36] has proposed that such an effect exists in bismuth. If our model of excess electrons is correct, then bismuth and graphite should behave quite similarly, that is, graphite should behave more like a poor metal than a semiconductor, and hence CHAMBER's explanation may also apply to graphite. Further investigation is necessary

before these differences can be understood. In this connection, the previously mentioned measurement of the de Haas–Van Alphen effect would be of interest, since such an experiment would test the general features of our model.

Acknowledgements—The financial assistance of the National Research Council of Canada in the form of a research grant to one of us (P.R.W.) and in the form of a studentship to the other is gratefully acknowledged.

REFERENCES

1. Ganguli N. and Krishnan K. S. *Proc. Roy. Soc.* A **177,** 168 (1941).
2. Hove J. E. *Phys. Rev.* **100,** 645 (1955).
3. McClure J. W. *Phys. Rev.* **104,** 666 (1956).
4. Peierls R. *Z. Phys.* **80,** 763 (1953).
5. Wilson A. H. *Proc. Camb. Phil. Soc.* **49,** 292 (1953).
6. Adams E. N. *Phys. Rev.* **89,** 633 (1953).
7. Luttinger J. M. and Kohn W. *Phys. Rev.* **97,** 869 (1955).
8. Wallace P. R. *Phys. Rev.* **71,** 622 (1947). (This reference is referred to as *A* in the text.)
9. Schoenberg D. *Trans. Roy. Soc.* **245,** 1 (1952).
10. Berlincourt T. G. and Steele M. G. *Phys. Rev.* **98,** 956 (1955).
11. Coulson C. A. and Taylor R. *Proc. Phys. Soc.* A **65,** 815 (1952).
12. Lifshitz I. M. and Kosevich A. M. *J. Exp. Theor. Phys.* **2,** 636 (1956).
13. Mrozowski S. *Phys. Rev.* **85,** 609 (1952).
14. Hennig, G. R., and Hove J. E. *Proceedings of the International Conference on the peaceful uses of Atomic Energy, Geneva, Switzerland* Vol. 7, Sec. 138, p. 666. Columbia University Press, N.Y. (1956).
15. Hennig G. R. and McClelland J. D. *J. Chem. Phys.* **23,** 1431 (1955).
16. Krishnan K. S. and Ganguli N. *Nature, Lond.* **144,** 667 (1939).
17. Dutta A. K. *Phys. Rev.* **90,** 187 (1953).
18. Primak W. and Fuchs L. H. *Phys. Rev.* **95,** 24 (1954).
19. Löwdin P. O. *J. Chem. Phys.* **18,** 365 (1950).
20. Luttinger J. M. *Phys. Rev.* **84,** 814 (1951).
21. Haering R. R. Ph.D. Thesis, McGill University (1957).
22. Hove J. E. *Phys. Rev.* **97,** 1717 (1955).
23. Carter J. L. and Krumhansl J. A. *J. Chem. Phys.* **21,** 2238 (1953).
24. Godin G. M.Sc. Thesis, McGill University (1955) unpublished.
25. Titchmarsh E. C. *Introduction to the Theory of Fourier Integrals* p. 60. Clarendon Press, Oxford (1937).
26. Seitz F. *The Modern Theory of Solids.* McGraw-Hill, New York (1940).
27. Dingle R. B. *Proc. Roy. Soc.* A **211,** 517 (1955).
28. Onsager L. *Phil. Mag.* **43,** 1006 (1952).
29. Jones H. and Zener C. *Proc. Roy. Soc.* A **145,** 268 (1934).
30. Kinchin G. H. *Proc. Roy. Soc.* A **217,** 9 (1953).
31. Soule D. E. *Bull. Amer. Phys. Soc.* **1,** 255 (1956).
32. Galt *et al. Phys. Rev.* **103,** 1506 (1956).
33. Chambers R. G. *Canad. J. Phys.* **34,** 1395 (1956).
34. Slonczewski J. C. Ph.D. Thesis, Rutgers University (1955), unpublished.
35. Tinkham M. *Phys. Rev.* **101,** 902 (1956).
36. Chambers R. G. *Phil. Mag.* **8,** 459 (1956).

VOL
3
195

J. Phys. Chem. Solids Pergamon Press 1957. Vol. 3. pp. 275–281.

INTERACTION ENERGY OF POINT IMPERFECTIONS IN METALS DUE TO THE FREE ELECTRONS

A. M. GAROFALO and J. S. PLASKETT

Physics Department, University of Virginia, Charlottesville, Virginia

(*Received* 4 *February* 1957; *revised* 9 *April* 1957)

VOL. 3 1957

Abstract—The interaction energy between two δ-function wells is calculated for a one dimensional model metal in which the potential is constant. For small wells, a large distance, a, apart, the energy is proportional to $\cos(2k'a)/a$, where k' is the wave vector of the maximum energy electron. (If the potential has a small time dependent fluctuation the above energy is multiplied by a factor $\exp(-\lambda a)$). By using a theorem on the average perturbation of degenerate levels the same result is obtained to the second order. It is shown that the perturbation theory diverges for low energy electrons. The interaction energy in three dimensions is proportional to $\cos(2k'a)/a^3$ according to perturbation theory.

1. INTRODUCTION

THE interaction energy of impurities in crystals has usually been regarded as an elasticity problem. Recently, however, it has been noticed that besides the static strain energy there is a temperature dependent interaction due to a coupling of the impurities with the phonon field.[1] In metals, and in general for crystals with wide energy bands, there is a further interaction due to a coupling of the impurities with the electrons of a crystal. This interaction will remain even if the ions of the crystal matrix are pinned down in their perfect lattice positions. In a perturbation theory this type of interaction can be attributed to a double scattering of the electrons by the two impurities. Since the intensity of an electron beam scattered by one impurity follows an inverse square law this interaction must be expected to be some sort of inverse power law, although it should be noticed that owing to incoherent scattering from other impurities and lattice vibrations the range will be limited by the mean free path of the electrons. Of course it may be that at some electron energies the scattering will be small, as in the Ramsauer–Townsend effect, but since all the Fermi electrons contribute to the effect, in contradistinction with electrical resistance, it cannot be expected that a careful calculation of the self-consistent potentials of the impurities will seriously diminish the interaction; any perturbing potential scatters at most energies.

A direct second-order perturbation calculation of the electron energy levels of the quasi-continuum can be criticized by a conscientious physicist on many counts. In an appendix to this paper we have attempted to meet a few of these criticisms. Apart from an explicit examination of these points this calculation is identical with one performed by RUDERMAN and KITTEL[2] on the spin-spin interaction of nuclei in metals. The three dimensional calculation is of considerable inherent difficulty—it is equivalent to a calculation of the continuum wave functions of a diatomic molecule—it therefore seemed sensible to solve the equivalent one-dimensional problem exactly. This is the major concern of this paper. The calculation shows that the perturbation expansion diverges for eigenvalues below a critical value but that it converges for all energies above this value.

Although the calculation has only been made for two impurities with δ-function potentials, the interested reader will find no difficulty in extending it to an arbitrary potential for the impurities, which has no qualitative effect on the answer, or to more than two impurities to show the non-additivity of the interaction due to multiple scattering.

We believe that the calculations show that

there is indeed a strong oscillating long-range interaction, but we hope also that it will discourage too sanguine a use of perturbation theory such as is to be found in PARMENTER.[3]

2. A PERFECT CRYSTAL

Let us suppose that the one dimensional crystal extends from $x = -L$ to $x = N$ and that at the points $x = 0$ and a $(a > 0)$ there are narrow potential wells. To be specific the wave equation is

$$\psi'' = (2m/\hbar^2)(V-E)\psi,$$

where $V(x) = 0$ except in the neighborhood of $x = 0$ and a, and in these regions

$$\int_{0-}^{0+} V\,dx = \hbar^2\delta_1/(2m)$$

$$\text{and} \quad \int_{a-}^{a+} V\,dx = \hbar^2\delta_2/(2m).$$

Furthermore we shall take for boundary conditions $\psi(-L) = \psi(N) = 0$. The equations of continuity at $x = 0$ are

$$\psi(0+) = \psi(0-)$$

and

$$\psi'(0+)-\psi'(0-) = \delta_1\psi(0)$$

and similarly at $x = a$. The solution in the three regions bounded by the points $-L$, 0, a, and N is of the form

$$\psi(x) = Ae^{ikx}+Be^{-ikx}$$
$$\text{with} \quad k^2 = 2mE/\hbar^2.$$

The eigenvalues are given by the zeros of the 6×6 determinant

$$\Delta(k,\delta) = \begin{vmatrix} e^{\mp ikL} & 0 & 0 \\ 0 & 0 & e^{\pm ikN} \\ 1 & -1 & 0 \\ (\mp ik-\delta_1) & \pm ik & 0 \\ 0 & -e^{\pm ika} & e^{\pm ika} \\ 0 & (\mp ik-\delta_2)e^{\pm ika} & \pm ike^{\pm ika} \end{vmatrix}.$$

Each column of this determinant should really be written out twice, once using the upper and once the lower of the two alternative signs.

The Laplace expansion of this determinant in terms of the first two rows gives

$$\Delta = h_1e^{-ik(L+N)}+h_2e^{ik(L+N)}-$$
$$-h_3e^{-ik(L-N)}-h_4e^{ik(L-N)},$$

where the h_i are the minors complimentary to the 2×2 determinants selected from the first two rows. In particular

$$h_1 = -h_2^*$$
$$= (2k+i\delta_1)(2k+i\delta_2)+\delta_1\delta_2e^{2ika}.$$

If L and N were equal and very large it would be possible to find the zeros of Δ to order $1/N$. It is, however, unnecessary to go into these details since an already existing theorem on the zeros of exponential sums gives the answer immediately. The theorem is (Theorem 2 of the Appendix to ATTREE and PLASKETT[4]): If the zeros of $\Delta(k, \delta)$ are $k_n(\delta)$ then

$$\sum_{k<k_n<k+dk}[k_n(\delta)-k_n(0)]$$
$$= \frac{1}{2\pi i}\left[\log\frac{h_1(k,\delta)}{h_2(k,\delta)}-\log\frac{h_1(k,0)}{h_2(k,0)}\right]dk$$

to an accuracy of order $1/N$ and $1/L$. The change of energy due to the small shift in these k_n's is of course

$$(\hbar^2k/m)\sum_{k<k_n<k+dk}(k_n(\delta)-k_n(0)].$$

If the explicit expressions are put in for h_1 and h_2, the following expression is obtained for the energy change due to all electrons with energies between 0 and $\hbar^2k'^2/2m$:

$$U_{12}{}^F(a) = \frac{\hbar^2}{m\pi}\int_0^{k'} k\arg\{(2k+i\delta_1)(2k+i\delta_2)+$$
$$+\delta_1\delta_2e^{2ika}\}\,dk.$$

If we put $\delta_2 = 0$, we obtain the self-energy of one well

$$U_1{}^F = \hbar^2/(m\pi)\int_0^{k'} k\arg(2k+i\delta_1)\,dk.$$

These are only the contributions to the energy from the free electrons and they should be multiplied by 2 since we have neglected spin degeneracy, as we shall throughout the rest of the paper.

The energies of the bound states are given by the imaginary zeros of $\Delta(k, \delta)$. If we look only at the zeros with $I_p(k) > 0$ then they are given, for large L and N, by the zeros of $h_1(k, \delta)$. This shows that the only zeros of $h_1(k, \delta)$, for $I_p(k) > 0$, lie along the imaginary axis, for otherwise there would be complex energy eigenvalues of an Hermitian operator. This result can also be easily verified directly by the principle of the argument. If we replace arg h_1 by $I_p \log h_1$, then we can deform the contour integral from 0 to k' so that it first runs up the imaginary axis with indentations to the right to avoid the branch points and then back down along any curve in the first quadrant to k'. If $k = i\kappa_1, i\kappa_2, \ldots$ are the zeros of $h_1(k, \delta)$ with $\kappa_1 > \kappa_2 > \ldots > 0$, then it can be immediately verified that $I_p \log h_1(i\kappa, \delta) = 0, -\pi i, -2\pi i, \ldots$ for $\kappa > \kappa_1, \kappa_1 > \kappa > \kappa_2, \kappa_2 > \kappa > \kappa_3, \ldots$ respectively. (The branch of the log is decided by taking k real and making δ_1 and δ_2 go to zero through real values when the arg should go to zero. It is easy to show that the branch is uniquely fixed by this criterion and that no change of branch is required with variation of k along the real axis. The branch for $I_p(k) > 0$ is fixed by analytic continuation, so that Cauchy's theorem is valid.) The integral up the imaginary axis is then easy to evaluate; it is just

$$(\kappa_1^2 + \kappa_2^2 + \ldots)\hbar^2/(2m)$$

or just the negative of the change of energy due to the introduction of the bound states, say $U_{12}{}^B(a)$. It follows that the total energy change due to the wells for all electrons with energy below $\hbar^2 k'^2/2m$ is

$$U_{12}(a) = U_{12}{}^F(a) + U_{12}{}^B(a)$$
$$= -\hbar^2/(m\pi) I_p \int_{k'}^{i\infty} \log h_1(k, \delta) k \, dk.$$

It is an interesting fact that this energy change is an analytic function of δ_1 and δ_2 although the energy change due to the bound or free states alone is discontinuous at the points where bound states are just about to appear or disappear. (For the corresponding result for the charge density, see PLASKETT.[5])

The interaction energy is obtained by subtracting from this the same expressions only with δ_1 or δ_2 put equal to zero, i.e. the two self-energies; explicitly

$$U_{12}(a) - U_1 - U_2 = -\frac{\hbar^2}{m\pi} \times$$
$$\times I_p \int_{k'}^{i\infty} \log \left\{ 1 + \frac{\delta_1 \delta_2}{(2k + i\delta_1)(2k + i\delta_2)} e^{2ika} \right\} k \, dk.$$

If $|\delta_i| < 2k'$ this rather unpleasant expression can be written as a power series in δ_1, δ_2 the first term of which is

$$-\frac{\hbar^2}{m\pi} \frac{\delta_1 \delta_2}{8k'a} \cos 2k'a + 0\left(\frac{1}{a^2}\right).$$

It is to be noted that our expression for the energy change due to the introduction of the wells, for electrons with wave vector between k and $k + dk$, can also be expanded into a series of terms, each of which is a homogeneous function of δ_1 and δ_2, provided k is not too small, e.g. if k is bigger than the positive root of $2k^2 - k|\delta_1 + \delta_2| - -|\delta_1 \delta_2|$. The result is

$$(\hbar^2/m\pi)\{(\delta_1 + \delta_2)/(2k) +$$
$$+ \delta_1 \delta_2 \sin 2ka/(4k^2) + \ldots\} k \, dk.$$

These two terms of the series agree with the similar expression obtained by first and second order perturbation theory according to PARMENTER.[3] (See Appendix.) This should not make one too sanguine, however, about the perturbation theory since for any fixed δ_1 and δ_2 the series diverges for small enough k. For very small k the correct expression for the energy change is

$$\frac{\hbar^2}{m\pi} \left\{ \frac{\pi}{2} \operatorname{sgn}(\delta_1 + \delta_2 + a\delta_1\delta_2) - \right.$$
$$\left. - \frac{k(2 - a^2\delta_1\delta_2)}{\delta_1 + \delta_2 + a\delta_1\delta_2} + \ldots \right\} k \, dk.$$

The discontinuity of the signum function is just another reflection of the fact that the energy change is a discontinuous function of δ_1 and δ_2.

In fact a changing sign of $\delta_1+\delta_2+a\delta_1\delta_2$ implies the appearance or disappearance of a bound state as the Table shows.

Table 1

sgn δ_1	sgn δ_2	sgn$(\delta_1+\delta_2+a\delta_1\delta_2)$	Number of bound states
-1	-1	$+1$	2
-1	-1	-1	1
-1	$+1$	-1	1
-1	$+1$	$+1$	0
$+1$	$+1$	± 1	0

It is perhaps worth mentioning that the interaction energy between a well and the boundary of the crystal, distant L from it, can easily be calculated by keeping L fixed but making N tend to infinity. The result is

$$-\frac{\hbar^2}{m\pi}I_p\int_{k'}^{i\infty}\log\left\{1-\frac{i\delta}{2k+i\delta}e^{2ikL}\right\}k\,dk.$$

If this is expanded in powers of δ the first term is

$$\frac{\hbar^2}{m\pi}\frac{\delta}{4L}\sin 2k'L+0\left(\frac{1}{L^2}\right).$$

3. A DISORDERED CRYSTAL

We now imagine that the potential, $V(x)$, is not zero between the wells, as it was before, but that it varies sufficiently slowly that the wave functions are given by the B.W.K. formula

$$\psi(x)=[\kappa(x)]^{-\frac{1}{2}}\exp\{\pm i\int^x\kappa(x')\,dx'\}$$

$$\text{with}\quad[\kappa(x)]^2=2m(E-V)/\hbar^2.$$

Furthermore, we shall suppose that in the neighborhood of the two δ-functions, at $x=0$ and a, $V(x)$ is zero. The previous calculations are unaltered and the interaction energy due to electrons in $(k,\ k+dk)$ is

$$\frac{\hbar^2}{m\pi}\arg\left\{1+\frac{\delta_1\delta_2}{(2k+i\delta_1)(2k+i\delta_2)}e^{2iJ}\right\}k\,dk,$$

where

$$J=\int_0^a\kappa(x)\,dx,\quad\text{and}\quad\hbar^2k^2/2m=E.$$

This result is only good if $E\gg V(x)$.

If $V(x)$, and so J, fluctuates then the interaction energy will also fluctuate. We imagine that the fluctuation is so slow that the electron wave functions are able to follow adiabatically. If the motion of the two wells is sufficiently slow their average motion will be determined by the average interaction energy. This will certainly be the case if the fluctuations in $V(x)$ are caused by thermal vibrations. The problem is clearly more involved if the fluctuations in $V(x)$ are caused by the motion of impurities.

The probability distribution for J will in general be Gaussian for large a, since J is then the sum of a large number of independent random variables. To get an idea of the order of magnitudes involved we make a computation of the distribution for J in a possible case.

Suppose that the interval a is composed of N equal subintervals of length τ and that in each subinterval $\int\kappa dx$ can have one of two different values, say $k_1\tau$ and $k_2\tau$. Then

$$\sum_{n=1}^{N}\int_{(n-1)\tau}^{n\tau}\kappa(x)\,dx=n_1k_1\tau+n_2k_2\tau,\qquad n_1+n_2=N,$$

if we assume that the $k_1\tau$ value of the integral occurs n_1 times. Let us further assume that k_1 occurs with a probability p_1 and k_2 with a probability $p_2=1-p_1$. Then, if there is no correlation between the subintervals, the probability of finding the above value of J is the binomial expression

$$\frac{N!}{n_1!\,n_2!}p_1^{n_1}p_2^{n_2}$$

$$\sim(2\pi Np_1p_2)^{-\frac{1}{2}}\exp\left\{-\frac{(n_1-Np_1)^2}{2Np_1p_2}\right\}.$$

The average interaction energy is

$$\frac{\hbar^2}{m\pi}k\,dk(2\pi)^{-\frac{1}{2}}I_p\int_{-\infty}^{+\infty}\exp(-\xi^2/2)\times$$

$$\times\log(1+Ae^{2ia\xi})\,d\xi,$$

where

$$A = \frac{\delta_1\delta_2}{(2k+i\delta_1)(2k+i\delta_2)} \exp[2ia(p_1k_1+p_2k_2)]$$

and $\alpha = \tau(k_1-k_2)\sqrt{(Np_1p_2)}$.

We have replaced the sum over n_1 by an integral. If we expand the log and integrate term by term we obtain the series

$$\sum_{n=1}^{\infty}(-1)^{n-1}\frac{1}{n}A^n \exp(-2n^2\alpha^2).$$

A very good value for the average interaction energy is given by the first term:

$$\frac{\hbar^2}{m\pi}k\,dk \exp[-2p_1p_2(k_1-k_2)^2a\tau]I_p(A).$$

Effectively the introduction of a random potential just multiplies the interaction energy by an exponentially decreasing factor.

4. APPENDIX. PERTURBATION THEORY

It can be easily shown that the energy change due to the two wells δ_1 and δ_2, which was calculated in section 2 for zero boundary conditions on the surface of the crystal, is independent of the boundary conditions. We therefore have our choice of boundary conditions for the perturbation calculations. Some boundary conditions make the unperturbed problem degenerate. If it were merely a matter of verifying the result of section 2 it would be wise to avoid such boundary conditions. Degeneracy is almost inevitable, however, in the three dimensional problem and it seems worthwhile, therefore, to face degeneracy in this simpler case, especially since the exact solution is known. It may be said parenthetically that the perturbation calculation with zero boundary conditions (no degeneracy) is easy and leads to the answer of section 2.

The calculation of the perturbation of a degenerate level with statistical weight g involves a calculation of the zeros of a $g\times g$ secular determinant. This only gives the first-order energy change and it is well known that the second-order calculation is much more tricky. We shall now prove a theorem that enables the sum of the g perturbed eigenvalues, corresponding to the original degenerate level, to be calculated as easily and, in fact, by the same formula as is used for a non-degenerate level. Effectively this means that if only the sums of eigenvalues are required, as in our case, the statistical weight of a level can be ignored.

The perturbed problem has the Hamiltonian $\mathscr{H}^0+\lambda\mathscr{H}^1$ (All the superscripts in the following discussion are just labels not powers): If we use the eigenfunctions of $\mathscr{H}^0$ to represent this operator it has the form of a matrix $H^0+\lambda H^1$, where H^0 is diagonal. To find the perturbed eigenfunctions and eigenvalues it is necessary to find a unitary matrix, U, that diagonalizes $H^0+\lambda H^1$, i.e. $(H^0+\lambda H^1)U = UE$. If U and E can be expanded in powers of λ, $U = \Sigma\lambda^nU^n$ and $E = \Sigma\lambda^nE^n$ and if we equate powers of λ, we obtain the equations

$$H^0U^0-U^0E^0 = 0,$$

$$H^0U^1-U^1E^0 = U^0E^1-H^1U^0,$$

$$H^0U^2-U^2E^0 = U^0E^2+U^1E^1-H^1U^1, \ldots$$

Because U is unitary we also have

$$U^0U^{0*} = 1, \quad U^0U^{1*}+U^1U^{0*} = 0, \ldots.$$

Let us arrange that the diagonal matrix H^0 has all its equal elements grouped next to each other. H^0 can then be regarded as a diagonal block matrix, the diagonal blocks of which are scalar matrices, the scalar being different for each diagonal block. We shall write $H^0{}_{kl}$ for the rectangular block matrix that has its rows the same as the kth eigenvalue and its columns the same as the lth eigenvalue. $H^0{}_{kl}$ is a $g_k\times g_l$ matrix if g_k is the statistical weight of the kth eigenvalue. We shall write all the other matrices H^1, E^n, and U^n in the same block notation. The first equation above can now be written (No sumation convention is used in the following.)

$$H_{kk}{}^0U_{kl}{}^0-U_{kl}{}^0E_{ll}{}^0 = 0.$$

Clearly we can choose $U_{kl}{}^0 = 0\,(k\neq l)$ and $E_{kk}{}^0 = H_{kk}{}^0$; $U_{kk}{}^0$ is then unitary. The second equation is

$$(E_k{}^0-E_l{}^0)U_{kl}{}^1 = U_{kl}{}^0E_{ll}{}^1-H_{kl}{}^1U_{ll}{}^0,$$

where $E_{kk}{}^0 = E_k{}^0 1$. This fixes the diagonal blocks of U^0 and the off diagonal blocks of U^1, in fact

$$U_{kk}{}^{0*}H_{kk}{}^1U_{kk}{}^0 = E_{kk}{}^1$$

and

$$U_{kl}{}^1 = \frac{H_{kl}{}^1}{E_l{}^0-E_k{}^0}U_{ll}{}^0, \qquad k\neq l.$$

The third equation is

$$(E_k{}^0-E_l{}^0)U_{kl}{}^2 = U_{kl}{}^0E_{ll}{}^2+U_{kl}{}^1E_{ll}{}^1-\sum_m H_{km}{}^1U_{ml}{}^1.$$

If k is put equal to l in this and $U_{ml}{}^1$ is given its known value, we obtain

$$U_{kk}{}^0E_{kk}{}^2+U_{kk}{}^1E_{kk}{}^1-H_{kk}{}^1U_{kk}{}^1-$$

$$-\sum_{m\neq k}\frac{H_{km}{}^1H_{mk}{}^1}{E_k{}^0-E_m{}^0}U_{kk}{}^0 = 0.$$

This gives

$$E_{kk}^{2} = -U_{kk}^{0*}U_{kk}^{1}E_{kk}^{1} - E_{kk}^{1}U_{kk}^{1*}U_{kk}^{0} + \\ + U_{kk}^{0*}\sum_{m\neq k}\frac{H_{km}^{1}H_{mk}^{1}}{E_{k}^{0}-E_{m}^{0}}U_{kk}^{0}.$$

If we use the fact that

$$U_{kk}^{0*}U_{kk}^{1} + U_{kk}^{1*}U_{kk}^{0} = 0$$

then it is easy to show that the trace of the sum of the first two matrices in the equation for E_{kk}^{2} is zero. It follows that

$$\mathrm{Tr}(E_{kk}) \\ = \mathrm{Tr}\left[E_{kk}^{0} + \lambda H_{kk}^{1} + \lambda^{2}\sum_{m\neq k}\frac{H_{km}^{1}H_{mk}^{1}}{E_{k}^{0}-E_{m}^{0}} + \cdots\right].$$

If the i, j element of the matrix H_{kl}^{1} is written $H_{ki,lj}^{1}$ and the eigenvalues occuring down the diagonal of E_{kk} are written E_{ki} then our expression is

$$\sum_{i} E_{ki} = g_{k}E_{k}^{0} + \sum_{i}\left[\lambda H_{ki,ki}^{1} + \right. \\ \left. + \lambda^{2}\sum_{m\neq k}\sum_{j}\frac{H_{ki,mj}^{1}H_{mj,ki}^{1}}{E_{k}^{0}-E_{m}^{0}} + \cdots\right].$$

This reduces the usual non-degenerate expansion when $g_k = 1$. It is to be noted that in calculating the second order effect all intermediate states are used that do not lead to a zero energy denominator.

Now let us apply this result to the problem of section 2 with periodic boundary conditions. The unperturbed wave functions are

$$\psi_{k} = (L+N)^{-\frac{1}{2}}e^{ikx} \\ \text{with} \quad k = 2\pi n/(L+N), \quad n \text{ integral}$$

The matrix elements for the perturbing potential are ($\lambda = 1$)

$$H_{kk'}^{1} = \frac{1}{L+N}\frac{\hbar^{2}}{2m}[\delta_{1} + \delta_{2}e^{ia(k'-k)}]$$

also, of course, $E_{kk'}^{0} = \delta_{kk'}\hbar^{2}k^{2}/2m$. There is a degeneracy between k and $-k$.
By our formula

$$E_{k}+E_{-k} = 2\frac{\hbar^{2}}{2m}k^{2} + \frac{2}{L+N}\frac{\hbar^{2}}{2m}(\delta_{1}+\delta_{2}) + \\ + \sum_{k'\neq\pm k}\frac{1}{(L+N)^{2}}\frac{\hbar^{2}}{2m}\frac{\delta_{1}^{2}+\delta_{2}^{2}+2\delta_{1}\delta_{2}\cos a(k-k')}{k^{2}-k'^{2}}.$$

If we replace $\Sigma_{k'}$ by $(L+N)(2\pi)^{-1}\int dk'$ (the Cauchy principle value), we find

$$E_{k}+E_{-k} = 2\hbar^{2}k^{2}/2m + \left\{\frac{\hbar^{2}}{2m\pi}(\delta_{1}+\delta_{2}) + \right. \\ \left. + \frac{\hbar^{2}}{4m\pi}\frac{\delta_{1}\delta_{2}}{k}\sin 2k|a| + \cdots\right\}\frac{2\pi}{L+N}.$$

This gives the expression of section 2 after multiplication by the number of states in dk. It was pointed out in section 2 that this series diverges for small k. It is of some interest to neglect this fact and calculate the interaction energy, for large a, due to all electrons with energy between 0 and $\hbar^{2}k'^{2}/2m$. The result is

$$\frac{\hbar^{2}}{4m\pi}\delta_{1}\delta_{2}\int_{0}^{k'}\frac{\sin 2k|a|}{k}\,dk \\ \sim \frac{\hbar^{2}}{4m\pi}\delta_{1}\delta_{2}\left(\frac{\pi}{2} - \frac{\cos 2k'a}{2k'|a|}\right).$$

The correct result does not contain the $\pi/2$ term.

It is amusing to make the perturbation calculation in three dimensions, although we have no means of knowing that it is ever correct. Let us use a cube of side L with periodic boundary conditions. The unperturbed wave functions are

$$\psi_{k} = L^{-3/2}e^{i\mathbf{k}\cdot\mathbf{r}} \\ \text{with} \quad k_{i} = 2\pi n_{i}/L \quad n_{i} \text{ integers}.$$

All k's that make $(n_1^{2}+n_2^{2}+n_3^{2})$ equal are degenerate. To make the expression for the matrix H^{1} easy we shall again imagine that we have δ-function impurities, i.e.

$$H^{1}(\mathbf{r}) = (\hbar^{2}/2m)\{\delta_{1}\delta(\mathbf{r}-\boldsymbol{a}_{1}) + \delta_{2}\delta(\mathbf{r}-\boldsymbol{a}_{2})\}.$$

This has the slight disadvantage that the self-energy of the wells is infinite, which is presumably connected with the fact that such a well has an infinite number of bound states, but we shall just subtract off the self-energy.

$$H_{kk'}^{1} = L^{-3}(\hbar^{2}/2m)\{\delta_{1}e^{i(\mathbf{k}'-\mathbf{k})\cdot\boldsymbol{a}_{1}} + \delta_{2}e^{i(\mathbf{k}'-\mathbf{k})\cdot\boldsymbol{a}_{2}}\}.$$

If the δ-functions were replaced by wells of finite radius and depth then the δ_1 and δ_2 in the above matrix element would be multiplied by

$$[3/(\alpha\kappa)^{3}](\sin\alpha\kappa - \alpha\kappa\cos\alpha\kappa) \quad \text{with} \quad \kappa^{2} = (\mathbf{k}'-\mathbf{k})^{2}$$

where α is the radius of the wells. This function acts as a convergence factor in the expressions obtained below for the perturbation. In other words we do the necessary sums, subtract off the finite self-energy, and then make α tend to 0.

The notation is simplified if we imagine that each of

a set of degenerate levels is shifted by the average shift of the whole set. This average shift for the level $\boldsymbol{k}$ is

$$\delta E_{\boldsymbol{k}} = \frac{\hbar^2}{2m} L^{-3} \left\{ (\delta_1 + \delta_2) + \right.$$

$$\left. + \frac{1}{L^3} \sum_{\boldsymbol{k}'}{}' \frac{\delta_1^2 + \delta_2^2 + 2\delta_1\delta_2 \cos(\boldsymbol{k}' - \boldsymbol{k}) \cdot \boldsymbol{a}}{k^2 - k'^2} \right\}$$

where $\boldsymbol{a} = \boldsymbol{a}_2 - \boldsymbol{a}_1$ and the dash on the summation sign means that all terms with $k'^2 = k^2$ are to be omitted. In all this we are only interested in the $\delta_1\delta_2$ term, which is the sole contribution to the interaction energy. If for large L it were permissible to replace the sum over $\boldsymbol{k}'$ by an integral using the Cauchy principle value, as it is in one dimension, then we should obtain

$$\delta E_{\boldsymbol{k}}(\text{interaction}) = \frac{\hbar^2}{2m} (2\pi L)^{-3} 2\delta_1\delta_2 \times$$

$$\times \frac{2\pi^2}{a} \cos ka \cos \boldsymbol{k} \cdot \boldsymbol{a}.$$

The convergence factor has been used in this to correctly evaluate the non-absolutely convergent triple integral. The interaction energy due to electrons between k and $\boldsymbol{k} + d\boldsymbol{k}$ is

$$-\hbar^2/2(m) \cdot (2\pi)^{-3} \cdot \delta_1\delta_2 k/a^2 \cdot \sin 2ka \, dk.$$

Now although it seems that the replacement of the sum over $\boldsymbol{k}'$, with a fixed $\boldsymbol{k}$, by an integral is not true in a region containing the singular sphere $k'^2 = k^2$ due to the peculiar distribution of $\boldsymbol{k}'$'s on concentric spheres, nevertheless it is reasonable that a further sum over $\boldsymbol{k}$ as in the last formula should average out these peculiarities.

If we assume that this formula for the contribution to the interaction energy due to electrons in $(k, k + dk)$ is correct down to $k = 0$ then we obtain the total interaction energy due to all free electrons up to an energy $\hbar^2k'^2/2m$ by integration:

$$(2\pi)^{-3} \frac{\hbar^2}{2m} \frac{\delta_1\delta_2 k'}{2a^3} \left[\cos 2k'a - \frac{\sin 2k'a}{2k'a} \right].$$

The interaction of a well with the crystal surface is a first-order effect, as in one dimension, and none of the above difficulties arise. When the surface of the crystal is given a zero boundary condition, the interaction energy due to electrons with the magnitude of their wave vector between k and $k + dk$ is

$$-(2\pi)^{-2} \frac{\hbar^2}{2m} \frac{\delta k}{a} \sin 2ka \, dk$$

where a is the distance of the well from the boundary. All free electrons up to energy $\hbar^2k'^2/2m$ give an interaction energy

$$\frac{1}{8\pi^2} \frac{\hbar^2}{2m} \frac{\delta k'}{a^2} \left[\cos 2k'a - \frac{\sin 2k'a}{2k'a} \right].$$

REFERENCES

1. Montroll E. W. and Potts R. B. *Phys. Rev.* **100**, 525 (1955); *Ibid.* **102**, 72 (1956).
2. Ruderman M. A. and Kittel C. *Phys. Rev.* **96,** 99 (1954).
3. Parmenter R. H. *Phys. Rev.* **97**, 587 (1955).
4. Attree R. W. and Plaskett J. S. *Phil. Mag.* Series 8, **1,** 885 (1956).
5. Plaskett J. S. *Phys. Rev.* **94**, 1420 (1954).

J. Phys. Chem. Solids Pergamon Press 1957. Vol. 3. pp. 282–302.

$M_{2,3}$ ABSORPTION SPECTRA OF THE ELEMENTAL SOLIDS Cr THROUGH Ge*

D. H. TOMBOULIAN, D. E. BEDO,† and W. M. NEUPERT

Cornell University, Ithaca, N.Y.

(*Received* 9 *May* 1957)

Abstract—The absorption by thin foils of the elements extending from Cr to Ge has been investigated in the vicinity of the $M_{2,3}$ edge by the use of a grazing incidence vacuum spectrograph. The spectral measurements fall in the 80 to 300 Å region. The $M_{2,3}$ discontinuity, which corresponds to the onset of $3p \rightarrow$ conduction band transitions, appears essentially as an unresolved feature above a high background absorption caused by valence band electrons. For each member of the sequence, measurements of the energy dependence of the mass absorption coefficient are presented graphically for incident photon energies extending to some 30 to 60 eV beyond the edge. The results regarding the spectral location of edges are compared with the information available from previous studies of the $M_{2,3}$ emission bands of the corresponding elements. In the region of secondary structures, the position of maxima in the absorption coefficient, as measured from the mean edge, are compared with reported values of characteristic energy losses suffered by electrons in passing through a foil of the same material.

1. INTRODUCTION

THE experimental results presented in this paper deal with the soft X-ray absorption by the group of nine elements extending from Cr to Ge. The spectral measurements fall in the 80 Å to 300 Å region, corresponding to incident photon energies of 155 eV to 41·3 eV. This sequential study is concerned with the energy dependence of the photoelectric absorption in the neighborhood of the $M_{2,3}$ discontinuity which marks the onset of absorption by $3p$ electrons. Nearly two decades ago, SKINNER and JOHNSTON[1,2] studied the $M_{2,3}$ absorption bands of Ni, Cu and Zn. More recently, similar measurements have been made for Fe[3] and Ge.[4] Except for a brief note[5] on the position of the $M_{2,3}$ edge of Co, no investigations have been carried out on the $M_{2,3}$ absorption band of the remaining transition elements of the third group. Lately, in connection with spectroscopic studies of the solid state, a series of publications[6–9] dealing with the $M_{2,3}$ emission bands (valence $\rightarrow 3p$ transitions) of the transition metals and neighboring elements have also appeared. A comparison of such measurements on the intensity distribution of M bands has revealed a number of differences as to the spectral locations and diffuseness of edges.

The present investigation was primarily undertaken to obtain complementary information on the general problem of the $M_{2,3}$ spectra of the light elements. It was our objective to examine the $M_{2,3}$ absorption spectra of the series of elements Cr $\rightarrow$ Ge, so as to review or extend the existing measurements and to obtain data on the heretofore unexplored spectra of Cr, Mn, Co, and Ga. A second aim of the research was to make observations of the fine structure found on the high energy side of the edge to see if any correlation existed between the position of secondary peaks in photoelectric absorption and the characteristic energy losses suffered by electrons traversing thin foils of matter. The possibility of such a correlation has recently been suggested by several authors.[10,30] Unfortunately, owing to technical difficulties and instrumental limitations we were unable to extend the absorption studies so as to include in the series the first five members (potassium to vanadium) for which the $3s^2 3p^6$ M subshell is also complete.

* Research supported by the Office of Ordnance Research, U.S. Army.

† Corning Glass Foundation Fellow.

2. EXPERIMENTAL

A description of the instrumental arrangement and the general procedure followed in soft X-ray absorption spectroscopy may be found in reference 1. The reader may also find it advantageous to consult the survey articles listed under references 11 and 12. Here the discussion will include technical details of relevance to the present work and special comments on the limitations of the customary procedures followed in carrying out absorption measurements in the particular spectral region.

The absorbers

Thin layers, deposited on a supporting substrate by vacuum distillation, served as absorbers. A glass slide, previously coated with a wetting agent (sodium octyl and capryl phosphates) was dipped in a Zapon (cellulose acetate) solution so as to form the supporting film. The material destined for absorption measurements was allowed to condense on the Zapon layer which was subsequently floated off and mounted. For convenience in the preparation of a large number of samples, a substrate film having a surface density of 15 $\mu g/cm^2$ was adopted as a standard. Such films possessed a sufficiently high transmission over the spectral range of interest and were not excessively fragile. The sample used as an absorber had an area of 1·50 cm^2. Excepting the case of Ge, the mass of each absorber was determined by weighing on a microbalance. The weighings were repeatable to within 5 μg. The masses of the various specimens whose thicknesses were suitable for the present absorption measurements ranged from 30 μg to 220 μg. The selection of optimum absorber thickness was governed by factors to be presented later.

The evaporation of Cr and Mn does not present any difficulties; both metals sublime so that no problems arise in the way of alloying with the tungsten wire used for the heater. On the other hand, Fe, Ni, and Co are evaporated from the liquid phase. These three metals dissolve in tungsten. One should employ a heavy tungsten filament and distribute the charge to be evaporated so that the amount of the molten metal which comes in contact with a given portion of the evaporator wire is limited. These precautions make it possible to keep the concentration of the solute in the metal-tungsten alloy to a low value. Otherwise, the filament will melt before appropriate temperatures are reached, since the melting point of the alloy is lowered with increasing amounts of the metal solute.

At 1500°K the evaporation rate[13] of Ni and Co is a million times faster than that of W. This datum is an assurance that only a small amount of W will be vaporized concurrently with the other metal and indicates that the absorbers will not be highly contaminated due to alloying if the evaporation is carried out at a low temperature consistent with an adequate deposition rate. Experience indicates that the presence of tungsten arises not from the direct evaporation of the metal, but rather from deposits of WO_2. Good vacuum techniques must be adhered to in order to avoid the formation of the volatile tungsten oxide which may seriously* contaminate the absorbing layer.

The evaporation of Cu is straightforward, but that of Zn requires a special approach. The metal has a high sublimation pressure at low temperatures (2×10^{-3} mm of Hg at 500°K). In addition, the deposits are likely to be patchy and to have a murky appearance. In the preparation of Zn absorbers, the glass slide was soldered to a brass plate using Ceroseal glass solder and the combination was clamped to the bottom of a metal trap containing liquid nitrogen. This arrangement did provide for efficient cooling (down to −120°C) of the substrate to be coated by Zn. The Zapon foils were not fractured by the chilling. The metal was evaporated at a slow rate and the resulting absorbers were free from cracks and were not cloudy in appearance.

Though Ga melts at 29°C, its vapor pressure rises very slowly, attaining a pressure of 1 mm of Hg at 1350°C. The evaporation technique adopted was the same as that used for Zn. The procedure followed in the preparation of Ge absorbers is described in reference 4.

The foils used as absorbers were free from pinholes and appeared quite uniform in thickness. SENNET and SCOTT[14] have examined thin films of Cr, Ni and Cu by the electron microscope and report no structural changes in films which were exposed to the atmosphere for half an hour after

* Due to its high atomic number, the absorption of low energy (~ 100 eV) photons by a few atomic layers of W is sufficient to reduce the transmission by the absorber to an intolerably low value.

evaporation. Excepting the case of Mn, the deposits of the remaining transition metals retained their luster and showed no visible signs of deterioration after several weeks of exposure to air. However, foils of Mn were found to react with moisture. All samples were prepared from materials of spectroscopic purity.

Subsequent to evaporation the absorbers were transferred to the spectrograph chamber without delay. From the repeatability of the results obtained with samples which were allowed to age, it is known that the amount of surface contamination incurred in the brief transfer process was not detectable in the case of the absorbers used in our measurements. This observation is confirmed in the case of Fe. CARTER and GIVENS[3] who did not allow the samples to come into contact with air, have reported results which are satisfactorily reproduced in the present measurements.

Studies[14] of the structure of evaporated layers

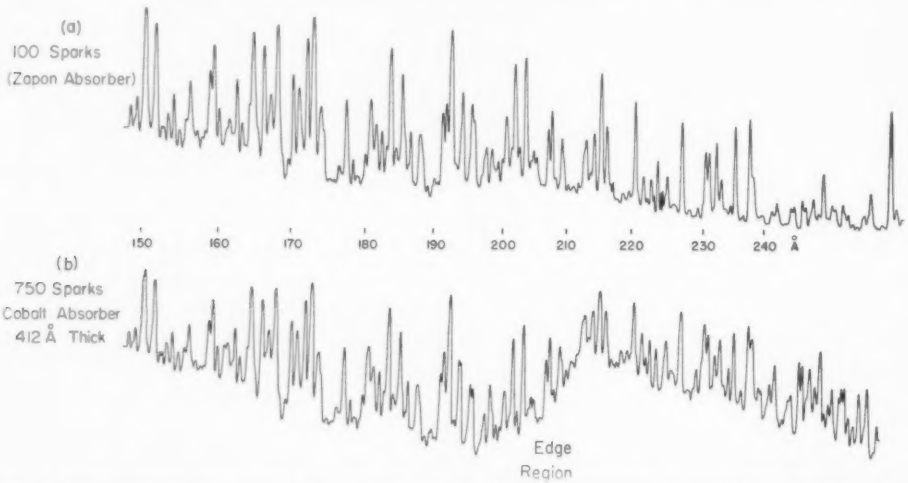

FIG. 1.[7] Microphotometer traces of a spectrogram obtained by DENNY[21] in connection with the $M_{2,3}$ absorption spectrum of Co, (a) the reference spectrum (b) the absorption spectrum. The particular exposure ratio K was equal to 7·5.

which are several hundred angstroms in thickness, offer evidence that such deposits are likely to have a microcrystalline and granular structure. We have no assurance that the layers did possess the crystalline properties of the bulk material. In particular an inhomogeneous structure is to be expected in the case of Zn and Ga. Owing to this consideration, thickness determinations derived from weighings by the use of bulk densities may not be meaningful, so that in presenting the data on the foils we have indicated the mass per unit area—a quantity characteristic of the atomic species and not necessarily on its state of aggregation.

Characteristics of the source

A microphotometer trace of the spectrum produced by a condensed discharge in a Pyrex capillary is shown in Fig. 1 (a). The deflection maxima correspond to line radiations emitted by excited atoms of O, N, Na, etc. This source was used in irradiating all the absorbers studied. The exposures in the various runs were controlled by changing the total number of discharges. The outstanding merits of the source are its high intrinsic brightness and long life. Where laborious measurements are involved, short exposures and freedom from failure are great conveniences.

These considerations led us to adopt the capillary source throughout the spectral range of interest. As an alternate choice, the condensed spark between metallic electrodes might have been used. Such a source has the advantage that by proper choice of electrode materials, dense line spectra may be produced over a limited wavelength range. But, the discharge between electrodes is subject to difficulties of operation such as, the need for frequent gap adjustments, the wandering of the spark within the gap resulting in inefficient illumination of the grating and the necessity for maintaining a high vacuum in the electrode chamber connected to the spectrograph. On the other hand, subsequent to the proper adjustment of the leakage rate, the discharge in a glass capillary requires little attention. Its operation needs no auxillary pumping system. It constitutes a source in depth, and alignment procedures are not critical.

Over the short wavelength region, the capillary spark emits a weak X-ray continuum. A faint continuum which sets in at about 300 Å, becomes gradually more intense as one proceeds towards longer wavelengths. This continuum is presumed to consist of temperature radiation emitted from the walls of the capillary. Superimposed on these background radiations is the intense characteristic spectrum of atomic and molecular origin.

Tests have indicated that under controlled conditions, the intensities of a series of lines within a spectrum, measured relative to the intensity of a reference line, are reproducible to within a few per cent from exposure to exposure. This property coupled with the assumed validity of homochromatic photometry, makes it possible to calibrate the emulsion and to put reliance in the observed shapes of absorption curves.

However, for a series of exposures obtained by varying the number of discharges, the intensity of a given line is found to deviate from the intensity ratio anticipated purely on the basis of the spark ratio. This variation may be as high as 10 per cent and arises from changes in the excitation conditions in the source.

Fig. 1 (b) shows a microphotometer trace of the spectrum emergent from a cobalt absorber, taken with an increase in the number of sparks so as to attain photographic densities comparable to those found in trace (a) of Fig. 1. In evaluating the absorption coefficient from the photographic record, the exposure ratio k between the two spectral strips is taken to be the ratio of the number of sparks used during each run. As remarked above, the actual exposure ratio may depart from this value of k. An error of this nature does not influence the shape of the absorption curve but may account for the lack of agreement between the values of the absorption coefficient deduced from a repetition of the measurement.

One unsatisfactory feature of the capillary source is paucity of lines below 120 Å and again at wavelengths in excess of 300 Å. The shortage of lines over the long wavelength region is not serious, since in the present measurements the corresponding photon energies fall on the low energy side of the $M_{2,3}$ edge. The situation over the short wavelength region is more consequential and constitutes a drawback in the accurate determination of the behavior of the absorption curve on the high energy side of the edge in question. The experimental data in the case of Cu, Zn, Ga and Ge suffer in particular from this defect.

Effects of order overlap

The experimental determination of the absorption coefficient involves the evaluation of the ratio I_0/I in which I_0 and I represent the beam intensities incident on and emergent from the absorber. In the photographic mode of recording, the beam intensity may be correlated with the energy which gives rise to the image of a spectral line on the plate.

In the beam incident on the grating from the source, let $E_s(\lambda)$ represent the energy associated with the radiation within a width $d\lambda$ centered at wavelength λ. Of this energy, the fraction $R_{\mathrm{I}}(\lambda)e^{-\mu(\lambda)t}$ will be collected in a distance interval* w centered at x on the Rowland circle (Fig. 2). The reduction in energy represented by this factor is brought about (1) by the degrading effect of the absorber of thickness t and coefficient $\mu(\lambda)$ and (2) by the reflecting power of the grating $R_{\mathrm{I}}(\lambda)$ which denotes the fraction of the incident energy diffracted into the image of order I.

However, the source also emits radiation of shorter wavelength such as $\lambda/2$, $\lambda/3$, ... These will also be focussed at the same point x thus contributing to the blackening of the image formed at the position of the first order line. For a line of wavelength $\lambda/2$ appearing in order II such a contribution may be represented by $E_s(\lambda/2)R_{\mathrm{II}}(\lambda/2)e^{-\mu(\lambda/2)t}$, in which $R_{\mathrm{II}}(\lambda/2)$ is the fraction of the incident energy $E_s(\lambda/2)$ diffracted into the second order and the exponential term accounts for the absorption at this shorter wavelength.

The total energy $E(x)$ collected at x can now be written as

$$E(x) = E_s(\lambda)R_{\mathrm{I}}(\lambda)e^{-\mu(\lambda)t} + E_s(\lambda/2)R_{\mathrm{II}}(\lambda/2)e^{-\mu(\lambda/2)t} + \ldots \quad (1)$$

if contributions coming from third or higher orders are considered negligible.

From (1) we obtain

$$e^{-\mu(\lambda)t} = \frac{E(x) - E_s(\lambda/2)R_{\mathrm{II}}(\lambda/2)e^{-\mu(\lambda/2)t}}{E_s(\lambda)R_{\mathrm{I}}(\lambda)}. \quad (2)$$

Studies[15] of the grating efficiencies for instrumental arrangements of the type used in these measurements show that, starting with the short wavelengths, $R_{\mathrm{II}}(\lambda/2)$ is essentially zero up to a certain critical value λ_c.

Over this region, the second term on the right hand side of equation 2 is zero and there is no blending of lines. Consequently $e^{-\mu(\lambda)t}$ can be computed directly from the information contained in the traces of Fig. 1(a) and 1(b) with the aid of the photometric process which is used to convert the observed deflections into the energies $E(x)$ and $E_s(\lambda)R_{\mathrm{I}}(\lambda)$ associated respectively with the corresponding line images in the absorption and reference† spectra.

At wavelengths greater than λ_c, it is necessary to include the correction arising from order overlap. In principle, this can be carried out since the reflecting powers are known and $e^{-\mu(\lambda/2)t}$ becomes available from the piecemeal determination of the absorption over the

* For simplicity, the line images will be regarded as rectangular in shape.

† By the term reference spectrum we mean the dispersed radiation which has passed only through (1) a foil of substrate identical to the one supporting the absorbing material or (2) through one of a pair of samples which are identical in all respects but differ in the thickness of the absorbing layers. In the second instance, effects arising from the transition layer between substrate and evaporated layer are eliminated.

region free from overlap. Also, the term $E_s(\lambda)R_I(\lambda)$ can be arrived at from the reference spectrum considering the energy associated with the blended line of wavelength λ.

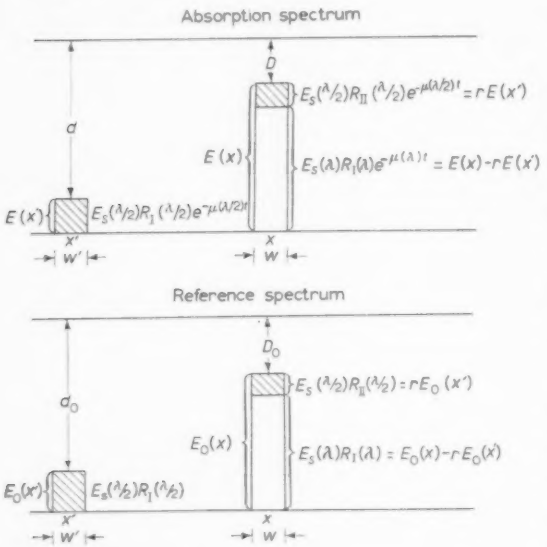

FIG. 2. A schematic diagram which illustrates the effect of order overlap in the idealized case where the second-order image of a line of wavelength $\lambda/2$ coincides with the first-order image of a line whose wavelength is λ.

From the contents of Fig. 2, equation 2 may be cast into the form

$$e^{-\mu(\lambda)t} = \frac{E(x) - rE(x')}{E_0(x) - rE_0(x')} \tag{3}$$

where

$$r = R_{II}(\lambda/2)/R_I(\lambda/2).$$

By the use of the calibration curve and the ratio of image widths* at x' and x the various energies can be expressed in terms of deflections d, D, d_0 and D_0 whose magnitudes are read directly from the traces.

The resulting formula for the linear absorption coefficient then reduces to

$$\mu(\lambda)t = \ln\left\{\frac{F(D_0) - rF(d_0)\cos\theta/\cos\theta'}{F(D) - rF(d)\cos\theta/\cos\theta'}\right\} + \ln K \tag{4}$$

where $F(D_0)$, $F(d_0)$, etc., represent relative energies per unit length along the trace corresponding to deflections D_0, d_0, etc. The second term on the right has been introduced to take care of the ratio between exposures.

A numerical example from the absorption spectrum of Cu is included here to show the magnitude of the discrepancies which may arise from order contamination. The strong OIII line $\lambda = 129{\cdot}9$ Å appearing in the second order overlaps with a first order line at $\lambda = 260$ Å. The $M_{2,3}$ edge of Cu is at 162·5 Å so that, in this example, while the absorption by the metal reduces the intensity of the offending line, the transmitted intensity is sufficient to contaminate a first order radiation chosen to evaluate $\mu(\lambda)t$ on the transparent side of the edge. From known reflectivities at $\lambda = 130$ Å, $r = 0{\cdot}40$ and for the particular angle of incidence the numerical value of $\cos\theta/\cos\theta'$ as calculated from the grating relation is 1·32. The values of $\mu(260)t$ as calculated from equation 4 for two different copper runs are listed in Table 1 along with the corresponding values of $\ln[F(D_0)/F(D)] + \ln K$ which would have been taken as the result if blending were disregarded.

The specially chosen illustration involving the coincidence of first- and second-order images of well isolated lines is not encountered frequently. More often, second-order images fall on shoulders of lines or appear in the background. Since photometric considerations necessitate the use of wide slits (~ 1 mil), the identification of and correction for partial overlapping becomes a hopeless task.

The foregoing account points out clearly that the absorption curve will be distorted if spurious results arising from blending of lines are not eliminated. Before undertaking the present measurements, the spectrum of the capillary spark was examined for the purpose of ascertaining the limits of the spectrum which could be regarded as essentially uncontaminated from order overlap. No strong evidence was found for second order blending in the 60 Å–180 Å region though at the upper end of this region some contribution to the background coming from intense lines at 85 Å was suspected. Above 180 Å, second- and third-order lines were definitely present. (Fortunately contamination by third-order lines was not a serious problem in our range of measurements.)

In the spectral region of interest, first-order lines subject to possible blending were excluded. The sorting was carried out on the basis of wavelength identification and consideration of intensities. Owing to the complexity of the spectrum and the distortion of line peaks and shapes resulting from overlap, this procedure does not insure the unambiguous identification of blends. Consequently, for further verification we resorted to the use of 6500 Å Al foils as band pass filters.[16]

* The widths of lines on the traces are assumed to be determined from geometrical considerations. If w_0 is the width of the slit on the Rowland circle, then the width w of a line diffracted at angle θ from the grating normal is given by $w = w_0/\cos\theta$. For a given position x measured from the central image along the Rowland circle, the angle θ can be calculated from the grating equation $n\lambda = a(\sin\varphi - \sin\theta)$ where a is the grating constant and φ is the angle of incidence measured from the grating normal.

Table 1. *An example which shows the effect of order contamination in the Cu spectrum*

t	k	$\mu(260)t$ from equation 4	$\mu(260)t$ uncorrected	Difference	Percentage difference
500 Å	8·11	1·69	2·01	0·32	19
986 Å	25·0	3·07	3·60	0·53	17

In this instance the first-order line at $\lambda = 260$ Å is overlapped by the intense line $\lambda = 129{\cdot}9$ Å appearing in the second order.

VOL. 3 1957

Needless to say, the exclusion of lines subject to overlap materially reduced the number of radiations which could be relied upon for carrying out the measurements. Although this circumstance makes it more difficult to ascertain the shape of and details in the absorption curve, we found it advantageous to work with only the spectrum of the capillary discharge. In this source the majority of the lines are emitted by the light elements and can be identified from existing analyses. In dealing with the denser spectra produced by the discharge between metal electrodes one is faced with a more difficult task of spotting the lines which suffer from overlap, since, in the heavier metals, the spectra are more complex and the observed transitions are only partially analysed.

In passing we note that even if a continuum were used for the incident radiation one would still face the prolems arising from the presence of higher order spectra in the dispersed radiation. As described elsewhere,[17] the absorption curve may be deduced from observations with the aid of instrumental characteristics related to the distribution of intensity among various orders.

Effects due to background radiation

A certain amount of background fogging is apparent in the spectrograms. As mentioned previously, the source emits a feeble continuum, which upon dispersion enhances the intensity of the characteristic line spectrum. It may consist of radiation appearing in the first order, but such a continuum may also contain shorter wavelengths in higher orders of diffraction. In the absence of order overlap, the presence of a background of this nature is not objectionable if the source characteristics remain unchanged. Because of the short wavelength cut-off in reflection imposed by the setting of the grating, no significant contribution is expected from the continuum emitted by the source at wavelengths shorter than 60 Å.

Fogging of plates is also caused by radiation scattered incoherently by the grating. Such diffuse illumination may contain *all wavelengths* present in the source from the far ultraviolet up to and including the visible. The amount of diffuse fogging depends on the transmission by the particular absorber. Thus the visible and near u.v. content of the scattered radiation will contribute differently to the reference and absorption spectrograms.

Because of the heterogeneous composition of the background there appears no ready means for applying a correction. In the course of our measurements, fog arising from this cause was kept to a minimum by keeping the grating as free as possible from scattering centers and by avoiding long exposures which tend to enhance the effect. The exclusion of long exposures prevented us from utilizing the weaker lines in the spectrum. In the interest of repeatability of results, plates with fewer usable lines were favored over those in which the spectrum was more fully developed at the expense of a noticeable background density.

Photometric considerations

Although the intensity distribution of soft X-ray emission bands has been determined by photomultiplier or counter techniques, the electrical recording of incident and emergent intensities has not been attempted in connection with absorption measurements in the 100 to 300 Å region, mainly because a convenient source of continuous radiation is not available. Intensity comparisons are therefore carried out by photographic registration. The method involves a calibration procedure which is described elsewhere.*

Special photographic materials must be used in this region, and in the present work, the Ilford QI emulsion came nearest to meeting the overall requirements. As will be pointed out, the main drawback of this emulsion is its limited range of usable densities. However, as tests have indicated,[17] the emulsion has the redeeming feature in that it possesses a flat wavelength response when densities produced by equal amounts of energy are compared over the 100 to 300 Å region.

The plates used for the entire set of measurements came from a single batch of the emulsion. Since the conditions under which plates are developed can be controlled quite closely, the critical step in intensity comparisons lies in determining the calibration of the emulsion. In our case, a calibration curve correlating

* See survey article by D. H. TOMBOULIAN in reference 12 for a discussion of the special considerations and difficulties which accompany intensity measurements by the methods of photometry in the far ultraviolet.

microphotometer deflections with relative intensities was prepared from spectrograms possessing a known exposure ratio K. The final curve was constructed from several individual calibrations. It was tested and found that it could predict the expected constant energy ratio between corresponding lines of two spectral traces independently of the line intensities involved.

It will now be shown that by virtue of the nature of the functional dependence of relative intensity on photographic density, errors associated with the reduction of traces can give rise to large fluctuations in the computed value of μx (linear absorption coefficient times sample thickness), unless the use of the calibration curve is limited to densities of intermediate value. The errors referred to stem from the estimation of deflections, from residual uncertainties in the microphotometer adjustments, and from the effect of inhomogenieties in the emulsion. The microphotometer was so adjusted that the readings associated with zero and full transmission corresponded to scale deflections of 0 and 100 divisions respectively. The graph in Fig. 3 shows the percentage

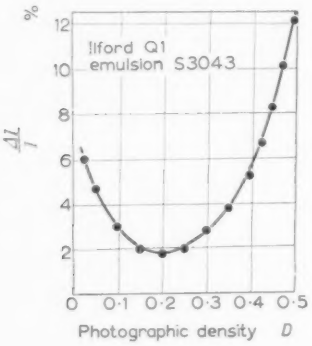

FIG. 3. A plot which shows the percentage error in intensity determinations arising from a given error in the microphotometer record. For the designated emulsion, $\Delta I/I$ represents the expected fractional error as a function of photographic density D.

error $\Delta I/I$ introduced into the determination of the relative intensities as a function of the photographic density D. The plot was deduced from our particular calibration curve, assuming an error of 1/2 division independent of deflection. From the relation $\mu x = \ln(I_0/I)$ it follows that the magnitude of the maximum error in the value of μx is given by

$$|\Delta \mu x| = |\Delta I_0/I_0| + |\Delta I/I|$$

in which the two terms on the right-hand side represent the magnitude of fractional error to be associated with the intensity measurement as deduced from the traces of the reference and absorption spectra respectively. The information contained in the graph of Fig. 3 indicates that the error in the value of μx can be kept below 10 per cent only if the densities are confined to values ranging between 0·005 and 0·40. The corresponding intensity variation is only eight fold, indicating the narrowness of the usable density range possessed by these special emulsions. The above mentioned error (1/2 of one division) is somewhat generous and as deduced from repeated measurements, the values of μx did not deviate by much more than 5 per cent. To achieve this precision it was often necessary to restrict our observations to lines whose photographic densities fell in an even smaller density range than quoted above. Furthermore, such a limitation often necessitated the exploration of the absorption spectrum in a piecemeal fashion, by varying the exposures of individual runs. Thus, spectrograms which were suitable for studying the behavior over regions of high absorption were over-exposed in the transparent regions for which lighter exposures had to be obtained.

Information gleaned from the construction of a large number of calibration curves indicates that over the density range specified above, the plot correlating deflection with intensity is sensibly linear. The slope or range of this portion does not appear to change materially from plate to plate or even from one preparation of the emulsion to the next. In view of this property, a master calibration curve was used for the reduction of plates, provided the stock emulsion remained unchanged.

3. EXPERIMENTAL RESULTS

General discussion

The measurements reported here are concerned with the photoelectric absorption by a $3p$ electron belonging to the $3s^23p^6$ subshell in the sequence of elements from Cr → Ge. Although this subshell becomes filled at A, the sequence from A → V could not be examined because of experimental restrictions described previously. Hence the present investigation was begun with Cr in which the $3d^54s$ configuration comprises the valence group. The M shell ($3s^23p^63d^{10}$) is completed at Cu which has one $4s$ electron outside the M shell. In the following three elements Zn, Ga and Ge, additional N electrons appear in the valence group. Thus, in the absorption process of interest here, the M_2 and M_3 levels constitute the initial states while the final states fall in the continuum of vacant levels above the $3d$, $4s$ or $4p$ bands as the case may be.

For each absorber, the outcome of the photometric reductions is presented by a graph which shows the variation of the mass absorption coefficient τ (in cm²/g) as a function of the incident photon energy E (in eV). The mass absorption coefficients are calculable directly from transmission data by using surface density determinations

as obtained from the mass and dimensions of each absorber. In our case, the calculation of the linear absorption coefficients would have involved the use of the density of the material in bulk.

Inspection of the results reveals the presence of considerable background absorption as witnessed by the values of τ on the low energy side of the main discontinuity. It is probable that this background arises from the absorption by valence band electrons. The binding energies and the numbers of $3d$ and $4s$ electrons compare favorably with the corresponding quantities associated with the $3p$ electrons of the completed subshell.

At the low energy end of the spectrum a rapid rise above the background indicates the onset of the M_3 absorption. At higher energies, the rising portion of the curve must begin to include the increase in absorption occasioned by the M_2 edge. Indeed, the blending of M_2 and M_3 absorption spectra is present over the region of higher energies and introduces a certain amount of diffuseness in the characteristic features of the observed curves.

The spectrographic resolving power, as deduced from a consideration of line spectra, was such that structures 0·1 eV apart could have been separated readily. The instrumental resolution was therefore adequate to show the individual edges. (In practice it was not always possible to establish the behavior of the absorption curve in such detail, mostly because of the sparse distribution of lines in the incident radiation.)

The observed spreading over the region of the absorption jump stems partly from the widths of the initial $3p$ states. Unfortunately no data are available on the widths of these states. As a crude estimate one may take a value of 0·2 eV as an upper limit. This estimate is arrived at in a roundabout manner from data on L_3 levels[18] and GWINNER's[19] measurements on the width of the $L_3 \rightarrow M_{4,5}$ radiative transition in Ge. In addition, the assumed width is consistent with the observed $M_{2,3}$ edge structure in Ge.[4]

Some insight regarding the (M_2-M_3) energy interval may also be gained from $M_{2,3}$ emission spectra of the metals in the sequence Ti $\rightarrow$ Zn. Estimates[6] for the (M_2-M_3) interval, as deduced from the shift in emission edges, lie between 1–2 eV. In view of the magnitude of inner level widths and separations, one might expect that, with the available instrumental resolving power, a break in the absorption curve corresponding to the onset of M_2 absorption should still be detectable. Indeed a suggestion of a break is present in some of the runs.

An additional contribution to the diffuseness of the edge structure comes from the energy dependence of the absorption coefficient on the high energy side of an individual edge (in our case the M_3 edge). Over the initial portion of the curve which is essentially free from overlap, the coefficient probably obeys the arctangent relation.* However, the shape of the arctangent is an idealization based on an assumed uniform density of states and may not be relied upon to correspond to the situation in reality. In the case of the well developed edge in the spectrum of Fe, attempts were made to match the observed shape over the rising portion of the curve by combining two arctangent curves in the intensity ratio expected from statistical weights. In this procedure, $h\Gamma$ was set equal to 0·2 eV and the coefficient C' was first deduced by a fit over the initial portion of the curve ascribable to the M_3 edge alone. It became clear that it was not possible to reconstruct the observed behavior of the absorption coefficient by the superposition of individual curves, even when reasonable allowances were made for the relative positioning and widths of the components involved. There is the possibility that the actual intensity relations are not properly represented by the simple assumption based on statistical weights and that the M_3 absorption might predominate. (In the corresponding emission spectra, the M_3 band appears to be more than twice as intense as the M_2 band.) In the main, it seems best to attribute the overall edge diffuseness to the shapes of the individual absorption curves, which, unlike the behavior predicted by the arctangent relation, may be expected to show an increase in absorption

* The reference here is to the formula developed by RICHTMYER, BARNES and RAMBERG *Phys. Rev.* **46,** 843 (1934),

$$K(\nu) = C' \left\{ \frac{1}{2} - \frac{1}{\pi} \arctan\left(\frac{E_{\text{edge}} - E}{h\Gamma/2} \right) \right\}.$$

In this relation, E is the incident photon energy, E_{edge} is the energy corresponding to the edge, $h\Gamma$ represents the width of the initial level and C' is a constant.

for energies extending several eV beyond the threshold.

It is instructive to attempt a decomposition of an observed curve into components which are to represent the individual M_2 and M_3 absorptions. For the illustrative example we have selected the Fe $M_{2,3}$ absorption spectrum for which we have reasonably complete and reliable measurements. We take the M_2-M_3 separation to be 1·5 eV—a value which is supported by evidence from emission spectra. Moreover, we assume that the cross-section for the M_3 absorption process is twice that of the M_2. We have regarded the observed composite curve to be free from overlap over the energy interval of 1·5 eV following the onset of the M_3 absorption. This uncontaminated portion of the curve enables us to construct the initial part of the individual M_2 absorption curve taking into account the postulated ratio between the coefficients. By subtracting the initial portion of the M_2 curve from the resultant, it becomes possible to extend the initial portion of the M_3 curve which extension in turn allows us to lengthen the M_2 curve. The two dotted curves shown in Fig. 4 were constructed in this manner from the experimentally observed curve shown by the solid line.

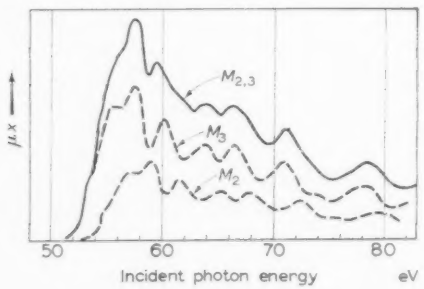

FIG. 4. An attempted resolution of the observed $M_{2,3}$ absorption curve of Fe into individual M_2 and M_3 component curves.

Over the region of the edge where the absorption is changing rapidly a meaningful decomposition is not possible unless the shape of the measured curve and the M_2-M_3 interval are known accurately. However, the analysis indicates that beyond 60 eV, the observed curve, though a blend, reproduces the features of the M_3 curve with little distortion and that the observed positions of peaks are shifted from those found in the component M_3 curve by not more than a few tenths of an electron volt. Also, the lack of symmetry apparent in the individual peaks of the observed curve, becomes less prominent in the decomposed curves. Actually, the contribution coming from the M_2 absorption may be less, so that the features of the observed curve would correspond even more closely to those of an uncontaminated absorption spectrum.

Excepting the cases of Cu and Ni[20] the authors are not aware of any detailed studies of the L_2 and L_3 absorption spectra of the sequence of elements dealt with in this investigation. Such spectra involve absorption by $2p$ electrons and on the basis of the selection rules should show features similar to those of the individual M_2 and M_3 spectra. In contrast to the $(M-M_3)$ separation (1 to 2 eV) the L_2-L_3 interval[6] ranges from 10 to 32 eV (Cr → Ge). Hence the blending effects alluded to above should be absent. For an investigation of the K absorption spectra of the transition elements the reader is referred to the work of BEEMAN and FRIEDMAN.[18]

Comments on individual spectra

The results of the present investigation are presented in graphical form by the plots appearing in Fig. 5 to Fig. 13. In each case the data were assembled from a consideration of several reductions of spectrograms obtained under varying conditions. By and large, the features portrayed by the graphs were repeatable from run to run. We shall now comment briefly on the absorption spectra of each of the elements.

Chromium. Evaporated Cr films even as thin as 20 Å are known to be continuous[14] in structure. This may perhaps be the reason for the fairly high values of τ obtained for this metal.

The spectrum covers the 200–300 Å region, the edge being located at 285 Å. At these comparatively long wavelengths the measurements suffer from (1) the increasing absorption by the substrate, (2) the gradual loss in the grating reflectivity and (3) the falling off of the emulsion response. Moreover, in our particular source, there was a scarcity of strong lines in the region above 260 Å. The use of filters to eliminate blending would have resulted in prohibitively long exposures. As a consequence the data on the short wavelengths side of the edge up

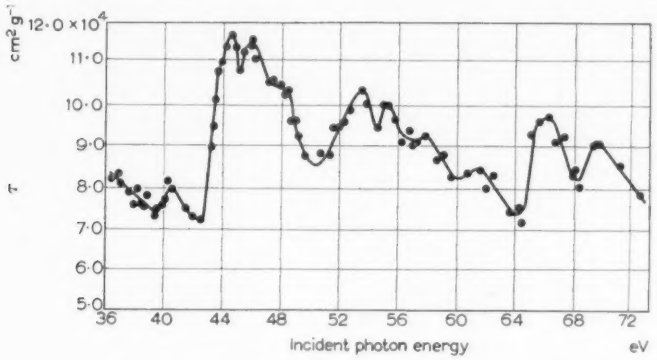

FIG. 5. The $M_{2,3}$ absorption spectrum of chromium. ($Z = 24$) 27 μg cm^{-2}

VOL. 3 1957

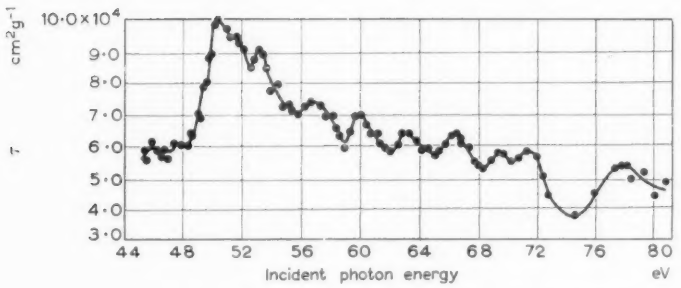

FIG. 6. The $M_{2,3}$ absorption spectrum of manganese. ($Z = 25$) 21 μg cm^{-2}

to about 50 eV are likely to be influenced by order contamination in spite of all efforts made to exclude errors arising from this cause.

Manganese. The information in Fig. 6 was obtained by combining the reductions of ten plates. (In all, close to 50 spectrograms were taken!) In the earlier stage of this work, some difficulty was encountered in confirming certain features of the curve. The edge absorption was seen to rise in an unusually steep manner and a narrow region of high transmission was repeatably noticed at a few electron volts from the edge. An examination of this region by means of filters showed that the above features originated from intensity distortions produced by second-order lines. In the result reported above, the entire region extending from 44 to 72 eV was investigated by the use of an Al filter.

Iron. Al foil filters were also utilized in this case. A striking characteristic of this spectrum is found in the large change in τ at the edge and the unusual width of the edge. The case of Fe is the only one in the entire sequence showing these features. However the values of $\Delta\tau$, ΔE (See Table 3 for definitions), the position of the first absorption maximum and the shape of the initially rising portion are in excellent agreement with the observations previously reported by CARTER and GIVENS.[3] These authors used a different source, a different emulsion and exercised greater care in avoiding possible oxidation of the evaporated absorbers. The correspondence found between the two sets of measurements may be taken to mean that the surface contamination of our samples was not serious. It is not possible to make a comparison over the region of higher energies, since in the data of

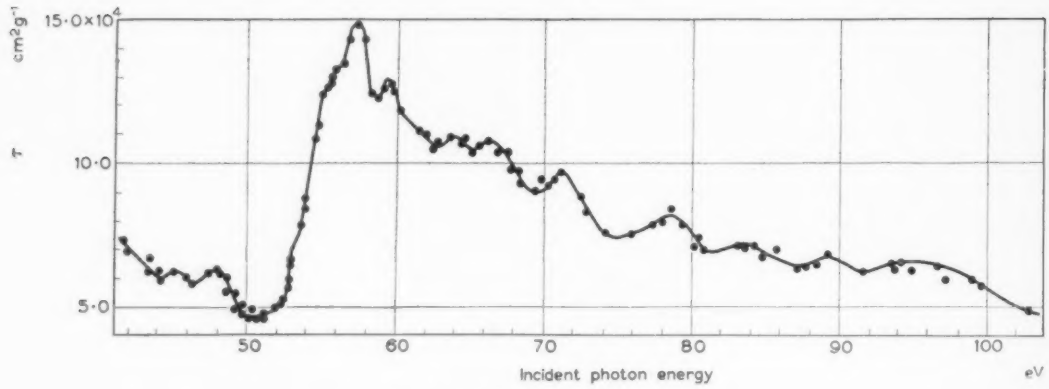

FIG. 7. The $M_{2,3}$ absorption spectrum of iron.
($Z = 26$) 19 μg cm^{-2}

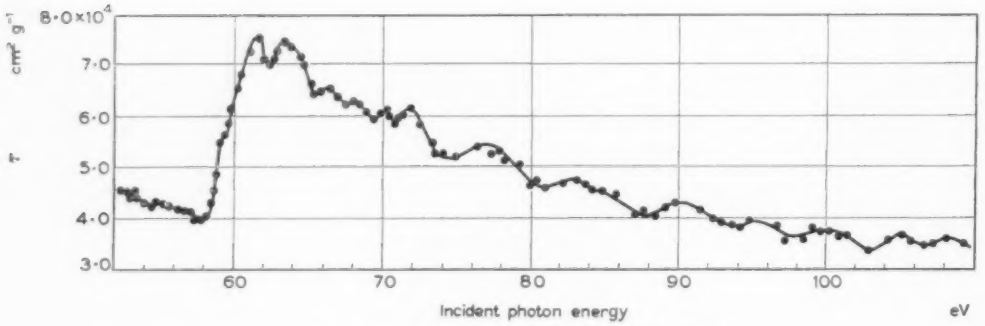

FIG. 8. The $M_{2,3}$ absorption spectrum of cobalt.
($Z = 27$) 33 μg cm^{-2}

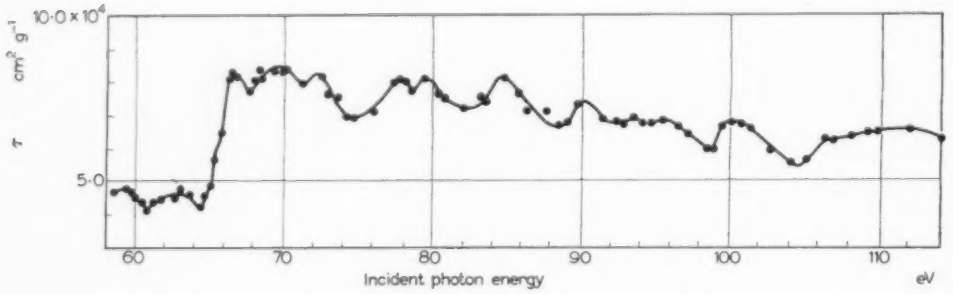

FIG. 9. The $M_{2,3}$ absorption spectrum of nickel.
($Z = 28$) 22 μg cm^{-2}

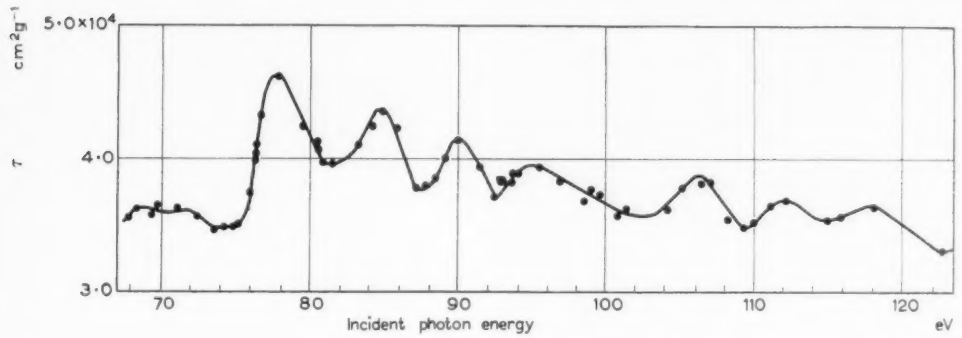

FIG. 10. The $M_{2,3}$ absorption spectrum of copper.
($Z = 29$) 88 μg cm^{-2}

VOL.
3
1957

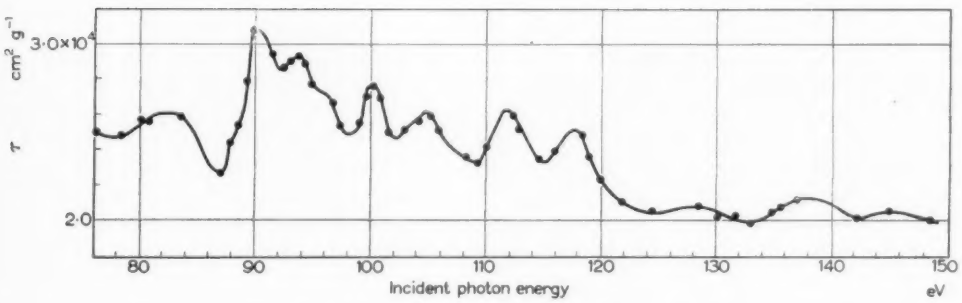

FIG. 11. The $M_{2,3}$ absorption spectrum of zinc.
($Z = 30$) 143 μg cm^{-2}

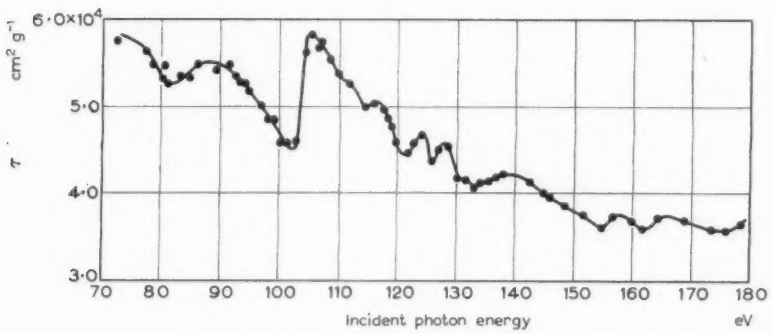

FIG. 12. The $M_{2,3}$ absorption spectrum of gallium.
($Z = 31$) 57 μg cm^{-2}

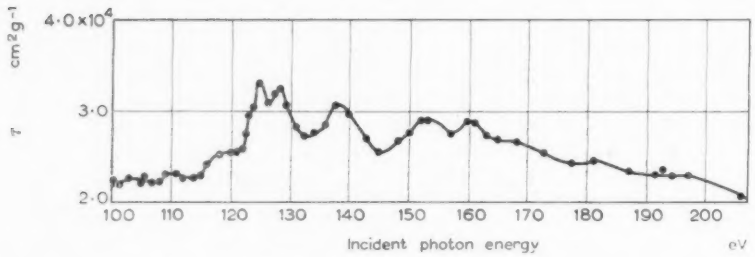

FIG. 13. The $M_{2,3}$ absorption spectrum of germanium. ($Z = 32$) 63 μg cm^{-2}

CARTER and GIVENS the highest incident photon energy is 70 eV. In passing we note that in the present measurements, the second peak appears at 59·5 eV which is 0·5 eV higher than the value given by the authors cited above.

As discussed in the introduction to this section, the magnitude of the entire rise at the edge is not to be associated strictly with the rise due to the individual M_2 and M_3 jumps, but is strongly influenced by the behavior of the individual curves. As can be seen from Fig. 4, the edge jump for each individual absorption is succeeded by a second prominent rise. For this reason the values of $\Delta\tau$, and ΔE, shown in Table 3 appear inordinately high when compared with the corresponding values listed for the remaining members of the sequence. Though the arctangent relation does not fit the data satisfactorily, yet a crude attempt at matching leads to an estimate of ~ 2 eV for the overall $M_{2,3}$ edge width. This corresponds to $\Delta\tau \cong 4\times10^4$ cm^2/g, in reasonable agreement with the magnitude of $\Delta\tau$ observed for the neighboring elements.

Cobalt. In 1936 SKINNER and JOHNSTON[5] reported that the $M_{2,3}$ edge was in the neighborhood of 202 Å, but gave no extended absorption measurements. More recently J. H. DENNY[21] has examined the Co spectrum.

As was done in the cases of Mn and Fe, the values of τ offered here were determined in part from runs made with an Al filter. The mean wavelength position of the $M_{2,3}$ discontinuity is seen to fall at 208 Å. The edge width again appears somewhat large, presumably for the reasons advanced in the preceding remarks on Fe. The absorption jumps found in the case of Cr, Mn and Ni are quite comparable and have an average value of $4{\cdot}20\times10^4$ cm^2/g. In Co, $\Delta\tau = 3{\cdot}6\times10^4$ cm^2/g.

Nickel, copper and zinc. In the M-series under study, the location of the $M_{2,3}$ edge recedes from 285 Å at Cr to 101 Å at Ge. In examining the spectra of the elements Ni → Ge, it was considered unnecessary to resort to the use of filters, since no serious effects are expected from the blending of orders below the Ni edge which falls at 189 Å. For Cu, the increase in τ at the edge is $1{\cdot}1\times10^4$ cm^2/g, a value which is only 25 per cent of the average jump observed in the case of the preceding metals Cr → Ni inclusive. For Zn, $\Delta\tau = 0{\cdot}8\times10^4$ cm^2/g and those of Ga and Ge are of the same order of magnitude.

Thus, the increases in τ at the edge seem to divide themselves into two groups, the values below copper being about four times as high as those found in Cu and the following three elements. This drop in absorption is undoubtedly associated with the modification in the density of states resulting from the completion of the 3*d* subshell at Cu.

To facilitate comparison with the earlier work on Ni, Cu and Zn the information derived from the present measurements is given in Table 2 along with the corresponding data obtained by other authors.[1,2] Values not quoted numerically by these writers were read from graphs and converted to energies using $V(\text{eV}) = 12397{\cdot}43/\lambda(\text{Å})$. It is seen that the agreement with older results is quite satisfactory as to the positions of mean edges and fine structure maxima.

Gallium and Germanium. We have no information regarding the structure of the gallium absorbers used. As reported by us in an earlier paper[4] there is reason to believe that the special preparation involved in the Ge absorbers led to films which were crystalline in nature. The results

Table 2. A comparison of the spectral positions of edges and secondary maxima with those obtained by previous investigators

Metal	Reference	Mean position of $M_{2,3}$ edge	Secondary maxima								
Nickel	*S–J*	65·8	66·6	69·3	—	78·5	84·4	90·2	99·6	110·2	—
	Present data	65·5	66·6	68·5	72·0	78·0	84·4	90·2	100·2	112·0	120·5
Copper	*J**	76·2	81·1	84·4	—	—	99·6	106·8	112·7	118·0	—
	Present data	76·3	—	84·5	89·8	95·0	—	106·2	112·0	117·8	126·0
Zinc	*J*	88·9	93·3	99·2	105·1	—	113·8	—	121·5	—	—
	Present data	88·8	93·5	100·0	105·0	111·5	—	117·5	—	128·0	137·0

Source designations and the meaning of symbols are listed below: *S–J*, H. W. B. SKINNER and J. E. JOHNSTON;[1] *J*, J. E. JOHNSTON;[2] *J**, edge value from *J* but secondary structure from *S–J*.†

† Value obtained by averaging M_2 and M_3 edge data for Cu and Zn as given in reference 2.

Table 3. Data on $M_{2,3}$ absorption edges for the sequence Cr → Ge *as obtained from the present measurements*

Element	Z	$M_{2,3}$ absorption						High energy emission limits (a)		(b)	
		E_1	E_2	ΔE	$\Delta\tau \times 10^4$	E_m	λ_m	M_2	M_3	M_2	M_3
Cr	24	42·5	44·6	2·1	4·5	43·5	285·6	42·0	43·0	41·6	42·1
Mn	25	48·3	50·3	2·0	4·0	49·5	250·4	47·6	48·8	46·2	46·8
Fe	26	51·4	57·4	6·0	10·2	54·3	228·3	52·8	54·2	51·7	52·3
Co	27	58·0	61·7	3·7	3·6	59·6	208·0	60·0	61·6	—	—
Ni	28	64·5	66·6	2·1	4·0	65·5	189·3	66·1	68·1	65·8	66·7
Cu	29	74·4	77·8	3·4	1·1	76·3	162·5	76·4	79·2	74·7	75·9
Zn	30	87·0	89·6	2·6	0·8	88·8	139·6	—	—	—	—
Ga	31	102·0	105·2	3·2	1·3	103·6	119·7	—	—	—	—
Ge	32	121·5	124·5	3·0	0·7	123·0	100·8	121·5	123·5	—	—

All energies are expressed in eV. Wavelengths corresponding to given energies are computed from $E(\text{eV}) = 12397{\cdot}43/\lambda(\text{Å})$. The known values of the high energy emission limits are also included for comparison. See below for the definition of column headings and references to sources:

E_1 The photon energy at which absorption increases due to $3p$ excitation.
E_2 The photon energy at which the first maximum is reached in $3p$ absorption.
ΔE The energy interval $E_2 - E_1$.
$\Delta\tau$ The change in the mass absorption coefficient in the energy interval ΔE.
E_m The mean edge energy i.e. a value of the energy in the interval ΔE at which the mass absorption coefficient has increased by $\Delta\tau/2$.
λ_m The wavelength corresponding to the energy E_m.
(a) Photographically recorded edges; Cr → Zn reference 6.
(b) Photoelectrically recorded edges; reference 8,9.
Data for Ge taken from reference 4.

on Ge are reproduced here only for the purpose of making the sequential comparison of $M_{2,3}$ spectra as complete as possible.

In Ga and Ge the magnitude of the jump at the edge is characteristic of the group of four elements with completed $3d$ shells. The background absorption in Ga is quite high before the onset of absorption by $3p$ electrons but shows a continuous

drop with increasing incident photon energy. In this respect the Ga spectrum is similar to that of the preceding metal Zn.

Numerical results

In Table 3 we list numerical information derived from the present study of the $M_{2,3}$ absorption bands of the elements Cr → Ge. The definitions of the various quantities appearing in the table are given under the caption. Where available, the high energy limits of the corresponding M_2 and M_3 emission bands investigated by various authors are also included for comparison. Except in the case of the semiconductor Ge, no energy gap is expected between the filled and unfilled portion of the valence bands.

In comparing the spectral locations of emission and absorption edges, it must be remembered that there is an element of diffuseness which is inherent in the nature of the emission or absorption process itself. An excited state has a finite lifetime, therefore the emission intensity or the absorption coefficient will possess an energy distribution which actually extends indefinitely but may be characterized by a width. In considering transitions between an inner state and various states of the continuum, the observations represent a superposition of distributions as modified by the instrumental response curve. Speaking loosely in terms of an energy level diagram depicting stationary states, one is led to designate such sharp features as the onset of absorption or the high energy limit in emission. However, only in the spirit of the remarks above, is one justified in expecting a sort of agreement between the highest observed energy of a photon emitted in the valence → $3p$ transition and the incident photon energy required to eject a $3p$ electron into the lowest empty state of the continuum.

The correspondence between emission and absorption edges in metals has also been explained[22] on the hypothesis that, below the conduction band, there exist excitation states associated with an ion in the metallic lattice. In this model, the absorption process is described on the basis of triple electron transitions. The view adopted here is the conventional one based on single electron transitions.

The values of E_m listed in Table 3 may not be related directly with the data taken from emission edges. In the sense of the foregoing comments it is not unreasonable to compare the values of the energy E_1 corresponding to the observed onset of the M_3 absorption with the designated M_3 high energy emission limits. E_1 should at least be equal to the M_3 limit and comparison shows that this requirement is met in the cases of Cr and Mn. In the sequence Fe → Cu there is an overlap between the observed emission and absorption limits by as much as 2 eV. The apparent overlap may arise from errors in establishing the energy scale or from experimental difficulties in judging the limits. It may be contended that an overlap of this sort may also originate from the width (~ 0·2 eV) to be associated with the $3p$ level. However, the magnitude of the overlap is inconsistent with this view.

The emission data of GYORGY and HARVEY[8,9] are consistently lower than those of SKINNER, BULLEN and JOHNSTON.[6] Also the M_2-M_3 interval derived from their edge data lies in the range 0·5–1·0 eV. On the basis of the diffuseness of the edge observed in our measurements, this interval would appear to be ~ 2·0 eV. The edge breadth should be at least equal to the M_2-M_3 interval plus the width of the inner level.

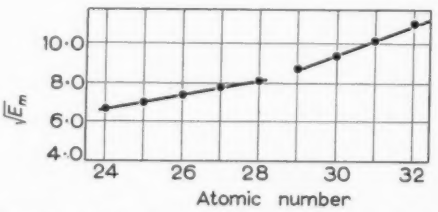

FIG. 14. A Moseley plot of the mean threshold energy corresponding to the onset of absorption by $3p$ electrons in the sequence Cr to Ge.

Fig. 14 shows a typical plot of $\sqrt{E_m}$ against the atomic number Z. It is interesting to note that the break in the otherwise linear portions occurs at $Z = 29$ (Cu).

Secondary maxima

On the high energy side of the initial steep rise, the absorption coefficient shows the customary fluctuations. In Table 4 we list the spectral positions of secondary maxima as read from the observed curves. As can be seen from the plots, the individual structures vary considerably in shape

Table 4. *Secondary structure*

Element	Secondary absorption maxima										
Cr	45·8	48·0	53·6	55·3	58·0	62·0	66·0	69·7			
Mn	51·5	53·1	56·7	59·9	63·0	66·6	69·5	71·5	78·0		
Fe	59·5	64·0	66·4	71·0	78·5	83·4	95·0	114·0	130·0		
Co	63·1	66·4	68·2	70·2	71·8	77·8	83·8	90·4	95·1	100·2	105·0
Ni	68·5	72·0	78·0	84·4	90·2	100·2	112·0	120·5			
Cu	84·5	89·8	95·0	106·2	112·0	117·8	126·0				
Zn	93·5	100·0	105·0	111·5	117·5	128·0	137·0				
Ga	116·5	124·5	128·0	140·0	157·0						
Ge	128·0	137·5	152·5	160·0							

The listed values represent the incident photon energies (in eV) at which maxima in the absorption coefficient are observed in the region of the fine structure.

VOL. 3 1957

and width, so that the peak positions are subject to uncertainties amounting to as much as 0·2 eV.

In a broad sense, such structures should be accounted for by the prohibitively difficult theory which underlies the photoelectric absorption by $3p$ electrons of a particular solid. The desired treatment would combine the roles played by the transition probabilities and the characteristic electronic level structure to predict the energy dependence of the absorption coefficient. In the absence of such a general approach, several more limited explanations of the structure exist. In KRONIG's view the secondary fluctuations in τ are regarded as characteristic of the crystalline structure alone and their origin is associated with Bragg reflections suffered by the ejected photoelectron. In other models, the structure in the neighborhood of the edge is regarded as atomic in character. Thus HAYASI[23] adopts the view that secondary maxima arise from transitions in which the final state of the photoelectrically ejected electron is a so-called "quasi-stationary" state. HAYASI points out that such stationary states are produced when the electron waves form a standing wave pattern in the close neighborhood of the atom from which the electron was emitted.

Moreover, in terms of a one-dimensional model containing a deviation from the periodic potential, he has concluded[24] that there is close correspondence between the energies of "quasi-stationary" states and those of the Brillouin zone boundaries. In the case of K absorption spectra, where $l = 1$ for the final state, the predictions of the model can be carried out in a relatively simple manner. Correlations[25] with data derived from K spectra lend some support to this concept.

It is of some importance to note that the Kronig model determines a state into which an electron may not make a transition by the absorption of a photon. In the HAYASI picture, the final level corresponds to a bound state into which photoelectrons may be transferred. In the first case the characteristic energy specification corresponds to an absorption *discontinuity*; in the second to an absorption *maximum*. In either model the expression for the critical energy in the case of cubic structures is the same and is given by

$$W = h^2(\alpha^2+\beta^2+\gamma^2)/8ma^2$$

where h is Planck's constant, m the electronic mass, a the lattice constant and α, β and γ are the reflection indices.

It is a characteristic of both theories that similar fine structures are to be associated with solids having the same type of crystal structure, since the fluctuations are correlated with a quantity which is

dependent on lattice parameters alone. However, the state density function characteristic of the material will in general be different, so that shapes of fine structure lines will show variations even in cases where the same crystal structure is involved.

A polyelectronic absorption process postulated by FRIEDEL[22] has also been used to predict the position of structure observed on the high energy side of the Li K absorption.

Also we must not ignore the possibility that maxima in close proximity to the edge may arise from a double excitation of inner levels by the incident photon. For instance, a K and possibly an L or M electron may be ejected simultaneously but the energy imparted to the K electron will be in excess of the energy required for the onset of K absorption in a single excitation process.

So far as is known, no theory of "quasi-stationary" states has been developed to treat the case in which the l-value of the final state is 0 or 2. In KRONIG theory, the liberated electron is represented by plane waves. This implies that experimental comparisons can only be made at energies sufficiently removed from the edge; that is, in a region where the lattice alone determines the fine structure. Experiments seem to point to improved agreement with theory for structures which are removed from the edge by 50 eV or more.

In the present work, the secondary structure lies within an energy interval of about 40 eV from the edge and the final states of the ejected electron have l-values of 0 or 2 ($4s$ or $3d$ states). The limitations imposed by the existing models prevent us for the present from attempting a correlation of the observed fine structure with predictions from theory.

Fine structure and characteristic electron losses

Recently attention has been called[26] to the possible existence of a similarity between characteristic energy losses of electrons and the fine structure found in the K absorption spectra of various materials. The comparison included most of the transition metals whose $M_{2,3}$ edge structure has been examined in this paper. Since the l-values of the core electron are different in the K and M absorption processes, it was thought worth while to see to what extent a similar correspondence could be made. The energy losses suffered by electrons transmitted by thin foils of matter range from a few eV up to 50 eV or more. Several mechanisms have been postulated[26–29] to account for these observations. In one approach, characteristic losses have been compared with the energies necessary to excite collective oscillations in the free electron gas of a metal. In another view, such losses are thought to arise from the transfer of a valence band electron into allowed states of the unfilled bands above. An alternative explanation[10] in terms of individual atomic ionization and excitation processes has also been proposed. However, primarily, it is the model based on the band to band transitions of individual electrons that leads one to consider the possibility of a correlation between absorption edge structure and characteristic losses. It must be realized that there are differences in the processes of X-ray fine structure absorption and interband transitions induced by incident primary electrons. In the absorption process as applied to $M_{2,3}$ bands it is an inner $3p$ electron that is transferred to a state above the valence band; while the characteristic losses in the case of the elements studied here are brought about by the transitions of $3d$, $4s$ and $4p$ valence electrons into higher vacant states.

PINES[29] who is a strong advocate of the plasma oscillation theory, has also considered the possibility of explaining characteristic losses on the band to band transition process. He has observed that, in the free electron approximation, a sharp line may be produced by this process only if the transition probability is large for a comparatively small number of band to band transitions, and that the favored transitions are those in which electrons occupying high energy states in the filled band are transferred to low lying states of the unfilled band.

In the absence of a clear formulation as to the reason why a correlation is expected, it was decided to compare the magnitudes of known characteristic losses, with the positions of absorption maxima as measured from an absorption edge. In dealing with the fine structure this procedure is tantamount to taking the zero of energy at the lowest unoccupied state above the filled bands.

In practice, the experimental evidence does not always allow a precise determination of energy differences owing to the diffuseness of edge and peak shapes. This state of affairs is particularly true of the $M_{2,3}$ spectra of metals belonging to the

Table 5. A comparison of secondary structures with characteristic energy losses of electrons

Cr	2·4	4·6	10·2	11·9	14·6	18·6	22·6	26·3	—		
	—	—	9·7	—	—	—	21·8	—	45·0		
Mn	2·0	3·6	7·2	10·4	13·5	17·1	20·0	22·0	28·5		
	—	—	—	9·9	—	—	—	22·1	—		
Fe	5·2	9·7	12·1	16·7	—	24·2	29·1	40·7	—	59·7	75·7
	—	—	—	15·8	19·4	—	—	—	56·1	—	—
Co	3·5	6·8	8·6	10·6	12·2	18·2	24·2	30·9	35·5	40·6	45·4
	—	5·7	—	—	—	18·3	24·0	—	—	—	47·0
Ni	3·0	6·5	—	12·5	18·9	24·7	34·7	46·5	55·0		
	—	6·0	9·4	12·5	17·6	23·4	—	47·0	—		
Cu	—	8·2	12·0	18·7	—	29·9	35·7	41·5	49·7		
	3·5	6·9	11·3	20·3	25·5	—	34·5	—	—		
Zn	4·7	11·2	16·2	22·7	28·7	39·2	48·2				
	5·7	9·9	17·0	23·1	—	—	—				
Ga	12·9	20·9	24·4	36·4	53·4						
Ge	5·0	14·5	29·5	37·0							
	—	16·0	30·1	—							

For each element, the number given in the first row represents the energy interval between the mean edge E_m and successive peaks in the fine structure. Characteristic electron loss data, taken from papers listed in references 26 and 30, are shown in the second row. For Ga, electron loss data are not available.

iron group, where one observes a superposition of the individual M_2 and M_3 absorption curves. This results in a certain blending of edges and secondary structures. As explained earlier, there is a close correspondence between the observed peak positions and those associated with the M_3 spectrum alone. The identification of the M_3 edge maxima in this manner, is likely to result in values which are shifted toward higher energies by about 0·2 eV. This error is not intolerable, in view of the fact that the energy corresponding to the M_3 edge can only be established in a makeshift manner. The energy differences given in Table 5 have been obtained by subtracting the values of E_m listed in Table 4 from the observed individual maxima. The error introduced by using E_m, instead of the energy corresponding to the M_3 edge, will depend on the degree of diffuseness produced by the overlapping of individual edge shapes. The correspondence between the two values will improve with increasing steepness of the combined edge structure. In the present treatment, a deviation toward higher energies of about 0·5 eV is to be expected. Consequently, the tabulated differences are subject to uncertainties of 0·3 eV arising only from our inability to isolate the M_3 curve. In addition, in the case of wide and flat structures, it is not possible to judge the peak positions to within $\pm 0{\cdot}2$ eV. Hence the overall error in the tabulated energy difference may run as high as 0·5 eV.

The characteristic loss values listed for a tentative comparison were taken from the measurements[26,30] of a single group of investigators, since in attempting to discover correlations one may easily be misled by the wide choice of loss values listed for the same material by different investigators. Furthermore, when the relatively large inaccuracies unavoidably present in X-ray and electron loss measurements are tolerated, one is bound to encounter fortuitous numerical coincidences. Indeed, it is possible to include in the comparison several additional loss values found in the literature. It may also be stated that with the given set of energy loss data, better agreement with

X-ray data could be attained by an allowed adjustment in the value of E_m. From the tabulation, it would appear that the evidence in favor of a correlation with M_3 edge data is less striking than that presented by LEDER, MENDLOWITZ and MARTON[26] in the corresponding comparison with K edge X-ray measurements.

Comments on the structure of the valence band

Theoretical investigations of the electronic band structure of the transition metals were initiated in 1935. Typical of this work[31,32] was the study of the energy bands in Cu and Ni. The $N(E)$ or the density of states curve deduced from the calculations was characterized by a broad $4s$ band of low density upon which was superimposed a narrower double-peaked $3d$ band of much higher density. A level density curve of this general type was considered applicable to the transition metals, except that in a given case the filled state of highest energy was governed by the number of valence electrons per atom. More recently more refined methods and more accurate boundary conditions have been applied to re-examine the band structure of a series of transition metals. The $N(E)$ curves deduced from these studies confirm the split-up character of the $3d$ band but predict somewhat narrower widths. For chromium,[33] the double peaks are nearly symmetrical and the Fermi level is located roughly at the midpoint between the peaks, in a region where the density of states is low and arises only from $4s$ electrons. For unmagnetized iron[34] the first high peak is followed by a dip at the Fermi level and a second narrower peak appears at higher energies. Much the same type of curve is found for nickel.[35] A calculation for copper[36] based on the cellular method, indicates that (1) there is a high density near the top of the $3d$ band which has a total width of 3·46 eV, (2) the top of the band lies 3·7 eV below the Fermi level, the Fermi band itself having a width of 7·1 eV.

While the authors of the various calculations referred to above believe that the general features of the $3d$ and $4s$ bands are correctly represented by the $N(E)$ curves, they still regard the calculated values of band widths to be quite tentative. In view of this situation and the fact that emission and absorption measurements yield only indirect information concerning the level density function, comparison of the present results with theory can only be made in a qualitative manner. However, such features as the widths of emission bands and the observed shapes of band edges in emission as well as in absorption will be governed primarily by the behavior of the $N(E)$ function.

Spectroscopic information derived from the study of L and M valence spectra furnish suitable material for making comparisons with the features associated with the $3d$ and $4s$ bands. The dipole transition rules prescribe that in L and M emission (valence $\rightarrow 2p$ or $3p$), intense contributions to the observed intensity distribution should result from transitions from the filled portion of the $3d$ band and to a much smaller extent from filled $4s$ states of low density. Similarly, in the complementary process, $2p$ or $3p \rightarrow$ conduction, intense absorption is expected when p electrons are transferred into the unfilled portion of the $3d$ band, though transfer of such electrons into the $4s$ states should also be present.

The L spectra of the transition metals and neighboring elements fall in the 13–27 Å region. In spite of the technical difficulties found in this region, bent crystal and ruled grating measurements have been attempted.[6,20]

There are discrepancies in the measurements, but the observed bands show no splitting of the $3d$ band contrary to what has been suggested on theoretical grounds. The L_2 and L_3 band widths as determined by grating measurements cluster around 6 eV, Ti $\rightarrow$ Cu. For the Ni and Cu L bands, bent crystal data indicate a somewhat smaller width of 5 eV. In agreement with what is expected from the general shape of the $N_s(E)$ and $N_d(E)$ curves, the emission intensities do not show an abrupt drop in the neighborhood of the high energy limit. Only a few[20] of the L series spectra of the Ti $\rightarrow$ Cu sequence have been investigated in absorption.

The $M_{2,3}$ spectra of the transition metals and neighboring elements lie in the far ultra-violet and extend from 100 Å–400 Å. Preliminary intensity measurements[6] on the $M_{2,3}$ emission bands ($3d+4s \rightarrow 3p$) have been carried out using photographic and photomultiplier techniques in recording. Since the final level in the emission process is again of the p-type, results similar to those found in L spectra are expected. Except for differences that may arise from the instrumental resolution and from the widths of the inner levels, there

is a correspondence between the widths and shapes of bands so far as the photographic studies of SKINNER are concerned. The results on M spectra for Cr, Mn, Fe, Ni and Cu as obtained by the photoelectric recording scheme of GYORGY and HARVEY,[8,9] show abrupt terminations at the high energy limit of the spectrum. This character of the observations implies that there are steep features at the Fermi limit in the $N_d(E)$ and $N_s(E)$ curves and also that the M_2 and M_3 levels are unusually narrow. It would seem reasonable that depending on the energy position of the highest occupied state relative to the peaks in the $N_d(E)$ curve, the intensity near the high energy limit will undergo a more or less gradual decline rather than suffer a sharp drop.

The evidence from absorption studies of the $M_{2,3}$ bands reported here does not contradict the theoretical model descriptive of the structure of $3d$ and $4s$ bands. As expected, the absorption is observed to be most intense in those cases where transitions into the unfilled portions of the $3d$ band are involved. As mentioned previously, in the presumed $N_d(E)$ curves for Cr and Fe the $3d$ states are filled up to a point in the low density region between the peaks, so that following the onset of $3p$ absorption there should be an intense absorption band corresponding to the energy spread of the unfilled $3d$ band. In the observations for the metals Cr $\rightarrow$ Ni, there is a considerable rise in absorption beyond the edge though the rise takes place over an energy interval which is several times that specified by theory for the empty part of the $3d$ levels. Beyond this region of high absorption, there is a more or less steady decline corresponding to the weaker $3p \rightarrow 4s$ transitions.

In Cu, Zn, Ga and Ge the $3d$ band is filled and the density of vacant levels, now arising from the intermingling of $4s$ and $4p$ is not as high. Also the transition probability of $3p \rightarrow 4s$ transitions is lower than that for the $3p \rightarrow 4d$ transition. Hence in these cases, one expects a reduction in the intensity of absorption. Indeed for Cu, Zn, Ga and Ge the rise in the absorption coefficient over the background on the low energy side of the edge is about 25 per cent of the corresponding rise in the spectra of the metals preceding copper. The behavior of the absorption curve beyond the region of the edge will be governed in part by the $N_s(E)/N_p(E)$ ratio of partial level densities.

According to the views of MOTT,[37] in Cu the highest occupied states have predominantly p symmetry and the $N_s(E)/N_p(E)$ ratio which is small at the onset of absorption is expected to rise particularly when energies corresponding to the beginning of the second Brillouin zone are reached. This prediction should manifest itself in a sharp rise in absorption but is not clearly identifiable in our measurements.

Acknowledgement—The authors wish to acknowledge the technical assistance rendered by Mr. LEON H. HINMAN in connection with the construction of the capillary light sources used in these measurements.

REFERENCES

1. SKINNER H. W. B. and JOHNSTON J. E. *Proc. Roy. Soc.* A **161,** 420 (1937).
2. JOHNSTON J. E. *Proc. Camb. Phil. Soc.* **35,** 108 (1939).
3. CARTER D. E. and GIVENS M. P. *Phys. Rev.* **101,** 1469 (1956).
4. TOMBOULIAN D. H. and BEDO D. E. *Phys. Rev.* **104,** 590 (1956).
5. SKINNER H. W. B. and JOHNSTON J. E. *Nature, Lond.* **137,** 826 (1936).
6. SKINNER H. W. B., BULLEN T. G., and JOHNSTON J. E. *Phil. Mag.* **45,** 1070 (1954).
7. KINGSTON R. H. *Phys. Rev.* **84,** 944 (1951).
8. GYORGY E. M. and HARVEY G. G. *Phys. Rev.* **87,** 861 (1952).
9. GYORGY E. M. and HARVEY G. G. *Phys. Rev.* **93,** 365 (1954).
10. STERNGLASS E. J. *Nature, Lond.* **178,** 1387 (1956).
11. NIEHRS H. *Ergebn. exakt. Naturw.* **23,** 359 (1950).
12. TOMBOULIAN D. H. *Handbuch der Physik* Vol. 30, p. 246. Springer-Verlag, Berlin (1957).
13. BOND W. L. *J. Opt. Soc. Amer.* **44,** 429 (1954).
14. SENNET R. S. and SCOTT G. D. *J. Opt. Soc. Amer.* **40,** 203 (1950).
15. SPRAGUE G. C., TOMBOULIAN D. H. and BEDO D. E. *J. Opt. Soc. Amer.* **45,** 756 (1955).
16. TOMBOULIAN D. H. and BEDO D. E. *Rev. Sci. Instrum.* **26,** 747 (1955).
17. TOMBOULIAN D. H. and HARTMAN P. L. *Phys. Rev.* **102,** 1423 (1956).
18. BEEMAN W. W. and FRIEDMAN H. *Phys. Rev.* **56,** 392 (1939).
19. GWINNER E. *Z. Phys.* **108,** 523 (1938).
20. CAUCHOIS Y. *Phil. Mag.* **44,** 173 (1953).
21. DENNY J. H. Thesis, Cornell University, 1957 (unpublished).
22. FRIEDEL J. *Phil. Mag.* **43,** 153 (1952).
23. HAYASI T. *Sci. Rep. Tôhoku Univ.* **33,** 123 (1949).

VOL. 3 1957

24. HAYASI T. and OKADA S. *Sci. Rep. Tôhoku Univ.* **37,** 331 (1953).
25. JOHNSTON R. W. and TOMBOULIAN D. H. *Phys. Rev.* **94,** 1585 (1954).
26. LEDER L. B., MENDLOWITZ H. and MARTON L. *Phys. Rev.* **101,** 1460 (1956).
27. MARTON L., LEDER L. B. and MENDLOWITZ H. *Advances in Electronics and Electron Physics* Vol. VII, pp. 183–238. Academic Press, New York (1955).
28. MARTON L. *Rev. Mod. Phys.* **28,** 172 (1956).
29. PINES D. *Rev. Mod. Phys.* **28,** 184 (1956).
30. MARTON L. and LEDER L. B. *Phys. Rev.* **94,** 203 (1954).
31. KRUTTER H. *Phys. Rev.* **48,** 664 (1935).
32. RUDBERG E. and SLATER J. C. *Phys. Rev.* **50,** 150 (1936).
33. SLATER J. C. and KOSTER G. F. *Phys. Rev.* **94,** 1498 (1954).
34. CALLAWAY J. *Phys. Rev.* **99,** 500 (1955).
35. KOSTER G. F. *Phys. Rev.* **98,** 901 (1955).
36. HOWARTH D. J. *Proc. Roy. Soc.* A **220,** 513 (1953).
37. MOTT N. F. *Phil. Mag.* **44,** 187 (1953).

J. Phys. Chem. Solids Pergamon Press 1957. Vol. 3. pp. 303–310.

NEUTRON-DIFFRACTION OBSERVATIONS ON THE PALLADIUM–HYDROGEN AND PALLADIUM–DEUTERIUM SYSTEMS

J. E. WORSHAM, JR.,* M. K. WILKINSON and C. G. SHULL†

Oak Ridge National Laboratory, Oak Ridge, Tennessee

(*Received* 1 *July* 1957)

VOL. 3 1957

Abstract—Neutron-diffraction investigations on powdered samples have shown that both hydrogen and deuterium atoms in β-phase Pd–H and Pd–D are located in the octahedral positions of the palladium lattice. Results obtained for samples with low gas concentration are inconclusive in determining the atomic positions in the α-phase, since at room temperature only a small amount of gas enters this phase. Although the vibrational amplitudes of hydrogen and deuterium are similar to those observed in other compounds, the total neutron-scattering cross-section for hydrogen in this system is abnormally low, indicating that the protons are more nearly free than in the other hydrogen compounds.

INTRODUCTION

THE palladium–hydrogen system has been of great interest for many years because of the unusual diffusion characteristics of the gas in the metal. Although extensive investigations have been made of the macroscopic properties of the system, a complete understanding of the fundamental nature of these gross characteristics has waited in part on a knowledge of the positions of the hydrogen atoms with respect to the crystal lattice. From an extensive review of the early experiments on this system, SMITH[1] has concluded that the hydrogen is present in an extensive "rift network" in the bulk of the metal. According to this concept, the hydrogen would be expected to be in a state similar to an extensive surface adsorption, and would therefore not be located within the palladium lattice. In contrast to this concept, recent diffusion experiments by DAVIS[2] have suggested that the hydrogen atoms occupy the tetrahedral positions of the face-centered-cubic palladium lattice.

X-ray investigations have shown that two different face-centered-cubic phases exist in this system, depending on the amount of hydrogen present. At low hydrogen concentrations, the α-phase exists and has a lattice constant of 3·89 Å, very nearly the same as that representative of pure palladium. However, as the hydrogen concentration is increased, the β-phase becomes present, in which the lattice is expanded to 4·02 Å. There are no intermediate values of the lattice constant, the two phases existing together at intermediate concentrations. Of course, the ranges of concentration for the two phases vary with sample temperature, and there is evidence which suggests a small amount of hysteresis, depending on whether the concentration is reached by absorption or evolution of the gas. The present investigation was initiated in an attempt to determine the positions of hydrogen and deuterium atoms in both phases of the palladium–hydrogen and palladium–deuterium systems.

EXPERIMENTAL PROCEDURE

Since there is considerable contradiction in the literature concerning the proper conditions required to aid the absorption process, some experiments were performed to determine a satisfactory

* Visiting scientist from the University of Richmond, Richmond, Virginia.

† Now at Massachusetts Institute of Technology, Cambridge, Massachusetts.

procedure by which absorption of hydrogen and deuterium could be obtained in the 100-mesh palladium powder used in the neutron-diffraction studies. These experiments admittedly were not accurately controlled, but some of the details will be given since they may be of interest.

For the neutron-diffraction investigation, it was necessary to seal the palladium powder in a thin-walled cylindrical cell made of aluminum to reduce scattering effects from the cell. The vacuum seal of this cell was made by lead gaskets and a glass stopcock, so that any high-temperature heat treatment of the sample had to be performed previously in a different container. Since these conditioning heat treatments were carried out in vacuum and convenience required that the sample be loaded in the diffraction cell at atmospheric pressure, it was necessary to expose the sample to some type of gas after the high-temperature process. The best method which was found for conditioning the samples according to these requirements was a vacuum heating at 450°C for 1 hr, after which dry air was admitted to the palladium when it had cooled. All samples prepared in this manner absorbed hydrogen readily. On the other hand, when argon was admitted to the sample after heating to 450°C, the palladium absorbed very little hydrogen. These results indicate that admitting air to the sample produces a surface oxide which aids in the absorption process. However, recent experiments by DAVIS[3] show that exposure of palladium to air or oxygen increases the absorbability of hydrogen only if small quantities of impurities are already present on the palladium surface.

Although this procedure was satisfactory in conditioning the palladium so that it would absorb hydrogen readily, when the hydrogen was admitted to the samples, a small part reacted to form water. Therefore, after exposure of the palladium in the diffraction cell to a small amount of hydrogen, it was necessary to remove the water vapor by heating the sample under vacuum for 4 hr at 100°C. This procedure also removed all measurable hydrogen from the palladium lattice. Because of the very large spin-incoherent neutron scattering from hydrogen, measurement of the diffuse scattering in the neutron-diffraction pattern is a reasonably accurate method for the detection of small quantities of hydrogen in the sample. Results of these measurements taken after the above heating procedure showed that the atomic ratio H/Pd was less than 0·003, so that subsequent measurements of the volume of gas absorbed gave the true amount of hydrogen in the palladium metal.

The cylindrical cell used in the neutron experiments was $\frac{3}{8}$ in. in diameter with a length of 3 in. and contained about 15 g of palladium powder. With a sample of this size, it was found from neutron-transmission measurements that non-uniform heating of the sample during absorption and evolution of the gas caused large inhomogeneities in the hydrogen content within the powder. The thermal gradients along the sample during the absorption and evolution processes were minimized by immersing the entire sample container in a constant-temperature water bath. The sample temperatures were maintained at about 95°C for hydrogen processes and at about 75°C for those with deuterium. At the completion of each process the water was very slowly reduced to room temperature, the temperature at which the diffraction data were obtained.

After these experimental procedures for sample preparation had been found to be satisfactory, a palladium sample was processed and placed in the diffraction cell. Neutron-diffraction data were obtained first for the pure palladium, and then hydrogen gas was admitted to give an atomic ratio H/Pd of 0·070. For this concentration at room temperature, it was expected that information could be obtained for the α-phase of the system. At the completion of the neutron experiments on this sample, hydrogen was again admitted to obtain an H/Pd ratio of 0·706, which gives only β-phase at room temperature. After the β-phase data had been obtained, hydrogen was evolved from the sample to give an H/Pd ratio of 0·064. This corresponded to a composition similar to the low hydrogen content on absorption and was produced in order to study possible hysteresis effects in the phase content for concentrations obtained by absorption and evolution of the gas. When sufficient results had been obtained with this preparation, all the hydrogen was removed, and the measured volume for the total amount of gas evolved agreed with that originally absorbed within 0·2 per cent. Diffraction data were again obtained for pure palladium, and then identical

VOL
3
195

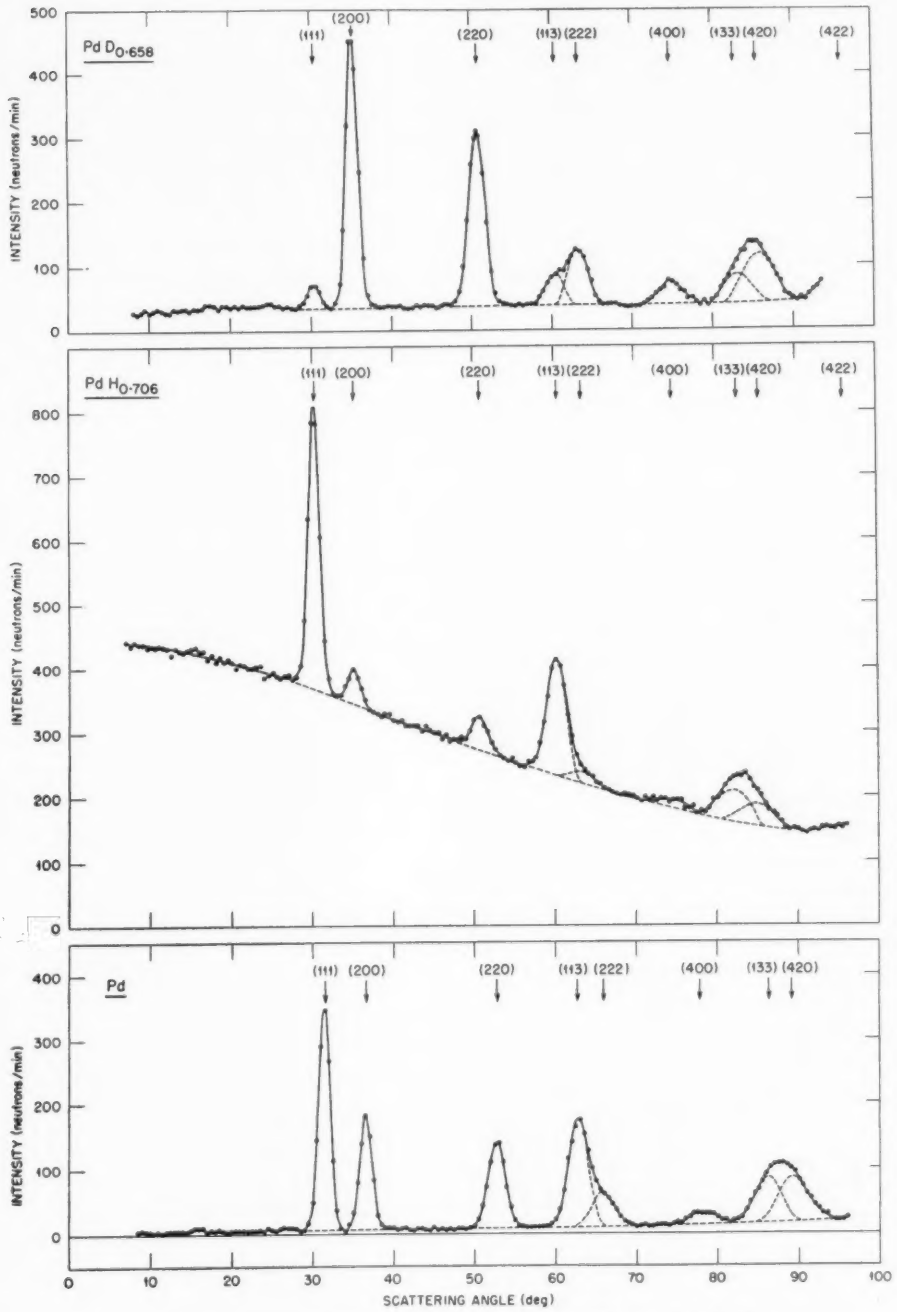

FIG. 1. Neutron-diffraction patterns of Pd, $PdH_{0.706}$, and $PdD_{0.658}$.

procedures were followed to study the palladium-deuterium system with D/Pd ratios of 0·068, 0·658, and 0·075. At each hydrogen and deuterium concentration, neutron-transmission data were used to check the homogeneity of the sample, and at the conclusion of each series the diffuse background in the neutron-diffraction pattern from the sample was checked to determine that no gas remained in the palladium lattice. The same sample of palladium powder was used throughout the entire investigation, and it was not exposed to the atmosphere between the time the diffraction cell was first loaded and the completion of the results on the palladium–deuterium system.

EXPERIMENTAL RESULTS

High-Concentration Samples

The neutron-diffraction patterns for pure Pd, $PdH_{0.706}$, and $PdD_{0.658}$ are shown in Fig. 1. These patterns have been corrected for background and scattering from the aluminum cell and consequently represent only scattering from the samples. The data for pure palladium show reflections from a simple face-centered-cubic lattice, and the changes which occur in the patterns for the β-phase samples of both hydrogen and deuterium are evidence that the gas atoms in this phase are present at definite positions in the crystal lattice. The changes in intensity for the deuteride are seen to be opposite to those for the hydride, which is the condition usually found when deuterium is substituted for hydrogen, since there is a reversed phase associated with the two nuclear scattering amplitudes. Expansion of the lattice in the β-phase is apparent from the shift in position of the diffraction peaks in the samples containing hydrogen and deuterium. The unusually high diffuse scattering from $PdH_{0.706}$ is the result of the nuclear spin-incoherent scattering from hydrogen and provides a rather sensitive test which was used for the detection of small amounts of hydrogen in the samples.

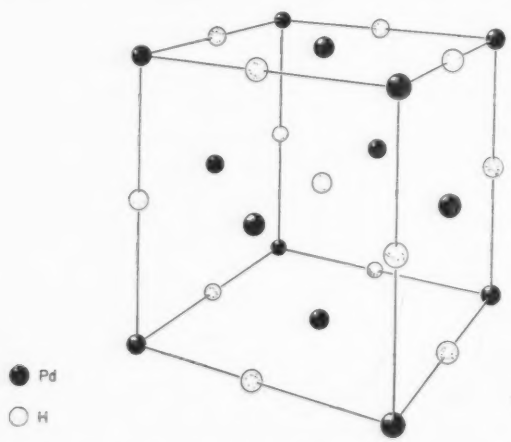

FIG. 2. Model showing the positions of hydrogen and deuterium atoms in the palladium lattice for β-phase Pd–H and β-phase Pd–D.

These diffraction patterns are representative of the NaCl-type structure, in which the hydrogen and deuterium atoms have entered the octahedral positions about the palladium atoms as shown in Fig. 2. For the hydride, the structure amplitude for an (hkl) reflection at a scattering angle of 2θ is given by

$$F_{hkl} = f_{\mathrm{Pd}} \exp(-b_{\mathrm{Pd}} \sin^2\theta/\lambda^2) \pm \pm\left(\frac{H}{\mathrm{Pd}}\right) f_H \exp(-b_{\mathrm{H}} \sin^2\theta/\lambda^2) \qquad (1)$$

in which the positive sign is used for even-indexed reflections and the negative sign for reflections with odd indices. A similar expression gives the structure amplitude for the deuteride. The f's represent the neutron-scattering amplitudes of palladium, hydrogen, and deuterium, and the b's represent coefficients in the temperature factors from which values of the root-mean-square vibrational amplitude, $(\overline{\mu^2})^{\frac{1}{2}}$, can be calculated for the various types of atoms. For pure palladium, only the first part of equation (1) is applicable, and the values of f_{Pd} and b_{Pd} were obtained from the plot of the logarithm of F_{obs} as a function of $\sin^2\theta/\lambda^2$ shown in Fig. 3. For the samples containing hydrogen and deuterium, values of the scattering amplitudes and temperature factor parameters were obtained from separate analyses[4] of the reflections with even indices and those with odd indices. The logarithmic plots for these analyses are also shown in Fig. 3, and the results obtained for the three samples are listed in Table 1. The scattering data from pure palladium taken at the start and finish of the investigation gave identical values of f_{Pd} and b_{Pd}, and the results for palladium from the

hydride and deuteride analyses agreed within experimental error. Structure amplitudes were calculated by substituting these experimental values in equation (1), and the calculated structure amplitudes are compared with the observed results in Table 2. The agreement is indicative of the correctness of the assumed NaCl-type structure. Furthermore, the good agreement between calculated and observed values, using the atomic ratios, H/Pd or D/Pd, determined from the measured volumes of gas absorbed, indicates that all the hydrogen or deuterium atoms enter the octahedral positions in the lattice and only a negligible amount is available for a rift network.

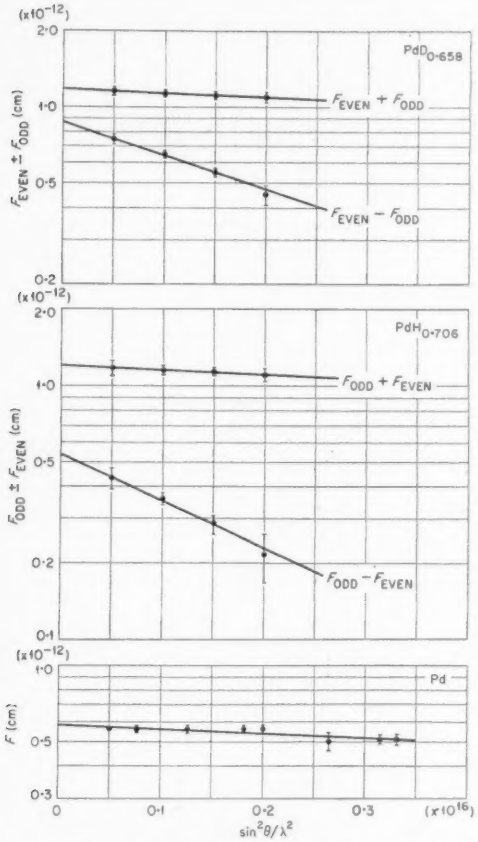

FIG. 3. Determination of the scattering amplitudes and temperature factor parameters for Pd, $PdH_{0.706}$, and $PdD_{0.658}$.

Low-Concentration Samples

Portions of the diffraction patterns for $PdH_{0.070}$ and $PdD_{0.068}$ prepared by absorption of the gases are shown in Fig. 4. These patterns were taken with Soller slit geometry to improve the resolution, and they have been corrected for background and scattering from the aluminum cell. Similar curves were also obtained from samples on evolution of the gases from the β-phase to compositions $PdH_{0.064}$ and $PdD_{0.075}$, but these are not shown.

The slight asymmetry of the large reflections can be ascribed to small unresolved reflections as shown by the cross-hatched area on the small-angle side of the reflections. These small reflections occur at the proper angle positions for reflections from the expanded β-phase, and a comparison of the relative intensities of these reflections with those of known β-phase in Fig. 1 indicates that, for both the hydride and deuteride, β-phase contamination was present in the low-concentration samples. Attempts to determine the intensities of these contaminating reflections so that estimates could be made of the amount of β-phase present in the samples were not very satisfactory, but the measurements indicated that for all four samples

Table 1. *Scattering amplitudes and temperature factor parameters for* Pd, Pd–H, *and* Pd–D *systems*

Element	Sample	f (10^{-12}cm/atom)	b (Å²)	$(\overline{\mu^2})^{\frac{1}{2}}$ (Å)
Pd	Pd	0·58±0·02	0·38±0·22	0·069
Pd	$PdH_{0.706}$	0·60±0·04	0·40±0·32	0·071
Pd	$PdD_{0.658}$	0·59±0·03	0·32±0·30	0·064
H	$PdH_{0.706}$	0·37±0·06	4·2 ± 1·5	0·23
D	$PdD_{0.658}$	0·66±0·05	3·1 ± 0·7	0·20

Table 2. Calculated and observed structure amplitudes (F) for Pd, Pd–H, *and* Pd–D *systems*

Reflection	Pd		$PdH_{0.706}$		$PdD_{0.658}$	
	$F_{calc.}$ (10^{-12} cm)	F_{obs} (10^{-12} cm)	$F_{calc.}$ (10^{-12} cm)	F_{obs} (10^{-12} cm)	$F_{calc.}$ (10^{-12} cm)	F_{obs} (10^{-12} cm)
(111)	0·58	0·56	0·80	0·80	0·19	0·20
(200)	0·58	0·56	0·38	0·40	0·93	0·93
(220)	0·56	0·56	0·41	0·39	0·86	0·87
(113)	0·55	0·56	0·68	0·69	0·30	0·30
(222)	0·55	0·56	0·43	0·45	0·80	0·77
(400)	0·54	0·50			0·74	0·72
(133)	0·53	0·51				
(240)	0·52	0·52				
R		2·8%		2·6%		1·8%

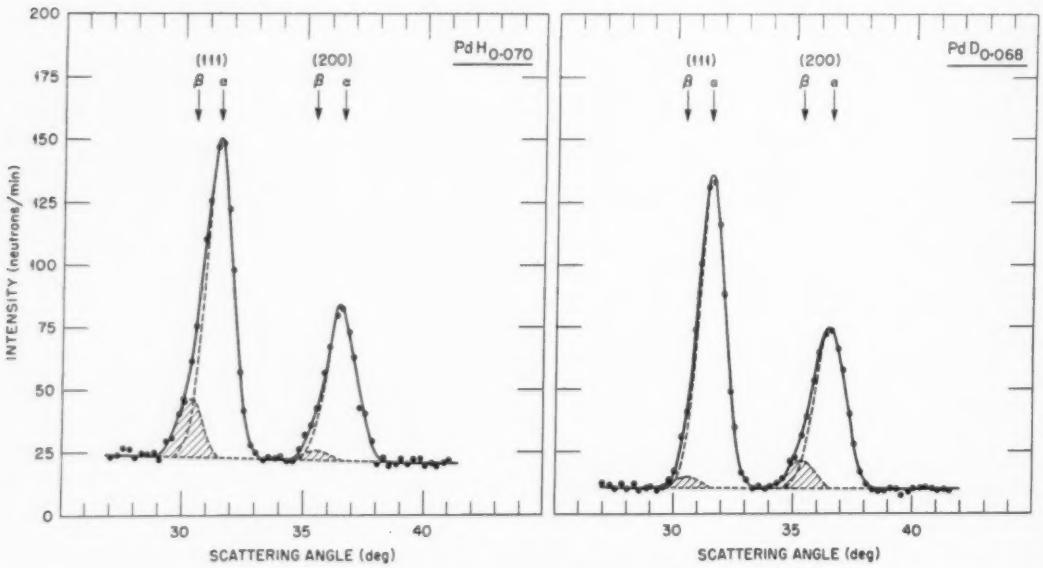

FIG. 4. Partial neutron-diffraction patterns for $PdH_{0.070}$ and $PdD_{0.068}$. The concentrations were obtained by absorption of the gases into pure Pd.

studied at least one-half of the gas was present in the β-phase. Furthermore, the relative intensities of the β-phase contamination strongly indicate that for this phase the lattice positions of the gas atoms are the same for low and high gas concentrations. However, the uncertainty of the small amount of gas atoms present in the α-phase made it impossible to determine their crystallographic positions in this phase.

DISCUSSION

The neutron-diffraction results obtained in this investigation show that in the expanded β-phase of both the palladium–hydrogen and palladium–

deuterium systems, the gas atoms are located in the octahedral positions of the face-centered-cubic palladium lattice. There is negligible hydrogen available for the rift network postulated by SMITH.[1] However, this result is not necessarily in disagreement with the predictions of DAVIS,[2] since a close inspection of his experimental conditions (low gas pressures and temperatures above 200°C) shows that his diffusion experiments were probably performed on systems in the α-phase. Attempts to determine the hydrogen and deuterium positions in the α-phase were unsuccessful, since only a very small amount of gas enters this phase at room temperature. This determination will have to be made at elevated temperatures and corresponding elevated gas pressures.

It is a well-known fact that palladium powder at room temperature will absorb hydrogen or deuterium at 1 atm pressure to a saturation value which occurs at an atomic ratio H/Pd of about 0·7. Since all of the octahedral crystallographic positions are not filled until H/Pd = 1·0, the gas atoms in the β-phase appear to be randomly distributed among the available positions and fill only about 70 per cent of them under normal absorption pressure. At elevated pressures, however, additional absorption can be made to occur. The apparent saturation at a 70 per cent value may be associated with an electronic saturation and not with the crystallographic saturation. Studies of the paramagnetic susceptibility extrapolated to low temperature by WUCHER[5] have shown that it decreases to zero as the hydrogen concentration approaches 0·7, and this is considered to represent the filling of the holes in the Pd 4*d*-band.[6] On this picture the hydrogen absorption in excess of 0·7 concentration would represent a different absorption process, since different conditions of absorption are necessary.

The values of the hydrogen and deuterium temperature parameters and root-mean-square vibrational amplitudes listed in Table 1 are seen to be very much larger than those for palladium, and indicate that there is considerable temperature motion of the hydrogen and deuterium atoms. However, these values are comparable with the values obtained for these atoms in other compounds, and therefore do not suggest any unusual mechanism for the large diffusion rates of these gases through palladium. On the other hand, the total scattering cross-section of hydrogen determined from transmission measurements with $PdH_{0.706}$ was found to be abnormally low. Specifically, a value of $28{\cdot}9 \pm 2{\cdot}5$ barns was measured for the hydrogen cross-section in this compound, while the average value obtained from many other compounds containing hydrogen is about 38 ± 4 barns. This low value more closely approaches that expected from a free hydrogen nucleus and suggests that, although the gas molecules are dissociated into atoms in the lattice, any bonds formed between gas atoms and palladium atoms have a strength less than that usually associated with chemical bonds. The large diffusion rate is undoubtedly associated with this rather weak bonding, and the vibrational amplitude due to thermal motion may be restricted by the relatively small pocket in which the gas atoms are located within the palladium lattice. The diffusion procedure is perhaps a process in which these loosely-bound gas atoms have considerable thermal motion and occasionally jump from one crystallographic position to an adjacent equivalent position which has a large probability of being unoccupied.

From this investigation it is, of course, not possible to determine the electronic structure of the compound and thus to state whether the hydrogen exists as a positive or negative ion or whether it is predominantly atomic. However, the results are conclusive in showing that only a negligible amount of hydrogen can possibly remain in the molecular state. The catalytic activity of palladium in hydrogenation probably results from the ability of this metal to furnish single hydrogen atoms from a lattice saturated with hydrogen. In this manner the large activation energy required in the dissociation of hydrogen molecules is effectively by-passed.

Acknowledgements—The authors wish to express their appreciation to S. W. MOSKO for considerable experimental assistance during the course of these investigations. They also are indebted to S. W. PETERSON and H. A. LEVY for helpful discussions concerning the results and for the use of their neutron-diffraction apparatus during part of the experiments.

REFERENCES

1. SMITH D. P. *Hydrogen in Metals.* University Press, Chicago (1948).
2. DAVIS W. D. *Knolls Atomic Power Lab. Rep.* No. **1227** (1954).
3. DAVIS W. D. *Knolls Atomic Power Lab. Rep.* No. **1375** (1955).
4. See, for example, James R. W. *Optical Principle of the Diffraction of X-Rays* p. 237. Bell, London (1954).
5. WUCHER J. *Ann. Phys., Paris* **7**, 317 (1952).
6. See discussion by WOHLFARTH E. *Rev. Mod. Phys.* **25**, 211 (1953).

J. Phys. Chem. Solids Pergamon Press 1957. Vol. 3. pp. 311–317.

THE DISTRIBUTION OF TRANSITION METAL CATIONS IN SPINELS

DONALD S. McCLURE

RCA Laboratories, Radio Corporation of America, Princeton, N.J.

(*Received* 18 *May* 1957)

Abstract—Crystal field theory in conjunction with spectroscopic data may be applied to give quantitatively the *d*-shell splitting and the resulting stabilization of a transition metal ion in a crystal site of given symmetry. The thermodynamic stabilization values are found for both octahedral and tetrahedral sites in the spinel lattice. The differences between these values is the site preference energy. The cation distributions predicted from this energy are in good agreement with known experimental data. The occurrence of a large Jahn–Teller effect is correlated with tetragonal phase formation.

VOL. 3 1957

1. INTRODUCTION

THE spinels are double oxides having the general formula $A[B]_2O_4$ where the oxygens lie in a nearly close packed cubic lattice. The A ions occupy tetrahedral interstices of the oxygen lattice and the B ions octahedral interstices. It is found that the so-called inverse structure $B[AB]O_4$ also occurs, and the problem is to explain the relative stability of the two forms.

If it were not for the fact that the most interesting spinels contain transition element ions, the relative stability would be primarily a question of Madelung energy and ion size. These two factors have been studied by many investigators and found not to be entirely sufficient.[1] The special features introduced by the unfilled *d*-shell were considered by ROMEIJN,[2] who suggested that extra stability could be achieved by the removal of the degeneracy of the *d*-shell, and also by GOODENOUGH and LOEB[3] who rejected ROMEIJN's idea, and instead invoked the use of covalent bonds of various hybridization types.

These two ideas are not actually very different. The first is based upon the crystal field theory and the second upon Pauling's theory of hybrid bonds. VAN VLECK showed how these theories were related many years ago.[4] In this paper we propose to show how the crystal field theory may be used to obtain quantitative information concerning the relative stability of normal and inverse spinels.

In order to obtain quantitative information it is necessary to interpret optical absorption data with the aid of crystal field theory; to derive from these data a crystal field splitting parameter called Dq; and then to find the extra stabilization (proportional to Dq) due to the crystalline environment of the ion. The reader is referred for details to a recent review.[5] ORGEL[6] has presented a systematic comparison of the theory with known spectroscopic data, and from this he derives the parameters of the theory for many ionic complexes in solution. HOLMES and MCCLURE[7] have shown that the parameters for the crystalline hydrates are nearly the same as for water solutions.

2. THE "SITE PREFERENCE" ENERGY

We might expect that the oxides of the transition metals would have nearly the same parameter values as the hydrates, since these parameters depend mainly upon the immediate surroundings of the ion. Recent spectroscopic studies in this laboratory have shown that, in the few cases studies, this expectation is borne out. The crystal field splitting parameter, Dq, has been obtained from the spectra of NiO, Cr_2O_3, 1 per cent NiO in solid solution in ZnO, and 1 per cent CoO in solid solution in ZnO shown in Figs. 1—4. The two solutions are of importance because the Ni^{++} and Co^{++} ions are in four-co-ordinated sites, whereas they are ordinarily found in six-co-ordinated sites.

The spectra shown in the figures were obtained

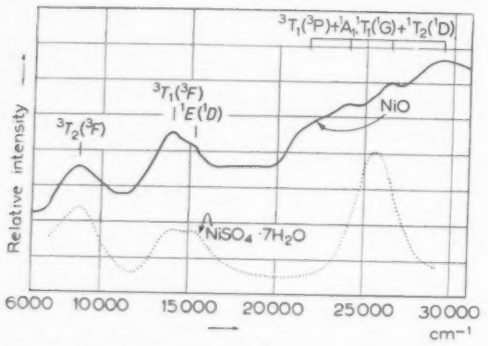

FIG. 1. Absorption spectra of NiO and $NiSO_4 \cdot 7H_2O$. In each compound the Ni^{++} is octahedrally co-ordinated to oxygen atoms. The probable assignments given in all figures are made on the basis of the crystal field calculation from free ion energy levels. The cubic field representation is given followed by the free ion state in parentheses.

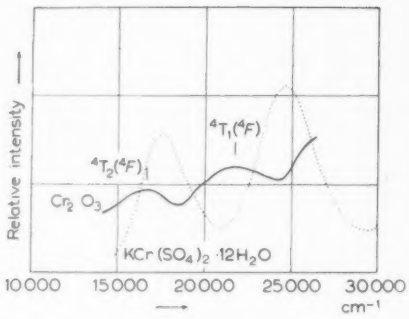

FIG. 2. Absorption spectra of $KCr(SO_4)_2 \cdot 12H_2O$ and Cr_2O_3. In each compound the Cr^{+++} is octahedrally co-ordinated to oxygen atoms.

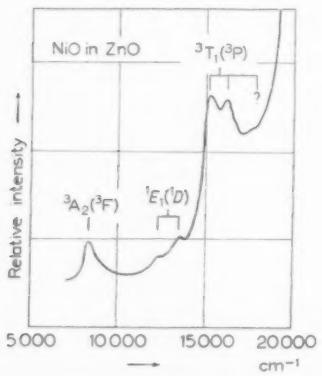

FIG. 3. Absorption spectrum of Ni (1 per cent) in ZnO. The Ni^{++} is presumed to lie on Zn^{++} lattice sites, where it is tetrahedrally co-ordinated to oxygen atoms.

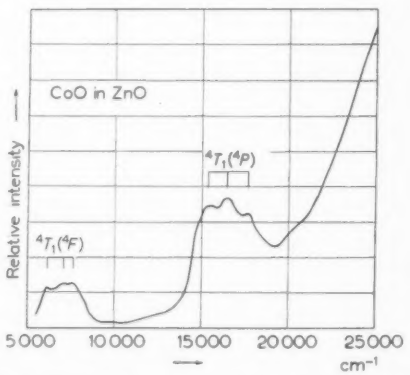

FIG. 4. Absorption spectrum of Co (1 per cent) in ZnO. The Co^{++} is tetrahedrally co-ordinated to oxygen atoms.

on a Cary Model 14 recording spectrophotometer by the KBr pellet technique.[9] The dried powdered substance is intimately mixed with KBr and pressed into a translucent pellet. Since this pellet scatters a great deal of radiation and thus lowers the contrast available, we used a method suggested by SHIBATA,[10] for reducing the scattering effect. Opal glass, which is a perfect diffuser in the visible and near infrared is placed in each beam of the spectrophotometer. Since it scatters completely, the scattering power of the sample is of no consequence and the spectral contrast is restored.

Each ion studied has an F ground state when free. When octahedrally co-ordinated (symmetry group O_h), this state splits into A_2, T_2 and T_1 states in this order with A_2 lowest for Cr^{+++} and Ni^{+++}, and T_1 lowest for Co^{++}. The order is exactly reversed for tetrahedral co-ordination. Each ion has in addition a P state of the same multiplicity as the ground state, and this appears unsplit in the spectrum as a T_1 state. The free ion F–P separation is somewhat larger than the one found in crystals, but the discrepancy is not often so large as to prevent a correct identification

of the levels. The symmetry assignments are given in the figures both for the free ion state and the combined ion. Some intercombination bands are observed for Co^{++} and Ni^{++} because of the large spin-orbit parameters. The Dq values are in each case obtained by making the best fit of the lowest energy peak, since this is the one least likely to be perturbed by higher transitions.

Our data are in agreement with those of ROMEIJN,[8] but are more complete, since the infra-red region has been included. The parameters are listed in Table 1. It can be seen that the

Table 1. Values of Dq in some crystalline solids compared with values for water solutions

	Dq (crystal)	Dq (H_2O)
NiO	885 cm^{-1}	860 cm^{-1}
Cr_2O3	1680	1760
NiO in ZnO	465	380*
CoO in ZnO	370	440*

* These values are the water solution values for Ni^{++} and Co^{++} multiplied by 4/9. (See text for discussion.)

Dq values are only slightly different for oxides than for hydrated ions.

In order to extend the data to the other ions of interest it seems quite safe to use the Dq values pertaining to water solution. We must also extend the data to include four-co-ordinated ions. We see from Table 1 that Dq for four-co-ordination is about half that for six-co-ordination. This agrees with what one calculates from a point charge model, where the Dq value for four-co-ordination is 4/9 that for six-co-ordination with the same neighbor distance. In order to treat all the data uniformly, we shall take Dq for four-co-ordination to be 4/9 that for six-co-ordination. This will have to be revised somewhat when complete spectroscopic data become available, but the errors are only a few kcal.

The stabilization energy derived by a transition metal ion from its surroundings is in part due to splitting the d-shell levels. This energy is purely electronic and arises because the d-shell is not spherically symmetric. The spatial properties of some of the d-orbitals are such that electrons in them may have their charge density maxima in low energy regions away from the ligands or anions. This results in a lowering of the energy with reference to a spherically symmetric shell, such as a rare gas configuration. The energy lowering for various d-electron configurations is equal to Dq times the following factors;* zero for d^0, d^5, d^{10} for any field type. For octahedral fields; 4 for d^1, d^6; 6 for d^2, d^4, d^7, d^9; 12 for d^3, d^8. For tetrahedral fields; 4 for d^4, d^9; 6 for d^1, d^3, d^6, d^8; 12 for d^2, d^7. The stabilization energies are given in Table 2. The fact that Dq's actually arise partly from electrostatic forces and partly from covalent forces is interesting but has no real bearing on the problem of cation distribution. The important fact is that by proper use of spectroscopic data we may derive a Dq value and make predictions depending only on the value of this number, and not on its origin.

The numbers in the last column of Table 2 give the energy per mole gained by the ion due to d-shell splitting when it is in an octahedral site, minus that gained when in a tetrahedral site. This is the "site preference" energy due to d-shell degeneracy and ranges from zero for Mn^{++} and Fe^{+++} to 46·7 kcal for Cr^{+++}.

These energies, although small, may be sufficient to determine whether a given spinel shall be normal or inverse. Before examining this possibility theoretically let us look at the data.

Table 3 compares the cation distribution in 2–3 spinels predicted from the last column of Table 2 with the observed cation distribution. Only the d-shell splitting has been considered. The good general agreement between predicted and observed results indicates that the d-shell splitting is indeed a key factor in determining whether normal or inverse structures occur in 2–3 spinels.

It is at first difficult to understand why this correlation should be as good as it is, since the energies are small compared to the energies involved in making rather small structural changes in the spinel structure. For example, according to the work of VERWEY and HEILMANN,[11] a change of 0·005 units in the oxygen parameter u for a normal 2–3 spinel having a 8·4 Å lattice parameter and $u = 0{\cdot}385$, requires an energy of 100 kcal/mole.

* Based on weak field theory.[6] In strong field theory the factors are the same except: in octahedral fields; 8 for d^2, d^7. In tetrahedral fields; 8 for d^3, d^8.

Table 2. Crystal field theory data for transition metal ions; The data given are

(1) Number of *d*-electrons.
(2) Free ion Russell–Saunders ground term (spin-orbit coupling is neglected in the term designation).
(3) The standard group theory symbol for the ground state of the octahedrally co-ordinated ion in a solid (using nomenclature of EYRING, WALTER and KIMBALL *Quantum Chemistry*).
(4) The group theory symbol for the tetrahedrally co-ordinated ionic ground state.
(5) *Dq* values for octahedral hydrates of the ions.
(6) *Dq* calculated for tetrahedral co-ordination. (See text.)
(7), (8) The thermodynamic stabilization in octahedral or tetrahedral fields.
(9) The octahedral site preference or the difference between columns 7 and 8.

Number of *d*-electrons	Ion	Free ion ground state	Octahedral field ground state	Tetrahedral field ground state	*Dq* cm^{-1} oct.	*Dq* cm^{-1} tetr.	Stabilization, kcal oct.	Stabilization, kcal tetr.	Oct. site preference energy kcal/mole
1	Ti^{+++}	^2D	$^2T_{2g}$	^2E_g	2030	900	23·1	15·4	7·7
2	*V^{+++}	^3F	$^3T_{1g}$	$^3A_{2g}$	1800	840	30·7	28·7	2·0
3	V^{++}	^4F	$^4A_{2g}$	$^4T_{1g}$	1180	520	40·2	8·7	31·5
	Cr^{+++}	^4F	$^4A_{2g}$	$^4T_{1g}$	1760	780	60·0	13·3	46·7
4	Cr^{++}	^5D	^5E_g	$^5T_{2g}$	1400	620	24·0	7·0	17·0
	Mn^{+++}	^5D	^5E_g	$^5T_{2g}$	2100	930	35·9	10·6	25·3
5	Mn^{++}	^6S	$^6A_{1g}$	$^6A_{1g}$	750	330	0	0	0
	Fe^{+++}	^6S	$^6A_{1g}$	$^6A_{1g}$	1400	620	0	0	0
6	Fe^{++}	^5D	$^5T_{2g}$	^5E_g	1000	440	11·4	7·5	3·9
	*Co^{+++}	^5D	$^1A_{1g}$	^5E_g		780	45	26	19
7	Co^{++}	^4F	$^4T_{1g}$	$^4A_{2g}$	1000	440	17·1	15·0	2·1
8	Ni^{++}	^3F	$^3A_{2g}$	$^3T_{1g}$	860	380	29·3	6·5	22·8
9	Cu^{++}	^2D	^2E_g	$^2T_{2g}$	1300	580	22·2	6·6	15·6
10	Zn^{++}	^1S	$^1A_{1g}$	$^1A_{1g}$	0	0	0	0	0

* *Note added in proof:* It is probably more accurate to use the strong field theory for the +3 ions. This changes the site preference energy of V^{+++} to 12·3 kcal.

The octahedral site stabilization of Co^{+++} was estimated from the heat of hydration increment caused by the crystal field (ref. 7, Fig. 3), and the tetrahedral site stabilization was taken to be the same as for Cr^{+++}.

This energy exceeds any of the *d*-shell splitting energies found. Actually the *u*-parameters of the structures we wish to consider differ by more than 0·005 units. On the other hand, the lattice parameters change also and may compensate for the change in *u*. The entire problem is very complicated, since the repulsion energies must also be considered in order to arrive at an equilibrium crystal structure. On the basis of empirical observation, however, one may conclude that within the accessible ranges of the parameters, there is both a normal and an inverse spinel structure having nearly the same energy except for special electronic forces, such as covalent bonding and *d*-shell splitting. For the transition metal ions therefore, it is not unreasonable to look for the

Table 3. Theoretical and experimental cation distributions in 2–3 spinels, AB_2O_4

A \ B	Al^{+++}		Ga^{+++}		Fe^{+++}		Cr^{+++}		Mn^{+++}		V^{+++}		Co^{+++}	
	Exp.	Th.	Exp.	Th.	Exp.	Th.	Exp.	Th.	Exp.	Th.	Exp.	Th.	Exp.	Th.
Mg^{++}	·88$I^{(e)}$	0	$I^{(c)}$	0	$I^{(a)}$	0	$N^{(a)}$	N		N	$N^{(d)(f)}$	N		N
Zn^{++}	$N^{(a)}$	0	N	0	$N^{(a)}$	0	$N^{(a)}$	N	N, $T^{(b,g)}$	N	$N^{(d)(f)}$	N		N
Cd^{++}	$N^{(a)}$	0	$N^{(d)}$	0	$N^{(a)}$	0	$N^{(a)}$	N		N		N		N
Mn^{++}	$N^{(a)}$	0		0	$I^{(a)}$	0	$N^{(a)}$	N		N	$N^{(f)}$	N		N
Fe^{++}	$N^{(a)}$	I		I	$I^{(a)}$	I	$N^{(a)}$	N		N	$N^{(f)}$	$I+N$		N
Co^{++}	$N^{(a)}$	I		I	$I^{(a)}$	I	$N^{(a)}$	N		N		$I+N$		N
Ni^{++}	$\frac{3}{4}I+\frac{1}{4}N^{(b)}$	I	$I^{(h)}$	I	$I^{(a)}$	I	$N^{(a)}$	N	$I+N$			I		I
Cu^{++}	$I^{(a)}$	I		I	0·86I, $T^{(e)}$	I	$N^{(a)}$	N		N		I		N

N = normal, I = inverse, T = tetragonal, 0 = no prediction is made by d-shell theory.

(*a*) VERWEY E. J. W. and HEILMAN E. L. *J. Chem. Phys.* **15,** 174 (1947).
(*b*) ROMEIJN F. C. *Philips Res. Rep.* **8,** 304 321 (1953).
(*c*) BARTH T. F. W. and POSNJAK E. *Z. Kristallogr.* **82,** 325 (1932).
(*d*) RUDORFF W. and REUTER B. *Z. Anorg. Chem.* **253,** 194 (1947).
(*e*) BERTAUT E. *J. Phys. Radium* **12,** 252 (1951).
(*f*) LOVELL G. H. B. *Trans. Brit. Ceram. Soc.* **50,** 315 (1951).
(*g*) MASON B. *Amer. Min.* **32,** 426 (1947).
(*h*) GREENWALD S., PICKART S. and GRANNIS F. *J. Chem. Phys.* **22,** 1597 (1954).

operation of the latter effect in spite of the large total energies involved.

There are a few disagreements between the predictions in Table 3 and the observed facts. These certainly are to be expected since we have not considered ion size and other factors. We can learn something about the site preference of non-transition metal ions from these cases. Thus for nickel aluminate, the inverse structure $Al(AlNi)O_4$ was predicted, but a 3/4 inverse, 1/4 normal structure is found. This indicates that Al^{+++} is able to compete somewhat with Ni^{++} for the octahedral site. The Ni^{++} ion has a 23 kcal preference for octahedral sites. The Al^{+++} ion must have nearly this same preference in this particular spinel. The lack of any information on the heat of reaction, normal > inverse, precludes a more exact estimate for Al^{+++}. But in view of this, it is not surprising to find that Fe^{++} and Co^{++}, whose octahedral site preferences are only a few kcal/mole, should be displaced by the Al^{+++} ion into the tetrahedral interstices. The site preferences of Al^{+++} and other non-transition metal ions have different origins from those of the transition metal ions, but they may nevertheless be evaluated by comparison, as has been done here.

Table 3 gives the results to be expected at low temperatures. In much of the experimental data available it is not indicated what the probable equilibrium temperature was, but because diffusion ceases for most ferrites below about 800°K, a cation distribution with a 2–3 kcal/mole preference at 0°K may be nearly obliterated. In borderline cases, the temperature effect is therefore important, and the figures in Table 2 could be used to estimate when these cases will occur.

In the 2–4 spinels of the type $X^{+2}Y^{+2}Z^{+4}O_4$, the relative site preference of X and Y may be compared if Z remains fixed in an octahedral site. In this case, one octahedral and one tetrahedral space is left. This is the case with the titanates. The Co-Mg titanates show a random distribution over the two kinds of site.[2] In view of the small (2 kcal/mole) preference of Co^{++} for octahedral sites and the high temperatures (1400°C) necessary to prepare Mg- and Ti-containing spinels, this result is understandable.

In the Co–Zn titanates, the Co goes to the octahedral site,[2] in accordance with the predictions derived from Table 2. The preparation temperature is probably lower, and the Zn seems to have a definite tetrahedral site preference, so that all factors work for the observed structure.

We can thus explain most of the observed cation distributions by using the site-preference energy derived from spectroscopically obtained Dq values.

There are, of course, other contributions to the site preference energy which have been discussed earlier.[1] If all ion sizes and charges were the same the *d*-shell effect would always predominate. The Al^{+++} ion causes the greatest departures from the predicted distribution, and this is because of its small size and high charge compared to the divalent transition metal ions.

3. TETRAGONAL PHASES

The detailed description of the ionic ground state given by crystal field theory is very important when considering tetragonal phase formation and magnetic anisotropy. The latter topic will form the subject of a future paper. The hypothesis we want to advance for tetragonal phase formation is that it occurs whenever the Jahn–Teller effect in the ionic ground state is large. According to JAHN and TELLER,[12] a non-linear molecule in a degenerate electronic state is unstable with respect to unsymmetrical displacements. A transition metal ion and its immediate anion neighbors may be considered as the molecule in this case, and the occurrence of degeneracy in the ground state of the "molecule" may be predicted from the otpical spectrum and the crystal field theory.

As we have already shown, the optical spectra are very nearly the same for the octahedrally coordinated solid oxides as for the hydrates, so that the electronic ground state of the ion in the *B* sites of a spinel lattice will usually be the same as for the hydrated ion. The electronic ground states are listed for the magnetically interesting ions in Table 2. VAN VLECK[13] showed that the Jahn–Teller splitting of an *Eg* type state in octahedral surroundings may be several thousand wave numbers, while for T_1- and T_2-type states it will be on the order of a few hundred wave numbers. Experimental confirmation of this exists. The splitting of the *Eg* excited state of $Fe^{++}(H_2O)_6$ ion is 1500 cm^{-1} or more.[7] The apparent *Dq* values for Mn^{+++}, Cr^{++} and Cu^{++} are much larger than for other ions having the same charge.[7] This can be explained if the extra stability is obtained not through the cubic field splitting alone, but through the addition of a Jahn–Teller splitting of several thousand wave numbers.

The form of the distortion of an octahedral site resulting from this effect is chiefly tetragonal for Cu^{++}, Cr^{++} and Mn^{+++}, since the tetragonal distortion completely removes any degeneracy in the ground state. For T_1 or T_2 ground states, the distortion is either tetragonal or trigonal, according to the recent work of OPIK and PRYCE.[14] Thus, one expects one or the other of these symmetries in the immediate surroundings of Ti^{+++}, Ti^{++}, Co^{+++}, Co^{++}, V^{+++} and Fe^{++}. Experimentally, the magnitude of the distortion in the T_1 or T_2 case is much less than for the *E* case, as the *Dq* values are not unusually high and the spectra do not show any evidence of large-scale energy splittings.[7] In Co^{+++} ion, a singlet state is very close to the quintet and in some compounds, for example $Co(NH_3)_6^{+++}$ the singlet is actually lower. The singlet state is orbitally non-degenerate, so that both the magnetism and the Jahn–Teller distortion disappear when it becomes the lowest state.

To return to the problem of cation distribution, if the Jahn-Teller effect is taken into account the predictions of Table 2 may be altered in some cases. This table is based upon spectroscopic *Dq* values which for Mn^{+++} and Cu^{++} contain large contributions from the Jahn–Teller effect. These values were derived from solution spectra where the full effect may be realized because of the absence of constraints. But if Mn^{+++}, for example, appears in solid solution replacing an ion such as Fe^{+++}, its environment will be largely determined for it by the other ions in the lattice and it will not have the configuration of nearest neighbors which entirely removes the electronic degeneracy. The effective *Dq* value will then be somewhat smaller than as given in Table 2. A critical test of this effect would be Ni^{++} and Mn^{+++} competing for the octahedral sites in zinc ferrite.

On the other hand, the Jahn–Teller effect occurring in a pure Mn^{+++} compound may give the stability predicted from Table 2, since the co-operative effects of a large number of Mn^{+++} ions should make it possible for the surroundings of each ion to attain the desired configuration with the resulting formation of a tetragonal phase.

The work of MASON[15] on the solid solutions $Mn_3O_4-Fe_3O_4$ gives some quantitative insight into this effect. He found that above 40 per cent Mn_3O_4, the solutions were tetragonal phases and below this cubic.

The spinel $Fe(CuFe)O_4$ is inverse when annealed, as would be predicted from Table 2, but when quenched from a temperature of 900°C the

Cu ions are found to be randomly distributed over both tetrahedral and octahedral sites.[16] This temperature effect is not in agreement with the 16 kcal. site preference energy. This spinel is also tetragonal, as would be expected from the large Jahn–Teller effect brought about by the Cu^{++} (^2Eg ground state). Experimentally it is found that as the Cu^{++} leaves octahedral sites, the tetragonality is reduced. GOODENOUGH and LOEB[3] expressed the experimental results in terms of the stress required in the octahedral sites to produce a tetragonal strain. This relation could presumably be converted into an energy relation giving the dependence of lattice energy on Cu^{++} ion distribution. The strain energy may be reduced if Cu^{++} ions are put on tetrahedral sites, but with a consequent loss in crystal field energy. The result of these two effects in working against each other is the observed temperature dependence of the ion distribution.

The principles of ligand field, or crystal field theory upon which the conclusions of this paper are based may be applicable to other systems, such as the garnet structure, where several ions compete for different sites. The crystal field stabilization can be shown to have important effects upon the thermodynamic properties of most transition metal compounds. Table 2 gives approximately the stabilization to be expected for oxides having either four- or six-fold co-ordination. This table could be improved and extended to other compounds and other co-ordination numbers by acquiring more spectroscopic data.

VOL. 3 1957

REFERENCES

1. For a review of cation distribution studies see GORTER E. W. *Philips Res. Rep.* **9,** 295 (1954). Also GREENWALD, PICKART and GRANNIS *J. Chem. Phys.* **22,** 1597 (1954).
2. ROMEIJN F. C. *Philips Res. Rep.* **8,** 321 (1953).
3. GOODENOUGH J. B. and LOEB A. L. *Phys. Rev.* **98,** 391 (1955).
4. VAN VLECK J. H. *J. Chem. Phys.* **3,** 803, 807 (1935).
5. MOFFITT W. and BALLHAUSEN C. J. *Ann. Rev. Phys. Chem.* **7,** 107 (1956).
6. ORGEL L. E. *J. Chem. Phys.* **23,** 1004 (1955).
7. HOLMES O. and MCCLURE D. S. *J. Chem. Phys.* **26,** 1686 (1957).
8. ROMEIJN F. C. *Philips Res. Rep.* **8,** 312 (1953).
9. FORD M. A. and WILKINSON G. R. *J. Sci. Instrum.* **31,** 338 (1954).
10. Private Communication K. SHIBATA, also SHIBATA K., BENSON A. and CALVIN M. *Biochem. Biophys. acta* **15,** 461 (1954).
11. VERWEY E. J. W. and HEILMANN E. L. *J. Chem. Phys.* **15,** 174 (1947).
12. JAHN H. A. and TELLER E. *Proc. Roy. Soc.* A **161,** 220 (1937).
13. VAN VLECK J. H. *J. Chem. Phy..* **7,** 79 (1939).
14. OPIK U. and PRYCE M. H. L. *Proc. Roy. Soc.* A **238,** 425 (1957).
15. MASON B. *Amer. Min.* **32,** 426 (1947).
16. PAUTHENET R. and BOCHIROL L. *J. Phys. Radium* **12,** 249 (1951).

Note—After the completion of this manuscript Dr. L. E. ORGEL informed me of several important references which express ideas similar to those in the present article. (Letter of 22 April 1957.) In 1952, ORGEL suggested that the Cu^{++} compounds have unsymmetrical environments because of the Jahn–Teller effect.[17] The relative stabilities of tetrahedral and octahedral complex ions were qualitatively discussed by him in 1956.[18] ORGEL and DUNITZ have recently published a survey of the stereochemistry of copper compounds.[19] In a paper to be published, DUNITZ and ORGEL discuss the occurrence of the Jahn–Teller effect in numerous compounds.

17. ORGEL L. E. *J. Chem. Soc.* 4756 (1952).
18. ORGEL L. E. *Report to the Tenth International Solvay Conference*, Brussells, May 1956.
19. ORGEL L. E. and DUNITZ J. D. *Nature, Lond.* **179,** 462 (1957).

J. Phys. Chem. Solids Pergamon Press 1957. Vol. 3. pp. 318–323.

ELECTRONIC PROPERTIES OF TRANSITION-METAL OXIDES—II

CATION DISTRIBUTION AMONGST OCTAHEDRAL AND TETRAHEDRAL SITES

J. D. DUNITZ* and L. E. ORGEL†

(*Received* 18 *June* 1957)

Abstract—The distribution of transition-metal ions amongst octahedral and tetrahedral sites in oxides, particularly of the spinel type, is discussed from the viewpoint of crystal field theory. It is shown that the available experimental information can be rationalized in terms of crystal field stabilizations, the magnitudes of which are determined from optical and magnetic data.

INTRODUCTION

In the first paper of this series[1] we discussed the stereochemistry of transition-metal oxides and showed that the deviations from cubic symmetry which occur in certain spinels and perovskites can be rationalized in terms of crystal field (ligand field) theory. We did not inquire into the factors determining the distribution of cations between octahedral and tetrahedral sites but utilized the available experimental evidence directly. Here we return to a discussion of the way in which the detailed electronic structure of the metal ion determines its preference for octahedral or tetrahedral sites, in particular in the close-packed oxygen arrangement of the spinel structure. We shall for convenience use simple electrostatic arguments throughout this paper since the more general arguments of ligand field theory would not lead to any new results. Covalent bonding is undoubtedly significant in these compounds and we are aware that part of the stabilization which we shall attribute to the crystal field effects is in fact covalent in origin. Fortunately this does not affect the validity of our arguments which depends only on the magnitude of the effects.

The cation distribution in spinels has previously been discussed in terms of crystal field theory by Romeijn.[2] We believe that his qualitative discussion is essentially correct, but that he did not appreciate the magnitude of the crystal field effects, and so was led to false conclusions, for example about the valency of the manganese ions in Mn_3O_4. We shall show that the crystal field stabilizations are large enough to account for all the observations on cation distribution and shall use spectroscopic data to make some quantitative estimates of the energies involved. This approach is essentially an application of ideas which have been used to discuss the relative stabilities of octahedral and tetrahedral complexes of the transition-metal ions in solution.[3,4,5]

CRYSTAL FIELD STABILIZATIONS

When a transition-metal ion is surrounded by an octahedron of negative ions or dipoles the d orbitals are split by the electrostatic field into a triply degenerate t_{2g} orbital which is stabilized and a doubly degenerate e_g orbital which is destabilized, relative to the mean d orbital energy. If the energies of these orbitals, referred to the mean, are $E(t_{2g})$ and $E(e_g)$ respectively, then obviously $E(t_{2g})/E(e_g) = -2/3$. We shall designate as Δ the energy separation between the two sets of orbitals, so that for the electronic configuration $(t_{2g})^m(e_g)^n$ the crystal field stabilization energy is $\Delta(4m-6n)/10$. In a tetrahedral field the situation is similar but the e orbitals are more stable than the t_2 orbitals. The corresponding crystal field stabilization for the configuration $(e)^p(t_2)^q$ is now $\Delta\,(6p-4q)/10$. These

* Davy Faraday Research Laboratory, The Royal Institution, London.

† University Chemical Laboratory, Cambridge.

Table 1. Stabilizations in terms of $\Delta/10$ *for transition-metal ions in crystal fields*

Ion	No. of *d* electrons	Stabilization in octahedral complex	Stabilization in tetrahedral complex
Ti^{3+}, V^{4+}	1	4	6
Ti^{2+}, V^{3+}, Cr^{4+}	2	8†	12
V^{2+}, Cr^{3+}, Mn^{4+}	3	12	8*†
Cr^{2+}, Mn^{3+}, Fe^{4+}	4	6*	4*
Mn^{2+}, Fe^{3+}, Co^{4+}	5	0	0
Fe^{2+}, Co^{3+}, Ni^{4+}	6	4	6
Co^{2+}, Ni^{3+}	7	8†	12
Ni^{2+}, Cu^{3+}	8	12	8*†
Cu^{2+}	9	6*	4*
Zn^{2+}	10	0	0

† The values given are correct only in the strong field limit, but are quite good approximations for real crystals.

* These ions have substantial additional Jahn-Teller stabilizations.

stabilizations are shown in Table 1 for different transition-metal ions, assuming integral values of m, n, p and q. The fields actually realized in oxide crystals are usually sufficiently strong to make the assumption of integral numbers of electrons in each type of orbital a good approximation even for ions with *d* electron configurations[6] for which it is not valid in very weak fields.

Since Δ does not vary too widely from one metal to another, provided the valencies of the ions are not different, and is substantially less for tetrahedral complexes than for octahedral ones, certain qualitative conclusions concerning the relative stabilities of transition-metal ions in octahedral and tetrahedral sites can be made immediately from Table 1. It is clear, for example, that Cr^{3+} and Ni^{2+} will be especially stable in octahedral sites while Mn^{2+} and Fe^{3+} will have no particular preference for either type of site insofar as crystal field effects are concerned. While these qualitative arguments might be pursued a little further we prefer to try to estimate the appropriate Δ values quantitatively from optical and magnetic data. It has been found that if crystal field stabilizations are obtained in this way, without correction for the numerous secondary effects which can be envisaged, the heats of formation of hydrated and complex transition-metal ions can be successfully rationalized.[7]

We require values of Δ appropriate to spinels but unfortunately the spectroscopic information on transition-metal oxides is rather limited and is available only for simple oxides and glasses. To make any progress we have to assume that the crystal field strengths for ions of a given valency in the spinels are roughly the same as in the simpler oxides with the same type of co-ordination. In the next section we shall discuss the available spectroscopic information and show that crystal field strengths in oxides are very similar to those in hydrates. We shall then be in a position to argue by analogy and thus to estimate Δ values appropriate to oxides from spectroscopic studies on hydrates.

OPTICAL EVIDENCE ON CRYSTAL FIELD STRENGTHS IN HYDRATES AND OXIDES

The absorption spectra of ions in aqueous solution have been studied extensively and values of the crystal field strength Δ have been determined for all the hydrated transition-metal ions, with the exception of Co^{3+}, which occur in spinels. The hydrates of ions containing only one *d* electron (or only one "hole" in the *d* shell) have a single absorption band, the frequency of maximum absorption corresponding to Δ, the separation between the t_{2g} and e_g orbitals. For ions containing more than one *d* electron the analysis is more complicated since transitions are possible to different excited states. We shall not discuss the optical data in detail since experimental and theoretical studies have already been reviewed.[8,9] Here we restrict our treatment to band assignments in oxides and hence to the determination of Δ values for them.

We shall now compare the available absorption spectra of transition-metal oxides and glasses with those in aqueous solution, to see how Δ varies on passing from an environment of water molecules to one of oxide ions. Optical data are available for glasses containing the trivalent ions Ti^{3+}, V^{3+} Cr^{3+}, and Mn^{3+}, and the divalent ions Cu^{2+}, Ni^{2+}, Co^{2+} and Fe^{2+}.[10]

Trivalent ions

The ion $[Ti(H_2O)_6]^{3+}$ in aqueous solution has a single absorption peak at 20300 cm^{-1} which is assigned as the $^2T_{2g} \rightarrow {}^2E_g$ transition. The only evidence that we have on Ti^{3+} in solid matrices refers to purple titanium glasses. In these there is

just one absorption band, clearly analogous to the band observed in hydrates, which has its maximum at 18700 cm^{-1} so that Δ is about 8 per cent smaller in the glass than in the hydrate.

The V^{3+} ion in glasses has absorption bands with maxima at 16000 cm^{-1} and 23500 cm^{-1}. Comparison with the hydrate $[V(H_2O)_6]^{3+}$ which has bands at 17700 cm^{-1} and 25600 cm^{-1} corresponding to the $^3T_{1g} \rightarrow {}^3T_{2g}$ and $^3T_{1g} \rightarrow {}^3T_{1g}$ transitions shows that Δ is reduced in the glass by about 10 per cent.

The spectra of Cr^{3+} complexes characteristically include sharp lines or narrow bands in the region 15000–17000 cm^{-1} and at about 22000 cm^{-1}. These are due to quartet-doublet transitions within the configuration $(t_{2g})^3$ and are particularly insensitive to crystal field effects. Thus the many careful studies of these bands which have been reported do not help us to determine Δ for chromic salts. The broad bands in the spectra of the Cr^{3+} ion have been investigated in very few solid matrices. In glass the positions of the $^4A_{2g} \rightarrow {}^4T_{2g}$ and $^4A_{2g} \rightarrow {}^4T_{1g}$ transitions at 22200 cm^{-1} and 15400 cm^{-1} respectively are consistent with $\Delta = 15400$ cm^{-1}. This Δ value is about 12 per cent smaller than that in the hydrate (17400 cm^{-1}).

While the value of 15400 cm^{-1} for Δ is probably typical for Cr^{3+} ions in oxides, e.g. in Cr_2O_3, there are one or two situations in which Δ is substantially larger, in particular for ruby and ruby spinel. This anomaly has been discussed elsewhere[11] and is, we believe, due to the "compression" to which the Cr^{3+} ions are subjected when they replace the smaller Al^{3+} ions in the octahedral sites of the corundum and spinel structures.

In manganese glasses the maximum of the one strong absorption band lies in the range 19000–21000 cm^{-1}. The corresponding band in the hydrate is the $^5E_g \rightarrow {}^5T_{1g}$ transition at 21000 cm^{-1}. Thus for Mn^{3+} also, Δ is usually somewhat smaller in glasses than it is in the hydrate.

Divalent ions

The correspondence between the absorption spectra of the hydrated cupric ion and the cupric ion when co-ordinated by oxide ions in solids might be expected to be rather poor since the extent of the JAHN–TELLER stabilization should be rather different in the two cases. In fact the correspondence is very close, the broad absorption band having its maximum at 12500 cm^{-1} in the hydrated ion and in the range 12000–13500 cm^{-1} in Cu^{2+} glasses.

The experimental evidence is more complete for Ni^{2+} in oxide matrices than for any other transition-metal ion. The solution of small amounts of NiO in MgO gives rise to a series of absorption bands in the visible and near ultra-violet.[12] The strongest of these are a relatively sharp peak at 25000 cm^{-1} and a double peak with maxima at approximately 14900 cm^{-1} and 13900 cm^{-1}. In addition there is a weaker, but well-defined peak at 21500 cm^{-1}. In the hydrated ion the corresponding peaks are at 25300 cm^{-1} ($^3A_{2g} \rightarrow {}^3T_{1g}$), 15400 cm^{-1} ($^3A_{2g} \rightarrow {}^1E_g$), 13500 cm^{-1} ($^3A_{2g} \rightarrow {}^3T_{2g}$) and 22000 cm^{-1} (unassigned triplet-singlet transition). The value of Δ is thus almost identical in the hydrate and the divalent oxide. Studies of the spectrum of Ni^{2+} in glasses confirm that the crystal field acting on octahedrally co-ordinated Ni^{2+} is very similar to that in the hydrate, although it varies a little with the composition of the glass.

For Co^{2+} also, in the red cobalt glasses, Δ is rather variable but, judging from the position of the $^4T_{1g} \rightarrow {}^4T_{1g}$ transition which is at 19600 cm^{-1} in the hydrate and at somewhat longer wavelengths in the glasses, the mean Δ value is about 8900 cm^{-1} compared with 9700 cm^{-1} in the hydrate.

The Fe^{2+} ion in glasses is transparent through the visible but has a strong absorption maximum at 10000 cm^{-1}. This band is clearly the $^5T_{2g} \rightarrow {}^5E_g$ transition which occurs in the hydrate at 10400 cm^{-1}.

In the purple nickel glasses and blue cobalt glasses, Ni^{2+} and Co^{2+} occur in tetrahedral co-ordination. This is particularly interesting since it throws some direct light on the magnitude of the crystal field effects for tetrahedral co-ordination, which cannot be determined easily in any other way. The absorption bands to be ascribed to the $^3T_1 \rightarrow {}^3A_2$ and $^3T_1 \rightarrow {}^3T_1$ transitions of tetrahedrally co-ordinated Ni^{2+} are probably at 5400 cm^{-1} and 15900–17500 cm^{-1}, respectively, corresponding approximately to a Δ value of about 3000 cm^{-1}. The spectrum of Co^{2+} in the blue cobalt glasses suggests, by analogy with the analysis given in reference 8, that for these $\Delta \approx 4800$ cm^{-1}.

VOL. 3 1957

CRYSTAL FIELD STRENGTHS FROM MAGNETIC SUSCEPTIBILITY DATA

Octahedrally co-ordinated transition-metal ions with from 3 to 7 *d* electrons form two kinds of compounds which differ in the number of unpaired electrons present on the metal atom. Thus Co^{3+} forms a complex fluoride $(CoF_6)^{3-}$ which has four unpaired spins, and a great variety of hydrates, amines, etc. which have no unpaired electrons, for example $[Co(H_2O)_6]^{3+}$. It has been shown that the type of compound formed with any given ligand is determined to a first approximation by the crystal field strength. There is a critical value for Δ such that if this value is exceeded the low-spin state is the ground state and otherwise the high-spin state is the ground state.[13,14] In the case of Co^{3+} the critical Δ is calculated to be 23500 cm^{-1} but seems to be a little smaller in practice. At temperatures above the absolute zero the two states are present in comparable amounts if Δ is near to this critical value.[15]

There is a great deal of evidence that the crystal field strengths for the hydrates of the divalent transition metals Cr^{2+}–Co^{2+} fall far short of the critical Δ values for spin pairing. Hence, in view of the similarity which we have noticed between values for divalent hydrates and divalent oxides we do not expect any low spin divalent ions in oxide matrices. Among the trivalent hydrates the ion $[Co(H_2O)_6]^{3+}$ has all its electrons paired while the other hydrates have much too small Δ values for spin-pairing. We may then expect that only with Co^{3+} will spin-pairing be important in the trivalent oxides. While we do not wish to discuss the tetravalent ions in detail here, we note that there is reason to believe that spin-pairing will complicate the magnetic behaviour of Co^{4+} ions in certain oxides.

The evidence from both optical and magnetic data on $[Co(H_2O)_6]^{3+}$ shows that this ion is diamagnetic, but there is much chemical evidence suggesting that the high-spin state is only slightly above the ground state and is accessible at room temperature.[15] It is interesting, therefore, that certain octahedrally co-ordinated cobalt oxides, particularly the spinels, have their spins paired while others, including the perovskites, are paramagnetic.[16] This suggests that the crystal field strengths are similar for oxides and for the hydrate, but somewhat larger in spinels than in perovskites, perhaps because of the greater polarizability of the oxide ions in the former.

EMPIRICAL CRYSTAL FIELD STABILIZATIONS

It seems clear from the optical evidence that the crystal field strengths for trivalent ions, octahedrally co-ordinated by oxide ions, are some 8 to 12 per cent lower than in the corresponding hydrates. For octahedrally co-ordinated divalent ions the crystal field strengths are about the same as in the corresponding hydrates. For the two ions Mn^{2+} and Fe^{3+} the available evidence is insufficient to derive values of Δ appropriate to oxides. For these we might make use of the analogies which we have found and infer their Δ values in oxides from the known values in hydrates. But in any case, a knowledge of these Δ values is not important for our present purposes since their crystal field stabilizations are zero, both in octahedral and tetrahedral co-ordination. For Co^{3+} in oxides we have no spectroscopic information but in the previous section we have discussed magnetic data which serve to fix the crystal field strength fairly accurately.

The experimental evidence on ions in tetrahedral co-ordination is so fragmentary that in estimating

Table 2. Crystal field stabilizations for transition-metal oxides

	A	*B*	*C*	*D*	*E*
Mn^{2+}			0	0	0
Fe^{2+}	10400	10400	11·9	7·9	4·0
Co^{2+}	9700	9700	22·2*	14·8	7·4
Ni^{2+}	8500	8500	29·2	8·6*	20·6
Cu^{2+}	12600	12600	21·6	6·4	15·2
Ti^{3+}	20300	18300	20·9	14·0	6·9
V^{3+}	18600	16700	38·3*	25·5	12·8
Cr^{3+}	17400	15700	53·7	16·0*	37·7
Mn^{3+}	21000	18900	32·4	9·6	22·8
Fe^{3+}			0	0	0

A $\Delta(cm^{-1})$ in hydrates
B $\Delta(cm^{-1})$ in oxides
C Octahedral Stabilization (kcal/mole)
D Tetrahedral Stabilization (kcal/mole)
E Excess Octahedral Stabilization (kcal/mole).

* We have used the strong field limit in calculating the stabilization energies from the observed Δ's. This means that we may overestimate the stabilization by a few per cent.

crystal field stabilizations we are forced to rely on the theoretical ratio of 4/9 between Δ for ions in tetrahedral and octahedral sites. This is liable to be in error by perhaps 25 per cent so that predictions which are very sensitive to the stabilizations of ions in tetrahedral sites are liable to be in error. Fortunately in most cases the octahedral stabilizations dominate the tetrahedral ones so that the uncertainty in Δ for tetrahedral sites is not very serious.

In Table 2 we have assembled our estimated crystal-field stabilization energies for transition-metal ions in spinels. We hope that new experimental data on the optical properties of spinels will become available and enable us to correct inaccuracies due to the assumptions which we are at present forced to make in estimating Δ.

EXPERIMENTAL EVIDENCE ON ION DISTRIBUTION

In Table 3 we have collected the available experimental evidence on the distribution of ions between tetrahedral and octahedral sites in binary spinels, XY_2O_4 where X is a divalent transition-metal ion and Y is trivalent aluminium, chromium, manganese, iron or cobalt. The atomic proportion of the divalent ion occurring in the octahedral sites is expressed as δ i.e. for a normal spinel, $\delta = 0$; for an inverse spinel $\delta = 1$; and for random distribution between the two kinds of site, $\delta = 0{\cdot}67$.

Interpretation

We compare first spinels containing the same divalent ion but different trivalent transition-metal ions. In every case we find that the chromite and manganite is normal, while for Mg^{2+}, Mn^{2+}, Fe^{2+}, Co^{2+}, Ni^{2+} and Cu^{2+} the ferrite is at least partially inverted. This is in excellent agreement with the stabilization energies shown in Table 2, which indicate that Cr^{3+} and Mn^{3+} have extra crystal-field stabilizations of 37·7 and 22·8 kcal respectively when in octahedral sites, while Fe^{3+} has no such stabilization energy.

We compare next spinels containing the same trivalent ion but different divalent ions. Among the aluminates we find that the nickel compound is largely inverted while Mn^{2+}, Fe^{2+}, Co^{2+} and Zn^{2+} aluminates are normal. This is consistent with the much greater preference of nickel than of any other of the divalent metals studied for octahedral sites.

The chromites, manganites and cobaltites are all normal, and so do not provide any further test of

Table 3. Experimental cation distributions in spinels

	Mg^{2+}	Mn^{2+}	Fe^{2+}	Co^{2+}	Ni^{2+}	Cu^{2+}	Zn^{2+}
Aluminates	$\sim 0^{(a)}$	$\sim 0^{(a)}$	$\sim 0^{(a)}$	$\sim 0^{(a)}$	$0{\cdot}76^{(a)}$	—	$0^{(a)}$
Chromites	$\sim 0^{(b)}$	$\sim 0^{(b)}$	$\sim 0^{(b)}$	$\sim 0^{(b)}$	$\sim 0^{(a)}$ $^{(b)}$	$0{\cdot}1^{(c)}$ $0^{*(d)}$	$0^{(e)}$
Ferrites	$0{\cdot}9^{*(e)}$ $0{\cdot}88^{*(f)}$	$0{\cdot}2^{*(g)}$	$1^{*(h)}$	$1^{*(i)}$	$1^{*(j)}$	$0{\cdot}95^{(c)}$ $1^{*(k)}$	$< 0{\cdot}05^{*(j)}$
Manganites	—	$\sim 0^{(a)}$	—	—	—	—	$\sim 0^{(l)}$
Cobaltites	—	—	—	$\sim 0^{(m)}$	—	—	$\sim 0^{(m)}$

* Neutron diffraction.

(a) Romeijn F. C. *Philips Res. Rep.* **8,** 304 (1953).
(b) Verwey E. J. W. and Heilmann E. L. *J. Chem. Phys.* **15,** 174 (1947).
(c) Miyahara S. and Ohnishi H. *J. Phys. Soc. Japan* **12,** 1296 (1956).
(d) Prince E. Paper presented at American Crystallographic Association Meeting, June 1956
(e) Bacon G. E. and Roberts F. F. *Acta Cryst.* **6,** 51 (1953).
(f) Corliss L. M., Hastings J. M., and Brockmann F. G. *Phys. Rev.* **90,** 1073 (1953).
(g) Hastings J. M. and Corliss L. M. *Phys. Rev.* **104,** 328 (1956).
(h) Shull C. G., Wollen E. O., and Koehler W. C. *Phys. Rev.* **84,** 912 (1951).
(i) Prince E. *Phys. Rev.* **102,** 674 (1956).
(j) Hastings J. M. and Corliss L. M. *Rev. Mod. Phys.* **25,** 114 (1953).
(k) Prince E. and Treuting R. G. *Acta Cryst.* **9,** 1025 (1956).
(l) Mason B. *Amer. Mineral.* **32,** 426 (1947).
(m) Cossee P. Thesis, Leiden (1956).

our theory. Among the ferrites only Mn^{2+} and Zn^{2+} are largely normal and these are just the metals which have no extra stabilization in octahedral sites.

Thus our simple theory accounts for all the available experimental evidence on cation distributions. It is perhaps worth emphasizing that the otherwise puzzling fact that Fe_3O_4 is a cubic inverted spinel while Mn_3O_4 is normal and tetragonally distorted receives an immediate explanation in terms of crystal field theory.

DISCUSSION

We have shown that the crystal field stabilizations of transition-metal ions in spinels vary in such a manner as to account for the changes in the degree of inversion which occur when one ion is replaced by another of the same charge. There are, however, some other factors which would be expected to have important effects on the cation distribution.

The variation with the nature of the metal ions of the difference in Madelung energy between the normal and inverse spinels has been ignored. The Madelung energy is a function of u, the oxygen parameter,[17,18] and is zero at $u = 0{\cdot}379$ for 2–3 spinels. For $u < 0{\cdot}379$ the inverse structure is stable, and for $u > 0{\cdot}379$ the normal structure is stable. In the 2–3 spinels, u is invariably a little larger than the critical value so that the normal structure appears to be slightly favoured. We may expect, however, that for a given cation distribution, the oxygen parameter will adjust itself as far as possible so as to maximize the electrostatic energy. The case of $NiAl_2O_4$, the only aluminate which is not normal, is interesting because it affords some confirmation that the crystal field stabilizations are approximately correctly scaled. ROMEIJN[2] has determined the value of u to be 0·381, for which value the normal structure is some 25 kcal/mole more stable than the inverse one in the absence of crystal field effects. The crystal field stabilization of octahedral Ni^{2+} of 21 kcal/mole is just about enough to compensate for this and the observed δ value of 0·75 is very close to that expected for a random distribution of cations.

Another important factor which has been ignored is that the irregular variation of crystal field stabilizations must be superimposed on a steady variation with atomic number of the difference in energy between octahedrally and tetrahedrally co-ordinated compounds. This is seen by comparing the octahedrally co-ordinated MnO structure with the tetrahedrally co-ordinated ZnO structure. Since neither ion is stabilized by crystal fields of either symmetry, it is clear that as the atomic number increases (and the ionic radius decreases) the tetrahedral structure becomes more stable relative to the octahedral.

It may seem surprising that the crystal field theory appears to work so well, since it takes no account of these variations. But it should perhaps be emphasized that its apparent success depends in part on the fragmentary and qualitative nature of the empirical evidence which we have interpreted. If we wished to calculate quantitatively the change in inversion on passing from say $MnFe_2O_4$ to $CoFe_2O_4$ or $ZnFe_2O_4$ it would be essential to allow for those parts of the cohesive energy which are not considered by the crystal field method.

REFERENCES

1. DUNITZ J. D. and ORGEL L. E. *J. Phys. Chem. Solids* **3,** 20 (1957).
2. ROMEIJN F. C. *Philips Res. Rep.* **8,** 304 (1953).
3. ORGEL L. E. *J. Chem. Soc.* 1756 (1952).
4. GRIFFITH J. S. *J. Inorg. Nucl. Chem.* **2,** 1 (1956).
5. JØRGENSEN C. K. and BJERRUM J. *Acta. Chem. Scand.* **9,** 180 (1955).
6. VAN SANTEN J. H. and VAN WIERINGEN J. S. *Rec. Trav. Chim. Pays-Bas* **71,** 420 (1952).
7. ORGEL L. E. *Proc. Tenth Solvay Conference in Chemistry* Brussels (1956).
8. ORGEL L. E. *J. Chem. Phys.* **23,** 1004 (1955).
9. JØRGENSEN C. K. *Proc. Tenth Solvay Conference in Chemistry* Brussels (1956).
10. WEYL W. A. *Coloured Glasses* Society of Glass Technology Monograph (1951).
11. ORGEL L. E. *Nature, Lond.* Submitted for publication.
12. KRÖGER F. A. and VINCK H. J. *Physica* **18,** 77 (1952).
13. ORGEL L. E. *J. Chem. Phys.* **23,** 1819 (1955).
14. GRIFFITH J. S. *J. Inorg. Nucl. Chem.* **2,** 229 (1956).
15. TAUBE H. *Chem. Rev.* **50,** 69 (1952); general discussion.
16. COSSEE P. Thesis, Leiden (1956).
17. DE BOER F., VAN SANTEN J. H., and VERWEY E. J. W. *J. Chem. Phys.* **16,** 1091 (1948).
18. GORTER E. W. *Philips Res. Rep.* **9,** 295 (1954).

J. Phys. Chem. Solids Pergamon Press 1957. Vol. 3. pp. 324–337.

LOW TEMPERATURE ELECTRICAL AND MAGNETIC BEHAVIOR OF DILUTE ALLOYS OF Mn IN Cu

R. W. SCHMITT and I. S. JACOBS

General Electric Research Laboratory, Schenectady, New York

(*Received* 4 *June* 1957)

Abstract—Measurements are reported of the magnetization, resistivity and magnetoresistivity of dilute alloys of manganese in copper. At very low temperatures the magnetization is hysteretic and remanence is observed in all except the most dilute alloys. The magnetoresistance also exhibits reproducible hysteretic behavior in cases where there is hysteresis in the magnetization. Furthermore the magnetoresistance is proportional to the square of the magnetization. From these experimental results it is inferred that within any volume of dimensions comparable to the electron mean free path the net magnetization in the virgin alloy is zero. The phenomenology of one possible magnetic structure fulfilling this requirement is developed and it is shown how the low-temperature resistance anomaly and peculiar magnetoresistive behavior could result from this magnetic structure.

1. INTRODUCTION

THE magnetic and resistive behavior of dilute alloys of transition metals in noble metals has received attention by many experimenters. The paramagnetism of these alloys at higher temperatures was first investigated and it was often found that the susceptibility followed a Curie–Weiss law.[1–9] More recently OWEN, BROWNE, KNIGHT and KITTEL[10] observed anomalous magnetic behavior at very low temperatures in such alloys. Our interest in the problem commenced independently at about the same time.[11]

The anomalous resistive behavior of these alloys was first noted by GERRITSEN and LINDE.[12] They observed that in addition to a minimum in the resistance versus temperature—an effect observed previously in a wider variety of dilute alloys by many investigators[13]—there was also a maximum in the resistivity at still lower temperatures. GERRITSEN and LINDE[12,14] also reported that at low temperatures the resistance of these alloys decreased in a magnetic field. KORRINGA and GERRITSEN[15] proposed an explanation of the anomalous resistive behavior. They postulated that the introduction of impurities in a noble metal matrix would result in extra electronic states which were spatially localized but nevertheless had energies near the Fermi energy. The consequence of this assumption is that there are anomalies in the resistance and magnetoresistance.

More recently one of us[11] suggested that if a co-operative magnetic transition occurred at low temperatures in the dilute alloys then the anomalous electrical behavior could be a result of this transition. We therefore examined explicitly the relation between the anomalous resistive behavior and the magnetic behavior of dilute alloys of manganese in copper. A preliminary report of these experiments was given at the Ottawa International Conference on Electron Transport in Metals and Solids.[16] In the present paper we present a more comprehensive report of the anomalous magnetic and electrical behavior of dilute alloys of manganese in copper. The principal new experimental results are the observation of reproducible hysteresis in the magnetoresistance as well as in the magnetization in some of the alloys and the correlation between the magnetization and magnetoresistance. From these results one can infer certain restrictions on the possible magnetic structure of the alloys.

2. MAGNETIC BEHAVIOR

(*a*) *Description of experiments*

In the present work, we investigated the properties of five dilute alloys. The nominal compositions of these

alloys were 0·05, 0·2, 0·4, 1·0 and 1·8 at. per cent Mn in copper. For convenience we shall designate the alloys by the nominal manganese content although the actual manganese content of a given magnetic or electrical sample may differ slightly from the nominal composition. The alloys were prepared by melting together American Smelting and Refining Company nominal 99·999 per cent pure copper and Electro-Manganese Corporation electrolytic manganese. The melting was done in sealed off, evacuated quartz tubes placed in a furnace and agitated mechanically during melting. Part of each melt was formed into a cylinder ($\frac{3}{16}$ in. diam. $\times \frac{3}{4}$ in. long) to be used in the magnetic measurements and an adjacent part of the melt was swaged and drawn into wire for the electrical measurements.

The magnetic samples were annealed at about 450°C for 30 min in a vacuum or in helium gas. After the experiments, they were analysed colorimetrically for manganese content and these results are shown in column 2 of Table 1. The 1·8 per cent alloy was examined spectroscopically for Fe, Ni, and Co and none was detected. The electrical samples were too small for an analysis but, as we shall see later, it appears that their manganese content did not greatly depart from that of the magnetic samples.

The magnetic properties of these alloys were studied by measuring their magnetization as a function of field. The more commonly measured susceptibility is obtained from the slope of such a curve, and in addition measurement of the magnetization can reveal both hysteretic behavior and deviations from a linear dependence of magnetization on field.

The technique of measurement is an adaptation of that described by ARROTT.[17] A coil is wound around the cylindrical surface of the sample and a current through this coil is adjusted to restore to uniformity the B field in which the sample is placed. The magnetization of the sample is calculated from this current, measured potentiometrically, and from the geometrical parameters. The null corresponding to the uniform B field is detected by moving the sample in to, or out of, a 2000 turn detector coil. The signal from the unbalance is amplified by a 75 c/s chopper amplifier and observed on a photoelectric recorder. The external magnetic field, measured by a Rawson rotating coil meter, was limited to a maximum of about 7150 oersteds by the space requirements of the double dewar cryostat. Small rapid field fluctuations from the motor-generator supply are approximately cancelled by a balanced dummy detector coil connected in opposition to the main one. These fluctuations constitute the principal limit to the sensitivity of the measurement. In the low temperature region where the magnetizations are higher, the relative error ranges between one per cent and one-fifth of one per cent.

The temperatures of measurement ranged between room temperature and about 2°K and were obtained by immersing the sample in constant temperature baths of liquid helium, hydrogen and nitrogen, and a CO_2-alcohol mixture. The temperatures achieved by pumping on the refrigerant were maintained within a few hundredths of a degree.

(b) Paramagnetic behavior

Although we are more interested in the low-temperature behavior, a few comments may be made about the "high" temperature results. As pointed out by previous workers, and most recently by OWEN *et al.*[10,18] the high-temperature susceptibility obeys a Curie–Weiss law $\chi = C/(T-\theta)$. Most previous workers[2,3,4,9] agree on the value of the Curie constant C, when correction is made for the diamagnetism of the copper. These data, except for two samples of OWEN *et al.*, all indicate effective magneton numbers p_{eff} approaching $\sim 4{\cdot}9$ per manganese atom for very dilute samples. This value is sometimes carelessly interpreted as that corresponding to a $3d^5$ electronic configuration of Mn, perhaps because of a confusion between the *effective magneton number* and the *saturation moment* expressed in Bohr magnetons.* On the other hand, MYERS and others have suggested a possible $3d^6$ configuration with the electronic spin

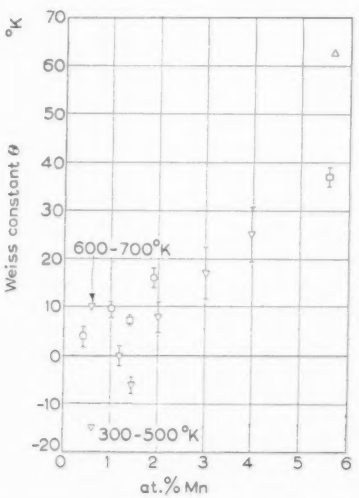

FIG. 1. Variation of Weiss constant, θ, with Mn concentration for dilute alloys of Mn in Cu. Data from several sources and temperature ranges, as follows: ○ present work, $T < 300$°K; □ OWEN *et al.*,[18] $T < 373$°K; ▽ GUSTAFSSON,[4] replotted and estimated, $300° < T < 600$°K, except as noted; △ VALENTINER and BECKER,[3] $T < 300$°K; data of NÉEL[2] omitted due to bad scatter.

* For clarification, see e.g. VAN VLECK J. H. *Electric and Magnetic Susceptibilities* p. 257. Oxford University Press (1932).

$S = 2$ for the Mn in these alloys. We shall henceforth assume a *saturation moment* of 4 Bohr magnetons (μ_B) per Mn atom as suggested by the high temperature susceptibility data. With other noble metals, Ag and Au, the effective magneton number is higher, approaching 5·9 in Ag.[7] The Weiss constant θ, in annealed samples is generally reported positive suggesting a ferromagnetic interaction and it increases with Mn concentration. The trend and reliability of these θ values may be seen in Fig. 1 which shows data derived from several sources, one using high temperature data (300°K to 600°K) and two using data up to room temperature. The limited utility of quantitative θ values is clear from this graph.*

(*c*) *Magnetic anomalies*

The magnetization curves in the low temperature region exhibit a number of interesting features. We have previously reported[16] that the magnetization is frequently not linear with field and that hysteresis and remanence may be present. Figs. 2, 3 and 4 show curves of the magnetization vs. field at low temperature for the five alloys of Mn in Cu described in Table 1. The results are expressed in terms of the relative magnetization $I = \sigma/\sigma_\infty$, where σ is the magnetic moment per gram of sample and σ_∞ is its saturation value assuming $4\mu_B$ per Mn atom. All our samples containing 0·4 atom per cent Mn or more exhibited hysteresis in the liquid helium range. The susceptibility of those samples which have hysteresis goes through a maximum at a temperature near to θ, in agreement with the findings of OWEN *et al.*[10,18] The extent of this maximum may be measured by the ratio of the susceptibility at the maximum to that at the lowest temperature of measurement (about 2°K). This ratio depends on the definition of the susceptibility in the presence of hysteresis, e.g.

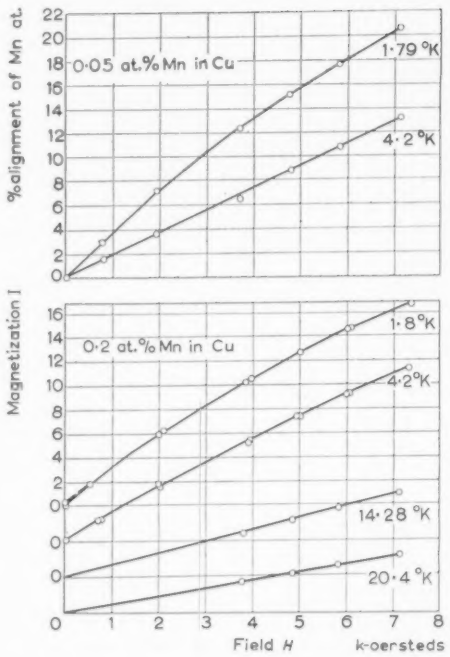

FIG. 2. Low-temperature isothermal magnetization curves for the nominal 0·05 and 0·2 at. per cent Mn in Cu alloys. The magnetization, I, is expressed in per cent alignment of Mn atoms assuming a saturation moment of 4 μ_B/Mn atom. These curves show deviations from linearity but no hysteresis.

$\chi = (\sigma/H)_{H=7000}$ or $\chi = (d\sigma/dH)_{H=0}$ or $\chi = [(\sigma_{7000} - \sigma_{\text{rem}})/H]_{H=7000}$, and varies between $\sim 1{\cdot}07$ and $\sim 1{\cdot}25$ for the 1·8 at. per cent Mn sample. The temperature at which the susceptibility is a maximum is near or slightly below that at which the hysteresis first appears. For example, the temperature of $\chi_{\max}$ for the 1·8 at. per cent Mn sample is less than 14°K but the data of Fig. 5, showing the approximate temperature dependence of the isothermal remanent magnetization, indicates that the remanence vanishes near 20°K. Similar behavior occurs in various alums at very low temperatures.[21] The existence of the maximum in the susceptibility has been interpreted by the Berkeley group as a gradual transition to antiferromagnetism. This view may be correct, but the evidence linking the maximum in χ to the presence of hysteresis and remanence can also be interpreted in other ways. One picture which has been

* In determining these θ values, the observed susceptibility has been corrected for diamagnetism in the popular way, i.e. considering the diamagnetism arising from the pure Cu in proportion to its concentration. One investigator, GUSTAFSSON,[4] has extrapolated his $\chi(T)$ data to obtain the temperature independent diamagnetism of the alloys as a function of Mn content. Recent experimental[19] and theoretical[20] work with other copper alloys has redirected attention to this diamagnetism problem. If GUSTAFSSON's values for the diamagnetism are used, the trend in the θ values in Fig. 1 remains, but the rate of increase of θ with concentration is less.

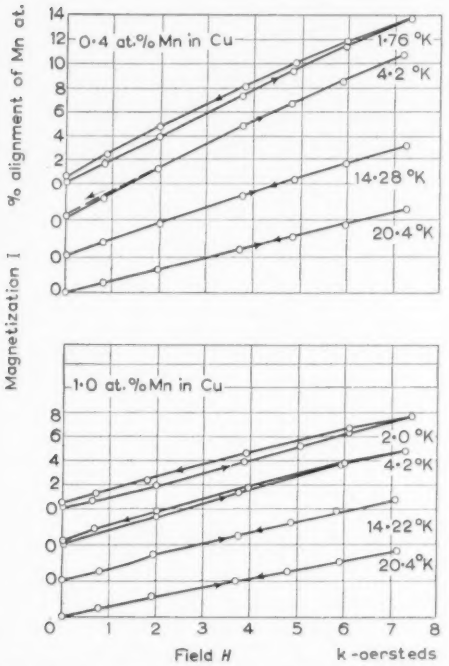

FIG. 3. Low-temperature isothermal magnetization curves for the nominal 0·4 and 1·0 at. per cent Mn in Cu alloys. Units of magnetization, I, as in Fig. 2. These curves show hysteresis.

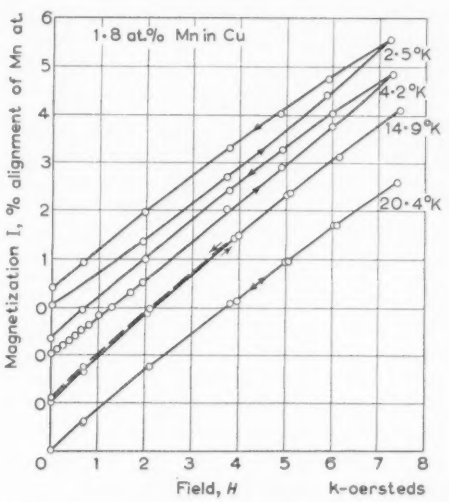

FIG. 4. Low-temperature isothermal magnetization curves for the nominal 1·8 at. per cent Mn in Cu alloy. Units of magnetization, I, as in Fig. 2. These curves show hysteresis.

suggested is that of small ferromagnetic domains coupled antiferromagnetically.[22,23]

The remanent magnetizations which can be obtained depend on temperature, as noted above, on composition, on time, on maximum magnetic field applied, and on whether that field is applied at temperature after cooling in zero field (isothermal remanent magnetization), or applied during cooling from a higher temperature such as 300°K or 77°K (thermoremanent magnetization). The magnitude of the isothermal remanent magnetization obtainable with a field of 7 k oersteds at about 2°K

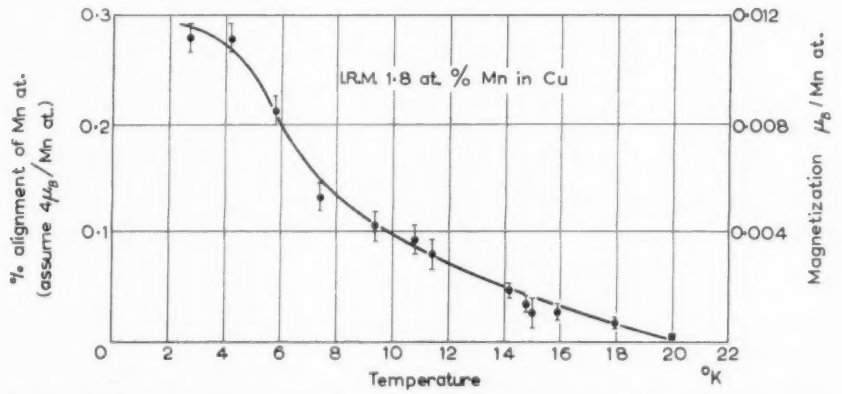

FIG. 5. Isothermal remanent magnetization (I.R.M.) vs. temperature for sample containing nominal 1·8 at. per cent. Mn. Measurements made after application of 5500 oersteds to demagnetized sample.

increases from 0·012 to 0·025 Bohr magnetons per Mn atom as the Mn content decreases from 1·8 at. per cent to 0·4 at. per cent. Assuming a saturation moment of 4 Bohr magnetons per Mn atom, these correspond to alignments of 0·3—0·6 per cent. These values are qualitatively similar to those of OWEN *et al.*, but quantitatively larger. The sample of lowest Mn content, 0·05 at. per cent, shows no remanence, while the 0·2 at. per cent sample shows a very small remanence ($\sim 0{\cdot}005\mu_B$/Mn) at 1·8°K and none at higher temperatures.

In many instances the remanent magnetizations decay isothermally with time. These decays were difficult to reproduce quantitatively and were not studied in detail. A representative figure for their rate is about 15 per cent fall-off in one hour. Remanent magnetizations measured immediately after the rapid removal of a field often are higher ($\sim$ 10 per cent) than those measured after a slow reduction of the field.

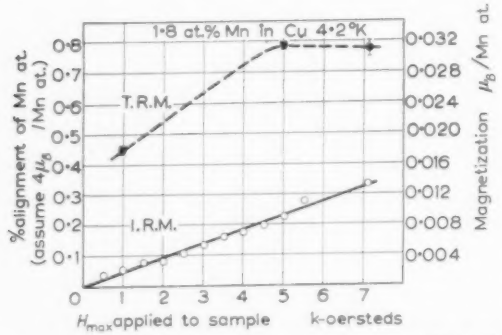

FIG. 6. Isothermal remanent magnetization (I.R.M.) vs. maximum applied field (H_{max}) for 1·8 at. per cent Mn sample at 4·2°K. Thermoremanent magnetization (T.R.M.) for same sample at 4·2°K measured after cooling sample in field H_{max} from temperatures above 77°K.

The field dependence of the isothermal remanence for one sample shown in Fig. 6 is approximately linear over the range of field employed. As noted by the Berkeley group, cooling the sample to low temperatures in the presence of a magnetic field produces a thermoremanent magnetization which is considerably larger than the corresponding isothermal remanence. Such a comparison appears in Fig. 6 for the 1·8 at. per cent Mn sample showing a twofold increase in moment to about 0·03 Bohr magnetons per Mn atom. If one begins at the quenching field just after cooling and traverses one cycle of the hysteresis loop, the loop is not closed. Thus, the magnetization of this field-quenched sample is initially enhanced just as is the remanence. Further traversals of the loop reveal a closed loop which is, however, biased so that the remanence is higher and coercivity smaller in the direction of the original quenching field than in the opposite direction. This behavior resembles that of samples showing thermoremanent effects when investigated over a limited range of field.[24] More detailed investigation of these hysteretic phenomena at both low and high fields may provide better understanding of the co-operative magnetic effect in these alloys. The present work substantiates the existence of anomalous magnetic behavior and supplies data needed for correlation of the electrical and magnetic properties.

3. RESISTIVE BEHAVIOR

(*a*) *Description of experiments*

The resistance of the samples was measured using standard potentiometric techniques. A Rubicon 6-dial "thermofree" potentiometer was used and the "galvanometer" consisted of a Liston-Becker Breaker Amplifier and a box galvanometer. Measurements were made with the current flowing in each direction through the sample so that the influence of thermal e.m.f. in the potential leads could be eliminated. Thermal e.m.f. in other parts of the measuring circuit was usually negligible.

High precision had to be attained in the magnetoresistance measurements. The fractional change in resistance on applying a magnetic field was small and we wished to measure these fractional changes with an accuracy of a few per cent. The limitations to precision arose from extraneous e.m.f. that could be as large as a few tenths of a μV. The total e.m.f. being measured varied from slightly less than 1000 μV to over 10^4 μV, depending on the sample being measured. Fortunately, the fractional change in resistance was greatest for those samples measured with least precision so that the desired accuracy of measuring the fractional change in resistance could be attained in all cases. The uncertainty of the resistivity itself is about ± 5 per cent owing to errors in measuring the dimensions of the samples.

The resistance samples were wires approximately 0·3 mm diam. by 20 cm long and were wound on small ceramic holders. Potential leads of the same material were spot welded on the sample and the mounted samples were annealed at 450°C for 30 min in a vacuum or in helium gas. The samples were wound bifilarly so as to reduce inductive pick-up from small fluctuations in the magnetic field when making magnetoresistance measurements.

The measurements of resistance versus temperature were made by immersing the sample in liquid helium,

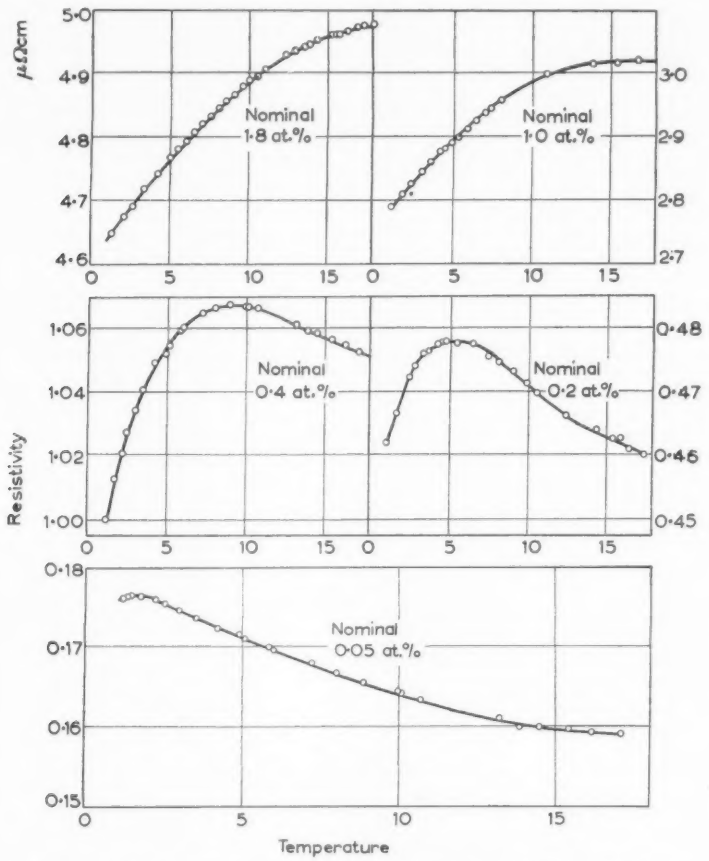

FIG. 7. Resistivity vs. temperature of Cu–Mn in liquid helium–hydrogen temperature range.

hydrogen, and nitrogen and determining the temperature from vapor pressure measurements. Intermediate temperatures were attained by using an activated charcoal "bath" and desorbing gas from the cold charcoal to maintain a constant temperature during a resistance measurement. The temperature was measured with a carbon thermometer or a copper-constantan thermocouple, depending on the temperature range of interest. Magnetoresistance measurements were made only in the liquid baths at a few fixed temperatures.

(*b*) *The resistivity anomaly*

Figs. 7 and 8 shows the resistivity versus temperature for five samples of Mn in copper. The lower concentration samples show a definite resistivity maximum while the highest concentration sample shows only an anomalous decrease in resistivity with decreasing temperature. These are the effects discovered by GERRITSEN and LINDE.[12] Fig. 9 shows the temperature of the resistivity maximum, T_{max}, versus the resistivity at 4·2°K. The disagreement with the data of GERRITSEN and LINDE is not surprising since they had to determine T_{max} for some of their samples by extrapolating data into the intermediate temperature region and this procedure is susceptible to considerable error.

We will not here discuss the dependence of T_{max} or of $\rho_{4\cdot2°K}$ on the concentration itself. The reason for avoiding this is the uncertainty, mentioned earlier, in the Mn content of the electrical samples.

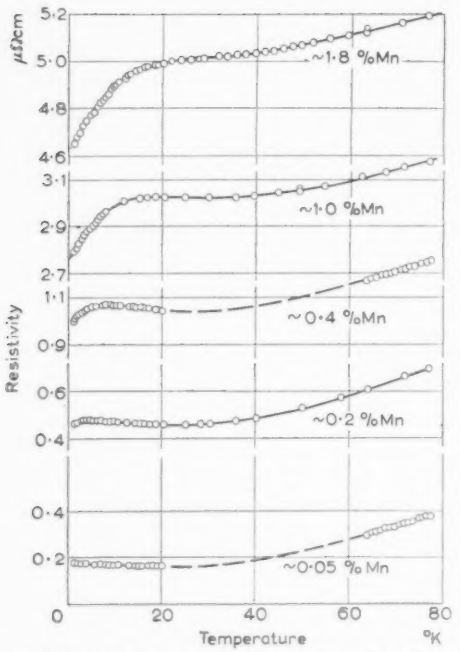

FIG. 8. Resistivity vs. temperature of Cu–Mn alloys from liquid helium temperatures to liquid nitrogen temperatures.

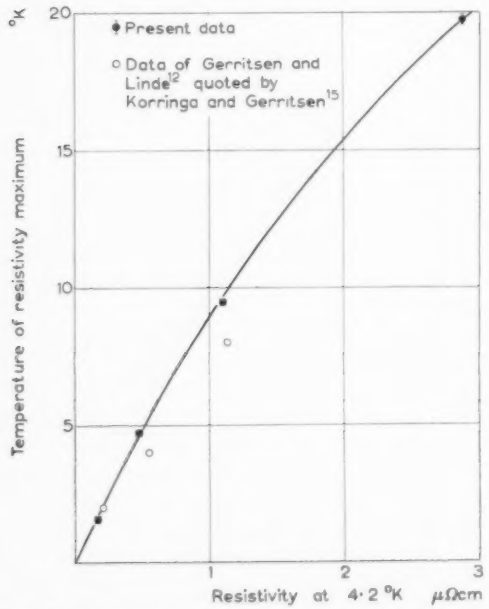
°K
Present data
Data of Gerritsen and Linde[12] quoted by Korringa and Gerritsen[15]
Temperature of resistivity maximum
Resistivity at 4·2 °K μΩcm

FIG. 9. Temperature of maximum resistivity, T_{max} vs. resistivity at 4·2°K for Cu–Mn alloys.

(c) *The magnetoresistance anomalies*

One of the most striking features of these alloys is that at low temperatures the resistance decreases on applying either a transverse or a longitudinal magnetic field. This is an effect discovered, again, by GERRITSEN and LINDE[12,14] who also showed that the size of the transverse and longitudinal effects is the same. Moreover, they showed that at low temperatures and high fields the resistance can be made to decrease by 20–30 per cent in some cases whereas the field-free resistance anomaly amounts to only a few per cent of the residual resistivity. In our experiments we did not use fields high enough to see decreases in resistance of more than a few per cent. However, we did observe reproducible hysteretic effects in the magnetoresistance that correspond to the hysteretic effects observed in the magnetizations.[16] Fig. 10 shows the transverse magnetoresistance of the 1·0 and 1·8 at. per cent samples. Hysteresis is observed at the lower temperatures just as it is observed in the magnetization. In addition, the magnetoresistance can be enhanced slightly by quenching the sample

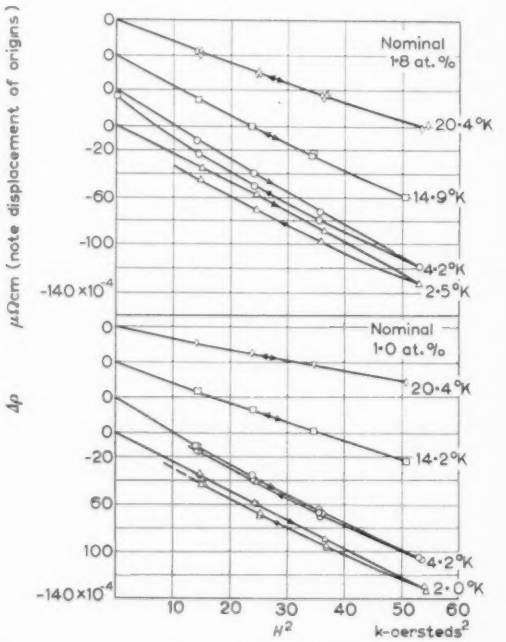

FIG. 10. Change in resistivity vs. square of magnetic field for the 1·0 and 1·8 at. per cent Mn in Cu samples.

in a magnetic field from liquid nitrogen or room temperature. This again corresponds to the similar effect observed in the magnetization. No hysteresis appears in any of the other three more dilute alloys; their magnetoresistance is shown in Fig. 11.

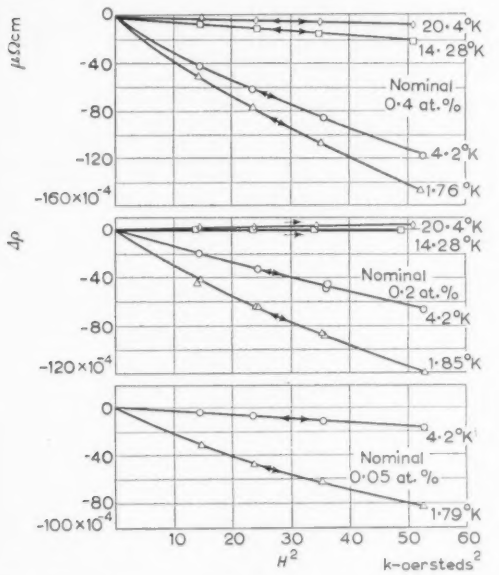

FIG. 11. Change in resistivity vs. square of magnetic field for the 0·05, 0·2, and 0·4 at. per cent Mn in Cu samples.

4. RELATION BETWEEN MAGNETIZATION AND MAGNETORESISTANCE

The appearance of hysteresis in both the magnetization and the magnetoresistance clearly indicates that the magnetoresistance depends not on the magnetic field alone but on the magnetization. Even in those cases where hysteresis does not appear, the relation between magnetoresistance and magnetic field is often not a simple quadratic one (Fig. 11). This corresponds to the fact that the relation between magnetization and field in these cases is not a simple linear one (Fig. 2). Thus, the magnetoresistance seems always to depend on the magnetization.

Before comparing the magnetoresistance and magnetization data, we should discuss the effect of small concentration differences between the magnetic and electrical samples. However, in the interest of simplicity we shall defer this discussion

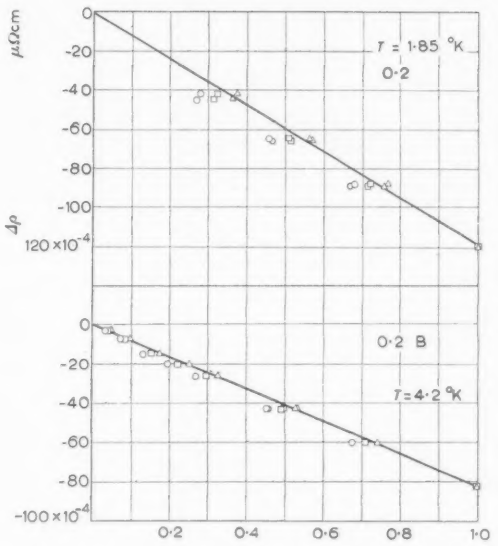

FIG. 12. Functional dependence of change in resistivity on magnetization for two 0·2 at. per cent Mn in Cu samples at liquid helium temperatures. $\triangle\rho$ vs. $(H/H_{max})^2$ —○; $\triangle\rho$ vs. $HI/H_{max}I_{max}$—□; $\triangle\rho$ vs. $(I/I_{max})^2$—△.

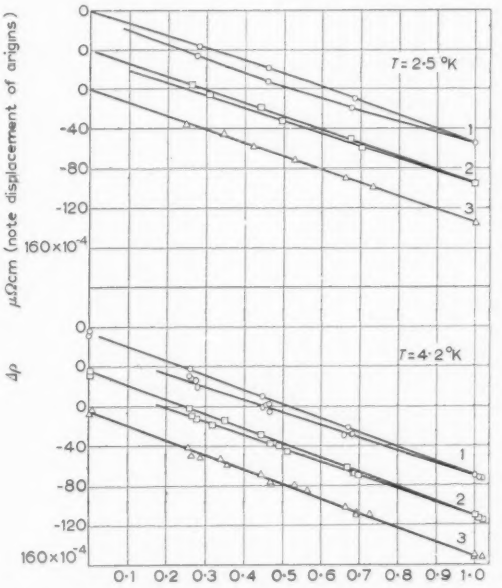

FIG. 13. Functional dependence of change in resistivity on magnetization for 1·8 at. per cent Mn in Cu at liquid helium temperatures. (See caption Fig. 12 for explanation of symbols.)

until later and pretend that the resistance samples have the same percentage manganese in them as the magnetic samples.

Those cases where either (a) the magnetization is not a linear function of the magnetic field even though no hysteresis is present or (b) there is measurable hysteresis in the magnetization can be used to ascertain the functional relation between magnetoresistance and magnetization. We have examined the data which complies with conditions (a) and (b) by plotting $\Delta\rho = \rho(H) - \rho(H = 0)$ vs. (1) $(H/H_{max})^2$, (2) $HI/H_{max}I_{max}$, and (3) $(I/I_{max})^2$. Figs. 12 and 13 show the result of this examination for a few cases at the lower temperatures. These are the four most favorable cases for distinguishing between an H^2, HI, or I^2 dependence. In some other cases, however, neither hysteresis nor deviation from linearity in the magnetization curve is sufficiently great to allow a distinction to be made. In the figures, it is seen that the magnetoresistance is a linear function of the square of the magnetization, I^2. We will not concern ourselves with the fact that there is sometimes a small remanent effect in the magnetoresistance as a function of I^2 and will consider only the slope of $\Delta\rho/\rho_v$ vs. I^2 curves (ρ_v resistivity of virgin sample). Table 1 summarizes the values of this slope.

We now return to the problem of the effect of slight composition differences between the electrical and magnetic samples. Let S be the slope of the $\Delta\rho/\rho_v$ vs. I^2 curve where $\Delta\rho$ and I are measured on two samples of slightly different composition. Suppose, however, that $\Delta\rho/\rho_v$ had been measured on a sample containing the same amount of manganese as the magnetic sample. This

Table 1

C (Nom.)	C (Mag.)	C (Elec.)	σ_∞ (e.m.u./g)	T (°K)	S	S'	S''
0·05	0·07	0·06	0·18	1·79	1·15	1·10	1·13
				4·2	0·60	0·64	0·77
0·2	0·20	0·17	0·69	1·85	0·96	0·88	0·89
				4·2	0·69	0·69	0·77
				14·3	(·04)	—	—
				20·4	—	—	0 (assumed)
0·2*B*	—	0·20	—	4·2	0·73	—	—
0·4	0·42	0·37	$1{\cdot}4_6$	1·76	0·72	0·65	0·66
				4·2	0·56	0·53	0·54
				14·3	0·26	0·27	0·30
				20·4	0·19	0·20	0·25
1·0	0·98	1·03	$3{\cdot}5_0$	2·0	0·81	0·89	0·91
				4·2	0·76	0·84	0·86
				14·2	0·61	0·61	0·63
				20·4	0·55	0·53	0·55
1·8	1·90	1·69	$6{\cdot}2_2$	2·5	0·93	0·84	0·87
				4·2	0·92	0·83	0·85
				14·9	0·73	0·71	0·73
				20·4	0·60	0·63	0·65

Explanation of Table: $C \equiv$ at. per cent Mn (column 1: nominal composition by which samples are designated in the text; column 2: composition of magnetic samples obtained from colorimetric analysis; column 3: composition of electrical samples estimated from residual resistivity), $\sigma_\infty \equiv$ saturation magnetization per gram assuming 4 μ_B per Mn atom; $S \equiv$ measured slope of $-\Delta\rho/\rho_v$ vs. I^2 curves; S', S'' corrected slopes (see text). (Samples 0·2 and 0·2*B* are two wires taken from the same melt.)

experiment would have yielded the correct slope S'. It is easily shown that

$$S' = S[1-\alpha\Delta c],$$

where $\alpha = \delta\ln(\Delta\rho/\rho_v)/\delta c$ and Δc is the excess concentration of manganese in the resistance sample. Approximate determinations of α can be obtained by plotting $\ln(\Delta\rho/\rho_v)$ for, say, the maximum field used, vs. the nominal composition of the samples and determining the slopes of these curves. The quantity Δc is obtained by knowing the composition of the magnetic samples from chemical analysis and by estimating the Mn content of the electrical samples from their resistivity at 4·2°K (the atomic resistivity increase of Mn in Cu at 4·2°K is taken to be 2·8 $\mu\Omega$cm/at. per cent.)[12] This procedure is very crude but our only purpose is to see whether or not slight composition differences between the electrical and magnetic samples are likely to be significant. Table 1 gives the values of S' obtained in this manner. One sees that the errors due to composition differences are probably small.

Fig. 11 shows that the magnetoresistance of the 0·2 at. per cent sample is positive at 20·4°K. This illustrates that the anomalous decrease in resistivity is sometimes so small that the effect of the normal increase of resistivity in a magnetic field cannot be neglected. We can estimate crudely, the importance of the normal magnetoresistance effect in the following way. Assuming that the Kohler–Justi rule holds for the normal magnetoresistance and that the normal and anomalous magnetoresistance effects are additive, one has

$$\Delta\rho/\rho_v = K(\rho_{00}H/\rho_v)^2 - S''I^2$$

where K is a constant, ρ_{00} is the resistance of a sample at 0°C, S'' is the proportionality factor between the anomalous magnetoresistance and I^2, and the other symbols have their usual meanings. For the purposes of estimating these corrections it is sufficient to take $H = (\sigma_\infty/\chi)\ I$, where σ_∞ and χ have been defined earlier. Then, S'' is related to our "measured" values S', by

$$S'' = S' + K(\sigma_\infty\rho_{00}/\rho_v)^2.$$

The quantity K is estimated by assuming $S'' = 0$ for the 0·2 at. per cent sample at 20·4°K; this yields $K = 7{\cdot}6\times10^{-13}$ (oersteds)$^{-2}$, a value three to six times higher than one would get by using data[25] on the magnetoresistance of pure copper at helium temperatures. Again one must emphasize the approximate nature of these calculations but, as a comparison of the tabulated values of S'', S', and S (Table 1) shows, the normal magnetoresistance is relatively unimportant except for the alloys of lower manganese content at the higher temperatures.

5. INTERPRETATION

The main problem that concerns us is the relation between the magnetic behavior and the anomalous resistive behavior. The anomalous resistive behavior in zero magnetic field is itself complex; as the temperature is lowered the resistance of the more dilute alloys passes through a minimum at a temperature T_{min} and then through a maximum at a temperature $T_{max} < T_{min}$. For higher concentration alloys the minimum and maximum both disappear but there is still an anomalously rapid decrease of resistance with decreasing temperature (cf. Figs. 7 and 8). The occurrence of a resistance minimum alone can be caused by non-transition impurities such as tin, gallium, bismuth, lead, etc.[13] The magnitude of the increase in resistivity with decreasing temperature is about two orders of magnitude smaller when caused by non-transition impurities than when caused by transition impurities. Nevertheless, we tentatively assume that the anomalous decrease of resistance with decreasing temperature and the decrease of resistance on applying a magnetic field are the only effects arising specifically from the magnetic character of the impurities. Consequently, in what follows we leave out of account a discussion of that part of the resistance which increases with decreasing temperature.*

There are three main experimental results upon which we wish to dwell; (1) in zero applied field there is an anomalous decrease of resistance with decreasing temperature, the anomaly amounting to 10 per cent or less of the "residual" resistance, (2) on application of a longitudinal or transverse field the resistance is decreased and, in sufficiently large fields, this decrease can be as much as 20 to 30 per cent; and (3) the decrease in resistivity in a magnetic field is proportional to the square of the magnetization. We will henceforth refer to (1) as the "resistance anomaly" and to (2) as the "magnetoresistance anomaly."

The experimental evidence indicates that some type of co-operative magnetic transition occurs. Below the transition temperature the spin degeneracy of each impurity ion is therefore removed and the scattering process that involves spin flips of the conduction electron and the ion becomes inelastic.[11,26] But this inelastic scattering

* It would have been possible to introduce an anomalous increase of resistance with decreasing temperature in the following discussion in the same *ad hoc* manner used previously by one of us.[11] However, since doing so would not change the following discussion we have avoided this complication.

cannot occur at $T = 0$; the scattering process in which an electron loses energy is not allowed because there are no vacant electronic states of lower energy, and the process in which the electron gains energy is impossible because there are no ions in the excited states to impart energy to the electron. Thus the scattering process involving spin flip does not contribute to the resistivity at $T = 0$ and its contribution increases with increasing temperature. This mechanism can therefore account qualitatively for the "resistance anomaly" regardless of the type of magnetic ordering.

The "magnetoresistance anomaly" and its dependence on the macroscopic magnetization of the sample are, on the other hand, sensitive to some features of the magnetic ordering. The experimental result that $\Delta\rho \propto I^2$ imposes certain restrictions on the type of magnetic ordering that can be present. For example, the possibility of a simple ferromagnetic structure with domains large compared to the electron mean free path can probably be ruled out immediately. In this case one would get $\Delta\rho \propto \Delta(M^2)$ where M is the intrinsic magnetization of a single domain. But the quantity $\Delta(M^2)$ would be only indirectly related to the observed magnetization and would not ordinarily be the square of the quantity measured.

We believe that from the experimental result $\Delta\rho \propto I^2$ we can infer the following: *within any volume of dimensions comparable to the electron mean free path, the net magnetization in the virgin alloy is zero.* One reason for this belief is provided by the counter-example of the large domained ferromagnetic model just noted. Secondly, several simple models that do not violate the condition—for example, antiferromagnetic, or very small domained ferromagnetic models—can easily yield the experimental result; we shall develop a phenomenology for one of these models below. It is probably also true that any type of short range magnetic ordering would yield the result $\Delta\rho \propto I^2$, provided the distance over which the spin directions are correlated is small compared to the electron mean free path.

There is another reason for believing the condition given in the preceding paragraph to be true. As previously remarked, the "magnetoresistance anomaly" can be large compared to the "resistance anomaly." The simplest way to account for this is that while ascribing the "resistance anomaly" to the inelastic scattering process, we assume a spin dependent elastic scattering[26] mainly responsible for the "magnetoresistance anomaly." But if the spin dependent elastic scattering is not to contribute also to the "resistance anomaly" then the conduction electrons must "see," within a mean free path, an average elastic scattering cross section in zero applied field that does not change with temperature. This condition is met if in the virgin alloy the net magnetization within a mean free path is zero.

Finally, OWEN *et al.*[18] have shown that a model fulfilling the above requirement can be used to account for the gross features of the susceptibility and spin resonance behavior. The particular model they have chosen is one in which the magnetic impurity ions are divided into two groups with ferromagnetic coupling between ions within a group and antiferromagnetic coupling between ions of different groups. They point out, however, that their result is not very sensitive to fine details of the magnetic structure and that a very fine domained ferromagnetic structure with antiferromagnetic coupling between domains would be equally acceptable.

In order to illustrate how one model that fulfills the requirement above can give rise to the experimental result, we shall develop the phenomenology for a simple case having impurity ions of spin 1/2, with orbital contribution to the moment quenched. Assume a ferromagnetic structure with very small domains, whose size must be small compared to the electron mean free path. This assumption seems justifiable since, for example, in a 1 at. per cent Mn in Cu alloy the average distance between Mn atoms is of the order of 10 Å whereas the mean free path is of the order of 200 Å. For more dilute alloys the ratio of mean free path to average distance of separation becomes even larger.

Assume, moreover, that nearby domains tend to align themselves antiparallel to one another, and that the temperature is sufficiently low so that the "intrinsic magnetization" of a domain is not changed significantly by the application of an external field. Finally, let us assume that when a field is applied the various domains align themselves either parallel or antiparallel to the field.*

* This is, of course, an unrealistic assumption. In the absence of sources of anisotropy, the antiferromagnetically coupled domains would align themselves perpendicular to the direction of the applied field. However, the essential result we wish to obtain—$\Delta\rho \propto I^2$—can be obtained in either case. For illustrative purposes we have therefore chosen the case for which one does not have to introduce the extra complication of writing down the expectation values for spin along more than one axis.

The hypothetical magnetization process then consists simply in the flipping of some antiparallel domains into the parallel orientation upon application of a field.

The spin states of magnetic impurity ions are shown in Fig. 14 where, for convenience, the states are numbered 1, 2, 3, 4. Let D_1 represent the average scattering cross section for elastic scattering of a conduction electron by

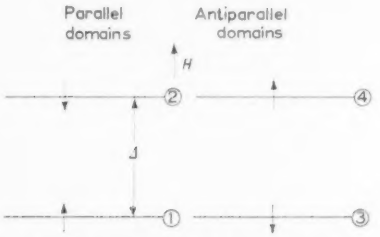

FIG. 14. Magnetic structure of hypothetical alloy. The spin states of magnetic impurity ions of spin 1/2 are shown. There is antiparallel coupling between the small ferromagnetic domains.

an ion of parallel spin and D_2 be the value when conduction electron and ion have opposite spins. Let D be an average scattering cross section for inelastic scattering of conduction electrons by the ions. Moreover, let n be the number of impurity ions per unit volume and $n_1, \ldots, n_4$ be the number per unit volume occupying each of the states shown in Fig. 14. If an external field is applied in the "spin up" direction, as shown in the figure, the relative magnetization, I, of the sample is given by $nI = (n_1+n_4)-(n_2+n_3)$. Also the magnetization M_0 within a domain is given by $M_0 = (n_1-n_2)/(n_1+n_2) = (n_3-n_4)/(n_3+n_4)$. The quantities $n_1, \ldots, n_4$ can then be expressed in terms of n, I, and M_0:

$$\begin{aligned} 4M_0n_1 &= n(M_0+I)(1+M_0) \\ 4M_0n_2 &= n(M_0+I)(1-M_0) \\ 4M_0n_3 &= n(M_0-I)(1+M_0) \\ 4M_0n_4 &= n(M_0-I)(1-M_0). \end{aligned} \tag{1}$$

(a) *Inelastic scattering.* In order to conserve the z-component of spin, inelastic scattering can occur only between electrons and ions of opposite spin. The probability of scattering from any state will be proportional to the occupation of the state, to the probability that there is a vacant electronic state into which the electron can be scattered, and to the probability that the initial electronic state is occupied. Thus, one can write an approximate collision time for the inelastic collisions for electrons of spin up and spin down:

$$\begin{aligned} 1/\tau_i\uparrow &\sim n_2[1-f(\zeta+\Delta)]\tfrac{1}{2}D+n_3[1-f(\zeta-\Delta)]\tfrac{1}{2}D \\ 1/\tau_i\downarrow &\sim n_1[1-f(\zeta-\Delta)]\tfrac{1}{2}D+n_4[1-f(\zeta+\Delta)]\tfrac{1}{2}D \end{aligned} \tag{2}$$

where $f(\varepsilon)$ is the Fermi function and ζ is the Fermi energy. One can easily express quantities like $[1-f(\zeta\pm\Delta)]$ in terms of the n_i's and there results the relation

$$\begin{aligned} 1/\tau_i\uparrow &= 1/\tau_i\downarrow \sim [n_1n_2/(n_1+n_2)+ \\ &\quad +n_3n_4/(n_3+n_4)]\tfrac{1}{2}D. \end{aligned} \tag{3}$$

(b) *Elastic scattering.* The probability of elastic collisions is proportional to the occupation of the appropriate state (for dilute alloys), to the scattering cross section, and to the probability that the initial electronic state is occupied and the final state vacant. Thus, again assuming domains small compared to the mean free path, one has

$$\begin{aligned} 1/\tau_e\uparrow &\sim (n_1+n_4)\tfrac{1}{4}D_1+(n_2+n_3)\tfrac{1}{4}D_2 \\ 1/\tau_e\downarrow &\sim (n_1+n_4)\tfrac{1}{4}D_2+(n_2+n_3)\tfrac{1}{4}D_1. \end{aligned} \tag{4}$$

(c) *Resistivity.* The total collision times for electrons of spin up and spin down are, respectively

$$\begin{aligned} 1/\tau\uparrow &= (1/\tau_i\uparrow)+(1/\tau_e\uparrow) \\ 1/\tau\downarrow &= (1/\tau_i\downarrow)+(1/\tau_e\downarrow). \end{aligned} \tag{5}$$

and

If only a small fraction of the collisions involve spin flip, i.e. are inelastic, then there is little "mixing" between spin up and spin down conduction electrons, and the spin up and spin down currents are essentially in parallel. Experimentally, the "resistance anomaly" which arises from the inelastic scattering processes is only a few per cent of the total resistivity so collisions involving spin flip are indeed only a small fraction of the total number of collisions. Under these circumstances the resistivity is given by

$$\rho \sim 1/(\tau\uparrow+\tau\downarrow). \tag{6}$$

Using equations (1), (3), (4) and (5) in (6) one obtains:

$$\begin{aligned} \rho &= \rho_0\{1+\beta(1-M_0^2)- \\ &\quad -(\gamma^2I^2)/[1+\beta(1-M_0^2)]\} \end{aligned} \tag{7}$$

where ρ_0 is a constant proportional to the concentration of the impurity, $\beta = D/(D_1+D_2)$, and $\gamma = (D_2-D_1)/(D_1+D_2)$. For the virgin sample $I = 0$ so that

$$\rho_v = \rho_0[1+\beta(1-M_0^2)]. \tag{8}$$

If we assume, as is plausible, that $M_0 \to 1$ as $T \to 0$, then ρ_0 is the resistivity at $T = 0°$K. Equation (7) can be re-written

$$\Delta\rho/\rho_v = (\rho-\rho_v)/\rho_v = -(\rho_0/\rho_v)^2\gamma^2I^2. \tag{9}$$

At low temperatures the slopes, S, of the $\Delta\rho/\rho_v$ vs. $-I^2$ curves are near the value 1 and they decrease as the temperature increases. In the context of the phenomenology presented above, this decrease in slope clearly must arise from a decrease in γ^2 with increasing temperature. (The temperature variation of ρ_0^2/ρ_v^2 is relatively

small.) This implies that in the elastic scattering process there remains a temperature dependence that has not been explicitly accounted for.

One can obtain an estimate of β, appearing in equation 8, as follows: clearly $\beta \gtrsim (\rho_{max}/\rho_0)-1$ where ρ_{max} is the resistivity of the sample at the maximum. The value obtained in this way is $\beta \gtrsim 0{\cdot}09 \pm 0{\cdot}02$ for four of our samples. (There is not enough data to estimate ρ_0 for the 0·05 sample). Thus, spin flip scattering processes contribute, in the paramagnetic limit, about 0·1 ρ_0 or 0·3 $\mu\Omega$ cm/at. per cent Mn to the resistivity. OWEN *et al.*[10] have indicated that this value is much larger than the value calculated using a free atom value for the s–d exchange interaction and a model based on the Zener mechanism for coupling the Mn atoms. However, we are informed[27] that a numerical error in the paper of OWEN *et al.*[10] causes their computed value to be incorrect by a factor of about 50. The correct numerical result is in somewhat better agreement with experiment.

6. CONCLUSIONS

The anomalous magnetic behavior at low temperatures of dilute alloys of manganese in copper indicates that some type of magnetic ordering occurs. Resistance and magnetoresistance anomalies also occur at low temperatures. At the lowest temperatures the change in resistance in a magnetic field is proportional to the square of the magnetization. The magnetic structure appears to be such that within any volume of dimensions comparable to the electron mean free path the net magnetization in the virgin alloy is zero. The gross magnetic and electrical behavior of these alloys is not sensitive to other fine details of the magnetic structure. For example, the structure may be a very fine-domained ferromagnetic one with antiferromagnetic coupling between domains or the structure may be simply a short ranged magnetic ordering that could arise from the RUDERMAN–KITTEL[28] type of interaction. Recent theoretical work of E. W. HART[29] and of KEI YOSIDA[30] make the latter alternative seem more likely.

It is probable, however, that details of the magnetic structure are important in determining features of the magnetic behavior such as the remanent and thermoremanent magnetizations and their time and temperature dependence. Thus, many aspects of the magnetic behavior outlined in Section 2 of this paper remain incompletely explored experimentally and unexplained theoretically.

The experimental results and phenomenological interpretation given in this paper indicate a possible relation between the co-operative magnetic effects and the anomalous resistive behavior. Neither the experiments nor the interpretation, however, are definitive in ascertaining whether or not the localized electronic states postulated by KORRINGA and GERRITSEN[15] are present. If such states exist, the phenomenology presented here would be complimentary to the treatment already given by KORRINGA and GERRITSEN. The latter treatment is concerned mostly with the scattering mechanism itself, i.e. with quantities such as D, D_1, and D_2 that appear as parameters in our equations. One consequence of the existence of the KORRINGA and GERRITSEN localized states would be to make D_1 and D_2 (and thus γ^2 in equation 7) temperature dependent. Experimentally, such a temperature dependence is observed but it is not clear that the KORRINGA and GERRITSEN model is unique in this respect. Further theoretical studies of the scattering mechanisms are clearly needed.

Acknowledgements—We have had many valuable discussions with C. P. BEAN and E. W. HART. Discussions with Prof. J. KORRINGA and Prof. C. J. GORTER contributed materially to our understanding. We have also benefited from discussions and interchange of data with many members of the Solid State Group of the University of California at Berkeley. Mr. RICHARD REA, Mr. PHILIP LAWRENCE, and Mrs. ETHEL FONTANELLA have rendered valuable technical assistance with the measurements and calculations.

REFERENCES

1. SHIH J. W. *Phys. Rev.* **38,** 2051 (1931).
2. NÉEL L. *J. Phys. Radium* **3,** 160 (1932).
3. VALENTINER S. and BECKER G. *Z. Phys.* **80,** 735 (1933).
4. GUSTAFSSON G. *Ann. Phys. Lpz.* **25,** 545 (1936).
5. KAUFMANN A., PAN S. and CLARK J. *Rev. Mod. Phys.* **17,** 87 (1945).
6. KRONQVIST E. *Ark. Mat. Astr. Fys.* B **34,** No. 7 (1947); *Ark. Fys.* **5,** 453 (1952).
7. KRONQVIST E. and GIANSOLDATI A. *Ark. Fys.* **7,** 343 (1954).
8. GIANSOLDATI A. *Arkiv. Fysik* **7,** 151 (1954).
9. MYERS H. P. *Canad. J. Phys.* **34,** 527 (1956).
10. OWEN J., BROWNE, M. E., KNIGHT W. D. and KITTEL C. *Phys. Rev.* **102,** 1501 (1956).
11. SCHMITT R. W. *Phys. Rev.* **103,** 83 (1956).
12. GERRITSEN A. N. and LINDE J. O. *Physica* **17,** 573, 584 (1951); **18,** 877 (1952).

13. MacDonald D. K. C. and Pearson W. B. *Acta Met.* **3,** 392, 403 (1955).
14. Gerritsen A. N. *Physica* **19,** 61 (1953).
15. Korringa J. and Gerritsen A. N. *Physica* **19,** 457 (1953).
16. Schmitt R. W. and Jacobs I. S. *Canad. J. Phys.* **34,** 1285 (1956).
17. Arrott A. *Phys. Rev.* **94,** 781 (1954); Arrott A. and Goldman J. E. *Rev. Sci. Instrum.* **28,** 99 (1957).
18. Owen J., Browne M. E., Arp V., and Kip A. F. *J. Phys. Chem. Solids* **2,** 85 (1957).
19. Henry W. G. and Rogers J. L. *Phil. Mag.* **1,** 237 (1956).
20. Friedel J. *Phil. Mag.* **43,** 153 (1952); *Adv. Phys.* **3,** 446 (1954).
21. deKlerk D. and Steenland M. J. *Progress in Low Temperature Physics* (Ed. C. J. Gorter). Vol I, p. 302. North Holland Publishing Company (1955).
22. Fisher J. C. Reported in references 16 and 18.
23. Gorter C. J., van den Berg G. J. and de Nobel J. *Canad. J. Phys.* **34,** 1281 (1956).
24. Néel L. *Adv. Phys.* **4,** 191 (1955).
25. Yntema G. B. *Phys. Rev.* **86,** 598 (1951).
26. Korringa J. *Canad. J. Phys.* **34,** 1290 (1956).
27. Kei Yosida. Private communication.
28. Ruderman M. A. and Kittel C. *Phys. Rev.* **96** 99 (1954).
29. Hart E. W. *Phys. Rev.* **106,** 467 (1957).
30. Kei Yosida *Phys. Rev.* **106,** 893 (1957).

VOL.
3
1957

BOOK REVIEW

J. F. NYE: **Physical Properties of Crystals: Their Representation by Tensors and Matrices,** Clarendon Press, Oxford, 322 pp., $8.00.

THERE is no other text in English with which to compare this book. The nearest text is W. VOIGT's *Lehrbuch der Kristallphysik*, published in 1910. W. G. CADY's book *Piezoelectricity* published in 1946 is, as the title indicates, primarily concerned with piezoelectricity and W. P. MASON's book *Piezoelectric Crystals and their Applications to Ultrasonics*, published in 1950 is more concerned with engineering uses of crystals. CADY's book is rather an encyclopedia of piezoelectricity and related matters. Since crystal physics is now considered to be more important than it was in 1910, and nomenclature has matured since then, a text with the academic viewpoint and modern nomenclature should be well received.

NYE's book is a systematic exposition on anisotropy as it applies to crystals. This reviewer wishes that the thirty-two point groups (into which crystals are classified by symmetry) were discussed early in the book instead of being left to the appendix. This would make the book seem to be more about crystals than about tensors.

The first forty-eight pages develop the ideas of Cartesian tensors, then these tensors are used to relate vector properties to other vector properties, the relations forming tensor properties. Tensor properties are then related to other tensor properties, these relations forming tensors of higher rank. In this way we find related to one another: magnetic field strength, magnetic induction, stress, strain, temperature, entropy, electric field and electric displacement. This entails the study of magnetic susceptibility, electric polarization, pyroelectricity, thermal expansion, piezoelectricity, the converse piezoelectric effect, elasticity, thermoelectricity, conductivity the electro-optic effect, the photo-elastic effect and optical activity.

About midway through the book matrices are introduced as a more compact representation that saves time in actual computation. A few sample calculations are presented. One gets the feeling that matrices are inferior to tensors since they are not necessarily tensors. This reviewer believes that tensors are an algebraic extension of geometry while matrices are pure algebra and not less powerful than tensors.

Is this book physics or applied mathematics? The spirit is mathematical but the usefulness is to physicists. This book could serve as a limited introduction to tensors—limited because Cartesian tensors lack the beautiful generality of general tensors. They lack it just because they are conceived entirely on right angles. However, most physical properties are always best expressed in rectangular co-ordinates and general tensors are much more complicated than Cartesian tensors. Hence crystal physics problems play right into the "hands" of Cartesian tensors. Triclinic assymmetric crystals have no symmetry but such physical properties as elastic effects are not more clarified by general tensors than by Cartesian tensors. However, some crystal geometry problems are simplified by the more general approach.

The problems of anisotropy in crystals are complex—such problems as the rotations of axes and what these rotations do to the numbers that represent, for example, the twenty-one independent elastic constants of a triclinic crystal. This book gives a systematic and useful treatment of these problems.

W. L. BOND

VOL
3
195

PAPERS TO BE PUBLISHED IN FUTURE ISSUES

E. M. LIFSHITS: Quantum theory of the electrical conductivity of metals in a magnetic field.

E. M. LIFSHITS and A. M. KOSEVICH: Theory of the Shubnikov—de Haas effect.

I. DZIALOSHINSKII: A thermodynamic theory of "weak" ferromagnetism of antiferromagnetics.

G. BARSCH: Wahrscheinlishkeitsverteilung und Korrelation von Schubspannungen um Kristall.

H. BROSS and A. SEEGER: Elektronen theoretische Untersuchungen über Fehlstellen in Metallen—V. Allgemeine Theorie des Einflusses von Gitter fehstellen auf die Transportvorgange in Metallen.

P. N. ARGYRES: Quantum theory of longitudinal magnetoresistance.

E. FELDTKELLER: Zum Energieumsatz bei röntgenphotochemischen Prozessen in KBr-Kristallen.

W. P. DOYLE: Absorption spectra of solids and chemical bonding—I. Arsenic, antimony and bismuth trioxides.

H. REISS and C. S. FULLER: The effect of ion pair and ion triplet formation on the solubility of lithium in germanium—effect of gallium and zinc.

S. I. PEKAR: Theory of electromagnetic waves in a crystal with excitons.

P. G. de GENNES and J. FRIEDEL: Anomalies de resistivité dans certains metaux magnetique.

H. J. KRUSEMEYER and D. G. THOMAS: Adsorption and charge transfer on semiconductor surfaces.

B. V. DERIAGIN and I. I. ABRIKOSOVAL: Direct measurements of molecular attraction in solids.

E. DANIEL and J. FRIEDEL: Sur l'annihilation de position dans les metaux.

W. LUDWIG: Über den Einfluss der Anharmonizität auf die Eigenschaften der Kristalle.

H. J. JURETSCHKE and R. STEINITZ: Hall effect and electrical conductivity of transition metal diborides.

R. J. WEISS and K. J. TAUER: Thermodynamics and magnetic structures of the allotropic modifications of manganese.

R. F. BREBRICK: Deviations from stoichiometry in binary ionic crystals.

D. M. WARSCHAUER and W. PAUL: Optical properties of semiconductors under hydrostatic pressure—I Germanium.

J. P. MAITA: Ion pairing in silicon.

A. C. DAMASK: Comparison of electron with neutron irradiation of a brass.

C. S. SMITH and D. R. WINDER: Single-crystal elastic constants of indium.

J. T. LAW: The interaction of oxygen with clean silicon surfaces.

R. F. WALLIS: Theory of cyclotron resonance absorption by conduction electrons in indium antimonide.

R. W. SOSHEA, A. J. DEKKER and J. P. STURTZ: X-ray induced color centers in MgO.

H. B. CALLEN: A ferromagnetic dynamical equation.

A. CHARLESBY and L. CALLAGHAN: Crystal distribution in various polyethylenes.

A. CHARLESBY and L. CALLAGHAN: Crystallinity changes in irradiated polyethylenes.

D. F. C. MORRIS: The lattice energy and heat of formation of lithium monosulphide.

L. A. GIRIFALCO and J. R. STREETMAN: A theoretical calculation of the relaxation of atoms surrounding a vacancy in the body centered cubic lattice.

J. C. PHILLIPS and H. B. ROSENSTOCK: Topological methods of locating critical points.

F. A. KRÖGER and H. J. VINK: Relations between the concentrations of imperfections in solids.

W. L. GORDON, C. N. SHAW and J. G. DAUNT: Radial atomic distribution in liquid helium-4 by X-ray scattering.

A. M. MONES and E. BANKS: Cation substitution in $BaFe_{12}O_{19}$.

D. M. WARCHAUER and W. PAUL: Optical properties of semiconductors under hydrostatic pressure—II silicon.

H. J. HROSTOWSKI and R. H. KAISER: Infra-red spectra of group III acceptors in silicon.

A. S. MILLER and R. J. MAURER: Self-diffusion and electrical conductivity in silver bromide.

H. B. ROSENSTOCK: Infra-red absorption by sodium chloride type lattices.

P. G. de GENNES: Inelastic magnetic scattering of neutrons at high temperatures.

A. M. CLOGSTON: Susceptibility of the three level maser.

H. SUHL: Quantum analog of the ferromagnetic microwave amplifier.

J. B. GOODENOUGH, D. G. WICKHAM and W. J. CROFT: Some magnetic and crystallographic properties of the system $Li_x^{+}N_{1-2x}^{++}Ni_x^{+++}O$.

H. J. HROSTOWSKI and R. H. KAISER: Absorption spectrum of bi-doped silicon.

J. W. NIELSEN and E. F. DEARBORN: Growth of single crystals of magnetic garnets.

B. T. MATTHIAS and S. GELLER: Superconductivity in the Pd–Se system.

D. S. TANNHAUSER: Self-diffusion of bromine in silver bromide.

H. M. BATH and M. CUTLER: Measurement of surface recombination velocity in silicon by steady-state photoconductance.

G. B. BENEDEK and T. KUSHIDA: Pressure dependence of the Knight shift in the alkali metals and copper.

H. A. GERSCH and W. C. KOEHLER: Types of magnetically ordered configurations on simple lattices.

R. J. SLADEK: Magnetically induced impurity banding in *n*-InSb.

J. R. DRABBLE and C. H. L. GOODMAN: Chemical bonding in bismuth telluride.

O. FLINT and J. H. O. VARLEY: On the mechanism of oxide film formation on zirconium.

H. KAWAMURA: The deformation potential of potassium chloride.

F. C. BROWN: Transient photoconductivity in AgCl at room temperature.

VOL.
3
1957